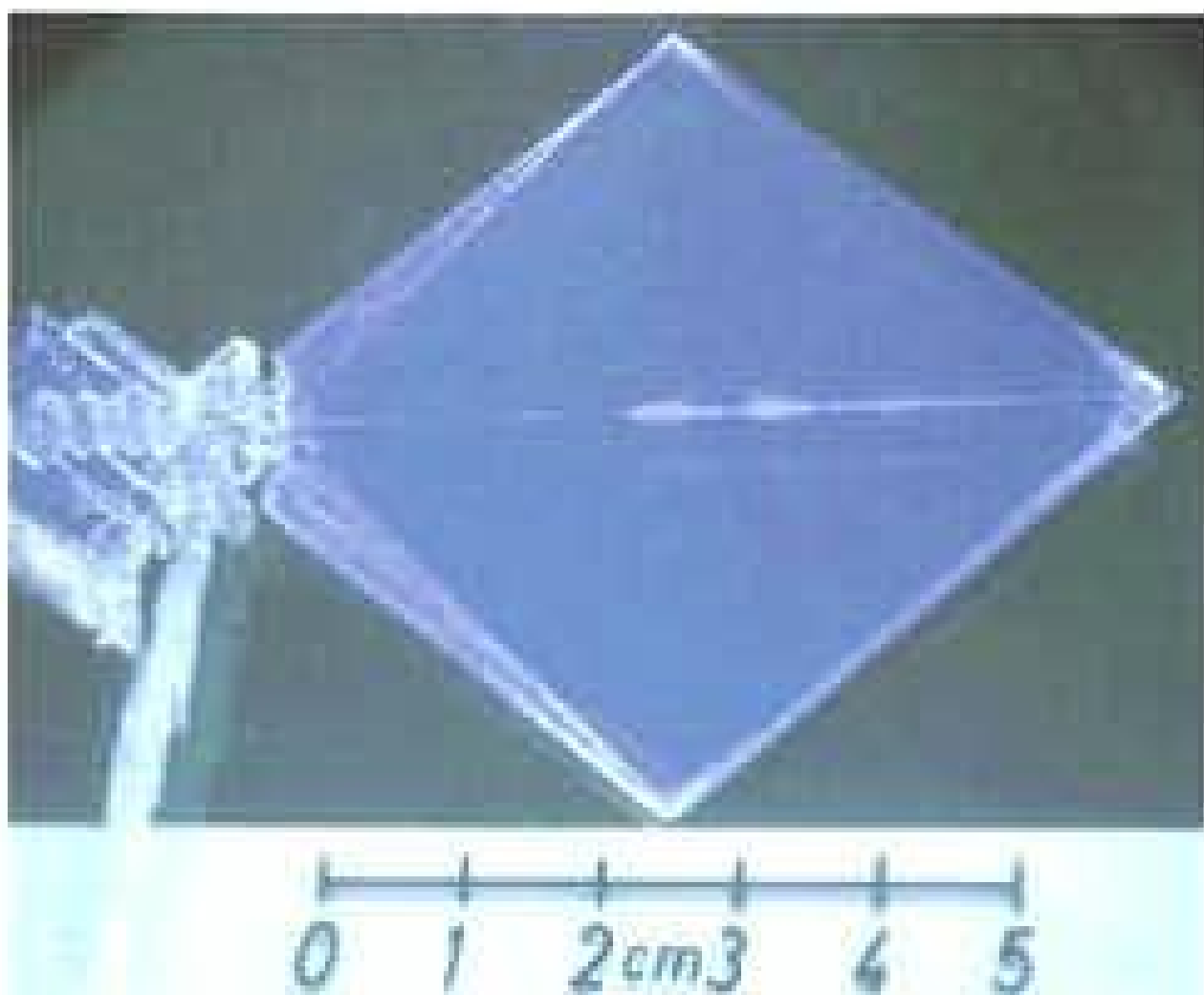


Markus Schwoerer
Hans Christoph Wolf

WILEY-VCH

Organic Molecular Solids



Markus Schwoerer
Hans Christoph Wolf
Organic Molecular Solids

1807–2007 Knowledge for Generations

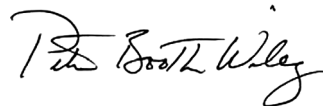
Each generation has its unique needs and aspirations. When Charles Wiley first opened his small printing shop in lower Manhattan in 1807, it was a generation of boundless potential searching for an identity. And we were there, helping to define a new American literary tradition. Over half a century later, in the midst of the Second Industrial Revolution, it was a generation focused on building the future. Once again, we were there, supplying the critical scientific, technical, and engineering knowledge that helped frame the world. Throughout the 20th Century, and into the new millennium, nations began to reach out beyond their own borders and a new international community was born. Wiley was there, expanding its operations around the world to enable a global exchange of ideas, opinions, and know-how.

For 200 years, Wiley has been an integral part of each generation's journey, enabling the flow of information and understanding necessary to meet their needs and fulfill their aspirations. Today, bold new technologies are changing the way we live and learn. Wiley will be there, providing you the must-have knowledge you need to imagine new worlds, new possibilities, and new opportunities.

Generations come and go, but you can always count on Wiley to provide you the knowledge you need, when and where you need it!



William J. Pesce
President and Chief Executive Officer



Peter Booth Wiley
Chairman of the Board

Markus Schwoerer, Hans Christoph Wolf

Organic Molecular Solids



WILEY-VCH Verlag GmbH & Co. KGaA

The Authors

Prof. Dr. Markus Schwoerer

Lehrstuhl für Experimentelle Physik II
Universitätsstr. 30
95447 Bayreuth
Germany

Prof. Dr. Hans Christoph Wolf

Universität Stuttgart
3. Physikalisches Institut
Pfaffenwaldring 57
70569 Stuttgart
Germany

Cover

A large anthracene crystal, prepared by plate sublimation under an inert gas atmosphere, 60 × 60 mm in size and with a thickness of 0.4 mm. Used with permission of Norbert Karl.

Original Title

Organische Molekulare Festkörper –
Einführung in die Physik von π -Systemen
©2005 WILEY-VCH Verlag GmbH & Co.
KGaA, Weinheim.

Translated from the German by Prof. William D. Brewer, Freie Universität Berlin, Germany.

All books published by Wiley-VCH are carefully produced. Nevertheless, authors, editors, and publisher do not warrant the information contained in these books, including this book, to be free of errors. Readers are advised to keep in mind that statements, data, illustrations, procedural details or other items may inadvertently be inaccurate.

Library of Congress Card No.

Applied for.

British Library Cataloguing-in-Publication Data

A catalogue record for this book is available from the British Library.

Bibliographic information published by Die Deutsche Bibliothek

Die Deutsche Bibliothek lists this publication in the Deutsche Nationalbibliografie; detailed bibliographic data is available in the Internet at <<http://dnb.ddb.de>>.

© 2007 WILEY-VCH Verlag GmbH & Co.
KGaA, Weinheim

All rights reserved (including those of translation into other languages).
No part of this book may be reproduced in any form – by photoprinting, microfilm, or any other means – nor transmitted or translated into a machine language without written permission from the publishers. Registered names, trademarks, etc. used in this book, even when not specifically marked as such, are not to be considered unprotected by law.

Typesetting VTEX, Vilnius, Lithuania

Printing Strauss GmbH, Mörlenbach

Binding Litges & Dopf Buchbinderei
GmbH, Heppenheim

Printed in the Federal Republic of Germany
Printed on acid-free paper

ISBN 978-3-527-40540-4

Foreword

The investigation of the physical properties of organic solids, in particular those whose structural elements contain conjugated π -electron systems, has in recent decades become an active and attractive subfield of solid-state physics and this field is now growing rapidly.

There are several reasons for this development. On the one hand, the great variety of phenomena and properties observed in the organic solids greatly exceeds that seen with inorganic materials: an example is energy transport via excitons, i.e. without charge transport, over comparatively long distances. Furthermore, organic chemical methods allow the variation of these interesting properties within wide limits. On the other hand, there are many promising new technological applications of these materials, e.g. in organic colour displays or in a novel molecular electronics which would complement and enlarge upon conventional electronics based on inorganic semiconductor materials. Finally, the organic solids form a link between the physics of inorganic materials and biophysics. The solid-state physics of organic materials has thus already made important contributions to the elucidation of elementary processes in photosynthesis.

In the organic solids, a hierarchy of forces can be observed: there are both strong covalent intramolecular chemical bonds and weak intermolecular van der Waals bonds. Many of the characteristic properties of the organic solids are due to the interplay of these two forces with their differing strengths.

In the usual course of studies, i.e. in the required courses, the student of physics learns nearly nothing about these materials and their properties. In the established textbooks on solid-state physics, there is almost no mention of the organic solids. Only in special-topics lectures and as electives is this topic treated in detail, if these are offered at all.

The present book is intended to fill this gap. It treats in particular the fundamentals of the physics of organic solids and is written for students taking such elective or special-topics courses and those who want to pursue research in the field of organic solids. In addition, it is intended for all physicists, photochemists and perhaps also chemists who want to broaden their knowledge of the solid state. We assume that the reader has a basic knowledge of solid-state physics corresponding to standard introductory courses on the subject. What do we intend to offer

the reader? An initiation into the fundamentals of the subject, links to the more detailed literature and an introduction to topics of current research are our goals.

Organic solid-state physics is a very broad field. In an introductory book such as this, it can be treated only with selected examples; an exhaustive treatment is neither possible nor desirable in an introduction.

We concentrate on π -electron systems. One can learn most of what is interesting in organic solid-state physics from them and they provide an entry to the physics of other materials. We use the term molecular crystals not only in the narrow sense, but also consider thin layers of oriented molecules which are attracting increasing interest.

We authors have been carrying our research in this area for several decades. We wish to thank our numerous students and co-workers with whom we have been able to explore much new territory in this fascinating subfield of solid-state physics. We also wish to thank Ms. Christine Leinberger for processing our texts which underwent numerous revisions, and Mr. Heinz Hereth for preparing a number of drawings. Ms. A. Tschörtner of the Wiley-VCH publishers is due thanks for excellent cooperation in the preparation of this book. It is a great pleasure for us to thank Prof. W. D. Brewer for his excellent translation from the German.

Bayreuth, Stuttgart,
September 2006

*Markus Schwoerer
Hans Christoph Wolf*

Contents

1	Introduction	1
1.1	What are Organic Solids?	1
1.2	What are the Special Characteristics of Organic Solids?	9
1.3	Goals and Future Outlook	15
	Problems for Chapter 1	16
	Literature	24
2	Forces and Structures	25
2.1	Forces	25
2.1.1	Inductive Forces	26
2.1.2	Van der Waals Forces	27
2.1.3	Repulsive Forces	29
2.1.4	Intermolecular Potentials	30
2.1.5	Coulomb Forces	33
2.2	Structures	34
2.2.1	Crystals of Nonpolar Molecules	34
2.2.2	Crystals of Molecules with Polar Substituents	39
2.2.3	Crystals with a Low Packing Density, Clathrates	40
2.2.4	Crystals of Molecules with Charge Transfer, Radical-ion Salts	42
2.3	Polymer Single Crystals: Diacetylenes	43
2.4	Thin Films	47
2.5	Inorganic-Organic Hybrid Crystals	51
	Problems for Chapter 2	52
	Literature	54
3	Purification of Materials, Crystal Growth and Preparation of Thin Films	57
3.1	Purification	57
3.2	Highest Purity	61

3.3	Crystal Growth	63
3.4	Mixed Crystals	70
3.5	Epitaxy, Ultrathin Films	71
	Problems for Chapter 3	72
	References	73
4	Impurities and Defects	75
4.1	Foreign Molecules, Impurities, and X traps	75
4.2	Structural Defects	78
4.2.1	Point Defects	78
4.2.2	Dislocations	79
4.2.3	Grain Boundaries	82
4.2.4	Dipolar Disorder	83
4.3	Characterisation and Analysis of Impurities	84
4.4	Characterisation of Defects	84
	Literature	86
5	Molecular and Lattice Dynamics in Organic Molecular Crystals	89
5.1	Introduction	89
5.2	Intramolecular Vibrations	91
5.3	Phonons	93
5.3.1	The Eigenvector	94
5.3.2	The Wavevector	95
5.3.3	The Frequencies Ω (K)	96
5.3.4	Excitations	97
5.4	Experimental Methods	97
5.4.1	Inelastic Neutron Scattering	97
5.4.2	Raman Scattering and Infrared Absorption	99
5.5	The 12 External Phonons of the Naphthalene Crystal	100
5.5.1	Dispersion relations	100
5.5.2	Pressure and Temperature Dependencies	104
5.6	Analytic Formulation of the Lattice Dynamics in Molecular Crystals	107
5.7	Phonons in other Molecular Crystals	109
5.8	Hindered Rotation and Diffusion	113
5.8.1	Nuclear Magnetic Resonance	113
5.8.2	Benzene Crystals	116
5.8.3	Methyl Groups	118
5.8.4	Diffusion	120
	Problems for Chapter 5	122
	References	123

6	Electronic Excited States, Excitons, Energy Transfer	125
6.1	Introduction	125
6.2	Some historical remarks	126
6.3	Optical Excited States in Crystals	127
6.4	Davydov Splitting and Mini-Excitons	134
6.5	Frenkel Excitons	139
6.5.1	Excitonic States, Fundamental Equations	140
6.5.2	Polarisation and Band Structure	143
6.5.3	Coherence	147
6.6	Charge Transfer (CT) Excitons	149
6.7	Surface Excitons	153
6.8	Excimers	154
6.9	Exciton Processes, Energy Conduction	156
6.9.1	Sensitised Fluorescence	157
6.9.2	Delayed Fluorescence by Triplet Excitons	160
6.9.3	Excitonic Processes	163
6.10	Excitonic Processes in other Systems	171
6.11	Future Developments	173
	Problems for Chapter 6	173
	Literature	174
7	Structure and Dynamics of Triplet States	177
7.1	Introduction and Historical Remarks	177
7.2	Spin Quantisation in Triplet States	181
7.3	The Dipole-Dipole Interaction, Fine Structure	183
7.3.1	Zero Field ($B_0 = 0$)	183
7.3.2	Zeeman Splitting ($B_0 \neq 0$)	189
7.3.3	Powder Spectra	191
7.4	Mini-Excitons	192
7.5	Triplet Excitons	199
7.5.1	Anthracene and Naphthalene Crystals: Two-dimensional Triplet Excitons	199
7.5.2	Dibromonaphthalene Crystals: coherent, one-dimensional Triplet Excitons	203
7.6	Optical Spin Polarisation (OEP)	204
7.7	Optical Nuclear-Spin Polarisation (ONP)	212
7.8	Perspectives	214
	Problems for Chapter 7	214
	Literature	215
8	Organic Semiconductors	217
8.1	Preliminary Historical Remarks	220
8.2	Conductivity and Mobility of nearly-free Charge Carriers	223

8.3	Charge Carriers in Organic Semiconductors: Polarons, Shallow Traps and Deep Traps	228
8.4	Generation of Charge Carriers and Charge Transport: Experimental Methods	234
8.4.1	The TOF Method: Gaussian Transport	234
8.4.2	Photogeneration of Charge Carriers	238
8.4.3	Contacts, Injection, Ejection, and Dark Currents	244
8.4.4	Space-Charge Limited Currents	255
8.5	Charge-Carrier Mobilities in Organic Molecular Crystals	263
8.5.1	Band- or Hopping Conductivity?	263
8.5.2	Temperature Dependence and Anisotropy of the Mobilities	265
8.5.3	Electric-field Dependence	269
8.5.4	Band Structures	272
8.5.5	Charge-Carrier Traps	277
8.6	Charge Transport in Disordered Organic Semiconductors	279
8.6.1	The Bässler Model	282
8.6.2	Mobilities in High-Purity Films: Temperature, Electric-Field, and Time Dependence	284
8.6.3	Binary Systems	289
8.6.4	Discotic Liquid Crystals	290
8.6.5	Stationary Dark Currents	292
	Problems for Chapter 8	303
	Literature	303
9	Organic Crystals of High Conductivity	307
9.1	Donor-Acceptor Systems	307
9.2	Strong CT Complexes, Radical-ion Salts	308
9.3	The Organic Metal TTF-TCNQ – Peierls Transition and Charge-Density Waves	314
9.4	Other Radical-ion Salts and CT Complexes	322
9.5	Radical-Anion Salts of DCNQI	323
9.6	Radical-Cation Salts of the Arenes	330
9.6.1	Direct-current Conductivity	330
9.6.2	X-Ray Scattering	334
9.6.3	Optical Reflection Spectrum	335
9.6.4	Magnetic Susceptibility	337
9.6.5	Spin Resonance of the Conduction Electrons (ESR)	339
9.6.6	Charge-Density-Wave Transport	343
	Problems for Chapter 9	346
	Literature	347
10	Organic Superconductors	351
10.1	Introduction	351

10.2	Mainly One-dimensional Charge-Transfer Salts as Superconductors; Bechgaard Salts	353
10.3	Quasi-Two-dimensional Charge-Transfer Systems as Superconductors	356
10.4	The Nature of the Superconducting State in Organic Salts	359
10.5	Three-dimensional Superconductivity in Fullerene Compounds	361
	Literature	363
11	Electroluminescence and the Photovoltaic Effect	365
11.1	Electroluminescence: Organic Light-Emitting Diodes (OLEDs)	366
11.1.1	Historical Remarks	366
11.1.2	The Principle of the OLED	368
11.1.3	Multilayer OLEDs	373
11.1.4	Electro-optical Properties	377
11.2	Photovoltaic Effect: Organic Photovoltaic Cells	381
11.2.1	Exciton Dissociation	382
11.2.2	Photovoltaic Characteristics	384
11.2.3	CuPc/C ₆₀ Solar Cells	386
	Literature	389
12	Towards a Molecular Electronics	391
12.1	What is Molecular Electronics and What Will it Do?	391
12.2	Molecules as Switches, Photochromic Effects	392
12.3	Molecular Wires	395
12.4	Light-Induced Phase Transitions	396
12.5	Molecular Rectifiers	400
12.6	Molecular Transistors	401
12.7	Molecular Storage Units	406
	Appendix: Coloured Plates	411
	Index	417

1 Introduction

Solid-state physics became an independent discipline only in the middle of the past century. In the intervening years, it has developed into the largest and in some respects most important branch of physics. Previously, in the first half of the 20th century, metals were at the focus of interest. Parallel to their increasing practical applications, theoretical understanding of metallic materials increased rapidly. In the second half of the century, inorganic semiconductors and superconductors took over the forefront of interest in basic research and applications of materials science. Indications are now strong that in the 21st century, a new group of materials will become similarly important and will be at the focus of interest: the organic solids.

In any case, in recent years the investigation of the physical properties of organic solids has attained greatly increased importance and attention. The wide variety of these compounds and the possibility to modify them in a practically unlimited fashion using the methods of synthetic organic chemistry have aroused high expectations for the development of new materials and their applications. Current interest focuses in particular on solids composed of those organic molecules which contain conjugated systems of π electrons. In this book, we give an introduction to the structure and especially to the dynamic, optical, electrical and electro-optical properties of this group of materials and show using selected examples their importance for practical applications.

This introduction can only attempt to summarise the typical properties and the most important concepts needed to understand organic solids. In the interest of brevity, we must often skip over the details of the experimental methods and of theoretical descriptions. The references given in each chapter can be consulted by the reader to provide a deeper understanding of the individual topics. In particular, we wish to draw attention to the few detailed monographs available in this area, which are relevant to all of the chapters in this book: [M1]–[M3].

1.1 What are Organic Solids?

Molecules or their ions (molecular ions or radical ions) from the area of organic chemistry, i.e. expressed simply, compounds with carbon atoms as their essential



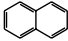
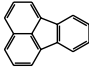
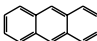
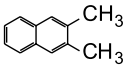
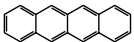
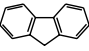
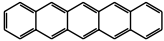

Molecule		Absorption	Molecule		Absorption
Benzene		254 nm	Perylene		434 nm
Naphthalene		311 nm	Fluoranthene		356 nm
Anthracene		375 nm	2,3-Dimethylnaphthalene		315 nm
Tetracene		471 nm	Fluorene		
Pentacene		582 nm			
Pyrene		352 nm			

Fig. 1.1 Molecular structures of some polyacene molecules, indicating the wavelengths of their lowest-energy optical absorption regions in solution at room temperature. All of these molecules have a conjugated π -electron system. The regions of absorption shift towards longer wavelengths

with increasing length of the conjugated electron chains. Many of these molecules are building blocks of still larger molecules, e.g. of dimers, oligomers, or polymers, or else they are components of the side chains in polymers or ligands to central metal ions.

structural elements, form solids as single crystals, polycrystals, or glasses. These are the organic solids. Polymers in the solid state also belong to this group. When we speak in the following sections of organic solids, then we include a broad category of materials under this generic term, but in particular those organic molecular crystals, radical-ion crystals, charge-transfer crystals, thin films or layered structures and polymers which include conjugated π -electron systems in their skeletal structures. These are in turn primarily constructed of carbon atoms but often contain also N, O, S, or Se atoms. To this class belong in particular the aromatic hydrocarbons and alkenes (olefins) (Fig. 1.1), but also N-, O- or S-containing heterocyclic compounds such as pyrrole, furane, thiophene, quinoxaline and others (Fig. 1.2). Also C_{60} and related molecules such as carbon nanotubes should be included here. The nanotubes, however, do not belong among the materials treated in this book. Only in exceptional cases will we treat the aliphatic hydrocarbons, which of course also form organic solids but contain no π electrons, only σ electrons and still more strongly bound (inner) electrons.

Why are molecules with π -electron systems of particular interest to organic solid-state physics? The electron configuration of the free carbon atom in its ground state is $1s^2 2s^2 2p^2$. Carbon has the valence four due to the fact that the electron configurations in chemically-bonded carbon are derived from the configuration $1s^2 2s^2 2p^3$. From molecular physics, we know that a so called double bond between two carbon atoms can form due to an sp^2 hybridisation: three degenerate orbitals are constructed out of one s and two p orbitals. They are coplanar and oriented at 120° relative to one another. Chemical bonds formed by these orbitals are called σ bonds; they are localised between the bonding C atoms. The fourth orbital, p_z , remains

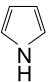
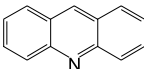
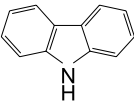
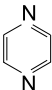
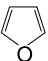
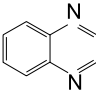
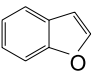
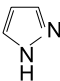

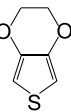
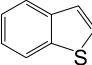
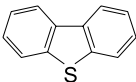
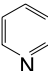
Molecule		Molecule	
Pyrrole		Acridine	
Carbazole		Pyrazine	
Furane		Quinoxaline	
Benzofurane		Pyrazole	
Thiophene		3,4-Ethylene-dioxithiophene	
Benzothiophene		Dibenzothiophene	
Pyridine			

Fig. 1.2 Some typical heterocyclic molecules.

unchanged and is directed perpendicular to the plane of the sp^2 orbitals, and thus to the plane of the C atoms.

The p_z orbitals of neighbouring atoms overlap. This leads to an additional bond, the so called π bond, and to a delocalised density of electrons above and below the plane of the molecule. This is the nodal plane for the π -electron density.

Fig. 1.3 shows the overall electron distribution in an aromatic molecule, anthracene. In addition to the total electron density, Fig. 1.3 also shows two π orbitals, the energetically highest which is occupied in the ground state (HOMO) and the energetically lowest which is unoccupied in the ground state (LUMO).

In comparison with the σ electrons, the contribution of the π electrons to bonding of the molecule is thus weak. Organic molecules and molecular crystals with conjugated π -electron systems therefore possess electronic excitation energies in the range of only a few eV and absorb or luminesce in the visible, the near infrared or the near ultraviolet spectral regions. The electronic excitation energies of this absorption shift towards lower energies with increasing length of the conjugated system; cf. Fig. 1.1. The lowest electronic excitation states are excitations of the π electrons. In the organic radical-ion crystals or the charge-transfer crystals, it are likewise the π -electron systems which are ionised. Most of the characteristic physical properties of the organic solids treated in this book are based on these π -electron systems. Above all they determine the intermolecular interactions, the

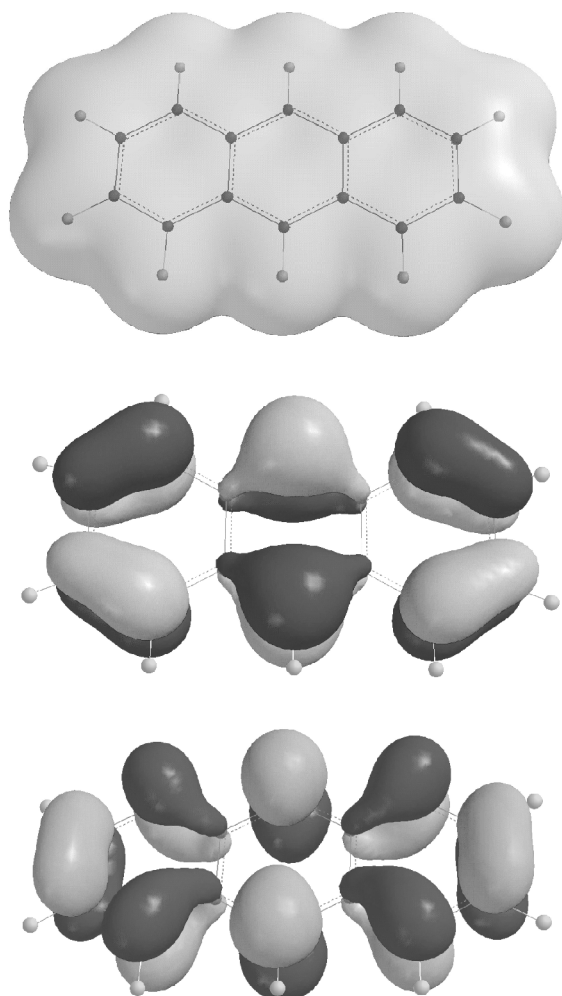


Fig. 1.3 Above: the overall distribution of the π electrons in the electronic ground state of the anthracene molecule, $C_{14}H_{10}$. The boundary was chosen so that ca. 90% of the total electron density was included. Centre: the distribution of a π electron in the highest occupied molecular orbital (HOMO). Below: the distribution of a π electron in the lowest unoccupied molecular orbital (LUMO). The figure was kindly provided by M. Mehring.

van der Waals interactions. They are essentially due to the outer, readily polarisable and readily-excited π electrons.

These intermolecular forces which hold the molecules together in the solid state are in general weak in molecular crystals in comparison to the intramolecular forces. Molecular crystals derive their name from the fact that the molecules as such remain intact within the crystals and thus directly determine the physical

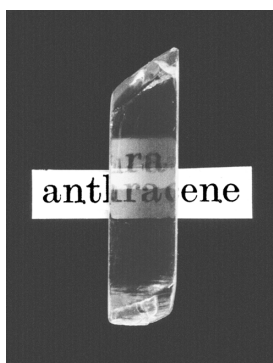


Fig. 1.4 An anthracene single crystal made by the Bridgman crystal-growth method, then cleaved and polished. The length of the crystal is about 2 cm and its thickness 1 cm. Along the direction of sight in this photograph, the c' direction, the strong double refraction is apparent. Image provided by N. Karl [1]. Cf. the coloured plates in the Appendix.

properties of the material. What an organic molecular crystal looks like to the naked eye is illustrated using the example of anthracene in Fig. 1.4.

In solid-state physics, it is a frequent and convenient practice to concentrate basic research on a few model substances. It is then attempted to apply what is learned from these substances to the large number of similar materials, i.e. those belonging to the same class of materials. An overview of the most important classes of materials treated in this book is given in Table 1.1.

Table 1.1 Organic molecular crystals and solids, important classes of materials, and characteristic examples treated in this book.

Class of materials	Examples	Figure
Aliphatic hydrocarbons	<i>n</i> -Octane	2.9
Aromatic hydrocarbons	Naphthalene, Anthracene	1.1, 1.3, 1.4, 2.10, 3.8
Weak donor-acceptor complexes, nonpolar in the ground state	Anthracene-Tetracyanobenzene (TCNB)	1.6
Strong donor-acceptor complexes, polar in the ground state	Tetrathiafulvalene- Tetracyanoquinodimethane (TTF-TCNQ)	2.8, 2.17
Radical-ion salts	$\text{Cu}^+(\text{DCNQI})_2^-$ $(\text{Fa})_2^+\text{PF}_6^-$ $\text{C}_{60}(\text{TDAE})^+$	1.7, 1.8, 2.18
Polymers	Poly(paraphenylene-vinylene) (PPV),	11.5,
Low-molecular-mass layers	CuPc, Alq ₃ , NPB	11.4
Polymer single crystals	Poly(diacetylene) (TS6)	1.10, 1.11

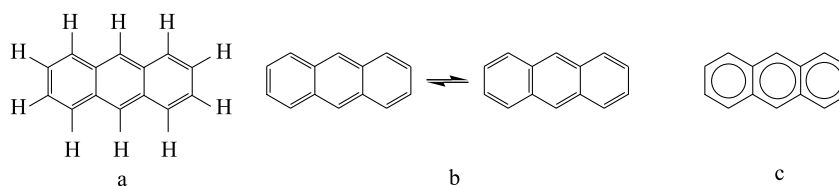


Fig. 1.5 Various typical representations of the structural formula of anthracene ($C_{14}H_{10}$). The C atoms are always left out, the H atoms often. Occasionally, structural formulas are written without indicating the π electrons, i.e. without showing the double valence lines or the circles in cyclic molecules. This, however, does not correspond at all to the usual rules.

The class which has been most intensively investigated in solid-state physics includes the crystals of simple **aromatic hydrocarbons** such as anthracene or naphthalene. Various usual versions of the structural formula of anthracene are given in Fig. 1.5. For the **aliphatic compounds**, we take *n*-octane as model substance. Here, the optically-excitable states lie at considerably higher quantum energies than in the case of the aromatic compounds, since here there are no π electrons. We will not treat them at any length in this book.

A further important class of materials are the **donor-acceptor complex crystals**. They consist of two partner compounds in a stoichiometric ratio, of which one transfers charge to the other. When the charge transfer occurs only in an electron-

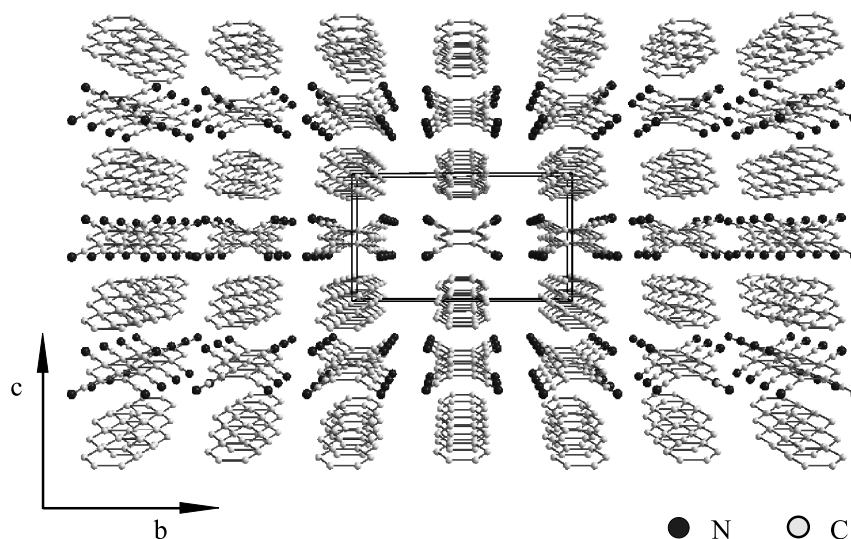


Fig. 1.6 The crystal structure of the weak donor-acceptor crystal anthracene-tetracyanobenzene (TCNB). One can clearly see how the two components alternate in parallel planes. The CN groups are indicated by a darker shade. The crystal structure is monoclinic, with $a = 9.528 \text{ \AA}$, $b = 12.779 \text{ \AA}$, $c = 7.441 \text{ \AA}$, $\beta = 92.39^\circ$.

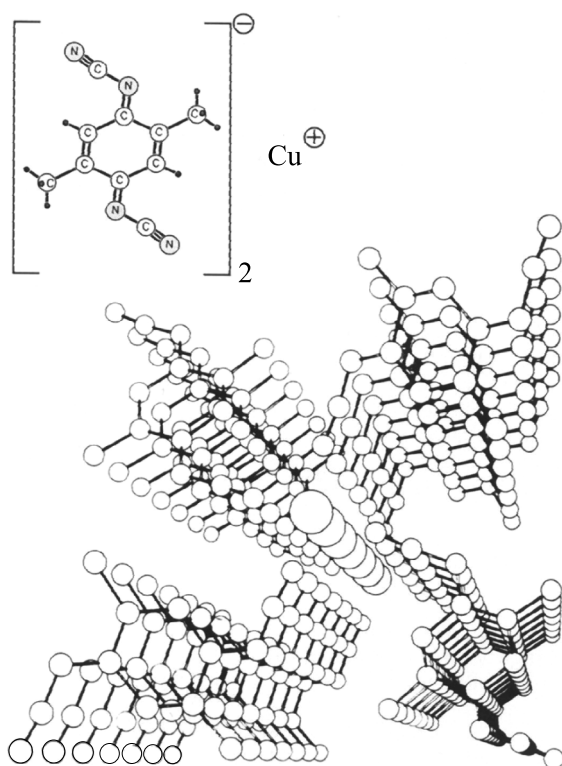


Fig. 1.7 Below: the crystal structure of the radical-anion crystal 2,5-dimethyl-dicyanoquinone-diimine, $\text{Cu}^+(\text{DCNQI})_2^-$. In the middle, one can discern a chain of Cu ions which are however not responsible for the metallic conductivity of the compound, as well as four stacks of the organic partner. The electrical conductivity takes place along these stacks. The stacks are connected via the CN groups and the central Cu ions to one another, so that their one-dimensionality is

reduced. In the molecular structure scheme (above), the H atoms are indicated as dots. The crystal structure is tetragonal, with $a = 21.613 \text{ \AA}$ and $c = 3.883 \text{ \AA}$. The DCNQI molecules are inclined with respect to the axis of the stacks, i.e. the c -direction, by $\phi = 33.8^\circ$. The perpendicular spacing of the planes between them is $\alpha = 3.18 \text{ \AA}$. This radical-anion salt is grown by electrocrystallisation from an acetonitrile solution containing the DCNQI and CuI ions. After [2].

ically excited state, they are termed weak D-A crystals. A good example of these is anthracene-tetracyanobenzene (TCNB) (Fig. 1.6). The crystal is constructed as a sandwich of planes which alternately contain the donor and the acceptor molecules. In the strong D-A or **charge-transfer complexes**, for example the compound $\text{TTF}:\text{TCNQ}$ or the **radical-ion salts**, the charge transfer takes place in the electronic ground state. Examples of these are shown in Fig. 1.7, the crystal structure of the radical-anion salt $\text{Cu}^+(\text{DCNQI})_2^-$ and in Fig. 1.8, a photograph of crystals of the radical-cation salt $(\text{Fa})_2^+\text{PF}_6^-$. These crystals are not transparent like the molecular crystals, but rather they look metallic, since they reflect visible light strongly over a broad bandwidth. An example of organic molecules in the form of an **epitaxial thin**

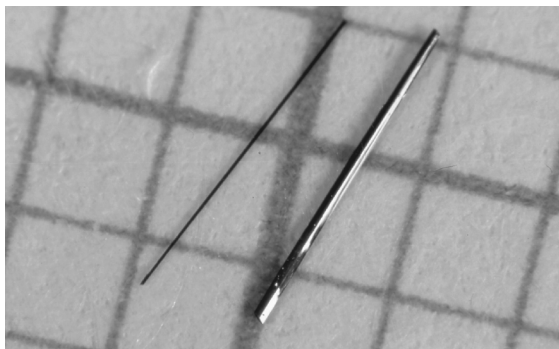


Fig. 1.8 Two crystals of the radical-cation salt (di-fluoranthene) hexafluorophosphate, $(\text{Fa})_2^+\text{PF}_6^-$. The right surface of the right-hand crystal is orientated in such a way that it reflects the light coming from the light source on the right. The reflectivity is metallic due to the high conductivity of the crystal along its long axis (a axis, see Fig. 2.18). The grid corresponds to 1 mm^2 . Cf. the coloured plates in the Appendix.

film is shown in Fig. 1.9. Finally, Fig. 1.10 shows the crystal structure and Fig. 1.11 a photograph of some crystals of a representative of the macroscopic **polymer single crystals** of poly-diacetylene. These two material classes, the non-crystalline polymers and low-molecular-mass evaporated films, are the most important classes which we shall describe as organic solids in the following chapters.

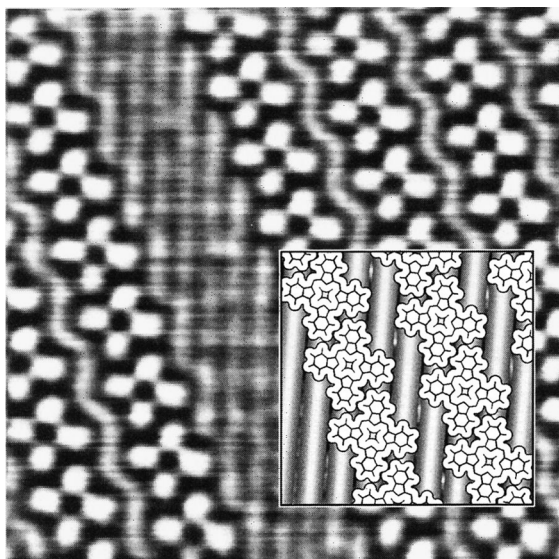


Fig. 1.9 Cu-phthalocyanine molecules on the surface of a MoSe_2 crystal; image made with a scanning tunnel microscope. The area shown has the dimensions $10 \text{ nm} \times 10 \text{ nm}$. The inset shows the molecular structure to the same scale. From [3].

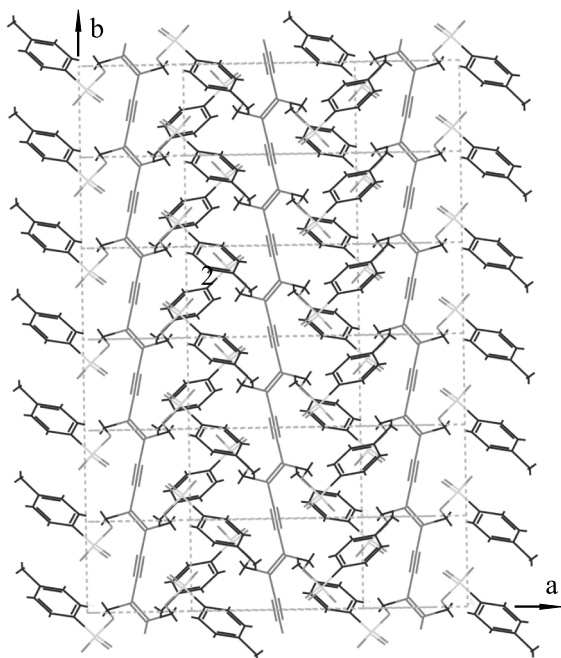


Fig. 1.10 The crystal structure of macroscopic poly-diacetylene paratoluylsulfonyloximethylene (p-TS6) single crystals. The picture shows the projection on the crystallographic (ab)-plane of the monoclinic crystal ($a = 14.993 \text{ \AA}$, $b = 4.910 \text{ \AA}$, $c = 14.936 \text{ \AA}$, $\beta = 118.14^\circ$ at $T = 295 \text{ K}$). The covalently bonded carbon chains with periodic

double-single-double bonds are oriented parallel to the twofold b axis. They carry a conjugated π -electron system. The side groups are covalently bonded to the chain. The chains are bonded to each other by van der Waals bonds. The unit cell contains two differently-oriented monomer units. After [4].

1.2

What are the Special Characteristics of Organic Solids?

In solids, one can distinguish four essential types of bonds: ionic bonds, metallic bonds, covalent bonds, and van der Waals bonds. In addition, in rare cases, hydrogen bonding is observed; it is indeed especially important in bio-macromolecules.

Ionic bonding results directly from the long-range Coulomb attraction between oppositely-charged ions. A typical representative of this type of bonding is sodium chloride. Ionically-bonded solids have as a rule a relatively high melting point, are brittle and, at least at lower temperatures, they are poor electronic conductors (insulators). **Metallic bonding** is likewise based mainly on the Coulomb interaction. In this case, a portion of the negative charges, the conduction electrons, are delocalised and more or less freely mobile. Their electrical conductivity, like their reflectivity, is high; the melting point is also relatively high. **Covalent bonding** results from the sharing of electrons between neighbouring atoms in the solid – the bonding electrons. This bonding type includes the inorganic semiconductors such

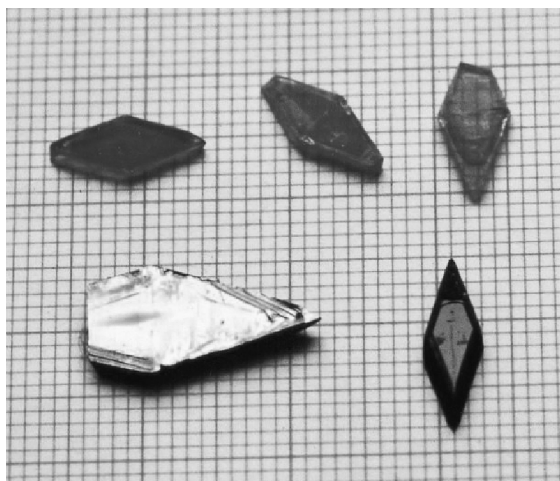


Fig. 1.11 Below: Two single crystals of the polydiacetylene paratoluyyl-sulfonyloximethylene-diacetylene (TS6). Above: three monomer crystals, illuminated with linearly polarised light. The polarisation direction of the light is horizontal, and the b axis of the polymer chains is oriented parallel to the long axis of the crystals. The polymer crystals strongly reflect light (below left) when the light

is polarised parallel, and almost not at all (below right) when the light is polarised perpendicular to the axis of the polymer chains. The monomer crystals contain only a small fraction of polymerised chains and are thus opaque (above left) when the light is oriented parallel, but transparent (above right) when the light is perpendicular to the b axis. Cf. the coloured plates in the Appendix.

as Si or Ge. These solids are semiconductors and as pure materials typically have a low electronic conductivity and a high melting point. They are hard and brittle. Polymer chains are also held together by the strong covalent bonds between the atoms within the chain. **Van der Waals** bonding is, finally, mainly responsible for the cohesion within molecular solids and is therefore particularly important for the topics in this book. It is based on weak electrical dipole forces between neutral molecules with fully-occupied molecular orbitals, i.e. molecular orbitals which can form neither ionic bonds, nor covalent bonds, nor metallic bonds. Molecular solids which consist of only one type of molecules, e.g. anthracene molecules, exhibit pure van der Waals bonding. They usually have a low electronic conductivity, are relatively soft and have a comparatively low melting point.

Van der Waals bonding is particularly weak in comparison to covalent bonding and has a very short range. Therefore, the properties of the individual molecules in all **nonpolar organic solids** remain intact to a much greater extent than those of the bonding units in the other materials classes. In the simplest approximation, a molecular crystal can be understood in terms of an **oriented gas**. This means that the solid structure simply holds the molecules in fixed positions without changing their (molecular) physical properties. Thus, for example, the molecular dimensions and the characteristic intramolecular vibrational frequencies are only slightly changed relative to those of the free molecules, since the intramolecular forces are dominant. Other properties such as energy and charge transport only become pos-

Table 1.2 Occupation probabilities for the phonons with the highest frequency ν in a typical molecular crystal as compared to Si.

T/K	$\exp(-h\nu/kT)$	
	$\nu = 3.5 \text{ THz}$ (Naphthalene)	$\nu = 14 \text{ THz}$ (Si)
300	0.57	0.11
100	0.19	1.2×10^{-3}
30	3.7×10^{-3}	1.8×10^{-10}
4.2	2.8×10^{-18}	

sible through the intermolecular forces and are therefore essentially determined by them.

A notable measure of the intermolecular forces is the maximum frequency ν of the lattice vibrations (optical phonons). In a typical organic molecular crystal, it is of the order of 3.5 THz; in Si, in contrast, it is 14 THz. Thus the difference in the Boltzmann factors $\exp(-h\nu/kT)$ for the thermal occupation of phonon states, which plays a decisive role in many solid-state properties, is already great when comparing organic and inorganic solids at room temperature, and it becomes very much greater at low temperatures (Table 1.2).

In Table 1.3, a number of the physical properties of the crystalline solids anthracene and germanium are compared with each other. Especially important are the lower binding energy, the lower melting point, and the higher compressibility of anthracene in comparison to the covalently-bonded inorganic semiconductor. The weak intermolecular interactions furthermore lead to a greater freedom of variation in the crystal structures and in structurally-determined properties as functions of the state variables such as pressure and especially temperature, and of external electromagnetic fields and waves, in particular UV, visible and IR radiation.

Polar organic solids, e.g. the radical-ion salts mentioned in Sect. 1.1, are bonded not only through van der Waals interactions but also through ionic bonds. Since molecules are larger than atoms, the distances between positive and negative charges are larger in the former and therefore, the ionic bonding energy of molecular ionic crystals is as a rule smaller than that of inorganic salts. However, it often determines the crystal structure. Electrically-conducting molecular crystals, e.g. $\text{Cu}(\text{DCNQI})_2$ or $(\text{Fa})_2\text{PF}_6$, additionally exhibit a metallic-bonding contribution to their crystal bonding.

Precisely those solid-state properties which are due to the relatively weak mutual bonding of the molecules in the crystal are what make the organic solids so interesting. This is the topic of the present book.

There are a whole series of properties and problems which distinguish the organic molecular crystals in characteristic ways from other solids and make them

Table 1.3 Comparison of the physical properties of anthracene and germanium crystals. From Pope and Swenberg, as well as from S. M. Sze, *Physics of Semiconductor Devices*, John Wiley and Sons, New York (1981).

Property	Germanium	Anthracene
Atomic weight	72.63	178.22
Melting point / °C	937	217
Density / (g cm ⁻³)	5.3	1.28
Density / molecules per cm ³	4.42×10^{22}	0.42×10^{22}
Crystal structure	Diamond structure	monoclinic
Lattice constant* / Å	5.66	6.04–11.16
Volume compressibility / (cm ² / dyn)	1.3×10^{-12}	9×10^{-12}
Dielectric constant** (static)	16	3.2
Electronic band gap E _g (at T = 300 K)/eV	0.66	4.0
Vacuum ionisation energy I _e /eV	4.8	5.8
Electron mobility* } (at T = 300 K)/ Hole mobility* } (cm ² /Vs)	3800 1800	} ≈ 1
Thermal expansion coefficient* / K ⁻¹	6.1×10^{-6}	140×10^{-6}
Specific heat (at T = 300 K)/(J/g K)	0.31	1.30
Longitudinal sound velocity*,**/(cm/s)	9.4×10^5	3.4×10^5

* These values are anisotropic in molecular crystals. The values given hold for a particular direction (see the corresponding chapters).

** For each case in the [100] direction.

attractive objects for study in solid-state physics. We shall list a few of these here. More information is to be found in later chapters.

First of all, we consider the **surfaces**: Due to the short range of the interaction forces, one can more readily produce surfaces and interfaces of high quality, with low defect and impurity concentrations, than in other types of crystals.

Then the **transport of electric charge**: among the organic solids there are insulators, semiconductors, metallic conductors and superconductors. To the solid-state physicist, it is a great challenge to understand how this enormous range of conductivity behaviours can be explained from the molecular and the crystal structures. Fig. 1.12 shows as an illustration the electrical conductivity of some radical-anion salts of DCNQI. The measured values are spread over more than 8 orders of magnitude, even though the variations in the molecules are small. Furthermore, the electrical conductivity of organic crystals is in general very anisotropic: many radical-ion salts are highly one-dimensional with respect to their conductivities. Closely connected to this is the Peierls instability. In this phase transition, the metallic conducting crystal becomes a semiconductor on cooling below the phase transition temperature T_p . Fig. 1.13 shows the specific electrical conductivity of the radical-cation salt (Fa)₂PF₆, which varies by more than 14 orders of magnitude within a relatively small temperature interval.

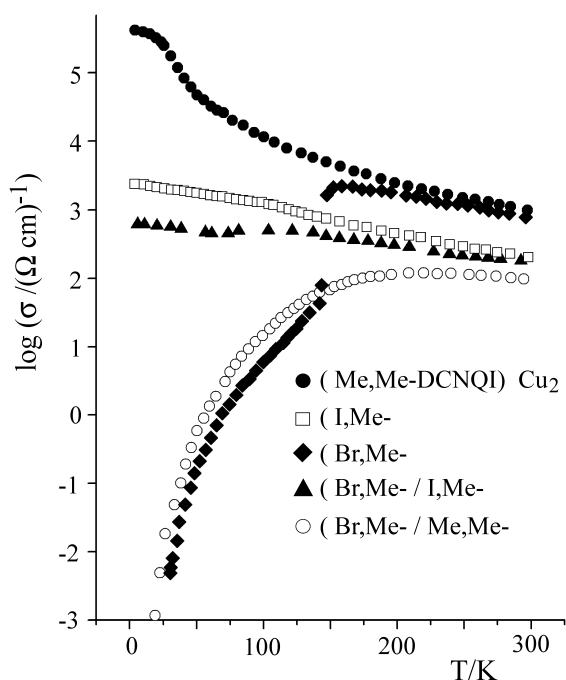


Fig. 1.12 The temperature dependence of the specific electric conductivity σ of some Cu^+ $(\text{DCNQI})_2^-$ radical-anion salts with different substituents of the two Me groups on the DCNQI molecules (cf. Fig. 1.7). Me refers to a methyl group, I and Br to an iodine or bromine atom; compare the image of the crystal

structure in Fig. 1.7. The crystal structure is very similar in all cases. The conductivity ranges from the organic metals down to the lowest temperatures (upper curve) to semimetallic semiconductors (the two lowest curves; one of them refers to an alloy). For details see Sect. 9.5.

In addition, these materials are particularly interesting owing to their enormous **variability**. Specifically, this means that their physical properties can be modified in often very small steps by comparatively minor chemical changes. The organic chemist can furthermore prepare molecules with a wide variety of properties in almost unlimited variations. Can this offering of the chemist be exploited in physics also, can crystals with the desired properties be so to speak synthetically “tailor-made”? Can one thus tell the chemists which molecule they should synthesize in order to produce a new semiconductor, or how a molecule is to be constructed in order to obtain a new superconductor with a high transition temperature? These are two of the problems which are currently key issues in the solid-state physics of organic molecular crystals. Such problems are often considered with a background of possible technical applications in mind.

An especially important and typical property of molecular crystals is the existence of **excitonic states**, in some cases with long lifetimes. These are neutral electronic excitation states with an excitation energy which is smaller than the energy required to excite an electron from the valence band into the conduction band, i.e. for the excitation of a dissociated electron-hole pair. One can also speak of an

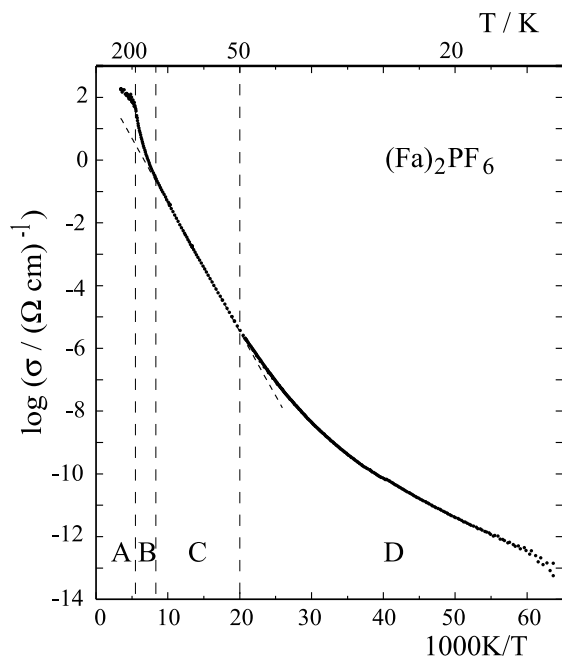


Fig. 1.13 The temperature dependence of the specific electrical conductivity σ of the radical-cation salt $(\text{Fa})_2^+\text{PF}_6^-$ (cf. Fig. 1.8). Fa refers to fluoranthene (Fig. 1.1). At $T_p = 182$ K, the crystal undergoes a structural phase transition (Peierls transition). At $T > T_p$ it behaves almost like a metal; at $T < T_p$ it is a semiconductor. In the region between 300 K and 20 K its electrical conductivity varies by 14 orders of magnitude. The temperature ranges A, B, C and D denote four different mechanisms of electrical conductivity. In the

range A ($T > T_p$), the conductivity is one-dimensional and metallic with strong fluctuations between metal and semiconductor. In the range B ($T < T_p$), the crystal is a semiconductor with a temperature-dependent activation energy. In the range C, the activation energy is constant. In the range D, the conductivity of the semiconductor is limited by thermal activation of charge carriers from defect states. See Sect. 9.6 for more details.

excitation below the conduction band. As a rule, the excitation energy of excitons in molecular crystals is so much smaller than the energy required to produce a non-bound electron-hole pair, that is a free electron in the conduction band and a free hole in the valence band, that thermal ionisation of the excitons cannot take place even at room temperature. When the quantum energy of the photons is not too great, the photo-excitation in molecular crystals thus does not produce free charge carriers, but rather bound electron-hole pairs, in which the distance between the electron and the hole is small in comparison to that of the so called Wannier excitons, excitations below the conduction band in the inorganic semiconductors. In the first approximation, the excitons in molecular crystals are molecular excitation states which are mobile within the crystal. They are termed Frenkel excitons and can be used to store and transport electronic excitation energy, i.e. for energy transport. Molecular crystals can in this case be used as model substances for the

investigation of energy conduction processes in polymers and in particular also in biological systems. Photosynthesis, the mechanism of sight, and questions of molecular genetics are among these.

The organic solids are also interesting as highly nonlinear optical materials and as highly and nonlinearly polarisable **dielectrics**, as **electrets**, as **ferroelectric materials** and as **photoelectrets**. In electrets, a macroscopic polarisation is present due to a macroscopic orientation of permanent dipole moments of the structural elements: the solid has a positive and a negative end. In photoelectrets, this state is induced by light excitation, and in ferroelectric materials by an external static electric field. These properties of organic materials are made use of in copying machines. In radiation physics, organic crystals such as anthracene are employed due to their high fluorescence quantum yields and their short relaxation times as **scintillator crystals**.

Finally, solid-state physicists make use of molecular crystals when they wish to understand certain aspects of solid-state physics better theoretically and experimentally. Weak intermolecular bonding forces, electrical conductivity with a very narrow bandwidth, large anisotropies in their electrical, optical and magnetic properties, one-dimensional conductivity, linear excitons, and linear magnetic ordering states are best studied in these material classes.

1.3 Goals and Future Outlook

In textbooks on solid-state physics, the organic materials, in particular molecular crystals, are traditionally left out entirely or are treated only in a cursory manner. One learns in detail how atoms or ions can form a crystal and which properties lead to insulators, semiconductors, or metals; but an understanding of the physical properties of solids which are composed of molecules is a neglected chapter in solid-state physics. This book has the goal of awakening or stimulating understanding of this interesting subfield of solid-state physics and in the process to show what these materials can contribute to our knowledge of other classes of materials. Therefore, most attention will be given to:

- the peculiarities of lattice dynamics, which are characterised by the fact that molecules, in contrast to atoms, may be excited not only to translational oscillations but also to rotational oscillations (librations);
- the Frenkel excitons with all the consequences which follow from the energy transport within the crystals which they make possible;
- the strong anisotropies with the possibilities they provide for low-dimensional transport processes;
- the notable delocalisation of electrons within the structural units of organic solids, but not between them, from which e.g. very narrow conduction bands result;

- as well as the great possibilities of variation of phases of the crystal structure and correspondingly of structurally-determined properties on varying the temperature and pressure.

Such specific properties are the reason why the organic molecular crystals and solids assume a special status within the wide field of the chemistry and physics of solid materials. We will thus make an effort to show which new concepts in solid-state physics are necessary or helpful for the understanding of these materials.

Technical applications of organic solids are as yet relatively few. The most important are based on their behaviour as dielectric materials or electrets in electrophotography. Furthermore, electrically-conducting polymers (e.g. poly (3,4-ethylenedioxythiophene) or PEDOT), mixed with polystyrolsulfonate (PSS) and called BAYTRON find application as antistatic or electrically-conducting coatings for photographic and X-ray films and for coating printed-circuit boards. It is becoming apparent that the semiconducting properties of organic solids will soon widen the spectrum of their applications. The **electroluminescence** of polymers and of low-molecular-mass vapour-deposited organic coatings is already being used in technology. In recent years, **transistors** and **integrated circuits** have been fabricated exclusively of organic materials. The “buzzword” **molecular electronics** covers all the efforts to employ molecules as the active components in logic and data-storage elements. The organic compounds can look to an important future role in electronics and optoelectronics as **new materials**. We will take up these topics also in the following chapters, with the intention of contributing to progress in research and applications through an improved understanding of the physical fundamentals.

Problems

Note: the problems for Chap. 1 involve the fundamentals of chemical bonding, electron transfer, electron and energy exchange and the Hückel model of the linear combination of the $2p_z$ atomic orbitals of the C atoms to yield the π orbitals of aromatic molecules (LCAO-MO). Knowledge of these fundamentals of molecular physics is a precondition for using this book. Solutions to the following problems 1–4 can be found in the corresponding chapters of textbooks on molecular physics.

Problem 1.1. Chemical Bonding 1; the hydrogen molecular ion, H_2^+ , electron and charge transfer:

The model system H_2^+ is the simplest for chemical bonding and for electron transfer. H_2^+ consists of two protons a and b at a distance R , with one electron. (See e.g. HERMANN HAKEN and HANS CHRISTOPH WOLF, *Molecular Physics and Elements of Quantum Chemistry*, 2nd ed., Springer-Verlag (2004), Sect. 4.3, page 58 ff.)

- a. Calculate the mean electronic energy and the energy splitting ΔE of the two eigenstates (bonding and antibonding states) in units of the Coulomb

integral C , the exchange or transfer integral D and the overlap integral S for the case $S \ll 1$.

- b. Look in the literature for the calculation of the three integrals C , D and S as a function of the reduced nuclear distance $R' = R/a_0$, where a_0 is the Bohr radius. (See e.g. MAX WAGNER, *Elemente der theoretischen Physik 1*, Rowohlt Taschenbuch Verlag (1975) or P. GOMBÁS, *Theorie und Lösungsmethoden des Mehrteilchenproblems der Wellenmechanik*, Verlag Birkhäuser, Basel (1950).)
- c. Calculate the equilibrium distance R_0 of the two protons.
- d. Show that for $S \ll 1$, the transfer integral D is proportional to the reciprocal of the transfer time t_{trans} of the electron from nucleus a to nucleus b. *Note:* Compute the time-dependent linear combination (sum) of the time-dependent wavefunctions Ψ_+ and Ψ_- .

Problem 1.2. Chemical Bonding 2; the hydrogen molecule, electron exchange and energy transfer:

The Heitler-London model for H_2 is the simplest model both for chemical bonding of two neutral species, here the bonding to two H atoms, as well as for electron exchange and energy transfer. (See e.g.: HERMANN HAKEN and HANS CHRISTOPH WOLF, *Molecular Physics and Elements of Quantum Chemistry*, 2nd ed., Springer-Verlag (2004), Sect. 4.4.) The two energetically lowest stationary states Ψ_u and Ψ_g of the H_2 molecule and their energies E_u and E_g are given by

$$E_u = 2E_0 + \frac{e^2}{4\pi\epsilon_0 R} + \frac{C-A}{1-S^2}, \quad \Psi_u = \frac{1}{\sqrt{2}}(\Psi_1 - \Psi_2) \quad (\text{P1.1})$$

and

$$E_g = 2E_0 + \frac{e^2}{4\pi\epsilon_0 R} + \frac{C+A}{1+S^2}, \quad \Psi_g = \frac{1}{\sqrt{2}}(\Psi_1 + \Psi_2) \quad (\text{P1.2})$$

where

$$\Psi_1(r_1, r_2) = \psi_a(r_{a1})\psi_b(r_{b2}) \quad (\text{P1.3})$$

and

$$\Psi_2(r_1, r_2) = \psi_a(r_{a2})\psi_b(r_{b1}). \quad (\text{P1.4})$$

These are the two mutually-degenerate stationary ground states of the non-interacting H atoms a and b; Ψ_1 describes the state in which electron 1 is around proton a and electron 2 is around proton b. In Ψ_2 , the electrons are exchanged. When the two H atoms interact at a proton spacing R , the degeneracy is lifted (see Eqns. (P1.1) and (P1.2)). The symbols used there are the overlap integral,

$$S^2 = \int \Psi_1 \Psi_2 d\tau_1 d\tau_2 \quad (\text{P1.5})$$

the Coulomb integral or the average Coulomb interaction of the two atoms,

$$C = \int \frac{1}{4\pi\epsilon_0} \left\{ -\frac{e^2}{r_{a2}} - \frac{e^2}{r_{b1}} + \frac{e^2}{r_{12}} \right\} \psi_a^2(r_{a1}) \psi_b^2(r_{b2}) d\tau_1 d\tau_2 \quad (\text{P1.6})$$

and the exchange integral,

$$A = \int \frac{1}{4\pi\epsilon_0} \left\{ -\frac{e^2}{r_{a2}} - \frac{e^2}{r_{b1}} + \frac{e^2}{r_{12}} \right\} \psi_a(r_{a1}) \psi_b(r_{b2}) \psi_a(r_{a2}) \psi_b(r_{b1}) d\tau_1 d\tau_2. \quad (\text{P1.7})$$

Show that the superposition of the two stationary states Ψ_u and Ψ_g to give a state $\Psi = \frac{1}{\sqrt{2}}(\Psi_u + \Psi_g)$ is no longer a stationary state, but describes the exchange of the two electrons. Determine the exchange frequency in units of A . For simplicity, set $S = 1$.

Problem 1.3. Hückel LCAO-MO theory 1: the allyl radical (See e.g.: LIONEL SALEM, *The Molecular Orbital Theory of Conjugated Systems*, W. A. Benjamin, Inc. (1974), Chap. 1, or PETER W. ATKINS, *Physical Chemistry*, Wiley-VCH (1988).)

In chemical bonding of the C atoms of a planar unsaturated hydrocarbon molecule, e.g. in benzene (Fig. P1.1), one can distinguish between σ bonds and π bonds or π electrons. The σ bonds are formed from the sp^2 hybrid orbitals of two neighbouring C atoms or from the sp^2 hybrid orbital of one C atom and the $1s$ orbital of an H atom. The sp^2 hybrid orbitals are orthogonal linear combinations of a $2s$ and the two $2p_z$ orbitals in the molecular plane. They make angles of 120° in the plane (Fig. P1.1b). The σ bonds are strongly localised and form the skeleton of the aromatic molecule. The energy levels of the sp^2 electrons bound in the σ bonds are therefore greatly reduced in comparison to the energy of the four valence electrons of the free C atom. Owing to their strong bonding, they can be excited only by high energies and are not considered further in the Hückel theory which follows.

The π bonds are formed by overlap of the $2p_z$ orbitals. Each carbon atom in the aromatic part of the molecule has one $2p_z$ electron (Fig. P1.1c). Their orbitals are orthogonal to the sp^2 orbitals. The spatial extent of the $2p_z$ orbitals is small in all directions within the molecular plane; the π bonds are therefore weak in comparison to the σ bonds. Owing to the equal C–C distances between all the C atoms in benzene (and nearly equal C–C distances in all other aromatic molecules) due to the σ bonds, and owing to the rotational symmetry of

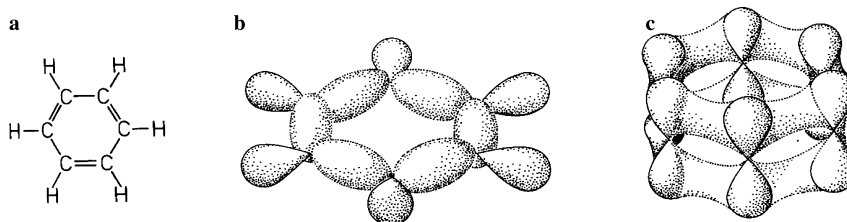


Fig. P1.1 Benzene molecule: a: skeleton, b: σ electrons, c: π electrons.

the $2p_z$ orbitals around the z axis, which is perpendicular to the molecular plane, all the $2p_z$ electrons together form the delocalised π -electron system (Fig. P1.1c). The π electrons are the most weakly bound of all the electrons in the molecule; they therefore have the lowest electronic excitation energies of the electronic system. These lie in the optical and near-ultraviolet spectral ranges. When aromatic molecules are ionised, it is from the π -electron system that electrons are ejected.

The goal of the Hückel theory is the determination of the energies E_j and the orbitals Ψ_j of the π -electron system. A radical simplification of this many-electron system is obtained by solving the Schrödinger equation in a single-electron approximation. The potential of the single electron chosen is a function of its coordinates within the average field of all the other electrons and the nuclei. The starting point for the molecular orbitals (MOs) is a linear combination of all N $2p_z$ atomic orbitals φ_r of the molecule:

$$\Psi_j = \sum_{r=1}^N c_{jr} \varphi_r. \quad (\text{P1.8})$$

The Hückel theory is described in detail in textbooks on molecular physics. Its results for the energies E_j and for the mixing coefficients c_{jr} are as follows: for each MO, the coefficients c_{jr} follow from the system of N secular equations ($s = 1, 2 \dots N$):

$$\sum_r c_{jr} (H_{rs} - E_j S_{rs}) = 0. \quad (\text{P1.9})$$

Here, the matrix elements of the effective Hamiltonian H_{eff} are given by

$$H_{rs} = \int \varphi_r^* H_{\text{eff}} \varphi_s d\tau \quad (\text{P1.10})$$

and

$$S_{rs} = \int \varphi_r^* \varphi_s d\tau \quad (\text{P1.11})$$

are the overlap integrals. Equations (P1.9) are a system of homogeneous linear equations for the determination of the coefficients c_{jr} . It has nontrivial solutions only when the determinant of the coefficients, the so-called secular determinant, is zero. If we carry out this calculation (see below), we find the energy eigenvalues E_j . To do this, however, we must know the values of the matrix elements H_{rs} and S_{rs} . Hückel made the following radical and effective simplification for them:

1. The Coulomb integral $H_{rr} = \int \varphi_r^* H_{\text{eff}} \varphi_r d\tau$, which roughly speaking represents the energy of a non-bound electron in a $2p_z$ orbital, is set equal to an empirical constant α for all r :

$$H_{rr} = \alpha. \quad (\text{P1.12})$$

2. All the resonance integrals H_{rs} ($r \neq s$) are likewise set equal to an empirical constant β , if a σ bond is present between r and s :

$$H_{rs} = \beta. \quad (\text{P1.13})$$

For all the other rs pairs, i.e. for second-nearest neighbours and all more distant neighbours, the resonance integrals are set equal to

$$H_{rs} = 0. \quad (\text{P1.14})$$

A justification for this is the fact that the product in the integrand of Eq. (P1.10) is vanishingly small. (The overlap of two $2p_z$ orbitals at a distance of 2 Å has a value of only about 0.04.)

3. The overlap integrals S_{rs} are set to 0 for ($r \neq s$) and to 1 for ($r = s$):

$$S_{rr} = 1 \quad (\text{P1.15})$$

$$S_{rs} = 0 \ (r \neq s). \quad (\text{P1.16})$$

For the simple but very instructive example of the allyl radical (Fig. P.1.2), the condition for the secular determinant thus becomes (see above):

$$\begin{vmatrix} \alpha - E_j & \beta & 0 \\ \beta & \alpha - E_j & \beta \\ 0 & \beta & \alpha - E_j \end{vmatrix} = 0. \quad (\text{P1.17a})$$

With the abbreviation

$$\frac{\alpha - E_j}{\beta} = x_j \quad (\text{P1.18})$$

the determinant becomes

$$\begin{vmatrix} x_j & 1 & 0 \\ 1 & x_j & 1 \\ 0 & 1 & x_j \end{vmatrix} = 0. \quad (1.17b)$$

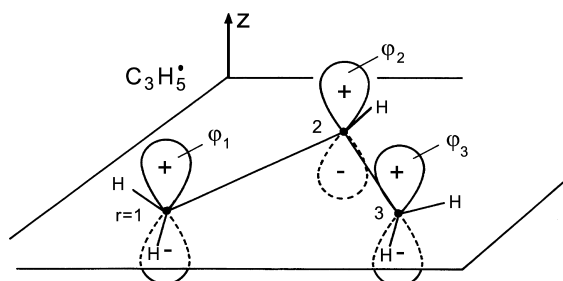


Fig. P1.2 The allyl radical, $\text{C}_3\text{H}_5^\bullet$. φ_1, φ_2 and φ_3 represent the $2p_z$ electrons from the three C atoms.

- Determine the energy eigenvalues E_j for the allyl group in units of α and β .
- Plot the energy eigenvalues in a term diagram with $\varepsilon_j = E_j - \alpha$ as ordinate, i.e. in a term diagram with its zero point at the energy of a non-bound $2p_z$ electron. Assume for the moment that $\beta < 0$ (see below) and enumerate the terms in order of increasing energy ε_j .
- Occupy three of these term diagrams taking the Pauli principle into account: the first with 2, the second with 3 and the third with 4 electrons in the lowest terms which can be filled in each case. These three term diagrams correspond to the cation, the radical and the anion of the allyl group. The energetically highest occupied MO in each case is called the HOMO, and the lowest unoccupied MO is called the LUMO.
- Which optical transitions could you use to determine the value of β within the framework of the Hückel model?
- One distinguishes between bonding, non-bonding and antibonding molecular orbitals. Give the names of the three molecular orbitals within this scheme. The electrons in the bonding molecular orbitals are denoted as π electrons, those in the non-bonding orbitals as n electrons, and those in the antibonding orbitals as π^* electrons. Denote the electrons in the term diagrams according to this convention.
- Using the system of equations (P1.9) and the simplifications (P1.12)–(P1.16), determine the three coefficients c_{jr} for each molecular orbital Ψ_j . To do this, you require the normalisation conditions

$$\sum_r c_{jr}^2 = 1 \quad (\text{P1.18a})$$

or

$$\sum_j c_{jr}^2 = 1. \quad (\text{P1.18b})$$

(P1.18a) means that each MO is normalised, and (P1.18b) means that each $2p_z$ orbital is distributed all together exactly once over the molecular orbitals.

- Draw a diagram for each MO Ψ_j with r ($r = 1, 2, 3$) as abscissa and c_{jr} as ordinate. You can see with the aid of this diagram that the number of nodes in the molecular orbitals increases with increasing j . A well-founded rule of quantum mechanics states that the number of nodes in the eigenfunctions of the stationary states increases with the eigenvalue of their energies. Therefore, Ψ_1 is the ground state, i.e. $\beta < 0$, as assumed above without proof.
- The occupation probability of an electron in a MO is found from Eqns. (P1.8), (P1.15) and (P1.16) to be

$$\begin{aligned} \int \Psi_j^* \Psi_j d\tau &= \int c_{j1}^2 \varphi_1^* \varphi_1 d\tau + \int c_{j2}^2 \varphi_2^* \varphi_2 d\tau + \int c_{j3}^2 \varphi_3^* \varphi_3 d\tau \\ &= c_{j1}^2 + c_{j2}^2 + c_{j3}^2 = 1. \end{aligned}$$

An electron in a MO is thus distributed inhomogeneously over the molecule. Calculate this distribution over the three carbon atoms for an electron in Ψ_1 and for an electron in Ψ_2 .

- Compute from this both the distribution of the sum of all the π electrons, i.e. the distribution n_r of the overall electron density over the three carbon atoms in the radical, as well as the distribution q_r of charge over the ions.
- Calculate the distribution ϱ_r of electron spins in the radical. This quantity is called the spin density ϱ_r . It can be determined for example from the hyperfine structure of electron-spin resonance (ESR) spectra.

Problem 1.4. The Hückel LCAO-MO Theory 2: Naphthalene ($C_{10}H_8$) (See e.g.: LIONEL SALEM, *The Molecular Orbital Theory of Conjugated Systems*, W. A. Benjamin, Inc. (1974), Chap. 1 and Appendix A-2, and Problem 1.3.)

Naphthalene is a molecule with the point group D_{2h} . It has a centre of inversion i, three twofold axes of rotational symmetry $1(R_z)$, $2(R_y)$ and $3(R_x)$, and three mirror planes perpendicular to the axes of rotational symmetry, xy , xz , and yz . The secular determinant for the calculation of the energy eigenvalues of the electronic system of the naphthalene molecule contains 10×10 coefficients c_{jr} (see Problem P1.3 and Fig. P1.3). The first row and first column of the determinant are shown in the following fragment:

$$\begin{vmatrix} x_j & 1 & 0 & 0 & 0 & 0 & 0 & 0 & 1 & 0 \\ 1 & & & & & & & & & \\ 0 & & & & & & & & & \\ 0 & & & & & & & & & \\ 0 & & & & & & & & & \\ 0 & & & & & & & & & \\ 0 & & & & & & & & & \\ 0 & & & & & & & & & \\ 1 & & & & & & & & & \\ 0 & & & & & & & & & \end{vmatrix} = 0.$$

- Complete the determinant.
- Try to determine the energy eigenvalues and the mixing coefficients from the completed determinant. This problem is not trivial. In case you cannot solve it, the Table P1.1 shows the results. Here, the notation for the symmetry types (= irreducible representations) of the molecular orbitals means: **a**,

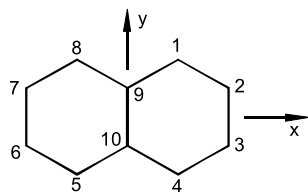


Fig. P1.3 Enumeration of the C atoms in the naphthalene molecule.

Table P1.1 Symmetry types and energies E_j of the 10 Hückel molecular orbitals ($j = 1 \dots 10$). The different contributions of the 10 $2p_z$ electrons to the 10 molecular orbitals are found from the coefficients a , b and c according to Eqns. (P1.19) a , b and c . The Coulomb integral α and the resonance integral β are defined in Problem P1.3.

MO	Symmetry types	$(E_j - \alpha)/\beta$	a	b	d
Ψ_{10}	b_{3g}	-2.3	0.300	-0.231	-0.461
Ψ_9	a_u	-1.62	0.263	-0.425	0
Ψ_8	b_{1u}	-1.30	0.400	-0.174	-0.347
Ψ_7	b_{3g}	-1.00	0	-0.408	+0.408
Ψ_6	b_{2g}	-0.62	0.425	-0.263	0
Ψ_5	a_u	+0.62	0.425	+0.263	0
Ψ_4	b_{1u}	+1.00	0	+0.408	-0.408
Ψ_3	b_{3g}	+1.30	0.400	+0.174	+0.347
Ψ_2	b_{2g}	+1.62	0.263	+0.425	0
Ψ_1	b_{1u}	+2.30	0.300	+0.231	+0.461

b: symmetric or antisymmetric behaviour with respect to a rotation around a twofold symmetry axis 1, 2 or 3; **g**, **u**: even or odd behaviour on inversion through a centre of inversion symmetry: in the case of **u**, the $2p_z$ atomic orbitals change their signs on inversion; in the case of **g**, they do not. In addition, the following notation was used:

$$a^2 = c_1^2 = c_4^2 = c_5^2 = c_8^2 \quad (\text{P1.19a})$$

$$b^2 = c_2^2 = c_3^2 = c_6^2 = c_7^2 \quad (\text{P1.19b})$$

$$d^2 = c_9^2 = c_{10}^2. \quad (\text{P1.19c})$$

- Justify Eqns. (P1.19).
- Complete the term diagram (β is negative) and fill in the electrons of the electronic ground state of the neutral molecule.
- Is the energetically lowest electronic transition from the ground state optically allowed? In which direction is it polarised?
- Show that the two next-highest electronic excited states are degenerate. Can they also be optically excited?
- Sketch the molecular orbitals by adding circles to the skeleton of the molecule (Fig. P1.3) at the positions of the carbon atoms, whose areas are proportional to the squares of the corresponding mixing coefficients; mark them with their relative signs. Draw in the nodal planes for each molecular orbital which are perpendicular to the molecular plane. (The molecular plane is always a nodal plane; cf. Fig. P1.2.)

Literature

Monographs related to the Field of this Book

- M1** M. POPE and C. E. SWENBERG, *Electronic Processes in Organic Crystals and Polymers*, 2nd ed., Oxford Univ. Press (1999)
- M2** E. A. SILINSH and V. CAPEK, *Organic Molecular Crystals*, AIP Press, New York (1994)
- M3** J. D. WRIGHT, *Molecular Crystals*, 2nd ed., Cambridge Univ. Press (1995)
- M4** H. HAKEN and H. C. WOLF, *The Physics of Atoms and Quanta*, 6th ed., Springer, Heidelberg, Berlin, New York (2004)
- M5** H. HAKEN and H. C. WOLF, *Molecular Physics and the Elements of Quantum Chemistry*, 2nd ed., Springer, Heidelberg, Berlin, New York (2004)

References

- 1** N. KARL, *Mol. Cryst. Liq. Cryst.* **171**, 157 (1989)
- 2** P. ERK, S. HÜNIG, J. U. v. SCHÜTZ, H. P. WERNER and H. C. WOLF, *Angew. Chem.* **100**, 286 (1988)
- 3** From C. LUDWIG *et al.*, *J. Vac. Sci. Technol.* **B12**, 1963 (1994). See also *Z. Phys.* **B86**, 397 (1992)
- 4** V. ENKELMANN, in: *Advances in Polymer Science* **63**, Polydiacetylenes, pp. 92–136, edited by H. J. Cantow, Springer (1984)

2

Forces and Structures

The structures of molecular crystals are determined both by the intramolecular forces as well as – in particular – by the *intermolecular* forces. When the latter are of short range, as is the case for van der Waals crystals, then the lattice energy will be minimised by a structure with the highest possible packing density. Simple molecular crystals are therefore densely-packed arrangements of molecules which interact only with their immediate neighbour molecules, and the decisive factors determining the crystal structure are to first order their size and shape. The question of the most effective molecular packing is thus determined to a large extent by the intramolecular forces. The intermolecular forces, on the other hand, can have a strong effect on the purely geometrically-allowed molecular packing arrangements via their strengths and their molecular anisotropy. Therefore, a knowledge of the intermolecular forces, their strengths, their ranges and their orientation dependence, is a necessary precondition for understanding the structures and many physical properties of molecular crystals.

2.1

Forces

How can electrically neutral and nonpolar molecules form a crystal? What are the forces between the molecules with filled orbitals which bind them together in a crystal? These forces are called inductive, dispersive, or, as a generic term, van der Waals forces. They are responsible for van der Waals bonding [M1].

To elucidate these forces, one best begins with the interaction of two permanent dipoles \mathbf{p}_1 and \mathbf{p}_2 at a distance \mathbf{r} from each another. Compare also Fig. 2.1a. The potential energy of the interaction of the two dipoles \mathbf{p}_1 and \mathbf{p}_2 is found from electrostatics to be

$$V = \frac{1}{4\pi\epsilon_0} \frac{\mathbf{p}_1\mathbf{p}_2 - 3(\mathbf{p}_1\mathbf{e}_r)(\mathbf{p}_2\mathbf{e}_r)}{r^3}. \quad (2.1)$$

Here, $\mathbf{e}_r = \mathbf{r}/r$ is the unit vector connecting the two dipoles and r is its magnitude.

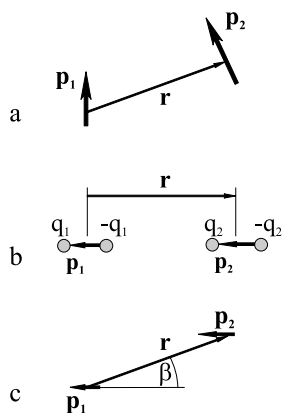


Fig. 2.1 The interaction of two dipoles p_1 and p_2 at a distance r from each other is found from the sum of the attractive and repulsive forces of the individual charges. See the explanation in the text.

For a parallel orientation of the dipole axes and the vector connecting them, corresponding to Fig. 2.1b, it follows from Eq. (2.1) that

$$V = -\frac{1}{4\pi\epsilon_0} \frac{2p_1p_2}{r^3} \quad (2.2)$$

where p_1 and p_2 are the magnitudes of the two dipole moments. The force F between the two dipoles is then attractive and has the magnitude

$$F = -\frac{dV}{dr} = -\frac{1}{4\pi\epsilon_0} \frac{6p_1p_2}{r^4}. \quad (2.3)$$

For the more general case that the relative orientation of the two parallel dipoles at a distance r is given by the angle β , cf. Fig. 2.1c, we find instead of Eq. (2.2)

$$V = -\frac{1}{4\pi\epsilon_0} \frac{p_1p_2}{r^3} (3\cos^2\beta - 1). \quad (2.4)$$

2.1.1

Inductive Forces

An attractive force between a molecule with a permanent dipole moment and a nonpolar molecule comes about when the first molecule induces a dipole moment in the second. Such attractive forces are called **inductive forces**. The induced moment obeys the following relation:

$$p_{\text{ind}} = \alpha E \quad (2.5)$$

where E is the electric field at the location of the second molecule and α is its polarisability.

For the field strength E at a distance r from a point charge q , we have

$$E = \frac{1}{4\pi\epsilon_0} \frac{q}{r^2} \mathbf{e}_r. \quad (2.6)$$

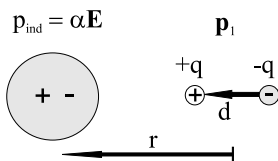


Fig. 2.2 A point dipole \mathbf{p}_1 can induce a dipole moment \mathbf{p}_{ind} in a nonpolar charge cloud with the polarisability α .

At the position of the polarisable molecule, one obtains for the relative orientation assumed in Fig. 2.2 a field strength due to the first dipole equal to

$$\mathbf{E} = \frac{1}{4\pi\epsilon_0} \left[\frac{+q}{(r-d/2)^2} + \frac{-q}{(r+d/2)^2} \right] \mathbf{e}_r \quad (2.7)$$

from which it follows for $d \ll r$ that

$$\mathbf{E} = \frac{1}{4\pi\epsilon_0} \frac{2\mathbf{p}_1}{r^3} \quad \text{with} \quad \mathbf{p}_1 = q \cdot \mathbf{d}. \quad (2.8)$$

If we denote the induced moment as $p_2 = p_{\text{ind}}$, we obtain with Eqns. (2.3) and (2.5) the attractive force between the molecule with a permanent dipole moment p_1 and the polarisable molecule:

$$F = -\frac{1}{4\pi\epsilon_0} \frac{6p_1 p_{\text{ind}}}{r^4} = -\frac{1}{(4\pi\epsilon_0)^2} \frac{12p_1^2 \alpha}{r^7} \quad (2.9)$$

and their potential energy

$$V = -\int_{\infty}^r F dr = -\frac{1}{(4\pi\epsilon_0)^2} \frac{2p_1^2 \alpha}{r^6}. \quad (2.10)$$

The forces calculated from Eq. (2.9) are called **inductive forces**. An important aspect is their strong dependence on the distance, corresponding to r^{-7} . Furthermore, they are proportional to the polarisability of the molecules.

2.1.2

Van der Waals Forces

The van der Waals forces in the strict sense, also called **dispersive forces**, are the attractive forces between two neutral, nonpolar molecules, for example anthracene molecules, which thus have no static dipole moments. Were the charge distribution within the molecules rigid, then there would indeed be no interactions between them. However, due to their temporally fluctuating charge distributions, they also have fluctuating dipole moments and these can induce dipoles in other molecules, compare Fig. 2.3. This results in an attractive force, as we already calculated in the section on inductive forces. To distinguish the two cases (of a permanent dipole and fluctuating dipoles), these forces due to fluctuations are also termed dispersive forces.

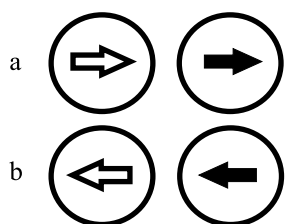


Fig. 2.3 Dispersive forces: a nonpolar molecule can have a fluctuating dipole moment (heavy arrow) and can thus induce another dipole in a nonpolar but polarisable molecule (light arrow). Its orientation is parallel to that of the inducing dipole. The interaction energy is thus always attractive.

From Eq. (2.9) we can find the dispersive force between two molecules with polarisability α

$$F = -\frac{1}{(4\pi\epsilon_0)^2} \frac{A'\alpha^2}{r^7}. \quad (2.11)$$

A' is here a factor whose magnitude is specific to a particular molecule. It takes into account the fact that the interacting molecules in general do not have spherical symmetry and that their mutual distance within the crystal is in general not much greater than their size. This means that F is anisotropic and moments higher than the dipole moment, i.e. at least quadrupole moments, must be taken into account in the charge distribution. Strictly speaking, the factor A' is thus only a symbol for the fact that the concrete calculation of the dispersive or van der Waals force between molecules – in contrast to that between noble-gas atoms – must be carried out in a differential manner, because the distance r in the integral equation (2.11) is only poorly defined or cannot be defined at all.

Like the inductive forces, the dispersive forces are of very short range owing to their r^7 dependence, and they are proportional to the square of the molecular polarisability. Thus, for larger organic molecules, especially for aromatic molecules like anthracene with their strongly polarisable π electrons, they are relatively strong. This is also shown by the comparison of the melting points of some molecular

Table 2.1 Melting points ($^{\circ}\text{C}$) of some molecular crystals. Van der Waals forces are determined by the polarisabilities of the molecules. Thus, cyclooctatetraene, with the same number of carbon atoms (8), has a higher melting point than o-xylol, because it has more polarisable π electrons. The same holds for benzene in comparison to *n*-hexane and for the series of polyacenes from benzene to hexacene.

o-xylol	–25
cyclooctatetraene	–4
<i>n</i> -hexane	–95
benzene	5.5
naphthalene	80
anthracene	216
tetracene	357
hexacene	380

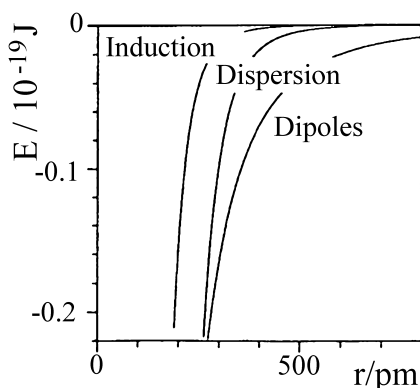


Fig. 2.4 Attractive energy E as a function of the distance r for the NH_3 molecule. At large distances, the dipolar interaction energy is predominant; at smaller distances, its contribution becomes comparable to that of the dispersive energy. After [M1].

crystals in Table 2.1. Benzene, for example, has a considerably higher melting point than n -hexane due to the greater polarisability of its π electrons.

From Eq. (2.11) we find the dispersion energy

$$V_{\text{disp}} = - \int_{\infty}^r F dr = - \frac{1}{(4\pi\epsilon_0)^2} \frac{A''\alpha^2}{r^6}. \quad (2.12)$$

The factor $A'' = A'/6$ has here of course the same meaning as in Eq. (2.11). A specific model for the differential calculation of the dispersion energy V_{disp} will be treated in Sect. 2.1.4.

Fig. 2.4 shows the different distance dependences of dipolar, inductive, and dispersive energies of attraction, computed for the NH_3 molecule, which has a permanent dipole moment. In this case, not only inductive and dispersive forces, but also dipole forces play a role.

2.1.3

Repulsive Forces

In addition to the attractive forces, there are also **repulsive forces** from the inner electrons and the atomic nuclei, which prevent the collapse of the crystal lattice. The superposition of the repulsion and the attraction yields the equilibrium distance r_0 between the molecules, cf. Fig. 2.5.

The repulsive forces are based on Coulomb repulsion and, according to the Pauli principle, on the interdiction for additional electrons to be found in a region of space where all the fully-occupied orbitals overlap. These effects become important only at very small distances and increase very rapidly with further decreasing distance. Their exact calculation is very difficult and laborious. They are generally treated using readily-applicable approximations.

The simplest approximation is that of a rectangular potential with the assumption

$$V = 0 \quad \text{for} \quad r > r_0, \quad V = \infty \quad \text{for} \quad r \leq r_0, \quad (2.13)$$

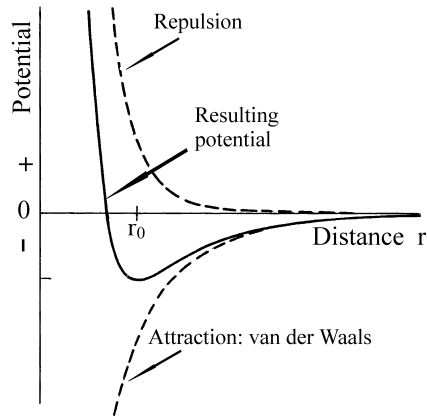


Fig. 2.5 The repulsive potential combined with the van der Waals attraction gives the overall potential. The interaction energy has its minimum at the equilibrium distance r_0 .

where r_0 is the smallest distance to which the atoms can approach each other. To refine this very rough model, one often uses the potential

$$V = \frac{C_n}{r^n}. \quad (2.14)$$

A value $n = 12$ is often used, yielding for the sum of repulsion and attraction the so called **Lennard-Jones potential**

$$V = \frac{C_{12}}{r^{12}} - \frac{A}{r^6}. \quad (2.15)$$

Compare also Fig. 2.5. The equilibrium distance where $dV/dr = 0$ will be denoted as r_0 .

As an alternative to the Lennard-Jones potential, one can also carry out calculations using an exponential repulsive potential

$$V = B \cdot e^{-\alpha r}. \quad (2.16)$$

This potential is called the **Born-Meyer potential**. The quantity α introduced here is of course not identical with the polarisability. The overall potential for repulsion and attraction is then called the **Buckingham potential** [1] and is given by

$$V = -\frac{A}{r^6} + B \cdot e^{-\alpha r}. \quad (2.17)$$

The two potentials (2.15) and (2.17) have proved reliable, e.g. for calculating the interaction between noble-gas atoms. For this purpose, the empirical constants A , B and α or A and C_{12} are determined for specific atoms from the crystal structures, the phonon energies, and from thermodynamic observables.

2.1.4

Intermolecular Potentials

To calculate the interaction between neutral and nonpolar molecules with closed electronic shells, Kitaigorodskii [2] originally suggested representing the intermole-

molecular potential as a sum of atom-atom potentials which each have the form (2.15) or (2.17). To calculate the intermolecular interaction of aromatic hydrocarbons, one then requires – using the Buckingham potential (2.17) – for the three different pairs of atoms, C-C, C-H and H-H, in each case three, i.e. all together nine constants. Table 2.2 contains two different sets of these nine parameters, as they were determined from the structural data and sublimation energies of various crystals by Kitaigorodskii [2] and by Williams [3]. The atom-atom potentials as shown in Fig. 2.6 and the intermolecular potentials found by summing over all the atom-atom pairs of neighbouring molecules obtained with these constants and using Eq. (2.17) have been found to be surprisingly reliable (see also Chap. 5.6).

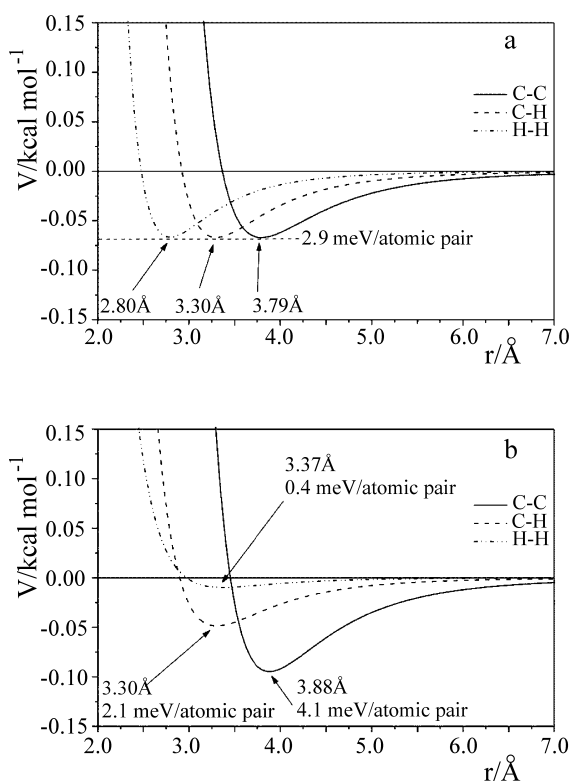


Fig. 2.6 Atom-atom potentials. For specific calculations of the intermolecular interaction of pure aromatic hydrocarbons, the overall potential is computed as the sum of individual atom-atom potentials $V(r)$. Here, r is the distance of the atoms of neighbouring molecules. Each of the three possible atom pairs (C-C, C-H and H-H) in neighbouring molecules is defined by its own set of parameters. Thus, using the Buckingham

potential (Eq. (2.17)), $3 \times 3 = 9$ parameters are necessary. The two parameter sets of Kitaigorodskii and of Williams (Table 2.2) have both proved to be good approximations, although they are very different in their details and the Williams parameter set appears to be more physically realistic than the Kitaigorodskii set. The overall intermolecular potential is the sum over all the atom-atom pairs in neighbouring molecules.

Table 2.2 Parameters of the exp-6 potential (Eq. (2.17)) for the three different atom-atom pairs of neighbouring hydrocarbon molecules (after Kitaigorodskii [2] and Williams [3]). The overall intermolecular potential is found as the sum of all the atom-atom potentials of neighbouring molecules.

atom pair	Kitaigorodskii			Williams		
	A kcal Å ⁶ mol ⁻¹	B kcal mol ⁻¹	α Å ⁻¹	A kcal Å ⁶ mol ⁻¹	B kcal mol ⁻¹	α Å ⁻¹
C-C	358	42 000	3.58	568	83630	3.60
C-H	154	42 000	4.12	125	8766	3.67
H-H	57	42 000	4.86	27.3	2654	3.74

In this summation process, the differences between the two potentials (2.15) and (2.17) are apparently almost canceled out, since both sets of parameters yield e.g. practically the same crystal structures, which in turn hardly differ from the observed crystal structures. In the calculation of the phonon dispersion curves (see Chap. 5) it has been found that the Kitaigorodskii parameter set describes the experimental dispersion curves somewhat better than the Williams set, although here, also, the differences are small and the agreement between theory and experiment is astonishingly good (see Chap. 5).

The binding energy of a hydrocarbon molecule in a crystal is thus found to a first approximation by addition from the interaction energies of the C and H atoms which compose the basic units of the molecule. The energies of sublimation of different crystals are therefore proportional to the masses of their molecules (cf. Fig. 2.7).

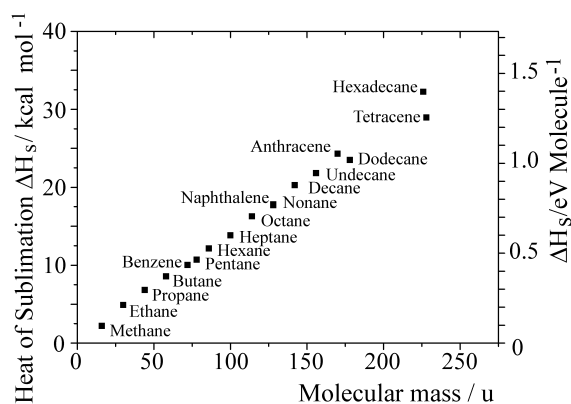
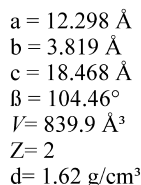


Fig. 2.7 Heats of sublimation of different molecular crystals as a function of the molecular mass. After [M6].

Coulomb Forces



(TCNQ), respectively. The distance between the molecular planes is 3.47 Å (TTF) and 3.17 Å (TCNQ). The direction of stacking is the *b* axis. Projections along the *a* axis (upper figure) and along the *b* axis (lower figure) are shown. The third dimension – above and below the plane of the drawing – is represented by black (above) and white (below) atoms. After [17] and [M4].

of such molecular crystals. Coulomb forces are particularly important for the interesting groups of crystals with charge transfer between the partners, i.e. the D-A complexes and the radical-ion salts. Here, we are dealing with crystals which consist of two different structural units, one of which acts as donor and gives up charge with a small ionisation potential to the acceptor. The latter is a structural unit with a larger electron affinity. See also Sect. 1.2 as well as Chap. 9.

In the complexes and salts which interest us here, at least one of the partners is an organic molecule. The other can also be such a molecule; an example of this is $\text{TTF}^+\cdot\text{TCNQ}^-$ (Fig. 2.8). It can also be an inorganic group with closed electronic shells, e.g. $(\text{FA})_2^+\text{PF}_6^-$ (Fig. 1.8). And finally, a metal ion is also a possible counterion, for example in $\text{Cu}^+(\text{DCNQI})_2^{\bullet-}$ (Fig. 1.7). In the radical-ion salts, the structural units crystallise as ions. In all cases, in addition to the van der Waals bonding determined to a great extent by the polarisability, there is also ionic bonding as we know it from ionic crystals such as NaCl. This ionic bonding may predominate, and it has an essential influence on the crystal structure. This can be seen particularly clearly in comparing the crystal structures of the typical molecular crystal naphthalene (Fig. 2.10) and the typical radical-ion salts $(\text{FA})_2\text{PF}_6$ (Fig. 2.18) and $\text{Cu}(\text{DCNQI})_2$ (Fig. 1.7).

2.2 Structures

Depending on the number of important intermolecular forces, the organic molecular crystals can be divided into three groups. The simplest to explain is the group of nonpolar molecules, in particular the simple aliphatic and aromatic molecules. Here, the dispersive and the repulsive forces as in Eq. (2.15) and Eq. (2.17) are important. In the second group, where the molecules have polar substituents, dipole-dipole forces and inductive forces as in Eq. (2.9) are also present. Finally, the third group consists of substances in which ionic forces, i.e. Coulomb forces between the different charges of the two partners, play an essential role. These are the strong donor-acceptor complexes and the radical-ion salts. Molecular solids in which hydrogen bonds make an essential contribution to the bonding can be considered to be a special case of the second group. However, we shall not discuss them further here.

2.2.1 Crystals of Nonpolar Molecules

In these crystals with relatively weak dispersive forces and strong short-range repulsion, one can make the assumption that the molecules will adopt the densest possible packing with the least possible repulsion. The arrangement of the molecules will be determined by atom-atom potentials. The lattice energy is minimised when the number of van der Waals atom-atom contacts is as large as possible.

According to Kitaigorodskii [M6], the packing density can be characterised by a packing coefficient K :

$$K = ZV_0/V$$

where V is the volume of a crystallographic unit cell in which each molecule has the volume V_0 , which can be calculated from the known atomic radii and the dimensions of the molecules. Z is the number of molecules in a unit cell. The values of K for the aromatic hydrocarbons lie between 0.68 (benzene) and 0.80 (perylene). For comparison: the packing coefficient of ice, which is bound through dipolar forces and hydrogen bonding, is only 0.38.

In considering the packing density within a crystal, we also need to remember that even with planar molecules, the molecular surfaces are not structureless. The positions of the atoms correspond to 'hills', the positions in between to valleys in the molecular contour; see Fig. 1.3. An arrangement in which the hills of one molecule lie above the valleys of the neighbouring molecules is therefore generally energetically more favourable for nonpolar molecules than one in which the molecules lie directly above one another. This is most noticeable in the 'herringbone' pattern in which many aromatic molecules crystallise; see below. In the case of the radical-ion salts, it is just the reverse: they generally crystallise in such a way that the overlap of the highest occupied molecular orbitals of neighbouring molecules is as large as possible (see e.g. Figs. 2.18 and 9.24).

The **long-chain alkanes**, in particular the linear hydrocarbons with n carbon atoms, are preferentially arranged in the solid state so that the CH_2 zig-zag chains of the individual molecules are parallel to each other, and thus form a layered structure with a parallel arrangement of the structural units (Fig. 2.9). Such an arrange-

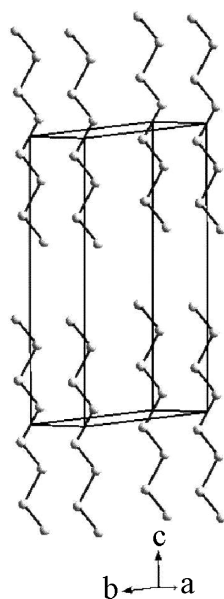


Fig. 2.9 The crystal structure of *n*-octane, $\text{CH}_3\text{-(CH}_2)_6\text{-CH}_3$, as an example of an aliphatic compound. The H atoms are not shown in the drawing. The bonds differ from those of the aromatic single bonds. The crystals are triclinic with $Z = 2$ molecules in the unit cell. $a = 4.22 \text{ \AA}$, $b = 4.79 \text{ \AA}$, $c = 11.02 \text{ \AA}$, $\alpha = 94.7^\circ$, $\beta = 84.3^\circ$, $\gamma = 105.8^\circ$, $Z = 2$.

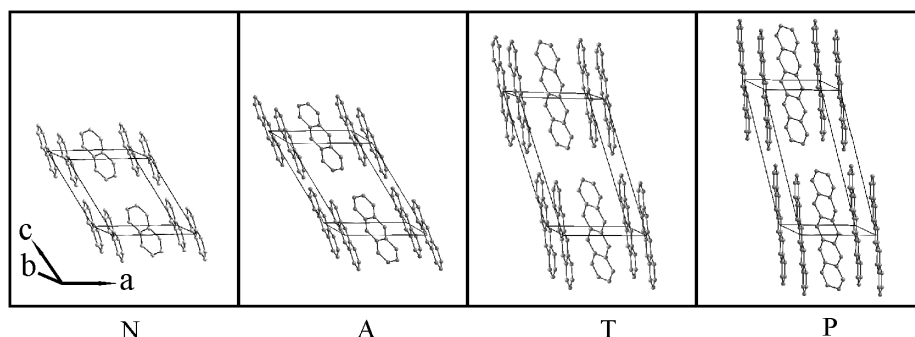


Fig. 2.10 The crystal structure of naphthalene, anthracene, tetracene, and pentacene. These aromatic compounds crystallise in the herringbone pattern. Their crystal-structure data are given in the first part of Table 2.3, and the orientation of the individual molecules in these crystals are indicated in the lower part of the Table.

ment guarantees the strongest dispersive interactions in view of the anisotropic polarisability of these molecules. In this case, the molecules need not be oriented perpendicular to the plane of the layers. For example, the molecules of fatty-acid derivatives, which are oriented parallel to each other following the same principle in Langmuir-Blodgett films, are frequently at an angle to the substrate if this is more favourable to the formation of closest packing due to steric interactions of the end groups. We shall not deal with the aliphatic crystals further in this book, as already mentioned in Chap. 1.

The **aromatic compounds** are of special interest. As an example, we show here the crystal structure of the very intensively investigated molecule anthracene (Fig. 2.10). The molecular structure, with the charge clouds of the π electrons perpendicular to the molecular plane (compare Fig. 1.2), shows in an understandable way that the polarisability is strongly anisotropic and has by far its largest value in the molecular plane. From the conditions of maximum dispersive interactions and optimum packing in space, the 'herringbone' structure seen in Fig. 2.10 is most favourable in a monoclinic crystal lattice with two molecules in the unit cell. Fig. 2.10 also shows the structures and Table 2.3 the structural data for the other crystals of polyacene molecules, i.e. for naphthalene, tetracene and pentacene with 2, 4 or 5 aromatic rings. All of these substances crystallise like many others also in the same pattern. Table 2.3 also contains data about the orientations of the individual molecules in the unit cell for these crystals.

From the structures shown in Fig. 2.10, one can see that the molecules are quite densely packed. Each molecule has ten nearest or next-nearest neighbours. Incidentally, note that the hydrogen atoms have been left out of the crystal structure drawings in order to make them clearer.

There are also aromatic molecular crystals with only one molecule in the unit cell, so that all the molecules in the crystal are equivalent under translations. The perhaps best-known example of this type of compound is hexamethylbenzene,

Fig. 2.11. It is worth mentioning that Lonsdale [4] in his structural analysis of this crystal found the first experimental proof that the molecules composed of aromatic rings are planar. In the case of hexamethyl benzene, as with many other organic crystals, there is a remarkable structural phase transition in which the triclinic structure (Fig. 2.11) is transformed into a monoclinic structure at 110 K [5].

Table 2.3 Above: crystallographic data from naphthalene (Nph), anthracene (Ac), tetracene (Tc), pentacene (Pc) and hexacene (Hc) molecular crystals. d : density, Z : number of molecules in the unit cell. Below: the orientation of the molecules in naphthalene, anthracene, tetracene and pentacene crystals. χ_L , ψ_L , ω_L ; χ_M , ψ_M , ω_M ; χ_N , ψ_N and ω_N are the angles between the molecular axes L (long axis), M (short axis) and N (perpendicular to the molecular plane) and the crystal axes a , b and c . From [M3, M4].

	Nph C ₁₀ H ₈	Ac C ₁₄ H ₁₀	Tc C ₁₈ H ₁₂	Pc C ₂₂ H ₁₄	Hc C ₂₆ H ₁₆
crystal structure	monoclinic	monoclinic	triclinic	triclinic	triclinic
space group	P2 _{1/a}	P2 _{1/a}	P1	P1	P1
$a/\text{\AA}$	8.24	8.56	7.90	7.90	7.9
$b/\text{\AA}$	6.00	6.04	6.03	6.06	6.1
$c/\text{\AA}$	8.66	11.16	13.53	16.01	18.4
$\alpha/^\circ$	90.0	90.0	100.3	101.9	102.7
$\beta/^\circ$	122.9	124.7	113.2	112.6	112.3
$\gamma/^\circ$	90.0	90.0	86.3	85.8	83.6
$V/\text{\AA}^3$	360	474	583	692	800
Z	2	2	2	2	2
$d_{\text{cal}}/(\text{g}/\text{cm}^3)$	1.17	1.24	1.29	1.33	1.35
$d_{\text{exp}}/(\text{g}/\text{cm}^3)$	1.15	1.25	1.29	1.32	1.34

Angle	Nph	Ac	Tc		Pc	
			Molecule I	Molecule II	Molecule I	Molecule II
χ_L	115.8°	119.7	105.8°	105.5°	104.4°	104.3°
ψ_L	102.6	97.0	105.5	103.6	106.4	104.0
ω_L	29.0	30.6	22.5	20.8	22.1	20.3
χ_M	71.2	71.3	69.2	115.4	67.9	118.5
ψ_M	29.45	26.6	30.1	26.0	30.7	29.2
ω_M	68.2	71.8	69.2	85.0	69.8	84.0
χ_N	32.8	36.2	26.6	30.6	26.6	32.4
ψ_N	116.3	115.5	115.2	67.8	115.7	65.0
ω_N	71.9	66.2	81.9	70.1	83.8	70.7

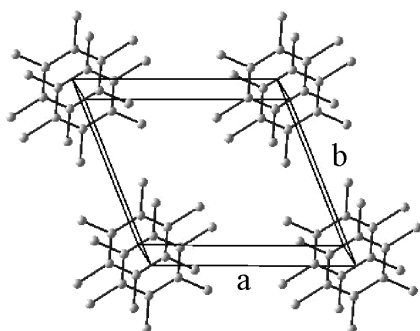


Fig. 2.11 The crystal structure of hexamethyl benzene as an example of a structure with only one molecule in the unit cell. The crystals are triclinic with $Z = 1$ molecules in the unit cell. $a = 8.92 \text{ \AA}$, $b = 8.86 \text{ \AA}$, $c = 5.3 \text{ \AA}$, $\alpha = 44.45^\circ$, $\beta = 116.72^\circ$, $\gamma = 119.57^\circ$, $Z = 1$.

Some aromatic hydrocarbons, for example pyrene and perylene, also crystallise in a herringbone pattern; however, the structural units of these lattices are pairs of molecules which form sandwich-like dimers (see Figs. 2.12 and 2.13 as well as Table 2.4). The two partners are bound together only weakly and absorb light like monomers, but they fluoresce as dimers. This interesting phenomenon is called excimer emission (excimer stands for “excited dimer”); more will be said about this topic later in Chap. 5. By the way, perylene (see also Table 2.4) crystallises not only in the dimer-like α phase but also in a β phase (Fig. 2.13). In the latter, which

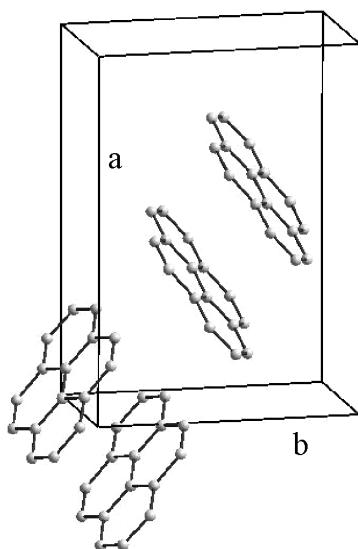


Fig. 2.12 The crystal structure (unit cell) of pyrene. Pairs of molecules are arranged in the herringbone pattern.

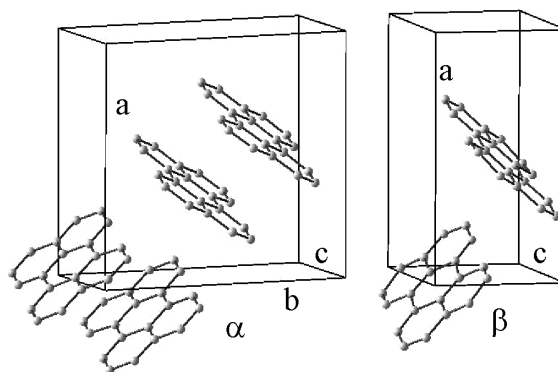


Fig. 2.13 α : The crystal structure (unit cell) of perylene, α phase. The unit cell contains 4 molecules, which are arranged like those of pyrene in pairs. Crystal-structure data are given in Table 2.4. β : The crystal structure (unit cell) of perylene, β phase. The unit cell contains 2 molecules. The structure is nearly isoenergetic with that of the α phase. Crystal-structure data are given in Table 2.4.

Table 2.4 The crystallographic data for pyrene and perylene crystals. From [M3].

	Pyrene C ₁₆ H ₁₀	Perylene C ₂₀ H ₁₂	
		α Phase	β Phase
crystal structure	monoclinic	monoclinic	monoclinic
space group	P2 ₁ /a	P2 ₁ /a	P2 ₁ /a
<i>a</i> /Å	13.65	11.35	11.27
<i>b</i> /Å	9.26	10.87	5.88
<i>c</i> /Å	8.47	10.31	9.65
β /°	100.28	100.8	92.1
<i>V</i> /Å ³	1052.9	1249	394.3
<i>Z</i>	4	4	2

has a very similar lattice energy, the molecules are arranged individually in the herringbone pattern, like those of anthracene, and there is no excimer emission. The two modifications thus lie energetically very close together and can both be grown at the same temperature by slight variations in the crystal-growth conditions. Their physical properties are, however, quite different.

For many crystals with pure van der Waals interactions, there are several phases with different lattice structure, but similar lattice energies. Phase changes driven by temperature variations or relatively low external pressure can thus readily be observed in many crystals. This is also true of the weak D-A-complex crystals, in which in the ground state no charge transfer has yet occurred.

Crystal **twinning** is also relatively easy to produce in these materials. In this process, crystals are formed which consist of two or more regions with the same structure, that is with the same stacking of the molecules, but however different orientations.

2.2.2

Crystals of Molecules with Polar Substituents

When directed dipolar interactions produced by polar groups or substituents are present in addition to the dispersive forces, then the variety of crystal structures increases.

Fig. 2.14 shows as a typical example the crystal structure of 1,4-dibromonaphthalene. The dipole forces decrease, in contrast to the dispersive forces, only as the fourth power of the distance. Therefore, a predominant structural principle is now that in the formation of crystals, the dipole-dipole interaction be maximised. On the other hand, the tendency to closest packing remains. Weak donor-acceptor crystals, in which in the electronic ground state only a very small charge transfer occurs,

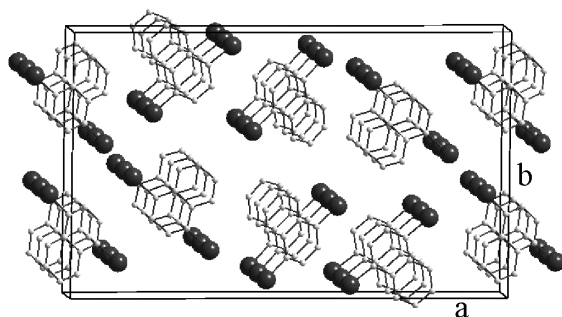


Fig. 2.14 The crystal structure of 1,4-dibromonaphthalene. The crystal consists of stacks of molecules, closely spaced with parallel molecular planes. This yields a strong one-dimensional behaviour in energy transport, i.e. linear excitons. The crystal is monoclinic, with $Z = 8$ molecules in the unit cell. The lattice constants are $a = 27.45 \text{ \AA}$, $b = 16.62 \text{ \AA}$, $c = 4.09 \text{ \AA}$. The angle between the c axis and the ab plane is $\beta = 91^\circ 55'$.

can also be included within this group. The crystal structure of anthracene-TCNB (Fig. 1.6) is an example of such a case.

2.2.3

Crystals with a Low Packing Density, Clathrates

There are also molecules whose crystals contain extended one-dimensional holes (channels) or two-dimensional cavities (planar cavities) in which other molecules can be trapped without covalent bonding, i.e. by van der Waals bonding alone. These are the **inclusion crystals** or **clathrates**.

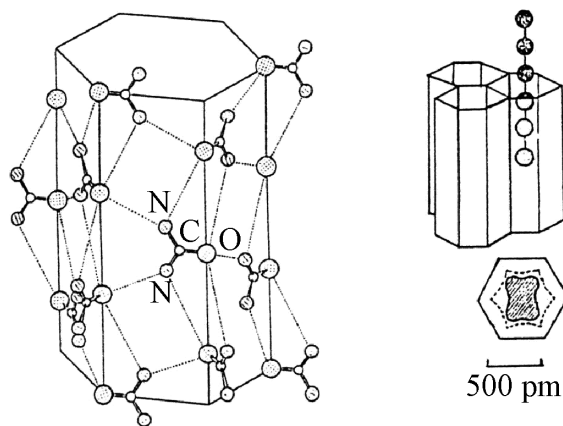


Fig. 2.15 Urea, which crystallises in a hexagonal structure as a clathrate together with n -alkanes. It is therefore suitable for separating linear and branched hydrocarbon chains. From [M2].

A typical example of them is urea, $\text{H}_2\text{N}-\overset{\text{O}}{\underset{\parallel}{\text{C}}}-\text{NH}_2$ (Fig. 2.15). Urea crystallises normally in a tetragonal structure. In the presence of specific hydrocarbons such as *n*-paraffins, however, the molecule forms hexagonal crystals on recrystallisation from the common solution, with open channels of ca. 520 pm diameter, in which even longer paraffins (alkanes) can be trapped as inclusions.

An example of crystals with planar inclusions are the clathrates of tetraphenylporphyrin (Fig. 2.16). Due to the steric requirements of the porphyrin molecule

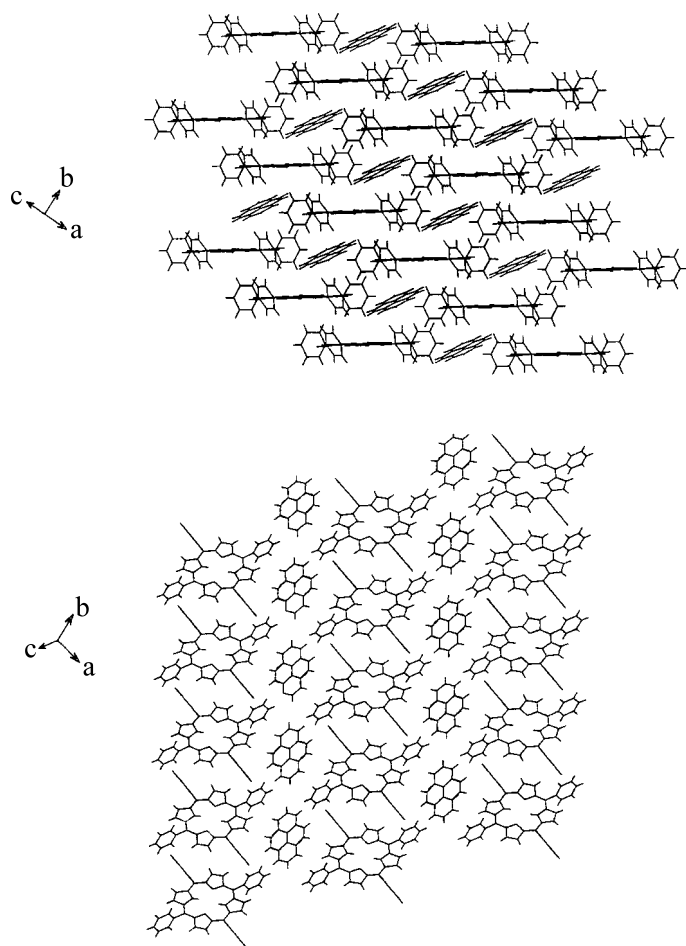


Fig. 2.16 The crystal structure of the triclinic TPP-pyrene clathrate. The lattice constants are $a = 9.727$, $b = 10.854$ and $c = 11.620$ Å, with $Z = 1$. The volume of the unit cell is expanded from 801.9 to 1073.5 (Å)³. *Above*: view along the channels which are filled with pyrene; *below*: view perpendicular to the channels. From [6].

which has multiple phenyl substituents, two-dimensional cavities are formed in the triclinic crystal structure. In these planar cavities, larger molecules such as anthracene, phenanthrene, pyrene, and many others can form well-ordered inclusions with a 1 : 1 ratio during crystal growth from solution. A certain amount of lattice expansion accompanies this growth. These crystals are also very descriptively termed ‘molecular sponges’. In this way, one can produce layers of aromatic molecules by self-organisation [6]. A large number of clathrate formers and inclusions are known.

Further examples of clathrates, clathrate formers and porous molecular structures can be found in Vögtle [M2] and also in [7].

2.2.4

Crystals of Molecules with Charge Transfer, Radical-ion Salts

Still more strongly influenced by dipolar and Coulomb forces are the structures of the strong donor-acceptor crystals and the radical-ion salts.

Charge-transfer interactions between an electron donor D and an electron acceptor A are stronger than van der Waals forces. This type of interaction is favoured by a low ionisation potential I of the donor and a high electron affinity A of the acceptor. The corresponding orbitals must have a sufficiently strong overlap with the smallest possible spacing and they should preferably have the same symmetry. The contribution of the charge-transfer interaction to the intermolecular forces thus depends strongly on the relative orientation of the donor and acceptor molecules.

The ground-state wavefunction Ψ_G of a charge-transfer complex is in the simplest case given by

$$\Psi_G = a\Psi_{DA} + b\Psi_{D^+A^-},$$

where Ψ_{DA} is the wavefunction without charge transfer. $a \gg b$ means that we are dealing with a complex with **weak** charge transfer in its ground state.

An example of a **strong** donor-acceptor-complex crystal is the compound TTF-TCNQ (Fig. 2.8). The ground state of this group of substances is at least partially ionic, due to the transfer of the fraction δ of an elementary charge, with $0 \leq \delta \leq 1$. $\delta = 1$ means complete charge transfer. In TTF:TCNQ, the degree of charge transfer from the donor TTF to the acceptor TCNQ at room temperature is $\delta = 0.59$. δ increases here with decreasing temperature. Frequently, one of the organic radical-ions also consists of a dimer, e.g. (perylene) $_2^+\bullet$ or (fluoranthene) $_2^+\bullet$ as radical cation or (TCNQ) $_2^-\bullet$ as radical anion.

The organic molecules are in these cases usually planar and form stacks, which can be mixed ($D^{\delta+}A^{\delta-}D^{\delta+}A^{\delta-}$) or separated ($D^{\delta+}D^{\delta+}D^{\delta+}D^{\delta+1+}$) and ($A^{\delta-}A^{\delta-}A^{\delta-}A^{\delta-}$). Stacks in which the neighbouring molecules are equidistant are termed regular, while those with dimerisation are termed alternating. The different stackings are of vital importance for determining the character of these materials as insulators, semiconductors, or metallic conductors. Fig. 2.17 indicates schematically that the TTF-TCNQ crystal is built up from separate stacks. An example of mixed stacks is the insulator anthracene-PMDA (Fig. 6.14).

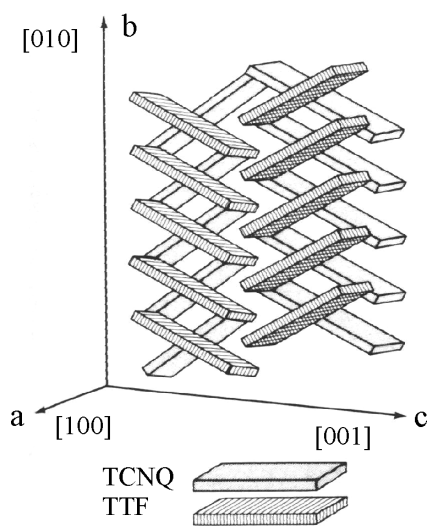


Fig. 2.17 Schematic of the TTF-TCNQ structure (see also Fig. 2.8). The molecular planes are not perpendicular to the stacking axis b here, but rather are slightly rotated towards the a axis. Along the a direction, the TCNQ and the TTF stacks alternate. From [M7].

Crystals with mixed stacks are insulators. Metallic conductivity, as we will find in the so called organic metals in Chap. 9, can, as we shall see there, only occur in crystals with separated stacks. Here, the acceptor stack takes on excess electrons from the donor stack. The charge transfer must be large, but not complete ($\delta < 1$). The charge carriers move preferentially along one of the stacks or sometimes along both. This also causes the high anisotropy in the conductivity, leading in the extreme case to one-dimensional behaviour of the metallic conductivity in many organic solids (more on this topic may be found in Chap. 9).

This is particularly true for the interesting members of the group of radical-ion salts, in which the acceptance or donation of an additional charge by an anorganic counterion occurs, such as in $(\text{Fa})_2^+\text{PF}_6^-$ (Fig. 2.18), or by a metal ion as in the salts of $\text{Cu}^+(\text{DCNQI})_2^\bullet$ (Fig. 1.7).

The computation of the structure of crystals with charge transfer is difficult, since here different, anisotropic intermolecular interactions contribute in the determination of the minimum energy. The crystal-growth conditions play a still stronger role than in crystals consisting of only one type of molecules, as do purity and the temperature. In general, the theoretical prediction of the structures of charge-transfer salts is hardly possible.

2.3

Polymer Single Crystals: Diacetylenes

There are also macroscopic polymer single crystals [8–11], which have a π -electron system along the polymeric carbon chains (Fig. 1.11): e.g. the poly-diacetylene crystals (Fig. 1.10). They are formed from monomeric diacetylene crystals via a so called topochemical reaction (Fig. 2.19 and Chap. 3). Topochemical refers to reactions of molecules in crystals in which the reactivity of the molecules is less important than

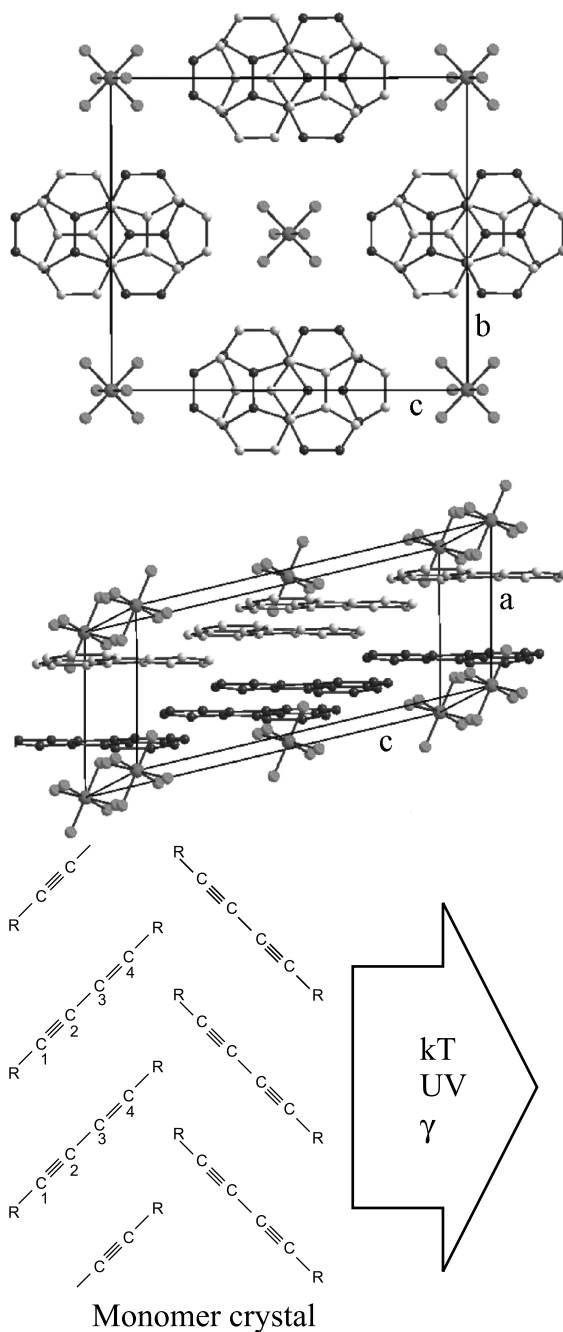


Fig. 2.19 The principle of the topochemical reaction of monomeric diacetylene crystals to give *poly*-diacetylene crystals. The reaction is irreversible and can be initiated thermally or also through UV radiation and/or through irradiation with γ rays.

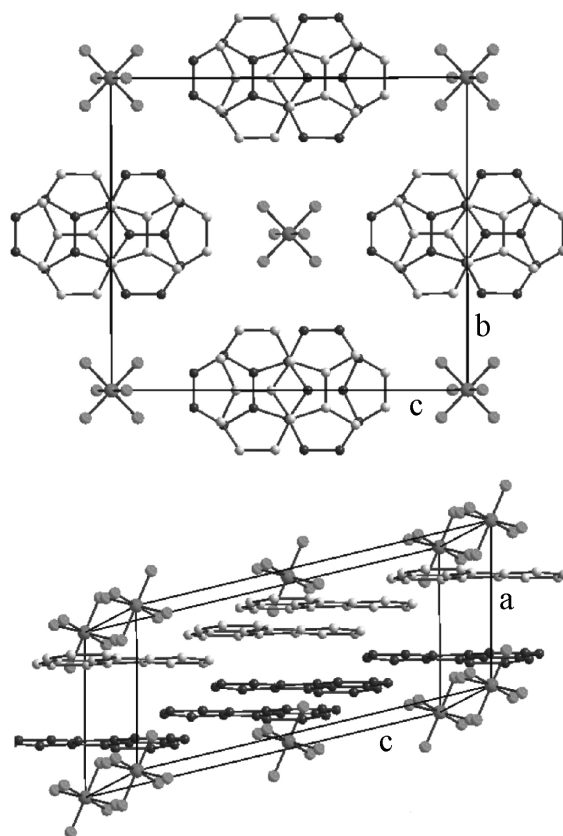


Fig. 2.18 The crystal structure of the radical cation salt $(Fa)_2^{2+\bullet}PF_6^-$. At room temperature, the crystal is monoclinic ($a = 0.66$ nm, $b = 1.257$ nm, $c = 1.477$ nm, $\angle(a, c) = 104^\circ$) and contains two fluoranthene molecules per unit cell. They are stacked along the a axis with two alternating spacings (0.328 nm and 0.333 nm). Two each of the fluoranthene molecules form the radical cation $(Fa)_2^{2+\bullet}PF_6^-$. The stacking axis a is perpendicular to the planes of the fluoranthene molecules. The PF_6^- anions are located in the channels between the fluoranthene molecules. From [10].

the arrangement of neighbouring molecules in the monomeric crystal. Its lattice structure determines whether the reaction can lead to a macroscopic polymer crystal or not, since the bond lengths and angles between the C atoms in the chain of the polymer crystal are largely determined by the strong covalent σ bonds. When the lattice parameters of the monomer crystal are not compatible with these bond lengths and angles in the polymer crystal, the reaction cannot progress to completion and produce macroscopic polymer crystals. Whether the structures of the monomer crystals are compatible with those of the polymer crystals or not depends on the molecular substituents R .

The solid-state polymerisation of the diacetylenes can be initiated thermally and/or through irradiation with UV or γ radiation and leads for many substituents R to macroscopic poly-diacetylene single crystals. For most substituents R , it is irreversible. Table 2.5 gives a selection of substituents R with which macroscopic diacetylene crystals have been successfully grown. Additional examples can be found in Enkelmann [11].

Poly-diacetylene crystals have unusually large anisotropies in their mechanical and in their optical properties. Along the linear chains of covalently-bound C atoms, they have a high tensile strength. In the perpendicular direction, there are cleavage planes because the polymer chains are bound together only by van der Waals forces. Along the chains, which carry the fully conjugated π -electron system, the crystals are highly (and nonlinearly) polarisable. Therefore, they are strongly dichroic: light which is polarised parallel to the chain is strongly reflected, while light with a perpendicular polarisation is practically not reflected (Fig. 1.11).

The crystal structures of the diacetylenes have been determined for many substituents R . A prominent example is shown in Fig. 2.20, which gives a section

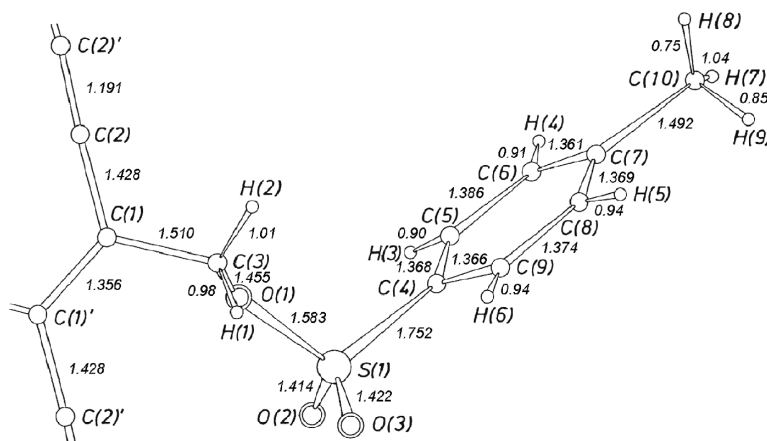


Fig. 2.20 A section through the crystal structure of the p-TS6 crystal. The crystal is monoclinic, with $a = 14.493$ Å, $b = 4.910$ Å, $c = 14.936$ Å, and $\beta = 118.14^\circ$ at room temperature. The distances between the atoms are in Å. The single-, double- and triple-bond lengths are 1.428 Å, 1.356 Å and 1.191 Å (Fig. 1.10). From [10].

Table 2.5 A selection of substituents R with which the topochemical reaction of the diacetylenes has been investigated. The right-hand columns indicate the reactivities qualitatively for the case of thermal activation and for γ irradiation. Other substituents have been given by Enkelman. After [10].

Examples for Substituents R				
$R_1 - C \equiv C - C \equiv C - R_2$				
Name	R_1	R_2	therm	γ
DNP		$=R_1$	+++	-
TS6		$=R_1$	+++	+++
PD-TS		$=R_1$	+++	+++
CD ₂ -TS		$=R_1$	+++	+++
FBS		$=R_1$	+++	+++
IPUDO		$=R_1$	-	+++
NP/PU			-	+
NP/4-MPU			-	+
NP/MPU			+	+
		(-)(S) or (+)(R)		
DNP/MNP			+++	
TS/FBS			+++	
FBS/TFMBS			+++	

through the structure of the poly-diacetylene crystal (p-TS6) with the substituents $R_1 = R_2 = \text{CH}_2$ -paratoluyyl-sulfonyl-oximethylene. Its crystal structure (Fig. 1.10) is monoclinic and contains two polymer units in the unit cell. The polymer chain is planar and the triple bonds are conjugated with the double bonds.

2.4

Thin Films

Finally, thin films are also relevant to the organic solids; they are the subject of increasing interest in research and for applications. Such films, which in some cases consist of only one or a few molecular layers, can be prepared by various methods. Many of the early works on thin molecular films used **Langmuir-Blodgett films**. Such films are made up of amphiphilic molecules, i.e. of molecules which have regions that are hydrophobic and others that are hydrophilic. An example of these is stearic acid, $\text{C}_{17}\text{H}_{35}\text{COOH}$, in which the COOH group at one end is water-soluble, i.e. hydrophilic, and the long saturated aliphatic chain in contrast is hydrophobic. Amphiphilic molecules cannot be fully dissolved in water owing to their long aliphatic chains. They remain on the water surface with their hydrophilic end groups two-dimensionally dissolved, whereby the polar head groups of the molecules point downwards into the water (Fig. 2.21).

For their preparation, a drop of a solution of the desired material in a volatile organic solvent, immiscible with water, is put onto the surface of highly pure water

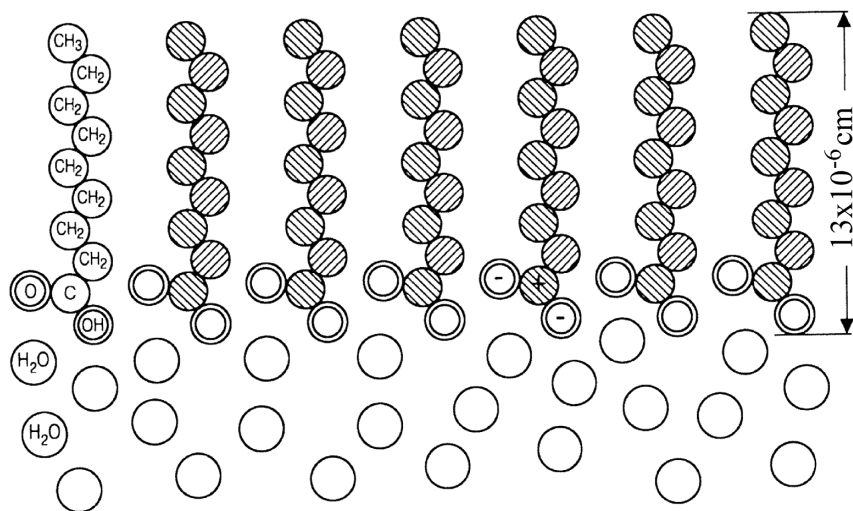


Fig. 2.21 Schematic of the arrangement of fatty-acid molecules on a water surface. The symbols mean: \bigcirc – water molecules, \bigcirc and OH – water soluble (hydrophilic) oxygen or hydroxyl groups, and CH_2 or CH_3 – water insoluble (hydrophobic) methylene or methyl groups in the saturated hydrocarbons (alkanes).

in a trough. The solvent evaporates and the molecules attached to the water surface can readily be compressed into a compact monomolecular film by means of a light lateral pressure in a so called Langmuir balance on the water-air interface. In these films, the molecules are parallel to each other and perpendicular or at an angle to the interface with a high packing density. They can be transferred to a solid substrate, for example a glass slide (cf. Fig. 2.22). This process can be repeated many times and thus thicker Langmuir-Blodgett films can be prepared, consisting of many monomolecular layers. It is, however, not easy to prepare Langmuir-

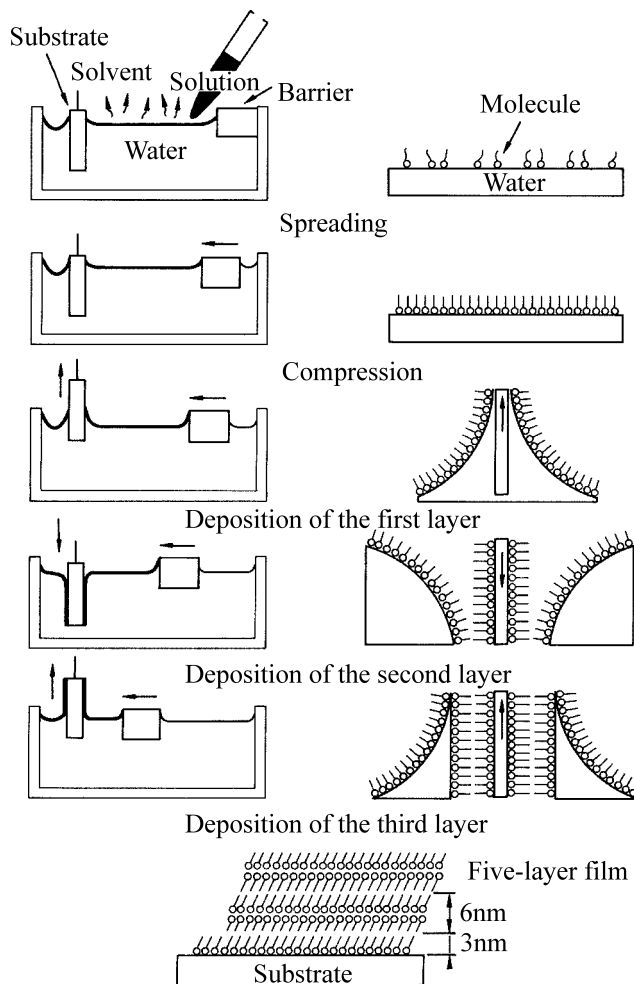


Fig. 2.22 The preparation of Langmuir-Blodgett films. Amphiphilic molecules, i.e. molecules with a water-soluble and an insoluble end, dissolve in a two-dimensional mode on a water surface (so called *spreading*). They can be compressed into

a two-dimensional monolayer and attached to a carrier by dipping and withdrawing it. This process can be repeated many times. In this way, one can produce ordered thin films with an arbitrary thickness.

Blodgett films which are free from defects or impurities over large areas. If this is intended, extreme care must be taken with the purity of the substances used, especially the water. It must in any case be free of surface-active impurities. Other disadvantages of LB films are their lack of mechanical strength and their limited thermal stability.

Both the molecules (also colouring agents, biologically relevant molecules and donor-acceptor complexes) and the liquid phase (instead of water for example glycerin or mercury) can be varied over a wide range. Thus, one can prepare a great variety of organic films. To be sure, the molecules must have rather special properties owing to their required amphiphilic nature.

Another method of preparing thin films, which is likewise limited to a particular class of molecules, is the technique of **self organisation** or self assembly [12]. Here, the molecule needs to carry an end group which can bond chemically to a substrate; we are thus dealing with a process of chemisorption. The best-known such end groups are the thiols, (R-SH, where R is the actual molecule), which can readily be attached to many organic molecules. The end groups can form a covalent bond, in particular with a gold substrate, and thus attach the molecules to the substrate. These molecules, bound on one side, can then, as with Langmuir-Blodgett films, organise themselves into more or less compact layers standing up from the surface of the substrate.

To obtain ordered films by self organisation, the molecules must be readily mobile on the substrate surface, so that they can find their optimal sites in the film. The intermolecular forces must be sufficiently strong so that a high packing density of the molecules on the surface is produced. The possibility or the tendency of organic molecules to form complex structures through self organisation is, by the way, not limited to the preparation of molecular films. It is also important for many structures and processes in biology.

A nice example of the self organisation of molecules from a solution onto a surface is shown in Fig. 2.23. Here, molecules of cyclo [12] thiophene – C[12]T for short – are arranged on the surface of highly-oriented pyrolytic graphite or HOPG, which readily allows the preparation of ideal surfaces. The C[12]T molecule is a planar ring consisting of 12 thiophene units. Every second thiophene molecule is substituted with two butyl side groups. As seen in the STM image in Fig. 2.23 (left), the molecules order on the HOPG surface at its interface with the solution, into a hexagonal lattice with the parameters $a = 2.36$ nm, $b = 2.39$ nm, and $\alpha = 59^\circ$. Details are given by Mena-Osteritz [13]. More information about self-assembled monomolecular layers of organic molecules (SAM) is given in Problems 2.2 and 2.3.

The most flexible methods, which can be applied in principle to nearly all molecules and which provide the most important techniques for the preparation of organic molecular films, are vacuum evaporation and molecular-beam epitaxy (cf. [14]). In both methods, the substance required is evaporated or sublimed and captured on a substrate which is cooled as necessary. In molecular-beam epitaxy, the substrate must be an (inorganic) single crystal. The nature of the substrate's surface, its temperature and the velocity of evaporation or sublimation, adjustable

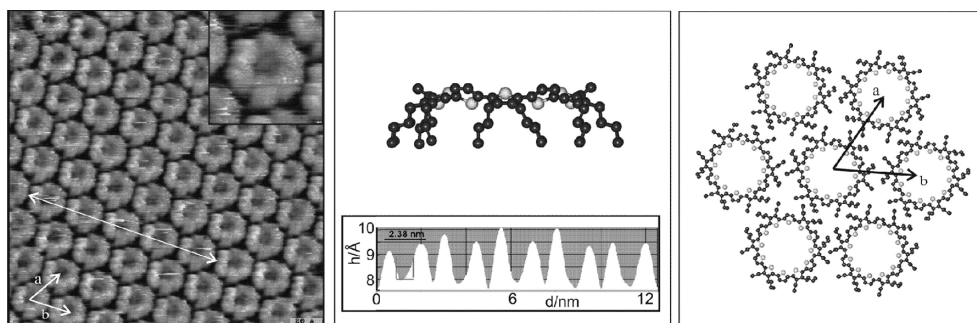


Fig. 2.23 The self organisation of cyclo [12] thiophene (C[12]T) on HOPG (Highly-Oriented Pyrolytic Graphite). The section shown on the left is an area of $28 \times 28 \text{ nm}^2$. At the upper right in the picture, an enlargement of $6.7 \times 6.7 \text{ nm}^2$ is shown. In the centre section, below, we see an STM scan along the white line in the left image, passing over seven

macrocycles. Above centre: the calculated equilibrium conformation of C[12]T. Right-hand portion of the figure: computed model of a two-dimensional hexagonal crystal of C[12]T. With kind permission of Ms. Mena-Osteritz [13]. Compare the coloured plate in the Appendix.

through the vapour pressure, are the most important parameters which determine the structure.

When the substrate is so cold that practically no motion of the arriving molecules on its surface can take place, then the molecules remain at the positions where they land. Since these positions are statistically distributed without any ordering, one in general obtains amorphous layers without measurable crystalline order at low temperatures. It is, however, surprising to observe how mobile even larger molecules such as anthracene can be on substrates even only a little above 4 K.

If the temperature of the film of molecules deposited onto a substrate at low temperature is slowly increased, their mobility also increases. The molecules can then move across the surface and can form an ordered structure which is energetically more favourable than the disordered amorphous phase. When the interactions of the evaporated molecules with each other are stronger than those with the substrate material, then the molecules can collect together to form island structures. The size and spacing of the islands depend particularly on the amount of the substance which was evaporated. With increasing temperature, a collection of microcrystals is formed on the substrate.

If, on the other hand, there is a stronger interaction between the substrate and the evaporated molecules than between the molecules themselves, then the molecules will tend to cover the substrate optimally, i.e. completely. Covalent bonds can also form between the molecules and the substrate, leading to changes in the molecular structure. One then refers to epitaxy, when the lattice parameter of the (single-crystal) substrate is commensurable with those which can exist in the crystalline phases formed by the evaporated molecules. Examples of epitaxy are shown in Figs. 2.23 and 1.9.

It should be mentioned that in principle, the same structures, island formation or epitaxy can also be obtained by evaporating the molecules onto a substrate which is already being held at a correspondingly higher temperature.

It is interesting to observe which structures the film adopts with increasing thickness during its deposition or on tempering. When the first molecular layers on the substrate have a structure determined by the latter, then this influence will decrease in importance with increasing layer thickness. Finally, the substance will continue to grow in its own crystal structure. This competition between different forces can lead to the occurrence of complex transition regions and to strains in the layers, or also to the formation of different phases.

There are also substances which sublime at higher temperatures and which can be collected at not-too-low temperatures (e.g. at room temperature) as large, very thin, free-standing crystal platelets of high quality. Among these are for example anthracene and pentacene. More about this subject will follow in Sect. 3.3, on crystal growth.

2.5 Inorganic-Organic Hybrid Crystals

An interesting class of crystals are the hybrid crystals, in which an organic partner is built into an inorganic crystal lattice in a stoichiometric ratio. A nice example of this are the lead halides.

Many lead halides grow from solution to form crystals with the Perovskite structure. Organic molecules with a functionally substituted end group which can act as a chemical anchor, such as NH_3 , can be built into the Perovskite layers, so that the crystal structure consists of alternating layers of the lead halide and the organic molecules. Two-dimensional organic crystals can also be formed by self organisation in an extended Perovskite structure. The general formula for the crystals is $(\text{RNH}_3)_2 \text{PbX}_4$, where R is an organic group, e.g. $\text{CH}_3-(\text{CH}_2)_n$ or $\text{C}_6\text{H}_5-\text{CH}_2)_2$, and X is a halogen. An example with anthracene as chromophore is shown in Fig. 2.24.

In the optical spectrum, one observes on the one hand the spectrum of the inorganic lead halide layers, with Wannier excitons as the lowest excited states and, on the other hand, spectra which are characteristic of the organic molecules. Here, Frenkel excitons are the lowest-lying excited states. With a suitable choice of the two partners, one observes energy transfer between the layers and can investigate the interaction effects between Wannier and Frenkel excitons [15, 16]. There are a large number of possibilities for varying both the inorganic as well as the organic partner. This appears to be a potentially productive field for further research.

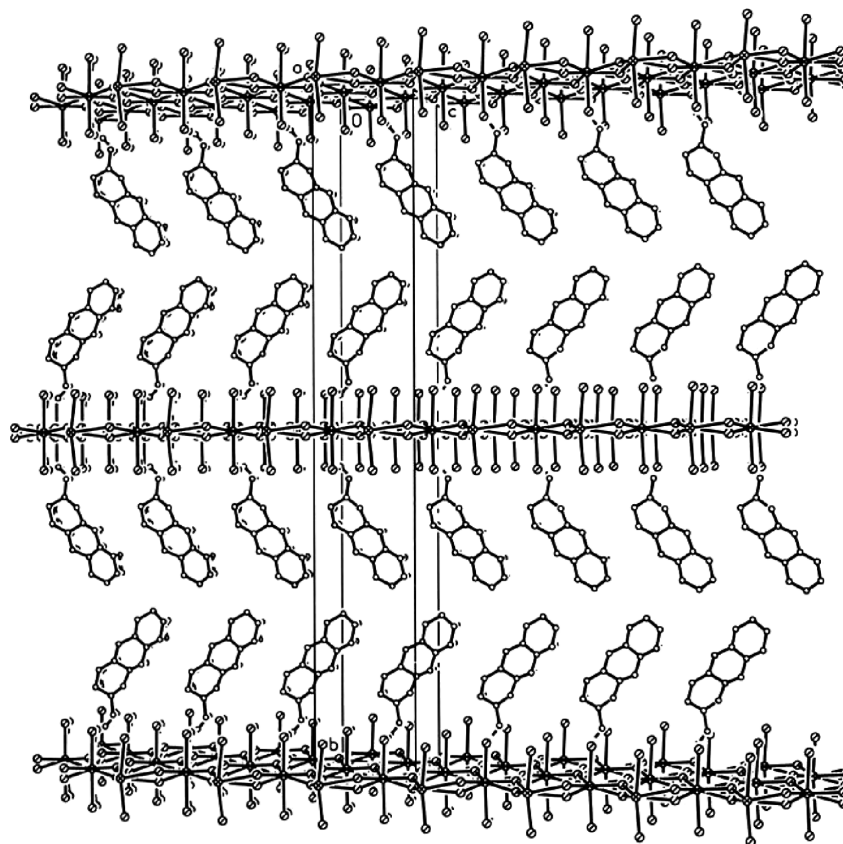


Fig. 2.24 The crystal structure of $(\text{anthryl-CH}_2\text{-NH}_3)_2 \text{PbCl}_4$. The lead halide layers are separated from each other by molecular double layers. The a , b , and c axes of the unit cell are shown in the figure. From [16].

Problems

Problem 2.1. Heat of sublimation:

Estimate the heat of sublimation of the anthracene crystal from the atom-atom potentials using the parameter set of Williams (Table 2.2 and Fig. 2.2b).

Problem 2.2. Self-assembled monolayers 1:

Self-assembled monomolecular layers of organic molecules (SAM) on a substrate can be prepared as follows (Fig. P2.1):

- a. The substrate is for example a Au single crystal with a (111) orientation, or a polycrystalline evaporated film, likewise with a preferential orientation of (111). The molecules are e.g. linear alkane chains, substituted at one of their

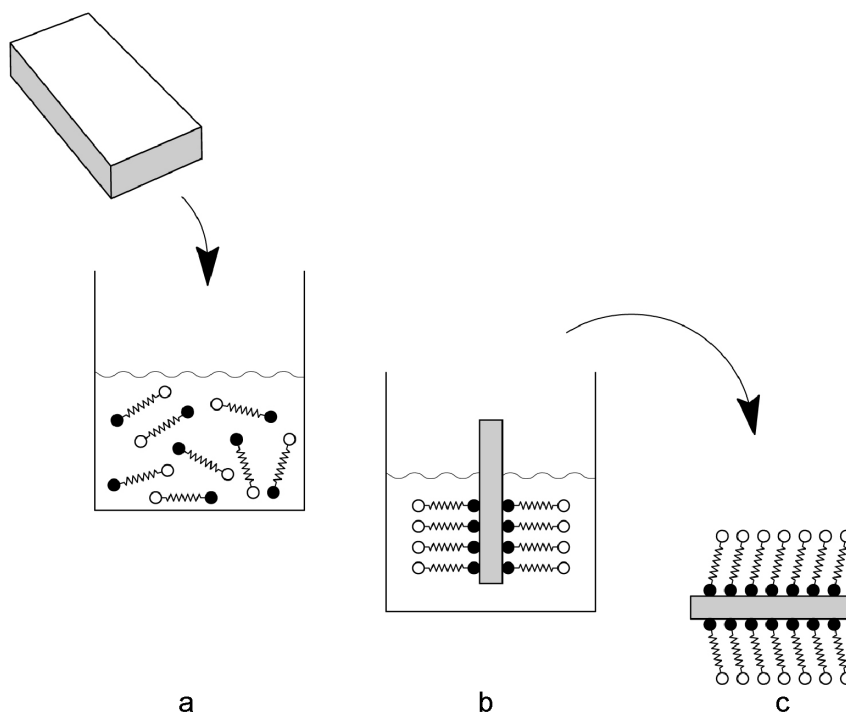


Fig. P2.1 Self-assembled monolayers (SAM).

ends by a thiol group (dark circles). They are thus *n*-alkane-thiols. The free ends may be substituted with arbitrary groups, for example with $-\text{CH}_3$ if hydrophobic layers are desired, or with $-\text{OH}$ or $-\text{COOH}$ if hydrophilic layers are needed (open circles).

- The substrate is dipped into the solution. It is left there a sufficient time to allow the reaction to go to completion, i.e. to obtain an optimal arrangement of the covalently-bound molecules on the substrate.
- The molecules are firmly bonded to the substrate. It can now be removed from the solution for further processing. Owing to the covalent bonding of the molecules to the substrate, these films are considerably more stable than LB films.

Estimate the number of molecules in an *n*-alkane-thiol SAM monolayer within the diffraction-limited focus of an optical microscope.

Problem 2.3. Self-assembled monolayers 2:

- One can follow the process of layer formation “*in situ*”. In the experiment described in Problem 2.2 (M. GRUNZE, *Physica Scripta* **T49**, 711 (1993)), the surface-sensitive method of second harmonic generation determines the time for formation of the layer to be 10 min., while ellipsometry measurements yield a time of 40 min. until thermal equilibrium is reached. Can

you explain this discrepancy without knowing the details of the two analytic methods?

- b. From systematic NEXAFS (near edge X-ray absorption fine structure) measurements, one finds that only when they have a certain minimum length ($n \geq 12$) do alkane-thiols form well-ordered films in which all the alkyl chains are stretched out and (for $n = 22$) form an angle of 35° with the normal to the plane of the substrate. Try to justify this effect.
- c. On studying the film with a scanning tunneling microscope, one can identify holes of 20 to 60 Å diameter and 2.5 Å depth. What is the cause of these?

Problem 2.4. Coulomb interactions in radical-ion salts

Estimate the contribution of the Coulomb binding energy in the radical-cation salt $(\text{Fa})_2^+\text{PF}_6^-$ (Fig. 2.18). To do so, choose a block B of 128 ($= 8 \times 4 \times 4$) unit cells EC with the following simplifying assumptions: $S(a, c) = 90^\circ$, $a = 0.66 \text{ nm}$, $b = c = 2a$. That is, assume a tetragonal lattice. Further assume that the charges of the $(\text{Fa})_2^+$ cations and the PF_6^- anions can be represented as point charges (Fig. P2.2). Now add up the Coulomb interaction energies of the central anion with all the ions in B. Compare the result with the van der Waals bonding of an arene molecular crystal composed of molecules with a similar number of carbon atoms as the Fa molecule.

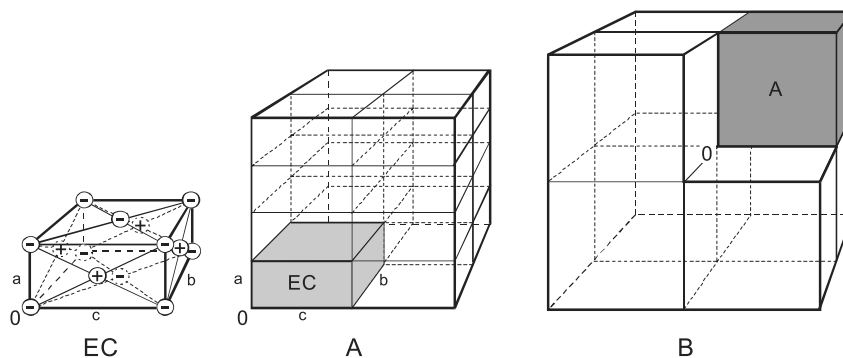


Fig. P2.2 EC: unit cell. A: A block of 16 unit cells, EC. b: A block of 8 blocks of type A, i.e. 128 unit cells; for clarity, the 8th block A (in front, upper right) is not shown.

Literature

Monographs

- | | |
|---|---|
| <p>M1 See also textbooks on physical chemistry, e.g. B. H. KUHN and H. D. FÖRSTERLING, <i>Principles of Physical Chemistry</i>, Wiley (1999)</p> | <p>M2 F. VÖGTLE, <i>Supramolekulare Chemie</i>, Teubner, Stuttgart (1992)</p> <p>M3 E. A. SILINSH, <i>Organic Molecular Crystals</i>, Springer, Heidelberg (1980)</p> |
|---|---|

- M4** N. KARL, *Organic Semiconductors*, in: *Landolt-Börnstein*, Vol. 17, Subvol. i, Springer, Heidelberg (1985)
- M5** A. I. KITAIGORODSKII, *Organic Chemical Crystallography*, Consultants Bureau, New York (1961)
- M6** A. I. KITAIGORODSKII, in: *Molecular Crystals and Molecules*, Academic Press, New York (1973)
- M7** M. POPE and C. E. SWENBERG, *Electronic Processes in Organic Crystals and Polymers*, 2nd ed., Oxford University Press (1999)

References

- 1** R. A. BUCKINGHAM and J. CORNER, *Proc. Roy. Soc. of London A* **189**, 118 (1947)
- 2** A. KITAIGORODSKII, *J. Chem. Phys.* **63**, 9–16 (1966)
- 3** D. E. WILLIAMS, *J. Chem. Phys.* **45**, 3770 (1966)
- 4** K. LONSDALE, *Proc. Roy. Soc. (Lond.) A* **123**, 494 (1929)
- 5** J. M. ROBINSON, *Organic Crystals and Molecules*, Cornell University Press (1953)
- 6** J. BLÖMKER and W. FREY, *Z. Kristallogr.* **215**, 265 (2000)
- 7** P. J. LANGLEY and J. HULLIGER, *Chem. Soc. Rev.* **28**, 279 (1999)
- 8** G. WEGNER, *Z. Naturforsch. (b)* **24**, 824 (1969)
- 9** M. SCHWOERER, E. DORMANN, TH. VOGTMANN and A. FELDNER, in: *Macromolecular Systems: Microscopic Interactions and Macroscopic Properties*, Wiley-VCH, pp. 122–180 (2000)
- 10** V. ENKELMANN, in: *Advances in Polymer Sciences* **63**, Polydiacetylenes, pp. 92–136, edited by H. J. Cantow, Springer (1984)
- 11** D. KOBELT and E. F. PAULUS, *Acta Cryst.* **B30**, 232 (1974)
- 12** G. M. WHITESIDES, *Selbstorganisation als Konstruktionsprinzip. Spektrum der Wiss. Special* **4** (1995)
- 13** E. MENA-OSTERITZ, *Adv. Mater.* **14**, 609 (2002)
- 14** ST. R. FORREST, *Chem. Rev.* **97**, 1793 (1997); S. R. FORREST, *Nature* **428**, 911 (2004)
- 15** M. BRAUN, W. TUFFENTSAMMER, H. WACHTEL and H. C. WOLF, *Chem. Phys. Lett.* **303**, 157 (1999)
- 16** M. BRAUN and W. FREY, *Z. Kristallogr.* **214**, 335 (2000)
- 17** T. J. KISTENMACHER *et al.*, *Acta Cryst. B* **30**, 763 (1974)

3

Purification of Materials, Crystal Growth and Preparation of Thin Films

As in every branch of solid-state physics, but especially in dealing with organic solids, it is very important to take great care in the preparation of the samples, in the effective purification of starting materials, and the growth of well-defined crystals or fully-characterised epitaxial crystalline or non-crystalline thin films. These steps form the fundamental basis for all investigations with and on these materials. Crystal growth, thin-layer preparation and extreme purification make up an art, which however with consistency, imagination and sufficient effort can be thoroughly mastered. It is unwise to try to economise on these efforts if one wishes to attain the goal of making progress in understanding the physical properties of molecular solids.

3.1

Purification

In later chapters, we shall show that impurity concentrations which one might consider to be extremely small, e.g. 1 ppm or 10^{-6} impurity molecules per host molecule, are often and decisively too large by orders of magnitude if the properties of the pure host material are to be investigated successfully. How can the required high degrees of purity be achieved? In any case, the starting material, whether commercially available or synthesised in the laboratory, must nearly always be purified to a high degree before one can begin the process of crystal growth. When extreme purity is required, chemical methods are in general much less successful than physical methods. As a rule, various procedures must be applied consecutively and purification steps must be repeated several times.

Special Chemical Methods are particularly important in cases in which impurities are difficult to remove using physical methods. In these cases, it is sometimes possible to resynthesise the substance to be purified into a material which is more readily purified. After the successful purification, the original substance must then be reconstituted. Chemical impurities can also be produced by oxygen, water, other solvents or by light, i.e. photochemically. Many organic compounds react sensitively to these influences. It is therefore often necessary to work under vacuum, in ultrahigh vacuum (UHV) or under inert gas, and to exclude light.

Most of the **physical methods** are based on processes involving phase separation. The most important are

- **Distillation**, presuming that the substances do not decompose thermally in the process;
- **Recrystallisation**, possibly repeated several times, presuming that the possibility of inclusion of solvent molecules ("water of crystallisation") is acceptable;
- **Chromatography**, a very efficient process in which however it is difficult to obtain the highest degree of purity; and finally
- **Sublimation** and
- **Zone refining**, the two processes with which the greatest levels of purification can be attained.

We will now describe these last methods in more detail.

Chromatography is a relatively simple method. It is based upon the fact that different molecules are retained to differing degrees by an adsorbing material. Typical adsorbents are aluminium oxide or silica gel. In liquid chromatography, the absorbent is placed in a long tube through which the starting material, which is to be purified, is carried by a suitable solvent. The more strongly a molecule is adsorbed, the higher up in the column it will be retained and this will allow the (less strongly adsorbed) starting material to be collected at the outlet in purified form. To be sure, even the more strongly adsorbed impurities reach the end of the column (with a reduced concentration), as well as those impurities which are less strongly adsorbed. It follows that the efficiency of this process depends essentially on the properties of the molecules involved and on those of the solvent and the adsorbent. The procedure can readily be repeated or extended to give a continuous process. Using chromatography, the highest degrees of purity cannot be attained. Its special value lies however in the fact that one can frequently obtain a strong reduction in the concentration of relatively crude contaminants. It is thus often suitable as a preliminary step before further purification by sublimation or zone refining.

Purification through **sublimation** is based on the fact that different molecular solids in general differ in their sublimation pressures and furthermore in their condensation temperatures. In the simplest case, the substance to be purified is heated in a tube which is evacuated or filled with protective gas, in which the sublimed material can be collected on a cold finger or a cooler region. With this simple procedure, which can also be repeated as often as needed, impurities cannot be removed if their sublimation pressure is too close to that of the substance to be purified. A similar but more effective procedure is **gradient sublimation** (Fig. 3.1). The material to be purified is sublimed along a temperature gradient. The sublimed molecules are transported with the aid of an inert carrier gas (N_2 , Ar) along the temperature gradient into the condensation region. When the different components of the sublimed material condense at different temperatures, they will be deposited at different locations along the tube. The inert carrier gas can be replaced or complemented by a reducing gas (H_2); this permits the simultaneous removal of

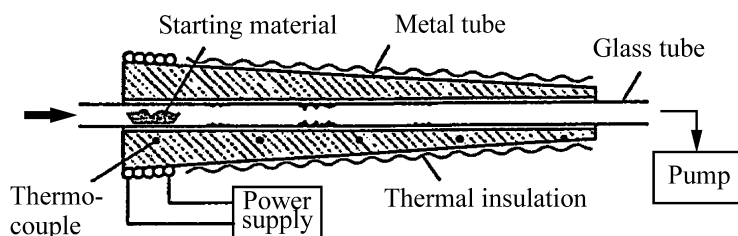


Fig. 3.1 Gradient sublimation. Here, a suitable temperature gradient is produced using a conical metal tube which is heated at one end – the inlet – and held at a constant, lower temperature at its other end. Molecules of the starting material which is initially in the inlet region sublime and are transported by a

current of inert gas (N_2 , Ar) at a pressure in the range of 1 mbar into the cooler region, where the various fractions of impurities and the purified material are deposited at various locations, depending on the temperature. The process can be repeated. From [1].

oxygen impurities. With the gradient sublimation process, one can attain extremely high degrees of purification. The apparatus can also be used to grow highly pure crystal platelets, since the condensation of many organic substances yields single-crystal platelets under suitable conditions of pressure and temperature. Examples of this are given in Sect. 3.4.

For all substances which melt without decomposition, **zone refining** is indeed the most effective method of purification. Following the development of the method in 1952 by Pfann for inorganic semiconductors, it was rapidly extended to organic materials [2]. Many sequential repetitions of the purification procedure can be carried out quite readily in the zone-refining process.

The principle of the process is shown in Fig. 3.2. A melting zone is moved from the beginning to the end of a tube made of glass or Pyrex containing the solid

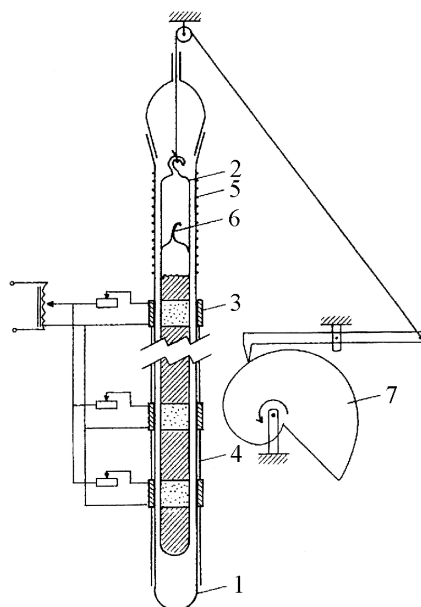


Fig. 3.2 An arrangement for zone refining. With this apparatus, several or many melting zones can be moved intermittently through the material to be purified. The apparatus consists of a tube made of Pyrex or quartz glass 1, on which ca. 20 heating elements 3 are wound, with glass tubes 4 as spacers. The material to be purified is enclosed in an additional tube of Pyrex or quartz glass from which air is excluded 2. The latter tube is closed off by a break joint 6. Thus, one can remove parts of the purified material without contact to the air. The Archimedean spiral 7 produces the required intermittent up and down motion of the tubes 2. After [1].

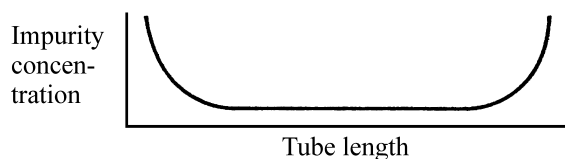


Fig. 3.3 A schematic representation of the distribution of impurities in a zone-refining tube. The impurities can, depending on their properties, be collected at either end, i.e. at the beginning or the end of the zone-refining tube.

material to be purified. Impurities which are more soluble in the melt than in the solid are then moved along the tube and concentrated at its end. Impurities which are less soluble in the melt exhibit the reverse behaviour. After repeated passes of the melting zone, they are concentrated at the beginning of the tube. A concentration gradient of the impurities as shown in Figs. 3.3 and 3.4 is then obtained.

The procedure can be repeated many times without difficulties. Furthermore, it is easy to move not just one, but many melting zones one after another through the tube. The effect of zone refining can in principle be calculated theoretically, if the distribution coefficients of the impurities are known. However, in practice such calculations are very difficult, since there are often many different impuri-

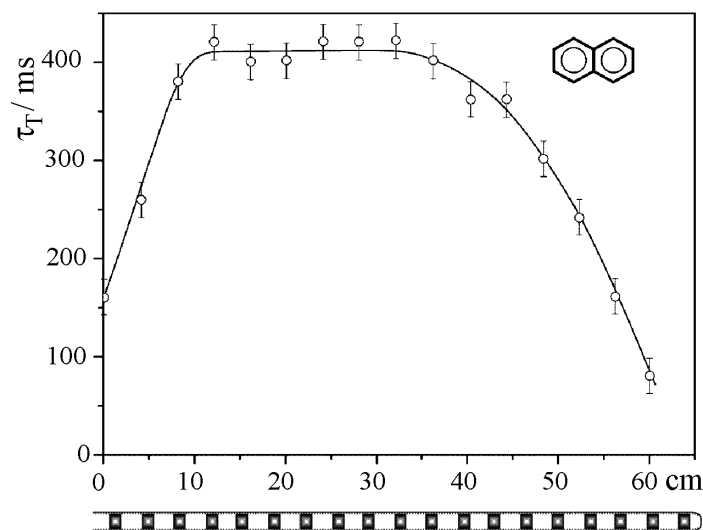


Fig. 3.4 In a tube filled with zone-refined naphthalene, in the centre region – where the purity is highest – a triplet-exciton lifetime of $\tau_T = 400$ ms (at room temperature) is measured as an indicator of the purity attained. At the beginning of the tube, the lifetime is ca. 160 ms, and at its end, it is less than 80 ms.

The purest region – here with a length of ca. 30 cm – can be separated and used as starting material for further purification. This purity test can be carried out on the sealed tube. The zone-refining tube shown here (at the lower edge of the picture) contains 16 melting zones. From [4].

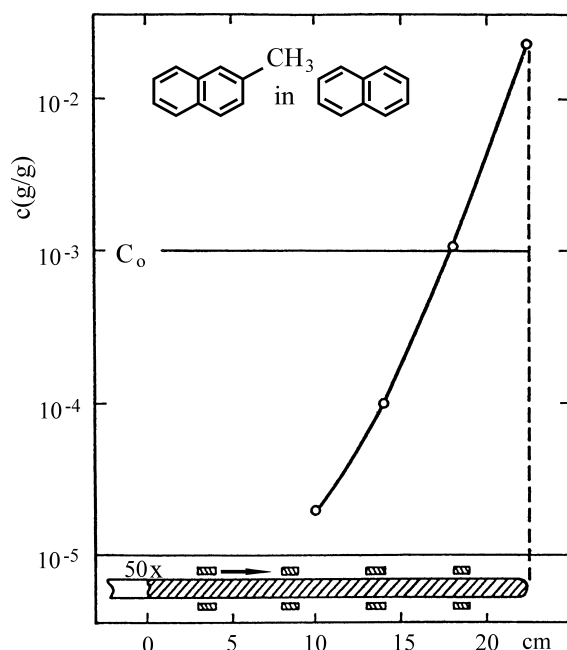


Fig. 3.5 The distribution of β -methyl-naphthalene in naphthalene after 50 passes in a zone-refining apparatus measured by gas-phase chromatography and mass spectrometry. Here, the purification effect is very strong; therefore, only one relatively short zone-refining tube was used (below). The measurement is of course carried out *ex situ*. c_0 is the concentration before purification, c the concentration measured afterwards.

ties. The apparatus is therefore automated to permit several hundred passes of the melting zone in the course of some days, and the purification is continued until a stationary distribution of impurities is attained. In favourable cases the distribution can be measured from outside the apparatus. In the case that the impurities are fluorescent, one can for example measure their fluorescence intensity. In the example shown in Fig. 3.4, the lifetime τ_T of triplet excitons (cf. Sect. 6.9) was determined. Another example, in which the impurities were determined by gas-phase chromatography, is shown in Fig. 3.5.

3.2 Highest Purity

A major problem in the production of high-purity organic crystals with an impurity content below 1 ppm is the qualitative and quantitative detection of the impurities. In the ppm region, gas-phase or liquid chromatography is usually sufficient, possibly together with a mass spectrometer (compare Fig. 3.5) and, for identification,

one or more spectroscopic methods (luminescence, IR, ESR ...). If still higher demands are made on the purity desired, other methods are however necessary.

For extreme purification, the total number of impurity molecules remaining at the end of the process is in general hard to measure and often also not very interesting. One is rather interested in specific impurities which even at the lowest concentrations still exert a serious influence on certain physical processes. The specific methods of measurement for these impurities are often based on the detection of the physical process which is influenced by the particular impurities. For such impurities one seeks specific detection methods.

One such method is sensitised fluorescence (see additional remarks on this subject in Chap. 6). Here, the detection limit for fluorescing compounds lies at less than 10^{-7} molecules/host molecule or ca. 10^{15} impurity molecules per cm^3 . Fig. 3.6 shows as an example of such a measurement the detection of β -methyl-naphthalene in naphthalene. Still more sensitive is the method of sensitised delayed fluorescence (Sect. 6.9). Here, the detection limit is at ca. 10^{-11} molecules/host molecule or 10^{11} impurity molecules per cm^3 [5, 6].

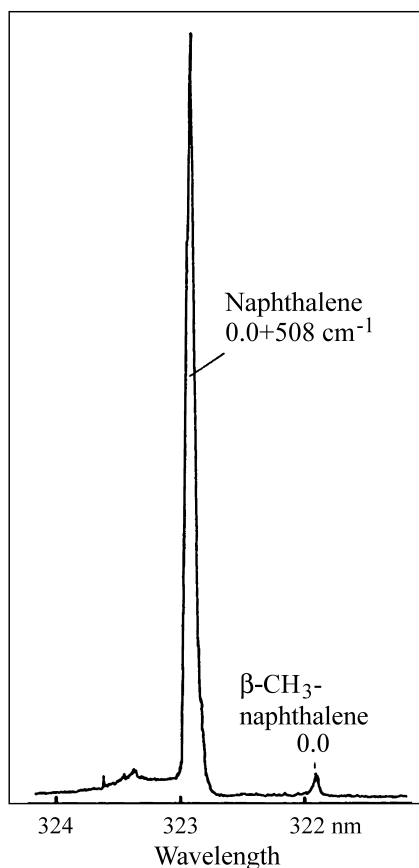


Fig. 3.6 In the fluorescence spectrum of naphthalene at 4.2 K, the impurity concentration of β -methyl-naphthalene can be estimated from the intensity ratio of a vibronic naphthalene line and the 0.0 line of β -methyl-naphthalene to be $3 \cdot 10^{-7}$. After [3].

Another very sensitive method is measurement of the lifetime of triplet excitons (Sect. 6.9), especially in aromatic molecular crystals. It can be very sharply decreased by specific impurities. Here, again, a detection limit of 10^{14} impurity molecules/cm³ can be attained [4]. An example is shown in Fig. 3.4.

Other methods with high detection sensitivity are based on the measurement of the electrical conductivity or the mobility of charge carriers and its modification by trapping. These can be due to structural defects or to impurity molecules. Free charge carriers in organic materials with their generally very low intrinsic charge-carrier concentrations can be produced either by injection from metallic electrodes, by field-effect doping, or by thermal or optical excitation of donors or acceptors. They can also be released thermally or through photoexcitation from traps, donors or acceptors. Thus, using photocurrent excitation spectroscopy, the detection limit for charged traps could be enhanced down to 10^{-12} mol/mol [7]. The investigation of space-charge limited currents can also permit measurement of extremely small concentrations of guest molecules. See Chap. 8 for more details.

3.3 Crystal Growth

Some purification methods are connected with the growth of single crystals. On the whole, the growth of organic crystals is an independent process which must be carried out with great care. There are growth methods starting from the gas phase, from the melt and from liquid solutions, as well as electrocrystallisation.

From the **gas phase**, i.e. by sublimation, all substances may be crystallised if they can be sublimed without decomposition. Good quality, large single crystals in the range of cm³ can be obtained by plate sublimation (Figs. 3.7 and 3.8). The sublimation chamber has the form of a flat pillbox with a thickness of a few cm. It can be filled with inert gas. The bottom plate and the lid of the pillbox are held at slightly different temperatures, so that the substance slowly sublimates from below to the top of the chamber and crystallises there. To obtain large, high-quality single crystals, the apparatus is operated over a period of many days following the formation of a good seed crystal. With this method, mixed crystals can also be grown, consisting of two or more different molecular species.

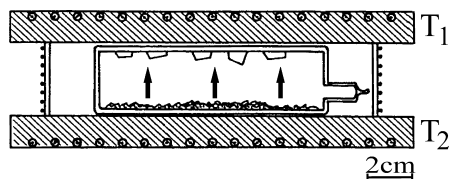


Fig. 3.7 A setup for plate sublimation. The temperature T_1 is somewhat lower than T_2 , so that the sublimate precipitates onto the upper wall and can grow into a single crystal if the process is carried out sufficiently slowly. After [3].

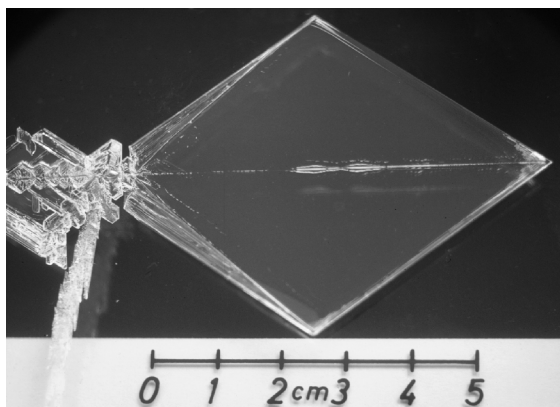


Fig. 3.8 A large anthracene crystal, prepared by plate sublimation under an inert gas atmosphere, 60×60 mm in size and with a thickness of 0.4 mm. From [3]. Compare the coloured plates in the Appendix and on the cover.

Using rapid growth from the vapour phase, one obtains in many cases extremely thin but crystallographically perfect platelets in a very simple manner; with thicknesses in the range of μm , they can have surface areas of cm^2 [8] (see also Fig. 3.9). Such crystals, which are frequently connected to the substrate only at a corner or an edge, but otherwise grow as a free-standing structure, have the highest degree of structural perfection among all known types of crystals. To be sure, only a single crystal orientation can be obtained in this way, i.e. that with its surface normal parallel to the direction of slowest growth. In the case of anthracene, this is the c direction. Often, the crystal structure requires that the seed crystals grow much more

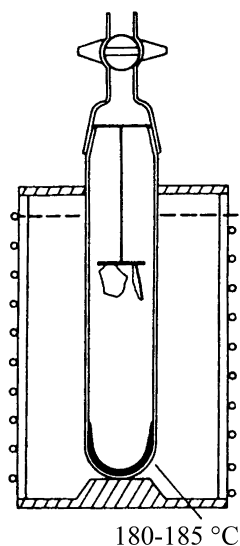


Fig. 3.9 An apparatus for the preparation of large, very thin anthracene crystals (flitter, thicknesses less than $1 \mu\text{m}$). The crystal growth takes place under an inert gas atmosphere very quickly following rapid heating of the chamber. From [8].

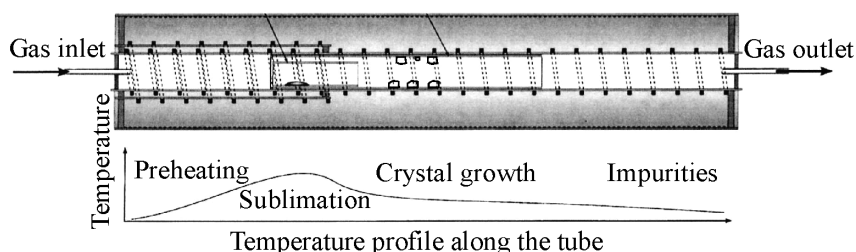


Fig. 3.10 A setup for carrying out gradient sublimation and crystal growth simultaneously. In three concentric glass tubes, which are heated to varying degrees, there is a flow of inert or reducing gas. Sublimation of the starting material takes place along the length of the apparatus, leading to the growth of thin crystal platelets and the precipitation of impurities. From [9].

rapidly along the edges than from the surface. In this way, platelets are formed with a ratio of length and breadth to thickness which can easily exceed 10^5 . The success of this method depends strongly on the number of seed crystals which form – thus upon the surface area for condensation of molecules, on the gas atmosphere in which the growth takes place, and on the rate of heating of the chamber.

The method of **gradient sublimation** with a carrier gas, as already described with reference to purification, has in recent years been employed to produce excellent single-crystal platelets. The combination of purification and crystal growth is carried out in the following manner [9, 10] (cf. also Fig. 3.10): along the length of a tube, a temperature gradient and a flow of gas (N_2 , Ar) are maintained. In the neighbourhood of the entrance to the tube, the temperature is high enough to cause the starting material (the source) to sublime; further along, it is reduced to the condensation temperature. Molecules which are heavier than the substance to be purified have a lower sublimation pressure and remain in the source region. Those with a higher sublimation pressure, i.e. lighter molecules, condense further along in the tube, past the region in which the base substance crystallises. Many volatile impurities are removed from the growing crystals by the carrier gas. Sublimation under convection in a carrier gas can also be carried out in a closed circulation system as a method for growing large (cm), thin (μm), highly pure crystals [11].

With this method, high-purity crystals of α -hexathiophene, pentacene and of many other substances can be grown. The method produces the best single crystals in terms of structural perfection and purity, and can be carried out rapidly (overnight). More details can be found in Kloc [10] and Laudise [9].

In crystal growth from the **melt**, the most important and widely-used procedure is that named for **Bridgman**. A closed ampoule containing the melted material is slowly lowered through a sharp temperature gradient so that the upper region containing the material lies above the melting point and the lower region lies below it (Fig. 3.11). One thus causes the melting zone to move through the material, but with only one melt zone and only one pass. Initially, the ampoule contains a

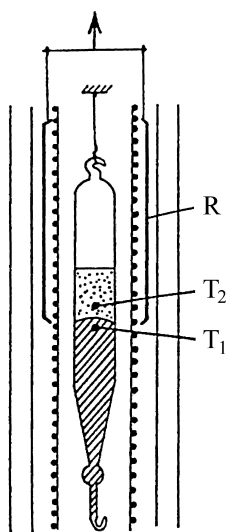


Fig. 3.11 A setup for crystal growth by the Bridgman method. Here, the whole growth tube is held at a uniform temperature T_1 slightly below the melting point of the substance to be crystallised. Melting at the temperature T_2 is effected by thermal radiation reflected from a half-silvered mirror on a glass cylinder R , which is slowly ($0.1\text{--}1\text{ mm/h}$) raised along the growth tube. Crystal growth begins at the lower end of the tube. The shape of this end is designed to assure that only one seed crystal can continue to grow, so that in the homogeneous volume of the tube, one single crystal grows. After [3].

capillary. It serves to select a seed crystal: if several seeds form, one of them will prove to be the fastest-growing along the capillary, and when the open volume at the end of the capillary is reached, this seed will guarantee the growth of a unique single crystal in the ampoule.

An advantage of this method is the possibility of growing large crystals. There are also disadvantages: the growing crystal has no characteristic crystallographic surfaces, but rather it takes on the shape of the ampoule. When the crystal grown at its melting point is cooled, it may undergo phase transitions. Owing to the different thermal expansion coefficients of the crystal and the ampoule, stresses occur. Even with very slow cooling and careful tempering and even with very cautious handling, e.g. in cleaving the crystal, samples grown by the Bridgman process contain noticeably more dislocations and structural inhomogeneities than those grown by other methods, especially with the sublimation technique.

When crystals are grown **from solution**, one has the advantage that an elevated temperature, as with melting or sublimation, is not necessary, so that thermal decomposition, stresses and the accompanying structural defects are less likely to occur. A considerable disadvantage is the fact that inclusion of solvent molecules within the crystals is often hard to avoid.

There are various methods for growing crystals from solution. The simplest is to allow the solvent to evaporate slowly and, through suitable experimental conditions, to prevent the number of seed crystallites from becoming too great. Another method consists of suspending a seed crystal in a saturated or slightly supersaturated solution and allowing it to grow further in a controlled manner.

In particular for crystal growth from solution, the morphology of the growing crystal and thus its habit can be critically influenced by additions of suitable impurity molecules at very low concentrations; this is called “dressing control”. The additive molecules are preferentially adsorbed onto a particular crystallographic plane

of the growing crystal with which they are topologically compatible, thus limiting the growth of this set of planes in favour of other directions within the crystal structure. The additive thus produces a relative increase in the growth of these planes relative to others, since the growth perpendicular to this plane is inhibited so that the growth rate in the corresponding direction is slower. In this way, for example, one can cause a substance to grow in the form of thin platelets or as long needles. More on this subject can be found in Vögtle [12], Chap. 6.

The growth and dissolution of crystals are opposing processes. It follows that an inhibitor for growth of a particular crystal plane can also influence the dissolution rate of the same plane. This increases the contrast between the protected planes and the exit points of defect lines, since there only a protected crystal plane is involved. In this way, etch craters are formed with whose aid one can count the defect lines (see also Fig. 4.8).

Donor-Acceptor-Crystals with an alternating arrangement of the molecules in their stacks frequently grow in the form of long needles along the direction of stacking. This can be explained by the fact that the charge-transfer interaction is strongest along the alternating stack direction. When the interactions between the stacks are sufficiently strong, then crystal platelets can also be formed.

A special procedure for crystal growth is **electrocrystallisation** (Fig. 3.12). With this method, the highly conducting radical-ion salts and the strong donor-acceptor crystals can be prepared. Here, the property of the crystals which is to be optimised – their electrical conductivity – is also employed for crystal growth: in electrocrystallisation, the crystals consisting of two differently-charged partners grow directly in the neighbourhood of an electrode. The crystals themselves thus form one of the two electrodes, which in turn effects an oxidation or reduction of the molecules. For example, in the electrocrystallisation of $(\text{DCNQI})_2\text{Cu}$ from a solution

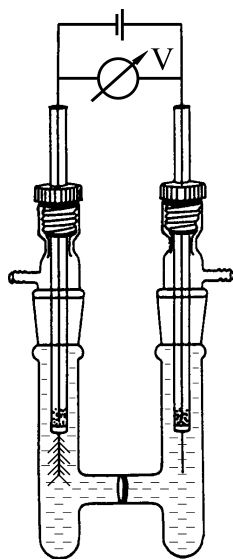


Fig. 3.12 An apparatus for electrocrystallisation. Depending upon the polarity, the crystals grow from a suitable solution when a voltage is applied to one of the two electrodes. A sintered-glass filter in the lower part of the apparatus prevents contamination from the reference electrode during the slow crystal-growth process.

containing both neutral (DCNQI) and CuI (cf. Fig. 1.12), the following processes take place: (DCNQI) accepts an electron according to the reaction $2(\text{DCNQI}) \rightarrow (\text{DCNQI})^- + (\text{DCNQI})^0$. CuI dissociates to $\text{Cu}^+ + \text{I}^-$. Finally, Cu precipitates onto the electrode according to the reaction $2(\text{DCNQI})^- + \text{Cu}^+ \rightarrow (\text{DCNQI})_2\text{Cu}$.

In the case of radical-cation crystals, the reaction follows a corresponding path. For example, the four steps for growth of $(\text{Fa})_2^+\text{PF}_6^-$ crystals are the following [13]:

1. $\text{Fa} \rightleftharpoons \text{Fa}^{\bullet+} + \text{e}^-$ (Oxidation)
2. $\text{Fa}^{\bullet+} + \text{Fa} \rightleftharpoons (\text{Fa})_2^{\bullet+}$ (Dimerisation)
3. $(\text{Fa})_2^{\bullet+} + \text{PF}_6^- \rightleftharpoons (\text{Fa})_2^{\bullet+}\text{PF}_6^-$ (Complex formation)
4. $\text{N} \cdot ((\text{Fa})_2^{\bullet+} + \text{PF}_6^-) \rightleftharpoons (\text{Fa})_2^{\bullet+}\text{PF}_6^-$ -crystal (Crystallisation)

Here, Fa = fluoranthene, ($\text{C}_{16}\text{H}_{10}$), and PF_6^- is the inorganic anion.

In this method, by varying the solvent, the voltage, and the current, one can control the crystal growth process. Often, thin needle crystals are formed. The growth process can take hours or in some cases days or weeks.

An interesting special case of crystal growth from solution are the macroscopic **polymer single crystals** of diacetylenene, the poly-diacetylene crystals. For their preparation, as a first step, macroscopic molecular crystals of substituted diacety-

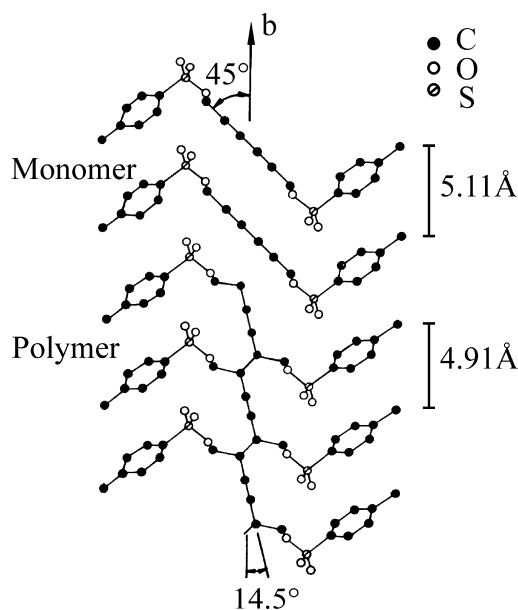


Fig. 3.13 Projections of the TS-diacetylene monomers (above) and polymers (below) onto the plane of the polymer backbone in the poly-diacetylene crystal. The lattice constant b of the monomer crystal and the polymer crystal differ by only 0.2 Å. Therefore, the crystal is not destroyed by the polymerisation: the macroscopic polymer crystal is formed from the macroscopic monomer crystal [13].

lene molecules are grown from solution in a common solvent. These monomer crystals are converted to polymer crystals in a second step [14]. In this process, the lattice constant along the b -axis changes only slightly (Fig. 3.13). This chemical reaction in the solid phase is termed a topochemical reaction. For some diacetylenes it can be activated thermally, for others by UV or γ -ray irradiation. In thermal activation, e.g. of the diacetylene TS6 (cf. Table 2.5), an activation energy of ca. 1 eV is necessary to form the dimers. The following reaction steps from the dimer via oligomers to the polymer are exothermic, with a polymerisation enthalpy of about 1.6 eV for each addition of an another monomer (Fig. 3.14). In photopolymerisation, the dimer is produced by the photoexcitation. The reaction then continues in the same manner as the thermal polymerisation, with a small activation energy and a large polymerisation enthalpy, i.e. exothermic and reversible [15].

The reactive species, which are responsible for the covalent bonding between the diacetylene molecules and thus lead to the formation of single-crystal polymer chains, have been identified spectroscopically [16, 17]. In the case of the shorter oligomers ($n \leq 6$), they are radicals, in which the two non-bonded electrons are each localised on one of the final C atoms of the oligomer. In the case of the long oligomers ($n \geq 7$), they are triplet-state carbenes, i.e. at each end of the oligomer

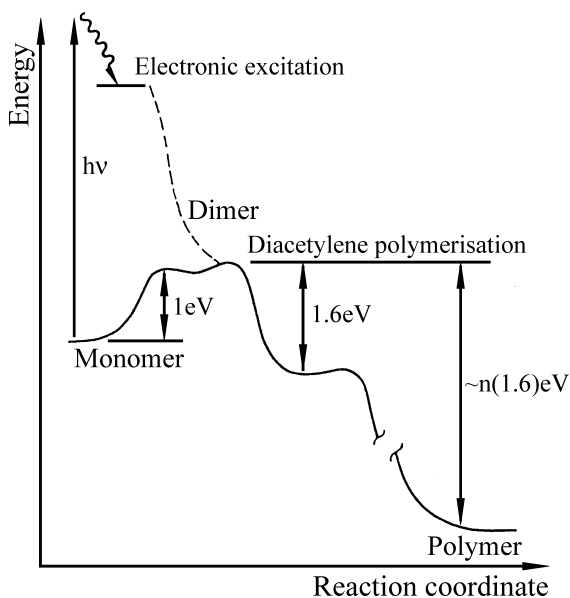


Fig. 3.14 The energy diagram of polymerisation of the TS-diacetylene crystal. In thermally-induced polymerisation, the first, thermally activated step is the covalent bonding of two monomers to form a dimer. The activation energy is about 1 eV. The bonding of an additional monomer onto the

dimer and to higher oligomers is an exothermic reaction with a reaction enthalpy of about 1.6 eV per monomer. The topochemical reaction of the monomer to a polymer crystal is therefore irreversible. In photoinduced polymerisation, the dimer is formed from an electronically-excited state. After [15].

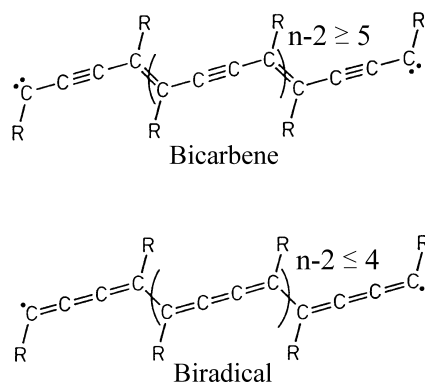


Fig. 3.15 Reactive species in the topochemical reaction of diacetylene crystals. The diradical and the dicarbene are the limiting structures for short and long oligomers, respectively. The free bonds at the ends of the oligomers react with the neighbouring monomers and thus form longer oligomers (see also Fig. 3.13). After [16, 17].

chain there are two free valence bonds with two electrons whose spins are not compensated, giving the total spin quantum number $S = 1$ (Fig. 3.15).

3.4

Mixed Crystals

Foreign molecules in a host crystal are **impurities** when they are unwanted. Otherwise, they are **guest molecules** or **dopants**. In these cases, all the purification and growth methods can be applied in a corresponding manner.

Guest molecules can often be inserted into the “simple” molecular crystals, whose crystal structure is determined solely by the van der Waals interactions, up to relatively high concentrations, if they are chemically and geometrically similar to the host molecules. Guest molecules are thus partially soluble in the host lattice. This is true, for example, in the cases of tetracene in anthracene or 2-methylnaphthalene and thionaphthene in naphthalene. Here, guest-molecule concentrations of up to the percent range can be obtained. The solubility limit for tetracene in naphthalene, in contrast, is in the range of 10^{-5} mol/mol. Such low solubilities, and still lower ones, are the rule for most guest molecules. This is indeed the basis of purification methods which are associated with crystal growth. Still higher concentrations than ca. 1% can be attained only in some special mixed-crystal systems. Examples are the fluorene-anthracene system, phenanthrene-anthracene, fluorene-dibenzofurane, and naphthalene- β -naphthol. More details can be found in Ref. [3].

An interesting special case is exhibited by the isotopic mixed crystals, e.g. perdeuteronaphthalene ($C_{10}D_8$) and naphthalene ($C_{10}H_8$), or perdeuteroanthracene ($C_{14}D_{10}$) and anthracene ($C_{14}H_{10}$). Here, the miscibility is nearly complete. When these crystals are grown from the melt, no noticeable separation of the

components occurs. These systems therefore play an important role in the investigation of highly concentrated mixed crystals. More on this subject can be found in Chaps. 6 and 7.

3.5

Epitaxy, Ultrathin Films

Usually, one speaks of epitaxial growth in cases where the structure of a film grown from the gas phase is essentially determined by the structure of the substrate. Epitaxy in the precise sense means that the crystal structure of the substrate is continued within the growing film. This is possible when the crystal structures of the substrate and the growing film are commensurate. Examples are shown in Figs. 1.9 and 2.23. Frequently, one refers also to Organic Molecular-Beam Epitaxy, OMBE.

In general, the structure of a film growing as a surface layer by evaporation or sublimation from the vacuum is also strongly influenced by its temperature, in addition to the structure of the substrate. If the latter is very low, for example 4 K, then the molecules which arrive at the surface of the substrate are hardly mobile; the evaporated film is then amorphous. A mobility of the molecules on the surface is necessary so that they can assume an ordered crystal structure after arriving at the growth surface, whether it is determined by the substrate structure or by the intermolecular forces of the evaporated molecules among themselves. This necessary thermal energy can be provided by warming and tempering the initially amorphous film; however, it can also be obtained by evaporating onto a substrate at a higher temperature. The optimal substrate temperatures must be determined empirically.

The preparation of well-defined thin or ultrathin crystalline films by sublimation or molecular-beam epitaxy is a technology which depends upon a large number of experimental parameters, which we cannot treat in detail here. Ultrahigh vacuum is in any case a prerequisite. More on this subject can be found for example in the review articles by Forrest [18].

The preparation of ultrathin films by the Langmuir-Blodgett method was already treated in Sect. 2.4. It is, to be sure, obviously very difficult to obtain films without defects or small holes in this manner.

Perhaps crystal film preparation by means of **self assembly**, which we also have already mentioned in Sect. 2.4, is the method of choice. One can obtain especially good films, that is, homogeneous and coherent films or self-assembling monolayers (**SAM**,) not from solution, but from the gas phase. For this purpose, one requires molecules with suitable end groups, which form a chemical bond with the substrate and remain perpendicular or canted relative to its surface, but parallel to one another. Examples of this kind of growth are thiol end groups on a gold substrate (cf. also Chap. 12). Another example are the trichlorosilane $-\text{SiCl}_3$ -end groups on suitably prepared Si surfaces. Such films are of interest for the fabrication of organic transistors [19]. More on this topic can likewise be found in Chap. 12.

An important goal is the preparation of films which are as far as possible free of defects, e.g. pinholes, which could lead to short-circuits in electrical measurements. The films should be sufficiently stable that electrodes (e.g. gold) can be attached to their free surfaces without the electrode material being incorporated into the film.

If, for example, alkane thioles or alkane silanes are used, then the thickness of the film is determined by the length of the molecules. With up to 20 CH₂ groups, film thicknesses of some nm are obtained. At the ends of the molecules pointing away from the substrate, various end groups can be attached. For example, with aromatic end groups and their mutual π - π interactions, the molecular film can be stabilised and sealed off. More details can be found e.g. in the review article by Schreiber [20], and in [19].

Problems

Problem 3.1. Contrast in transmission electron microscopy:

Imaging of organic molecules with the transmission electron microscope is possible only under favourable conditions. According to Freyer (J. R. FREYER, *Mol. Cryst. Liq. Cryst.* **96**, 275 (1983)), the following inequality holds for the resolution d_p of a molecule:

$$d_p \geq \frac{S/N}{C \cdot \sqrt{f \cdot N_{Cr}}}$$

In this expression, we have used the following symbols:

d_p = point resolution in Å (1 Å = 10⁻¹⁰ m)

S = required signal/noise ratio (ca. 5)

C = contrast (ca. 0.1 for one layer of scattering centres)

f = electron-efficiency factor (ca. 25%, i.e. only every 4th electron contributes)

N_{Cr} = damage threshold (in electrons per surface area (in Å⁻²)).

The contrast C is proportional to \sqrt{n} , where n is the number of scattering centres (atoms) which lie behind each other. A commercial microscope requires a dose of ca. 100 Å⁻² to attain a theoretical resolution of 1 Å (naturally, only the theoretical resolution is quoted in the specifications); this dose lies near the damage threshold N_{Cr} for organic molecules.

How many molecules would have to be stacked up to yield $d_p = 1$ Å? With hexadecachloro-copper-phthalocyanine molecules of thickness 3.4 to 3.8 Å, one obtains the typical layer thickness used for organic microscopy samples.

Problem 3.2. C₆₀ Langmuir-Blodgett film: C₆₀ is dissolved in benzene (concentration 1.297 · 10⁻⁴ mol/l) and spread onto water in a Langmuir trough. C₆₀ is water-

insoluble and hydrophobic, and forms a Langmuir-Blodgett film after the benzene has evaporated.

How large is the area per molecule which is occupied by a C_{60} molecule if the total surface area of the film is 16.87 cm^2 and 0.1 ml of the solution was used to make it?

The van der Waals area of C_{60} is 78.5 Å^2 . (P. HEINEY *et al.*, *Phys. Rev. Lett.* **66**, 2911 (1991)). What follows from this for the film described above?

References

- 1 N. KARL, *Organic Electronic Materials*, in: *Organic Electronic Materials*, edited by R. Farchioni and G. Grosso, Springer, Heidelberg (2001)
- 2 H. C. WOLF and H. P. DEUTSCH, *Naturwiss.* **41**, 425 (1954)
- 3 N. KARL, *High Purity Organic Molecular Crystals*, in: *Crystals, Growth, Properties and Applications*, vol. 4, edited by H. C. Freyhardt, Springer, Heidelberg (1980); N. KARL, *J. Cryst. Growth* **99**, 1009 (1990)
- 4 K. W. BENZ, *Zs. Naturforsch.* **24a**, 298 (1969)
- 5 H. C. WOLF, in: *Adv. in Atomic and Molecular Physics*, edited by R. Bates and I. Estermann, Vol. III, Academic Press, New York (1967)
- 6 K. W. BENZ, H. PORT and H. C. WOLF, *Zs. Naturforsch.* **26a**, 787 (1971)
- 7 N. KARL and H. FEEDERLE, *phys. stat. sol.* **34a**, 497 (1976)
- 8 E. GLOCKNER and H. C. WOLF, *Chem. Phys.* **10**, 479 (1975)
- 9 R. A. LAUDISE, CH. KLOC, P. G. SIMPKINS and T. SIEGRIST, *J. Cryst. Growth* **187**, 449 (1998)
- 10 CH. KLOC, P. G. SIMPKINS and R. A. LAUDISE, *J. Cryst. Growth* **182**, 416 (1997)
- 11 M. ICHIKAWA *et al.*, *Adv. Mater.* **15**, 213 (2003)
- 12 F. VÖGTLE, *Supramolekulare Chemie*, Teubner, Stuttgart (1992)
- 13 V. ENKELMANN, B. S. MORRA, CH. KRÖHNKE, G. WEGNER and J. HEINZE, *Chem. Phys.* **66**, 303 (1982); D. BLOOR, in: *Polydiacetylenes*, NATO A.S.I. Series, Martinus Nijhoff Publishers, p. 1 (1985)
- 14 G. WEGNER, *Z. Naturforsch.* **24b**, 824 (1969)
- 15 R. R. CHANCE and M. L. SHAND, *Chem. Phys.* **72**, 948 (1980)
- 16 H. SIXL, in: *Advances in Polymer Science*, **63**, *Polydiacetylenes*, edited by H. J. Cantow, Springer, p. 49 (1984)
- 17 M. SCHWOERER, E. DORMANN, TH. VOGTMANN and A. FELDNER, in: *Macromolecular Systems: Microscopic Interactions and Macroscopic Properties*, Wiley-VCH, pp. 122 (2000)
- 18 ST. R. FORREST, *Chem. Rev.* **97**, 1793 (1997); *Nature* **428**, 911 (2004)
- 19 M. HALIK, H. KLAUK, U. ZSCHIESCHANG, G. SCHMID, CH. DEHM, M. SCHÜTZ, M. MAISCH and F. EFFENBERGER, *Nature* **431**, 963 (2004)
- 20 F. SCHREIBER, *Progress in Surface, Science* **65**, 151 (2000)

4

Impurities and Defects

As in many cases in solid-state physics, defects in organic solids, even at very low concentrations, can be extremely important for their physical properties. Even the most successfully purified and carefully grown molecular crystals contain a residue of impurities and structural defects. Both can give rise to considerable structural or electronic deviations from the behaviour expected of ideal crystals. Impurity molecules can strongly influence the optical and electronic properties of the host crystal either directly or indirectly by disturbing the host lattice structure. In particular, the emission spectra (fluorescence and phosphorescence), excitonic energy transport and charge transport (the charge-carrier mobility and the charge-carrier concentration) are often determined by impurities. Structural defects disturb the coherence of excitation states and of the conduction electrons in the crystal.

4.1

Foreign Molecules, Impurities, and X traps

Foreign molecules in a crystal can be **guest molecules** or **impurities**. Guest molecules are molecules which are intentionally added to the crystal by doping. As was already mentioned in the preceding chapter, the solubility limit is usually very low. Guest molecule concentrations of more than 10^{-3} are obtainable only for a few host-guest pairs, if a thermodynamically stable solubility is required. Isotopically mixed crystals, e.g. perdeuteronaphthalene : naphthalene ($\text{N-d}_8(x) : \text{N-H}_8(1-x)$), about which we shall have more to say in Chaps. 6 and 7, can in contrast be obtained in the whole range of concentrations between 0 and 100% and are stable over this whole range.

Every foreign molecule differs in shape and electronic structure from the host molecules. Its interactions with the neighbouring host molecules are therefore different from those of a host molecule in the same host environment. Thus, the immediate neighbours of a foreign molecule in the host lattice also differ in their precise positions and their electronic structure more or less strongly from the undisturbed host molecules. The degree of this disturbance naturally depends on how strongly the foreign molecule and the host molecules differ in their shapes and electronic structures. If the electronic excitation states of a foreign molecule lie en-

ergetically above those of the host crystal, then they will hardly be observable in absorption for low concentrations owing to the superposed absorption of the host. Even in emission it will be difficult to observe the foreign molecules, since the lower-lying host exciton band will take up the excitation energy without emitting radiation. The foreign molecule nevertheless represents a defect within the host crystal and can make its appearance in terms of a perturbation of its host environment. Likewise, a foreign molecule can act as a defect even when it exhibits no immediate spectroscopic signature.

Such local or **point defects** in a host lattice are called **X traps** [1]. X stands here for unknown, since one quite possibly does not know the chemical nature of the defect molecules. X traps are the most important point defects for molecular crystals. Their local character is a result of the short range of the van der Waals forces. The fluorescence spectrum of an X trap differs from that of a guest molecule in that it, in contrast to the latter, exhibits the vibronic structure of the host lattice.

The oldest and also a very characteristic example of an X trap is that produced by thionaphthene (= benzothiophene) in naphthalene (Fig. 4.1). The thionaphthene molecule is very similar to the naphthalene molecule. One of the two six-membered rings is however replaced by a five-membered ring, and in it, a CH group is replaced by an S atom (see Fig. 1.2). It is always contained in commercially-available naphthalene in concentrations in the percent- to the ppm range, because naphthalene is obtained from coal tar, which always contains sulphur. It is difficult to remove by zone refining.

In the absorption spectrum, one does not observe it for concentrations below 10^{-3} , because its orbital energies and therefore its electronic states lie somewhat above those of naphthalene and therefore overlap with the absorption of the host. Thus, one can also not observe it in the fluorescence radiation: that of the host lies at somewhat lower energy and absorbs the thionaphthene fluorescence with a high efficiency. However, one can observe a fluorescence with the vibronic structure typ-

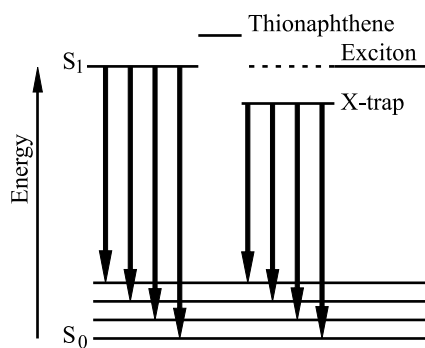


Fig. 4.1 The energy scheme of an X trap. The lowest electronic excitation state S_1 of the foreign molecule (here thionaphthene) lies above the S_1 state of the host (here naphthalene). Naphthalene molecules act as traps, which are disturbed by neighbouring

thionaphthene molecules. One observes a host (naphthalene) emission, that is an emission with the vibronic structure of the host, with a quantum energy somewhat reduced as compared to the pure host.

ical of naphthalene and a 0.0 transition which lies 29 cm^{-1} lower than that of the pure naphthalene crystal. This is the emission of the naphthalene molecules which are neighbours to a thionaphthene impurity, i.e. an X trap [1]. The process of sensitised fluorescence (cf. Chap. 6) has the result that these X traps act as efficient traps for the excitation energy and extinguish the intrinsic naphthalene fluorescence. Thionaphthene concentrations of $< 10^{-7}$ molecules/molecule can be detected in this manner. This is depicted schematically in Fig. 4.1. The exact structure of the X traps can in favourable cases be determined by means of ENDOR [2]. With this method, one can show that X traps often consist of only a single host molecule. It is slightly rotated from its ideal lattice position due to a neighbouring foreign molecule. An example is shown in Fig. 4.2. When the perturbation of the host lattice by the foreign molecule affects several host molecules, then the X trap can also act as a local funnel in the energy scheme of the crystal, with the central host molecule in the lowest position. If one follows the time dependence of the capture of an exciton by a trap, it can be observed in some cases that first a “pre-capture” takes place before the energy has arrived at the bottom of the funnel.

The word “trap” also expresses the fact that these point defects can frequently capture electronic excitation energy. Other well-studied X traps are those of pyrene in anthracene, with a trapping depth of $\Delta E = 59\text{ cm}^{-1}$. Naturally, there are also triplet X traps, e.g. in 1,2,4,5-tetrachloro-benzene, with $\Delta E = 21.3\text{ cm}^{-1}$. Host molecules can also act as X traps when they are perturbed not by foreign molecules but by a specific structural defect. Occasionally, in the literature a distinction is made between X and Y traps, depending on whether the lattice perturbation is caused by a structural defect in the crystal (Y trap) or by a foreign molecule (X trap). Plastic deformation of crystals can also produce discrete trapping states, for example in

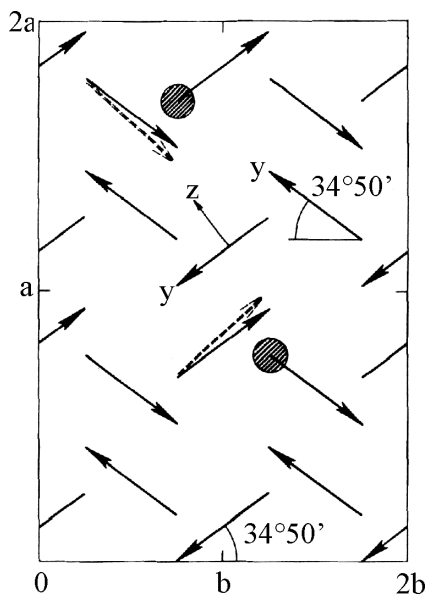


Fig. 4.2 The structure of an X trap. Here, we show a dibenzo-thiophene molecule (Fig. 1.2) in a fluorene single-crystal host (Fig. 1.1). The scheme shows the orientation of the dibenzo-thiophene molecules (arrows with circle) due to the increased space taken up by the sulphur atom in the dibenzo-thiophene molecule. The fluorene molecules nearest to the dibenzo-thiophene (arrows, dashed) are rotated about 2.5 degrees out of their equilibrium positions in the pure crystal. After [3], based on ENDOR measurements.

naphthalene. There, after plastic deformation, in the fluorescence spectrum one observes, in addition to a continuous background stretching out towards longer wavelengths, discrete trapping states 165 cm^{-1} below the exciton band. The continuous background is due in part to excimer configurations. By annealing, the fraction of defect fluorescence can be reduced [4].

Foreign molecules can in addition have the following effects on the electronic properties of the host crystal:

- They can themselves produce or act as traps for excitons and also for charge carriers if their excitation energies are lower than those of the host molecules. Later (in Chap. 8), we will see that impurities which act as traps can have a strong influence on space-charge limited currents and on the drift mobilities of charge carriers.
- They can contribute to the generation of free charge carriers, if they are more readily ionised than the host molecules. They thus act as donors or acceptors within the semiconductor.
- They can perturb the conduction-band structure of the ideal crystal. They act as scattering centres for the charge carriers. If, e.g. in CT or radical-ion salts, the high conductivity of the host is based on the overlap of neighbouring molecules in one-dimensional stacks, then evidently foreign molecules in the stacks can strongly reduce the charge-carrier mobility and thus the electrical conductivity.

4.2

Structural Defects

Defects in a crystal which extend in all directions over not more than a few intermolecular distances are termed **point defects**. They can be impurities or structural defects. Dislocations are, in contrast, structural defects which affect larger regions of the crystal.

4.2.1

Point Defects

X traps are localised at a particular point in the lattice, without extending over larger distances in one or more dimensions. They thus belong to the class of point defects. Other point defects can be caused by missing molecules in the lattice, i.e. **lattice vacancies** or so-called Schottky defects, or by interstitial molecules, i.e. Frenkel defects, or finally by improperly oriented molecules on regular lattice sites. Point defects can usually be observed only indirectly, through the effects they have on other physical properties of the crystal.

Frenkel defects in general do not play an important role in molecular crystals. The asymmetric shape of the molecules and the steeply increasing repulsive potential between molecules at short intermolecular distances make the occurrence of interstitial molecules in molecular crystals thermodynamically improbable. The

energy required for their formation is considerably higher than for Schottky defects.

Schottky defects are thus easier to produce. The energy required is composed of the sublimation enthalpy and an energy of relaxation of the lattice. With these energies, the concentration of lattice vacancies in thermal equilibrium can be calculated. Estimates for the density of vacancies yield for anthracene at 300 K $1.5 \cdot 10^{14} \text{ cm}^{-3}$ and for naphthalene $7 \cdot 10^{15} \text{ cm}^{-3}$. At the melting point, for anthracene one finds $2 \cdot 10^{19} \text{ cm}^{-3}$ and for naphthalene, $3 \cdot 10^{17} \text{ cm}^{-3}$ ([M1], p. 223). Notably, the density at 300 K roughly corresponds to the minimum density of specific impurities which can be achieved with the best purification processes and detected with the best analytic methods (cf. Sect. 3.2).

If such vacancies are considered to represent an inner free surface within the crystal, it becomes clear that they can act as anti-traps both for excitons (owing to the smaller solvent shifts for molecules at a surface) and for charge carriers (due to the lower polarisation energies for molecules at a surface). They thus do not capture excitons and charge carriers, but instead they act as scattering centres. This is for example quite different in ionic crystals: there, a vacancy has an effective charge and therefore captures charge carriers of opposite charge. An anion vacancy in an alkali-halide crystal becomes for example a colour centre, called an F centre, on capturing an electron. Since the number density of vacancies increases exponentially with temperature, corresponding to their thermal activation, the vacancies, along with phonons, contribute to the temperature dependence of the charge-carrier mobilities and the exciton coherence. Due to the fact that also the host molecules which are neighbours of a vacancy have reduced polarisation energies, the scattering cross-section of a vacancy can be very large, much larger than that of a single molecule, up to 10^{-13} cm^2 [M2].

Vacancies are furthermore of decisive importance for the process of self-diffusion of a molecule within the crystal (cf. Sect. 5.8). This is a thermally-activated process. Its measured activation energy (2.4 eV for naphthalene) is assumed to be about twice as large as the activation energy for the production of a vacancy ([M1], p. 223). One can calculate from this that the vacancy concentration will be in the ppm range at 300 K.

4.2.2

Dislocations

Organic molecular crystals are relatively soft and can readily be deformed. Therefore, structural defects can easily be produced in them. Some of these structural defects can be considerably reduced by careful annealing. The structural perfection of the crystals depends strongly on this possibility as well as on the growth conditions.

The well-known dislocations in inorganic crystals, with the aid of which one can explain the plastic mechanical properties of metals and alloys, naturally also occur in molecular crystals. They are formed when a part of a crystal is displaced relative

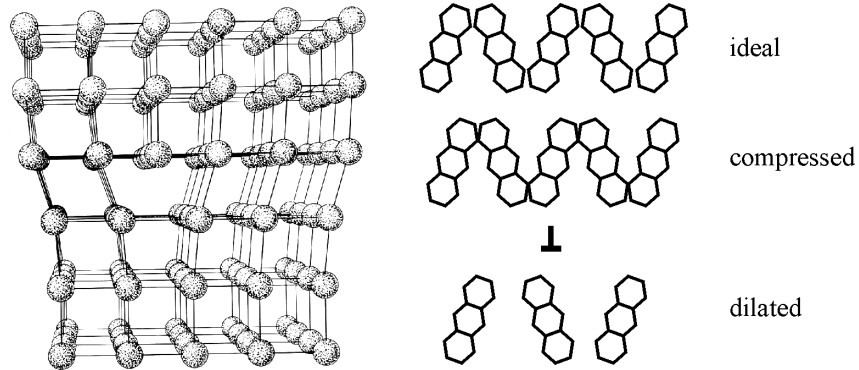


Fig. 4.3 The structure of a step dislocation. The deformation can be graphically represented as due to the insertion of an additional lattice plane into the upper part of the crystal. In the neighbourhood of the dislocation, there are expanded and compressed regions. Due to the strong dependence of the intermolecular potential on distance, the excitation states react very sensitively to the presence of these regions.

to its neighbourhood. As a rule, they consist of a superposition of step and spiral dislocations.

A step dislocation can be understood as a slippage of part of the crystal relative to the rest. The boundary between the slipped and the unslipped regions is the dislocation line (Fig. 4.3). A step dislocation can also be considered to be an extra lattice plane inserted into the undisturbed crystal. The dislocation line is a line along this step (the edge of the plane). The neighbourhood of a dislocation line is strained. In the case of spiral dislocations, a section of the crystal lattice is rotated by one lattice constant through a slippage (Fig. 4.4).

The dislocation density is defined as the number of dislocation lines which pass through a unit surface of the crystal. In some cases, they can be counted as etch pits which are formed on partially dissolving or etching a crystal surface. More about this subject will be given in Sect. 4.4 and Fig. 4.8.

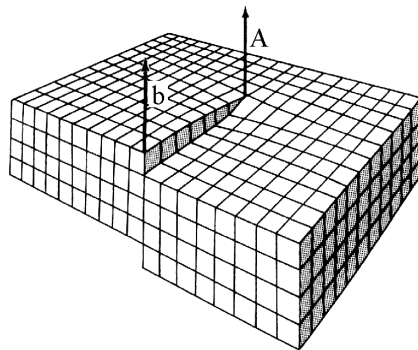


Fig. 4.4 Schematic representation of a spiral dislocation. The line of dislocations A runs parallel to the shear strain. This line of dislocations is surrounded by distorted material.

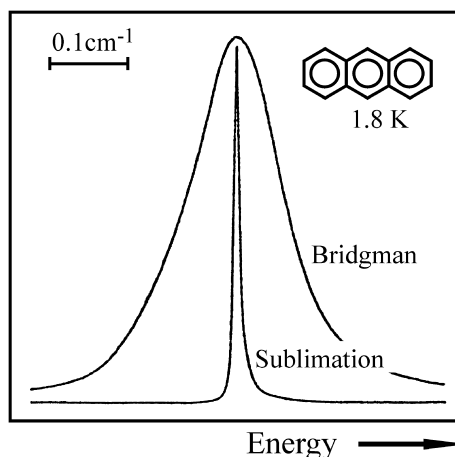


Fig. 4.5 The excitation spectrum ($T_1 \leftarrow S_0$) of the energetically lower of the two Davydov components ($14\,738\text{ cm}^{-1}$) of the triplet 0,0 transition in anthracene at 1.8 K in a Bridgman crystal and in a sublimation crystal. The spectral line is strongly inhomogeneously broadened in the Bridgman crystal. See Fig. 6.5.10 and Sect. 6.5.2. After [7].

Dislocation densities depend strongly on the method of crystal growth and the following treatment of the crystals. They can often be considerably reduced by annealing. In the best organic crystals, which were grown as free-standing platelets from the vapour phase and then annealed, the dislocation density can be as low as 10 cm^{-2} [5]. This value is comparable with the dislocation densities in the best Si or Ge crystals.

Crystals grown from the melt necessarily have internal strains, and their dislocation densities can easily be in the range of 10^5 to 10^7 dislocations/ cm^2 . The difference is made clear in Fig. 4.5. The 0,0 line of the $T_1 \leftarrow S_0$ transition in an anthracene crystal grown by the Bridgman procedure shows more inhomogeneous broadening by a large factor than that of a sublimation platelet. There, the linewidth is only 0.009 cm^{-1} . Fig. 4.5 makes it very clear that the sublimation crystals are vastly superior in terms of the number of defects in the crystal lattice. Here, we already refer to the characteristic features in the optical spectrum of molecular crystals. These will be treated in more detail in Chap. 6.

The number of disturbed lattice sites is considerably larger than the number of dislocations, since lattice distortions in the neighbourhood of a dislocation line extend out further than a lattice constant. A dislocation density of 10^6 cm^{-2} implies a density of 10^{14} or more of disturbed lattice sites per cm^2 . This can in turn mean that more than 1% of all the molecules within a plane are disturbed.

Dislocations, and the associated internal strains, are thermodynamically unstable as we have mentioned, and to a certain extent can be eliminated by annealing. They have a strong influence on the mobility of charge carriers and of excitons in the crystal. In any case, they disturb the periodicity of the lattice and act as scattering centres. They also modify the distribution and the concentration of impurity molecules in the crystal. It thus becomes clear with the example of step dislocations (Fig. 4.3) that the lattice above the slippage plane is compressed by the insertion of an additional lattice plane, while it is expanded below the slippage plane. Smaller molecules than those of the host can then occupy lattice sites in the upper region,

while larger ones preferentially occupy sites in the lower region below the slippage plane. Impurities are therefore usually enriched in the neighbourhood of dislocations, just as are all point defects.

4.2.3

Grain Boundaries

Real crystals differ from ideal crystals in that they are composed of mosaic blocks, i.e. small crystallites. Typical values of their sizes lie in the range of some 100 up to some 1000 lattice constants. They are tilted relative to one another by a few minutes of arc (Fig. 4.6). The intersection of two of these blocks forms a so called small-angle grain boundary. This is known from the maxima in X-ray diffraction spectra; their widths for an ideal crystal should theoretically be only a few seconds of arc. In reality, one measures instead values of at least one minute of arc, due to the distribution of orientations of the mosaic blocks.

The mosaic structure and small-angle grain boundaries are found to a greater or lesser extent in all apparently perfect single crystals. The extent of inhomogeneity can be determined from the angular width of the Bragg reflections from selected lattice planes. The corresponding “rocking curves” are obtained by scanning slowly through the angular range of the Bragg reflection between the incident X-ray beam and the crystal with a high angular resolution and registering the intensity of the Bragg reflection. For good Bridgman crystals of anthracene and naphthalene, one finds angular widths of 0.5° .

The grain boundaries are thus a third type of extended defect. They can be considered to be a row of dislocations which are formed between neighbouring crystallites or mosaic blocks.

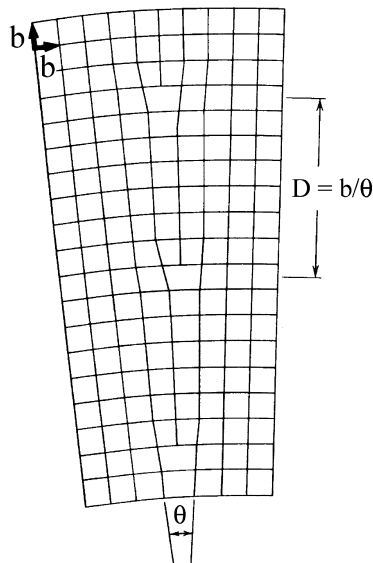


Fig. 4.6 A small-angle grain boundary, from C. KITTEL, *Introduction to Solid-State Physics*, 13th ed., Oldenbourg Press, Munich (2002).

4.2.4

Dipolar Disorder

Another class of structural disorder can occur when the crystal structure allows the molecule to assume two different orientations within the lattice with a similar or even identical lattice energy. A nice example is 2,3 dimethylnaphthalene (DMN), Fig. 4.7 (cf. also the analogous molecule dimethylantracene, Fig. 5.17). The two methyl groups at one end of the naphthalene molecule reduce its symmetry. The molecule has a dipole moment pointing in the direction of its long axis. 2,3 DMN crystallises like naphthalene in a herringbone pattern with two molecules in the unit cell. The molecules are distributed statistically within the crystal with respect to the two possible orientations of their dipole moments. There are thus a large number of possible local environments for the molecules, each with a different interaction energy. This so called dipolar disorder has the result, among other things, that the width of the observed absorption and emission lines of ca. 200 cm^{-1} even at low temperatures remains more than an order of magnitude larger than the width observed in naphthalene and anthracene crystals [8]. This structural disorder strongly modifies the energy transfer, the spectrum of the coupled lattice vibrations or phonons, and all the exciton states and processes – one observes a so-called dispersive instead of a diffusive energy transport. In diffusive transport, the lattice sites which are involved in the transport have the same energy (within kT), while in dispersive transport, the energy distribution is spread out over a larger region.

In some weak $\pi-\pi^*$ donor-acceptor crystals, the acceptor lattice is ordered, while the donor has an additional degree of freedom. An example is the anthracene-tetracyano-benzene crystal (cf. Fig. 1.6). Here, the donor has two equivalent sites,

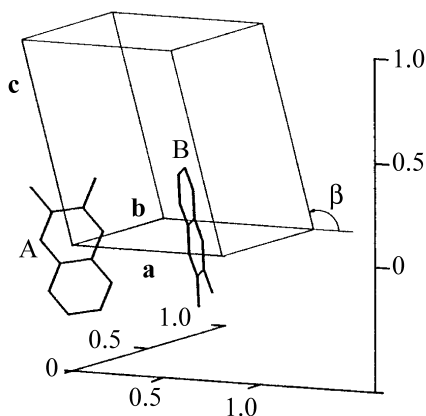


Fig. 4.7 The unit cell of a 2,3-dimethylnaphthalene crystal with the carbon skeleton of the two differently oriented molecules A and B. They are in fact statistically distributed with respect to the two possible orientations of their dipole moments. The units of length are nm. The lattice constants at $T = 290\text{ K}$ are: $a = 0.7916\text{ nm}$; $b = 0.6052\text{ nm}$; $c = 1.0017\text{ nm}$; $\beta = 105.43^\circ$. From [6].

which differ only by a small rotation of 8.6° around an axis perpendicular to the plane of the molecules. At room temperature, the molecule oscillates between these two positions [9].

4.3

Characterisation and Analysis of Impurities

A complete analysis of the nature, number and distribution of all the impurities in a crystal is difficult and not always possible. In practice, one considers only those impurities which are important for a particular investigation, and the detection limit is extended only as far as is necessary and practical with the given detection method.

The first method is visual examination. For example, in the zone refining of aromatic hydrocarbons, one often observes a brownish discolouration at the end of the zone refining tube, where impurities collect. Using gas-phase chromatography, when possible combined with a mass spectrometer, the chemical nature of these impurities can often be identified.

Particularly important are the spectroscopic techniques. Absorption and emission spectroscopy or, in the case of paramagnetic impurities, also ESR spectroscopy in many cases permit the detection and identification of impurities down to very low concentrations. In Sect. 6.9.2, we show that for example using the method of sensitised fluorescence, a detection limit of better than 10^{-10} molecules/molecule can be attained.

Impurities which act as traps for charge carriers can be detected from the space-charge limited conductivity or from measurements of charge-carrier mobility in favourable cases, and their concentrations can be determined, but not their identities (see Sect. 8.5.5).

If extreme purity is required, then the procedures of purification and crystal growth must be repeated until no further progress can be detected with a suitable analysis technique. The goal of this process must be to allow research groups in different laboratories to work with materials of comparable purity.

4.4

Characterisation of Defects

In characterising defects, one must also limit oneself to the methods and the extent which are important for the particular investigation at hand.

In the optical methods, the microscope within its limited spatial resolving power plays an important role. Working with polarised light, one can readily recognise twinning, grain boundaries and other inhomogeneities within a crystal. In particular, one can use the method of **etch pits** to identify dislocations and to count them. This method, which we already mentioned above, is based on the fact that molecules in disturbed regions of a crystal can be more readily dissolved or sublimed than those in undisturbed areas. The crystal surface is therefore lightly etched with

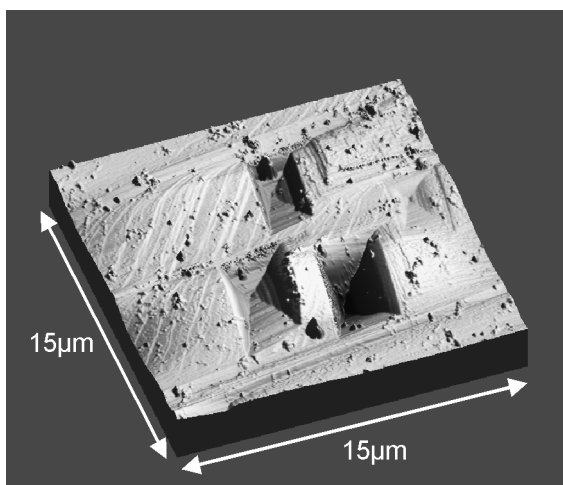


Fig. 4.8 Etch pits on the *a-b* surface plane of a tetracene crystal, after etching with oleum ($\text{H}_2\text{S}_2\text{O}_7$). The edges of the pits correspond to the crystallographic directions 110 and $\bar{1}\bar{1}0$. The number density is ca. 10^5 cm^{-2} . From J. NIEMAX, Dissertation, Stuttgart (2004).

a suitable solvent; for example, methanol, ethanol, acetone or sulphuric acid are often used. The etch pits mark the intersections of dislocations with the crystal surface. Fig. 4.8 shows as an example the etch pits on a tetracene single crystal. From the shape of the etch pits, the direction of the dislocations can also be determined. The density of the etch pits and thus of the dislocations is in this case 10^5 cm^{-2} . It can be reduced by annealing the crystal.

A further very successful method for investigating structural defects is **X-ray topography** [10,11]. Here, in the simplest version, monochromatic X-radiation is incident through an entrance slit at a fixed angle onto the crystal to be investigated, and the reflected beam is detected as a function of the angle of incidence and the orientation angle. When the Bragg condition is fulfilled for a particular family of crystal planes, one obtains a reflection maximum for the given orientation. This reflection may be perturbed if the crystal contains defects. For example, a small-angle grain boundary between two regions of the crystal with slightly different orientations leads to a region of contrast in the reflected X-ray beam. With this method, dislocations, grain boundaries and other extended structural defects can be imaged (cf. Fig. 4.9).

At this point, we shall not treat further methods for the investigation of defects in crystals, such as e.g. electron microscopy, for which one requires crystals with a thickness of less than 5000 \AA , or positron annihilation. In any case, a careful analysis of the quality of the crystal to be investigated belongs among the indispensable operations which must be carried out in studying molecular crystals.

Surface defects can in some cases be identified using scanning tunnel microscopy. An extremely fine probe tip is positioned close to the surface under study (for example at a distance of 8 \AA) and a relatively low voltage is applied (a few mV),

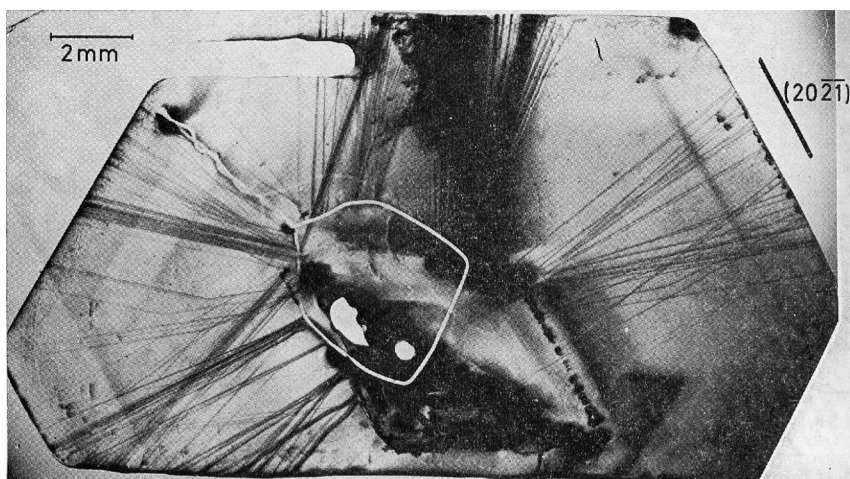


Fig. 4.9 X-ray topography to allow the visualisation of dislocations; here, defects in a benzene crystal which was grown from solution. In the centre, one can recognise the loop of a platinum wire which suspended the seed crystal platelet in the solution. Many linear dislocations start at inclusions in the surface of

the seed crystal and from certain points on the platinum wire, and they run parallel to the plane of the platelet. The image shows the reflection $20\bar{2}1$; the platelet is oriented perpendicular to 0001, and its thickness is 3 mm. After [11].

giving rise to a tunneling current whose strength depends sensitively on the distance between the tip and the surface. A change of the distance by 1 Å can change the tunneling current by an order of magnitude.

Just as in Chap. 3, where we treated the purity of materials, crystal growth and crystal quality, we must here also limit ourselves to the most important topics and be aware of the fact that our treatment cannot be exhaustive. However, we hope that these two chapters will provide the reader with an introduction and with a more ready access to the extensive technical literature on these subjects.

Literature

Monographs

- | | |
|--|--|
| <p>M1 M. POPE and C. SWENBERG, <i>Electronic Processes in Organic Crystals and Polymers</i>, Oxford University Press (1999)</p> | <p>M2 E. A. SILINSH, <i>Organic Molecular Crystals</i>, Springer Scientific Publishers (1980)</p> |
|--|--|

References

- | | |
|---|--|
| <p>1 A. PRÖPSTL and H. C. WOLF, <i>Z. Naturforsch.</i> 18a, 724, 822 (1963)</p> <p>2 H. DÖRNER and D. SCHMID, <i>Phys. Lett.</i> 54, 154 (1978); <i>Phys. Lett.</i> 61, 171 (1979)</p> | <p>3 H. C. WOLF, in: <i>Die feste Materie</i>, edited by L. Genzel, Umschau-Verlag, Frankfurt (1973)</p> <p>4 R. SCHNAITHMANN and H. C. WOLF, <i>Z. Naturforsch.</i> 20a, 76 (1965)</p> |
|---|--|

- 5 J. N. SHERWOOD, *Mol. Cryst.* **9**, 37 (1969)
- 6 N. KARL, H. HEYM and J. J. STEZOWSKII, *Mol. Cryst. Liq. Crist.* **131**, 163 (1985)
- 7 H. C. WOLF, in: *Organic Molecular Aggregates*, edited by P. Reineker, H. Haken and H. C. Wolf, Springer (1983)
- 8 W. SCHROF, E. BETZ, H. PORT and H. C. WOLF, *Chem. Phys.* **118**, 57 (1987)
- 9 C. A. FYFE, *J. Chem. Soc. Faraday II*, 1633, 1642 (1974)
- 10 B. K. TANNER, *X-ray Diffraction Topography*, Oxford, Pergamon (1976)
- 11 H. KLAPPER, *X-Ray Topography in Crystals, Growth, Properties and Applications* vol. 13, edited by H. C. Freyhardt, Springer, Heidelberg (1991)

5

Molecular and Lattice Dynamics in Organic Molecular Crystals

5.1 Introduction

In all molecular crystals, there are both vibrations and stochastic rotations or translational motions of the molecules.

In the case of the vibrations, one distinguishes two types: the intramolecular vibrations (molecular vibrations), which are also referred to as internal modes and whose frequencies differ from those of the free molecules only slightly or not at all; and the external vibrations (lattice vibrations), which are also termed external modes, where the organic molecules as a whole oscillate around their equilibrium positions. Usually, only the external vibrations are called phonons.

The internal modes with few exceptions have much higher frequencies than the external modes and they also in general have little or no dispersion, i.e. no dependence on the wavevector. Only in the case of larger, more or less planar molecules (anthracene, tetracene, pentacene ...) are there also internal modes with low frequencies and dispersion.

In the case of the external vibrations, the molecules, which are to first order treated as rigid blocks, undergo either translational vibrations or libration, or else a mixed translational-libration oscillation (Fig. 5.1). The motions of the molecules in the crystal are coupled to form a wave with the wavevector \mathbf{K} . Their frequency Ω is a function of \mathbf{K} . (To distinguish the intermolecular vibrations from electronic excitations by neutrons or light, the frequencies Ω and the wavevectors \mathbf{K} of the external vibrations, i.e. the phonons, are written as capital letters; see e.g. [5].) There are two types of phonons, the acoustic phonons (AP), for which $\Omega(\mathbf{K})$ approaches zero for $\mathbf{K} \rightarrow 0$, and the optical phonons (OP), for which $\Omega(\mathbf{K})$ has finite values for $\mathbf{K} \rightarrow 0$ (Fig. 5.2). The frequencies Ω or the corresponding quantum energies $\hbar\Omega$ of all the phonons in organic molecular crystals are as a rule not only lower than the energies of the internal modes, but are also notably smaller than the frequencies or the phonon energies in covalently-bonded inorganic crystals such as *Si*. This is a direct result of both the large masses and the large moments of inertia of the organic molecules, and of the weak intermolecular van der Waals bonding.

A direct and important consequence of the small quantum energies of the phonons in molecular crystals is their thermal excitation: in thermal equilibrium at

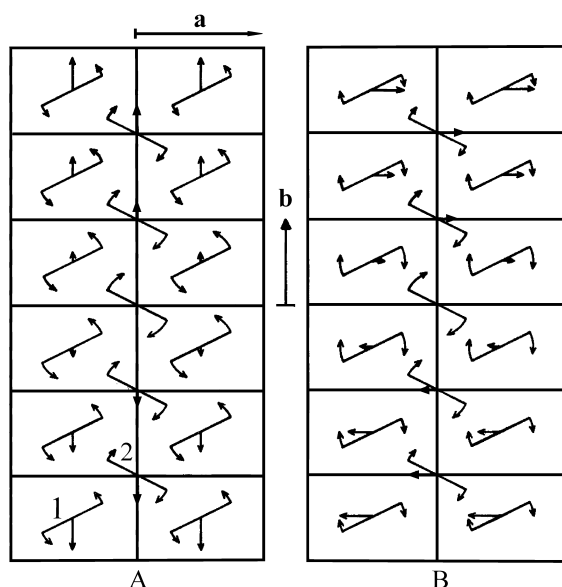


Fig. 5.1 A schematic drawing of a mixed translational-libration wave in a monoclinic molecular crystal, which has two molecules in the primitive unit cell and a twofold axis of symmetry (b). The two molecules 1 and 2 are represented by straight lines. A rotation of 180° around the b -axis and a following translation by $(a/2, b/2)$ converts molecule 2 into molecule 1 and *vice versa*. The wavevector

\mathbf{K} is oriented along the b direction ($\mathbf{K} = (0, K, 0)$). The vectors of the translational and the libration motions away from the equilibrium position are indicated by arrows and they are either identical (A) or reverse their signs (B) under the above-mentioned rotation of the crystal by 180° around the b -axis followed by a translation of $(a/2, b/2)$.

room temperature, the probability that lattice vibrations will be excited in organic molecular crystals, i.e. that phonon states are occupied, is larger than in covalently bound inorganic crystals. Thermally-excited phonons thus play an important role in their interactions with excitons or with charge carriers in organic molecular crystals.

Besides the internal and external vibrations of the molecules, there are, as already mentioned, also stochastic or at higher temperatures nearly free rotations of entire molecules in some molecular crystals (e.g. the benzene molecules in a benzene crystal or the $-\text{CH}_3$ groups in methyl-substituted aromatics). And finally, molecules in molecular crystals, like atoms in atomic crystals, can diffuse.

In the following sections of this chapter, we first treat intramolecular vibrations; then, in much more detail, phonons using typical examples; and finally, very briefly, stochastic rotational motions (“reorientations”) and translational diffusion of molecules. Although the experimental methods for the characterisation of dynamics in molecular crystals are in principle no different from those used to investigate inorganic crystals, we shall briefly describe inelastic neutron diffraction, Raman scattering, infrared and far-infrared spectroscopy, as well as NMR spectroscopy to the extent necessary or useful for the specific understanding of molecular and lattice

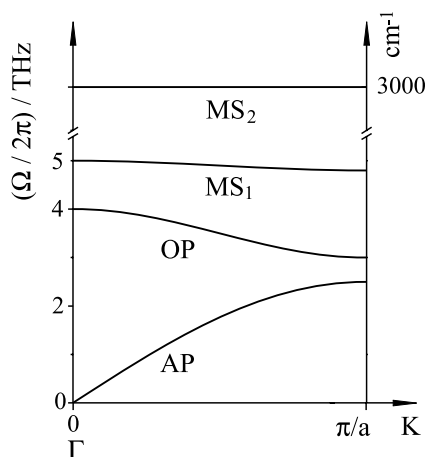


Fig. 5.2 A schematic energy diagram $\Omega(\mathbf{K})$ of the internal and the external molecular vibrations in molecular crystals. Ω is the frequency, $\hbar\Omega$ the energy and K is the magnitude of the wavevector in a particular direction, e.g. in the direction \mathbf{a} . $K=0$ is the centre and $K=\pi/a$ the boundary of the Brillouin zone, with the lattice constant a . Γ is the usual notation for the centre of the Brillouin zone. MS_1 is a low-frequency internal molecular oscillation with a small or vanishing dispersion ($\Omega \approx \text{const.}$). MS_2 is a high-frequency internal molecular oscillation. All together, there are $3N-6$ internal modes; N is the number of atoms per molecule. OP is an optical phonon in which whole molecules are excited to carry out translational or libration oscillations whose frequencies are

nonvanishing at the centre of the Brillouin zone: $\Omega_{OP}(0) \neq 0$. The highest frequency of the optical phonons is about the same in all aromatic molecular crystals and has a value of roughly 4 THz (corresponding to a wavenumber of 130 cm^{-1} , an energy of 16 meV or a temperature of 190 K). All together, there are $6Z-3$ optical phonons, whose frequencies depend on their wavevectors, $\Omega(\mathbf{K})$; this is termed their dispersion relation or their dispersion branch. Z is the number of molecules in the primitive unit cell. AP is an acoustic phonon whose frequency vanishes at the Γ -point: $\Omega(0) \rightarrow 0$. Acoustic phonons have a velocity of sound given by $\frac{d\Omega}{dK}(K \rightarrow 0) = c_s$. All together, there are 3 acoustic phonons. The velocities of sound in all aromatic molecular crystals lie in the range of a few 10^5 cm/s .

dynamics in molecular crystals. Theoretical methods of calculating phonon spectra and their dispersion relations $\Omega(\mathbf{K})$ (Sect. 5.6) always start in the first approximation from the model of an “oriented gas”, in which the molecules are treated as rigid bodies with a given mass and moment of inertia, coupled by the van der Waals forces.

5.2

Intramolecular Vibrations

A molecule in vacuum has $3N-6$ normal modes. Here, N is the number of atoms in the molecule. A free anthracene molecule thus has $3 \times 24-6 = 66$ normal modes or normal vibrations. As an example, Table 5.1 lists the frequencies of these 66 internal modes in the anthracene crystal. They were determined from the vibrational

Table 5.1 Intramolecular normal vibrations in anthracene crystals: vibrational modes, symmetry notation and wavenumbers. Where two different wavenumbers are given for a single normal vibration, a Davydov splitting was observed. From [1–3]. Non-planar (out-of-plane) vibrations are marked with *.

Vibrational mode	Symmetry	Wavenumber (cm ⁻¹)	Vibrational mode	Symmetry	Wavenumber (cm ⁻¹)
ω_1	b_{1g}^*	247/244.5	ω_{34}	b_{3u}^*	129/111
ω_2	b_{2g}^*	290	ω_{35}	a_u^*	172
ω_3	b_{3g}	390	ω_{36}	b_{1u}	235
ω_4	a_g	395	ω_{37}	b_{3u}^*	475
ω_5	b_{3g}	478.5/481	ω_{38}	a_u^*	
ω_6	b_{1g}^*	477	ω_{39}	b_{3u}^*	603
ω_7	b_{2g}^*	577	ω_{40}	b_{2u}	600
ω_8	a_g	622	ω_{41}	b_{1u}	650
ω_9	b_{1g}	747	ω_{42}	b_{3u}^*	727
ω_{10}	a_g	753	ω_{43}	a_u^*	
ω_{11}	b_{2g}^*	762.5/764	ω_{44}	b_{2u}	808
ω_{12}	b_{2g}^*	896	ω_{45}	a_u^*	870
ω_{13}	b_{1g}^*	904	ω_{46}	b_{3u}^*	883
ω_{14}	b_{2g}^*	918/916	ω_{47}	b_{1u}	903
ω_{15}	b_{3g}	954/959	ω_{48}	b_{3u}^*	954
ω_{16}	b_{2g}^*	980/978.5	ω_{49}	a_u^*	
ω_{17}	a_g	1008	ω_{50}	b_{2u}	998
ω_{18}	b_{3g}	1103	ω_{51}	b_{2u}	1068
ω_{19}	a_g	1163	ω_{52}	b_{1u}	1145
ω_{20}	b_{3g}	1187	ω_{53}	b_{2u}	1163
ω_{21}	a_g	1261	ω_{54}	b_{1u}	1270
ω_{22}	b_{3g}	1274	ω_{55}	b_{1u}	1314
ω_{23}	b_{3g}	1376	ω_{56}	b_{2u}	1346
ω_{24}	a_g	1403	ω_{57}	b_{2u}	1398
ω_{25}	a_g	1482	ω_{58}	b_{1u}	1447
ω_{26}	a_g	1557	ω_{59}	b_{2u}	1462
ω_{27}	b_{3g}	1576	ω_{60}	b_{2u}	1533
ω_{28}	b_{3g}	1634	ω_{61}	b_{1u}	1616
ω_{29}	b_{3g}		ω_{62}	b_{1u}	3024
ω_{30}	b_{3g}		ω_{63}	b_{2u}	3050
ω_{31}	a_g	3066	ω_{64}	b_{1u}	3050
ω_{32}	a_g	3088	ω_{65}	b_{2u}	3093
ω_{33}	a_g	3108	ω_{66}	b_{1u}	3108

structure of optical spectra, from Raman spectra and from *IR* spectroscopy. The table contains as well as the frequencies, also the symmetries of the molecular normal vibrations. The anthracene molecule has D_{2h} symmetry. In the notation for the molecular normal motions, b_{1u} represents a polarisation of the oscillation parallel to the short axis (M), b_{2u} is parallel to the long axis (L), and b_{3u} is parallel to the per-

pendicular axis (N) of the planar molecule. The parity-odd vibrations (u) are active in the infrared, while the even vibrations (g) are Raman active. Vibrations out of the molecular plane are denoted by a $*$.

In the limiting case of a negligible intermolecular coupling, every molecule in the crystal can be excited to its molecular oscillations independently of every other molecule. The intermolecular coupling of the internal modes is so weak in comparison to their quantum energies that they are observed only for a few very low-frequency intramolecular vibrations. Then, in analogy to the Davydov splitting for excitons (Chap. 6), there exists a splitting also for these internal oscillations. In Table 5.1, these Davydov splittings are found as the difference of the two frequencies which are given for some of the 66 normal vibrations. For example, for the mode ω_{34} , the Davydov splitting is $(129 - 111) \text{ cm}^{-1} = 18 \text{ cm}^{-1}$. All the other Davydov splittings observed are considerably smaller. The mode ω_{34} was assigned to a “butterfly mode”. The likewise very low-energy mode ω_{35} is the oscillation of a torsional motion around the long molecular axis (“twist mode”).

The spectrum of the intramolecular vibrations in the anthracene crystal includes the region from 111 cm^{-1} to 3108 cm^{-1} . For larger aromatic molecules, the lower limit shifts towards lower wavenumbers (frequencies); for smaller aromatics, it shifts towards higher wavenumbers. In naphthalene, the smallest wavenumber (frequency) of an internal mode is around 170 cm^{-1} (5 THz). An analysis of the internal modes as given in Table 5.1 for anthracene has to our knowledge not been published for other molecular crystals with a similarly large number of atoms in such a complete form. Selected values of the wavenumbers of the intramolecular vibrations of other molecular crystals can, however, be found, e.g. in [3].

5.3 Phonons

Phonons in organic molecular crystals are quantised coupled oscillatory displacements of the molecules from their equilibrium positions in the periodic crystal lattice. As mentioned, in contrast to the oscillations in atomic crystals, in molecular crystals there are not only translational vibrations, but also rotational vibrations, which frequently are called libration. In the model of an oriented gas (where the molecules are treated as rigid bodies with given masses and moments of inertia), in a molecular crystal with Z molecules in the primitive unit cell, there are 3 translational and 3 rotational degrees of freedom per molecule, i.e. all together $6Z$ degrees of freedom. In the naphthalene crystal, $Z = 2$, as in the anthracene, tetracene and pentacene crystals. Therefore, in these crystals, there are 12 degrees of freedom and thus 12 normal vibrations or 12 phonon branches. The restoring forces of the translational vibrations and the restoring torques of the rotational vibrations are the forces and torques of the van der Waals bonds (see Chap. 2 and Sect. 5.6).

Every phonon is characterised by its eigenvector of the displacement of the molecules, its wavevector \mathbf{K} and its frequency $\Omega(\mathbf{K})$.

5.3.1

The Eigenvector

The eigenvector of the displacement defines the direction of the translation or the direction of the axis of rotation of the molecules. The eigenvectors must obey the symmetry of the crystal. The naphthalene crystal belongs to the space group C_{2h}^5 . Its symmetry elements are the unit operation (E), a rotation around the \mathbf{b} axis by 180° (C_2), a reflection in the $a-c$ plane (σ_h), and the inversion (I). Here, C_2 and σ_h project the crystal onto itself with an additional translation of $1/2(\mathbf{a} + \mathbf{b})$. The $a-c$ plane is therefore termed the mirror-glide plane. According to the rules of group theory [6], there exist four possible symmetries A_g , B_g , A_u and B_u for the eigenvectors (Table 5.2). Eigenvectors of type A are self-identical under a 180° rotation around the b axis (C_2) and are termed symmetric; those of type B reverse their signs under C_2 and are called antisymmetric (Fig. 5.3). Eigenvectors are denoted by an index g when they are self-identical under inversion (I), while those with index u change their signs under I .

Table 5.2 Character table of C_{2h} .

	E	C_2	σ_h	I
A_g	1	1	1	1
B_g	1	-1	-1	1
A_u	1	1	-1	-1
B_u	1	-1	1	-1

The eigenvectors of the twelve phonons in the naphthalene crystal are sketched in Fig. 5.4 for the special case $\mathbf{K} = 0$, that is at the Γ point of the 1st Brillouin zone (1st BZ). The modes 1, 2, 3, 5, 7 and 10 are pure translational vibrations. The vectors are roughly parallel to the crystal axes a , b and c' . c' is perpendicular to the $a-b$ plane. Each of these 3 directions corresponds to a mode in which the two molecules in the unit cell oscillate in phase (1, 2 and 3) and to a mode in which

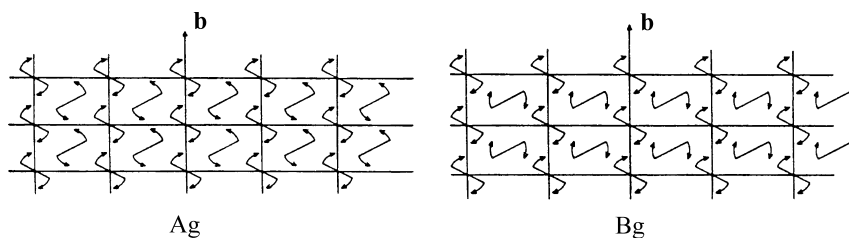


Fig. 5.3 Vibrational modes of the (Raman active) phonons A_g and B_g , schematic representation. b is the twofold axis of the monoclinic crystal. For the B_g phonons the axes of rotational symmetry of the two molecules in the unit cell are parallel, while for the A_g phonons, they are oriented antiparallel. $K = 0$.

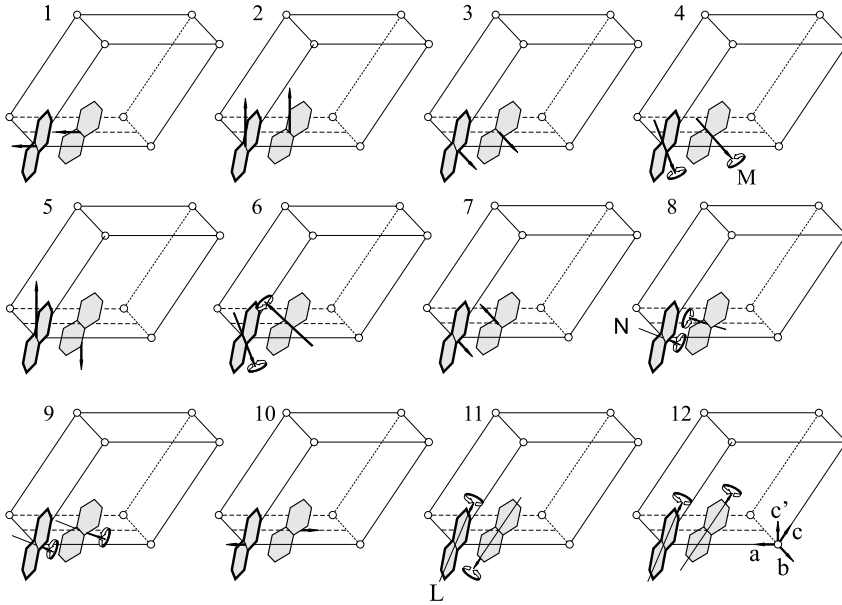


Fig. 5.4 Displacement vectors and their symmetries for the 12 phonons in the naphthalene crystal at the Γ point, i.e. at $K=0$. In each mode, at the Γ point all the unit cells oscillate in phase. In the rotational vibrations 4, 9 and 12, the two molecules in the unit cell

oscillate in phase, while in the modes 6, 8 and 11, they oscillate in opposing phase. N , M and L are the perpendicular (normal), the middle and the long molecular axes; a , b and c are the monoclinic crystal axes.

they oscillate with opposing phase (5, 7 and 10). The modes 4, 6, 8, 9, 11 and 12 are pure rotational vibrations at $K=0$. The directions of their axes of rotation are to first order the directions of the principal axes of the molecular moments of inertia, i.e. the axes M , L and N . The precise directions of the axes and the symmetry of the modes (A_g , B_g , A_u , and B_u) follow from the solution of the equations of motion (Sect. 5.6).

5.3.2

The Wavevector

The wavevector K can take on an arbitrary magnitude and an arbitrary direction within the 1st BZ. The 1st BZ of the naphthalene crystal (Fig. 5.5) follows from the usual rules and can be constructed in three steps as follows:

- 1.) The primitive vectors \mathbf{a}^* , \mathbf{b}^* , and \mathbf{c}^* of the reciprocal lattice are derived from the primitive vectors \mathbf{a} , \mathbf{b} , and \mathbf{c} of the crystal lattice: e.g.

$$\mathbf{a}^* = 2\pi(\mathbf{b} \times \mathbf{c})/(\mathbf{a} \cdot \mathbf{b} \times \mathbf{c}) \quad (5.1)$$

\mathbf{b}^* and \mathbf{c}^* are obtained by cyclic permutation.

- 2.) From \mathbf{a}^* , \mathbf{b}^* , and \mathbf{c}^* , the reciprocal lattice follows by means of periodic continuation.

- 3.) The 1st Brillouin zone follows from the reciprocal lattice by construction of the planes which are perpendicular to the lines connecting neighbouring points in the reciprocal lattice at their midpoints. The smallest closed volume which is bounded by these planes is the 1st BZ. For the naphthalene crystal, we find from the lattice parameters at $T = 300\text{ K}$ (Table 2.3) the following magnitudes for the reciprocal lattice vectors: $a^* = 2\pi \cdot 0.145\text{ \AA}^{-1}$, $b^* = 2\pi \cdot 0.167\text{ \AA}^{-1}$, $c^* = 2\pi \cdot 0.138\text{ \AA}^{-1}$; and for the volume V of the primitive unit cell of the crystal lattice, $V = \mathbf{a} \cdot \mathbf{b} \times \mathbf{c} = 359\text{ \AA}^3$. Γ denotes the centre, and Y , Z and A the boundaries of the 1. BZ in the a^* , b^* and c^* directions. Δ , R and Θ are points within the 1. BZ in the directions shown in Fig. 5.5.

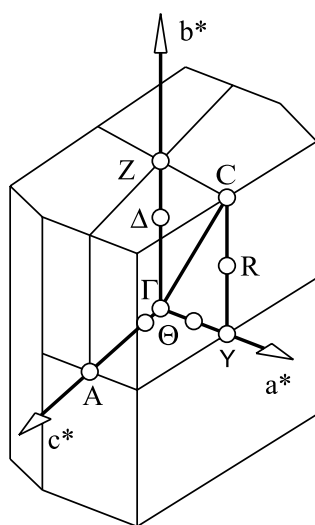


Fig. 5.5 The 1st Brillouin zone (1st BZ) of the naphthalene crystal. Γ denotes its centre. Y , Z and A are the usual notations for the boundaries of the 1st BZ in the a^* , b^* and c^* directions. For example, at A , the magnitude of the wavevector is $1/2c^*$ and c^* is perpendicular to the $(a-b)$ plane; it is thus parallel to the c' direction and not parallel to the c direction. Δ , Θ and R are points in or on the boundary of the 1st BZ.

5.3.3

The Frequencies $\Omega(\mathbf{K})$

Each phonon in a molecular crystal is characterised by its phonon dispersion relation $\Omega_j(\mathbf{K})$ with $j = 1, 2, \dots, j, \dots, 6Z$; (Z = the number of molecules in the unit cell). The individual phonon dispersion relations are also termed phonon branches. At each point $\Omega(\mathbf{K})$ along the dispersion relation curve, all the molecules oscillate with the same frequency Ω and with the same amplitude, but with phase differences defined by \mathbf{K} . At the Γ point, the molecules with the same orientation oscillate in phase in all the unit cells. An example is shown in Fig. 5.3. An example for $\mathbf{K} \neq 0$ and thus for a phase difference between neighbouring unit cells is shown schematically in Fig. 5.1.

5.3.4

Excitations

Besides thermal excitation of phonons, they can also be excited systematically by inelastic neutron scattering, by Raman scattering, by infrared absorption, by coupling to optical transitions or by coupling to charge carriers within the crystal. The first three of these methods can be applied to determine the phonon frequencies Ω or the entire dispersion relations $\Omega(\mathbf{K})$ quantitatively. This will be treated in the following Sect. 5.4.

5.4

Experimental Methods

For the experimental determination of the phonon dispersion relations $\Omega(\mathbf{K})$, inelastic neutron scattering is by far the most powerful method, but it also requires the most effort. Important complements to this method are however Raman scattering of light and infrared absorption spectroscopy. In particular, Raman scattering permits a precise determination of the frequencies of the Raman-active optical phonons with wavevectors $\mathbf{K} \approx 0$. It is thus particularly well suited to the evaluation of pressure and temperature dependences, which are especially prominent in the case of the soft organic molecular crystals.

5.4.1

Inelastic Neutron Scattering

Thermal neutrons have unique advantages over other particle-beam methods for the investigation of the lattice dynamics of solids: their average energy $E = \hbar^2 k^2 / 2M_n$ (M_n is the mass of the neutrons and $\hbar \mathbf{k}$ their momentum) lies near 25 meV and is thus of the same order as the phonon energies. At the same time, their average wavelengths λ , the de Broglie wavelengths $\lambda = 2\pi/k \approx 0.2$ nm, are comparable to the interatomic distances in crystals. The dimensions of the 1st BZ thus correspond to the magnitude of the wavevectors of thermal neutrons. Therefore, neutron scattering, in contrast to Raman or infrared spectroscopy, offers the possibility to determine the energies of all the lattice vibrations for each wavevector \mathbf{K} in the 1st BZ, that is the dispersion relations $\Omega(\mathbf{K})$. In contrast to beams of other particles such as electrons, neutrons furthermore interact with matter only weakly, which allows them to penetrate deeply into the substances being investigated. To be sure, this latter property means that neutron scattering requires large sample crystals.

In inelastic neutron scattering, neutrons from a cold source are selected by a monochromator M and collimated to yield a monoenergetic beam (Fig. 5.6). The neutron matter wave thus has a well-defined wavevector \mathbf{k}_i and a quantum energy $\hbar^2 k_i^2 / 2M_n$, before it reaches the crystal Cr which is to be investigated. In the crystal, it is scattered elastically and inelastically. In the case of the inelastic scattering,

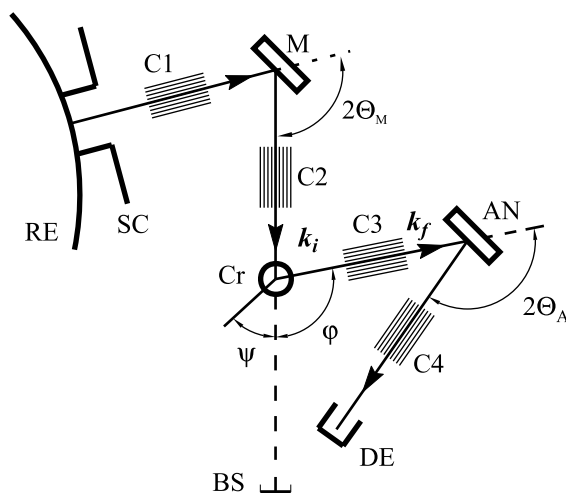


Fig. 5.6 The setup of a three-axis neutron spectrometer, schematic: RE = nuclear reactor, SC = shielding, M = monochromator crystal, C₁–C₄ = collimators, $2\Theta_M$ = scattering angle of the monochromator, AN = analyser crystal, $2\Theta_A$ = analyser scattering angle, Cr = sample (crystal), ψ = sample orientation relative to k_i , k_i = wavevector of the incident neutron waves, φ = scattering angle of the sample, k_f = wavevector of the inelastically-scattered neutron wave, DE = detector, BS = beam stop.

both the magnitude and direction of the wavevector k_f are different from k_i . The measurement of this difference using the analyser AN yields $\Omega(\mathbf{K})$, i.e. the frequency of the phonon created by the inelastic scattering process as a function of its wavevector. This follows directly from the two conservation laws for momentum and energy:

$$\mathbf{k}_i + \mathbf{G} = \mathbf{k}_f + \mathbf{K} \quad (5.2)$$

$$\hbar^2 k_i^2 / 2M_n = \hbar^2 k_f^2 / 2M_n \pm \hbar\Omega. \quad (5.3)$$

Here, \mathbf{G} is a lattice vector in the reciprocal-space lattice. Fig. 5.7 illustrates the principle of the experiment in reciprocal space. Only when Eqns. (5.2) and (5.3) are simultaneously fulfilled is there a finite intensity of the inelastically-scattered neutron wave. The observable quantity in the experiment is the intensity of the scattered neutron wave as a function of the energy loss and of the scattering vector \mathbf{Q} :

$$\mathbf{Q} = \mathbf{k}_i - \mathbf{k}_f. \quad (5.4)$$

By rotating the sample crystal, one can in principle investigate any arbitrary direction in the reciprocal lattice and any magnitude of \mathbf{K} , thus the entire first Brillouin zone.

The two usual types of spectrometers are the three-axis spectrometer and the time-of-flight spectrometer.

In the three-axis spectrometer (Fig. 5.6), the energies of both neutron waves, $\hbar^2 k_i^2 / 2M_n$ and $\hbar^2 k_f^2 / 2M_n$, are determined by diffraction from a monochromator

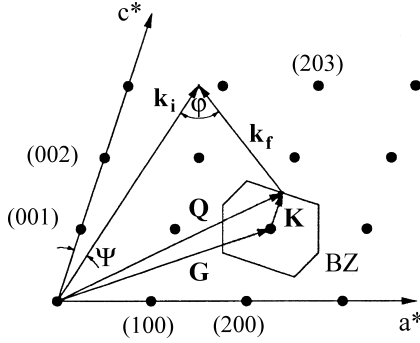


Fig. 5.7 A scattering diagram in reciprocal space. The scattering vector \mathbf{Q} is the difference between the wavevectors \mathbf{k}_i of the incident wave and \mathbf{k}_f of the scattered wave. \mathbf{Q} is an observable of inelastic neutron scattering. It determines the value of the phonon wavevector \mathbf{K} : $\mathbf{Q} = \mathbf{K} - \mathbf{G}$ up to a lattice vector \mathbf{G} in the reciprocal lattice. φ and ψ are the scattering angle and orientation of the sample (see Fig. 5.6).

crystal M or measured by an analyser crystal AN. In the monochromator, neutrons from the “white” beam of the reactor are diffracted by the monochromator crystal through an angle $2\Theta_M$ if and only if the Bragg condition is fulfilled: $2d \cdot \sin \Theta = n \cdot \lambda = n \cdot 2\pi/k$; the diffracted neutrons are thus monoenergetic. Here, d is the spacing of the lattice planes in the diffracting crystal, n is the order of the diffraction, λ is the wavelength and k is the magnitude of the wavevector of the neutron beam. The same relations hold for the analyser.

In a time-of-flight spectrometer (TOF spectrometer), the energy of the incident neutrons is determined, for example also by diffraction from a monochromator crystal M, but instead of a continuous neutron beam, a neutron pulse or a series of pulses is used, produced by periodic interruption of the neutron beam by a so-called chopper. The energy of the scattered neutron wave then is found from the velocity of the scattered neutrons, which is calculated from the distance and the measured time of flight of the neutrons between the sample crystal and the detector.

5.4.2

Raman Scattering and Infrared Absorption

Raman Scattering is inelastic scattering of photons of energy $\hbar\omega$. In this case, the laws of conservation of momentum and energy analogous to Eqns. (5.2) and (5.3) also hold:

$$\mathbf{Q} = \mathbf{k}_i - \mathbf{k}_f = \mathbf{K} \quad (5.5)$$

and

$$\omega_i = \omega_f \pm \Omega. \quad (5.6)$$

Since the wavelengths of visible and infrared photons are always large in comparison to the lattice constants, the scattering vector \mathbf{Q} can take on only vanishingly small values. Therefore, Raman scattering detects phonons only at $\mathbf{K} \approx 0$, i.e. at the centre Γ of the first BZ ($\mathbf{G} = 0$). In addition to the conservation laws, symmetry selection rules hold, which take into account the fact that Raman scattering is a two-quantum process. When g and u states are present, it is found for Raman processes that $g \leftrightarrow g$ transitions are allowed and $u \leftrightarrow g$ transitions are forbidden. Therefore, the lines in the Raman spectrum can be associated with the symmetry of the excited phonons.

Infrared Absorption is a single-photon process. Here, also, $\mathbf{k}_{\text{IR}} = \mathbf{K} \approx 0$ applies. Thus, infrared absorption detects only phonons at the Γ point of the first BZ. In this case, we have $\omega = \Omega$, where $\hbar\omega$ is the quantum energy of the infrared radiation. The frequencies or the wavenumbers of the optical phonons in molecular crystals are of the order of 3 THz or 100 cm^{-1} ; thus the wavelengths of infrared absorption are of the order of $100 \text{ }\mu\text{m}$. Infrared spectroscopy of phonons in molecular crystals is therefore in fact far-infrared spectroscopy. The symmetry selection rules are complementary to those for Raman scattering for vibrations with u and g states: $u \leftrightarrow g$ transitions are allowed and $g \leftrightarrow g$ transitions are forbidden.

Inelastic neutron scattering, Raman scattering and infrared absorption are thus complementary: Raman scattering and IR absorption have the advantage that Raman scattering in particular requires only very small samples; and the disadvantage that they detect phonons only at $\mathbf{K} = 0$. The great advantage of inelastic neutron scattering is that it can be used to determine the phonon dispersion relations throughout the whole Brillouin zone. In Sect. 5.5, we shall see on the basis of some examples that for a naphthalene crystal, the twelve phonon branches could in fact be determined in the entire first BZ by inelastic neutron scattering and that furthermore, all nine optical phonons are “visible” at the Γ point, six by Raman scattering and three by infrared absorption.

5.5

The 12 External Phonons of the Naphthalene Crystal

Naphthalene and anthracene belong to the organic molecular crystals on which extensive experimental investigations of the lattice dynamics have been carried out. They will therefore be used as examples in this and the following Sect. 5.6. Other organic molecular crystals will be discussed in Sect. 5.7.

5.5.1

Dispersion relations

Fig. 5.8 shows the experimental phonon dispersion relations of a perdeuterated naphthalene crystal (N-d_8) determined at a temperature $T = 6 \text{ K}$ by inelastic neutron scattering [7]. Deuterium (D) has a much higher scattering cross section for coherent inelastic neutron scattering than the isotope H. Nevertheless, to gain a

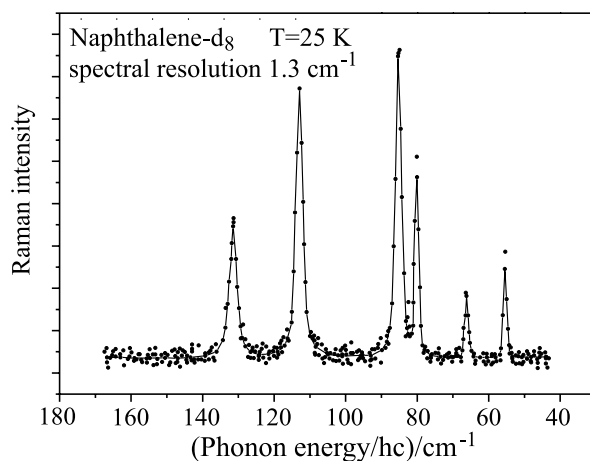


Fig. 5.9 The Raman spectrum of a N-d₈ crystal at $T = 25$ K. From [12].

- i. The number of external phonon branches is in fact twelve. Of these, three are acoustic and nine are optical branches.
- ii. The highest frequency or energy of an external phonon is that of an optical phonon at $\mathbf{K} = 0$. It has the value 3.9 THz or 16.1 meV. Compared to the optical phonon of Si at $\mathbf{K} = 0$, these values are about a factor of 4 smaller.
- iii. The width of the whole spectrum of the optical phonons is around 2.5 THz. Above the maximum frequency of 3.9 THz, the spectrum exhibits a gap which is about half as wide as the overall width of the spectrum of the optical phonons. The frequencies of the internal molecular vibrations are observed only above this gap. Their dispersion is weaker than that of the external modes. The gap in the spectrum, the number of phonon branches below

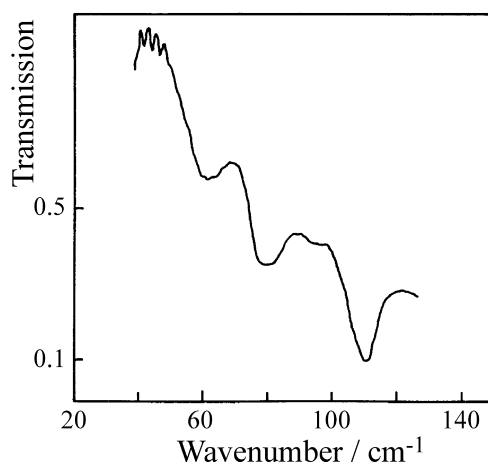


Fig. 5.10 The infrared absorption spectrum of a non-deuterated naphthalene crystal (N-h₈), at $T = 1.5$ K. From [13].

Table 5.3 Frequencies and symmetries of the 9 optical phonons (Nos. 12-4) at the Γ point ($\mathbf{K} = 0$) in a perdeuterated naphthalene crystal, N-d₈. The experiments were carried out at different temperatures: inelastic neutron scattering at $T = 6$ K [7], Raman scattering at $T = 25$ K [12], and infrared absorption at $T = 1.5$ K [13]

Optical phonon No.	Symmetry notation		Frequency at $\mathbf{K} = 0$ / THz (Naphthalene-D ₈ , $p = 1$ bar)		
			n scattering	Raman	IR
12	Γ_3	B_g	3.90	3.96	–
11	Γ_1	A_g	3.37	3.39	–
10	Γ_2	A_u	3.20	–	3.2
9	Γ_1	A_g	2.52	2.58	–
8	Γ_3	B_g	2.38	2.40	–
7	Γ_4	B_u	2.34	–	2.3
6	Γ_1	A_g	1.93	1.98	–
5	Γ_2	A_u	1.73	–	1.7
4	Γ_3	B_g	1.63	1.67	–

the gap, and the low dispersion above the gap are the experimental proof that here, a differentiation between internal and external modes is justified.

- iv. The optical phonons in the centre of the first BZ were detected also by Raman scattering or by IR absorption. Fig. 5.9 shows the Raman spectrum of a N-d₈ crystal [12] at $T = 25$ K and Fig. 4.10 gives the IR absorption spectrum of a N-H₈ crystal at $T = 1.5$ K [13]. The frequencies of the nine optical phonons at $\mathbf{K} = 0$ are collected in Table 5.3. (In the table, the IR frequencies from the spectra were multiplied by a factor $\sqrt{m(\text{N-H}_8)/m(\text{N-D}_8)} = 0.97$; since the IR-active phonons correspond to pure translational oscillations, this isotope correction is correct to the first approximation). The agreement of the experimental values from inelastic neutron scattering and from Raman and infrared spectroscopy is very good. In Table 5.3 and in Fig. 5.8, the symmetries of the optical phonons at $\mathbf{K} = 0$ are also given. They follow in the one hand from the theoretical calculation of the phonon dispersion relations (Sect. 5.6) and on the other from the selection rules for optical excitations: $\Gamma_1 = A_g$ and $\Gamma_3 = B_g$ are Raman-active, $\Gamma_2 = A_u$ and $\Gamma_4 = B_u$ are infrared-active phonons.
- v. Of the three acoustic phonon branches, in each case that with the largest slope is the branch of the longitudinal acoustic phonons (LA), while the two others are the transverse acoustic branches (TA). From this we can derive immediately the longitudinal sound velocity

Table 5.4 Longitudinal sound velocities $c_{s,l}$ in the perdeuterated naphthalene crystal (N-d₈ at $T = 6$ K) and in the perdeuterated anthracene crystal (A-d₁₀ at $T = 12$ K). The values were computed directly from the phonon dispersion relations.

K	N-d ₈	A-d ₁₀
// a^*	$3.2 \cdot 10^5$ cm/s	$3.1 \cdot 10^5$ cm/s
// b^*	$3.6 \cdot 10^5$ cm/s	$3.4 \cdot 10^5$ cm/s
// c^*	$3.3 \cdot 10^5$ cm/s	$4.0 \cdot 10^5$ cm/s

$$c_{s,l} = \frac{d\Omega_{LA}}{dK} \quad (5.7)$$

in the three directions a^* , b^* and c^* (Table 5.4).

5.5.2

Pressure and Temperature Dependencies

Organic molecular crystals are soft, and their thermal expansion coefficients are large. Both properties are a direct consequence of the van der Waals bonding, which is weak and anharmonic. Fig. 5.11 shows the temperature dependence of the relative volume V/V_0 of the naphthalene crystal with $V_0 = V(300\text{ K})$. Phenomenologically, it can be described by the function

$$V(T) = AT^2 + B. \quad (5.8)$$

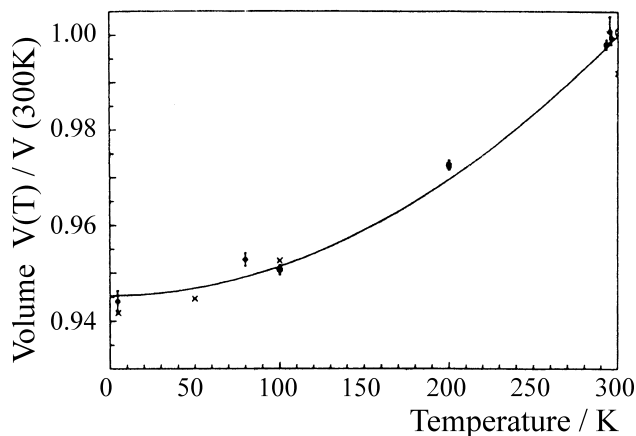


Fig. 5.11 The temperature dependence of the relative volume (V/V_0) of the naphthalene crystal N-d₈. The solid curve is a fit of the measured values to the parabolic dependence (Eq. (5.8)). $V_0 = V(300\text{ K})$. After [12].

Table 5.5 Parameters of Eq. (5.8) for the temperature dependence of the volume of the naphthalene and the anthracene crystals [12].

	$A/(\text{\AA}^3/\text{K}^2)$	$B/(\text{\AA}^3)$
Naphthalene-D ₈	$0.2190 \cdot 10^{-3}$	340.65
Anthracene-D ₁₀	$0.20 \cdot 10^{-3}$	456.2

The constants A have similarly large values for naphthalene and anthracene, while the constant B is naturally much larger for anthracene than for naphthalene, since the anthracene molecule is larger than the naphthalene molecule (Table 5.5).

Fig. 5.12 shows the pressure dependence of the relative volume of the naphthalene crystal. The isothermal compressibility κ is defined by

$$\kappa^{-1} = B(p) = -V \left(\frac{\partial p}{\partial V} \right)_{T=\text{const}}. \quad (5.9)$$

p is the pressure. The function $B(p)$ is called the module of compressibility. The pressure dependence of the volume can be described phenomenologically by the function

$$\left(\frac{V}{V_0} \right)^{B_1} = \frac{B_0}{B_1 p + B_0} \quad (5.10)$$

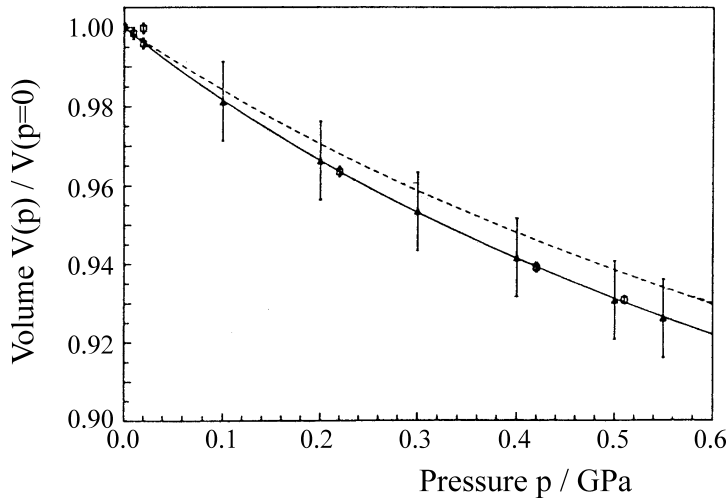


Fig. 5.12 The pressure dependence of the relative volume V/V_0 of the naphthalene crystal N-d₈ at room temperature. The measured values with different symbols are from different, independent experiments. The solid curve is a fit to the so called Murnaghan equation (Eq. (5.10)). The dashed line is a fit to a “modified” Murnaghan equation. From [12].

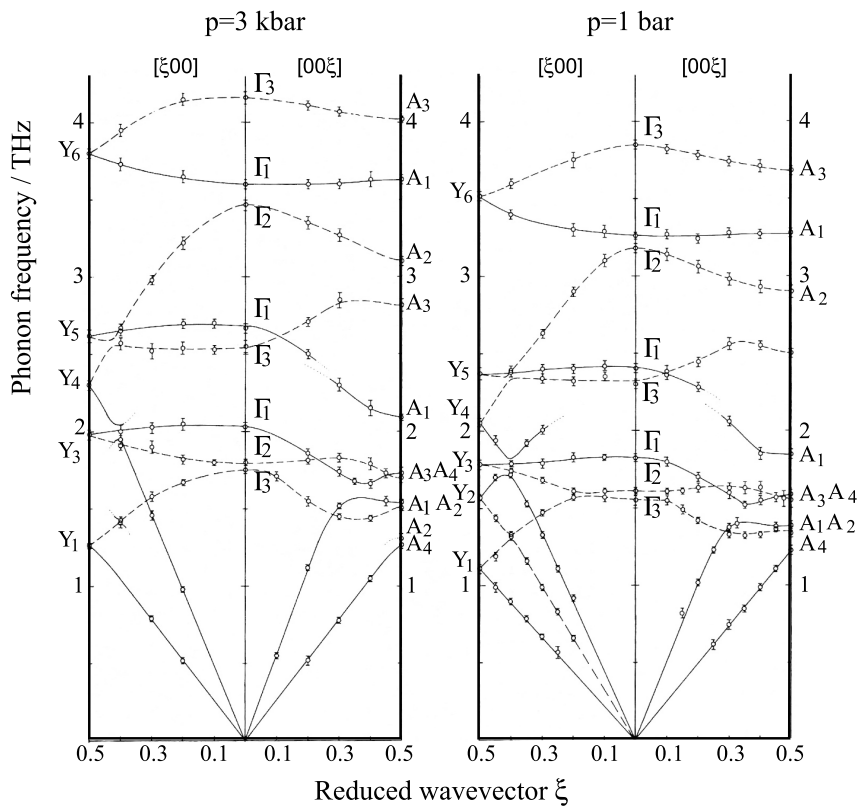


Fig. 5.13 The pressure dependence of the phonon dispersion relations of the N-d₈ crystal at $T = 100$ K. At high pressures, nearly all the phonon frequencies are higher than at normal pressure. After [8].

[12]. Here, the constants for naphthalene have the values:

$$B_0 = 4.95 \text{ GPa} \quad \text{and} \quad B_1 = 9.2.$$

As a result of the strong variation of the crystal volume and therefore of the lattice parameters on changing the temperature and pressure, the frequencies of the external phonons change. An example of the dependence of the phonon dispersion relations on the hydrostatic pressure p is shown in Fig. 5.13. At $p = 3$ kbar, the crystal is compressed and all the phonon frequencies are higher than at $p = 1$ bar [8]. With increasing temperature, the crystal expands and the phonon frequencies become lower [10]. The frequency shifts were determined for each phonon branch by inelastic neutron scattering and, for the Raman-active modes, also by Raman scattering, and analysed quantitatively. The mean frequency shift $\Delta\nu/\nu$ is about -10% on increasing the temperature from 6 K to 300 K. However, we cannot treat these details further here and refer the reader to the original literature [8, 9, 10, 12]. In a quantitative analysis of the temperature and pressure

dependence of scattering processes, e.g. by excitons or by charge carriers, the temperature and pressure dependencies of the phonons must be taken into account.

5.6

Analytic Formulation of the Lattice Dynamics in Molecular Crystals

Under the assumptions that the intermolecular interactions in molecular crystals can be represented as the sum of the atom-atom interactions (Table 2.2 and Fig. 2.6), and that the molecules are rigid, i.e. their masses and their inertial tensors are constant, Pawley [14] carried out the first analytical formulation of the lattice dynamics. In the following, we will sketch the physical fundamentals of his model and describe its results in the harmonic approximation in comparison with the experimental phonon dispersion relations (Fig. 5.8). As we shall see, the model of an oriented gas describes the experimental results in detail, and furthermore, it yields both the similarities of the lattice dynamics of different molecular crystals and their differences qualitatively, even when the same parameters for the intermolecular atom-atom potentials are used for all of the molecular crystals (Table 2.2 and Fig. 2.6).

For the formulation of the lattice dynamics in a molecular crystal, only six coupled equations of motion are necessary: three for translation and three for rotation of a single molecule, if all the molecules in the unit cell are connected by symmetry operations. (This assumption does not hold e.g. for dipolar disorder in dimethyl-naphthalene or dimethyl-anthracene crystals (see Sect. 5.7).) The translational-rotational displacements $\mathbf{u}(lk)$ of the k th molecule in the l th unit cell are taken to be given by propagating plane waves $\mathbf{u}(lk) = \mathbf{U}(lk)e^{i(\mathbf{K} \cdot \mathbf{r} - \Omega(\mathbf{K})t)}$. Here, $\Omega(\mathbf{K})$ is the frequency of the phonon with wavevector \mathbf{K} . \mathbf{u} is a vector with six components u_i . The u_i refer for $i = 1, 2, 3$ to the translational displacements and for $i = 4, 5, 6$ to the rotational displacements. For the formulation of the equations of motion, the “force constants” are required. They are computed from the overall lattice potential Φ . Φ is the sum over all the intermolecular pair-potentials $V_{lk,l'k'}$:

$$\Phi = \frac{1}{2} \sum_{ll'} \sum_{kk'} V_{lk,l'k'} . \quad (5.11)$$

Here, for the second summation the condition $k \neq k'$ within the same lattice cell $l = l'$ is required. The factor $1/2$ avoids double counting. Each intermolecular pair-potential $V_{lk,l'k'}$ is taken to be a superposition of atom-atom central potentials $V_{mn}(r_{mn})$ (see Sect. 2.1.3 and Fig. 2.6):

$$V_{lk,l'k'} = \sum_{mn} V_{mn}(r_{mn}) . \quad (5.12)$$

Here, m denotes the atoms of molecule lk , n the atoms of molecule $l'k'$, and r_{mn} the distances between the atoms m and n .

For small displacements u_i , the “force constants” (force constants for the translational vibrations and torque constants for the rotational vibrations) are the second derivatives Φ_{ij} of the lattice potential Φ with respect to the corresponding displacements:

$$\Phi_{ij}(lk, l'k') = \frac{\partial^2 \Phi}{\partial u_i(lk) \partial u_j(l'k')} . \quad (5.13)$$

With these expressions, the equations of motion for the molecule (lk) become

$$M_i \ddot{u}_i(lk) = - \sum_{l'k'j} \Phi_{ij}(lk, l'k') u_j(l'k') . \quad (5.14)$$

Here, the M_i for $i = 1, 2, 3$ refer to the masses of the molecules and for $i = 4, 5, 6$ to their moments of inertia on rotation around the principal axes of the inertial tensor.

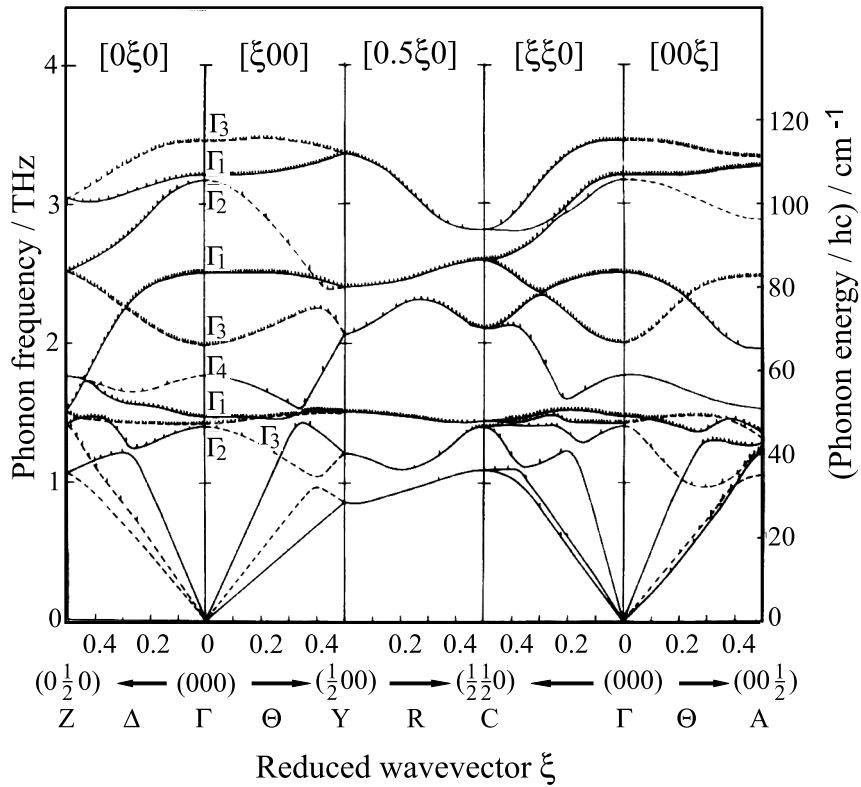


Fig. 5.14 Calculated phonon dispersion relations in the harmonic approximation for perdeutero-naphthalene, (N-d₈). The agreement with the experimental dispersion relations (Fig. 5.8) provides a good justification of the rigid-molecule model, because the parameters of the intermolecular potentials

used in the calculations are independent of the dispersion relations and were not determined in a way specific to a particular polyacene (here: naphthalene); nevertheless, the discrepancies between the calculated and the experimental dispersion relations are not more than at most 20%. From [7].

The limitation to second derivatives in computing the “force constants” is called the harmonic approximation. The calculation does not take into account either the zero-point oscillation or the anharmonicity of the potentials. It is, strictly speaking, valid only at $T = 0$. Thermal expansion, thermal conductivity and other nonlinear effects are thus not contained in this model.

In detail, the solution of the equations of motion requires strict observance of the crystal symmetry and precise equilibrium coordinates of the molecules and their atoms in dependence on the temperature (and the pressure), since only then can the atom-atom potentials be computed correctly. Natkaniec *et al.* [7] solved the equations of motion numerically at $T = 0$ K for the perdeuterated naphthalene crystal N-d₈ (and later for many other molecular crystals). The lattice sum in Eq. (5.14) was limited to 24 neighbouring molecules j , after it had been found that inclusion of additional neighbour shells had no influence on the results. This is a direct consequence of the short range of the van der Waals interaction.

The results of the calculations of the phonon dispersion relations for the N-d₈ crystal are shown in Fig. 5.14 with the parameter set of Kitaigorodskii (Table 2.2 and Fig. 2.6). A comparison with the experimental dispersion relations (Fig. 5.8) to be sure exhibits numerical deviations of up to 20%; however, the qualitative shape of the curve is well reproduced, including many details. This is all the more surprising since the intermolecular atom-atom potential parameters used were obtained from macroscopic properties (crystal structure, compressibility, sublimation energy) of many different organic molecular crystals and not simply taken from the dispersion relations or from data for the naphthalene crystal alone. The good general agreement between experiment and theory therefore justifies the model of atom-atom potentials as a good approximation for the bonding and dynamics of the molecules in organic molecular crystals. In this model, the differences due to the use of the parameter sets of Kitaigorodskii or of Williams are not very significant.

5.7 Phonons in other Molecular Crystals

Qualitatively, the dynamic properties of different polyacene crystals are similar, since both the intermolecular van der Waals forces and also the molecular masses are to first order proportional to the number of C atoms per molecule. Therefore, for example all the sound velocities are of the same order of magnitude (Table 5.4). The same is true for the maximum frequencies of the optical phonons and of the intramolecular oscillations. A clear and general difference is however to be found between smaller and larger molecules in terms of the lowest frequencies of the intramolecular modes: with increasing molecular mass, the frequency of the low-energy intramolecular vibrations shift towards lower values. These molecular excitations are either bending or torsional oscillations. This frequency shift can cause the gap and the strict separation of internal and external modes to become less sharp.

In the following section, the peculiarities of the dynamic properties of a few selected molecular crystals will be treated briefly.

Anthracene: The six libration modes in perdeuterated anthracene have the following frequencies at the Γ point ($\mathbf{K} = 0$) at $T = 12$ K (in THz, [15]): 1.43 (1.41), 1.62 (1.62), 2.06 (2.04), 2.32 (2.34), 3.65 (3.6) and 3.87 (3.84). The frequencies in parentheses were measured with Raman scattering. Using inelastic neutron scattering, not only were the dispersion relations of the above-named six modes determined, but all together 16 dispersion branches were measured. Of these, as for naphthalene, twelve are external modes (three acoustic and nine optical). The remaining four branches are the four lowest-energy internal modes. In contrast to naphthalene, they show a noticeable dispersion and their frequency spectrum overlaps with that of the external modes. As for the naphthalene crystal, all the dynamic properties of the anthracene crystal, i.e. all the phonon branches and the crystal volume, are strongly dependent on the temperature and the pressure [16, 12].

Perylene: The two different crystalline phases, α perylene and β perylene (see Chap. 2, Fig. 2.12) differ strongly also in their dynamic properties: α perylene has four molecules or two dimers per unit cell. From this, 24 internal modes result, 21 optical and three acoustic. They have also been observed and identified by inelastic neutron diffraction [17] and by Raman scattering [18]. Their spectrum has a width of about 4 THz, again similar to the cases of naphthalene and anthracene. For α perylene, the model treated in Sect. 5.6 again yields satisfactory theoretical dispersion relations. The low-energy internal modes are torsional (twisting) and butterfly modes. Their spectrum overlaps with that of the external modes.

β Perylene, in contrast, has only two molecules per unit cell and thus again nine optical and three acoustic phonons [18]. Fig. 5.15 shows the molecular displacements of characteristic phonons in both phases of the perylene crystals. There, one can readily see that the doubling of the modes in α perylene in comparison to β perylene has its origin in the differences between the cophase and the corresponding counterphase displacements of the two molecules in the dimers. The counterphase modes have higher frequencies and can therefore be considered to be excitation states of the dimers within the crystal.

Biphenyl: The molecule (Fig. 5.16) is not planar in the gas phase; the angle between the two planes is about 45° . In the biphenyl crystal, the molecules are planar. At 40 K and at 17 K, there are structural phase transitions within the biphenyl crystal. The molecules thereby lose their centres of inversion. Below 40 K, the molecule is twisted by about 10° around the central C–C axis. This means that the intermolecular coupling is larger than the intramolecular torsion potential and that the coupling between torsional and lattice oscillations cannot be neglected in every case, but instead can even induce phase transitions. A similar conclusion holds for the coupling of low-frequency bending vibrations (Fig. 5.16, lower part) to external lattice vibrations (see e.g. [19, 20]).

2,3-Dimethyl-naphthalene (DMN) and 2,3-Dimethyl-anthracene (DMA): These two molecules crystallise similarly to naphthalene and anthracene (see Chap. 4.2.4). In particular, they form macroscopically apparently perfect single crystals. The lattice parameters of the triclinic 2,3-DMA crystal at room temperature are $a =$

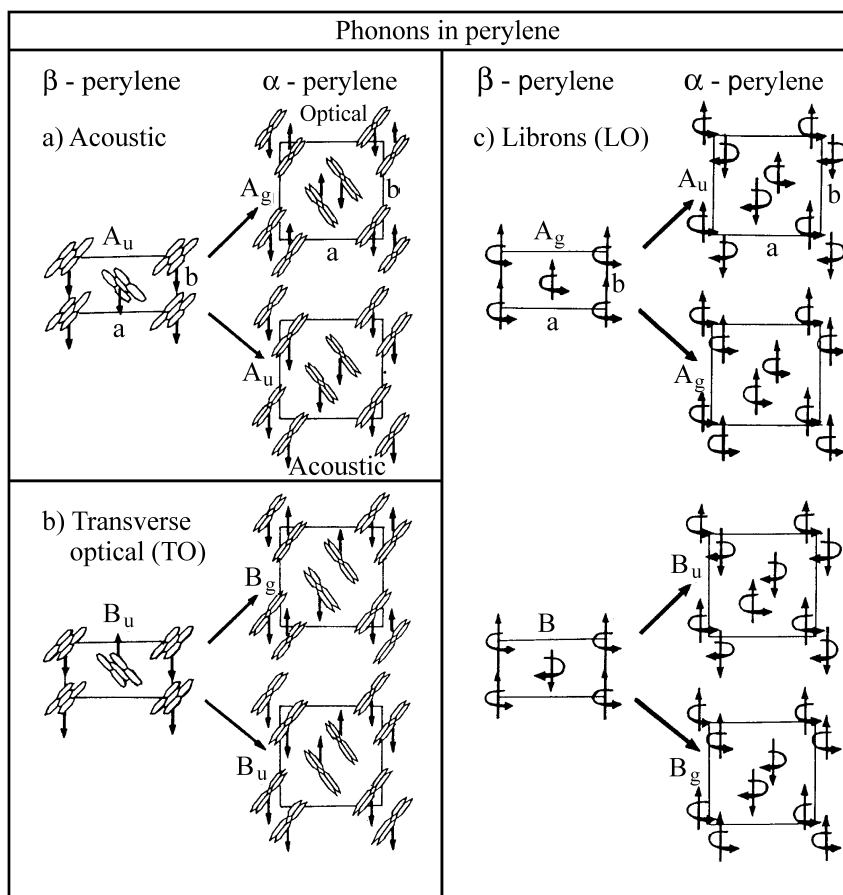


Fig. 5.15 The characteristic phonons in perylene crystals (see also Fig. 2.12). $\mathbf{K} = 0$. From [18].

0.762 nm, $b = 0.596$ nm, $c = 1.252$ nm, $\alpha = 93.3^\circ$, $\beta = 105.4^\circ$, and $\gamma = 89.99^\circ$ [21]. The crystal symmetry is described by the space group P1. This means that the molecules would have to have point symmetry and that their centres of symmetry

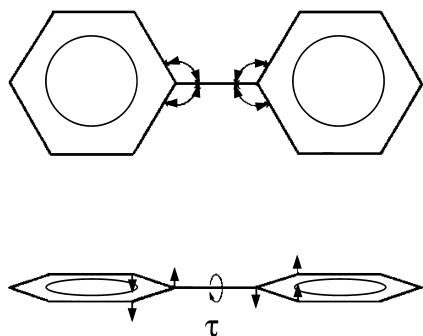


Fig. 5.16 Low-frequency intramolecular excitations in biphenyl. The arrows indicate low-molecular bending vibrations. τ = torsional vibration.

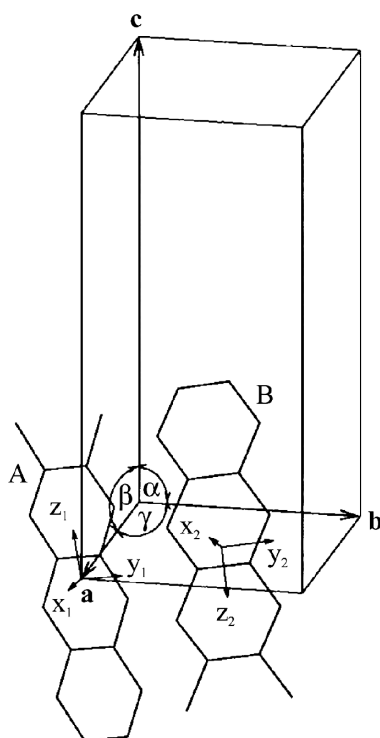


Fig. 5.17 The unit cell of 2,3 dimethyl-anthracene (DMA).

x_1, y_1, z_1 and x_2, y_2, z_2 define the molecule-fixed coordinate systems of the molecules A and B.

would occupy the crystalline inversion centres (000) or $(1/2 \ 1/2 \ 0)$ (Fig. 5.17). In reality, the molecules do not have centres of inversion. Therefore, one has to assume a so called dipolar disorder in the crystals, in the sense of an “up-down” orientation of the methyl groups. Thus in Fig. 5.17, instead of molecule B, a molecule with the reversed orientation of its z_2 axis could be located with the same probability. X-Ray structural analysis thus shows a reference lattice which consists of averaged inversion-symmetrical molecules formed by averaging the two possible orientations, whose centres of symmetry occupy the inversion centres of the crystal (Fig. 5.18).

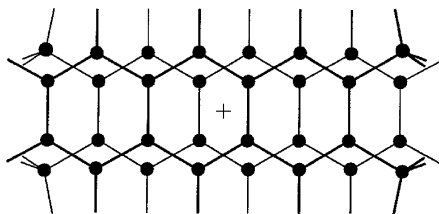


Fig. 5.18 An inversion-symmetric 2,3-DMA molecule as is exhibited by X-ray structural analysis through an average superposition of the two possible orientations within the real crystal. After [21].

The crystals are thus not single crystals with a strictly periodic lattice, but rather they possess an intrinsic structural dipolar disorder. This disorder leads among other effects to a strong broadening of the reflections in inelastic neutron scattering. Their analysis using the Pawley model verifies the dipolar disorder and yields details of the molecular and crystalline distortions, which we will not treat further here (see [21–23]). In terms of couplings of other degrees of freedom (excitons, charge carriers...) with the phonons, this example of dipolar disorder shows that even small perturbations of the lattice periodicity will give rise to a broad phonon spectrum.

5.8

Hindered Rotation and Diffusion

As already mentioned, in some molecular crystals, a hindered or nearly free rotation of entire molecules is observed, e.g. of benzene molecules in crystals of benzene, or of molecular groups, e.g. of CH_3 groups in crystals of methyl naphthalene. These motions are stochastic and are termed pseudorotations or reorientations. These two terms denote the two limiting approximations, that of free rotation and that of a fixed orientation of the molecules or molecular groups. Experimental methods which have proved useful for the investigation of these stochastic motions are nuclear-spin magnetic resonance (NMR) [24] and quasielastic neutron scattering [35, 36].

Furthermore, molecules in molecular crystals can diffuse from their lattice sites to a neighbouring vacancy. This translational or self-diffusion has been investigated in a number of molecular crystals, e.g. using radioactive tracer molecules [31, 32].

In the following sections, we treat briefly or sketch the relevant observable quantities in NMR spectroscopy for the investigation of rotational motions and the examples of molecular or molecular-group rotations mentioned, as well as the tracer methods and their results for translational diffusion.

5.8.1

Nuclear Magnetic Resonance (NMR): the Second Moment of the Line shape and Nuclear Spin-Lattice Relaxation

The NMR spectrum of a rigid solid, e.g. the proton (^1H)NMR spectrum of a polyacene crystal, consists as a rule of a single broad line. It is inhomogeneously broadened, i.e. it is a statistical superposition of spectrally unresolved components. The spectral width of the statistical distribution and thus the solid-state NMR linewidth is greater than the linewidth of the individual components and it is in particular very much greater than the NMR linewidth in liquids (see e.g. [28]). In a static magnetic field \mathbf{B}_0 and a high-frequency magnetic field $\mathbf{B}_1 \cos \omega t$, the resonance condition is given by $\hbar\omega = \hbar\omega_L = g_I\mu_N B_0$. The symbols used here are: $\omega = \omega_L$ = Larmor frequency, g_I = nuclear g -factor, μ_N = nuclear magneton, and $B_0 = |\mathbf{B}_0|$ = resonance field strength, with $\mathbf{B}_0 \perp \mathbf{B}_1$. The width of the inhomoge-

neous NMR line and thus the width of the statistical distribution are denoted as ΔB . The cause of the inhomogeneous broadening in a rigid lattice is the magnetic dipole-dipole coupling of neighbouring nuclei. A nucleus with the magnetic moment μ produces a local magnetic field B_{loc} at a distance r of the order of $B_{loc} = \mu_0 \mu / 4\pi r^3$. Here, $\mu_0 = 4\pi \cdot 10^{-7} \text{ VsA}^{-1}\text{m}^{-1}$ is the magnetic induction constant (permeability of vacuum). For a proton ($\mu = 1.4 \cdot 10^{-26} \text{ Am}^2$), and at a distance $r = 2 \text{ \AA}$, $B_{loc} \approx 2 \cdot 10^{-4} \text{ Tesla} = 2 \text{ Gauss}$.

To compute the lineshape $f(B)$ and its width ΔB , one has to sum over the dipole-dipole interactions of all nuclei $1, 2, \dots, i, \dots, j, \dots, N$ with their different distances \mathbf{r}_{ij} . For N nuclei and using a quantum-mechanical treatment, the contribution \mathcal{H}_{DD} of the dipole-dipole interaction to the spin Hamiltonian is

$$\mathcal{H}_{DD} = \frac{\mu_0}{4\pi} \cdot \frac{1}{2} \sum_{i=1}^N \sum_{j=1}^N \left\{ \frac{\boldsymbol{\mu}_i \boldsymbol{\mu}_j}{r_{ij}^3} - \frac{3(\boldsymbol{\mu}_i \mathbf{r}_{ij})(\boldsymbol{\mu}_j \mathbf{r}_{ij})}{r_{ij}^5} \right\}. \quad (5.15)$$

Here, $\boldsymbol{\mu}_i = g_i \mu_N \mathbf{I}_i$, $\boldsymbol{\mu}_j = g_j \mu_N \mathbf{I}_j$, \mathbf{I}_i and \mathbf{I}_j are the nuclear spin operators, and $r_{ij} = |\mathbf{r}_{ij}|$.

The factor $1/2$ takes into account the fact that the pairs of nuclei should not be doubly counted in the summation, and naturally all summands with $i = j$ are excluded. Each summand leads to a single component of the inhomogeneous NMR line. In a rigid lattice, the different directions of the \mathbf{r}_{ij} are constant in time. The nuclear spins are directionally quantised in the external magnetic field \mathbf{B}_0 when $B_0 \gg B_{loc}$.

For a known crystal structure, each summand in Eq. (5.17) can be computed, and thus in principle the statistical distribution $f(B)$ of the resonance field strengths, i.e. the shape of the inhomogeneous resonance line (see e.g. [26]).

For a simple comparison with experiment, the calculation of the **second moment** $\langle \Delta B^2 \rangle$ of the NMR line suffices:

$$\langle \Delta B^2 \rangle = \frac{\int_0^\infty (B - \langle B \rangle)^2 f(B) dB}{\int_0^\infty f(B) dB}. \quad (5.16)$$

Here, $\langle B \rangle$ is the central resonance field strength. The second moment $\langle \Delta B^2 \rangle$ is roughly equal to the square of the inhomogeneous linewidth ΔB and is of the order of the square of the local field: $\langle \Delta B^2 \rangle \approx B_{loc}^2$. Van Vleck [27] was the first to compute the second moment for a rigid lattice. For protons ($I_i = I_j = I = 1/2$ and $g_i = g_j = g_I = 5.58$), the Van Vleck formula gives:

$$\langle \Delta B^2 \rangle = \frac{3}{4} \left(\frac{\mu_0}{4\pi} \right)^2 I(I+1) g_I^2 \mu_K^2 \frac{1}{N} \sum_k \frac{(1 - 3 \cos^2 \Theta_{jk})^2}{r_{jk}^6}. \quad (5.17)$$

In this expression, r_{jk} is the magnitude of the distance of proton k from proton j , and Θ_{ij} is the angle between the external magnetic field \mathbf{B}_0 and the distance vector \mathbf{r}_{jk} . The sum runs over all the protons k and is independent of j . To each \mathbf{r}_{jk} in the

rigid lattice corresponds a fixed value of Θ_{ij} . The largest contribution to the second moment comes naturally from the nearest-neighbour protons. Equation (5.18) permits an immediate comparison between the calculated and measured inhomogeneous linewidths in a rigid lattice. For benzene, the calculation gives, in good agreement with the measured value at $T < 90$ K, the result $\langle \Delta B^2 \rangle = 9.7$ Gauss², (cf. Fig. 5.19).

If the lattice is not rigid, i.e. if the molecules or individual molecular groups can reorient rapidly and statistically, then in the calculation of the second moment in Eq. (5.18), an average must be carried out over all the orientations Θ_{jk} of the proton-proton position vectors, which change during the motions. The reason for this is motional narrowing: when the inverse correlation time τ_c^{-1} of the reorientation is greater than the inhomogeneous linewidth of the rigid lattice in frequency units ($\tau_c^{-1} > \Delta\omega = g_I\mu_N\Delta B/\hbar$), then the anisotropic contributions to the second moment are averaged out. The linewidth thus becomes smaller. Owing to their small absolute linewidths in comparison to optical spectral lines, the process of motional narrowing is often observed in NMR and ESR spectroscopies (see also Chap. 7.4), and the NMR lines in liquids are very sharp.

Along with the inhomogeneous linewidth ΔB or its second moment $\langle \Delta B^2 \rangle$, another directly observable quantity in nuclear magnetic resonance is the longitudinal or spin-lattice relaxation time T_1 . It characterises the relaxation of the nuclear-spin magnetisation $\mathbf{M}(t)$ towards thermal equilibrium after it has previously been perturbed, e.g. by a resonant high-frequency pulse or a sudden change in the external magnetic field B_0 . In the simplest case, the process of spin-lattice relaxation follows an exponential function, $\mathbf{M}(t) = \mathbf{M}_0 e^{-t/T_1}$, and is thus uniquely defined by the constant T_1 . Methods for determining T_1 are described in basic textbooks on NMR (see e.g. [26, 28]) and will not be treated here. However, it is important for the treatment of statistical rotational reorientation motions to understand the mechanism of the spin-lattice interaction. When the reorientation of the molecules and thus also of the position vectors of neighbouring nuclear spins relative to the external field B_0 is a stochastic time-dependent process, then the dipole-dipole coupling also fluctuates with time, due to its anisotropic character, and with it the local field B_{loc} ; the fluctuations are characterised by a correlation time τ_c . A temporally fluctuating local field induces nuclear spin transitions. The spin-lattice relaxation time T_1 has its minimal value when $\tau_c^{-1} \approx \omega_L$, where ω_L is the nuclear spin Larmor frequency (precession frequency in the external magnetic field). Bloembergen, Purcell and Pound [25] derived the following formula for this process:

$$\frac{1}{T_1} = C \left[\frac{\tau_c}{1 + \omega_L^2 \tau_c^2} + \frac{2\tau_c}{1 + 4\omega_L^2 \tau_c^2} \right]. \quad (5.18)$$

Here, C is a coupling constant. For a particular molecule, C has a fixed value. From a measurement of $T_1(\omega_L)$, τ_c can be determined in principle.

When the molecular reorientation process is thermally activated, one expects the following temperature dependence for τ_c :

$$\tau_c = \tau_\infty e^{\Delta E/kT} \quad (5.19)$$

where ΔE is the activation energy for the reorientation. It is defined by the potential of the molecule or molecular group whose stochastic reorientation is being considered. From a measurement of $T_1(T)$, one can thus use Eqns. (5.18) and (5.19) to determine the activation energy of the reorientation. For this purpose, analysis of the function $\lg T_1(T^{-1})$, which can be determined directly from experiment, is suitable. It exhibits a characteristic V-shape, whose minimum depends on the Larmor frequency (cf. Fig. 5.21).

5.8.2

Benzene Crystals

Andrew and Eades [24] investigated the proton spin resonance spectra and spin-lattice relaxation in polycrystalline benzene (C_6H_6) in the temperature range between 75 K and 278 K. The second moment (the square of the linewidth) of the proton spin resonance line exhibits a characteristic temperature dependence (Fig. 5.19): at $T < 80$ K the width of the motionally-narrowed NMR line is independent of the temperature. In the range between 80 K and 120 K, the resonance line becomes less broad due to motional narrowing. At $T > 120$ K, the narrow linewidth again becomes temperature independent.

At $T < 80$ K, the linewidth is quantitatively attributable to the magnetic dipole-dipole coupling of the protons in the rigid benzene lattice. It follows directly from the crystal structure (see Sect. 5.8.1) that each pair of protons ij gives a contribution to the second moment proportional to r_{ij}^{-6} . All together, Andrew and Eades obtained for the second moment in polycrystalline, non-deuterated hydrocarbons a value of $7.159 \cdot 10^{-46} N^{-1} \sum_{i>j} r_{ij}^{-6} \text{ Gauss}^2$. N is here the number of proton pairs whose interactions contribute to the linewidth, and r_{ij} is the magnitude of the proton-proton distances in units of cm. The sum consists of two types of terms, those for the in-

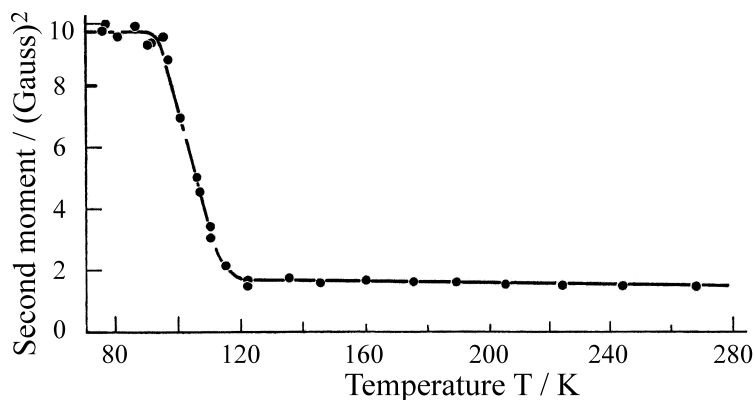


Fig. 5.19 The temperature dependence of the second moment (the square of the linewidth) of the proton spin resonance line of a benzene crystal, (C_6H_6). 1 Gauss = 10^{-4} Tesla $\hat{=}$ 4.2576 MHz for protons. From [24].

tramolecular pairs and those for the intermolecular pairs. In the case of benzene, the sum yields a result of 9.7 Gauss^2 (cf. Fig. 5.19).

The narrowing above $T > 90 \text{ K}$ results from the molecular reorientation of the pairs. Here, the benzene molecules undergo rotational jumps around the hexagonal symmetry axis. These jumps are thermally activated. At $T > 120 \text{ K}$, they have become so rapid that most, but not all, of the contributions of the dipole-dipole interaction to the second moment are averaged out. The resulting theoretical value for the second moment in benzene is 1.55 Gauss^2 , in good agreement with the experimental value of 1.61 Gauss^2 (cf. Fig. 5.19).

When the process of reorientation can be described by a single correlation time τ_c , then τ_c can be determined from the spin-lattice relaxation time T_1 (see Sect. 5.8.1). Fig. 5.20 illustrates the temperature dependence of τ_c in an Arrhenius plot. The reorientation is evidently a thermally activated process over the whole temperature range (Eq. (5.23)): $\tau_c = \tau_\infty \exp(\Delta E/kT)$. The activation energy ΔE is found to be $3.7 \text{ kcal/mol} \cong 160 \text{ meV/molecule}$ and is within its error limits the same for the two partially deuterated benzenes, $\text{C}_6\text{H}_5\text{D}$ and $\text{C}_6\text{H}_3\text{D}_3$. The value of ΔE is about 35% of the sublimation energy. The activation barrier for the reorientation in benzene is thus a significant portion of the binding energy of the crystals.

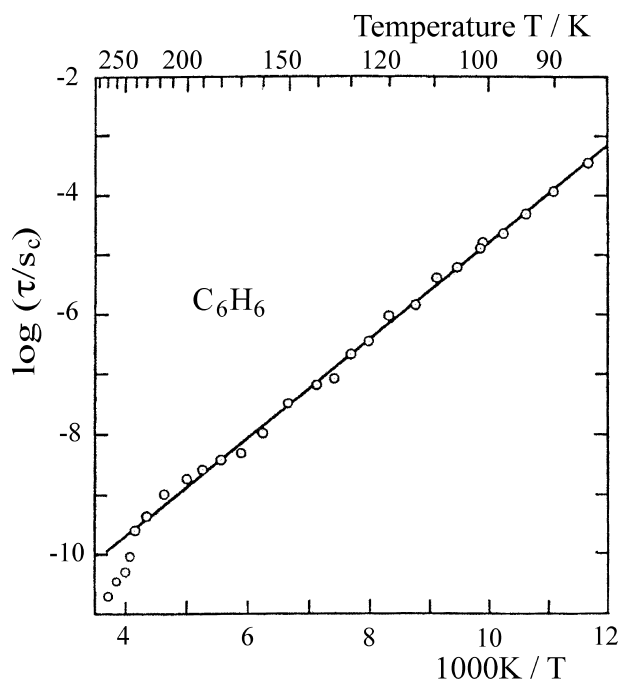


Fig. 5.20 The temperature dependence of the correlation time τ_c of the protons in a benzene crystal, C_6H_6 . It was obtained from the proton spin-lattice relaxation time T_1 . The corresponding activation energy is $\Delta E = 160 \text{ meV}$. After [24].

The frequencies $\nu_c = 1/(2\pi\tau_c)$ and $\nu_\infty = 1/(2\pi\tau_\infty)$ can be considered to represent an average reorientation frequency and its maximum value at $T \rightarrow \infty$. From Fig. 2.20, we find e.g. for C_6H_6 : $\nu_c(90\text{ K}) = 1.6\text{ kHz}$. Compared with the static linewidth expressed in frequency units, $\Delta\nu = 13.6\text{ kHz}$, $\nu_c(90\text{ K})$ is rather small. At $T = 110\text{ K}$, $\nu_c(110\text{ K}) = 79\text{ kHz}$ and is thus large compared to the static linewidth. Therefore, motional narrowing must be considered in the range between 90 K and 110 K. At $T \rightarrow \infty$, $\nu_\infty = 1/(2\pi\tau_\infty) = 1.5\text{ THz}$. A simple numerical estimate shows that $h\nu_0$ is still small compared to the quantum energy of the highest rotational states of the free benzene molecule around its sixfold symmetry axis, which are thermally excited at $T = 300\text{ K}$. The reorientation motion can therefore not be considered to be a free rotation even at high temperatures, but is rather a stochastic process, whose average frequency at high temperatures lies in the range of the acoustic phonons.

Further details of the dynamics of polycrystalline benzene were obtained with advanced NMR methods and with quasielastic incoherent neutron scattering [35, 36].

5.8.3

Methyl Groups

Von Schütz and Wolf [29] have likewise investigated a second typical stochastic reorientation motion using NMR in molecular crystals: the hindered rotation of methyl (CH_3 -) groups in ten different methyl-substituted naphthalene crystals. The reorientation motions are, at not-too-low temperatures, the dominant source of nuclear spin-lattice relaxation in these highly purified molecular crystals. Only at very low temperatures do thermally-activated reorientation processes cease to play a role. The spin-lattice relaxation is then determined essentially by paramagnetic impurities.

In non-substituted naphthalene crystals, the activation energy for the reorientation of whole naphthalene molecules is about 25 kcal/mol or 1 eV per molecule. It can thus only become important for spin-lattice relaxation in the neighbourhood of the melting point. In methyl-substituted naphthalene crystals, the reorientation of whole methyl-naphthalene (NM) molecules is still more strongly sterically hindered but nevertheless the proton spin-lattice relaxation times are much shorter, up to five orders of magnitude, over the whole temperature range of the measurements, than in non-substituted naphthalene crystals. This can be attributed exclusively to the reorientation motions of the CH_3 groups. They are also called rotation-diffusion jumps and are to first order characterised by a correlation time τ_c , i.e. by the correlation time constant τ_∞ and the activation energy ΔE . As examples, Figs. 5.21a and b show the experimentally-determined values of the proton spin-lattice relaxation time T_1 of two different dimethyl-naphthalene (DMN) single crystals as a function of the inverse temperature. T_1 was measured over the temperature range from the melting point down to about -200°C and at four different proton Larmor frequencies, $\omega = 4\text{ MHz}$, 22 MHz , 44 MHz , and 86 MHz . In 1,5-DMN (Fig. 5.21b), the two CH_3 groups are attached to the molecule in such a way

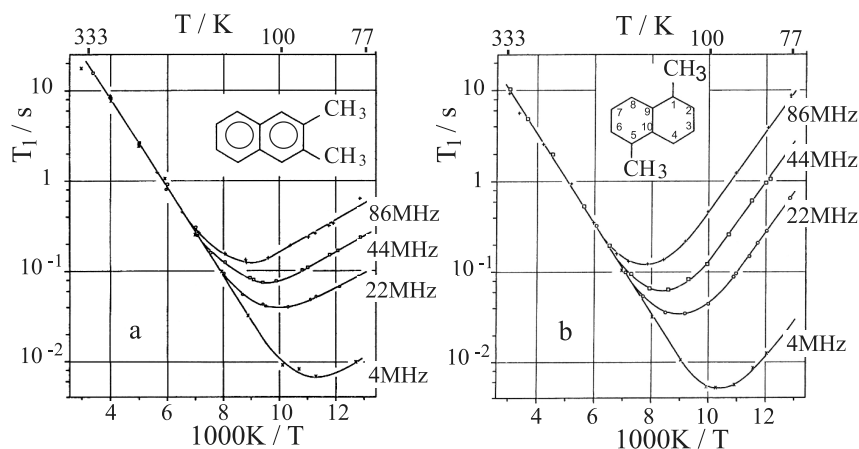


Fig. 5.21 The proton spin-lattice relaxation time T_1 of 2,3 β -dimethyl-naphthalene (a) and of 1,5 β -dimethyl-naphthalene crystals (b) as a function of the inverse temperature and at the proton spin Larmor frequencies 4 MHz, 22 MHz, 44 MHz and 86 MHz. After [29].

that they cause no steric hindrance to each other. The $\lg T_1(T^{-1})$ curve exhibits the V-shaped form mentioned in Sect. 5.8.1, which can be derived from Eqns. (5.18) and (5.19). The analysis yields the values for τ_∞ and ΔE as listed in Table 5.6. In 2,3-DMN (Fig. 5.21a), the high-temperature and the low-temperature branches of the $\lg T_1(T^{-1})$ curves are not symmetric. Presumably, this asymmetry is due to a

Table 5.6 Correlation time constants τ_∞ and activation energies ΔE for the reorientation motions in methyl-substituted naphthalene crystals. The correlation time is $\tau_c = \tau_\infty \cdot e^{\Delta E/kT}$ (* = single crystals).

Substance	Activation energy $\Delta E/\text{meV}$	Frequency constant τ_∞/s	Relaxation-determining motion
Naphthalene	1100	10^{-18}	Whole molecule
β -MN*	35	—	CH ₃ group at position 2
2,6-MN*	17	—	CH ₃ groups at positions 2 and 6
2,3-MN*	104	$0.24 \cdot 10^{-13}$	CH ₃ groups at positions 2 and 3
2,3,6-MN*	106	$0.14 \cdot 10^{-13}$	CH ₃ groups at positions 2 and 3
α -MN	104	$0.5 \cdot 10^{-13}$	CH ₃ group at position 1
1,2-MN	65	—	CH ₃ groups at positions 1 and 2
1,3-MN	106	$1.0 \cdot 10^{-13}$	CH ₃ group at position 1
1,5-MN*	100	$1.0 \cdot 10^{-13}$	CH ₃ groups at positions 1 and 5
1,7-MN	110	$1.2 \cdot 10^{-13}$	CH ₃ group at position 1
1,8-MN*	140	—	CH ₃ groups at positions 1 and 8

coupling of the two neighbouring CH₃ groups during their reorientation motions [29].

The activation energies of the CH₃ reorientation motions are similar for nearly all the MN crystals (Table 5.6). However, the values of ΔE in β -MN and in 2,6 DMN are noticeably smaller than those for α -MN and for all the other MN crystals. Here, β denotes a bonding position at the C atoms 2, 3, 6 and/or 7, while α denotes bonding at the positions 1, 3, 5 and/or 8 in naphthalene. Presumably, the low barriers for β -MN and 2,6 DMN are essentially determined by the intermolecular potential. In all the other crystals, the intramolecular potential and/or the mutual steric hindrance of the neighbouring CH₃ groups evidently plays a decisive role. All of the components of the potential mentioned here are in principle van der Waals interactions and could be treated with a Buckingham potential *ansatz* (Chap. 2 and Eq. (2.17)) [29].

The values of ΔE in the MN crystals are nearly as large as that for benzene (Sect. 5.8.2). This result is also typical: the order of magnitude of the van der Waals interactions is similar in all the polyacene crystals. A typical correlation time τ_c at room temperature can be found e.g. for 1,5 DMN from the values in Table 5.6 and Eq. (5.23) to be τ_c (1,5 DMN, 300 K) = $2.4 \cdot 10^{-12}$ s. Compared with the period of rotation of a free CH₃ group around its threefold symmetry axis, similarly to the case of benzene, the corresponding rotational frequency is much lower than that of the free groups or molecules [30]. The reorientation motions of the CH₃ groups are thus hindered rotations.

5.8.4

Diffusion

The diffusive translation of molecules has been extensively investigated in a number of molecular crystals. When the diffusing molecules are identical to the molecules of the crystal, one terms this motion *self diffusion*. Microscopically, it consists of a hopping motion of a molecule from its original lattice site to a neighbouring vacancy (see Chap. 4). For diffusion and self diffusion to take place at all, there must therefore be vacancies present in the lattice. They can either be attached to dislocations or small-angle grain boundaries, or they can be thermally activated.

An experimental procedure for the direct measurement of self diffusion is the “radiotracer” technique. Here, molecules are marked with radioactive atoms, e.g. with ¹⁴C, and deposited onto the surface of the crystal at a time $t = 0$. Thereafter, layers are sliced off the crystal surface sequentially at times $t > 0$ using a microtome. A typical layer thickness is 5 μm . The crystal is thus dissected layer by layer and the quantity of tracer molecules in each layer is analysed with a spatial resolution given by the layer thicknesses [31, 32].

Another method, which was originally developed for the investigation of noble-gas crystals, begins at $t = 0$ with a molecular crystal homogeneously doped with radioactive tracer molecules. The radioactive molecules which diffuse to the crystal surface exchange at times $t > 0$ with non-radioactive molecules in the vapour phase

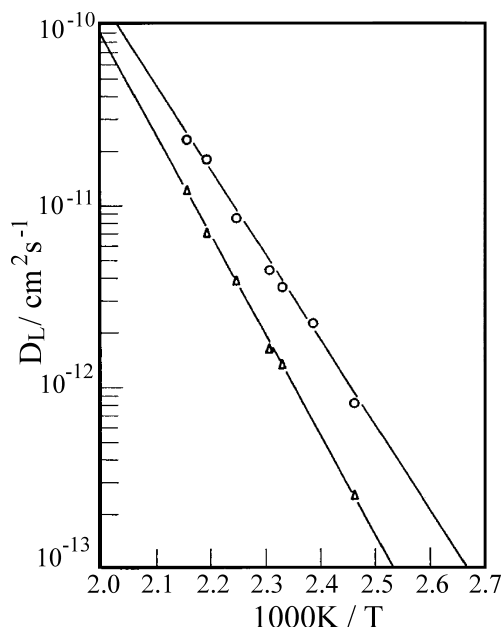


Fig. 5.22 Temperature dependence of the diffusion coefficient of phenanthrene in anthracene crystals between 400 and 450 K. Δ : $\perp a-b$ plane, O: $\perp a-c$ plane. After [34].

above the crystal, and the radioactivity of the vapour is analysed as a function of time t [33].

The goal of these experimental investigations is the determination of the diffusion coefficient D as a function of the temperature. In the typical molecular crystals naphthalene or anthracene, the diffusion is thermally activated:

$$D = D_0 e^{-Q/RT}. \quad (5.20)$$

Q is the activation energy for diffusion. Fig. 5.22 shows this temperature dependence for the diffusion coefficient of phenanthrene in anthracene crystals. In the relatively small temperature range between 400 and 450 K, D changes by a factor of about 100 [35]. Table 5.7 lists measured values of D for self diffusion in naphthalene crystals, and Table 5.8 contains characteristic values for D in naphthalene and anthracene crystals. The two important experimental results are the following:

1. The activation energy Q for self diffusion is larger than the sublimation energy L_s . From this, one can qualitatively derive the conclusion that in a diffusion jump, the activation of a lattice vacancy and the activation of the jump from a lattice site to the vacancy are necessary.
2. The diffusion along a small-angle grain boundary is very much more rapid than that in a perfect single crystal. For the diffusion of phenanthrene in anthracene, the ratio of the diffusion coefficients D_L along the small-angle grain boundaries to D in a perfect crystal was found to be between 10^6 and 10^7 , depending on the direction in the crystal. Furthermore, the value of the

Table 5.7 Self-diffusion coefficient D in high-purity naphthalene crystals. For more details, we refer to the review article by Sherwood [31].

Temperature $T/^{\circ}\text{C}$	Diffusion coefficient $D/\text{cm}^2 \text{ s}^{-1}$
56.8	$2.77 \cdot 10^{-13}$
60.0	$3.20 \cdot 10^{-13}$
64.2	$8.5 \cdot 10^{-13}$
69.7	$1.9 \cdot 10^{-12}$
74.4	$5.3 \cdot 10^{-12}$

Table 5.8 Parameters of the self diffusion in anthracene and naphthalene crystals. D = diffusion coefficient, $(D_g/D)_m$ = ratio of the diffusion coefficients for diffusion along the small-angle grain boundaries (D_g) and in a perfect crystal (D) at its melting point (m). D_0 : (see Eq. (5.20)), $D = D_0 e^{-Q/RT}$. Q = Activation energy. L_s = Sublimation energy.

Crystal	$(D_g/D)_m$	$D_0/\text{cm}^2 \text{ s}^{-1}$	$Q/\text{kJ mol}^{-1}$ (eV/molecule)	Q/L_s
Naphthalene	106	$2 \cdot 10^{-15}$	179 (1.86)	2.5
Anthracene	105	$1 \cdot 10^{-10}$	202 (2.10)	2.1

activation energy for diffusion along the grain boundaries is only 26% to 60% of that for the perfect crystal.

Problems

Problem 5.1. Comparison of inorganic semiconductor crystals (Si or Ge) with organic molecular crystals (naphthalene or anthracene):

Look in textbooks on solid-state physics (e.g. CHARLES KITTEL, *Introduction to Solid State Physics*, John Wiley and Sons; or: N. W. ASHCROFT, N. D. MERMIN, *Solid State Physics*) for the values of the following fundamental properties of inorganic semiconductor crystals (in particular Si and/or Ge) and compare them with the corresponding values for organic semiconductor crystals (in particular naphthalene and/or anthracene), which you can find in the present book. Discuss the reasons for the differences.

- minimum spacing of the lattice structural elements (atoms or molecules)
- binding energy per lattice structural element (atom or molecule)

- density
- melting point
- volume compressibility
- sound velocity
- ionisation energy
- electron affinity
- maximum frequency of the phonons (in molecular crystals internal and external phonons).

Problem 5.2. Nuclear spin-lattice relaxation and activation energy for the reorientation of $-\text{CH}_3$ side groups

- a. Explain the longitudinal nuclear spin-lattice relaxation time T_1 and describe a standard method for determining it.
- b. Find from Fig. 5.21b the activation energy of the $-\text{CH}_3$ side groups in the 1,5-dimethyl-naphthalene crystal.

References

- 1 T. A. KRIVENKO, V. A. DEMENTJEV, E. L. BOKHENKOV, A. I. KOLESNIKOV and E. F. SHEKA, *Mol. Cryst. Liq. Cryst.* **104**, 207–230 (1984)
- 2 E. A. SILINSH and V. ČÁPEK, *Organic Molecular Crystals*, AIP Press (1994)
- 3 N. KARL, *Organic Semiconductors*, in: *Landolt Boernstein (New Series) Group III*, Vol. 17, Subvolume 17i, pp. 106–218
- 4 B. DORNER, *Coherent Inelastic Neutron Scattering in Lattice Dynamics*, Springer Tracts in Modern Physics, Springer Verlag (1982)
- 5 C. KITTEL, *Einführung in die Festkörperphysik*, Oldenbourg-Verlag, 13th ed. (2002)
- 6 R. M. HOCHSTRASSER, *Molecular Aspects of Symmetry*, W. A. Benjamin, New York (1966)
- 7 I. NATKANIEC, E. L. BOKHENKOV, B. DORNER, J. KALUS, G. A. MACKENZIE, G. S. PAWLEY, U. SCHMELZER and E. F. SHEKA, *J. Phys. C: Sol. St. Phys.* **13**, 4265 (1980)
- 8 U. SCHMELZER, E. L. BOKHENKOV, B. DORNER, J. KALUS, G. A. MACKENZIE, I. NATKANIEC, G. S. PAWLEY and E. F. SHEKA, *J. Phys. C: Solid State Phys.* **14**, 1025–1041 (1981)
- 9 J. KALUS, B. DORNER, V. K. JINDAL, N. KARL, I. NATKANIEC, G. S. PAWLEY, W. PRESS and E. F. SHEKA, *J. Phys. C: Solid State Phys.* **15**, 6533–6544 (1982)
- 10 E. F. SHEKA, E. L. BOKHENKOV, B. DORNER, J. KALUS, G. A. MACKENZIE, I. NATKANIEC, G. S. PAWLEY and U. SCHMELZER, *J. Phys. C: Solid State Phys.* **17**, 5893–5914 (1984)
- 11 J. KALUS, *Röntgen und Neutronenstreuung*, in: *Spektroskopie amorpher und kristalliner Festkörper*, edited by D. Haarer and W. Spiess, Steinkopff Verlag (1995)
- 12 W. HÄFNER and W. KIEFER, *J. Chem. Phys.* **86**, 4582–4596 (1987)
- 13 R. OSTERTAG, Dissertation, Universität Stuttgart (1972)
- 14 G. S. PAWLEY, *phys. stat. sol. (b)* **49**, 475 (1972)
- 15 B. DORNER, E. L. BOKHENKOV, S. L. CHALPOT, J. KALUS, I. NATKANIEC, G. S. PAWLEY, U. SCHMELZER and E. F. SHEKA, *J. Phys. C: Solid State Phys.* **15**, 2353 (1982)
- 16 J. F. J. JORDAN, J. KALUS, U. SCHMELZER and G. ECKOLD, *phys. stat. sol. (b)* **155**, 89 (1989)

- 17 J. SCHLEIFER, J. KALUS, U. SCHMELZER and G. ECKOLD, *phys. stat. sol. (b)* **154**, 153 (1989)
- 18 T. J. KOSIC, C. L. SCHOSSER and D. D. DLOTT, *Chem. Phys. Lett.* **96**, 57 (1983)
- 19 H. TAKEUCHI, S. SUZUKI, A. J. DI-ANOUX and G. ALLEN, *Chem. Phys.* **55**, 153 (1981)
- 20 P. LAUNOIS, F. MOUSSA, M. H. LEMÉE-CAILLEAU and H. CAILLEAU, *Phys. Rev. B* **40**, 5042 (1989)
- 21 M. DÖRR, H. GERLACH, J. KALUS, N. KARL, M. MONKENBUSCH, I. NATKANIEC, U. SCHMELZER, W. SCHMIDT, J. J. STREZOWSKI, P. VORDERWISCH, G. VOSS and M. WARTH, *J. Phys.: Condens. Matter* **10**, 10879 (1998)
- 22 J. KALUS, H. GERLACH, J. SCHLEIFER, F. WÖRLEN, G. VOSS, M. GODLEWSKA, I. NATKANIEC, N. KARL and M. PRAGER, *phys. stat. sol. (b)* **134**, 53 (1986)
- 23 F. WÖRLEN, J. KALUS and U. SCHMELZER, *Mol. Cryst. Liq. Cryst.* **159**, 297 (1988)
- 24 E. R. ANDREW and R. G. EADES, *Proc. Roy. Soc., London A* **218**, 537 (1953)
- 25 N. BLOEMBERGEN, E. M. PURCELL and R. V. POUND, *Phys. Rev.* **73**, 679 (1948)
- 26 C. P. SLICHTER, *Principles of Magnetic Resonance*, 3rd ed., Chapter 3.4, p. 80, Springer-Verlag (1990)
- 27 J. H. VAN VLECK, *Phys. Rev.* **74**, 1168 (1947)
- 28 A. ABRAGAM, *The Principles of Nuclear Magnetism*, Oxford, Clarendon Press (1961)
- 29 J. U. v. SCHÜTZ and H. C. WOLF, *Z. Naturforsch.* **27a**, 42 (1972)
- 30 H. HAKEN and H. C. WOLF, *Molecular Physics and the Elements of Quantum Chemistry*, 2nd ed., Springer-Verlag (2004)
- 31 J. N. SHERWOOD, in: *Surface and Defect Properties of Solids*, Vol. 2, p. 250, edited by M. W. Roberts and J. M. Thomas, London, the Chemical Society (1973)
- 32 J. N. SHERWOOD and D. J. WHITE, *Phil. Mag.* **16**, 975 (1967)
- 33 A. V. CHADWICK and J. A. MORRISON, *Phys. Rev.* **B1**, 2748 (1970)
- 34 P. J. REUCROFT, H. K. KEVORKIAN and M. M. LABES, *J. Chem. Phys.* **44**, 4416 (1966)
- 35 F. FUJARA, W. PETRY, W. SCHNAUSS and H. SILLESCU, *J. Chem. Phys.* **89**, 1801 (1988)
- 36 O. ISFORT, B. GEIL and F. FUJARA, *J. Magn. Res.* **130**, 45 (1998)

6

Electronic Excited States, Excitons, Energy Transfer

6.1

Introduction

One of the most interesting aspects of the physics and chemistry of organic solids is their ability to conduct optical excitation energy within the crystal or even in amorphous material and to transfer it. Energy which is absorbed at one place in the solid can be transported to another place where it can be used to induce various processes which require energy. Such processes include sensitised luminescence, the generation of free charge carriers and photochemical reactions.

To investigate and understand this type of energy transfer processes, one needs to make use of many different spectroscopic techniques, in particular absorption, luminescence, and excitation spectroscopy in the visible and the ultraviolet spectral regions, with which one can obtain information about the electronic excited states. These methods are assumed here to be known to the reader.

The measurement of absorption spectra of molecular solids is made difficult by the high concentration of the molecules within the solid phase, in contrast to solutions. For the study of the absorption of strong optical spectra, one therefore requires extremely thin samples. An extinction coefficient of $10^4 \text{ l mol}^{-1} \text{ cm}^{-1}$ in solution, according to the Lambert-Beers law, corresponds to an absorption coefficient of ca. 10^5 cm^{-1} in a crystal (cf. Fig. 6.6). This means that for a measurement of the absorption spectrum, the crystal must have a thickness of less than 10^{-5} cm . Thus, often one has to measure reflection spectra instead of absorption spectra, and then recalculate them using a Kramers-Kronig transformation. Another, less frequently-used method is photoacoustic spectroscopy. In this case, one makes use of the heating of the sample by the absorbed light. This heat is converted into an acoustic wave by modulating the light and enclosing the sample in a sealed volume of gas. The amplitude of the acoustic wave is then related to the optical absorption coefficient.

Furthermore, excitation spectroscopy is an important technique. Here, one measures the emission from the sample as a function of the quantum energy of the exciting light. We will treat this method in detail later.

In this chapter, we discuss the processes which are important for spectroscopy, in particular using organic molecular crystals as examples. Our knowledge of their

spectroscopic properties was obtained in the main from simple, non-doped or doped crystals of aromatic hydrocarbons such as naphthalene or anthracene. These substances will be emphasized in the present chapter. However, the special properties of charge-transfer crystals as well as the photosynthetic apparatus as an example from biological physics will also be treated.

6.2

Some historical remarks:

differences between the spectra of molecules in a crystal and free molecules

The first systematic investigation of the optical spectra of organic crystals was due to P. Pringsheim and A. Kronenberger [1]. They were able to show that at low temperatures (at that time 20 K), the spectrum of solid benzene showed great similarities to its spectrum in liquid solutions and in the gas phase. Since the electronic and spectroscopic properties of the molecules were thus only slightly modified by crystallisation, the model of an **oriented gas** seemed to offer a good first approximation for understanding the crystal spectra. This is in strong contrast to most inorganic crystals: there, the basic units of the crystal are hardly recognisable as such in the optical spectra.

In the following 20 years, a group of physicists in the Ukraine [2] studied a series of other aromatic crystals spectroscopically. It developed that there are also very characteristic differences from the spectra of free molecules. In the year 1948, A. S. Davydov [3] formulated the basic theoretical explanation for the observable interaction processes in the crystal spectra, between the molecules in electronically excited states within the crystal. He made use of the model of **Frenkel excitons** [4] and was able in particular to give a quantitative explanation of a characteristic line splitting, the **Davydov splitting**, as a fundamental property of organic molecular crystals. Fig. 6.1 shows as an example the splitting of the $0,0$ -transition in the $T_1 \leftarrow S_0$ absorption spectrum of anthracene at room temperature.

Energy Transfer and **Excitons** are, as we have already mentioned, perhaps the most interesting and in any case the most characteristic photophysical processes in molecular crystals. The investigation of these processes began in 1934, when A. Winterstein, U. Schön and H. Vetter [5] were able to explain the green fluorescence radiation from anthracene crystals, which had been described as due to the effect of an unknown “chrysogen”, in terms of sensitised fluorescence. This fluorescence is emitted by tetracene molecules which are present at very low concentration in the anthracene. Pure anthracene fluoresces in the crystalline phase just as in solution with a blue-violet colour. This observation set off a large number of spectroscopic studies of the sensitised emission from mixed crystals. Very soon, J. Franck and E. Teller [6] pointed out in a summary report of this field that there was an important connection here to the primary processes of photosynthesis and other biophysical processes.

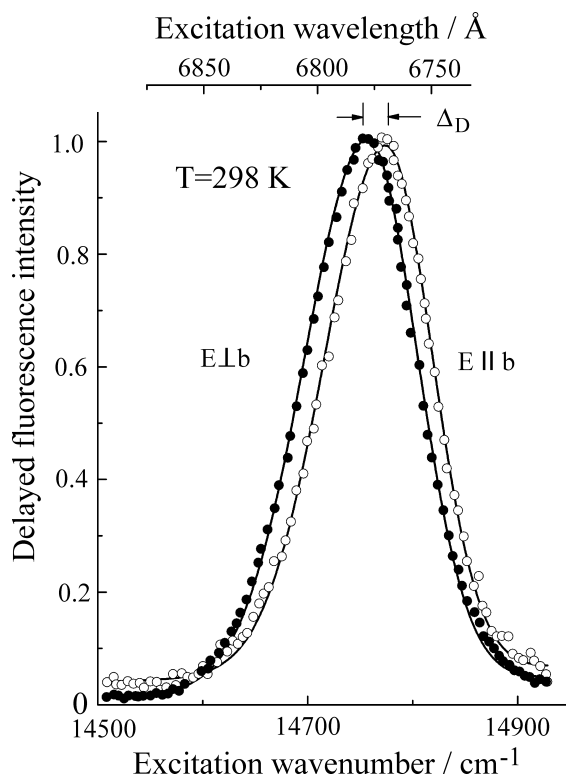


Fig. 6.1 The Davydov splitting $\Delta_D = 21.5 \text{ cm}^{-1}$ of the 0.0-transition in the $T_1 \leftarrow S_0$ absorption spectrum of anthracene at 300 K. This is the excitation spectrum of the triplet excitons. The absorption was detected via the intensity of the delayed fluorescence

(see Sect. 6.9.2). The two bands with differing polarisations relative to the crystalline a and b axes are normalised to the same intensity. The true intensity of the band $\perp b$ is about seven times smaller than that of the band $\parallel b$ (see also Fig. 6.10). After Avakian *et al.* [7].

Since these early works, the field of the spectroscopic properties of molecular solids has grown enormously. In the following sections, we shall present the most important phenomena and discoveries from this field.

6.3

Optical Excited States in Crystals

The electronic excited states of organic molecular crystals are clearly and in a readily understandable way derived from those of the free molecules (or of molecules in liquid solutions). This follows, as was already discussed in Chap. 2, from the fact that the intermolecular forces in crystals are relatively weak in comparison to the binding forces within the molecules. The excited states and the transitions between them are studied by means of optical spectroscopy, particularly in the visible and the ultraviolet spectral ranges. Here, we will explain the essential facts using

as examples the aromatic hydrocarbons, in particular anthracene and naphthalene. These crystals have been more extensively investigated than all the other molecular crystals with conjugated π electron systems.

Light can be absorbed by organic molecular crystals in their singlet or in their triplet term systems (Fig. 6.2). The term diagram shown here is equally valid for free molecules and for molecular crystals. In an ideal crystal, the excited states

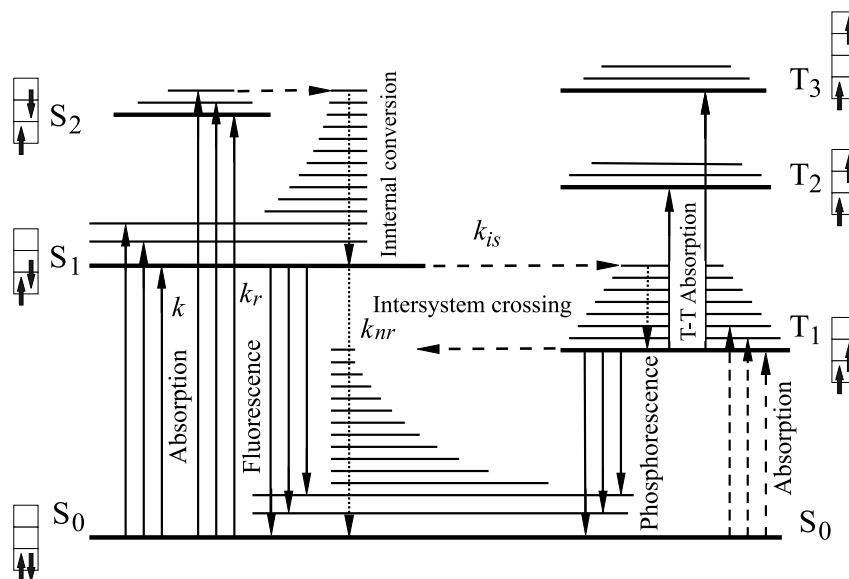


Fig. 6.2 The energy terms of a molecule or also of a molecular crystal, shown schematically. The electronic ground state S_0 , the electronic singlet (S_1 , S_2) and triplet (T_1 , T_2 , T_3) excited states as well as the vibronic states are shown. In the crystal, all the terms are narrow excitonic bands. Radiative transitions: absorption by the singlet and by the triplet system, fluorescence, phosphorescence. Radiationless transitions: internal conversion from the higher to the lowest electronic excited states S_1 and T_1 , as well as intersystem crossing (ISC) from the singlet into the triplet system. Singlet states are diamagnetic. Triplet states have a total spin quantum number of $S = 1$, while for singlet states, $S = 0$. Light-induced transitions between the singlet and the triplet systems are therefore in general forbidden. k is the rate constant for absorption, k_r for fluorescence and k_{nr} for radiationless transitions. For naphthalene, the following number applies: the energy difference/ hc $S_1 - S_0 = 31\,500\text{ cm}^{-1}$. Its fluorescence therefore lies in the ultraviolet.

The energy difference/ hc for $T_1 - S_0 = 21\,200\text{ cm}^{-1}$; the phosphorescence is therefore in the green. The zero-field splitting of the triplet states is not shown here (see Chap. 7). In the naphthalene or the anthracene crystal, the width of the excitonic band S_1 is ca. $150\text{--}200\text{ cm}^{-1}$, that of the T_1 band is ca. $10\text{--}20\text{ cm}^{-1}$. The spacing between subsequent electronic excited states S_1 , S_2 , $S_3 \dots$ or T_1 , T_2 , $T_3 \dots$ lies in general in the range of a few 1000 cm^{-1} , those between the vibronic levels are a few 100 cm^{-1} (see Chap. 5). Thermal excitation of the absorbing (S_0) and emitting levels (S_1 , T_1) is not taken into account in the diagram. The energy terms are also sketched in a molecular-orbital scheme. There, the energetically lowest level is the highest occupied molecular orbital (HOMO). The direction of the arrows indicates the relative orientation of the spins of the two electrons in the two partially-occupied orbitals of each excited state. After [M6].

are however waves, which are characterised by their energy E and their wavevector \mathbf{k} . Therefore, each term is in fact a band with an energy $E(\mathbf{k})$ that depends on its wavevector \mathbf{k} . Singlet terms are energy states in which the electronic spins are coupled pairwise to a total spin quantum number of $S = 0$. As a rule, the electronic ground state of a molecule with an even number of electrons is a singlet state and is denoted by S_0 . In the state S_0 , the crystal is, as in all singlet states, diamagnetic. In the triplet states, the spins of two electrons are parallel to each other, and the total spin quantum number is $S = 1$. Crystals with excited triplet states have a paramagnetic contribution to their susceptibilities and can thus also be investigated using electron spin resonance (ESR) (see also Chap. 7). All excited states with the exception of the two lowest excited-state terms S_1 and T_1 are very short-lived. They give up their excess energy very rapidly in comparison to the terms S_1 and T_1 , typically in times of the order of psec, via the vibronic sublevels with non-radiative transitions to the surrounding crystal lattice. This process of conversion of electronic excitation energy into heat is called **internal conversion** (IC).

The lowest excited states S_1 and T_1 have, in contrast, long lifetimes, usually between 10^{-9} and 10^{-6} s for S_1 and 10^{-4} to 20 s for T_1 in typical crystals. The radiative transitions $S_1 \rightarrow S_0$ are termed fluorescence and the $T_1 \rightarrow S_0$ radiative transitions are called phosphorescence. Transitions between the pure singlet and the pure triplet systems, so called **intersystem crossings** (ISC), are forbidden.

The classification of states according to their total spin quantum numbers ($S = 0$ and $S = 1$) however assumes a vanishing spin-orbit coupling. For the smaller nuclear charges of C and H, this criterion is to a large degree fulfilled, but still not completely. Therefore, the lifetime of the state T_1 in aromatic hydrocarbons is long but not infinite. The forbiddenness of the transitions is partially lifted by the very weak spin-orbit coupling. The absorption coefficients for $T_1 \leftarrow S_0$ transitions are typically in the range 10^{-4} to 10^{-5} cm^{-1} . When the molecules or the molecular crystals contain atoms heavier than C, H, N, or O, for example Br or I, then owing to the stronger spin-orbit interaction, the intersystem crossing rate between the singlet and the triplet systems increases strongly. The intersystem crossing rate $S_1 \rightarrow T_1$ for naphthalene is for example $1.6 \cdot 10^6 \text{ s}^{-1}$, but for 1-bromo-naphthalene, in contrast, it is over $1.85 \cdot 10^9 \text{ s}^{-1}$. The singlet-triplet absorption is stronger in the latter case. The phosphorescence also has an increased intensity in comparison to the fluorescence and its decay time becomes shorter.

As shown in Fig. 6.2, within the purely electronic terms S_n ($n \geq 0$) and T_n ($n \geq 1$) there are superposed vibronic terms, that is terms with excited molecular vibrations. In the crystal, the intramolecular vibrations are only slightly different from those in the free molecules (cf. Chap. 5). Electronic transitions between levels with zero vibrational quantum numbers are called 0,0 transitions.

If one continues the term diagram in Fig. 6.2 upwards, i.e. into a higher-energy region, it ends at the ionisation limit, that is with the emission of an electron from the crystal. For anthracene, the ionisation limit of the free molecule lies at 7.5 eV and the work function for emission of an electron out of the crystal at 5.75 eV.

For the allowed optical singlet-singlet transitions, the **absorption coefficient** of organic crystals lies typically in the range of 10^5 cm^{-1} . The oscillator strength f of the

optical transitions of polyacene molecules and crystals lie between 10^{-3} for “weak” and more than 2 for “strong” transitions. If the thickness of the crystal is more than a few μm , a homogeneous optical excitation of the crystal bulk is thus not possible with single-photon excitation. In the case of singlet-triplet excitations, the situation is different: the absorption coefficient for the transition $T_1 \leftarrow S_0$ in anthracene lies in the range 10^{-4} cm^{-1} . With intense laser light, for example a He-Ne laser, one can generate such a high homogeneous triplet concentration in the bulk of an anthracene crystal that the lifetime of the triplet excitons is essentially determined by mutual annihilation of two excitons (see Sect. 6.5 and Fig. 6.21).

In addition to single-photon spectroscopy with only one absorbed photon, lasers, with their high photon densities, also permit **two-photon** (and **multiphoton**) **spectroscopy** [8]. Two-photon processes, in which two photons are simultaneously absorbed by the ground state, connect states of equal parity. A single-photon process, in contrast, induces dipole-allowed transitions between states of different parity. Conjugated π -electron systems in general have strongly field-dependent polarisabilities – i.e. their polarisability is not constant – and large values of the higher-order dielectric susceptibilities, as required for multiphoton processes. Two-photon spectroscopy in organic solids even with moderate laser intensities thus provides access to excited states in the molecules or in the crystal which cannot be reached with single-photon spectroscopy (or only indirectly, through vibronic contributions). Such contributions are also important in relaxation by means of internal conversion to the emitting S_1 state. Detection of two-photon absorption can be carried out by using the (single-photon) fluorescence from the S_1 state.

Two-photon absorption can be very useful in molecular crystals if one wishes to generate a homogeneous excitation of singlet states within a “thick” crystal (i.e. thicker than ca. $1 \mu\text{m}$). The two-photon absorption intensity increases, to be sure, quadratically with increasing light intensity; but with strong laser sources it is still weak in comparison to single-photon absorption, that is, the absorption depth for two-photon excitation is comparatively large.

Figure 6.3 shows the excited states of free molecules and their crystals in another representation. Here, the energy scale begins at the vacuum level ($E = 0$), as is usual in semiconductor physics and in photoelectron spectroscopy. The (negative) binding energies are then plotted downwards. In the reverse direction, the series of energetically higher states continues up through the occupied valence states in the valence band (corresponding to the doubly-occupied molecular HOMO), followed by the lowest triplet state T_1 , the lowest excited singlet state S_1 , charge-transfer states (CT), and finally the conduction band. S_1 and T_1 correspond to excitations into excitonic states in which the HOMO and the LUMO in the same molecule are each only singly occupied. The highest valence band and the conduction band correspond to an excitation in which the HOMO of one molecule and the LUMO of another, distant molecule are each singly occupied, thus in which no coupled ion pairs are present. Further important quantities are explained in the figure caption. The energy range between the triplet state T_1 and the lowest edge of the conduction band is the region of occurrence of Frenkel excitons.

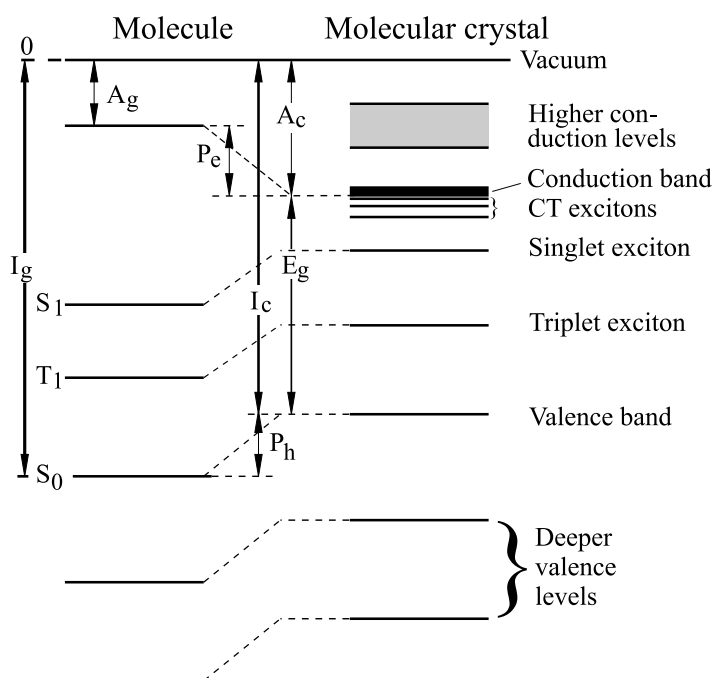


Fig. 6.3 The energy term diagram in a different representation. The 0 at the upper edge denotes the vacuum level, i.e. the threshold at which the molecule or the crystal is just positively ionised by sufficient excitation of an electron. Here, I_g = the ionisation potential of the molecule, A_g = the electron affinity of the molecule, A_c = the electron affinity of the

crystal, P_e , P_h = the polarisation energies for the transition from the molecule to the molecular crystal, I_c = the ionisation potential of the crystal, and E_g = the energy difference between the upper edge of the valence band and the lower edge of the conduction band, i.e. the band gap.

The fluorescence transitions of crystals in general begin at low temperatures at the vibrational ground state of the S_1 term and end at the various vibrational levels of the ground state S_0 . The notation 0,0-line denotes the transition from the vibrational ground state of the S_1 term to the vibrational ground state of S_0 . At helium temperature, the fluorescence lines are frequently very narrow. The **fluorescence spectrum** $S_1 \rightarrow S_0$ thus consists of a series of relative sharp lines whose spacings correspond to the vibrational levels of the ground state. Figure 6.4 shows as an example a high-resolution fluorescence spectrum from an anthracene crystal [9]. One can barely discern transitions in this spectrum which are due to trapping states in the crystal. The **absorption spectrum** $S_1 \leftarrow S_0$ begins at low temperatures likewise with a 0,0 transition and is the mirror image of the fluorescence spectrum. It consists of transitions to the vibrational levels of S_1 [10, M5], cf. also Fig. 6.6. At sufficiently high temperature, absorption by the thermally-occupied lowest vibronic levels of the ground state S_0 is also possible. The **phosphorescence spectra** $T_1 \rightarrow S_0$ start at T_1 and end in the same vibronic ground-state levels as the flu-

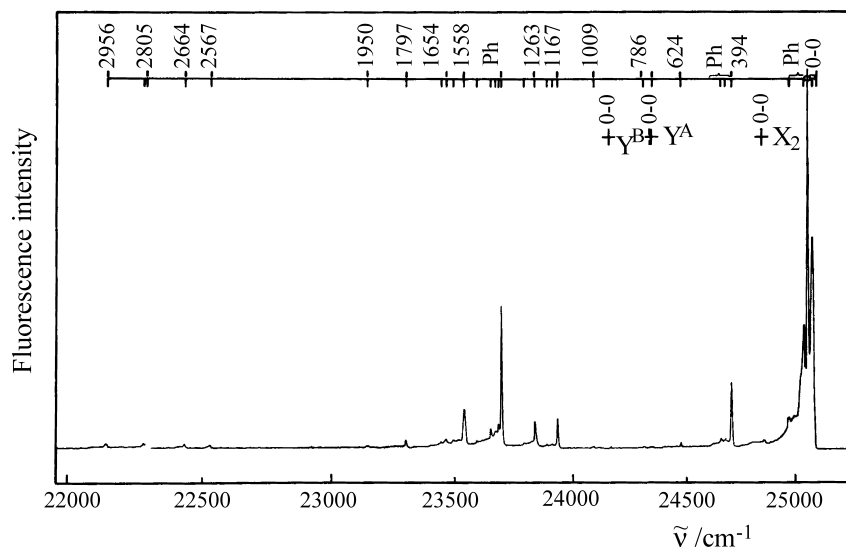


Fig. 6.4 The fluorescence spectrum of an anthracene crystal at $T = 4.2$ K. The spectrum consists of numerous sharp lines, which can be attributed to four different vibronic series. The **intrinsic fluorescence** begins at 0,0 and contains a progression of vibronic transitions. The line spacings can be associated with known molecular vibrations of anthracene. The 0,0 spacings listed at the top of the figure belong to this vibronic series. The direct 0,0 transition is forbidden, since in the anthracene exciton band, the state $k = 0$ does not lie at the lower band edge. The position of the true 0,0 spacing is obtained from an extrapolation of the vibronic transitions and is found to be

$25\,097\text{cm}^{-1}$. The forbiddenness of the transition is lifted by participation of phonons (denoted by Ph in the figure). Furthermore, the spectrum contains **three series of traps**, here very weak and barely recognisable through the 0,0 transitions. X_2 is an X trap which is due to a structural defect. Y_A and Y_B denote another type of X-traps, which here presumably are due to anthracene molecules with a low deuterium content resulting from the natural abundance of D in H; these act like structural defects. More details are given in the complete analysis of the fluorescence spectrum of anthracene-perdeuteroanthracene mixed crystals. From [9].

orescence spectra. The vibronic structures of the spectra are thus the same. The linewidths are determined by the – generally very efficient – internal conversion (IC); cf. [M6, Chap. 14]. Furthermore, the crystal spectra are very similar to those of the molecules. However, one observes the following most important differences in the terms and the spectra:

- A general shift in the terms, mostly to lower energies (Fig. 6.5). This **solvent shift** is based on the interaction of the molecules within the crystal with their neighbouring molecules, i.e. on the van der Waals bonding. It is molecule-specific and has a different magnitude for different excited states.
- A splitting of each molecular term into a maximum of Z terms in the crystal, where Z is the number of molecules in the unit cell (Fig. 6.6). It is called the **Davydov splitting** and is due to the resonant interaction between non-translationally equivalent molecules in excited states. The Davydov splitting is also different in magnitude for different excited states and transitions.

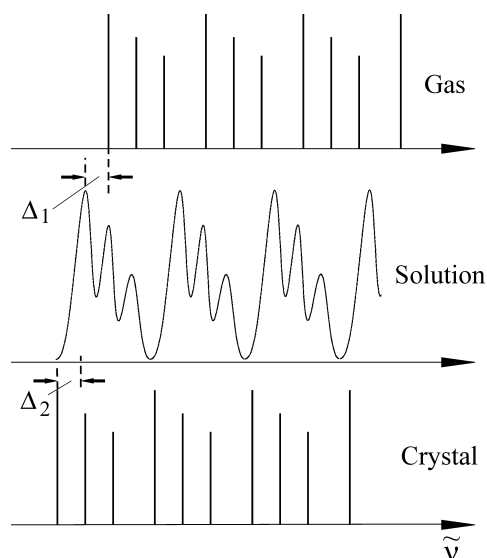


Fig. 6.5 A schematic diagram illustrating the typical changes in linewidths and line positions in the spectrum on going from the gas phase to solutions (solvent shift Δ_1) and to the crystal (additional shift Δ_2), without the Davydov splitting. The linewidths in solution and in the crystal are typical of low-temperature spectra. After [M5].

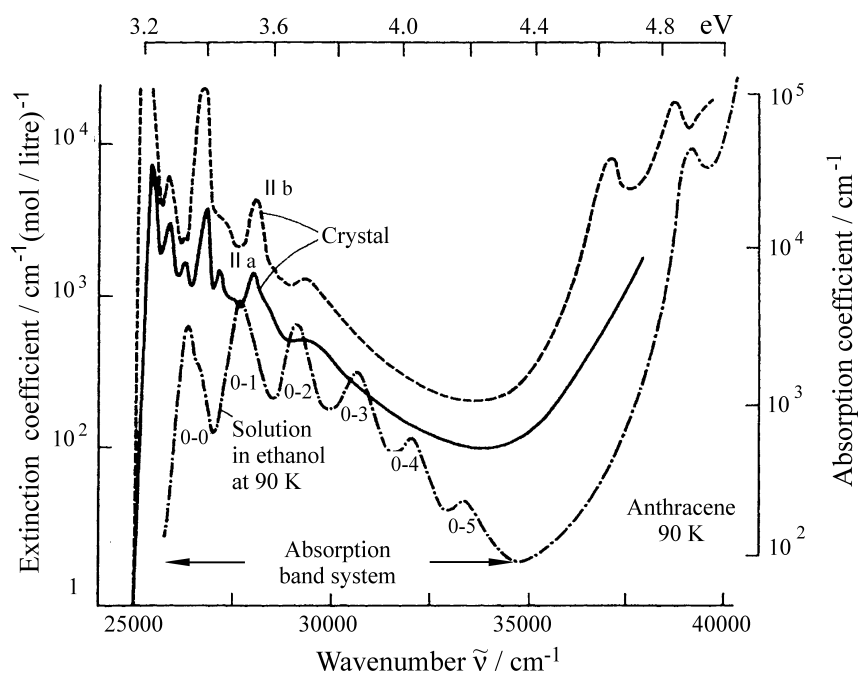


Fig. 6.6 The absorption spectrum of an anthracene crystal and of anthracene in an ethanolic solution. The crystal is oriented with its $a-b$ plane perpendicular to the optical beam direction. Transitions from the S_0 into the vibronic levels of the S_1 and S_3 states are

detected at 90 K. One can discern the shift in the crystal spectrum and its Davydov splitting into two components with different polarisations, \parallel to the crystalline a and b axes. The spectrum in solution has been expanded by a factor 10 along its ordinate. From [10, M5].

The Davydov components of the spectra also differ in their polarisation: in the monoclinic aromatic crystals with $Z = 2$ (differently-oriented molecules within the unit cell), the excitation of one of the two Davydov components is possible when the electric field vector \mathbf{E} of the light is polarised parallel to the twofold \mathbf{b} axis. For the excitation of the second Davydov component, $\mathbf{E} \perp \mathbf{b}$ is required.

- A broadening of the terms: from discrete terms in the molecule, bands are formed in the crystal, the **excitonic bands** $E(\mathbf{k})$, since the excitation energy in the periodic potential of the ideal crystal is delocalised over all the molecules.
- A complete or partial **lifting of degeneracies** between excited molecular states and the **breaking of selection rules** which hold for transitions in the free molecules, because now not just the symmetry of the molecules, but that of the whole crystal is the determining factor. For example, the $0,0$ transition $S_1 \leftarrow S_0$ at a wavenumber of $48\,000\text{ cm}^{-1}$ is forbidden in the benzene molecule for optical dipole radiation by reasons of symmetry; in benzene crystals, however, it is allowed.
- In transitions with a very **high oscillator strength**, the shifts and Davydov splittings can become so large that the similarity to the spectrum of the free molecule vanishes. This will be discussed in more detail later in Sect. 6.5.2.

The interaction between all the molecules in the crystal is responsible for the shifts in the terms, while the Davydov splitting is caused by the resonant interaction (which is also called the exchange interaction) between the non-translationally-equivalent sublattices. The widths of the terms and transitions are determined by both interactions together.

6.4

Davydov Splitting and Mini-Excitons

The theory of the line shifts and splittings in crystals is due in particular to A. S. Davydov and is known by his name. Here, we shall dispense with a detailed treatment of this theory and refer the reader to the specialised literature (Davydov [11, 12], Craig *et al.* [13, 14], McClure [15], Knox [16]). Instead, we want to turn our attention to its more important physical consequences and to concentrate on crystals with no more than two molecules in their unit cells.

In a **first step**, we consider a **physical dimer**. This is a pair of equivalent molecules, denoted by 1 and 2, whose distance and relative orientation are the same as in the crystal lattice. In the case of anthracene, let these be the two molecules in a unit cell. Such a configuration gives a mini-exciton [17] in an optically-excited state. This model is explained in Fig. 6.7. Later, we will expand it to include the whole crystal lattice, and will thus obtain the Frenkel excitons.

We denote the ground-state wavefunctions and energies of the two non-coupled molecules by ϕ_1 and ϕ_2 and $E_1 = E_2 = E_0$. For the wavefunction Φ_G and the energy

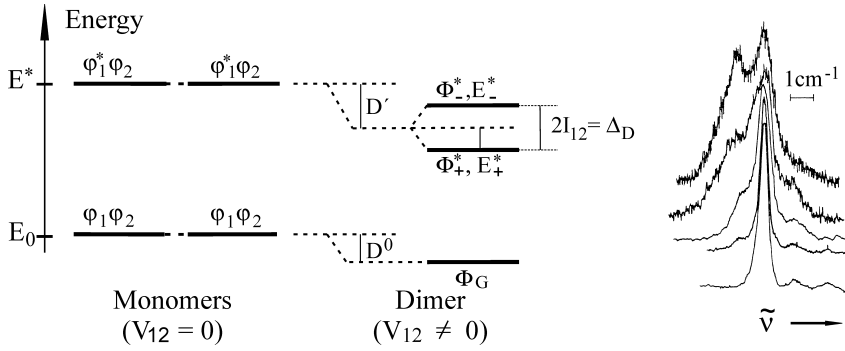


Fig. 6.7 Left: The splitting Δ_D and shift $D' - D^0$ of the excited term of a physical dimer or mini-exciton, relative to the monomer. The quantities V_{12} , D^0 , D' and I_{12} are defined in the text. The energetic ordering of the terms E_+^* and E_-^* depends on the sign of I_{12} ; the case shown here is for $I_{12} < 0$. There are two optical transitions.

Right: Monomer and pair emission (mini-exciton). The 0,0-transition of the phosphorescence of $C_{10}H_8$ as a guest molecule in a $C_{10}D_8$ host crystal is shown. The spectra from crystals with 0.2, 2, 5, 10 and 20 mole % $C_{10}H_8$ are shifted vertically for

clarity; the upper spectrum was taken at 1.8 K, the others at 4.2 K. The central line belongs to the isolated guest molecule (the monomer). All the curves have been normalised to the same amplitude relative to this line, which is at 21208.9 cm^{-1} . The intensities of the two dimer lines at $\pm 1.2 \text{ cm}^{-1}$ increase with increasing guest concentration, correspondingly. They are not equal, owing to the different thermal occupations of the two dimeric states. The transitions at $+1.3 \text{ cm}^{-1}$ and $+5 \text{ cm}^{-1}$ belong to naphthalene with ^{13}C in the α and β positions. After [18].

E_G of the physical dimer, we then have

$$\Phi_G = \phi_1\phi_2 \quad \text{and} \quad E_G = 2E_0. \quad (6.1)$$

We now assume that one of the two molecules is excited into a state ϕ_1^* or ϕ_2^* . Their energy is then E_1^* or $E_2^* = E^*$. In principle, the probability of a molecule being excited is equally great for either of the two molecules. The wavefunctions Φ_{\pm}^* for the singly-excited system are then the linear combinations

$$\Phi_{\pm}^* = \frac{1}{\sqrt{2}}(\phi_1\phi_2^* \pm \phi_1^*\phi_2) \quad (6.2)$$

with the dimer energies $E_{\pm}^* = E_{\mp}^* = E_0 + E^*$.

If, however, there is an interaction between the two molecules, whose Hamiltonian V_{12} depends on the coordinates of the electrons of both molecules, then the degeneracy will be lifted and the two states with energies E_+^* and E_-^* and wavefunctions Φ_+^* and Φ_-^* differ by the interaction energy $2I_{12}$. Furthermore, there is an additional energy shift D' . For the energies of the two states we then have:

$$E_{\pm}^* = E^* + E_0 + D' \pm I_{12} \quad (6.3)$$

(compare Fig. 6.7).

Here, I_{12} is the **resonance interaction energy**

$$I_{12} = \langle \phi_1^* \phi_2 | V_{12} | \phi_1 \phi_2^* \rangle. \quad (6.4)$$

It describes an exchange of the excitation energy between molecules 1 and 2.

If – as a thought experiment – at time $t = 0$ only one of the two molecules is excited, then the excitation energy oscillates coherently between them. The oscillation frequency is found from the energy difference: $\hbar\omega = \Delta E = 2I_{12}$. The steady-state solutions Φ_+^* and Φ_-^* from Eq. (6.2) are the quantum-mechanical equivalent of the two normal modes of a pair of coupled oscillators.

The quantity $2I_{12}$ is called the Davydov splitting Δ_D . Its numerical value, $\Delta_D/\hbar c$, is between a few and a few thousand cm^{-1} for the systems of interest here. More on this subject will be given in Sect. 6.5.

D' is the so called **Coulomb interaction energy** in the excited state, i.e. the Coulomb interaction of the charge distribution of the excited state in molecule 1 with that of the ground state of molecule 2. We then have:

$$D' = \langle \phi_1^* \phi_2 | V_{12} | \phi_1^* \phi_2 \rangle = \langle \phi_1 \phi_2^* | V_{12} | \phi_1 \phi_2^* \rangle. \quad (6.5)$$

The Coulomb interaction D^0 in the ground state

$$D^0 = \langle \phi_1 \phi_2 | V_{12} | \phi_1 \phi_2 \rangle \quad (6.6)$$

is identical to the van der Waals binding energy of the molecules involved. This interaction is in general smaller than when one of the molecules is in an excited state. Even without the Davydov splitting, the 0,0 transition of the dimer is thus red-shifted by an amount $D = D' - D^0$. This shift is termed the “solvent shift” in molecular physics when one of the two molecules involved is a solvent molecule.

The simple dimer model as in Fig. 6.7 can be called a mini-exciton. It shows how intermolecular interactions can lead to shifts and splittings in the spectra. An example is shown on the right-hand side of Fig. 6.7. D^0 and D' are based to first order on the molecular polarisability in the ground and excited states, and the resonance energy I_{12} in the singlet state is due to the resonance interaction between molecule 1 in an excited state and molecule 2 in its ground state or *vice versa*. In the triplet state, I_{12} is determined in the main by the overlap of the orbitals of the two molecules, one of which is excited.

The **polarisation** of the optical transitions in the two Davydov components is determined by the transition dipole moments \mathbf{M} in the case of allowed optical transitions. This is explained in Fig. 6.8. For two monomeric molecules 1 and 2, they are

$$\mathbf{M}_{s_1 \leftarrow s_0}^1 = \langle \phi_1 | e\mathbf{r} | \phi_1^* \rangle \quad \text{and} \quad \mathbf{M}_{s_1 \leftarrow s_0}^2 = \langle \phi_2 | e\mathbf{r} | \phi_2^* \rangle.$$

For the dimer, we have

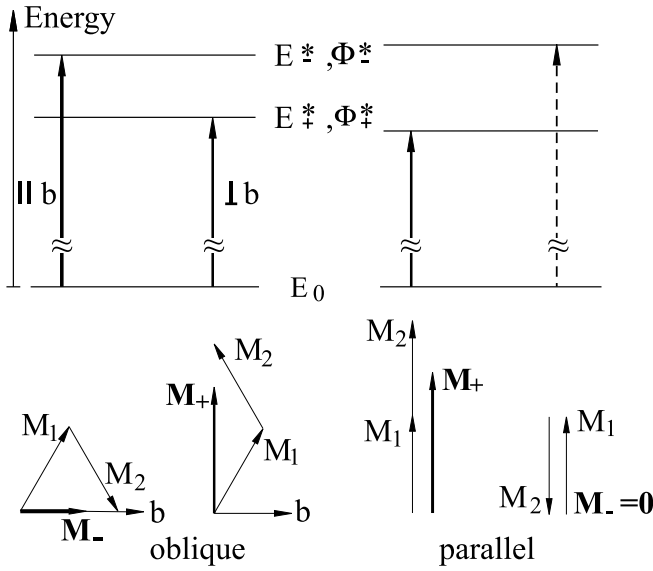


Fig. 6.8 A sketch showing the orientation and magnitude of the transition dipole moments \mathbf{M} for various mini-exciton geometries. When the two transition moments are parallel (beside one another or in a line), a blue or red shift occurs relative to the monomer. Only one optical transition is allowed. In the general

case of non-parallel orientation, shown on the left, there are two allowed transitions. These are the two Davydov components. Their transition moments can be constructed by vector addition of the individual moments. The solvent shift is left out here for simplicity.

$$\begin{aligned}
 \mathbf{M}_{S_1 \leftarrow S_0}^{\pm} &= \langle \Phi_G | e\mathbf{r} | \Phi_{\pm}^* \rangle \\
 &= \frac{1}{\sqrt{2}} \langle \phi_1 \phi_2 | e\mathbf{r} | \phi_1 \phi_2^* \pm \phi_1^* \phi_2 \rangle \\
 &= \frac{1}{\sqrt{2}} [\langle \phi_1 \phi_2 | e\mathbf{r} | \phi_1 \phi_2^* \rangle \pm \langle \phi_1 \phi_2 | e\mathbf{r} | \phi_1^* \phi_2 \rangle] \\
 &= \frac{1}{\sqrt{2}} [\mathbf{M}^2 \pm \mathbf{M}^1].
 \end{aligned} \tag{6.7}$$

In the case of translational equivalence, i.e. molecules oriented parallel to one another, the transition moments are either parallel or antiparallel (Fig. 6.8 right). In this case, only one of the two optical transitions $S_1 \leftarrow S_0$ of the dimer is allowed, with

$$\mathbf{M}_+^{Dimer} = \frac{1}{\sqrt{2}} 2\mathbf{M}^1 \quad (\text{or } \mathbf{M}^2).$$

For the other state, we find

$$\mathbf{M}_-^{Dimer} = 0$$

that is, the transition is forbidden (Fig. 6.8, below).

When the two molecules are on the other hand not translationally equivalent, as is the case in the unit cell of anthracene – Fig. 6.8, left – then both excited states have nonvanishing transition moments. Their magnitudes and directions can be computed with the aid of Eq. (6.7); for dipole transitions by addition or subtraction of the individual vectors. This is demonstrated schematically in Fig. 6.8.

There are thus two allowed transitions with the energy difference $2I_{12}$. This holds equally well for excitons in the crystal and for the mini-exciton. In the monoclinic anthracene crystal lattice, the orientation 1 is converted into orientation 2 by a mirror-glide operation (and *vice versa*). The mirror-glide plane is the a-c plane (Fig. 2.10). \mathbf{M}^+ and \mathbf{M}^- are therefore polarised parallel and perpendicular to the \mathbf{b} axis. The two Davydov components thus differ in both energy and polarisation.

The **magnitudes** of the level shift D and of the Davydov splitting $2I_{12}$ are found from Eqns. (6.5) and (6.4). For singlet terms which belong to allowed optical transitions, one can calculate the interaction potential V_{12} and the resonance energy I_{12} to a good approximation as a dipole interaction of the transition dipole moment of the excited molecular state with the neighbouring molecule in the ground state [13]. We thus have

$$I_{12} \propto z \cdot \frac{\mathbf{M}^i}{R_{1,2}^3} \hat{=} \text{const.} \frac{f}{\Delta E_M^i}. \quad (6.8)$$

In this expression, the meanings of the symbols used are:

- z is an orientation factor of the order of 1,
- \mathbf{M} is the transition dipole moment of the optical transition in the molecule,
- f is the oscillator strength of the transition,
- R is the distance between the molecules in the crystal,
- ΔE_M^i is the molecular excitation energy in the state i .

In going from the mini-exciton to a crystal exciton (cf. Sect. 6.5), to calculate D and I , a sum over the interactions with all the non-excited neighbours must be carried out. For oscillator strengths f between 0.001 and 0.1, numerical values for I_{12} between ca. 10 and ca. 1000 cm^{-1} are obtained in the singlet state. In the triplet state, the interaction energy between the excited and the non-excited states is smaller and cannot be computed as a simple dipole interaction. The splittings are also smaller. More on this topic will be given in the following section.

The measurement of pair or dimer spectra in a crystal thus allows the determination of the resonance interaction between an excited and a ground-state molecule in the crystal if their distance and orientations are known. Since guest molecules are not in general soluble at a sufficiently high concentration to produce a high enough pair concentration, one preferably uses **isotopic mixed crystals** for pair (or also aggregate) spectroscopy. Naphthalene is soluble in deuterated naphthalene to an arbitrarily high concentration, likewise anthracene in perdeuteroanthracene. In these cases, the electronic terms of the non-deuterated substances lie energetically lower than those of the perdeuterated host crystal by the order of 100 cm^{-1} . They therefore act as traps for the fluorescence or phosphorescence.

On irradiating the triplet levels T_1 of these traps, one can sensitively observe the $T_1 \leftarrow S_0$ absorption of the traps by high-resolution excitation spectroscopy using delayed fluorescence as detection channel in spite of the very small absorption constant. More on this will be given in Sect. 6.9.2, cf. also [19] and [20]. With increasing guest concentration, one also obtains the spectra of the various possible pair configurations in addition to A-B pairs; also A-A pairs and thereby the resonance interactions in different crystal directions (cf. Sect. 6.5.2). With still higher guest concentrations, there are, corresponding to their statistical probabilities, also trimers and larger aggregates of guest molecules at concentrations which make possible the analysis of their spectra. As the size of the aggregates increases, the magnitude of the Davydov splitting also increases from the value for the dimer up to that of the crystal.

Here, excitation spectroscopy shows its strength. One irradiates the sample with an extremely sharp laser line (down to 0.001 cm^{-1}). Detection is accomplished via the integrated fluorescence, which can readily be separated from the excitation light using filters, as the absorption and the fluorescence do not overlap. The emission lies at a higher quantum energy. With this method, it is even possible to identify and distinguish the isotope ^{13}C , present with its natural abundance of only 1.1%, at different positions within the molecules [21].

Even with simple UV-VIS spectroscopy, the exchange interaction I_{12} of a naphthalene dimer in naphthalene, i.e. in a mini-exciton, could be detected as a splitting of the 0,0 transition in the phosphorescence spectrum, yielding $1.2 \pm 0.2 \text{ cm}^{-1}$ [18]. In the phosphorescence spectrum of naphthalene in perdeuteronaphthalene, the transitions at $\pm 1.2 \text{ cm}^{-1}$ relative to the monomer line, which belong to the A-B pair, can be uniquely assigned on the basis of their concentration dependence (cf. Fig. 6.7, right-hand side). The exchange interaction in all the other possible neighbour configurations which can be investigated using the so called pair spectroscopy provides the data which are needed to compare with the quantitative calculation of exciton dispersion relations [19]. More in Sect. 6.5.2.

6.5 Frenkel Excitons

We now wish to extend the dimer model to encompass an “infinitely large” three-dimensional crystal lattice; this is very similar to the transition from the covalent bonding of two atoms to the band structure of a metal or a semiconductor with delocalised states. Starting from the more or less sharp energy levels in the two-body system, we arrive at a band of energy states whose width depends on the interactions of the individual molecules or the overlap of the molecular orbitals in the lattice. We must then take the interaction of an excited molecule with all the other molecules in the crystal and with the periodic lattice potential into account. The levels E^+ and E^- in the dimer model of Fig. 6.7 are transformed into a more or less broad band of energy levels. These are the excitonic bands of the crystal, which we shall treat in this section.

6.5.1

Excitonic States, Fundamental Equations

We assume that the crystal consists of N unit cells. We will limit ourselves here to crystals with no more than two molecules in the unit cell. The Hamiltonian H of the pure molecular crystal is given by

$$H = \sum_{m\alpha} H_{m\alpha} + \sum_{m\alpha < n\beta} V_{m\alpha; n\beta}. \quad (6.9)$$

Here, $H_{m\alpha}$ is the Hamiltonian of the molecule α in the m -th unit cell of the crystal, $V_{m\alpha; n\beta}$ describes the pairwise interaction between the molecule α in unit cell m with molecule β in unit cell n (cf. the fundamental work of Silbey *et al.* [22]). With two molecules in the unit cell, the indices α and β run over these two sites, and m and n run over all the N unit cells.

For the ground state of the crystal, in analogy to Eq. (5.1) we obtain with the ground-state functions $\phi_{m\alpha}$ of the individual molecules the function

$$\Phi_G = \mathcal{A} \prod_{m\alpha} \phi_{m\alpha}. \quad (6.10)$$

\mathcal{A} is here an antisymmetrisation operator. For the excited state in which one molecule $n\alpha$ is excited and all the others remain in their ground states, the wavefunction is:

$$\Phi_{n\alpha}^* = \mathcal{A} \phi_{n\alpha}^* \prod_{n\alpha \neq m\beta} \phi_{m\beta}. \quad (6.11)$$

The localised single-exciton wavefunctions $\Phi_{n\alpha}^*$ are not eigenfunctions of the crystal Hamiltonian. A wavefunction appropriate to the crystal symmetry and the periodic potential can be found using the Bloch-wave *ansatz*. From the localised basis functions $\Phi_{n\alpha}^*$, one obtains the delocalised wavefunction

$$\Psi_\alpha(\mathbf{k}) = \frac{1}{\sqrt{N}} \sum_n \Phi_{n\alpha}^* \exp(i\mathbf{k}\mathbf{R}_{n\alpha}). \quad (6.12)$$

In this expression, $\mathbf{R}_{n\alpha}$ is the position vector of molecule $n\alpha$ (for more details see [22]).

$\Psi_\alpha(\mathbf{k})$ is the wavefunction of an **exciton**, that is, of a neutral, delocalised excitation state with the wavelength λ , defined by $k = 2\pi/\lambda$. \mathbf{k} is the wavevector of the exciton. The exciton is a quasiparticle with the momentum $\mathbf{p} = \hbar\mathbf{k}$. For $\mathbf{k} \rightarrow 0$, the wavelength is large compared to the lattice constant d . $\mathbf{k} = 0$ corresponds to an infinitely long wavelength, i.e. the excitation phase is the same within all N unit cells of the crystal.

Equation (6.12) describes an exciton whose excitation energy is delocalised over the whole crystal, but is limited to a set of translationally-equivalent molecules α . This “one-site” wavefunction thus holds for **linear crystals** or for crystals with only **one molecule in the unit cell**. Quasi-one-dimensional excitons can for example be

observed in dibromonaphthalene (cf. Fig. 2.14). Hexamethylbenzene (Fig. 2.11) has only one molecule in its unit cell. With these “one-site” wavefunctions and the Hamiltonian given above, we can in principle compute the energy eigenvalues of the ground and excited states.

For the experimentally measurable energy difference between the excited state E^* and the ground state E_0 , we obtain

$$\Delta E(\mathbf{k}) = E^* - E_0 = E_{\text{Mol}}^* + D^* + 2I_{11} \cos \mathbf{k}\mathbf{d} \quad (6.13)$$

if we compute the Coulomb and the resonance interactions as in Eqns. (6.4) and (6.5). This is allowed when the interaction with the neighbouring molecules has a short range, so that only nearest neighbours need to be taken into account. In particular, owing to the translational equivalence, there is **no** Davydov splitting. The width of the exciton band is here to a good approximation given by $4 I_{11}$.

With the “one-site” wavefunctions for the two sublattices α and β as basis functions and using the Hamiltonian in Eq. (6.9), the energy eigenvalues of the ground and excited states can also be calculated for a crystal with **two molecules in the unit cell**. We obtain for the energy difference between ground and excited state the result:

$$\Delta E(\mathbf{k}) = E_{\text{Mol}}^* + D^* + E_{\alpha\beta}(\mathbf{k}). \quad (6.14)$$

Here, as in Eq. (6.13), E_{Mol}^* is the molecular excitation energy and D^* the static solvent shift

$$D^* = \sum_{n\alpha} \left[\left\langle |\phi_{m\beta}^*|^2 V_{n\alpha;m\beta} |\phi_{n\alpha}|^2 \right\rangle - \left\langle |\phi_{m\beta}|^2 V_{n\alpha;m\beta} |\phi_{n\alpha}|^2 \right\rangle \right]. \quad (6.15)$$

D^* is in general < 0 .

The determination of the \mathbf{k} eigenvalues yields the band structure of the crystal from the \mathbf{k} -dependent part:

$$E_{\alpha\beta}(\mathbf{k}) = L_{\alpha\alpha}(\mathbf{k}) \pm L_{\alpha\beta}(\mathbf{k}) \quad (6.16)$$

with the sum over translationally-equivalent interactions

$$L_{\alpha\alpha}(\mathbf{k}) = \sum_n I_{n\alpha;m\alpha} \exp(i\mathbf{k}(\mathbf{R}_{n\alpha} - \mathbf{R}_{m\alpha})) \quad (6.17)$$

and the sum of the translationally-inequivalent interactions

$$L_{\alpha\beta}(\mathbf{k}) = \sum_n I_{n\alpha;m\beta} \exp(i\mathbf{k}(\mathbf{R}_{n\alpha} - \mathbf{R}_{m\beta})). \quad (6.18)$$

In these expressions, the $I_{n\alpha;m\beta}$ are the matrix elements which describe the excitonic energy exchange

$$I_{n\alpha;m\beta} = \langle \phi_{n\alpha} \phi_{m\beta}^* | V_{n\alpha;m\beta} | \phi_{m\beta} \phi_{n\alpha}^* \rangle. \quad (6.19)$$

If, as in anthracene, the two molecules in the unit cell are connected by the symmetry operation C_{2h} , then by diagonalising the matrix $||H_{\alpha\beta}||$ for each value of \mathbf{k} , one obtains two exciton states (Davydov components). They can, if the interactions are predominantly of short range, be written in the simple form

$$\Psi_{\pm}(\mathbf{k}) = \frac{1}{\sqrt{2}}[\Psi_{\alpha}(\mathbf{k}) \pm \Psi_{\beta}(\mathbf{k})]. \quad (6.20)$$

Via transitions between the zero-vibrational ground state ($k = 0$) and the exciton band, the states with $\mathbf{k} = 0$ are directly accessible optically. This follows from momentum conservation. The momentum of the incident photon is namely very small compared to a reciprocal lattice vector. The Davydov splitting is

$$\Delta_D = 2L_{\alpha\beta}(0) = 2 \sum_n I_{\alpha\beta}^{ij} \approx 8I_{12}. \quad (6.21)$$

Here, the sum is carried out over all the translationally-inequivalent neighbours j of a chosen molecule i . In a molecular crystal of the anthracene type, these are to a good approximation the four nearest neighbours in the ($a-b$) plane; thus the value $8I_{12}$.

The translational shift, i.e. the shift of the centre of the Davydov components relative to the origin of the exciton band, is $L_{\alpha\alpha}(0) = \sum I_{\alpha\beta}^{ij}$, with summation over all the translationally-equivalent neighbours.

The splitting of the molecular energy levels into exciton bands is shown schematically in Fig. 6.9.

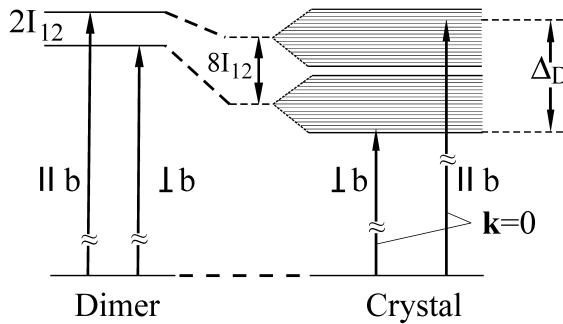


Fig. 6.9 In a crystal with two molecules in the unit cell, a molecular state splits into two Davydov bands. The dimer levels, which are split by the energy $2I_{12}$, are further shifted energetically by their interaction with translationally-equivalent molecules in the crystal. The splitting then becomes $2 \cdot 4I_{12}$ in the case of 4 nearest translationally-inequivalent neighbours and interactions

limited to the nearest neighbours. The width of the two Davydov bands is, from Eq. (6.22), given by the interaction with the equivalent and the inequivalent molecules in the crystal. The Davydov splitting Δ_D is defined as the energy difference of the $k = 0$ levels in the two bands. The optical transitions to the two bands have different polarisations ($\parallel b$ and $\perp b$).

6.5.2

Polarisation and Band Structure

The two Davydov components differ as in the dimer in the polarisation of their optical transitions. In monoclinic anthracene, they are polarised parallel to the **b** axis (cf. Fig. 2.10) or in the $a-c$ plane, i.e. $\perp \mathbf{b}$, corresponding to Ψ_+ and Ψ_- in Eq. (6.20). The polarisation results from the symmetry of the molecules and the crystal. The excitonic wavefunctions must obey certain symmetry conditions which agree with the crystal symmetry (its space group) and the symmetry of the individual molecules. For the molecule anthracene, this is the point-group symmetry D_{2h} and for the crystal, C_{2h} . Frenkel excitons, in the language of space-group terminology, must therefore transform as the irreducible representations A_u , B_u , A_g , B_g (Table 5.2). If, as in the case of anthracene, the S_1 state has B_u symmetry, then the states of the Frenkel excitons transform as B_u (symmetric) or as A_u (antisymmetric) in Eq. (6.20). Which of the two Davydov components lies energetically higher depends on the sign of the interaction I_{12} .

The strength of the **resonance interaction**, which is responsible for the Davydov splitting, can be calculated for a singlet state, and when the transition is allowed in the free molecule, as the Coulomb interaction of the transition dipole moment of the excited state D^* with the neighbouring molecules in their ground states. This was already pointed out in Sect. 6.4, Eq. (6.8). The transition moment can be represented as a vector in a certain direction relative to the molecular axes. It corresponds to a particular dipole moment. For sufficiently large oscillator strengths, the dipole interaction is predominant and leads to results which are in agreement with experiments. Cf. also the extensive calculations for anthracene and naphthalene [22, 23]. For singlets, the interaction takes on the form $^1D^* + ^1A \rightarrow ^1D + ^1A^*$, ¹. In this scheme, the excited molecule D , the donor, gives an electron back to the ground state, while simultaneously another electron in the initially not excited neighbouring molecule A , the acceptor, is raised into an excited state. In triplet states, this interaction is forbidden by the Pauli principle. However, the exchange interaction is then allowed; it is based on the overlap of the wavefunctions following the scheme $^3D^* + ^1A \rightarrow ^1D + ^3A^*$, i.e. the triplet state is exchanged between D and A . The exchange interaction is in general weaker than the dipole interaction, and its range is shorter. Triplet splittings are therefore usually noticeably smaller than singlet splittings and they can be understood by including only interactions with the nearest neighbours [19]. In this connection, we mention also the calculation of the triplet-exciton dispersion in anthracene [24].

Typical values for the magnitude of the Davydov splitting for triplet states lie in the region of 10 cm^{-1} and for singlet states between 100 and some 1000 cm^{-1} , as we have already mentioned for dimers.

Band shifts and Davydov splitting thus depend strongly on the electronic structure of the transitions. In the case of strong transitions with an oscillator strength $f > 0.3$, the dipole approximation is good, as in Eq. (6.8). The splittings are so large that one can recognise the two Davydov components as parts of a common molecular transition only with the aid of their polarisations. Thus, the strong $S_3 \leftarrow S_0$

transition in anthracene (oscillator strength $f = 2.3$) is split into a b -polarised component at $37\,000\text{ cm}^{-1}$ and an a - c component at $53\,000\text{ cm}^{-1}$. The Davydov splitting is here $16\,000\text{ cm}^{-1}$. For the $S_1 \leftarrow S_0$ transition in anthracene, $f \approx 0.1$. Such transitions are termed medium-strong; they have Davydov splittings of 220 cm^{-1} . In α -perylene, the splitting of the transition in the visible with $f = 5.4$ is several thousand cm^{-1} [13].

The $S_1 \leftarrow S_0$ transition in naphthalene has a similarly large Davydov splitting as in anthracene, ca. 150 cm^{-1} , in spite of its much smaller oscillator strength, $f < 0.01$. Here, the dipole approximation is no longer sufficient by itself for the calculation of the splitting. Electric quadrupole moments must also be taken into account [23].

In triplet transitions, the resonance interaction and thus the Davydov splitting can, as mentioned, no longer be understood in terms of a dipole interaction, but rather as an exchange between orbitals which overlap. Measured values are available only for T_1 states. Figure 6.10 shows as an example, similar to Fig. 6.1, the two 0,0 components of the excitation spectrum $T_1 \leftarrow S_0$, of the triplet exciton T_1 in an anthracene crystal; here, however, the spectrum was taken at $T = 1.8\text{ K}$. 0,0 transition means that the excitation affects only excitons and that no additional phonons or vibrons are excited. In anthracene, the Davydov splitting of the T_1 excitonic state is 21.5 cm^{-1} (cf. Fig. 6.10). In naphthalene, it is 9.8 cm^{-1} [34].

In Table 6.1, some numerical values for the S_1 and T_1 states in anthracene and naphthalene are collected.

The vibronic levels also have a Davydov splitting, which in the excited state can be comparable to those of the zero-vibrational states; cf. [25] and [22]. The Davydov splitting of vibronic levels in the ground state is however very small, because the resonance energy between an oscillating and a non-oscillating molecule in the ground state is very low. Correspondingly, the width of a “vibronic band” in the electronic ground state is small.

When vibrons and phonons are thermally populated, then all possible k values are occupied. With the selection rule $\Delta k = 0$, it is clear that absorption transitions

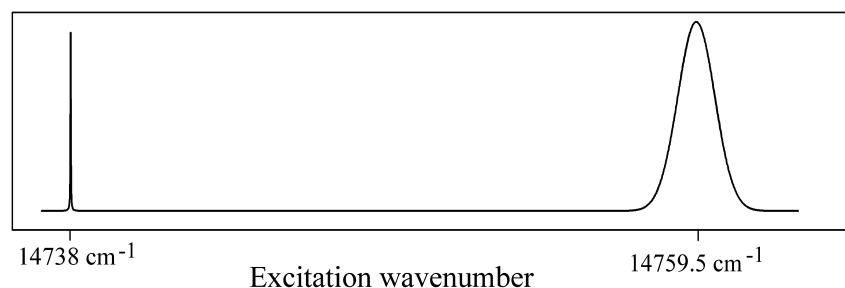


Fig. 6.10 The Davydov splitting of the 0,0 transition in the $T_1 \leftarrow S_0$ spectrum of anthracene at 1.8 K . This excitation spectrum was detected with an extremely narrow-band laser. The Davydov splitting is 21.5 cm^{-1} . These are the same transitions shown in Fig. 6.1 at 300 K ; there, however, they have a half-width of

ca. 150 cm^{-1} . The half-width of the low-energy component here is only 0.009 cm^{-1} , and that of the other component is 0.9 cm^{-1} . This, like the broadening with increasing temperature, is a result of the exciton-phonon coupling. The two lines have here been normalised to the same intensity. After [20].

Table 6.1 Some characteristic numerical values for S_1 and T_1 excitons in naphthalene and anthracene crystals.

	0,0 region, cm^{-1}	Solvent shift, eV	Davydov splitting, cm^{-1}	Absorption constant of S_0 , cm^{-1}	Lifetime τ of the excitons (without trapping), s
Anthracene S_1	25 300	0.29	220	10^5	$2 \cdot 10^{-8}$
Anthracene T_1	14 750		21	$3 \cdot 10^{-4}$	$4 \cdot 10^{-2}$
Naphthalene S_1	31 500	0.43	150	10^4 – 10^5	10^{-7}
Naphthalene T_1	21 200		10	$5 \cdot 15^{-4}$	< 0.5

* For the quantities given in this table, slightly differing values can be found in the literature. We dispense here with a detailed discussion and literature citations.

from the ground state into **all** the k -states of the exciton band are permitted. With this “hot band” spectroscopy, the bandwidth and the density of states of the exciton band can thus be determined optically [26]. The Boltzmann factors for the thermal population of phonon states show that even at low temperatures, a considerable occupation of phonon states is to be expected.

To compute the complete exciton dispersion relations $E(k)$, we start from Eqns. (6.16)–(6.18). Denoting the two possible sites within the unit cell by A and B, we write the k -dependent part of the energy as:

$$E_{\pm}(\mathbf{k}) = L_{AA}(\mathbf{k}) \pm L_{AB}(\mathbf{k}). \quad (6.22)$$

L_{AA} and L_{AB} contain the summation over all the N unit cells of the crystal (compare Eqns. (6.17) and (6.18)).

Owing to the small range of the resonance interactions, we can, to a good approximation, especially in the triplet state, limit the sums to those terms which describe the interaction of a molecule with its nearest neighbours. If we now replace $\exp(i\mathbf{k}\mathbf{R})$ by its real part and insert the corresponding lattice vectors for \mathbf{R} , we obtain the dispersion relation from Eqns. (6.17), (6.18) and (6.22):

$$E_{\pm}(\mathbf{k}) = 2[I_{AA}^a \cos(\mathbf{k}\mathbf{a}) + I_{AA}^b \cos(\mathbf{k}\mathbf{b}) + I_{AA}^c \cos(\mathbf{k}\mathbf{c})] \pm 4 I_{AB}^{ab} \cos\left[\mathbf{k} \cdot \frac{1}{2}(\mathbf{a} + \mathbf{b})\right]. \quad (6.23)$$

The expressions I_{AA}^a , I_{AA}^b , and I_{AA}^c refer to the resonance interaction of translationally-equivalent $A-A$ pairs along the crystal directions \mathbf{a} , \mathbf{b} , and \mathbf{c} , while I_{AB}^{ab} denotes the interaction between inequivalent $A-B$ pairs in the $a-b$ plane of the crystal. The factor 4 takes into account the number of similar $A-B$ pairs.

These quantities can be measured using pair spectroscopy [19], and with them the dispersion relations can be computed quantitatively (cf. Fig. 6.11). To calcu-

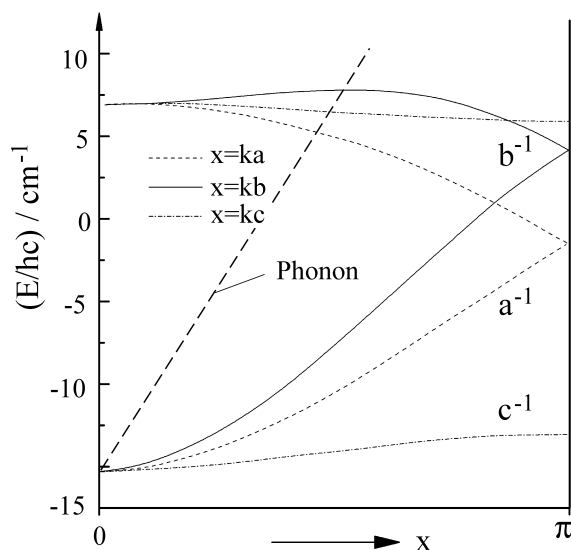


Fig. 6.11 Calculated exciton band structure of the T_1 state of anthracene for three directions in the reciprocal lattice. The experimentally-determined numerical values for the triplet resonance interactions are given in the text (from [19]). The dashed curve is a typical dispersion relation for acoustic phonons in anthracene [28].

late these relations, the following resonance-interaction values were used: $I_{AA}^b = -2 \text{ cm}^{-1}$, $I_{AA}^{a+c} = -0.6 \text{ cm}^{-1}$, $I_{AA}^c = +0.5 \text{ cm}^{-1}$, $I_{AB}^{ab} = -2.55 \text{ cm}^{-1}$. The quantities I_{AA}^b and I_{AB}^{ab} dominate the results. The exciton therefore moves preferentially in the $a-b$ plane. The resonance interactions outside this plane are much smaller, but are not negligible. The magnitude of the measured resonance interactions corresponds within the errors of the measurement and the simplifications used (interactions only with the nearest neighbours) to the measured Davydov splitting of $\Delta_D = 8 I_{AB} = 21.5 \text{ cm}^{-1}$.

In the 1,4-dibromonaphthalene crystal (compare Fig. 2.14), the crystal structure leads to a one-dimensional exciton motion along the c' direction. The pair-interaction energy is here $I_{AA} = 6 \text{ cm}^{-1}$; the excitons are thus faster than in anthracene.

Whether the $\mathbf{k} = 0$ state lies at the upper or the lower edge of the exciton band depends, according to Eq. (6.19), on the sign of the resonance interaction energies I_{12} and I_{11} (or I_{AA} and I_{AB}).

Dispersion relations of singlet excitons are not so simple to calculate, because the range of the important interaction forces is larger than for the triplet states. One therefore has to take interactions with more neighbours into account [23]. A simplified calculation for anthracene can be found in [25]. Furthermore, the number of Davydov components increases correspondingly, when the unit cell of a crystal contains more than two molecules.

6.5.3

Coherence

Exciton waves with a definite value of \mathbf{k} are coherent and in the ideal case are delocalised over the entire crystal. This holds as long as there is no exchange of momentum with defects in the crystal or with phonons. A measure of the coherence time of excitons in the purely coherent case is the inverse optical linewidth. During its coherence time τ_k , the exciton remains in its \mathbf{k} -state. During this time, it travels a distance l_k , its coherence length. One refers to coherent excitons when l_k is large compared to the lattice constant d . In the limiting case $l_k = d$, the motion is an incoherent hopping from one lattice site to another. The coherence time decreases strongly with increasing temperature due to the increasing density of states of the phonons. At room temperature, the hopping time is a measure of the coherence time. For naphthalene and anthracene, values of 10^{-13} – 10^{-14} s [30] are obtained. While one can consider the limiting cases of purely coherent or incoherent exciton motion at very low temperatures or sufficiently high temperatures, respectively, in the general case one is dealing with a coupled coherent and incoherent process. The theory for such processes is due to Haken and Strobl [31]. The diffusive character of the exciton motion corresponds to stochastically distributed hopping processes from one site to another in the lattice.

An experimental approach to measurement of the spatial coherence of excitons is offered by analysis of optical line shapes and linewidths. However, a quantitative understanding of the exciton-phonon interaction is rendered difficult by the fact that the bandwidths of exciton bands are relatively small (in the singlet state $\sim 100 \text{ cm}^{-1}$, in the triplet state $\sim 10 \text{ cm}^{-1}$). The exciton-phonon interaction is not small in comparison to this. In the literature, one thus can find rather widely divergent numbers for coherence times which were measured by different methods.

The interaction of the excitons with phonons causes a drastic broadening of the optical transitions with increasing temperature (see Fig. 6.12). This temperature broadening is especially striking in comparing Figs. 6.1 and 6.10. Both figures show the same transitions to the T_1 state of anthracene, namely the absorption of the S_0 state into the two $\mathbf{k} = 0$ states of the Davydov-split exciton bands, measured with excitation spectroscopy. They lie here at the lower edge and nearly at the upper edge of the bands – see the dispersion relation in Fig. 6.11. In Fig. 6.1, (at room temperature), the linewidth is $\Gamma/hc = 70 \text{ cm}^{-1}$. The resulting lifetime of the $\mathbf{k} = 0$ state is $\tau = \hbar/2\Gamma = 4 \cdot 10^{-14}$ s. In Fig. 6.10, at 1.8 K, the lower Davydov component has $\Gamma/hc = 0.009 \text{ cm}^{-1}$, corresponding to $\tau = 3 \cdot 10^{-10}$ s. The residual linewidth is determined by the scattering of excitons from structural defects [21]. The width of the upper component, $\Gamma/hc = 0.9 \text{ cm}^{-1}$, yields for the lifetime of this $\mathbf{k} = 0$ state a value of $\tau = 3 \cdot 10^{-12}$ s. The lifetimes quoted here correspond to the coherence times. They thus decrease by two orders of magnitude between low temperatures and room temperature.

The large linewidth of the upper Davydov component, which is also a factor of 100 greater than that of the lower component, is due to the interaction with (acoustic) phonons from \mathbf{k}/\mathbf{k}' scattering. The low-energy $\mathbf{k} = 0$ state is at the same

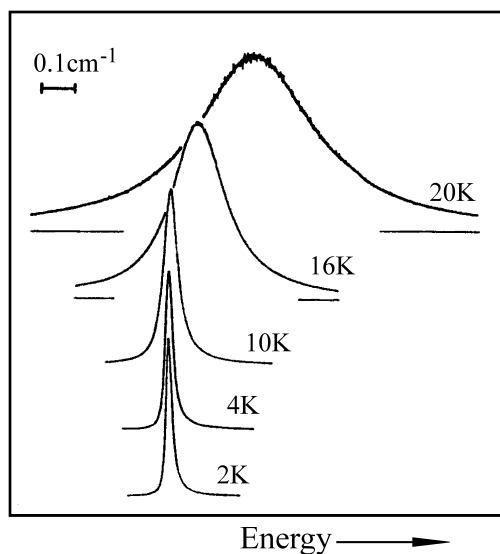


Fig. 6.12 The temperature dependence of the linewidth of the low-energy Davydov component from Fig. 6.10, for the triplet 0,0 transition in anthracene. The curves are normalised to the same height. The exciton-phonon interaction broadens the lines between 2 K and 20 K by more than two orders of magnitude. From [20] and [29].

time the lower edge of the exciton band. It therefore cannot relax to a different \mathbf{k} state through emission of phonons. For interband scattering, the absorption of an acoustic phonon with an energy of at least $15 \text{ cm}^{-1} \cdot hc$ is necessary. Such phonons are however practically non-existent at a temperature of 1.8 K. The high-energy state with $\mathbf{k} = 0$, in contrast, can relax to the lower Davydov component or to other \mathbf{k} states via phonon emission through interband scattering. The lifetime of the exciton in a particular \mathbf{k} state is thus reduced. This makes the larger residual linewidth even at 1.8 K and the Lorentz line shape understandable [32].

The quality of the crystal also has a decisive influence on the coherence time, the coherence length, and the linewidth of excitons. Defects due to dislocations or internal strains (see Chap. 4) can likewise act as scattering centres for excitons and thereby shorten their coherence times. Furthermore, they cause changes in the interaction integrals I (Eq. (6.19)) and thus lead to an inhomogeneous line broadening. An impressive example of this was already shown in Fig. 4.5. A direct determination of exciton coherence by means of interference experiments has yet to be carried out. As an indirect determination, the measurement of the exciton band structure using “hot band” spectroscopy (cf. Sect. 6.5.2) appears very convincing.

In the incoherent limiting case, the hopping time is proportional to I^{-1} (cf. Eq. (6.4)). Typical hopping times for singlet excitons in aromatic crystals lie as mentioned in the range of 10^{-13} s, while for triplet excitons, they are 10^{-11} to 10^{-12} s. From these times and from the lifetimes, the diffusion lengths can be computed (see Sect. 6.9.1).

Additionally, in the case of triplet excitons, there is not only a spatial coherence, but also a spin coherence, which can be investigated using ESR (see also Chap. 7). It is limited by intraband scattering of excitons with k -dependent resonance frequencies due to selective spin-orbit coupling. The measured spin coherence times

Table 6.2 Static interaction parameters from optical spectroscopy. Further measurements using ESR spectroscopy are considered in Chap. 7.

Observation	Information	Quantities derived from the measurements	Singlet or triplet	Technique or measurement method
Davydov splitting	Sum of the interaction elements ("Resonance energy")	ΣI_{ik}	S, T	Absorption and emission spectroscopy
Solvent shift	Coulomb interaction	D	S, T	"
Splitting of energy levels through aggregation, also exciton dimensionality	Individual interaction matrix elements	I_{11}, I_{12} etc.	S, T	Pair spectroscopy, high-resolution excitation spectroscopy, isotopic mixed crystals
Band-band transitions including vibronic bands	Density of states in the exciton band	Band properties -widths of exciton bands	S, T	"Hot band" – optical spectroscopy, absorption and emission

are clearly longer than those for the spatial coherence of the exciton. Thus, for the linear excitons (due to the crystal structure) in α -dichloro-anthracene crystals, from the ESR linewidths the scattering rates $P_{kk'}(1.6\text{ K}) = 7 \cdot 10^6\text{ s}^{-1}$ and $P_{kk'}(4.2\text{ K}) = 7 \cdot 10^8\text{ s}^{-1}$ were found [33].

To finish off this section, we have again collected in Table 6.2 the (static) interaction parameters which can be determined with the aid of optical spectroscopic methods.

6.6 Charge Transfer (CT) Excitons

Frenkel excitons are the limiting case of excitonic excited states in which the correlated electron-hole pair is localised on the same molecule and can move through the lattice in this form. These excitons are the normal case in a molecular crystal. The other limiting case, the Wannier excitons, describes the neutral excitation states in inorganic crystals such as Cu_2O , Si or Ge. For these excitons, the distance between the excited electron and the hole which it has left is an order of magnitude larger than the distance between the lattice structural units, namely 40–100 Å (for an illustration, see Fig. 6.13). The excited states of Wannier excitons can often be analysed to a good approximation in terms of hydrogen-like Rydberg series, with energy values given by $E = E_\infty - E_1/n^2$ where $n = 1, 2, 3, \dots$, E_∞ = energy required

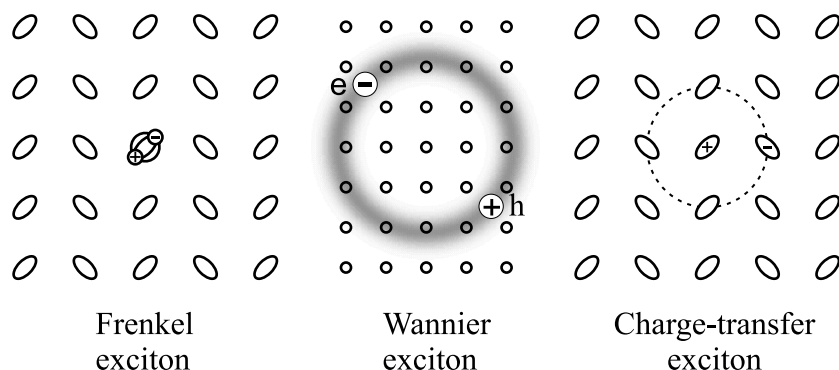


Fig. 6.13 Excitons with different radii: diagram of a Frenkel exciton, a Wannier exciton, and a charge-transfer (CT) exciton. Wannier excitons have not been observed in organic crystals.

to create an electron-hole pair with an infinite distance within the solid, and E_1 = energy of the lowest Wannier exciton state. Setting $E_\infty = 0$, one obtains as in the H atom

$$E = -\frac{e^4 m_0}{32\pi^2 \varepsilon^2 \varepsilon_0 \hbar^2} \frac{1}{n^2}.$$

ε is the dielectric constant of the crystal. In organic molecular crystals, they have not yet been observed.

In organic crystals, the term **charge transfer exciton** is applied to electronic excitations which are neutral but polar, and in which the electron-hole distance is one or two times greater than the distance of the molecular structural units. Charge transfer excitons thus lie in terms of their binding energies as well as in terms of their spatial extension between the Frenkel excitons and the Wannier excitons. Previously, they were also referred to as ionic states. They are thus excitations in which an electron or a hole is transferred to a molecule in the neighbourhood and thus gives rise to an ion pair.

The energy of a CT exciton, E_{CT} , in which the electron and the hole are located on neighbouring molecules, is given by

$$E_{CT} = I_D - E_A - P_{eh}(r) - C(r) \quad (6.24)$$

with

- I_D = Ionisation potential of the donor (at the site of the hole),
- E_A = Electron affinity of the acceptor (at the site of the electron),
- $P_{eh}(r)$ = Polarisation energy of the lattice due to the electron-hole pair at the distance r ,
- $C(r)$ = Coulomb attractive energy between the electron and the hole at the distance r .

Such CT excitation states are found, in addition to the Frenkel excitons, in the aromatic molecular crystals such as anthracene which we have already treated, that

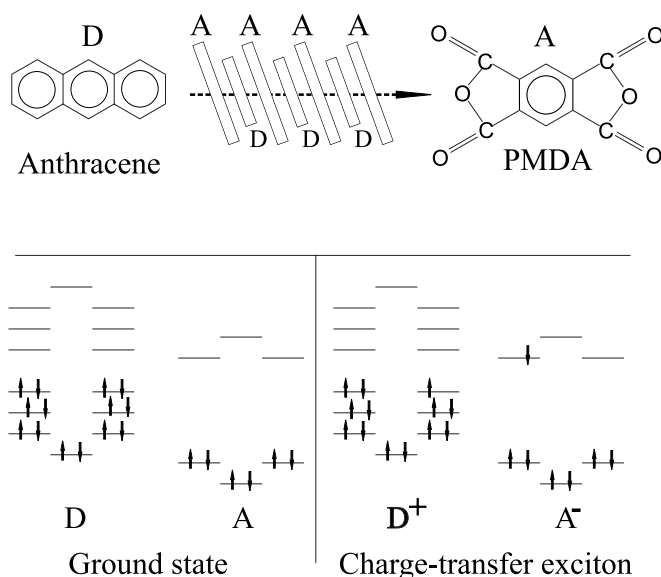


Fig. 6.14 The anthracene-pyromellitic acid dianhydride (A-PMDA) mixed-crystal system as an example of a weak donor-acceptor crystal with mixed stacks. The ground state is neutral, nearly without charge transfer. The lowest CT state is formed by a transition of an electron

from the HOMO of the donor (anthracene) to the LUMO of the acceptor (PMDA). It lies energetically lower than the transition to the LUMO in anthracene. The molecules form DADA... stacks. From [M1].

consist of only **one type of molecules**. They are difficult to observe in the usual optical spectrum, because their absorption is very weak (typical oscillator strengths for the transition from the neutral ground state are $f = 10^{-4}$ to 10^{-2}), and because they lie in the spectral range of the much stronger $S_n \leftarrow S_0$ absorption, i.e. at excitation energies which are higher than those of the Frenkel excitons. For anthracene, the absorption edge, that is the 0,0 threshold for the $S_1 \leftarrow S_0$ transition, lies at 3.11 eV, and the CT excitation at 3.9 eV. These excited states become important and observable in the photoconductivity of anthracene and similar crystals. We will return to this topic in Chap. 8. Their investigation is most expediently carried out in reflection or absorption in an applied electric field. The field is modulated and only the correspondingly modulated part of the absorption or reflection is measured. This spectroscopic method is called electroabsorption or electroreflection [35].

In crystals which are composed of **two different partner molecules**, CT excitations and with them CT excitons are frequently the predominant lowest excitation states and are thus responsible for the lowest-energy transitions in the singlet system. We will illustrate this using the example of the weak donor-acceptor complex **anthracene/pyromellitic acid dianhydride**, (A/PMDA) (Fig. 6.14). The ground state is neutral and nonpolar, with only a small charge-transfer fraction. The lowest optical excitation starts from the ground state of the donor *D*, anthracene, (from its highest occupied orbital or HOMO) and leads to the lowest unoccupied orbital (LUMO) of the acceptors *A*, PMDA, within the mixed stack DADADA. A polar ex-

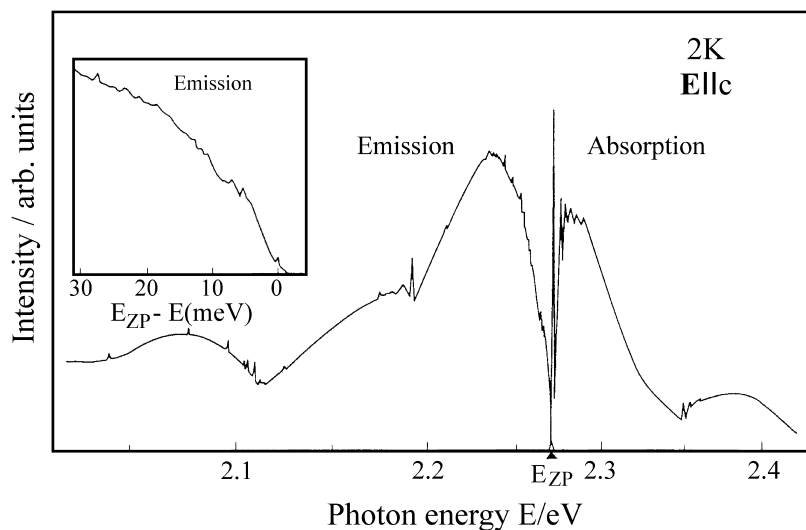


Fig. 6.15 The absorption and emission spectra of an anthracene-PMMA crystal at 2 K with the polarisation of the light parallel to the stacking axis. The zero-phonon line ZP can be clearly seen in the absorption spectrum, likewise in the emission spectrum (enlarged scale, upper left). The spectrum is furthermore severely broadened, because the CT excitation is accompanied by strong phonon interactions. From [37].

cited state is produced by this absorption, which is characterised by a CT absorption band. The optical transition is polarised along the stacking axis. Figure 6.15 shows the absorption and the fluorescence spectra, measured with the optical polarisation parallel to the stacking axis [36]. The absorption band, which is strongly broadened by phonon interactions, contains a sharp zero-phonon line as a 0,0 transition. The vibronic structure is barely visible, except for the sharp 0,0 zero-phonon line ZP, because the strong electron-phonon interaction broadens the transitions severely. The ionic complex partners produce a local lattice deformation and polarise their surroundings. This can also lead to self trapping of the excitonic energy of excitation and thus of the CT exciton. Note the energy of the 0,0 transition in Fig. 6.15. It is smaller by ca. 8000 cm^{-1} than that of the 0,0 transition of Frenkel excitons in the anthracene crystal (compare Figs. 6.4 and 6.6).

The lowest excited triplet state T_1 of this crystal belongs, in contrast, only to the anthracene molecule and corresponds to triplet Frenkel excitons with no polar character, as we described in Sect. 6.5. This follows from the energetic position (not shown here) and the vibronic structure of the phosphorescence spectrum [36].

A local CT state can be represented as a linear combination of the states $\psi(A^-D^+A^0)$ and $\psi(A^0D^+A^-)$. The optical transition from the electronic ground state $\psi(A^0D^0A^0)$ is allowed only into the state with odd parity, $\psi_u = \frac{1}{\sqrt{2}}[\psi(A^-D^+A^0) - \psi(A^0D^+A^-)]$. When an electric field is applied along the stacking axis, the transition into the state with even parity is also allowed. The energy difference between

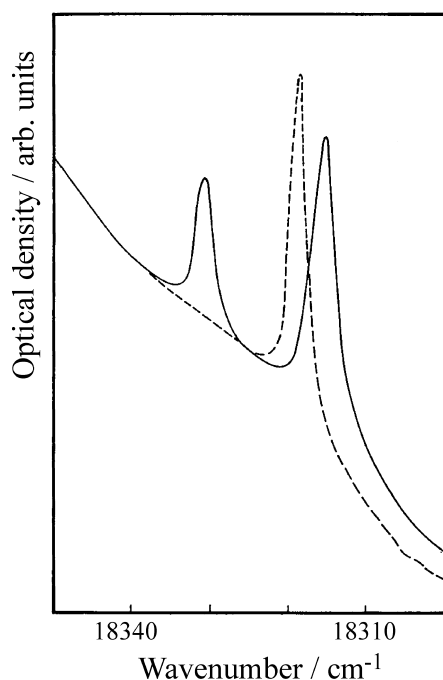


Fig. 6.16 Detection of a CT exciton in anthracene-PMDA by means of the Stark effect. The sharp zero-phonon line at the absorption edge (dashed line, without an electric field) splits in the presence of an electric field (of ca. $4 \cdot 10^4 \text{ V cm}^{-1}$) into two components (solid line). From [38].

the two states is here equal to 12 cm^{-1} . It corresponds to the splitting of the exciton band at $k = 0$ (see also Fig. 6.16). Transport of the CT state within the crystal requires the motion of a pair excitation state. Expressed in simple terms: the CT state is polar. The configuration with dipole moments along the direction of the applied field differs in its energy from that in the opposite direction [38].

The optical spectra of strong D-A complexes or radical-ion salts, that is of crystals in which a charge separation already exists in the ground state, are typified by the metallic character of these materials. They will be treated in Chapter 9.

6.7

Surface Excitons

Molecules which are located at the surface of a crystal are not surrounded on all sides by other molecules as are those in the bulk. Therefore, surface excitons differ from bulk excitons. Due to the smaller number of neighbouring molecules, the shifts and splittings D and I etc. in the equations of Sect. 6.4 are smaller. The electronic terms of surface excitons are thus less shifted relative to those of the free molecules, i.e. the energies of the transitions lie at somewhat higher values than those of the bulk excitons. This is demonstrated in Fig. 6.17 using the example of anthracene. It shows the reflection spectrum from the (001) surface of an anthracene crystal. One can discern resonance and antiresonance lines which belong to the bulk excitons as well as to excitons in the first, second, and third surface lay-

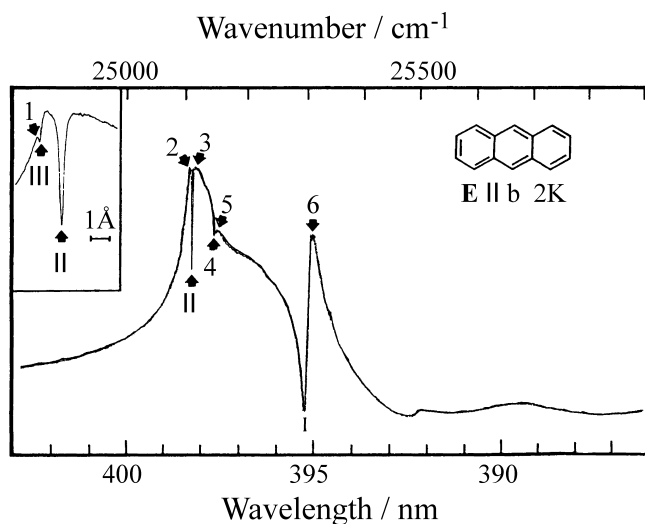


Fig. 6.17 Surface excitons in anthracene, observed in the reflection spectrum, **b** polarised with perpendicular incidence onto the (001) surface of the crystal (the cleavage surface of a Bridgman crystal). The minima I, II and (III) (the latter with an enlarged scale in the inset) in the broad reflection of the bulk exciton are identified as excitons from the

first (I), the second [II] and the third layer from the surface (III). The structures denoted by 1 and 6 correspond to the 0,0 transitions $||a$ and $||b$ of the bulk excitons. This yields a Davydov splitting of 225 cm^{-1} . That of the surface exciton in I is equal to 218 cm^{-1} . The remaining structures 2 to 5 belong to phonon satellites. After [39].

ers. The identification of the lines is made possible by comparing the spectrum to the reflection from a crystal on whose surface a thin CH_4 layer had been deposited.

In the usual crystals, surface excitons are hard to observe. Their absorption is naturally weak compared to that of the bulk and it lies in an energy range in which the bulk also absorbs. They are therefore best observed in reflection. For naphthalene and anthracene, Davydov splittings and solvent shifts are seen in the 0,0 transitions $S_1 \leftarrow S_0$ which are about 10–20% smaller than the known bulk transitions in these crystals. See also [39].

These surface excitons become important for very thin crystals, which consist to a large extent of surfaces. Here, the somewhat different excitons in the second and third layers from the surface can be more readily identified. Experimental results for ultrathin films are not yet available.

6.8

Excimers

The term excimer denotes molecular configurations which absorb as monomers but in the excited state form (physical) dimers and fluoresce as such. One also speaks of resonance dimers. These excimers (excited dimers) have been extensively investigated in solution. Their emission is red-shifted compared to the monomer

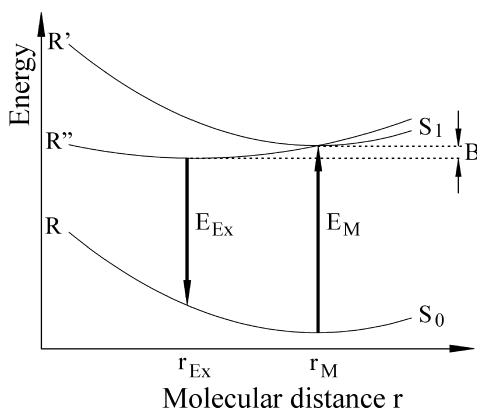


Fig. 6.18 Potential curves and an emission transition for excimers in a crystal. Absorption occurs at the equilibrium spacing r_M in the ground state and leads to the excited state S_1 . From there, a radiationless relaxation into the excimer state with the smaller equilibrium spacing r_{Ex} takes place. The excimer emission

leads from this state back to the ground state. R , R' and R'' symbolise the potential curves of the molecules in their ground states (R) and in the excited state (R') as well as the excimer state (R''). B is the binding energy of the excimer. From [40, 41].

emission, their vibronic structure is not or at best poorly resolved, and their lifetimes are longer. For more information, cf. ([M6], Sect. 14.5).

There are also crystals of aromatic hydrocarbons whose fluorescence is an excimer emission. For this to occur, the molecules in the crystal must be ordered pairwise in parallel planes, with a small distance between neighbouring planes. In the pyrene crystal, this distance is 3.53 Å. The molecules are thus already ordered as physical sandwich dimers within the crystal. Prime examples of this – as also in solution – are pyrene and perylene (cf. the crystal structures in Chap. 2, Figs. 2.11 and 2.12).

The binding between the two partners of a pair is weak in the ground state; they absorb light as monomers, “excitonically”. In the excited state S_1 , the binding of the pairs increases due to resonant exchange. In this process, the two partners change their mutual configuration somewhat and approach the state of maximum resonance stabilisation, so that in particular, their planar spacing becomes smaller – in the case of pyrene, it decreases from 3.53 to 3.37 Å. This approach is accompanied by a radiationless energy relaxation. From the relaxed state, the excimer emission leads back to the ground state S_0 , whose potential at the smaller molecular spacing is repulsive (Fig. 6.18). It is thus strongly Stokes-shifted relative to the absorption, in pyrene by ca. 0.5 eV. In the ground state, the energy relaxes by a further ca. 3000 cm⁻¹ and the spacing increases by 0.16 Å back to that of the initial state. Fig. 6.19 illustrates the (excimeric) emission spectrum of a pyrene crystal. The absorption, not shown here, begins with the 0,0 transition which is only weakly indicated in the emission, at 26 720 cm⁻¹. The excimeric emission is broad and nearly featureless, since there are no discrete vibrational levels in the non-bonding ground-state potential. The excimer formation also implies a strong exciton-phonon interaction, which further broadens the emission.

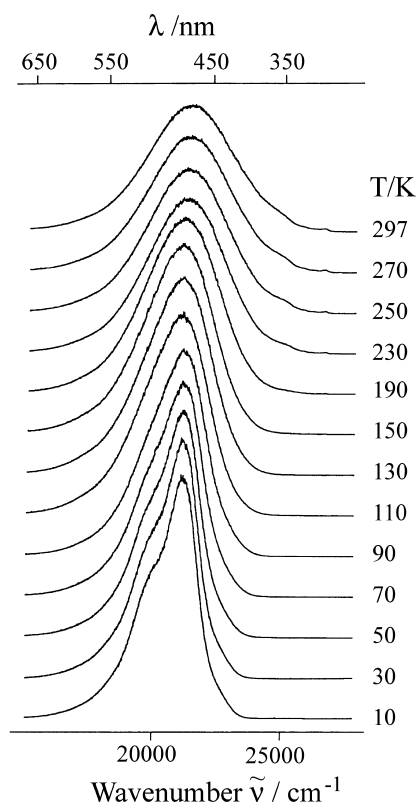


Fig. 6.19 Excimer emission from a pyrene crystal. At 297 K, in the region of the absorption edge of the crystal at $26\,595\text{ cm}^{-1}$, one can see a weak signal which corresponds to the 0,0 transition of the monomeric exciton emission of pyrene. From [42].

Excimer formation can also be understood in terms of self trapping of the (monomeric) exciton. To be sure, the excimer states are mobile during their lifetime of some 100 ns on their own as excimer excitons. This can be detected by guest molecules which act as deeper traps that can collect the excitation energy (sensitised fluorescence, Sect. 6.9.1).

Excimer emission is observed from many crystals when they are subjected to pressure or when they are strongly deformed in some other manner. In the deformed crystals, molecular configurations are produced which favour excimer emission. Through annealing, these defects can often be removed again. Also in vapour-deposited films which are initially amorphous at low temperatures, excimer structures can frequently be formed by a suitable annealing process.

6.9

Exciton Processes, Energy Conduction

Electronic excitation energy can be conducted within molecular crystals by excitons from one location to another. This is a very important and characteristic process in molecular crystals. In this section, we show how this energy conduction can be investigated and what consequences it has. See also [30].

6.9.1

Sensitised Fluorescence

The fundamental observable of exciton mobility and energy conduction in molecular crystals is sensitised fluorescence (compare Fig. 6.20). One irradiates a host crystal H , for example anthracene, which has a very low doping or impurity concentration of a guest G , for example tetracene, with light that can be absorbed by the host

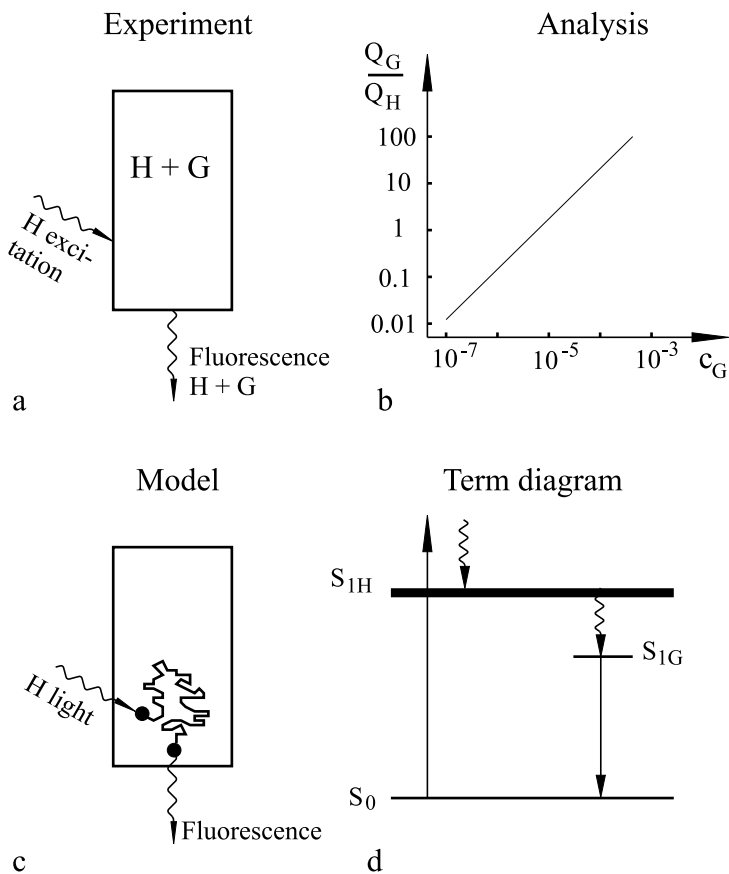


Fig. 6.20 Sensitised fluorescence, schematic representation. **a:** the host crystal H contains a low concentration of guest molecules, G . The crystal is excited by light which is mainly absorbed by the host. The fluorescence contains mainly guest light. **b:** the emitted fluorescence light quanta from the host and the guests, Q_H and Q_G , differ spectrally in their wavelengths and can therefore be detected separately. The quantum ratio Q_G/Q_H is plotted against the guest concentration c_G .

c: the excitation light is absorbed in the crystal by the host. The excitation energy diffuses in the form of S_1 excitons within the crystal. When the exciton reaches a guest molecule G within its lifetime, it is trapped there and G -light is emitted. **d:** Excitation energy from the exciton band S_{1H} of the host is transferred to a guest molecule which is isolated in the host lattice. Emission follows from the guest excitation state S_{1G} . From [43].

crystal (Fig. 6.20a). The electronic energy states of tetracene are lower than those of anthracene. It can therefore act as a trap for the excitation energy. The fluorescence spectrum of the mixed crystal contains relatively little anthracene light (blue), but much tetracene light (green). Figure 6.20b shows that for a tetracene concentration c_G of only 10^{-5} guest molecules per host molecule, the emission intensities from host and guest are approximately equal. Or, expressed differently: the relative excitation probability for the guest molecule tetracene in the host anthracene is amplified 10^5 -fold and (for $c_G \ll 1$) is also independent of c_G . The tetracene emission is thus sensitised by the host.

How this can be explained with exciton diffusion and in the term diagram is shown by Figs. 6.20c and d. If we initially assume the incoherent limiting case for the excitonic motion – at room temperature, this assumption is fulfilled – then the exciton diffuses stochastically from one lattice site to another. When this hopping excitation state meets up underway with a guest molecule, it will fall into the trap represented by the guest, and the guest fluorescence can be emitted. If an exciton has a lifetime of 10^{-8} s and if it requires 10^{-13} s for one step in the hopping process, then during its lifetime it can pass through 10^5 molecular sites in the lattice. The hopping time can be estimated from the resonance energy I between neighbouring molecules (Eq. (6.3)) to be $t_h = h/4I$. Its order of magnitude can also be obtained from the Heisenberg uncertainty relation using the width of the exciton band, ΔE , giving $\tau^{-1} = \Delta E/h$. Only one of these 10^5 molecules need be a guest in order to transfer the energy from the host to a guest. Table 6.1 contains some numerical values for the absorption constants and lifetimes, and Table 6.3 lists diffusion coefficients of singlet and triplet excitons. Typical diffusion lengths of excitons in molecular crystals are $0.1 \mu\text{m}$ for singlet and up to $10 \mu\text{m}$ for triplet excitons.

Table 6.3 Some numerical values for the diffusion of S_1 and T_1 excitons in anthracene and naphthalene. (1) The hopping time in the $a-b$ plane (see Sect. 6.9.1), average values from various measurements. (2) k : transport constant as in Eq. (6.25), Sect. 6.9.1, also average values. (3) Diffusion coefficient D , numerical values from [M2] and [M4]. See additional references there. (4) The diffusion length can be computed from $L = \sqrt{D\tau}$ up to a numerical factor between $\sqrt{2}$ and $\sqrt{6}$ for different dimensionalities. These values are from [M2] and [M4].

	(1) t_h/s , 4.2 K	(2) k	(3) $D/\text{cm}^2\text{s}^{-1}$, 300 K	(4) $L = \sqrt{D\tau}/\text{cm}$
Anthracene S_1	10^{-13}	$6 \cdot 10^4$	$4 \cdot 10^{-3}$ a-b plane $6 \cdot 10^{-4}$ c direction	$1 \cdot 10^{-5}$
Anthracene T_1	10^{-12}		$1.6 \cdot 10^{-4}$ a-b plane $1.2 \cdot 10^{-5}$ c plane	10^{-3}
Naphthalene S_1	$4 \cdot 10^{-12}$ $5 \cdot 10^{-13}$	$2.5 \cdot 10^4$	$2 \cdot 10^{-4}$ a direction $5 \cdot 10^{-5}$ c direction	$5 \cdot 10^{-6}$
Naphthalene T_1	10^{-12}		$3 \cdot 10^{-5}$ a-b plane	

From measurements of the sensitised fluorescence, one can determine diffusion coefficients D and diffusion lengths L of excitons. The ratio of the intensities from the guest molecules and the host, I_G/I_H as a function of the concentration c_G (in molecules/molecule) can be empirically described by a dimensionless transfer constant k (cf. also Fig. 6.20c). The following relation holds:

$$\frac{I_G}{I_H} = k c_G. \quad (6.25)$$

In the simplest model, the model of statistical hopping of the exciton from lattice site to lattice site with a hopping time t_h , k is found to be

$$k = \tau_H / t_h. \quad (6.26)$$

Here, τ_H is the lifetime of the host excitons without traps. We furthermore make the simplifying assumption that every exciton is captured when it reaches a trap and that the excitation density is constant with time and remains homogeneous. If, in addition, the mean free path of the exciton is smaller than the capture radius R of the traps for excitons, and D is the exciton diffusion coefficient, then we obtain

$$k = 4\pi D R \tau_H N_H \quad (6.27)$$

with N_H = number density of the host molecules. This follows from the classical theory of diffusion of Smoluchowski [44]. More details may be found in Pope and Swenberg.

Measurement of the transfer constants thus yields the unknown quantities DR and D , if one assumes that R is given by the molecular spacing in the crystal.

In the case of the tetracene fluorescence in anthracene, one finds $k = 10^5$. This is, as mentioned, at the same time the number of jumps during the lifetime of the excitons. We then obtain using $R = 10 \text{ \AA}$, for the known values of τ_H and N_H , the diffusion coefficient of singlet excitons at room temperature, $D = 5 \cdot 10^{-3} \text{ cm}^2 \text{ s}^{-1}$. This is an average value for three-dimensional crystals. The diffusion is of course anisotropic.

Table 6.3 lists some values related to the diffusion of singlet and triplet excitons in anthracene and naphthalene.

From the diffusion coefficients D , the diffusion length L can be extracted:

$$L = \sqrt{Z \cdot D \cdot \tau_H}, \quad (6.28)$$

where Z is a number between 2 and 6, depending on the dimensionality of the diffusion process. With $\tau_H = 10^{-8} \text{ s}$, one finds the value $L = 500 \text{ \AA}$ for singlet excitons in anthracene. Given the numerous approximations and simplifications in the analysis, this can only be an order-of-magnitude estimate. The diffusion length defined in Eq. (6.28) is a measure of the mean spatial displacement of the exciton. For the displacement in a given direction, the correct expression is $L = (D\tau_H)^{1/2}$.

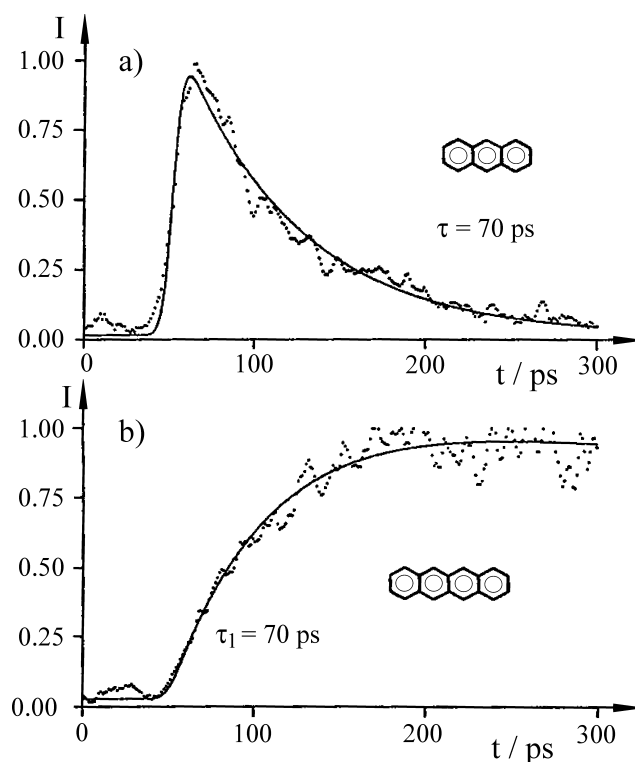


Fig. 6.21 Sensitised fluorescence of anthracene doped with $2.3 \cdot 10^{-3}$ mol/mol of tetracene, at 1.6 K in a time-resolved measurement. The two-photon excitation was carried out with a 10 ps pulse of wavelength 614.5 nm. It was chosen in order to excite the bulk of the crystal as homogeneously as

possible and to reduce the contribution of the surfaces. The initial exciton density was 10^{15} cm^{-3} . The anthracene emission increases with the excitation pulses and then decays with the same time constant as the growth of the emission of the guest molecule tetracene. From [45].

Assuming coherent exciton motion during the coherence time τ , the mean free path L can also be estimated: $L = \frac{1}{2} \tau v$ (v is the velocity of the excitons). The velocity v can be obtained from the relation $\frac{1}{2} m v^2 = \frac{3}{2} k T$, with the effective exciton mass m .

The energy transfer from the host to the guest molecules can also be measured in a time-dependent way. Figure 6.21 shows the decay of the host emission and the increase of the sensitised guest emission in a doped crystal, indicating that the two processes have the same time constant (here 70 ps), as is to be expected from the model of sensitised fluorescence in Fig. 6.20.

6.9.2

Delayed Fluorescence by Triplet Excitons

Triplet excitons in aromatic molecules are still more effective energy conductors than singlet excitons. Their lifetimes are longer and their hopping times are not

much shorter than those in the singlet state. The number of steps per lifetime and thus the number of sites visited by an exciton in the crystal can thus be much greater (compare Table 6.3).

The existence of triplet excitons was first discovered through the observation of **delayed fluorescence** (Fig. 6.22). This is a particularly characteristic process for organic crystals. In this process, two triplet excitons can combine their energy and form a singlet exciton, according to the scheme $T_1 + T_1 \rightarrow S_1 + S_0$. The delayed fluorescence is then emitted by the S_1 state. This is explained in Figs. 6.22c and d. Delayed fluorescence is thus an emission with a lifetime determined by the triplet excitons and the quantum energy of singlet excitons. This triplet-triplet annihilation process can also lead to a delayed fluorescence from guest molecules (exciton-guest annihilation, Fig. 6.22d). In this way, **sensitised delayed fluorescence** can occur. It is illustrated in the term diagram in Fig. 6.22d and in the experimental result in Fig. 6.22b. It is remarkable that already at a concentration of 10^{-7} guest molecules per host molecule, the intensities of the guest and the host emissions are equal. It follows from this that impurity or dopant concentrations down to 10^{-10} molecules/molecule can be detected with this method.

As already mentioned in Sect. 6.4, delayed fluorescence measured with excitation spectroscopy is an especially efficient method for observing $T_1 \leftarrow S_0$ absorption spectra. The triplet state can namely be excited directly without the necessity of passing through the singlet state, using a tunable narrow-band laser and detecting the excitation via the integrated delayed fluorescence. In this way, one can resolve very sharp absorption lines, as is shown using the example of triplet excitons in anthracene in Fig. 6.10. The linewidth of the exciting laser was here ca. 0.001 cm^{-1} . Furthermore, in the excitation spectrum the splitting of the triplet state into its three fine-structure components could also be observed (see Chap. 7), in spite of its small value of ca. 0.05 cm^{-1} [46].

As we have seen in Sect. 6.5, the physical cause of the existence of triplet excitonic bands in molecular crystals is the exchange interaction between the π orbitals of the molecules, in particular between an excited molecule and its ground-state neighbours. This depends very strongly on the distance between the molecules and on their mutual orientation. Excitonic bands $E(\mathbf{k})$ and energy conduction are therefore very anisotropic. In naphthalene and anthracene (see Fig. 2.9), the interaction between the two non-translationally equivalent molecules in the unit cell predominates (cf. Sect. 6.4). The energy conduction therefore takes place primarily two-dimensionally in the $a-b$ plane. Dibromonaphthalene (Fig. 2.13), on the other hand, is an example of a crystal with nearly one-dimensional or linear excitons. The interaction between the molecules which are packed plane on plane with small spacings in the c direction is notably stronger than any interactions in the $a-b$ plane. The energy is thus transferred preferentially along the linear chains of molecules and only occasionally from one chain to another. This was shown clearly using electron spin resonance in [47] (see also Chap. 7).

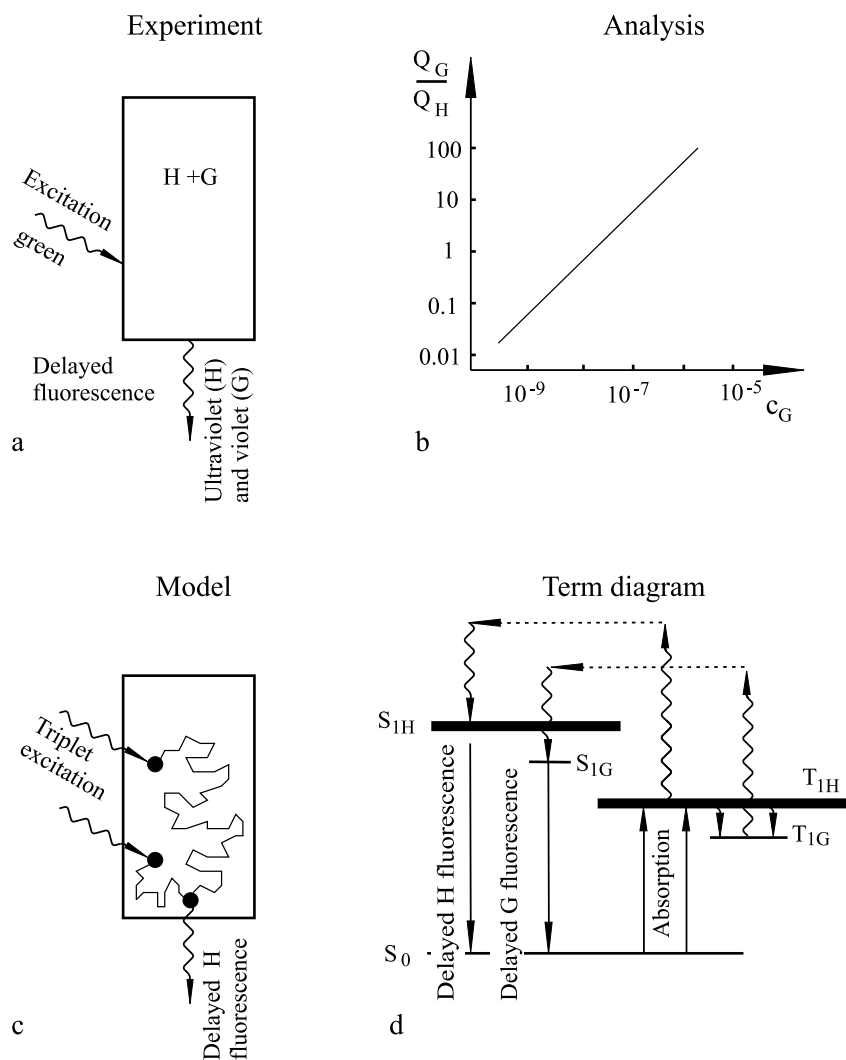


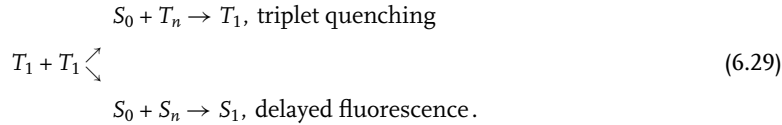
Fig. 6.22 Sensitised delayed fluorescence, schematically. **a:** The mixed crystal $H + G$ is excited into the triplet band T_1 of the host (naphthalene: green light). The delayed fluorescence contains a relatively large proportion of guest light (anthracene: violet light) and little host light (naphthalene: ultraviolet). **b:** The ratio of guest intensity Q_G to host intensity Q_H in the delayed fluorescence is plotted against the guest

concentration. **c:** Two triplet excitons meet during their diffusion in the mixed crystal. This leads to the emission of a light quantum of delayed fluorescence. **d:** Two triplet excitons combine; this can give rise to a singlet exciton. When two free excitons T_{1H} mutually annihilate, the excitonic band S_{1H} is preferentially populated. Annihilation at a localised guest T_{1G} populates preferentially the singlet ground state S_{1G} . After [43].

6.9.3

Excitonic Processes

Excitons can, as we have seen in Sect. 6.9.2, react with one another and also with other excitation states. The most important processes are exciton annihilation or fusion and exciton splitting or fission. The **annihilation of two triplet excitons**, which leads to delayed fluorescence, takes place more precisely via the alternate reaction mechanism



Here, the symbols T_n and S_n each refer to a particular vibronic state of an electronically-excited triplet or singlet state, so that energy conservation is fulfilled.

In the first case, only a triplet state remains. It relaxes from the higher level T_n back to the lowest level T_1 , and from it, light emission occurs, i.e. phosphorescence, or else a radiationless decay. To be sure, this process has combined two T_1 states into one with a correspondingly reduced emission intensity. In this case, we thus have a partial quenching. In the second case of the reaction mechanism (6.29), in contrast, a higher singlet excitation state S_n is produced. This state relaxes towards S_1 . From there, the fluorescence light is however emitted with a delay. That is, the lifetime of the triplet excitons is now the determining factor. One thus obtains, for example from anthracene, a blue delayed fluorescence if the T_1 excitons are excited directly with red light. A third possible case, the excitation of quintet states from the mutual annihilation of two triplet states, has yet to be observed, presumably because its electronic energy is larger than twice the energy of the triplet excitons.

Making use of delayed fluorescence, one can investigate in particular trapping states which are energetically close to the T_1 excitonic band, owing to the high probability that they will relax to the excitonic band following direct excitation. Pair spectroscopy (cf. Sect. 6.4) takes advantage of this fact.

In order to obtain the dependence of the phosphorescence intensity I_P and the intensity of delayed fluorescence, I_{DF} , on the incident power I_E or the absorption coefficient α , the kinetics of the triplet state must be investigated. From the solution of the balance equations for mono- and bimolecular decay, one finds for the steady state in the limiting cases of “strong” and “weak” excitation the following expressions [32]:

strong excitation weak excitation

$$I_P \sim \sqrt{\alpha I_E}$$

$$I_P \sim \alpha I_E$$

$$I_{DF} \sim \alpha I_E$$

$$I_{DF} \sim (\alpha I_E)^2 .$$

Studies of the delayed fluorescence are usually carried out in the range of strong excitation. The phosphorescence is in this case unimportant.

To investigate the kinetics, the delayed fluorescence is observed after switching off the excitation. The decay curve of the delayed fluorescence intensity $I_{DF}(t)$ can then be computed using the following rate equations. This calculation is independent of the details of the excitation; it assumes only that at time $t = 0$, a concentration $[T_1]_0$ of triplet excitons has been generated. For the time dependence of the triplet concentration $[T_1]$, shortly after the optical excitation, i.e. after the decay of the prompt fluorescence of the optically excited singlet excitons (or, more simply, after a few nanoseconds) and assuming a homogeneous exciton density in the crystal, we have:

$$\frac{d[T_1]}{dt} = -k_T[T_1] - \gamma_{tot}[T_1]^2. \quad (6.30)$$

In this expression, the following quantities are used:

k_T is the rate constant for the decay of the triplet excitons in the absence of bimolecular processes (it includes all the radiative and radiationless processes except for the bimolecular processes); and

γ_{tot} is the total rate constant for all processes of bimolecular annihilation (or fusion).

Depending on the excitation density $[T_1]$, either the monomolecular depopulation ($-k_T[T_1]$) directly from T_1 or the bimolecular ($-\gamma_{tot}[T_1]^2$) via annihilation predominates.

If f represents the fraction of triplet-triplet annihilation processes which lead to singlet excitons – compare the reactions (6.29) – then for the time dependence of the singlet exciton density $[S_1]$, we find:

$$\frac{d[S_1]}{dt} = -k_s[S_1] + \frac{1}{2}f\gamma_{tot}[T_1]^2. \quad (6.31)$$

Here, $[k_s]$ is the rate constant for the decay of the singlet state.

The factor $1/2$ in the last term takes the fact into account that two T_1 excitons are required to produce one S_1 exciton.

The decay time of the singlet excitons is very short in comparison to the lifetime of the triplet excitons. Therefore, after the decay of the prompt fluorescence, i.e. after less than $1 \mu s$ following the end of the optical excitation, a quasistationary equilibrium is established. All of the singlet excitons produced by triplet-triplet annihilation decay immediately; the rates of their production ($1/2f\gamma_{tot}[T_1]^2(t)$) and decay ($k_s[S_1](t)$) are equal:

$$\frac{1}{2}f\gamma_{tot}[T_1]^2 = k_s[S_1]. \quad (6.32)$$

The intensity of the delayed fluorescence in quanta per cm^3 and s is thus found to be

$$I_{DF} = k_s^r [S_1] = \frac{k_s^r}{k_s} \frac{1}{2} f \gamma_{\text{tot}} [T_1]^2 \quad (6.33a)$$

or

$$I_{DF}(t) = \Phi_F \cdot \frac{1}{2} \cdot f \cdot \gamma_{\text{tot}} [T_1]^2(t). \quad (6.33b)$$

Here, k_s^r is the radiative decay probability (fluorescence probability) and $\Phi_F = k_s^r/k_s$ is the quantum yield of the fluorescence from S_1 . The fraction f for anthracene is found experimentally to be 0.3 to 0.4.

The time dependence of the decay of the delayed fluorescence, $I_{DF}(t)$, is thus found according to Eq. (6.33b) from the time dependence of the square of the triplet exciton concentration $[T_1]^2$. The latter can be obtained from Eq. (6.30), which is readily solved for two limiting cases:

In the limit of short times, i.e. immediately after the end of the optical excitation, the bimolecular term can predominate: ($\gamma_{\text{tot}}[T_1]^2 \gg k_T [T_1]$). For this limiting case, the solution of Eq. (6.30) is

$$\frac{1}{[T_1]} = \frac{1}{[T_1]_0} + \gamma_{\text{tot}} t. \quad (6.34)$$

With Eq. (6.33b), it follows from this that the time dependence of the decay of the delayed fluorescence in the limit of high triplet exciton concentration is

$$\frac{1}{\sqrt{I_{DF}}} = \frac{1}{\sqrt{I_{DF}(t=0)}} + ct. \quad (6.35)$$

In this expression, $c = \left(\sqrt{\Phi_F \frac{1}{2} f / \gamma_{\text{tot}}} \right)^{-1}$. This limiting case was observed for anthracene in about the first 4 ms after the end of the excitation [48]. In the further course of the decay of the triplet excitons, the relative fraction of the bimolecular decay continues to decrease until the limit of long times is reached, in which the monomolecular decay predominates ($k_T [T_1] \gg \gamma_{\text{tot}} [T_1]^2$). The solution of Eq. (6.30) is then given by $[T_1] = [T_1]_{00} e^{-k_T t}$. With this and Eq. (6.33b), the decay of the delayed fluorescence in the limit of very small triplet exciton concentration, i.e. in the later part of the decay curve, is found to be

$$I_{DF} \propto e^{-2k_T t}. \quad (6.36)$$

This limit was also observed in the experiments on anthracene crystals by Hall *et al.* [48] for $t > 40$ ms (Fig. 6.23). In the limit of long times, the delayed fluorescence thus decays twice as fast as the phosphorescence.

The intensity of the delayed fluorescence produced by triplet-triplet annihilation as in reaction 6.29 can be influenced by an **applied magnetic field** [49, 50] (see also Fig. 6.24). This takes the form of a modulation of the bimolecular rate constant γ

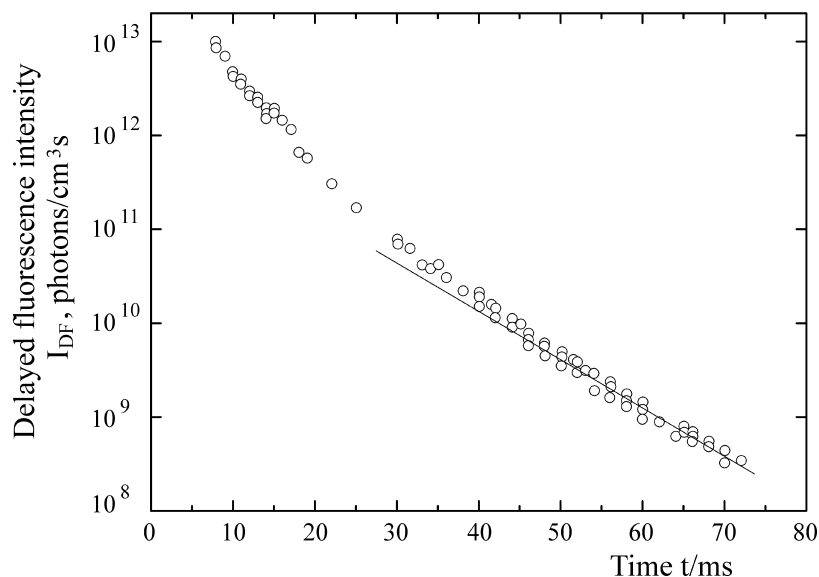


Fig. 6.23 The intensity of the delayed fluorescence of anthracene after an excitation pulse, plotted logarithmically vs. time. The plot shows that the delayed fluorescence, as would be expected for a bimolecular process, decays as $e^{-2\beta t}$, where β is the decay rate of the triplet excitons (here $(17.2 \text{ ms})^{-1}$). After [48].

for the annihilation. The constant and thus the intensity of emission depend on the strength and the direction of the field relative to the crystal axes. For a given orientation, the intensity of the delayed fluorescence from an anthracene crystal increases slightly with increasing magnetic field up to ca. 350 G, then decreases until it reaches a saturation value at ca. 2 kG, where it is about 80% of the intensity in zero magnetic field [50].

To explain the field dependence, we have to assume that the applied field has an influence on whether the spin selection rules can be obeyed in the fusion process. A kinetic explanation by Merrifield and Johnson [49, 50] assumes in the reaction $T_1 + T_1 \rightleftharpoons (T_1 \cdots T_1) \rightleftharpoons S_1 + S_0$ the existence of an intermediate pair state $(T_1 \cdots T_1)$, in which the two excitons repeatedly collide before they react. The possible spin correlations in this pair state have both triplet as well as singlet character. The triplet fraction in the pair state is also influenced by an applied magnetic field via the Zeeman interaction of the coupled individual spins with the field. The strength and direction of the field thus determine the relative fraction of triplet and singlet states in the pair. The singlet fraction leads to the states S_1 and S_0 , and thus to delayed emission. Therefore, the intensity and lifetime of the emission can be modulated by an applied magnetic field. This holds for all biexcitonic processes in which two triplet states participate.

A similar magnetic-field dependence is found in photoconductivity which is stimulated by triplet excitons.

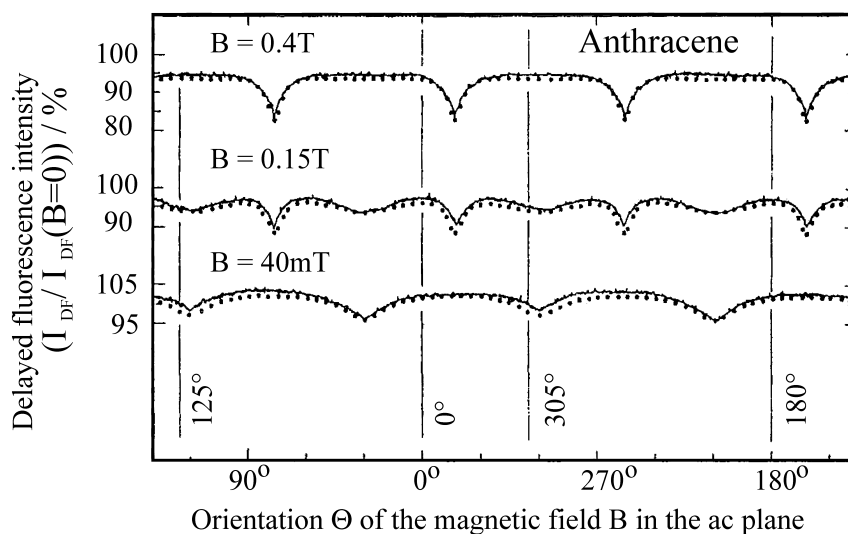


Fig. 6.24 The intensity of the delayed fluorescence in a magnetic field \mathbf{B} , relative to the intensity at $B = 0$, as a function of the orientation of \mathbf{B} in the $a-c$ plane of anthracene. 0° corresponds to the a axis. The measurements at three values of the applied

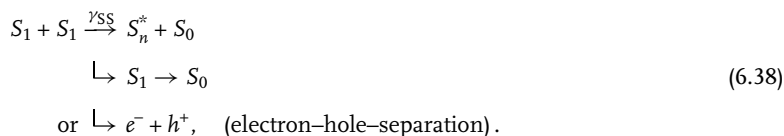
field show low-field resonances (bottom curve) and high-field resonances (top curve). The low-field resonances correspond to the principal-axis directions x and y of the fine-structure tensor. After [50].

There is also **singlet-triplet annihilation** according to the reaction scheme



Here, the triplet excitons act as fluorescence quenchers by reacting with the singlet excitons. The singlet excitons give up their energy to the triplet excitons in an allowed transition from a lower to a higher triplet state. Due to their longer lifetimes, the steady-state triplet exciton concentration increases relative to the singlet concentration with increasing excitation intensity and the quenching process becomes stronger. This is important in the application of organic crystals as scintillation detectors for radiation. γ_{ST} is the rate constant for this quenching reaction.

In addition, one observes **singlet-singlet annihilation** or fusion according to the reaction scheme



S_n^* is here a vibronically-excited singlet state with $n > 1$, and γ_{SS} is the bimolecular rate constant. At least one of the two participating S_1 states is therefore deactivated without emitting radiation and thus is lost for fluorescence emission. With

Table 6.4 Bimolecular exciton annihilation rate constants, in $\text{cm}^3 \text{s}^{-1}$. γ_{tot} is the total rate constant for triplet-triplet annihilation, γ_{ST} the rate constant for quenching of the S_1 emission through singlet-triplet reactions, and γ_{SS} is the rate of singlet-singlet annihilation. From [M1] and [M4]. Further references can be found there.

	γ_{tot}	γ_{ST}	γ_{SS}
Anthracene	$2 \cdot 10^{-11}$	$5 \cdot 10^{-9}$	$1 \cdot 10^{-8}$
Naphthalene	$3 \cdot 5 \cdot 10^{-12}$	$5 \cdot 10^{-11}$	$1 \cdot 10^{-10}$

increasing excitation intensity, i.e. with an increasing steady-state concentration of S_1 excitons, one observes for example a decrease in the fluorescence quantum yield of crystalline tetracene.

With a sufficiently high total energy, this process can even cause the ejection of an electron from the crystal; that is, the exciton annihilation leads to ionisation. In the case of anthracene, the ionisation limit of 5.75 eV lies lower than twice the S_1 energy, $2 \times 3.15 = 6.30$ eV. Measurement of the kinetic energy of the emitted photoelectrons permits the verification of the fusion process. In general, the fusion of two excitons allows higher excited states to be reached with smaller energy quanta. Table 6.4 contains numerical values of the rate constants for exciton annihilation processes.

Finally, we which to mention here that excitons can also react with free or trapped **charge carriers**, for example according to the reaction scheme



2D here stands for the doublet state (Spin 1/2) of a charge carrier or a charged molecule. This is interesting for photoconductivity (Chap. 8). Singlet excitons can also be quenched readily by free or trapped charge carriers.

The complementary process to fusion is **exciton fission** or splitting (Fig. 6.25). Here, an exciton decays into two other excitons of correspondingly lower energies, for example



This process was discovered in tetracene. In this case, the energy of a singlet exciton, 2.4 eV, is nearly degenerate with that of two triplet excitons, $2 \times 1.28 = 2.56$ eV. The process of fission is thermally activated and follows the scheme



It is a competing process to $S_1 \rightarrow S_0$ emission and is partly responsible for the low fluorescence quantum yield from crystalline tetracene. Fission is also a biexcitonic process, which, like triplet exciton fusion, can be modulated by an applied magnetic field with a similar dependence as shown in Fig. 6.24 for fusion (see also Fig. 6.26). The fluorescence intensity of tetracene is therefore magnetic-field dependent [51].

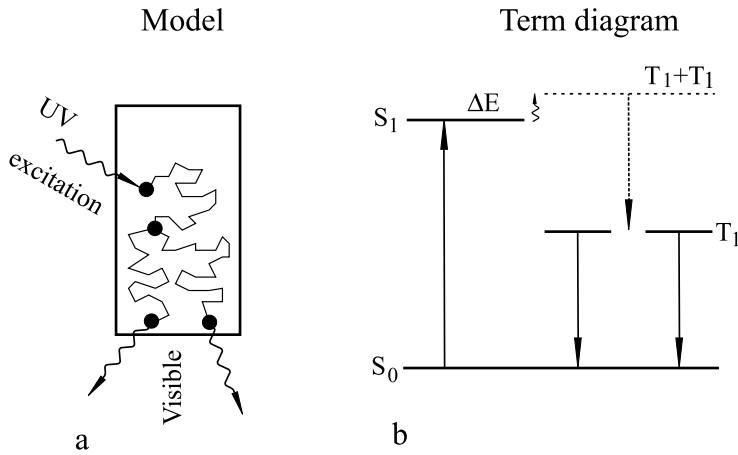


Fig. 6.25 Exciton fission, schematically. **a:** The excitation takes place from the singlet absorption region of the crystal. The singlet exciton splits into two triplet excitons. Their emission is observed. **b:** When the energy of the excited S-state is somewhat smaller than twice the energy T_1 , then exciton fission can be activated by the thermal energy ΔE . After [43].

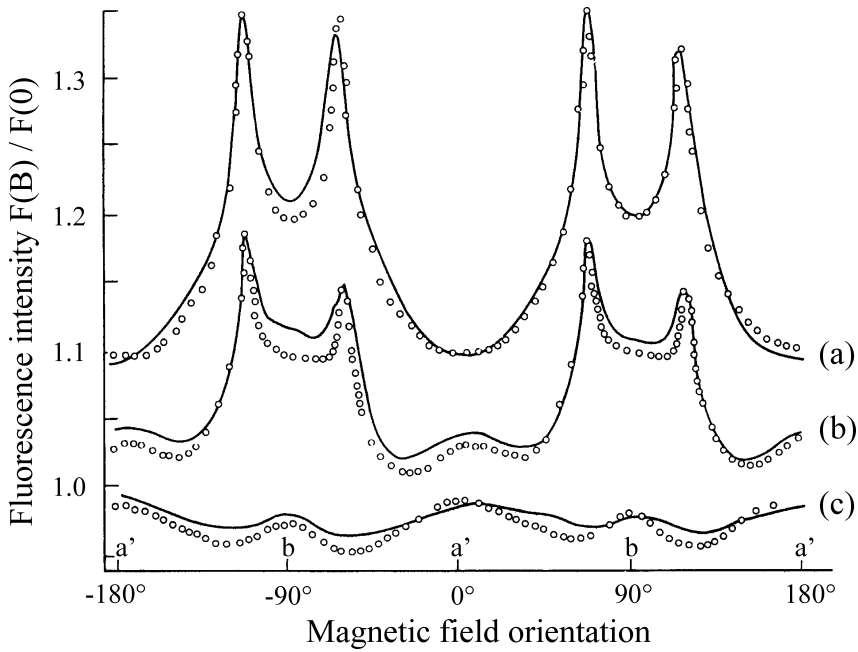


Fig. 6.26 The magnetic field dependence of the prompt fluorescence in a tetracene crystal. The ratio $F(B)/F(0)$ of the prompt fluorescence intensity with and without a magnetic field B is plotted against the orientation of the magnetic field relative to the $a-b$ plane. The constants are $a = 0.5$ T, $b = 75$ mT, and $c = 15$ mT. The dotted curves are calculations. From [51].

Highly-excited singlet excitons of suitable energies can also decay into two singlet excitons of lower energy. Such processes are important for the interaction of energetic radiation with molecular crystals. In this case, one is often faced with the problem of how large energy quanta can be divided up into such small quanta that they are finally comparable to the elementary excitation energies of the material in question, i.e. of excitons, charge carriers, molecular vibrations and phonons.

To complete this section, Table 6.5 again collects some important dynamic interaction parameters which can be determined from measurements of the sensitised and delayed fluorescence.

Table 6.5 Dynamic interaction parameters, from measurements of sensitised and delayed fluorescence. Other results for the triplet states can be found in Chap. 7.

Observation	Information	Quantity derived from the measured values	Singlet or triplet	Method
Sensitised fluorescence	Energy transport	Reaction velocity rate constant k_{HG} , Diffusion coefficient D , Trapping velocity	<i>S</i>	Host and guest fluorescence, intensity in mixed crystals
Sensitised fluorescence, time-resolved	Exciton transfer and trapping times	k_{HG} , Trapping velocity	<i>S</i>	Time-resolved (ps) spectroscopy
Sensitised delayed fluorescence	Energy transport	Reaction velocity rate constant k_{HG} , Diffusion coefficient D , Trapping velocity as well as triplet lifetime	<i>T</i>	Host and guest delayed fluorescence
Kinetics of delayed fluorescence	Exciton diffusion and annihilation	Annihilation coefficient γ , Diffusion coefficient D	<i>T</i>	Time-resolved optical spectroscopy
Sensitised emission in isotopic mixed crystals at higher (> 1%) concentrations	Exciton transfer in "dilute" exciton systems	k_{HG} , D in dilute exciton systems	<i>S, T</i>	Intensity of the guest emission with varying trap depth in isotopic mixed crystals as a $f(T)$

6.10

Excitonic Processes in other Systems

Energy conduction processes by excitons and various excitonic phenomena also play an important role in other molecular systems besides molecular crystals; especially in biological systems. Molecular crystals provide an exemplary field from which a fundamental understanding of these processes can be gained.

A nice example is the **primary photosynthesis process**. Here, light energy which is absorbed by the “antenna” chlorophyll molecules is conducted to a chlorophyll dimer in the reaction centre. Only there do the chemical reactions take place which lead to charge separation and finally to photosynthesis. For more details, cf. [M6], Sect. 20.7.

The antenna molecules are arranged in ring-shaped structures, the so-called *light harvesting systems* LH I and LH II (cf. Fig. 6.27 for a concrete example). These ring structures were elucidated in particular by Cogdell and by Schulten. When light absorption takes place in one of the bacterio-chlorophyll molecules (BChl) in LH II, the energy distributes itself like an exciton very quickly over the entire ring, due

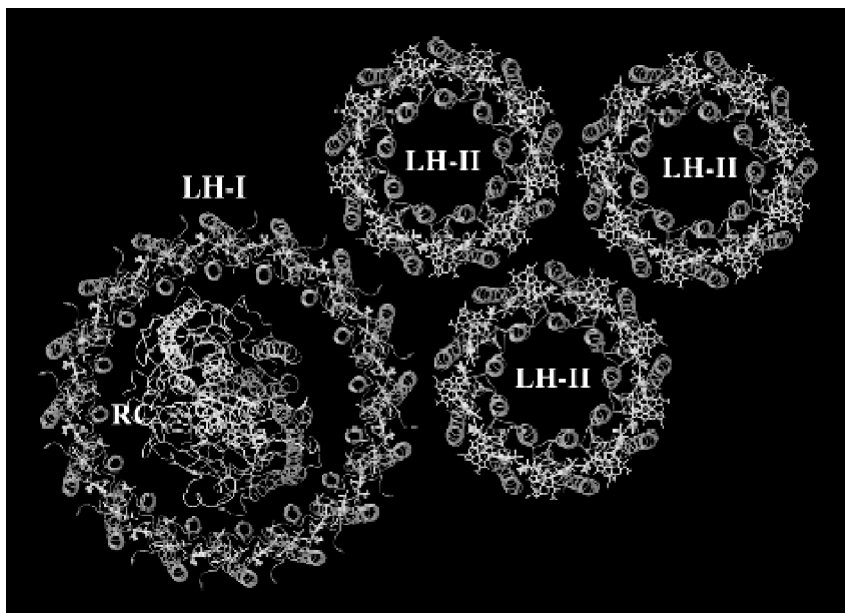


Fig. 6.27 The reaction centre (RC) and the light-harvesting complex in the photosynthetic apparatus of the bacterium *rhodospirillum rubrum*. Between the helices of the apoproteins (magenta and blue), the bacterio-chlorophyll (BChl) molecules (green and blue) of the light-harvesting complexes

LH II (outer part) and LH I (inner part) are ordered in a ring-shaped and nearly coplanar arrangement. In the middle of LH I is the reaction centre with the two BChl molecules of the “special pair”. From [53]. See also [M6], Sect. 20.7, and compare the coloured plate in the appendix.

to the favourable molecular spacings and the nearly coplanar orientations of the molecules.

The sizes of the complexes LH I and LH II differ somewhat in different species. In the purple bacterium *rhodospseudomonas sphaeroides*, the LH II units contain 8 BChl molecules of type B 800 with their absorption maxima at 800 nm, and 16 BChl molecules of type B 850 with a maximum at 850 nm. The excitation energy is delocalised coherently over the ring. It can be transferred to the LH I unit, which acts as a trap. The latter contains 32 BChl molecules of type B 875, with their absorption maxima at 875 nm. Here, again, the excitation is delocalised. It can, finally, be transferred to the “special pair” located in the middle of the ring. In this BChl dimer, charge separation begins, and with it the actual process of photosynthesis. The absorption of the special pair is, like that of mini-excitons in dimers, shifted still further into the red, namely to 965 nm. The pair thus acts as a trap for the excitation energy of the antennae. This allows the light energy to be transferred efficiently (yield ca. 95%) and rapidly (in ca. 100 ps) from an antenna and storage system – the antennae serve also as an exciton reservoir – to the site in the complex where it is needed.

In Fig. 6.28, the path of the excitation energy is again shown schematically. The spectroscopic and time-resolved analysis of these systems shows that the S_1 states of the chlorophyll molecules are in fact split excitonically. Their resonance energy lies at 300 cm^{-1} for chlorophyll molecules with the mutual orientation shown schematically in Fig. 6.28; these are the B 850 molecules. One can also distinguish between coherent excitons and more-or-less incoherent excitons.

In polymers, also, excitons are frequently the lowest-lying excited states. They can therefore play an important role for photoprocesses in polymers. This is also true of the key substance of genetics, the DNA helix. Here, again, the excitation energy can be conducted to reactive side groups via excitonic processes.

An improved understanding of excitons and their reactions in molecular crystals will thus lead to progress in elucidating the processes and reactions of photochemistry, solid-state chemistry, and, not least, of biological systems.

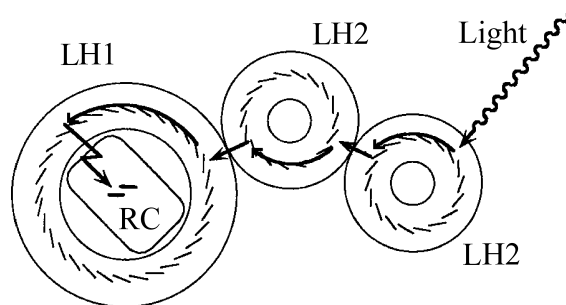


Fig. 6.28 Model of the energy flow in the bacterial light-collecting complexes from LH II to LH I and to the “special pair” in the reaction centre RC. The diagram corresponds to a plan view onto the membrane. The number of molecules in the rings is somewhat different in different species.

6.11

Future Developments

In the coming years, excitons in disordered systems and strongly-coupled excitons will be a focus of attention. In mixed crystals consisting of two components, the guest molecules can be included into the exciton band of the host, i.e. amalgamated. The influence of such an amalgamation on the electrical, optical, and magnetic properties of the mixed crystals is an interesting, old, but still current research topic in the physics of molecular crystals [43].

At the end of this chapter on optical spectra, we must emphasize once again that we have limited ourselves here to a small selection out of the extensive area of organic crystals. Molecules with π -electron systems and their lowest electronic excited states are the most important topics in current research and for applications, and they are the subject of the greatest interest at present.

Problems

Problem 6.1. Why are no excitons observed in the spectra of inorganic semiconductors at room temperature, e.g. in CuO or GaAs?

What is the essential difference in comparison to excitons in organic molecular crystals, e.g. in the anthracene crystal? Give a quantitative comparison of the binding energies.

Problem 6.2. Compare and discuss the term diagram (Fig. 6.9), the spectra (Figs. 6.1 and 6.12), and the band structure (Fig. 6.11) of the triplet excitons in the anthracene crystal.

Problem 6.3. Surface excitons:

At $T = 2$ K, in the π -polarised reflection spectrum of the (001)-cleavage planes of anthracene crystals, one observes spectrally-resolved surface excitons (Fig. 6.17). The Davydov splittings of their 0,0 transitions are only 10–20% smaller than those of the volume excitons (Sect. 6.7 and Ref. [39]). Discuss this experimental result qualitatively (cf. Sect. 6.5.2).

Problem 6.4. Charge-transfer excitons:

Estimate the electron-hole gap of a “hot” (highly excited) exciton in a typical molecular crystal (anthracene), when the electron-hole binding energy of this hot exciton is only about equal to the mean thermal energy at room temperature. Compare this value with the relevant lattice constant.

Literature

Monographs

- M1** M. POPE and C. E. SWENBERG, *Electronic Processes in Organic Crystals and Polymers*, 2nd ed., Oxford Univ. Press, New York/Oxford (1999)
- M2** E. A. SILINSH and V. ČÁPEK, *Organic Molecular Crystals*, AIP Press, New York (1994)
- M3** J. D. WRIGHT, *Molecular Crystals*, Cambridge Univ. Press, New York (1987)
- M4** H. C. WOLF, *Energy Transfer in Organic Molecular Crystals. A Survey of Experiments*, in: *Adv. Atomic and Molec. Physics*, edited by D. R. Bates and I. Estermann, vol. 3, Acad. Press, New York (1967)
- M5** H. C. WOLF, *The Electronic Spectra of Aromatic Molecular Crystals*, in: *Adv. in Solid State Physics*, edited by F. Seitz and D. Turnbull, vol. 9, Acad. Press, New York (1959)
- M6** H. HAKEN and H. C. WOLF, *Molecular Physics and the Fundamentals of Quantum Chemistry*, 2nd ed., Springer (2004)

References

- 1** P. PRINGSHEIM and H. KRONENBERGER, *Z. Physik* **40**, 75 (1926)
- 2** I. W. OBREIMOV and A. F. PRICHOTJKO, *Phys. Zs. Sowjetunion* **1**, 203 (1932)
- 3** A. S. DAVYDOV, *J. Exp. Theor. Phys. USSR*, **18**, 210 (1948); **21**, 673 (1951); *Sov. Phys.-Usp.* (English Transl.) **7**, 145 (1964)
- 4** J. FRENKEL, *Phys. Rev.* **37**, 17, 1276 (1931)
- 5** A. WINTERSTEIN, U. SCHÖN and H. VETTER, *Naturwiss.* **22**, 237 (1934)
- 6** J. FRANK and E. TELLER, *J. Chem. Phys.* **6**, 861 (1938)
- 7** AVAKIAN, P., V. ERN, R. E. MERRIFIELD and A. SUNA, *Phys. Rev.* **165**, 974 (1968)
- 8** W. KAISER and C. G. GARRET, *Phys. Rev. Lett.* **7**, 229 (1961)
- 9** E. GLOCKNER and H. C. WOLF, *Chem. Phys.* **10**, 479 (1975)
- 10** H. C. WOLF, *Z. Naturforsch.* **13a**, 414 (1958)
- 11** A. S. DAVYDOV, *J. Exp. Theor. Phys. USSR* **18**, 210 (1948)
- 12** A. S. DAVYDOV, *Theory of Molecular Excitons*, Mc Graw Hill, New York (1962)
- 13** D. P. CRAIG and S. H. WALMSLEY, *Visible and UV Absorption by Molecular Crystals in The Physics and Chemistry of the Organic Solid State*, edited by Fox, Labes, Weissberger, Interscience Publ., New York (1963)
- 14** D. P. CRAIG and S. H. WALMSLEY, *Excitons in Molecular Crystals*, W. A. Benjamin, New York (1968)
- 15** D. S. MC CLURE, *Solid State Physics* **8**, 1 (1958)
- 16** R. S. KNOX, *Theory of Excitons*, Academic Press, New York (1963)
- 17** H. C. WOLF, *J. Phys. C* **5a**, 101 (1971)
- 18** C. L. BRAUN and H. C. WOLF, *Chem. Phys. Lett.* **9**, 260 (1971)
- 19** H. PORT, D. RUND and H. C. WOLF, *Chem. Phys.* **60**, 81 (1981)
- 20** H. C. WOLF, *Mat. Sci.* **X**, 419 (1984)
- 21** U. DOBERER, H. PORT, D. RUND and W. TUFFENTSAMMER, *Molec. Physics* **49**, 1167 (1983)
- 22** R. SILBEY, J. JORTNER and S. A. RICE, *J. Chem. Phys.* **42**, 1515 (1963)
- 23** R. SILBEY, J. JORTNER, M. T. VALG and S. A. RICE, *J. Chem. Phys.* **42**, 2948 (1965)
- 24** J. JORTNER, S. A. RICE and J. L. KATZ, *J. Chem. Phys.* **42**, 309 (1965)

- 25 M. R. PHILPOTT, *J. Chem. Phys.* **54**, 2039 (1971); **54**, 111 (1971)
- 26 E. I. RASHBA, *Fiz. Tverd. Tela* **5**, 1040 (1963)
- 27 U. DOBERER and H. PORT, *Z. Naturforsch.* **39a**, 413 (1984)
- 28 G. S. PAWLEY, *Phys. Stat. sol.* **20**, 347 (1967)
- 29 H. PORT, D. RUND, G. J. SMALL and V. YAKHOT, *Chem. Phys.* **39**, 175 (1979)
- 30 H. C. WOLF, *Adv. in Atomic and Mol. Phys.*, edited by I. Estermann, Vol. 3, Academic Press (1967)
- 31 H. HAKEN and G. STROBL, *Zs. Physik* **262**, 135 (1973)
- 32 D. RUND, Dissertation, Stuttgart (1982)
- 33 R. KRAUSS, W. SCHROF, H. C. WOLF and D. SCHMID, *Chem. Phys.* **73**, 55 (1982)
- 34 D. M. HANSON and G. W. ROBINSON, *J. Chem. Phys.* **43**, 417 (1965)
- 35 L. SEBASTIAN, G. WEISER and H. BÄSSLER, *Chem. Phys.* **61**, 125 (1981)
- 36 D. HAARER and N. KARL, *Chem. Phys. Lett.* **21**, 49 (1973); D. HAARER, *Chem. Phys. Lett.* **27**, 19 (1974)
- 37 Y. TOKURA and K. SEKI, in: *Functionality of Molec. Systems* Vol. 1, p. 197 Springer Verlag (1998)
- 38 D. HAARER, M. R. PHILPOTT and A. MORAWITZ, *J. Chem. Phys.* **63**, 5238 (1975)
- 39 J. M. TURLET and M. R. PHILPOTT, *J. Chem. Phys.* **62**, 4260 (1975); M. R. PHILPOTT and J. M. TURLET, *J. Chem. Phys.* **64**, 3852 (1976)
- 40 A. WALKER, Dissertation, Universität Stuttgart (1984)
- 41 A. WALKER, H. PORT and H. C. WOLF, *Chem. Phys.* **92**, 177 (1985)
- 42 SEYFANG, R., E. BETZ, H. PORT and H. C. WOLF, *J. Lumines.* **34**, 57 (1985)
- 43 H. C. WOLF, *Die feste Materie*, edited by L. Genzel, Umschau-Verlag, Frankfurt (1973)
- 44 M. SMOLUCHOWSKI, *Ann. Phys.* **48**, 103 (1915)
- 45 A. BRAUN, U. MAYER, H. AUWETER, H. C. WOLF and D. SCHMID, *Z. Naturforsch.* **37a**, 103 (1982)
- 46 H. PORT and D. RUND, *Chem. Phys. Lett.* **69**, 406 (1980)
- 47 R. SCHMIDBERGER and H. C. WOLF, *Chem. Phys. Lett.* **16**, 402 (1972); **25**, 185 (1974)
- 48 J. L. HALL, D. A. JENNINGS and R. H. McCLINTOCK, *Phys. Rev. Lett.* **11**, 364 (1963)
- 49 R. E. MERRIFIELD, *J. Chem. Phys.* **48**, 4318 (1968)
- 50 R. C. JOHNSON and R. E. MERRIFIELD, *Phys. Rev.* **B1**, 896 (1970)
- 51 H. V. BOUCHRIHA, J. L. ERN, C. FAVE, M. GUTMANN and M. SCHOTT, *J. de Physique* **39**, 257 (1978)
- 52 A. M. VAN OIJEN, M. KETELAARS, J. KÖHLER, T. J. AARTSMA and J. SCHMIDT, *Science* **285**, 400 (1999)
- 53 X. HU, TH. RITZ, A. DAMJANNOVIC and K. SCHULTEN, *J. Phys. Chem. B* **101**, 3854 (1997)

7 Structure and Dynamics of Triplet States

7.1

Introduction and Historical Remarks

In Chap. 6, we discussed low-energy optical excitation states, the singlet and triplet excitons and energy transfer. The primary experimental method applied there was optical spectroscopy in the visible, in the near IR and in the UV spectral ranges. In the present chapter, we treat the structure and the dynamics of localised triplet states, of triplet mini-excitons, and of triplet excitons in molecular crystals. The primary experimental method for the investigation of the lowest-energy triplet level T_1 is electron-spin resonance (ESR) (Fig. 7.1).

In all the systems dealt with here, the T_1 states have three notable properties: their lifetime is many orders of magnitude longer than that of the S_1 states, their total spin quantum number is $S = 1$, and they consist even without an applied

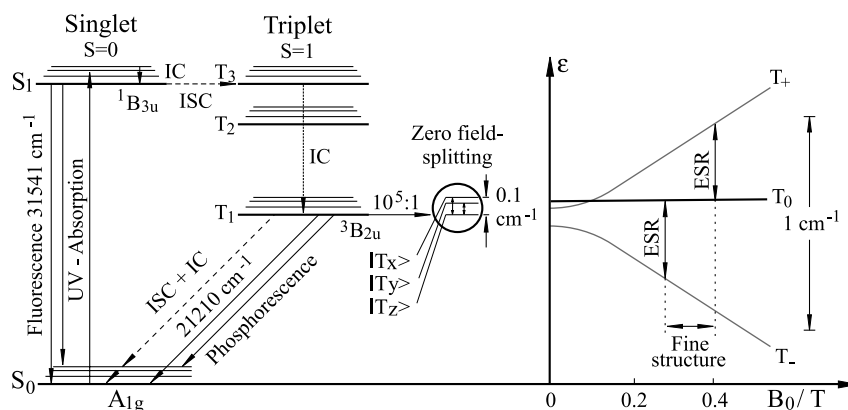


Fig. 7.1 An electronic term diagram for a molecular π -electron system (left), zero-field splitting (centre) and splitting in an applied magnetic field B_0 (right). Between the left and centre parts of the figure, the energy scale is expanded by a factor of 10^5 . S_0 , S_1 are singlet states; T_1 , T_2 , and T_3 are triplet states; S is the

total spin quantum number; ISC = intersystem crossing; IC = internal conversion; $|T_u\rangle$ ($u = x, y, z$) are zero-field states; $|T_i\rangle$ ($i = +, 0, -$) are Zeeman states. The wavenumbers and symmetries given apply to the naphthalene molecule. ϵ is the energy (cf. also Fig. 6.2).

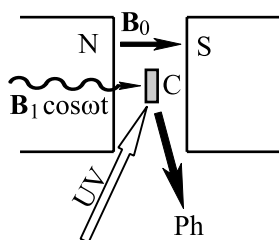


Fig. 7.2 The principle of an ESR experiment in excited triplet states. C = crystal; $B_1 \cos \omega t$ = high-frequency field; N \rightarrow S = magnet; B_0 = static magnetic field strength; UV = optical excitation; Ph = phosphorescence.

magnetic field B_0 of three non-degenerate components. For $B_0 = 0$, these three components of the triplet state are referred to as its zero-field components $|T_x\rangle$, $|T_y\rangle$ and $|T_z\rangle$, and their energy differences as the **zero-field splitting** of the triplet state. It is characterised by two parameters, the fine-structure constants D and E (see Fig. 7.6), which are molecule-specific and which can in many cases be measured with high precision. Their order of magnitude is 0.1 cm^{-1} or less. The zero-field splitting is thus in every case small compared to the excitation energy of the T_1 state (cf. Fig. 7.1).

In an applied magnetic field $B_0 \neq 0$, the triplet states have in addition a Zeeman energy. The Zeeman splitting then consists of three non-equidistant terms. For technical reasons, the ESR spectrum is usually measured at a constant microwave frequency, e.g. 9.4 GHz (X band) or 35 GHz (Q band). It exhibits a fine-structure splitting between the resonance fields of the $\Delta m_s = 1$ transitions which is also termed the **fine structure** (Fig. 7.1); this is a direct result of the zero-field splitting.

The ESR spectra yield not only the magnitude of the fine structure, but also particularly detailed information on the dynamics of the T_1 states. To show this, we briefly sketch the principle of an ESR experiment in optically-excited triplet states (Fig. 7.2). It differs from the principle of ESR in electronic ground states in various ways. First, the state T_1 must be populated through irradiation by UV light, with which primarily the S_1 states, but also – via intersystem crossing (ISC) – the three components of the T_1 state are populated in a steady state. After switching off the optical excitation, the triplet state begins to decay. However, the lifetimes of the three zero-field components are not only long, they are usually more or less different. Secondly, owing to the zero-field splitting, ESR spectroscopy can – often to advantage – be carried out without an applied magnetic field, that is in zero field ($B_0 = 0$). One refers to ESR then as the **zero-field resonance**. And thirdly, the detection of ESR transitions can often be achieved not only via the absorption of microwave power, $B_1 \cdot \cos \omega t$, but also optically through a change in the intensity of the phosphorescence, the optical absorption or the fluorescence. The method is then referred to as **Optical Detection of Magnetic Resonance (ODMR)**.

ODMR is as a rule possible when an optical transition probability coupled to T_1 depends on the orientation of the spin; when for example the phosphorescence probabilities of the three components of the triplet state ($|T_x\rangle$, $|T_y\rangle$, and $|T_z\rangle$ at $B_0 = 0$ or $|T_+\rangle$, $|T_0\rangle$, and $|T_-\rangle$ at $B_0 \neq 0$) are different. Frequently, the sensitivity of optical detection is much greater than that of detection via the microwave absorp-

tion, since in the ideal case of ODMR, each microwave quantum gives rise to an optical quantum of much higher energy and thus more sensitive detection.

The first experiments with ESR on electronically excited molecular triplet states were published by Hutchison *et al.* [1]. A few years later, the first optical detection of ESR in a magnetic field followed [2], as well as the first optical detection of the zero-field resonance [3]. For these experiments, molecular crystals (host crystals doped with guest molecules) were investigated. The host crystal in these mixed-crystal systems serves mainly as an orienting matrix and the result of these ESR measurements are values for the fine structure and the dynamic properties of the T_1 state of the guest molecules.

A typical 9.4 GHz-ESR triplet spectrum of such a host-guest system is shown in Fig. 7.3. The host crystal was a perdeuterated naphthalene crystal, ($N-d_8$), with 2%

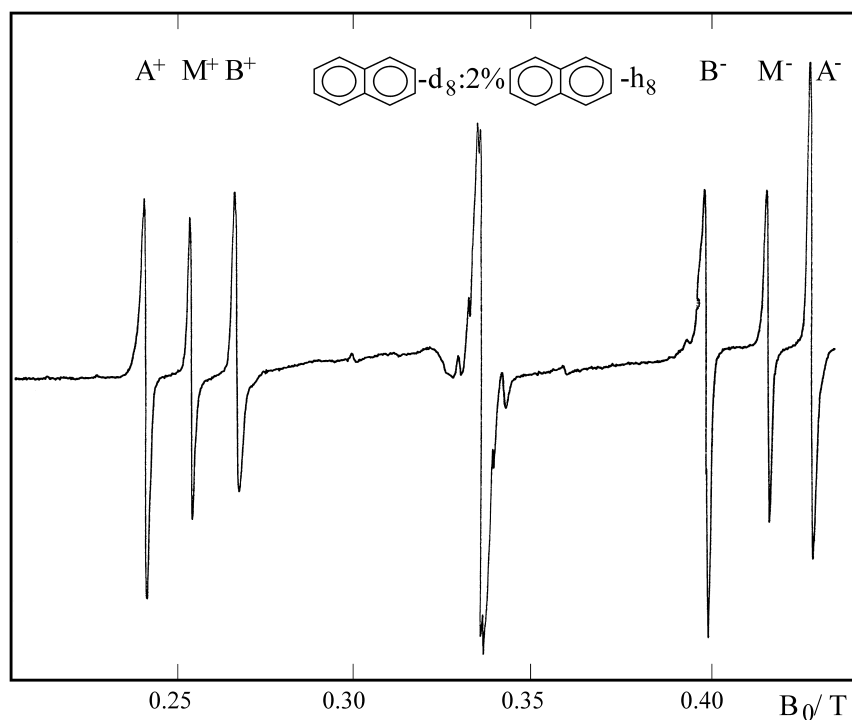


Fig. 7.3 The ESR spectrum of a perdeuterated naphthalene–naphthalene ($N-d_8 + 2\% N-h_8$) mixed crystal at $T = 4.2$ K. A^+/A^- and B^+/B^- are ESR transitions in isolated $N-h_8$ molecules with the two different orientations A and B (see Fig. 7.11); M^+/M^- are transitions in $N-h_8$ $A-B$ pairs (mini-excitons); the lines in the centre ($g \approx 2$) are transitions in free radicals of the crystal mount. The relative concentrations of the T_1 states of the isolated guest molecules (A, B)

and of the mini-excitons (M) are not proportional to the relative heights of the corresponding ESR lines in this spectrum, because the A and B ESR transitions were saturated, while the M ESR transitions were not saturated. From the unsaturated spectra, the relative concentration of the mini-excitons can be found, and they correspond to what would be expected for a statistical distribution of the guest molecules (see Sect. 7.4). From [4].

non-deuterated naphthalene (N-h₈) as guest: N-d₈ + 2% N-h₈. At 4.2 K, the N-h₈ molecules and – in their statistical abundance – also pairs of neighbouring N-h₈ molecules form traps for the triplet excitons of the host crystal N-d₈. Thus, in these mixed crystals, it is principally the T_1 states of the isolated N-h₈ molecules, and not the free triplet excitons of the host crystal, that have a steady-state population. As mentioned before, the crystal also contains directly-neighbouring pairs of N-h₈ molecules (dimers), i.e. unit cells which are occupied by two non-equivalently oriented N-h₈ molecules A and B . These also form traps for triplet excitons. The T_1 states of these $A-B$ pairs are thus also populated in a steady state; they are referred to as triplet mini-excitons (compare Sect. 6.4). The spectrum thus contains three pairs of two fine-structure components each: A^+/A^- , B^+/B^- , and M^+/M^- . These represent the ESR transitions in the isolated A and B molecules as well as those in the $A-B$ mini-excitons M . All three spectral regions exhibit an anisotropic fine structure; Fig. 7.4 shows the anisotropy of each of the resonance fields on rotating the applied magnetic field \mathbf{B}_0 in a particular crystal plane, here the $\gamma-z$ plane of the A molecules [4].

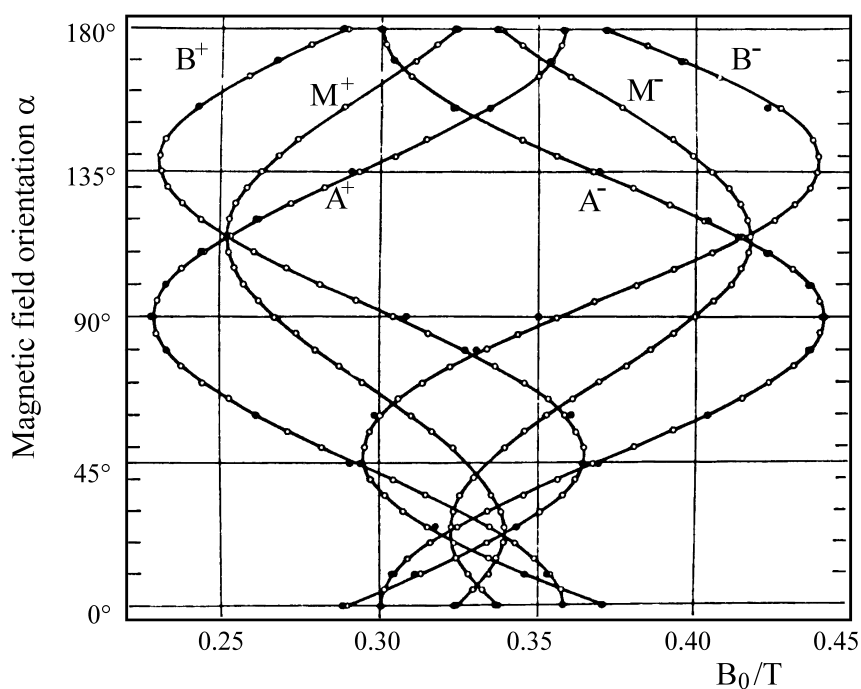


Fig. 7.4 The anisotropy of the resonance fields of the ESR transitions in a (N-d₈ + 2% : N-h₈) mixed crystal on rotating the magnetic field \mathbf{B}_0 in the $\gamma-z$ plane of the A molecules (cf. Figs. 7.9 and 7.11); $\alpha = 0^\circ \simeq \mathbf{B}_0 \parallel \gamma_A$, $\alpha = 90^\circ \simeq \mathbf{B}_0 \parallel z_A$; x_A^* indicates a principal axis of the mini-excitons (cf. Fig. 7.11). Open circles are the experimental values; filled circles are calculated values; $\omega \approx 2\pi \cdot 9.4$ GHz. $T = 4.2$ K. After [4].

For an understanding of ESR in crystals, a detailed discussion of the molecular fundamentals is necessary. We deal with this primarily in Sections 7.2 and 7.3. There, the spin quantisation in triplet states, magnetic dipole-dipole coupling, zero-field splitting, Zeeman splitting and fine structure are explained. These fundamentals apply both to isolated molecules and to **excitons** (Sects. 7.4 and 7.5). In the two later Sects. 7.6 and 7.7 of this chapter, the so called optical spin polarisation in excited triplet states and dynamic nuclear spin polarisation will be treated.

7.2

Spin Quantisation in Triplet States

Triplet states in π -electron systems are formed by the coupling of two π -electrons to give states with a total spin quantum number $S = 1$. These two electrons also have a magnetic dipole-dipole coupling. In spherical symmetry, the spatial average of the latter is zero. In triplet states of molecules or molecular crystals with their non-spherical symmetry, the spatial average of the magnetic dipole-dipole coupling of the two unpaired electrons is however generally nonzero. Therefore, the triplet state is triply split even when $\mathbf{B}_0 = 0$. This is the previously-mentioned zero-field splitting.

In the following, we shall see that the magnetic quantum number m_s for triplet states is not a good quantum number in zero applied magnetic field or in weak applied fields, and that the three Zeeman components are described approximately by the quantum numbers $m_s = +1, 0$ and -1 only when a strong magnetic field \mathbf{B}_0 is applied. (The precise meanings of “weak” and “strong” depend in each case on the ratio of the Zeeman energy to the magnetic dipole-dipole interaction energy.)

The spin eigenfunctions of a system consisting of two coupled π -electrons $i = 1$ and 2 are, in the absence of an applied magnetic field ($\mathbf{B}_0 = 0$), given by the following four linearly-independent, orthonormal linear combinations of the products of the single-electron spin functions $|\alpha_i\rangle$ and $|\beta_i\rangle$ with the spin quantum number $s = 1/2$:

$$|T_x\rangle = \frac{1}{\sqrt{2}}|\beta_1\beta_2 - \alpha_1\alpha_2\rangle, \quad (7.1a)$$

$$|T_y\rangle = \frac{i}{\sqrt{2}}|\beta_1\beta_2 + \alpha_1\alpha_2\rangle, \quad (7.1b)$$

$$|T_z\rangle = \frac{1}{\sqrt{2}}|\alpha_1\beta_2 + \beta_1\alpha_2\rangle, \quad (7.1c)$$

$$|\Sigma\rangle = \frac{1}{\sqrt{2}}|\alpha_1\beta_2 - \beta_1\alpha_2\rangle. \quad (7.1d)$$

Here, $|\alpha_i\rangle$ and $|\beta_i\rangle$ are defined as usual by the action of the components of the spin operator $\mathbf{s}_i = s_{xi} \mathbf{e}_x + s_{yi} \mathbf{e}_y + s_{zi} \mathbf{e}_z$ (Table 7.1) (see e.g. [M2, M5]).

	$ \alpha\rangle$	$ \beta\rangle$
\hat{s}_x	$\frac{\hbar}{2} \beta\rangle$	$\frac{\hbar}{2} \alpha\rangle$
\hat{s}_y	$i\frac{\hbar}{2} \beta\rangle$	$i\frac{\hbar}{2} \alpha\rangle$
\hat{s}_z	$\frac{\hbar}{2} \alpha\rangle$	$\frac{\hbar}{2} \beta\rangle$

Table 7.1 The action of the components \hat{s}_u of the spin operator $\hat{\mathbf{S}}$ on the spin functions $|\alpha\rangle$ and $|\beta\rangle$. $u = x, y, z$, with the total spin quantum number $S = 1/2$.

The physical properties of the four two-electron spin functions $|T_u\rangle$ ($u = x, y, z$) and $|\Sigma\rangle$ follow from the action of the three vector components $\hat{S}_u = \hat{s}_{u1} + \hat{s}_{u2}$ of the total spin operator $\hat{\mathbf{S}} = \hat{\mathbf{s}}_1 + \hat{\mathbf{s}}_2 = \hat{S}_x \mathbf{e}_x + \hat{S}_y \mathbf{e}_y + \hat{S}_z \mathbf{e}_z$ on the four two-electron spin functions (Eq. (7.1)). For the three functions $|T_x\rangle$, $|T_y\rangle$, and $|T_z\rangle$, these actions are collected in Table 7.2 and have the following physical significance:

- The three functions $|T_u\rangle$ are eigenfunctions of the square of the total spin operator with the total spin quantum number $S = 1$; for all $|T_u\rangle$ we thus have

$$\hat{S}^2|T_u\rangle = (\hat{S}_x^2 + \hat{S}_y^2 + \hat{S}_z^2)|T_u\rangle = 2\hbar^2|T_u\rangle = S(S+1)\hbar^2|T_u\rangle.$$

- The three functions $|T_u\rangle$ are eigenfunctions of the component \hat{S}_u of the total spin operator with the eigenvalue $S_u = 0$: $\hat{S}_u|T_u\rangle = 0$. The total spin in the state $|T_u\rangle$ is thus oriented in the $u = 0$ plane, i.e. in the $v - w$ plane.
- The expectation value of the spins in every direction perpendicular to the direction u is for the three eigenfunctions $|T_u\rangle$ likewise equal to 0: $\langle T_u|\hat{S}_v|T_u\rangle = 0$.
- For the function $|\Sigma\rangle$ (Eq. (7.1d)), the relation $\hat{S}^2|\Sigma\rangle = 0$ holds, i.e. $|\Sigma\rangle$ is the spin eigenfunction for the singlet state with total spin quantum number $S = 0$.

In Fig. 7.5, the quantisation of the directions for two of the three triplet components in zero field is visualised: in the $|T_z\rangle$ state, the total spin lies in the $z = 0$ plane but there, it has no preferred direction. For the two other directions, x and y , the analogous result holds. Which orientation the coordinate system x, y, z will have in a

	$ T_x\rangle$	$ T_y\rangle$	$ T_z\rangle$
\hat{S}_x	0	$+i\hbar T_z\rangle$	$-i\hbar T_y\rangle$
\hat{S}_y	$-i\hbar T_z\rangle$	0	$+i\hbar T_x\rangle$
\hat{S}_z	$+i\hbar T_y\rangle$	$-i\hbar T_x\rangle$	0
\hat{S}_x^2	0	$\hbar^2 T_y\rangle$	$\hbar^2 T_z\rangle$
\hat{S}_y^2	$\hbar^2 T_x\rangle$	0	$\hbar^2 T_z\rangle$
\hat{S}_z^2	$\hbar^2 T_x\rangle$	$\hbar^2 T_y\rangle$	0

Table 7.2 The action of the components \hat{S}_u and \hat{S}_u^2 of the total spin operator $\hat{\mathbf{S}}$ on the zero-field spin functions $|T_u\rangle$, $u = x, y, z$; total spin quantum number $S = 1$.

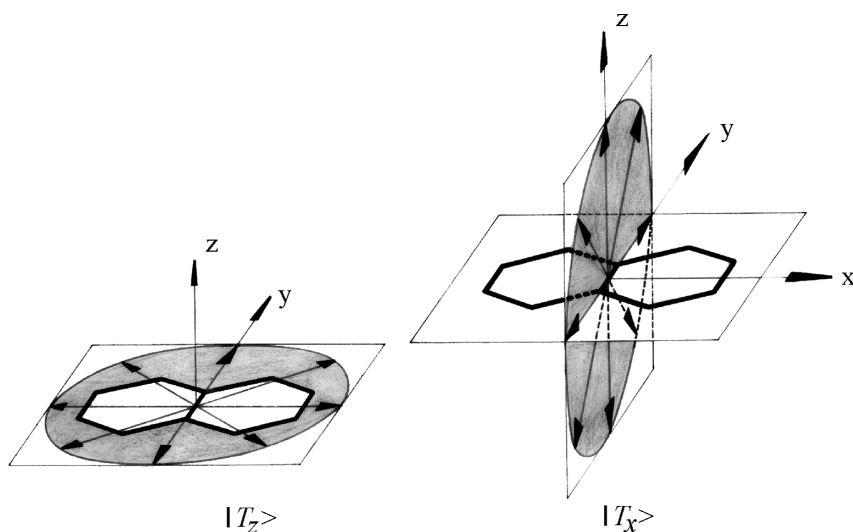


Fig. 7.5 The three spin functions $|T_u\rangle$, ($u = x, y, z$) of the triplet state are eigenfunctions of the component S_u of the total spin operator \mathbf{S} : $S_u|T_u\rangle = 0$. The total spin is thus oriented in the $u = 0$ plane. It has no preferred direction in this plane. The three spin functions $|T_u\rangle$ therefore transform like rotations around the $u = 0$ axis.

real system, e.g. in a molecule or a crystal, cannot be derived from our treatment of the triplet spin functions up to now. This requires an internal field direction, which will be discussed in the following section.

7.3

The Dipole-Dipole Interaction, Fine Structure

In the following section, we summarise the calculation of the magnetic dipole-dipole interaction for the components of the T_1 state. The individual steps in this calculation are treated in detail in [M2] or [M5].

7.3.1

Zero Field ($B_0 = 0$)

Neglecting the spin-orbit coupling, the wavefunctions Ψ of the molecules, i.e. the molecular orbitals, are the product of a spatial part $\Phi(R_j, r_i)$ and a spin part. The spatial functions Φ depend only on the position variables R_j of the nuclei and r_i of the electrons, while the spin part depends only on the spin variables of the electrons (and in some cases of the nuclei). As long as no applied magnetic field is present

($\mathbf{B}_0 = 0$), and as long as the magnetic dipole-dipole interaction can be neglected, we can write e.g. for the three components of the triplet state T_1 :

$$|^3\Psi_{1u}\rangle = |^3\Phi_1(R_j, r_i)\rangle \cdot |T_u\rangle. \quad (7.2)$$

Here, the spatial functions $^3\Phi_1$ are all identical and the three spin parts make no contribution to the energy. Therefore, the three states $^3\Psi_{1u}$ are degenerate with the approximations made up to now. This degeneracy is lifted by the magnetic dipole-dipole interaction W_{DD} of the two unpaired electrons. To estimate the order of magnitude of W_{DD} , it suffices to consider a particular relative orientation, e.g. that in which the two magnetic moments μ_B are parallel to the vector which connects them, \mathbf{r}_{12} . In this case, we have:

$$|W_{DD}|/hc = \frac{\mu_0}{4\pi} \cdot \frac{2\mu_B^2}{r_{12}^3} \cdot \frac{1}{hc}.$$

Here, μ_B is the Bohr magneton. For the distance $r_{12} = 2 \text{ \AA}$, $W_{DD}/hc = 0.108 \text{ cm}^{-1}$. This energy is very small compared to the electronic excitation energy of the triplet state, but only about $\frac{1}{3}$ of the Zeeman energy $g\mu_B B_0/hc$ of an electronic spin in an applied magnetic field of $B_0 = 0.3 \text{ T}$, a typical value for ESR spectroscopy. The magnetic dipole-dipole coupling can thus not be neglected, but it can be included using perturbation theory with degeneracy.

The Hamiltonian \mathcal{H}^{DD} for the magnetic dipole-dipole coupling is, in complete analogy to the electric dipole-dipole coupling, a function of the distance \mathbf{r}_{12} between the two spins \mathbf{s}_1 and \mathbf{s}_2 and of their relative orientations:

$$\mathcal{H}^{DD} = \frac{\mu_0}{4\pi} \cdot \frac{g^2 \mu_B^2}{\hbar^2} \cdot \left\{ \frac{\hat{\mathbf{s}}_1 \hat{\mathbf{s}}_2}{r_{12}^3} - \frac{3(\hat{\mathbf{s}}_1 \hat{\mathbf{r}}_{12})(\hat{\mathbf{s}}_2 \hat{\mathbf{r}}_{12})}{r_{12}^5} \right\}. \quad (7.3)$$

In this expression, g represents the gyromagnetic ratio (g -factor) and r_{12} is the magnitude of \mathbf{r}_{12} . To compute the matrix elements \mathcal{H}_{uv}^{DD} in the basis of the three triplet components $|^3\psi_{1u}\rangle$ (Eq. (7.2)), we can (virtually) first carry out the integration over the spatial variables, so that the remaining operator \mathcal{H}_s^{DD} contains only the total spin operator $\hat{\mathbf{S}}$ and its components \hat{S}_u . The calculation for the resulting so called *spin Hamiltonian* \mathcal{H}_s^{DD} yields

$$\mathcal{H}_s^{DD} = \frac{D}{\hbar^2} \left(\hat{S}_z^2 - \frac{1}{3} \hat{\mathbf{S}}^2 \right) + \frac{E}{\hbar^2} (\hat{S}_x^2 - \hat{S}_y^2). \quad (7.4)$$

Here, the fine-structure constants D and E have the following expectation values:

$$D = \frac{\mu_0}{4\pi} \cdot g^2 \mu_B^2 \cdot \frac{3}{4} \left\langle \frac{r_{12}^2 - 3z_{12}^2}{r_{12}^5} \right\rangle \quad (7.5a)$$

$$E = \frac{\mu_0}{4\pi} \cdot g^2 \cdot \mu_B^2 \cdot \frac{3}{4} \left\langle \frac{y_{12}^2 - x_{12}^2}{r_{12}^5} \right\rangle. \quad (7.5b)$$

x_{12} , y_{12} and z_{12} are the components of \mathbf{r}_{12} . The term $\frac{1}{3} \hat{\mathbf{S}}^2$ in Eq. (7.4) is in general (and in the following) left off, since it causes only a small and furthermore identical

shift of all three triplet components by $-\frac{2}{3}D$. It could be measured only if the dipole-dipole coupling could be “switched off”, which is of course impossible.

The matrix of the spin Hamiltonian \mathcal{H}_s^{DD} (Eq. (7.4)) in the basis of the three spin functions $|T_u\rangle$ then follows directly from Table 7.2:

$$\|\mathcal{H}_{s,uv}^{DD}\| = \begin{vmatrix} D-E & 0 & 0 \\ 0 & D+E & 0 \\ 0 & 0 & 0 \end{vmatrix}. \quad (7.6)$$

The three spin functions $|T_u\rangle$ are thus also eigenfunctions of the spin Hamiltonian \mathcal{H}_s^{DD} . Their energy eigenvalues are $\varepsilon_x = D-E$, $\varepsilon_y = D+E$ and $\varepsilon_z = 0$ (Fig. 7.6).

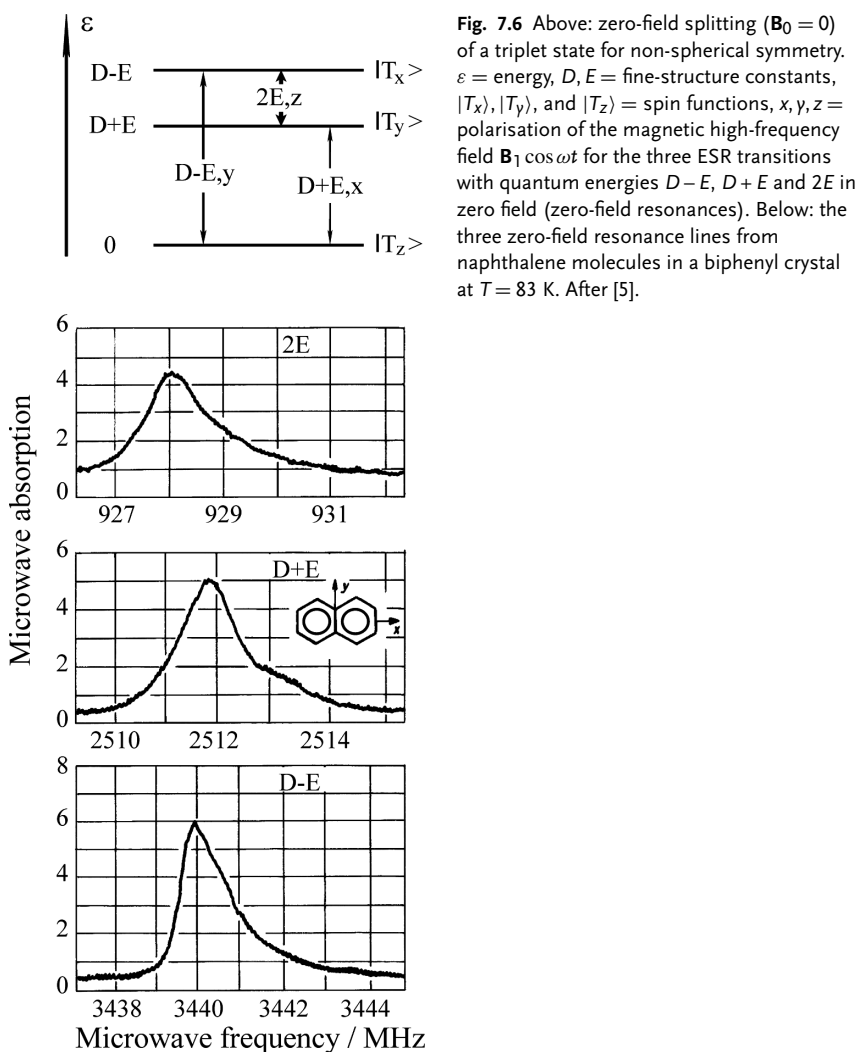


Fig. 7.6 Above: zero-field splitting ($\mathbf{B}_0 = 0$) of a triplet state for non-spherical symmetry. ε = energy, D, E = fine-structure constants, $|T_x\rangle, |T_y\rangle$, and $|T_z\rangle$ = spin functions, x, y, z = polarisation of the magnetic high-frequency field $\mathbf{B}_1 \cos \omega t$ for the three ESR transitions with quantum energies $D-E$, $D+E$ and $2E$ in zero field (zero-field resonances). Below: the three zero-field resonance lines from naphthalene molecules in a biphenyl crystal at $T = 83$ K. After [5].

Since the dipole-dipole interaction is an internal interaction, the coordinate axes must correspond to the symmetry of the system being investigated. In a planar molecule, e.g. in naphthalene, the coordinate system x, y, z must therefore be identical to the principal-axis system of the molecule. In the T_1 exciton, the coordinate system must reflect the symmetry of the crystal. The identification of the three axes x, y , and z , i.e. also of the three states $|T_x\rangle$, $|T_y\rangle$, and $|T_z\rangle$ relative to the molecular or crystal axes however requires a measurement in an applied magnetic field.

The magnitudes and signs of D and E are defined with respect to the chosen coordinate system x, y, z (see Eq. (7.5a,b)). Without knowledge of the orientation of these coordinates relative to the system being investigated, the interpretation of D and E according to Eq. (7.5) permits no conclusions to be drawn about the orientation of \mathbf{r}_{12} .

The three transitions between the three terms are referred to as zero-field transitions or the zero-field resonances. In an applied high-frequency field $\mathbf{B}_1 \cos \omega t$, all three transitions are allowed. This follows immediately by computation of the transition matrix elements $(g\mu_B/\hbar)\langle T_u | \mathbf{B}_1 \cdot \hat{\mathbf{S}} | T_v \rangle$ using Table 7.2: for example, the transition matrix element for the zero-field transition $T_x \leftrightarrow T_z$ (Fig. 7.5), the transition matrix element $\langle T_x | (B_{1x}\hat{S}_x + B_{1y}\hat{S}_y + B_{1z}\hat{S}_z) | T_z \rangle$ is nonzero only for the y component. For this transition, \mathbf{B}_1 must thus have a component in the y direction. From Fig. 7.5, this becomes intuitively clear: for this transition, all the spins must precess around the y axis. The other two zero-field transitions follow by cyclic permutations.

The most precise measurements of the fine-structure parameters D and E have in fact been carried out using zero-field resonance. Figure 7.6 shows the three zero-field transitions in the T_1 state of naphthalene molecules in a biphenyl crystal at $T = 83$ K. In these experiments, the absorption of the microwaves was detected as a function of their frequency [5]. The lines are inhomogeneously broadened and nevertheless only about 1 MHz wide. Owing to the small linewidth of the zero-field resonances, the fine-structure constants can be determined with a high precision. This small inhomogeneous broadening is due to the hyperfine interaction with the nuclear spins of the protons (see e.g. [M2] and [M5]). For triplet states in zero field, the hyperfine structure vanishes to first order in perturbation theory, since the expectation value of the electronic spins vanishes in all three zero-field components (cf. Sect. 7.2). The hyperfine structure of the zero-field resonances is therefore a second-order effect [5].

As a second example, Fig. 7.7 shows the optical detection of the zero-field resonance (ODMR) from **X-traps** (cf. Sect. 4.1) in an anthracene crystal at $T = 1.2$ K [6]. Here, both the variation of the intensity of the phosphorescence, ΔI_P , and also the changes in the intensity ΔI_{DF} of the delayed fluorescence (cf. Sect. 6.9.2) were measured as functions of the microwave frequency. With both methods, all three zero-field resonances were detected. The optical detection of the resonance at 1850 MHz requires simultaneous irradiation at one of the other two resonance frequencies. The method of (optical) detection of this resonance is therefore referred to as electron-electron double resonance (EEDOR). From the three zero-field resonances and their structures, the three fine-structure parameters of two different X-traps in the anthracene crystal were found to be

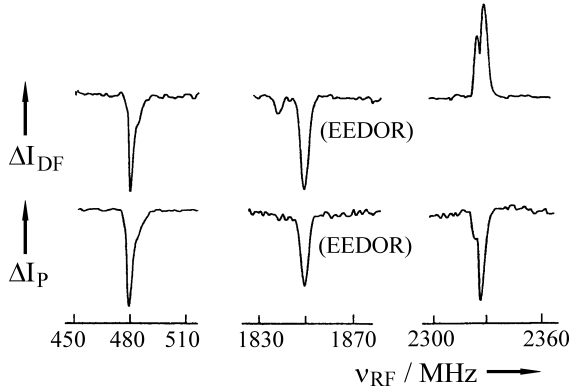


Fig. 7.7 ODMR signals from X-traps in an anthracene crystal at $T = 1.2$ K. The variations ΔI_P in the phosphorescence intensity and ΔI_{DF} of the intensity of the delayed fluorescence are plotted as functions of the microwave frequency ν_{RF} . The signal at 1850 MHz (EEDOR) was detected via simultaneous irradiation with one of the other resonance frequencies. From [6].

	X-trap 1	X-trap 2
$\frac{D}{hc}/\text{cm}^{-1}$	0.06967	0.06940
$\frac{ E }{hc}/\text{cm}^{-1}$	0.00793	0.00808

A third example of a zero-field resonance is shown in Fig. 7.8; it is the optically-detected $D + |E|$ transition of **triplet excitons** in 1,2,4,5-tetrachlorobenzene crystals at a temperature of $T = 4.2$ K [7]. In this measurement, the phosphorescence intensity

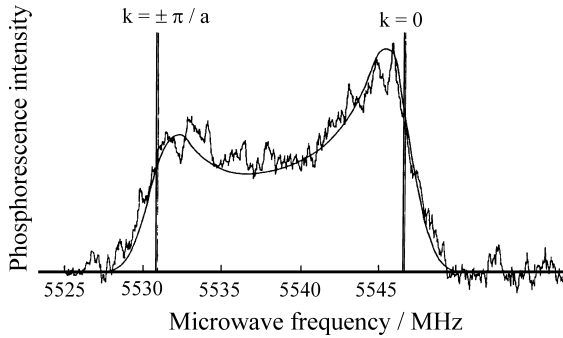


Fig. 7.8 The optically-detected $D + |E|$ band-band transition in triplet excitons of 1,2,4,5-tetrachlorobenzene crystals. The intensity of the 0,0 transition of the phosphorescence was measured as a function of the microwave frequency at $T = 4.2$ K.

Owing to the crystal structure, the excitons are one-dimensional. The solid line is an image of the dispersion curves of the triplet exciton bands of the two triplet components between which the zero-field ESR transition was induced. After [7].

was detected as a function of the microwave frequency in the range from 5525 MHz to 5550 MHz. The solid curve was calculated from the dispersion curves $\varepsilon(\mathbf{k})$ of the two triplet components between which the zero-field ESR transition was induced: each triplet component $|T_u\rangle$ is a coherent, one-dimensional triplet exciton wave in these crystals, with the energy $\varepsilon_u(\mathbf{k})$. Here, \mathbf{k} is the wavevector ($-\pi/a < k \leq \pi/a$) and, in addition to the spin selection rules, the selection rule $\Delta k = 0$ applies to the ESR transitions. At $T = 4.2$ K, all the \mathbf{k} states in the first Brillouin zone are thermally populated and can therefore be observed in the ODMR signal. The ODMR signal is thus an image of the combined density of states of the two triplet exciton components. This is one of the few cases where the coherence of the triplet excitons has been directly observed.

Table 7.3 gives experimental values of the fine-structure constants D and E for some aromatic molecules in their excited triplet states T_1 and for the carbene $:\text{CH}_2$ (methylene) in its electronic ground state, which is a triplet state. In molecules or in molecular crystals which have a three- or more-fold axis of symmetry that is chosen to be the z axis, it is $\langle x_{12}^2 \rangle = \langle y_{12}^2 \rangle$. For this cylindrical symmetry, it follows from Eq. (7.5b) that $E = 0$. For benzene molecules, however, $E \neq 0$. This shows that benzene in its triplet state T_1 no longer has a 6-fold axis of symmetry. The molecule is so distorted owing to its Jahn-Teller instability in the T_1 state that it has – like the higher aromatics – at most a twofold axis of symmetry. E is thus a measure of the deviation from cylindrical symmetry.

In molecules with a discus shape, $\langle z_{12}^2 \rangle \ll \langle x_{12}^2 \rangle \approx \langle y_{12}^2 \rangle$. It follows from this using Eq. (7.5a) that:

$$D = \frac{3}{4} \cdot \frac{\mu_0}{4\pi} \cdot g^2 \mu_B^2 \cdot \frac{1}{r_{12}^3}.$$

With $D/hc = 0.1 \text{ cm}^{-1}$ (naphthalene), we obtain from this expression the mean distance of the two electrons: $\langle r_{12} \rangle \approx 2.5 \text{ \AA}$. For rod-shaped molecules, $\langle x_{12}^2 \rangle \approx \langle y_{12}^2 \rangle \ll \langle z_{12}^2 \rangle$. With Eq. (7.5a), we obtain:

$$D = -\frac{3}{4} \cdot \frac{\mu_0}{4\pi} \cdot g^2 \mu_B^2 \cdot \frac{2}{r_{12}^3}.$$

From the sign of D , we thus gain information about the shape of the molecules. Measurement of this sign is not simple and is usually possible only by performing

	$(D/hc)/\text{cm}^{-1}$	$(-E/hc)/\text{cm}^{-1}$
Benzene	0.1581	0.0046
Naphthalene	0.0994	0.0154
Anthracene	0.0718	0.0080
Pyrazine	0.33923	0.00791
Quinoxaline	0.1007	0.0182
Phenazine	0.0744	0.0110
$:\text{CH}_2$	0.6636	

Table 7.3 The fine-structure parameters D and E from selected molecules in the electronically excited triplet state T_1 and from methylene, (CH_2), in its electronic triplet ground state. The parameters are weakly dependent both on the temperature and also on the host matrix.

a double-resonance experiment. For the T_1 state of all isolated polyacene molecules, $D > 0$ when the z axis is chosen to be the direction perpendicular to the molecular plane.

7.3.2

Zeeman Splitting ($B_0 \neq 0$)

To compute the energy of the three triplet components in an applied static magnetic field \mathbf{B}_0 , the spin Hamiltonian of the dipole-dipole interaction, \mathcal{H}_s^{DD} , Eq. (7.4), must be added to the spin Hamiltonian of the Zeeman interaction, $\mathcal{H}_s^z = (\mu_B/\hbar)\mathbf{B}_0 \cdot \hat{\mathbf{S}}$.

The overall spin Hamiltonian \mathcal{H}_s then becomes

$$\mathcal{H}_s = \frac{D}{\hbar^2} \hat{S}_z^2 + \frac{E}{\hbar^2} (\hat{S}_x^2 - \hat{S}_y^2) + \frac{\mu_B}{\hbar} (\mathbf{B}_0 \cdot \hat{\mathbf{S}}). \quad (7.7)$$

In the general case, the g -factor is a second-rank tensor. For the simplified case of an isotropic g -tensor, ($\tilde{g} = g = \text{isotrop}$), the Zeeman term becomes $(g\mu_B B_0/\hbar)(p\hat{S}_x + q\hat{S}_y + r\hat{S}_z)$. Here, $B_0 = |\mathbf{B}_0|$ and p, q , and r are the direction cosines of the magnetic field relative to the three space coordinates x, y , and z : $p = \cos \alpha$, $q = \cos \beta$, $r = \cos \gamma$ (Fig. 7.9). In the basis of the zero-field spin functions $|T_u\rangle (u = x, y, z)$, and referring to Table 7.2, the matrix of the overall spin Hamiltonian becomes:

$$\|\mathcal{H}_{s,uv}\| = \begin{vmatrix} D - E & -irg\mu_B B_0 & iqq\mu_B B_0 \\ irg\mu_B B_0 & D + E & -ipg\mu_B B_0 \\ -iqg\mu_B B_0 & ipg\mu_B B_0 & 0 \end{vmatrix}. \quad (7.8)$$

This matrix is not diagonal. The three states $|T_u\rangle$ are therefore mixed by the magnetic field. The mixing coefficients and the energies ε of the states in the magnetic field are as usual calculated from the system of secular equations. The energies are found from $\text{Det}[\mathcal{H}_{s,uv} - \varepsilon\delta_{uv}] = 0$. Explicitly, this third-order equation for the calculation of the Zeeman energies ε with $p^2 + q^2 + r^2 = 1$ is given by:

$$\varepsilon^3 - 2D\varepsilon^2 + (D^2 - E^2 - g^2\mu_B^2 B_0^2)\varepsilon + [(D - E)g^2 p^2 + (D - E)g^2 q^2]\mu_B^2 B_0^2 = 0. \quad (7.9)$$

Figure 7.10 shows these energies for the example of the N-d₈:N-h₈ mixed crystal with the fine-structure constants of naphthalene, N-h₈, and the g -factor of the free

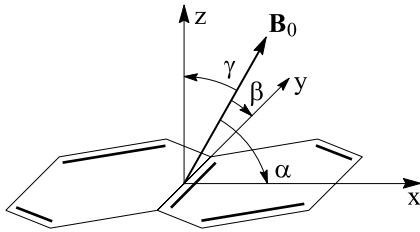


Fig. 7.9 The definition of the orientation of the applied magnetic field \mathbf{B}_0 relative to the principal-axis system x, y, z of the magnetic dipole-dipole interaction.

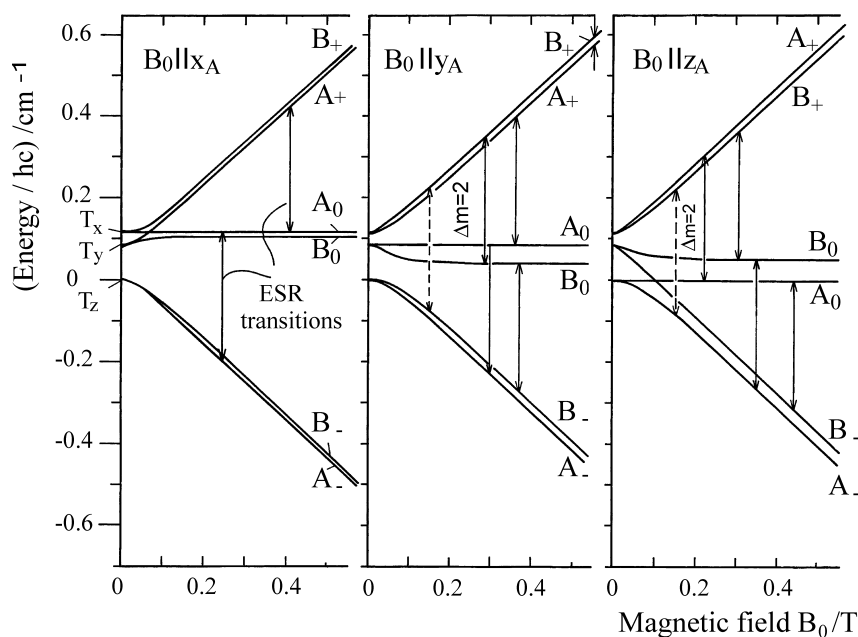


Fig. 7.10 The Zeeman splitting of the triplet states of the two differently-oriented molecules A and B in the naphthalene crystal (see Fig. 7.11) for three different orientations of the applied magnetic field \mathbf{B}_0 , each parallel to one of the principal axes of the A molecules. There are two “allowed” $\Delta m = 1$ ESR transitions for each of the two molecular orientations A and B. (In the term diagram for $\mathbf{B}_0 \parallel x_A$, these transitions are shown for simplicity only for the molecular orientation A).

At high field strengths of B_0 , the three Zeeman components A_+ , A_0 and A_- or B_+ , B_0 and B_- are defined by the magnetic directional quantum numbers $m_s = +1, 0, -1$. The ESR transitions are shown for a microwave frequency $\omega = 2\pi \cdot 9.4$ GHz. For $\Delta m_s = 1$ transitions, $\mathbf{B}_1 \cos \omega t \perp \mathbf{B}_0$ must hold. $\Delta m_s = 2$ transitions are weakly allowed, as long as the Zeeman splitting is not large in comparison to the zero-field splitting and m_s is therefore not a good quantum number. After [4].

electron. The orientation of \mathbf{B}_0 is chosen as follows: \mathbf{B}_0 is parallel to one of the three principal axes x_A , y_A , or z_A of one of the two naphthalene molecules (A) in the unit cell (Fig. 7.11). Then \mathbf{B}_0 relative to the second molecule (B) is *not* oriented parallel to a molecular principal axis.

When the field B_0 becomes so strong that the Zeeman energy is larger than the zero-field splitting, then the $|T_u\rangle$ states become so mixed that they turn into the states $|T_+\rangle$, $|T_0\rangle$, and $|T_-\rangle$, which are characterised for high applied fields by the magnetic directional quantum numbers $m_s = +1, 0$, and -1 . For intermediate field strengths, the terms are curved as a function of B_0 and the m_s are not good quantum numbers. At high fields, the terms are linear and the selection rule $\Delta m_s = \pm 1$ holds for ESR transitions with an orthogonal orientation of \mathbf{B}_1 and \mathbf{B}_0 ($\mathbf{B}_1 \perp \mathbf{B}_0$). For the molecules A or B, these transitions are observed separately (see Fig. 7.3). On rotation of \mathbf{B}_0 , e.g. in the $y-z$ plane of the A molecules, the terms and the transitions are shifted (Fig. 7.4). From this anisotropy of the fine structure of the

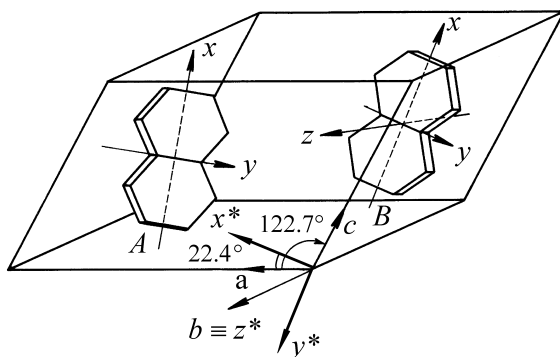


Fig. 7.11 The unit cell of the naphthalene crystal. x, y , and z are the two-fold symmetry axes of the two differently-oriented molecules A and B, and also the principal axes of the magnetic dipole-dipole coupling in the excited triplet state of the molecules. a, b , and c are the crystal axes. x^*, y^*, z^* are the principal axes of the magnetic dipole-dipole coupling of the triplet excitons (cf. Sects. 7.4 and 7.5).

ESR spectra, D, E, g and the orientation of the molecules within the crystal can be determined by applying Eq. (7.9).

7.3.3

Powder Spectra

The ESR spectra of T_1 states in a magnetic field ($\mathbf{B}_0 \neq 0$) discussed thus far were the spectra of $\Delta m = 1$ transitions in single crystals. Their fine structure is anisotropic, i.e. it depends on the direction of the applied magnetic field \mathbf{B}_0 relative to the crystal axes (cf. Fig. 7.4). In crystalline powders or in glasses, the orientations of the principal axes x, y, z of the molecules or x^*, y^*, z^* of the excitons (see Sects. 7.4 and 7.5) are statistically distributed in space. The ESR spectrum is therefore an inhomogeneous superposition of the spectra of all the orientations. Figure 7.12 shows a characteristic example: the experimental ESR spectrum of the T_1 state of naphthalene- d_8 in tetrahydrofuran at 77 K [8]. In this sample, the naphthalene- d_8 molecules are statistically oriented.

A simulation of such a superposition, using the fine-structure constants of the naphthalene molecule ($D/hc = 0.100 \text{ cm}^{-1}$, $E/hc = -0.015 \text{ cm}^{-1}$, and $g = g_e$), and with a linewidth of $\Delta B = 1.2 \text{ mT}$ for each component is shown in Fig. 7.13a. The discontinuities in the broad $\Delta m = 1$ ESR spectrum correspond to the principal-axis orientations $\mathbf{B}_0 \parallel u$ ($u = x, y, z$). They occur because of the high density of resonance-field values in the neighbourhood of the principal-axis directions (compare Fig. 7.4). For $E = 0$, two of these discontinuities occur at the same place. The $\Delta m = 2$ spectrum is narrow because the anisotropy of the $\Delta m = 2$ transitions is to first approximation zero. The ESR signal (Fig. 7.13b) is – as usual in ESR due to the method of measurement – the first derivative of the spectrum (absorption vs. frequency or field strength, Fig. 7.13a). Even with a powder or a glass sample,

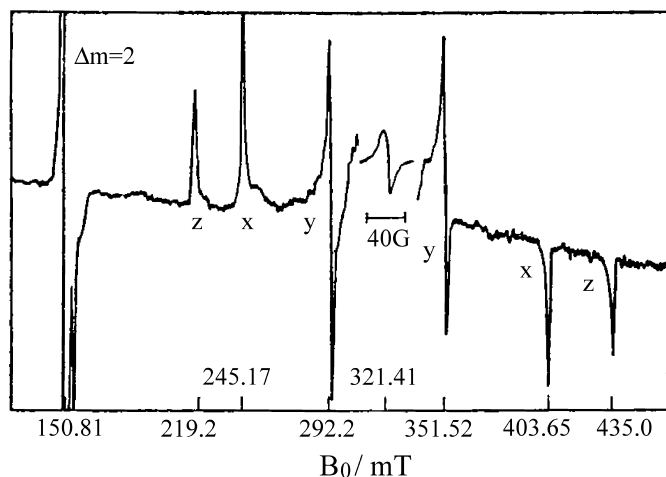


Fig. 7.12 The experimental ESR signal from the T_1 state of statistically-oriented naphthalene- d_8 molecules in tetrahydrofuran at $T = 77$ K. The signal at 321.4 mT (shown on an expanded scale) is a two-quantum transition. This denotes a $\Delta m = 2$ ESR transition, whereby with two microwave quanta, half the energy difference is induced. It corresponds to two-photon absorption in optical spectroscopy. For x , y , and z , see Fig. 7.13. From [8].

the determination of the fine-structure constants is thus also possible (providing the quantity of sample material is sufficient). For the simulation of ESR powder spectra, extensive programme packages are available (see e.g. [9, 10]).

7.4

Mini-Excitons

Along the path from isolated, oriented molecules to excitons in non-doped crystals, we next take up the triplet states of oriented dimers, which we called mini-excitons in Sect. 6.4. Mini-triplet-excitons are excitations of triplet states which are spatially distributed over exactly two molecules, for example the two A and B molecules in the unit cell of Fig. 7.11, and they are localised there. In principle, mini-excitons can also be localised on a pair of molecules with the same orientation in crystals with a dimeric structure, e.g. in the α -perylene crystal (Fig. 2.12). We will however restrict ourselves in this section to the treatment of $A - B$ mini-excitons.

$A - B$ mini-excitons exist in sufficiently concentrated mixed crystals, for example in perdeuteronaphthalene-naphthalene mixed crystals $N-d_8 : x-N-h_8$, in statistical abundance, because $N-h_8$ can be inserted at arbitrary concentration x into the $N-d_8$ crystal. There, nearest-neighbour $N-h_8$ pairs are formed, in whose immediate neighbourhood only $N-d_8$ molecules of the host crystal, and no other $N-h_8$ guest molecules are found, when the $N-h_8$ concentration x is not too high. If w_{AB} denotes

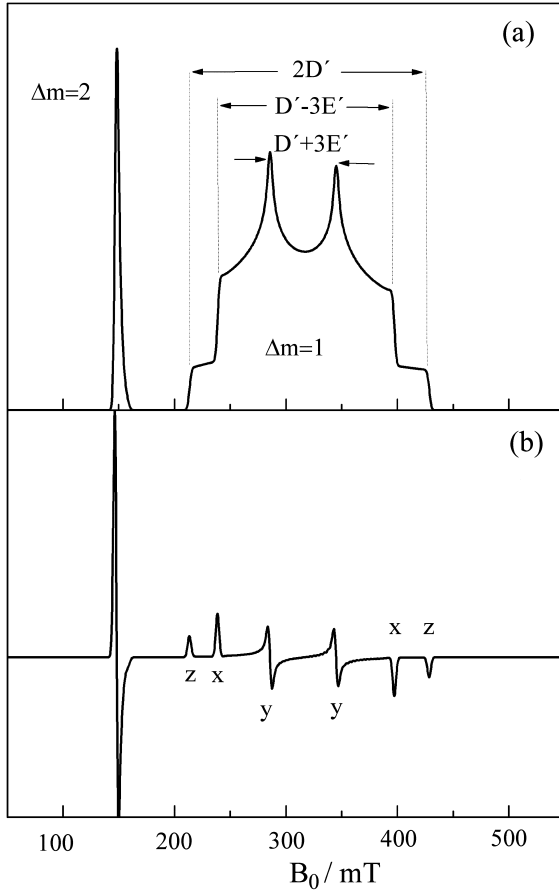


Fig. 7.13 A simulated absorption spectrum (a) of the ESR from the T_1 state of statistically-oriented naphthalene molecules ("powder spectrum") and its first derivative (b). Because of the way the signals are measured, the ESR signal is as a rule the first derivative of the ESR absorption frequency or field spectrum. $D/hc = 0.100 \text{ cm}^{-1}$, $E/hc = -0.015 \text{ cm}^{-1}$, $g = g_e$, $\nu = 9.0096 \text{ GHz}$, $\Delta B = 1.2 \text{ mT}$.

the ratio of the abundance of neighbouring $A-B$ $N-h_8$ pairs to the abundance of the isolated $N-h_8$ molecules, i.e. to the abundance of the $N-h_8$ molecules which have no nearest neighbour $N-h_8$, then for not-too-large $N-h_8$ concentrations ($x \leq 5\%$) for this relative concentration of the $N-h_8$ pairs we have: $w_{AB} \approx \frac{1}{2}x$.

In $N-d_8 : x-N-h_8$ mixed crystals, one observes in the triplet ESR spectrum (Fig. 7.3) in addition to the ESR lines A^+/A^- and B^+/B^- from the isolated molecules also two additional lines, M^+/M^- , whose intensity relative to the intensities of the lines from the individual molecules matches the ratio of their statistical probabilities, w_{AB} . This result was found for $N-h_8$ concentrations between $x = 0.2\%$ and $x = 10\%$ [4].

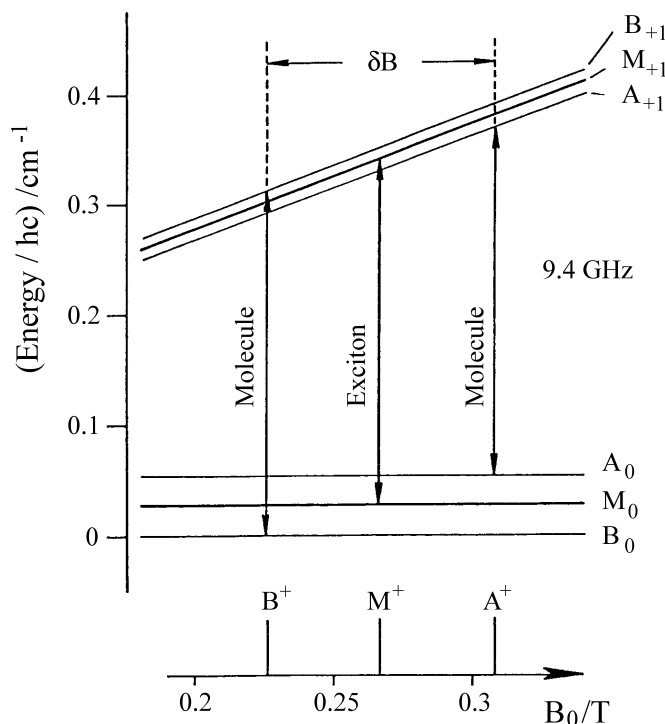


Fig. 7.14 Schematic portion of the term diagram of the triplet states of the molecules A and B and the mini-excited states M in the naphthalene crystal for a selected orientation of the applied magnetic field \mathbf{B}_0 . $\delta\mathbf{B}$ is the difference in the fine structure of the two $m_s = +1 \leftrightarrow m_s = 0$ ESR transitions A_+ and B_+ of the molecules A and B. The magnitude of $\delta\mathbf{B}$ is independent of the magnitude $|\mathbf{B}_0|$, if

$|\mathbf{B}_0| \gg D/g\mu_B$ holds. The terms and the ESR resonance fields M of the excitons are then each given by the mean values of the terms and resonance fields for the two molecules A and B. Therefore, the exciton resonance field M^+ is – independent of the orientation of the applied field \mathbf{B}_0 – always halfway between the resonance fields for A^+ and B^+ of the individual molecules. The same holds for M^- .

The characteristic property of the M lines is their spectral position: they lie in the centre between the corresponding A and B lines, i.e. M^+ between A^+ and B^+ , and M^- between A^- and B^- (Fig. 7.3). This result holds for all orientations of \mathbf{B}_0 (Fig. 7.4). Figure 7.14 gives an intuitively clear explanation for this mean value: in this scheme, the Zeeman terms $|T_+\rangle$ and $|T_0\rangle$ as well as the resonance fields of the corresponding $\Delta m_s = 1$ transitions of the two molecules A and B are shown. The diagram also shows the mean values M_+ and M_0 of the two molecular Zeeman terms and the resulting resonance field M_+ for the mini-exciton.

Quantitatively, the ESR spectra of the M lines are obtained from the spin Hamiltonian:

$$\mathcal{H}_{s,AB} = \frac{1}{2}(\mathcal{H}_{s,A} + \mathcal{H}_{s,B}) \quad (7.10a)$$

and thus from the mean value of $\mathcal{H}_{s,A}$ and $\mathcal{H}_{s,B}$, the spin Hamiltonians of the isolated N-hg molecules [11]. In order to carry out this averaging, $\mathcal{H}_{s,A}$ and $\mathcal{H}_{s,B}$ must

first be transformed to a mutual coordinate system (x^*, y^*, z^*) . Choosing the z^* axis parallel to the two-fold crystal axis b , we obtain

$$\mathcal{H}_{s,AB} = \frac{D^*}{\hbar^2} \hat{S}_{z^*}^2 + \frac{E^*}{\hbar^2} (\hat{S}_{x^*}^2 - \hat{S}_{y^*}^2) + \frac{g\mu_B}{\hbar} \mathbf{B}_0 \hat{\mathbf{S}}. \quad (7.10b)$$

$\mathcal{H}_{s,AB}$ is thus formally identical to \mathcal{H}_s (Eq. (7.7)). The values of D^* and E^* for the mini-exciton as well as the orientations of x^* and y^* depend on the fine-structure constants D and E of the isolated molecules and on their orientations in the crystal. They are clearly derived uniquely through the averaging process. For naphthalene, a tedious but simple calculation according to Eq. (7.10) yields the values

$$\begin{aligned} D^*/hc &= -0.0058 \text{ cm}^{-1} \\ E^*/hc &= +0.0485 \text{ cm}^{-1} \\ \mathbf{z}^* &= \mathbf{b} \\ \angle(x^*, a) &= 22.4^\circ. \end{aligned}$$

The orientations of the principal axes x^* , y^* and z^* are illustrated in Fig. 7.11, while Fig. 7.15 shows the term diagram of the mini-excitons in comparison to that of the isolated molecules in zero field.

The M lines are the ESR lines of the mini-exciton, whose triplet state represents the mean value of the triplet states of the two individual molecules A and B . This means that the excitation energy can be rapidly exchanged between the two molecules. The interesting question is how quickly this exchange takes place and whether it is characterised by a coherent oscillation with the exchange frequency $\omega_{AB} = 2I_{AB}/\hbar$, where $2I_{AB}$ is the Davydov splitting (see Sect. 6.4), or instead by an incoherent hopping process with a hopping probability P .

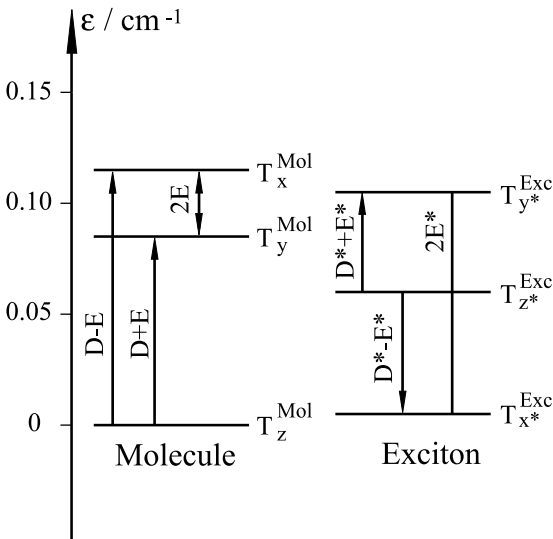


Fig. 7.15 The zero-field splitting of the triplet states of the molecules (Mol) and of the triplet excitons (Exc). The scale corresponds to the values for naphthalene.

To answer this question, we consider in the following the experimentally determined line shape and the linewidth Δ of the mini-exciton ESR spectra, and then analyse them in terms of the theory of exchange or motional narrowing.

The linewidths ΔB_M of the two mini-exciton ESR lines M^+ and M^- depend in a very characteristic manner on the spectral spacing of the two associated lines $A^+ - B^+$ and $A^- - B^-$, i.e. on the difference of the fine structures of the two inequivalently-oriented molecules A and B : ΔB_M has a finite value when the $A - B$ spacing goes to zero and then increases quadratically with increasing $A - B$ spacing (Fig. 7.16). In frequency units, ($\Delta\omega_M = g\mu_B\Delta B_M/\hbar$), the empirical result is then

$$\Delta\omega_M = \Delta\omega_M^0 + \tau(\omega_A - \omega_B)^2. \quad (7.11)$$

Here, τ is in the first instance a constant fit parameter, which will be analysed later. A further empirical result is the shape of the M lines: for a vanishing $A - B$ spacing, they have a Gaussian line shape and for a large $A - B$ spacing, they are approximately Lorentzian.

These two results will be analysed below in terms of the model of **motional or exchange narrowing**, which was originally developed by Anderson [12] as well as by Kubo and Tomita [13]. This model is the basis of many methods in magnetic resonance, in particular in nuclear-spin resonance. It was treated in detail theoretic-

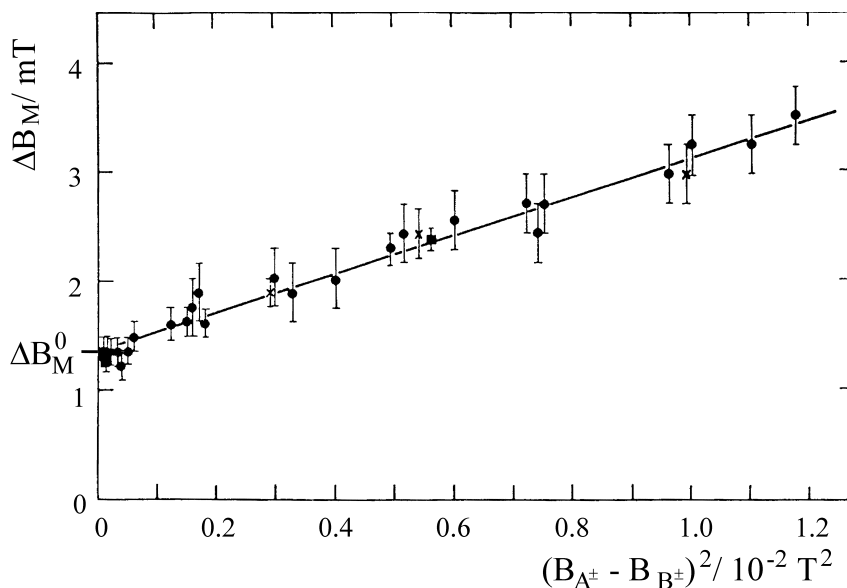


Fig. 7.16 The width ΔB_M of the ESR lines from the mini-excitons in a naphthalene crystal as a function of the square of the line spacing $(B_{A^+} - B_{B^+})$ or $(B_{A^-} - B_{B^-})$ of the ESR lines of the isolated molecules. ΔB_M is the total width of the derivative of the ESR lines at the points of their extreme values (distance between the

inflection points). ΔB_M^0 is the minimum M linewidth; it is observed for crystal orientations at which the fine-structure components of the isolated molecules have the same resonance fields, that is at $(B_{A^+} - B_{B^+}) = (B_{A^-} - B_{B^-}) = 0$ (see e.g. Fig. 7.4, $\alpha = 115^\circ$). From [4].

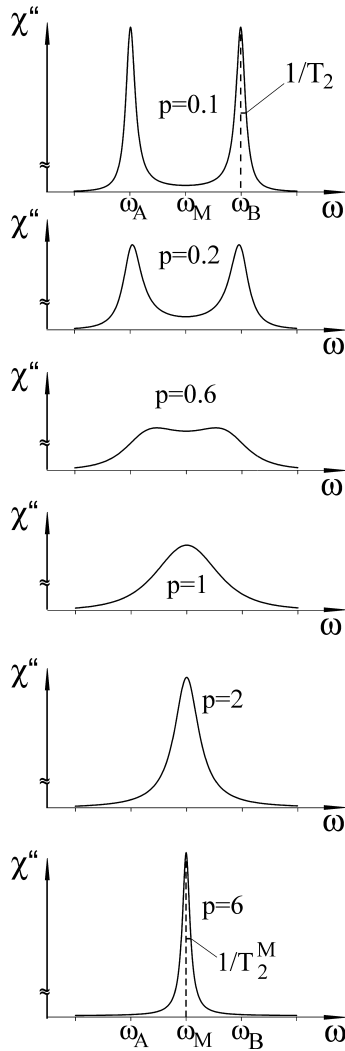


Fig. 7.17 The lineshape of ESR lines for a purely incoherent motion of the excitation energy between *A* and *B*. ω_A and ω_B are the eigenfrequencies of the localised states. The jump probability *P* between *A* and *B* is given in units of $1/2 (\omega_A - \omega_B)$. From [14], [15].

cally by Reineker and Haken [14, 15] for application to the ESR of mini-excitons and makes the following statements:

When a system of molecules is either in the state *A* or in the state *B* and these two states are each characterised by a frequency ω_A or ω_B , one then observes two separate spectral lines when the lifetimes or the correlation times τ_c of the states *A* and *B* are arbitrarily long (Fig. 7.17). The linewidths of the spectral lines are then determined by the transverse relaxation times T_2 : $\Delta\omega = 1/T_2$. When an incoherent dynamic process permits exchange or hopping between the two states, this causes a shortening of the correlation times of the isolated states *A* and *B* and thus a broadening of the lines from *A* and *B*. For a large exchange or hopping frequency, the two-line spectrum becomes a single-line spectrum, when the hopping frequency

is roughly equal to the difference frequency $\omega_A - \omega_B$. (The cause of the vanishing spectral resolution is intuitively clear: the frequency of a periodic motion, here the beat frequency $\omega_A - \omega_B$, can no longer be measured when the lifetime or the correlation time becomes shorter than its period, here the period $2\pi/(\omega_A - \omega_B)$ of the beats.) For a further increase in the hopping frequency, the single line, termed an exchange-narrowed line, becomes still narrower. Its linewidth $1/T_2^M$ is then given by the classical formula for motional narrowing:

$$1/T_2^M = \frac{(\omega_A - \omega_B)^2}{8P}. \quad (7.12)$$

In this expression, P is the jump probability per unit time for a jump from A to B .

With mini-excitons, we have an example of the rare case that both the spacing $\omega_A - \omega_B$ and also the linewidth $\Delta\omega_M$ of the exchange-narrowed M line can be varied continuously and can be simultaneously measured: $\omega_A - \omega_B$ follows from the spacings $A^+ - B^+$ and $A^- - B^-$ (cf. Fig. 7.3), and can be varied by rotating the crystal in a magnetic field (see Fig. 7.4). $\Delta\omega_M$ follows from ΔB_M (Fig. 7.16). With the exception of the constant part of the linewidths, ΔB_M^0 , the experimental result (Eq. (7.11)) and the theoretical width of the exchange-narrowed line (Eq. (7.12)) are formally identical: the linewidth of the mini-exciton ESR line increases quadratically with the $A - B$ spacing (Fig. 7.16). From these experimental results, we find the $A - B$ jump probability within the naphthalene triplet mini-exciton at 4.2 K to be $P_{4.2K} = 1.5 \cdot 10^{11} \text{ s}^{-1}$. Defining the correlation time τ_c by $\tau_c = 1/2P^{-1}$, then we have

$$\tau_c^{4.2 \text{ K}} = 0.3 \cdot 10^{-11} \text{ s}.$$

Compared with the exchange frequency $\omega_{AB} = 2I_{AB}/\hbar$ ($2I_{AB}$ is the Davydov splitting), the jump probability is smaller: $\hbar P/2I_{AB} = 0.32$. The energy and spin exchange in the mini-exciton must therefore be considered to be an incoherent process even at 4.2 K. At high temperatures ($T \gg 4.2 \text{ K}$), the mini-excitons are not observable, since they can then be thermally activated into the excitonic band of the host crystal.

The constant part of the linewidth, $\Delta\omega_M^0$ (or ΔB_M^0), and the Gaussian lineshape for a small $A - B$ spacing, i.e. for a small difference in the fine structure of the isolated molecules A and B , mean that the M lines are also inhomogeneously broadened. The reason for this broadening is the hyperfine structure (hfs). In the case discussed here, with many nuclei (protons) involved and an anisotropic hyperfine coupling, the hfs in the ESR spectra of the isolated molecules A and B is maximal for an orientation of \mathbf{B}_0 along the molecular principal axes, and even then it is only partially resolved; for all other field directions it is unresolved. The envelope curve of the ESR lines is then approximately Gaussian in shape and has a linewidth of $\Delta\omega_A$ or $\Delta\omega_B$.

In the mini-exciton, the difference of the fine structure averages to an arbitrarily narrow value when it becomes very small, that is when the $A - B$ spacing is negligible. This process of motional or exchange narrowing of the fine structure was analysed above. If the two molecular partners A and B of all the mini-excitons had

one and the same nuclear spin configuration, the M line of width ΔB_M^0 would be extremely sharp. Since however each molecule in the $A-B$ pair has its individual nuclear spin configuration, the two Gaussian ESR lineshapes of the molecules A and B are folded during the averaging, because the correlation times of the nuclear spins are orders of magnitude longer than the inverse jump probability P^{-1} for the mini-excitons (see above): the hyperfine structure of the mini-excitons is not completely averaged out. At a very low temperature ($T = 1.34$ K), it can even be spectrally resolved [16]. Only the second moment $\langle \Delta B^2 \rangle$ is smaller. As one can readily understand, this folding process leads to a new Gaussian distribution and to a linewidth $\Delta \omega_M^0$ which is reduced by a factor $1/\sqrt{2}$.

The reduction of the inhomogeneous linewidth follows from Van Vleck's calculation of the second moment $\langle \Delta B^2 \rangle$. It states that $\langle \Delta B^2 \rangle$ is proportional to N^{-1} ; N is here the number of nuclear spins. In an $A-B$ pair, the number of nuclear spins is doubled in comparison to an isolated molecule. Therefore, the inhomogeneous linewidth is reduced by the factor $1/\sqrt{2}$. The experimental values in naphthalene confirm this interpretation: in the immediate neighbourhood of the $A-M-B$ crossing points ($\alpha = 120^\circ$ in Fig. 7.4), the experimental value for the ratio of the linewidths of the mini-excitons to those of the isolated molecules is $\Delta B_M/\Delta B_{AB} = 1/1.6$. The width ΔB_M^0 is thus an additional confirmation of the model for a mini-exciton: it consists of the two molecules in a unit cell. At higher $N\text{-}h_8$ concentrations ($x = 10\%$), $A-A-B$ and $A-B-B$ mini-excitons have also been observed [4].

7.5

Triplet Excitons

Triplet excitons have been investigated by ESR in several organic molecular crystals. Here, we take as a typical example the anthracene and naphthalene crystals [17–18], as well as 1,4-dibromonaphthalene crystals [20, 21].

7.5.1

Anthracene and Naphthalene Crystals: Two-dimensional Triplet Excitons

In non-doped anthracene crystals, as in non-doped naphthalene crystals at $T = 300$ K, two sharp Lorentzian ESR lines from excitons are observed (Figs. 7.18 and 7.21). They have, in complete analogy to the M lines of mini-excitons, a large and anisotropic fine structure (Fig. 7.19). The fine-structure constants of the triplet excitons in the anthracene crystal are $D^*/hc = -0.00575$ cm^{-1} and $E^*/hc = +0.0330$ cm^{-1} . The choice of axes is here the same as for the mini-excitons (cf. Fig. 7.11): $\mathbf{z}^* \equiv \mathbf{b}$. From the measurements, the angle $\angle(\mathbf{x}^*, \mathbf{a}) = 27.25^\circ$ is determined. With the methods treated in Sect. 7.4, this yields the fine-structure constants of the isolated anthracene molecule at room temperature, $D/hc = +0.0694$ cm^{-1} and $E/hc = -0.00836$ cm^{-1} . (The small deviations from the values obtained for isolated anthracene molecules in a single-crystal matrix (see

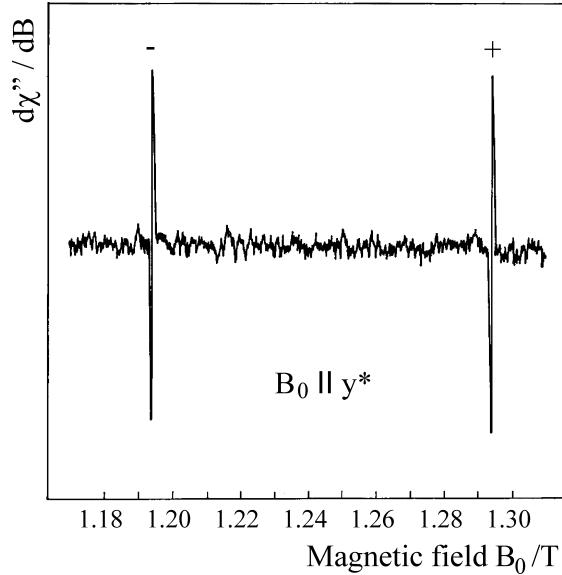


Fig. 7.18 The ESR spectrum of triplet excitons in an anthracene crystal at $T = 300$ K. $\omega = 2\pi \cdot 35$ GHz. For y^* , see Fig. 7.11. After [17].

Table 7.3) are not surprising, since the fine-structure constants are somewhat dependent on the local environment of the molecules.) In complete analogy to the mini-excitons, the width of the Lorentzian exciton ESR lines increases quadratically with the spacing of the ESR lines of the associated isolated molecules A and B (Fig. 7.20). The latter can, to be sure, not be observed directly, since in the non-doped crystal only excitons but not isolated molecules can be excited; however, their fine structure and thus the spacing of their ESR lines can be calculated unambiguously. The quantitative evaluation of the anisotropy of the ESR linewidth (Fig. 7.20) using the method described in Sect. 7.4 yields the correlation time $\tau_{c,\text{exc}}$ in a pure anthracene crystal at room temperature:

$$\tau_{c,\text{exc}}^{300\text{ K}} = 3.6 \cdot 10^{-12} \text{ s}.$$

From this, we find the jump rate $P_{300\text{ K}}^{\text{anthracene}} = 1.4 \cdot 10^{11} \text{ s}^{-1}$ and the diffusion coefficient D_{ab} for two-dimensional, incoherent diffusion of the triplet excitons in the $(a-b)$ plane of the anthracene crystal:

$$D_{ab} = \frac{1}{2} l^2 P = 1.9 \cdot 10^{-4} \text{ cm}^2/\text{s}.$$

Here, $l = (1/2)\sqrt{a^2 + b^2} = 5.24 \text{ \AA}$ was used. The value obtained in this way for the diffusion coefficient is in good agreement with that obtained from optical experiments, $D_{aa} = 1.8 \cdot 10^{-4} \text{ cm}^2\text{s}^{-1}$ and $D_{bb} = 1.5 \cdot 10^{-4} \text{ cm}^2\text{s}^{-1}$.

Independently of the technique of electron spin resonance, the influence of the triplet excitons on the nuclear-spin relaxation of the protons in anthracene

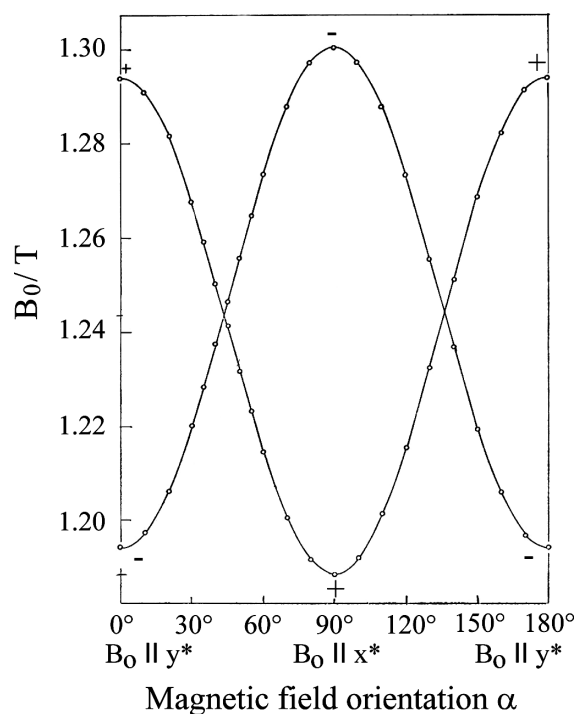


Fig. 7.19 The angular dependence of the ESR resonance fields B_0 for triplet excitons in anthracene crystals on rotating \mathbf{B}_0 in the plane $\mathbf{b} = 0$. $\omega = 2\pi \cdot 35$ GHz, $T = 300$ K. After [17].

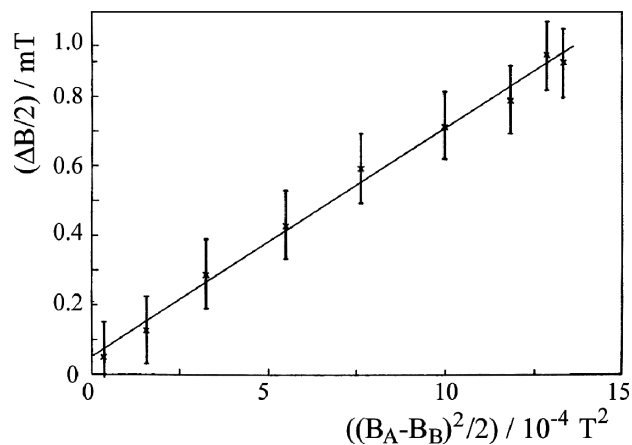


Fig. 7.20 The half-width $\Delta B/2$ of the ESR transitions belonging to the triplet excitons in anthracene crystals as a function of the square of the spacing of the corresponding calculated resonance fields of the isolated molecules. The definition of ΔB is given in Fig. 7.21. From [17].

crystals allows the hopping rate of triplet excitons to be determined, yielding $\tau_c = (5 \pm 1) \cdot 10^{-12}$ s [19]. The spin-lattice relaxation of protons in an anthracene crystal which was not optically excited is very slow (e.g. several hours at $B_0 = 25$ mT and $T = 300$ K). From the time dependence of the hyperfine interaction with the triplet excitons, it becomes considerably faster. The dependence of this effect on the applied magnetic field provides the value quoted above. It agrees within the error limits with the value found from the ESR spectra.

Taking the lifetime of the triplet excitons to be $\tau \geq 10$ ms, we find the mean squared displacement or diffusion length L for triplet excitons in anthracene crystals at room temperature to be

$$L = \sqrt{2D\tau} = 20 \mu\text{m}.$$

It is thus about 1000 times longer than that of singlet excitons in anthracene crystals (see Sect. 6.9.1), and therefore makes energy transfer via the long-lived triplet states possible over long distances, i.e. even to traps or reaction centres whose concentrations are very low.

The large mean squared displacement can by the way explain the small residual linewidth of the triplet ESR lines in a natural way (for small $A - B$ spacing); this was also observed for the triplet excitons in naphthalene crystals (Fig. 7.21). It is due to the complete averaging-out of the hyperfine structure, because the number N of molecules over which the average is carried out is not 2, as for the mini-excitons, but rather is very large ($N \gg 1$). The second moment is then not reduced by the factor $1/2$, as for the mini-excitons, but instead by the factor $1/N$. The exciton ESR linewidth is therefore narrowed in relation to the linewidths of the isolated

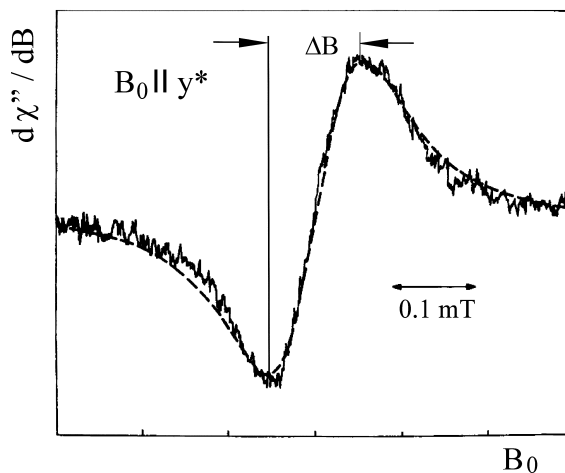


Fig. 7.21 The narrow ESR line from triplet excitons in a naphthalene crystal. The dashed curve indicates a Lorentzian line shape. $T = 300$ K, $\omega = 2\pi \cdot 35$ GHz, $B_0 || y^*$ (see Fig. 7.19). From [17].

molecules by a factor of $1/\sqrt{N}$; so strongly, that it is limited only by the exchange narrowing of the fine structure.

7.5.2

Dibromonaphthalene Crystals: coherent, one-dimensional Triplet Excitons

The dibromonaphthalene (DBN) crystal differs in its crystal structure (Fig. 2.14) considerably from the structure of the polyacene crystals (Fig. 2.10): the unit cell of DBN contains eight molecules, which belong to two non-equivalent sublattices I and II. The excitation energies of the triplet excitons in the sublattices I and II differ by 50 cm^{-1} . At low temperatures, therefore, only the excitons in one of the sublattices are excited. Each sublattice consists of linear stacks of DBN molecules along the c axis of the crystal. The exciton transport along this stacking axis is also predominant: the triplet excitons in DBN crystals are quasi-one-dimensional excitons.

Figure 7.22 shows the ODMR and the ESR signals from a DBN crystal at $T = 1.4 \text{ K}$. The ODMR signals were detected via the 0,0 transition of the excitonic phosphorescence from ($T_1 \rightarrow S_0$); it is clearly separated spectrally from the 0,0 transition of localised triplet states. In an applied magnetic field B_0 , the ($T_1 \rightarrow S_0$)–0,0 transition is furthermore split into its three Zeeman components, which were used individually in the ODMR experiment for detection of the signals [20, 21].

At higher temperatures, e.g. at room temperature, the exciton states of both sublattices I and II are occupied in the steady state. Since I and II are magnetically not equivalent due to differing molecular orientations leading to different fine structures, they can be observed separately in the ESR spectrum. Figure 7.23 shows a characteristic portion of the ESR spectra at room temperature for three different orientations; only for $B_0 \parallel a^*$ are I and II equivalent, for reasons of symmetry. Rotation by even a small angle causes a separation of the ESR transitions from I and II.

From the analysis of the ESR line shape and width using the model of motional narrowing, one obtains the following results for the dynamics of the quasi-one-dimensional triplet excitons in DBN:

- At $T < 16 \text{ K}$, the triplet exciton motion within the one-dimensional stacks is coherent and is determined by the exchange integral $I_{AA} = I_{BB} = 7 \text{ cm}^{-1}$. This corresponds to an exchange frequency of $\omega_{AA} = 2 I_{AA}/\hbar = 2.7 \cdot 10^{12} \text{ s}^{-1}$. For $T > 16 \text{ K}$, the exciton motion within the stacks becomes increasingly incoherent.
- The hopping probabilities between the two one-dimensional stacks in sublattices I and II are found from the analysis of the ESR spectra at room temperature to be $P_{I,II} = 1.6 \cdot 10^8 \text{ s}^{-1}$ and $P_{II,I} = 2.8 \cdot 10^8 \text{ s}^{-1}$. Their ratio is about the same as the Boltzmann factor, $\exp(-\Delta E/kT) = 0.8$ at $T = 300 \text{ K}$, and the energy difference between I and II is $\Delta E/\hbar c = 50 \text{ cm}^{-1}$. The incoherent motion of the triplet excitons between the one-dimensional stacks is thus at least 1000 times slower than that within the stacks: the triplet excitons in DBN crystals are therefore indeed one-dimensional.

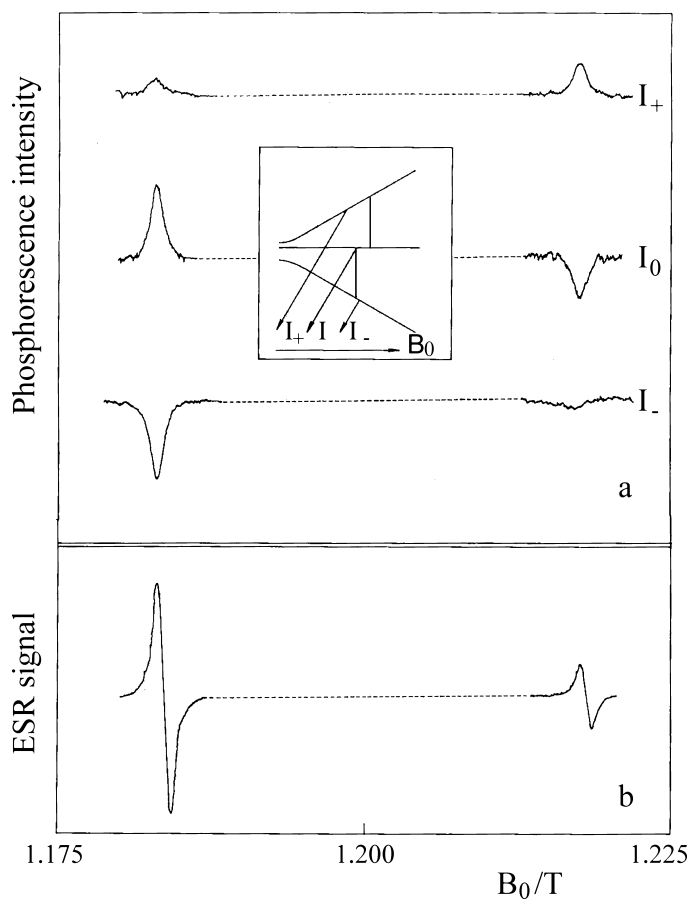


Fig. 7.22 ODMR and ESR of triplet excitons in the dibromonaphthalene (DBN) crystal. $T = 1.4$ K, $\omega = 2\pi \cdot 35$ Ghz. (a) The intensities I_+ , I_0 and I_- of the three individual Zeeman components of the 0,0 transition of the $T_1^{\text{exc}} \rightarrow S_0$ phosphorescence at $20\,192\text{ cm}^{-1}$ were measured as functions of the applied magnetic field B_0 for constant microwave power. (b) The ESR spectrum measured with the usual microwave detection. After [20].

7.6

Optical Spin Polarisation (OEP)

Optical electron spin polarisation (OEP) is the term used to describe a non-Boltzmann distribution of the populations of the three zero-field or Zeeman components of an optically-excited triplet state. This non-thermal equilibrium can be a stationary or a non-stationary state. The optical excitation, that is e.g. the UV excitation, must be neither narrow-band nor polarised, and at low temperatures, OEP is the normal case for most triplet states in organic π -electron systems. The OEP is

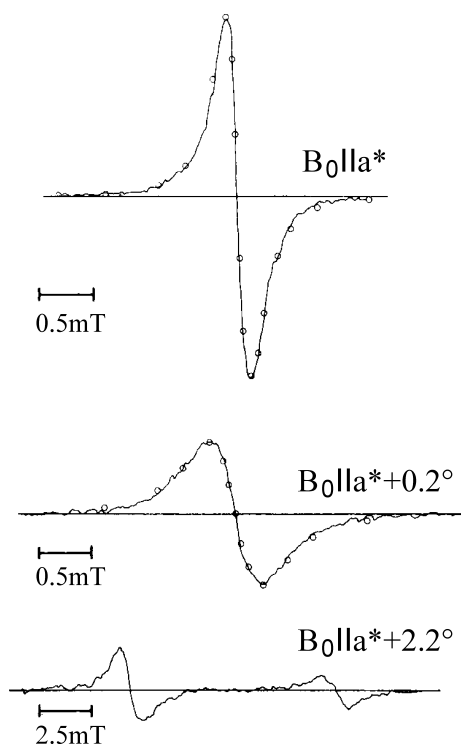


Fig. 7.23 A portion of the ESR spectrum of DBN triplet excitons at $T = 300$ K for three neighbouring orientations of the applied magnetic field \mathbf{B}_0 . The splitting for $\mathbf{B}_0 \parallel (\mathbf{a}^* + 2.2^\circ)$ indicates the two non-equivalent sublattices I and II. The circles represent a Lorentzian lineshape. From [21].

primarily due to symmetry conservation in intersystem crossing processes, which are in turn caused by the spin-orbit coupling between the singlet system and the triplet system. Each of the three zero-field components has its individual occupation probability, lifetime, and phosphorescence probability. When the spin-lattice relaxation probability is not sufficient to equalise these differences, OEP results. This is usual at low temperature, but is also occasionally the case at higher temperatures.

The direct (and the first) experimental detection of this non-thermal population of the triplet components was the observation of **stimulated emission** of microwaves from one of the two $\Delta m = 1$ ESR transitions in an applied magnetic field ($\mathbf{B} \neq 0$). Figure 7.24 shows the ESR spectrum of the N-h₈ guest molecules in an N-d₈:0.2% N-h₈ mixed crystal at $T = 4.2$ K [22,23], and Fig. 7.25 gives the ESR spectrum of triplet excitons in a non-doped and in a doped naphthalene crystal at room temperature [24]. In the ESR spectrum of the isolated N-h₈ molecules (Fig. 7.24), the two low-field transitions corresponding to the two molecular orientations *A* and *B* take place via stimulated emission (Em) of microwaves and the two high-field transitions via absorption (Abs). In the triplet exciton ESR spectrum of the doped naphthalene crystal (Fig. 7.25), the low-field transition occurs likewise via stimulated emission and the high-field transition via absorption of microwaves. Which of the two $\Delta m = 1$ transitions is emissive and which is absorptive depends on the orientation of the crystals in the applied magnetic field. But the fact that the

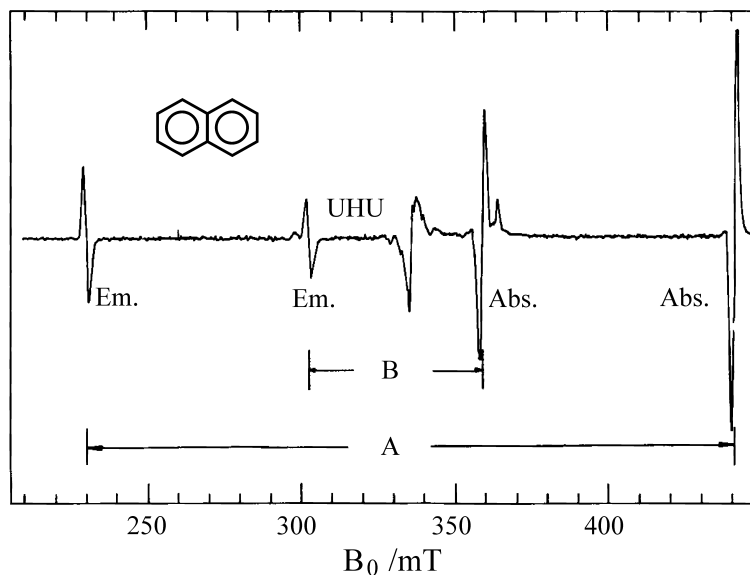


Fig. 7.24 The ESR spectrum of the T_1 state of a naphthalene- d_8 : 0.2% naphthalene- h_8 mixed crystal at $T = 4.2$ K, $\nu = 9.4$ GHz. The ESR signal is as usual the first derivative of the microwave absorption spectrum. In the centre of the signal UHU, which is due to free radicals in the sample holder and not to an optically-excited state, the first derivative is

positive. The UHU signal is an ESR *absorption* signal. Therefore, the two ESR lines denoted by Abs are also *absorption* signals. At the centres of the two ESR signals denoted by Em, however, the first derivative is negative; thus, these two ESR transitions of the T_1 spectrum correspond to stimulated *emission* of microwaves. From [22].

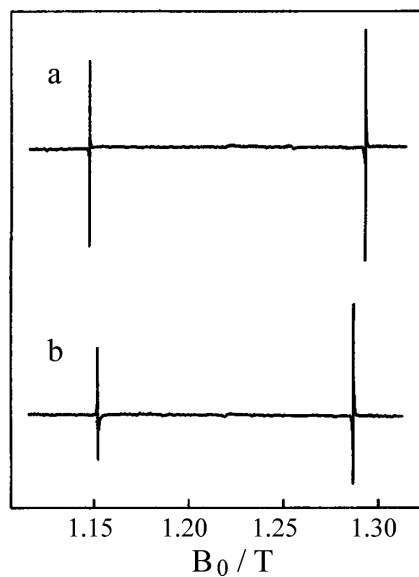


Fig. 7.25 Triplet exciton ESR lines from naphthalene crystals at room temperature and $\nu = 35$ GHz. a) $B_0 \parallel \gamma^*$, non-doped crystal; the different intensities result from a weak optical spin polarisation. b) Naphthalene + 0.5% quinoxaline, with $B_0 \parallel \gamma^* + 10.5^\circ$; the low-field transition takes place by stimulated emission, but the high-field transition exhibits absorption of microwaves. From [24].

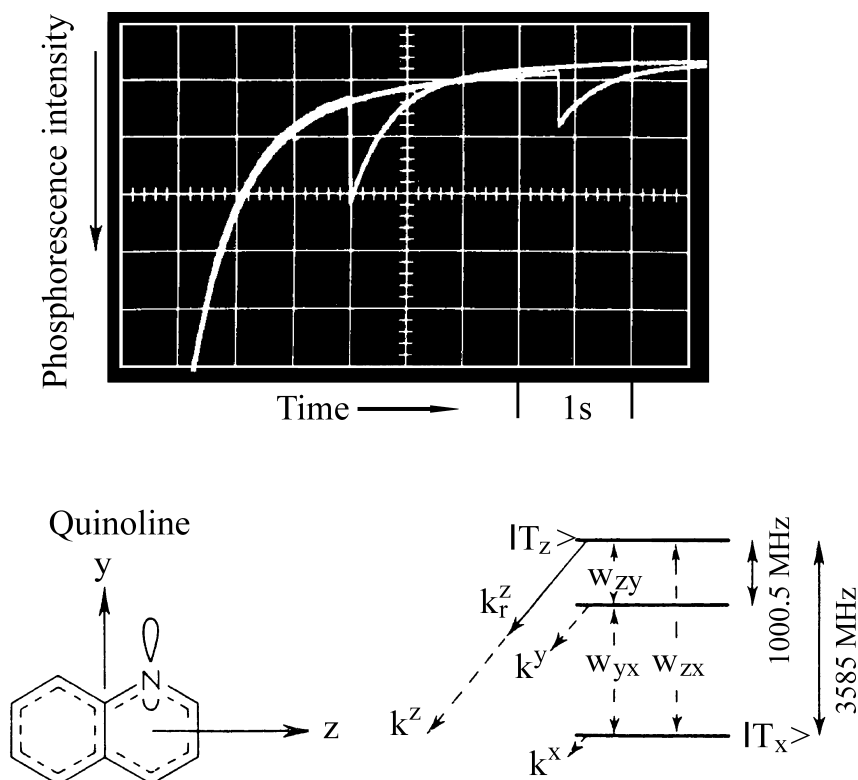


Fig. 7.26 Microwave-induced delayed phosphorescence. Above: two superposed phosphorescence-intensity decays of quinoline in a durene crystal at $T = 1.35$ K and $\mathbf{B}_0 = 0$. The phosphorescing triplet component is $|T_z\rangle$. The delayed phosphorescence signals, delayed in the first experiment by ca. 2 s and in the second by ca. 4 s, are produced by resonant 1000.5 MHz pulses, which saturate the zero-field transition $T_y \leftrightarrow T_z$ at these times after the end of the UV excitation and thus

pump population from the longer-lived state $|T_y\rangle$ into the phosphorescing state $|T_z\rangle$. They are readily visible as flashes of light to the naked eye. Time scale: 0.5 s per scale unit. Below: zero-field splitting of the T_1 state of quinoline. k^u ($u = x, y, z$) are the rate constants for the decay of the zero-field component $|T_u\rangle$; k_r^u are the phosphorescence probabilities; w_{uv} the spin-lattice relaxation probabilities. After [25].

three triplet components are not in thermal equilibrium when stimulated emission is observed, and instead that a population inversion is present between in each case two of the three components, is evident.

A second direct optical-detection method for selective population and depopulation is **microwave-induced delayed phosphorescence** in zero field ($\mathbf{B}_0 = 0$) [25]. Figure 7.26 shows the phosphorescence intensity from quinoline in a durene (tetramethyl benzene) host crystal at $T = 1.35$ K as a function of the time after the end of the UV excitation. The phosphorescing zero-field component here is $|T_z\rangle$. Its lifetime is considerably shorter than those of the other two zero-field components, from which furthermore no phosphorescence is emitted. If the zero-field transition

$T_y \leftrightarrow T_z$ is rapidly saturated by a short resonant microwave pulse (1000.5 MHz) after the end of the UV excitation, thus when the radiative component $|T_z\rangle$ has already mostly decayed, then the radiative component $|T_z\rangle$ will again be populated from the non-radiative component $|T_y\rangle$, thus inducing renewed phosphorescence. With a still longer delay of the microwave pulse, the increase in the phosphorescence intensity is smaller. From this, the lifetime of $|T_y\rangle$ can be derived. With this method, the decay constants of all three zero-field components can be determined.

The physical reason for the selective population and depopulation of the three triplet components are selection rules for the intersystem crossing processes, i.e. the processes of converting singlet states into triplet states and *vice versa*. The intersystem crossing is made possible by spin-orbit coupling. In hydrocarbons and also in azo-aromatics, it is weak owing to the small nuclear charges, but nevertheless it mixes a small portion of singlet character into the triplet states and *vice versa*. The Hamiltonian H_{SO} of the spin-orbit coupling [26] is invariant to permutation of the axes x, y , and z and it has non-vanishing matrix elements only between states whose overall symmetry is identical to that of the product orbit \otimes spin. In the intersystem crossing processes, the overall symmetry of the states is thus conserved. The singlet states S_i have a well-defined orbital symmetry, $\Gamma_O(S_i)$, which is determined by the spatial wavefunction $|S_i\rangle$. The symmetry of the three triplet

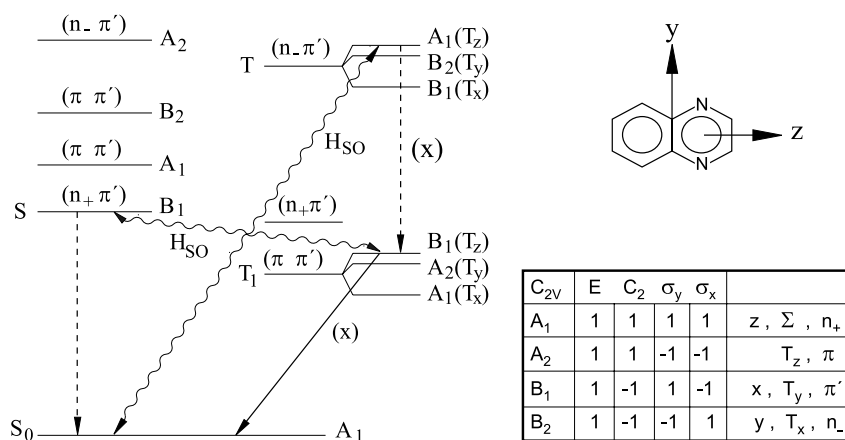


Fig. 7.27 The lowest electronic states of quinoxaline and its overall symmetries (orbit \otimes spin) A_1, A_2, B_1 , and B_2 in the group C_{2v} . The spin-orbit couplings marked by wavy lines indicate the couplings H_{SO} between the pairs of singlet and triplet states which are important for the phosphorescence. Only states of the same overall symmetry can be mixed by H_{SO} . The phosphorescence is from the x -polarised radiative $B_1 - A_1$ transition $T_z \rightarrow S_0$. The dashed lines indicate the allowed $B_1 - A_1$ dipole transitions within the singlet or the triplet terms. The symmetry properties of

the molecular orbitals n_+, n_-, π and π' , the spin functions $|T_x\rangle, |T_y\rangle$, and $|T_z\rangle$ of the triplet states and $|\Sigma\rangle$ of the singlet states as well as the polarisation directions x, y and z of the phosphorescence radiation are given in the character table. Here, π and π' are the highest bonding and the lowest antibonding π orbitals; n_+ and n_- are linear combinations of the non-paired ("lone pair") sp^2 hybrid orbitals of the two nitrogen atoms N_1 and N_4 :

$$n_{\pm} = \sqrt{\frac{1}{6}}[(s + \sqrt{2}p_y)N_1 \pm (s - \sqrt{2}p_y)N_4].$$

From [27].

components T_{ju} is found from the products $\Gamma_O(T_j) \otimes \Gamma_S(T_u)$. Here, $\Gamma_O(T_j)$ are the orbital symmetries and $\Gamma_S(T_u)$ with ($u = x, y, z$) are the spin symmetries. The latter are different, because the three spin functions $|T_u\rangle$ each transform like rotations around the u axis (see Fig. 7.5). It is therefore to be expected that of the three matrix elements $\langle S_i | H_{SO} | T_j \cdot T_u \rangle$ for a particular state $|S_i\rangle$, at most one will be nonzero in each case and that the mixture of different singlet states into the triplet components $|T_{ju}\rangle$ varies in strength.

The selection rules for intersystem crossing were treated theoretically by van der Waals *et al.* [26] for selected molecules in detail. Figure 7.27 shows the particularly simple example of the energetically lowest electronic states of quinoxaline. The spin-orbit coupling mixes two pairs of singlet and triplet states in such a way that both contributions select the triplet component $|T_z\rangle$ as the radiative (phosphorescing) component.

For pure hydrocarbons, e.g. for naphthalene, there exist several pairs of singlet and triplet states with non-vanishing spin-orbit coupling, but here also, one triplet component ($|T_x\rangle$) is predominant in the phosphorescence. Both in the pure hydrocarbons as well as in the hetero-aromatics, the main contributions to the spin-orbit coupling result from states which contain a σ orbital. Contributions from states which contain only π orbitals are small enough to be neglected.

Figure 7.28 lists all the rate constants in zero field and in an applied magnetic field which must be experimentally determined in order to have a complete understanding of the dynamics of the triplet state and therefore a quantitative understanding of optical spin polarisation: the individual population rates s_u ($u = x, y, z$)

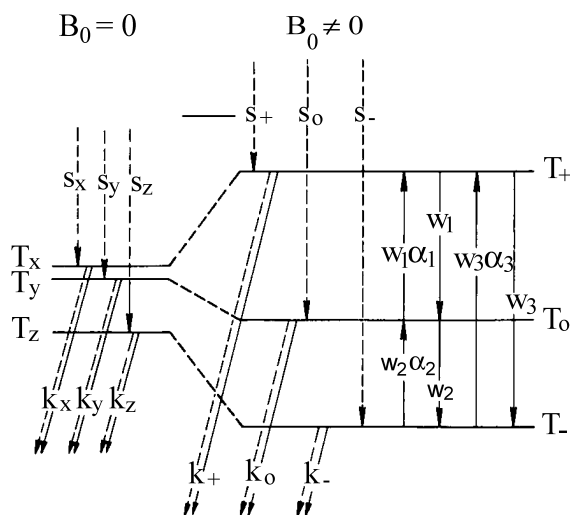


Fig. 7.28 Notation for the rate constants of the populations (s), the decays (k), and the spin-lattice relaxation (w) of the triplet components T_u ($u = x, y, z$) in zero field ($B_0 = 0$) and T_i ($i = +, 0, -$) in an applied magnetic field ($B_0 \neq 0$). α_i are the Boltzmann factors. After [28].

and s_i ($i = +, 0, -$), the individual depopulation rates k_u and k_i , which each consist of a non-radiative part, k^{nr} , and the radiative part (the phosphorescence probability) k^r , with ($k = k^r + k^{nr}$), and the spin-lattice relaxation rates w . There is a simple relation connecting the rate constants in zero field to those in a magnetic field, because the states $|T_i\rangle$ in a magnetic field are linear combinations of the zero-field states $|T_u\rangle$: $|T_i\rangle = \sum_u c_{iu} |T_u\rangle$. The mixing coefficients c_{iu} are found uniquely from the solution of the secular equations defined in Eq. (7.9). They are complex and depend on the magnitude and orientation of \mathbf{B}_0 . The relation between the rate constants in zero field and those in a magnetic field for the decay rates are thus given by:

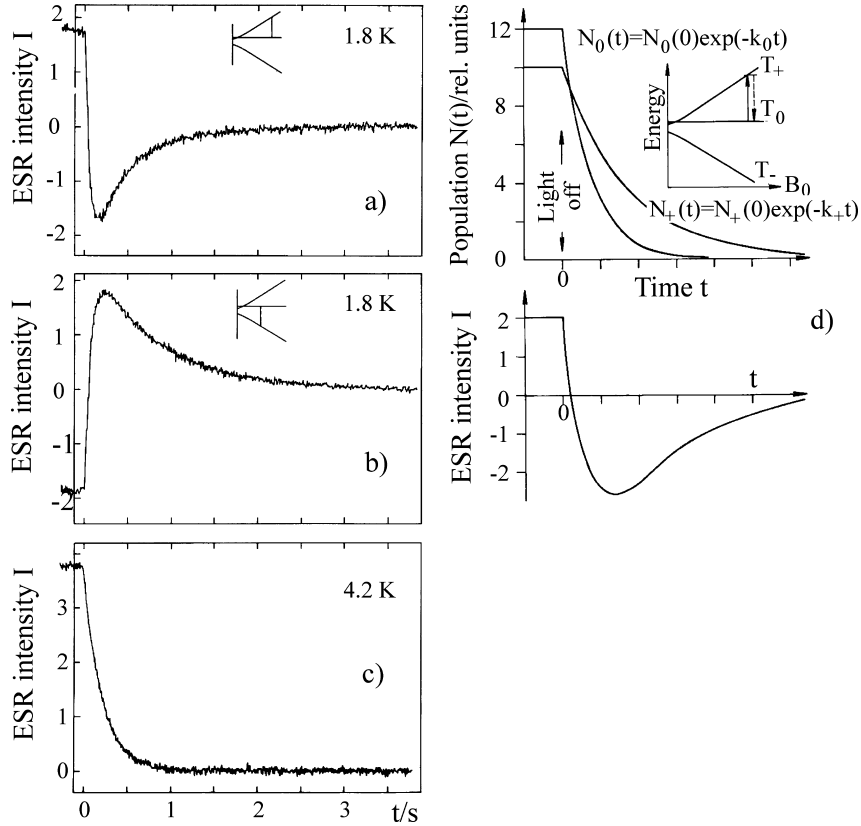


Fig. 7.29 a) and b) Decay of the signal intensities I of the two fine-structure components of the ESR spectrum of quinoxaline in a naphthalene-d₈ host crystal at $T = 1.8$ K, and $\mathbf{B}_0 \parallel x$ after the end of the UV excitation at $t = 0$. $I > 0$ corresponds to absorption, $I < 0$ to stimulated emission of microwaves. c) $T = 4.2$ K. d) Model for a). N_+ , N_0 are the populations of the Zeeman states $|T_+\rangle$ and $|T_0\rangle$; k_+ and k_0 are the decay-rate constants for the two Zeeman states. The

difference of the populations $\Delta N = N_0 - N_+$ is proportional to the ESR intensity I of the $\Delta m_s = 1$ transition $T_+ \leftrightarrow T_0$. In a steady state, $\Delta N (t \leq 0)$ is positive; shortly after the end of the excitation, ΔN becomes negative. Therefore, shortly after the end of the excitation, the steady-state ESR absorption signal becomes a stimulated ESR emission signal. This time dependence was observed in a). From [23].

$$k_i = \sum_u |c_{iu}|^2 k_u \quad (7.13a)$$

and for the population rates,

$$s_i = \sum_u |c_{iu}|^2 s_u \quad (7.13b)$$

(see e.g. [27], [28]).

An example of a quantitatively-analysed experimental result for these constants is shown in Fig. 7.29: in mixed crystals of naphthalene-d₈ : 0.1% quinoxaline, the ESR transition $T_+ \leftrightarrow T_0$ for the field direction $\mathbf{B}_0 \parallel x_{\text{quinoxaline}}$ and at a temperature $T = 1.8$ K is an absorption signal in the stationary state (Fig. 7.29a), while the transition $|T_0\rangle \leftrightarrow |T_- \rangle$ in the stationary state exhibits stimulated emission of microwaves (Fig. 7.29b). After the end of the UV excitation at $t = 0$, the absorption line temporarily becomes an emission line and *vice versa*. The interpretation of these results is simple (Fig. 7.29d): due to the negligible spin-lattice relaxation at $T = 1.8$ K, the three Zeeman components decay after the end of the UV excitation independently of one another, each with its own lifetime $\tau_i = k_i^{-1}$ into the S_0 ground state. Since the difference of the populations of the three states is directly proportional to the intensity of the ESR signals, their time dependence can be used to determine the individual lifetimes of the Zeeman components involved. In the case of the particular orientation $B_0 \parallel x$, the state is $|T_0\rangle = |T_x\rangle$, and one obtains directly from the measurements, e.g. the decay constant $k_0 = k_x$ and thus the lifetime of the zero-field constant $|T_x\rangle$ of quinoxaline.

Even at $T = 4.2$ K, the spin-lattice relaxation is so effective that the three triplet components are approximately in thermal equilibrium. Their populations then correspond roughly to the Boltzmann distribution and the two ESR lines thus decay with the same average lifetime of the states (Fig. 7.29c).

With these and similar experiments in zero field and also from the time dependence of the Zeeman components of the phosphorescence spectra in high magnetic fields ($B_0 = 5$ T) [30], the decay rates k_u , their radiative contributions k_u^r , and the relative occupation probabilities s_u could be determined. Table 7.4 contains the

Table 7.4 Rate constants for the population and depopulation of the three zero-field components $|T_u\rangle$, ($u = x, y, z$) of the quinoxaline triplet states in a N-d₈ : quinoxaline crystal. B_0 is the applied field at which the measurement was carried out. The rate constants in zero field can be uniquely computed from those measured in a magnetic field; see Eq. (7.13).

Overall decay rate constants/s ⁻¹			Occupation probabilities /%			Phosphorescence probabilities /%			B_0/T
k_x	k_y	k_z	s_x	s_y	s_z	k_x^r	k_y^r	k_z^r	
12	1	0.4	95	4	1				0.3
12	1	0.4				98	≤ 2	≤ 2	5
12.0	0.80	0.42	96.4	2.3	1.3	97.4	1.3	1.3	0

values for the example that was discussed above. An extensive table of these rate constants for a large number of different systems which have been investigated can be found in the article by Hausser and Wolf [29].

The differences in the population and depopulation rate constants and the phosphorescence probabilities of the three components of the triplet states form the basis of all the methods for **Optical Detection of Magnetic Resonance** in triplet states of π -electron systems. These methods were developed after the discovery of optical spin polarisation and extended to inorganic solids. The essential physical difference from the optical double resonance in atoms developed by Alfred Kastler is to be found in the selection mechanism: in optical double resonance, the polarisation of the resonant UV light, i.e. the symmetry of an applied field, is responsible for the selection. In optical spin polarisation, the selection is due to the spin-orbit coupling, and thus to an internal field.

7.7

Optical Nuclear-Spin Polarisation (ONP)

A well-known and important phenomenon in the area of nuclear-spin resonance (NMR) in gases, liquids, or solid samples is dynamic nuclear-spin polarisation (DNP) (see e.g. [M6]). This term refers to deviations of the nuclear magnetisation from its thermal-equilibrium value, thus a deviation from the Boltzmann distribution of the populations of the nuclear Zeeman terms, which is produced by optical pumping (Kastler [31]), by the Overhauser effect [32], or by the *effet solide* or *solid-state effect* [33]. In all these cases, the primary effect is a disturbance of the Boltzmann distribution in the electronic-spin system. In the Overhauser effect and the *effet solide*, this disturbance is caused for example by saturation of an ESR transition. Owing to the hyperfine coupling, a nuclear polarisation then results from coupled nuclear-electronic spin relaxation processes, whereby the polarisation of the electronic spins is transferred to the nuclear spins.

The optical electron-spin polarisation in triplet states (Sect. 7.6) can give rise to a non-equilibrium magnetisation of the nuclear spin system and thereby produce a deviation from the Boltzmann distribution of the nuclear Zeeman terms. This effect was discovered in anthracene crystals and was called **optical nuclear-spin polarisation (ONP)** [34]. The direct and historically first detection of ONP was the measurement of proton-spin relaxation with and without excitation of the triplet excitons (Fig. 7.30). The crystal is in this case magnetised at room temperature before the measurement in a high applied magnetic field (1.5 T). Thereafter, the applied field is reduced to a small value, here $B_p = 25$ mT, and the nuclear-spin magnetisation is measured in this field B_p by means of NMR as a function of time. It relaxes relatively slowly in the dark to its new thermal equilibrium value M_0 . When the triplet excitons are excited, i.e. under stationary UV irradiation, the nuclear magnetisation relaxes firstly faster and secondly towards a dynamic equilibrium value M_0^p , which differs in magnitude and direction from the thermal equilibrium

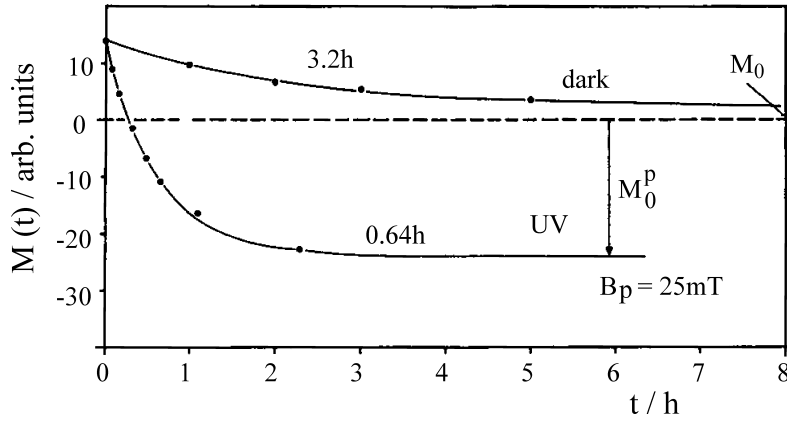


Fig. 7.30 Relaxation of the nuclear magnetisation $M(t)$ of an anthracene crystal after switching the polarising field from the value $B_0(t \leq 0) = 1.5$ T to a value $B_p(t > 0) = 25$ mT with and without UV irradiation for the excitation of the triplet excitons. M_0 is the thermal nuclear-spin polarisation, M_0^p is the nuclear-spin polarisation with optical pumping. After [34].

magnetisation M_0 , owing to the hyperfine coupling between the electronic spins and the nuclear spins (cf. Fig. 7.30).

Quantitatively, the characteristic parameter for ONP is either the amplification factor $V = M_0^p/M_0 - 1$, or the polarisation

$$p = (N_+ - N_-)/(N_+ + N_-). \quad (7.14)$$

Here, N_+ and N_- are the populations of the nuclear Zeeman terms $m_I = \pm 1/2$. V and p are strongly dependent on the magnitude and direction of B_p . As an example, Fig. 7.31 shows the equilibrium polarisation p_L on UV excitation of the triplet excitons in a fluorene- d_8h_{10} crystal which was doped with 1000 ppm of acridine [35], as a function of the orientation of the magnetic field, whose value was $B_p = 8$ mT. Aside from the apparent anisotropy, the absolute value of the maximum stationary-state polarisation, $p_L \approx 10^{-3}$, is notable. This value, which is not yet a saturated in terms of a possible higher UV intensity, that is a higher exciton density, corresponds to the thermal polarisation at room temperature in an applied magnetic field of 300 T or, at $B_p = 8$ mT, to a nuclear spin temperature of 8 mK. These two values show that ONP, when compared to thermal-equilibrium nuclear-spin polarisation, can be very effective. To be sure, this holds only for polarising fields up to about 100 mT, that is for field strengths in which the three components of the T_1 state are neither the pure zero-field states $|T_u\rangle$ ($u = x, y, z$) nor the nearly pure high-field states $|T_i\rangle$ ($i = +, 0, -$); instead, they are mixed electron spin states. In zero field and at high fields, ($B_p \gg D/g\mu_B$), the ONP vanishes. Hopes of being able to apply ONP in nuclear physics have thus far not been fulfilled.

The mechanism of ONP is based on the hyperfine coupling and on the selection rules for intersystem crossing. In detail, it is complicated. We refer the reader to the relevant literature, which is cited in the article by Hausser and Wolf [29].

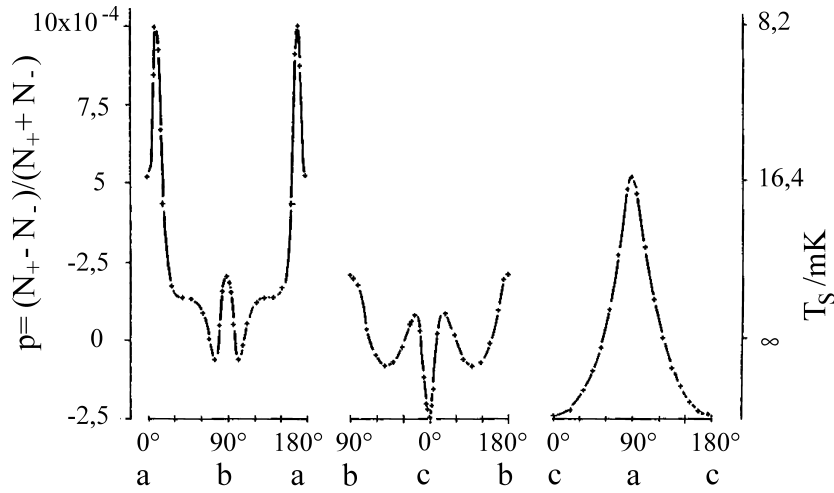


Fig. 7.31 The steady-state value of the optical nuclear-spin polarisation $p = p_L$ in a fluorene- d_8h_{10} crystal doped with acridine, measured at room temperature, as a function of the orientation of the polarising magnetic field whose value is $B_p = 8$ mT. p_L is the equilibrium polarisation, and T_S is the nuclear-spin temperature. From [35].

7.8

Perspectives

In contrast to inorganic semiconductors or insulators, the triplet states in organic molecular solids have an important and characteristic special property. They are as a rule the energetically-lowest excited states and have long lifetimes. We shall meet up with the triplet states again several times in later chapters of this book.

Problems

Problem 7.1. The magnetic dipole-dipole interaction:

Show explicitly that the fine structure of the triplet states which is due to the magnetic dipole-dipole coupling of two electrons is a specific property of molecules, but not of atoms. For example, the triplet state 3P_1 of the Hg atom has no zero-field splitting.

Problem 7.2. The fine structure of triplet excitons:

Compute explicitly, starting from the fine-structure constants D and E of the anthracene molecule (Table 7.3), the fine-structure constants D^* and E^* and the orientation of the principal axis x^* of the triplet excitons in the anthracene crystal (Fig. 7.15). **Hint:** First derive the spin Hamiltonian \mathcal{H}_s^{DD} in the form $\mathcal{H}_s^{DD} = \hat{S}F_0\hat{S}$. Here, $\hat{S} = \hat{s}_1 + \hat{s}_2$ is the sum of the spin operators of the two electrons 1 and 2, and

F_0 is the fine-structure tensor, which is diagonal in the principal-axis system of the molecule. Then compute the spin Hamiltonian of the exciton, $\mathcal{H}_{s,AB}$ with the aid of Eq. (7.10a).

Problem 7.3. The hopping time of triplet excitons:

In the ESR spectrum of pure anthracene crystals, one observes neither a hyperfine structure nor the fine structure of isolated molecules, but rather only the fine structure of the excitons, which is described by their spin Hamiltonian, $\mathcal{H}_{s,AB}$ (see Sect. 7.5.1). What follows from this observation for the motion of the excitons?

Problem 7.4. Absorption-detected magnetic resonance (ADMR):

In the method known as ADMR, the microwave transitions between the individual triplet sublevels are detected by means of a change in the optical absorption of the singlet ground state. This is based on a redistribution of the population between the three different triplet substates (zero-field states without, or Zeeman states with an external magnetic field) with different decay constants ("spin-polarisation"): if for example the spin population is pumped by microwave irradiation from a short-lived sublevel to a long-lived one, then the overall triplet population is increased, while the population of the singlet ground state decreases.

- Sketch an ADMR spectrum in which the change $\Delta I/I$ in the transmission of a sample at a fixed optical wavelength of observation is plotted versus the applied microwave frequency. Assume that there is always a redistribution of the population into a more rapidly decaying sublevel.
- Derive a linear relation between the relative transmission $\Delta I/I$ and the change in the fraction S_0 of molecules in the S_0 state.
- With a sample of the photosynthetic bacterium *Rhodobacter spaeroides* GA, an optical density of 0.23 is measured at 894 nm. In the ADMR-spectrum at 10 K, irradiation with a microwave frequency of 659 MHz (corresponding to the $D + E$ transition) produces a relative transmission change of -440 ppm. Calculate from this change ΔS_0 in the population of the S_0 state.

Literature

Monographs

- | | |
|---|--|
| <p>M1 C. P. SLICHTER, <i>Principles of Magnetic Resonance</i>, 3rd ed., Springer, Heidelberg (1990)</p> <p>M2 A. CARRINGTON and A. D. McLACHLAN, <i>Introduction to Magnetic Resonance</i>, Chapman and Hall, John Wiley and Sons, New York (1979)</p> <p>M3 S. P. McGLYNN, T. AZUMI, and M. KINOSHITA, <i>Molecular Spectroscopy of the Triplet State</i>, Prentice-Hall, Englewood Cliffs, New Jersey (1969)</p> | <p>M4 <i>The Triplet State</i>, edited by A. B. Zahlan <i>et al.</i>, Cambridge University Press (1967)</p> <p>M5 H. HAKEN and H. C. WOLF, <i>Molecular Physics and the Elements of Quantum Chemistry</i>, 2nd ed., Springer, Heidelberg (2004)</p> <p>M6 A. ABRAGAM, <i>The Principles of Nuclear Magnetism</i>, Oxford Clarendon Press (1961)</p> |
|---|--|

References

- 1 C. A. HUTCHISON and B. W. MANGUM, *J. Chem. Phys.* **29**, 952 (1958); *J. Chem. Phys.* **34**, 908 (1961)
- 2 L. KWIRAM, *Chem. Phys. Lett.* **1**, 272 (1967)
- 3 J. SCHMIDT and J. H. VAN DER WAALS, *Chem. Phys. Lett.* **2**, 640 (1968)
- 4 M. SCHWOERER and H. C. WOLF, *Molecular Crystals* **3**, 177 (1967)
- 5 C. A. HUTCHISON JR., J. V. NICHOLAS and G. W. SCOTT, *J. Chem. Phys.* **53**, 1906 (1970)
- 6 J. U. v. SCHÜTZ, F. GÜCKEL, W. STEUDLE and H. C. WOLF, *Chem. Phys.* **53**, 365 (1980)
- 7 A. H. FRANCIS and C. B. HARRIS, *Chem. Phys. Lett.* **9**, 188 (1971)
- 8 E. WASSERMANN, L. C. SNYDER and W. A. YAGER, *J. Chem. Phys.* **41**, 1763 (1964)
- 9 M. J. MOMBOURQUETTE, J. A. WEIL and D. G. MCGAVIN, *EPR-NMR User's Manual*, Dep. of Chemistry, University of Saskatchewan, Canada (2001)
- 10 Høgni WEIHE, Inst. of Chemistry, University of Copenhagen, The Program SIM (1998)
- 11 H. STERNLICHT and Harden M. MCCONNELL, *J. Chem. Phys.* **35**, 1793 (1961)
- 12 P. W. ANDERSON, *J. Phys. Soc. Jap.* **9**, 316 (1954)
- 13 R. KUBO and K. TOMITA, *J. Phys. Soc. Jap.* **9**, 888 (1954)
- 14 P. REINEKER and H. HAKEN, *Z. Physik* **250**, 300 (1972)
- 15 P. REINEKER, *Z. Naturforsch.* **29a**, 282 (1974)
- 16 H. HINKEL, H. PORT, H. SIXL, M. SCHWOERER, P. REINEKER and D. RICHARDT, *Chem. Phys.* **31**, 101 (1978)
- 17 H. HAARER and H. C. WOLF, *Molecular Crystals and Liquid Crystals* **10**, 359 (1970)
- 18 D. HAARER, D. SCHMID and H. C. WOLF, *Phys. Stat. Sol.* **23**, 663 (1967)
- 19 G. MAIER and H. C. WOLF, *Z. Naturforsch.* **23a**, 1068 (1968)
- 20 R. SCHMIDBERGER and H. C. WOLF, *Chem. Phys. Lett.* **16**, 402 (1972)
- 21 R. SCHMIDBERGER and H. C. WOLF, *Chem. Phys. Lett.* **25**, 185 (1974)
- 22 M. SCHWOERER and H. C. WOLF, in: *Magnetic Resonance and Relaxation*, edited by R. Blinc, North Holland Publishing Company (1967)
- 23 M. SCHWOERER and H. SIXL, *Chem. Phys. Lett.* **2**, 14 (1968); *Z. Naturforsch.* **24a**, 952 (1969)
- 24 D. HAARER and H. C. WOLF, *phys. stat. sol.* **33**, K117 (1969)
- 25 J. SCHMIDT, W. S. VEEMAN and J. H. VAN DER WAALS, *Chem. Phys. Lett.* **4**, 341 (1969)
- 26 W. S. VEEMAN and J. H. VAN DER WAALS, *Molecular Physics* **18**, 63 (1970)
- 27 J. H. VAN DER WAALS and M. S. DE GROOT, in: *The Triplet State*, edited by A. B. Zahlan, Cambridge University Press (1967); M. S. DE GROOT, I. A. M. HESSELMANN, J. SCHMIDT and J. H. VAN DER WAALS, *Molecular Physics* **15**, 17 (1968)
- 28 H. SIXL and M. SCHWOERER, *Chem. Phys. Lett.* **6**, 21 (1970); *Z. Naturforsch.* **25a**, 1383 (1970)
- 29 K. H. HAUSSER and H. C. WOLF, in: *Advances in Magnetic Resonance*, edited by J. S. Waugh, **Vol. 8**, 85, Academic Press, New York (1976)
- 30 A. HAMMER, M. SCHWOERER and H. SIXL, *Chem. Phys. Lett.* **5**, 434 (1970)
- 31 A. KASTLER, *J. Physique* **11**, 255 (1950)
- 32 A. W. OVERHAUSER, *Phys. Rev.* **92**, 411 (1953)
- 33 A. ABRAGAM and W. G. PROCTOR, *Comp. Rend.* **246**, 1258 (1958)
- 34 G. MAIER, U. HAEBERLEN, H. C. WOLF and K. H. HAUSSER, *Phys. Lett.* **25A**, 384 (1967); G. MAIER and H. C. WOLF, *Z. Naturforsch.* **23a**, 1068 (1968)
- 35 P. LAU, D. STEHLIK and K. H. HAUSSER, *J. Magn. Resonance* **15**, 270 (1974)

8

Organic Semiconductors

Many organic solids and polymers are perfect insulators and are used to a considerable extent technically as such. There is, however, also a large number of organic semiconductors. Furthermore, there are organic solids with a high dark conductivity or with a quasi-metallic conductivity (Chap. 9), as well as organic superconductors (Chap. 10).

Anthracene crystals and all comparable organic molecular crystals and organic solids which consist of only one type of molecules with conjugated π -electron systems and are highly pure, are **insulators** at room temperature and below. This is however only true when the applied electric voltage, i.e. the “external” electric field strength, is low and when the organic solid is not irradiated by light, electrons, or other particles. It is also true of non-crystalline organic solids or polymers with conjugated π -electron systems, e.g. also for non-doped polyacetylene. All these organic crystals or solids only become conductors of electric current – and are thus **semiconductors** – when excess charge carriers are either produced by the internal photoeffect or are injected by high applied voltages. If, however, such organic crystals or solids contain defects, impurities, dopant atoms, or guest molecules at low concentrations, they can become conductors (semiconductors) at moderate temperatures. The cause of this is that the defects can be thermally ionised and thus release mobile charge carriers. On the other hand, defects can act as traps for excess charge carriers and thereby also reduce the electrical conductivity.

The specific electrical conductivity σ is determined by the product of the charge-carrier concentration n and the charge-carrier mobilities μ : $\sigma = qn\mu$. q is the charge, for electrons, $q = -e$ and for holes, $q = +e$, where e is the elementary charge. The mobility μ is the mean drift velocity v_D of the charge carriers in the given electric field F : $v_D = \mu F$. The charge-carrier concentration n can be varied over many orders of magnitude by photoexcitation or injection in the usual organic semiconductors.

The charge carrier mobilities μ differ fundamentally in ultrapure aromatic molecular crystals from those in less-perfect organic crystals or disordered organic solids or polymers. Fig. 8.1 shows the temperature dependence of μ in an ultrapure perylene crystal: between 300 K and 30 K, the mobility **increases** with decreasing temperature. This holds generally for high-purity single crystals. In this particular case, μ increases from about 1 cm²/Vs at room temperature to around

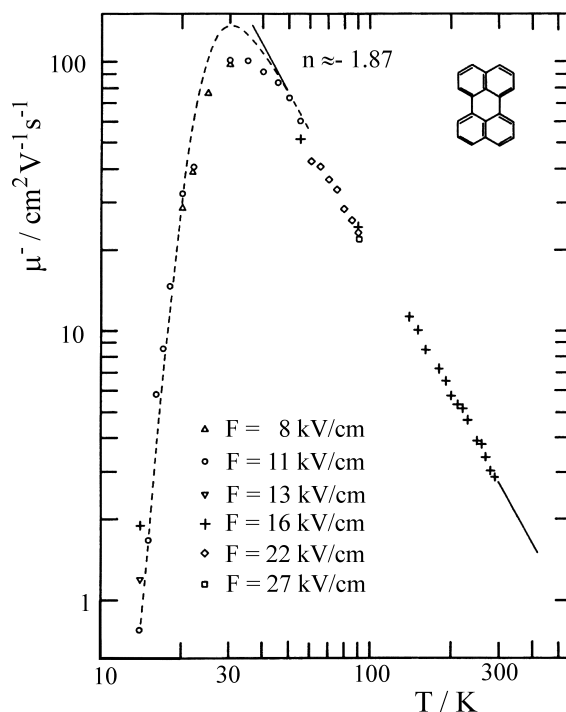


Fig. 8.1 The temperature dependence of the electron mobility μ in a 370 μm thick perylene crystal with an oblique orientation of the electric field \mathbf{F} ($\angle(\mathbf{F}, \mathbf{a}) = 45^\circ$, $\angle(\mathbf{F}, \mathbf{b}) = 66^\circ$, $\angle(\mathbf{F}, \mathbf{c}') = 55^\circ$). At 30 K $< T < 300$ K, μ increases with decreasing temperature. At $T < 30$ K, the

mobility is limited by shallow traps. From the analysis of $\mu(T)$ (dashed curve), the trap depths $E_t = 17.5$ meV and the relative trap concentration $c_t = 5 \cdot 10^{-4}$ can be determined (for details see Sects. 8.4 and 8.5). After [23].

100 cm^2/Vs at 30 K (for details see Sects. 8.4 and 8.5). Precisely the inverse temperature dependence of the mobility is exhibited by all *disordered* organic solids. This is true both of disordered low-molecular films as well as of polymer films. Figure 8.2 shows a characteristic example: the temperature dependence of the mobility of the holes in a disordered low-molecular film of (4-N,N-diethylamino-2-methylphenyl)-4-methylphenylmethane (MPMP), which was prepared by sublimation of the MPMP molecules onto a substrate [49]. MPMP is typical of many disordered films of evaporated molecules. The values for the mobility are here, as in all non-crystalline solids, orders of magnitude smaller than in crystals, and they **decrease** with decreasing temperature, in the present case from about $10^{-3} \text{ cm}^2/\text{Vs}$ at 350 K to around $10^{-6} \text{ cm}^2/\text{Vs}$ at 200 K. Furthermore, the mobilities depend on the electric field strength F (for details see Sect. 8.6).

The reason for the two fundamentally different temperature dependencies and the different magnitudes of the mobilities lies in processes occurring in the motion of the charge carriers. In ultrapure crystals, the charge carriers have a quasi-momentum $\hbar\mathbf{k}$ and are scattered by phonons. Here, \mathbf{k} is the wavevector of the electron or hole waves. With **decreasing temperature**, the phonon density and with it

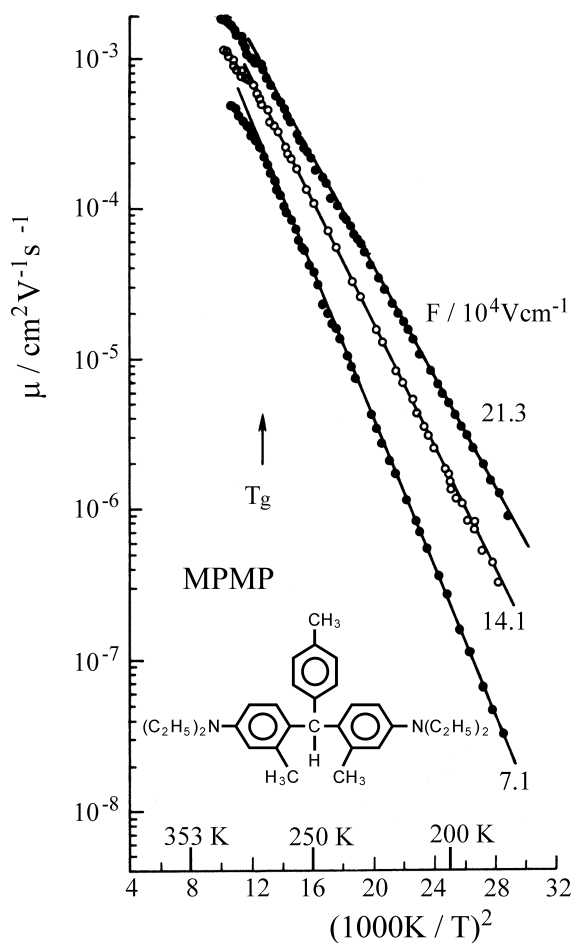


Fig. 8.2 The temperature dependence of the hole mobility μ in an $8.7 \mu\text{m}$ thick disordered film of MPMP molecules at different field strengths F . MPMP = bis(4-*N,N*-diethylamino-2-methylphenyl)-4-methylphenylmethane. The film was prepared by vapour-deposition (sublimation) [49]. T_g is the glass point (for details see Sect. 8.6). After [49].

the scattering probability decrease, and therefore the mobilities increase. One then refers to the process of electrical conductivity as **band conductivity** (cf. Sect. 8.5).

In contrast to ultrapure crystals, the charge carriers in disordered molecular solids are localised on the molecules and for transport, they must be thermally activated in order to hop from molecule to molecule. Therefore, in the disordered molecular solids, the mobility becomes greater with **increasing temperature**. The process of electrical conductivity is then termed **hopping conductivity** (cf. Sect. 8.6).

The boundary between band and hopping conductivity is naturally not well-defined. However, if the mean free path of the charge carriers is of the order of

magnitude of only one lattice constant, then the conductivity will take place via a hopping process.

In the following sections, after some preliminary historical remarks and a more precise characterisation of the charge carriers in terms of polarons, we will introduce the more important experimental methods. After that, we treat ultrapure crystals (Sect. 8.5) and disordered organic solids (Sect. 8.6).

All together, the organic semiconductors have increased enormously in importance both in basic research and for applications since the 1960's. They have developed in this time from a special topic of interest to only a few researchers to a respected branch of solid-state research which is active worldwide.

8.1

Preliminary Historical Remarks

The earliest research papers on the electrical and optoelectronic properties of fluorescing organic solids were published in the first two decades of the 20th century. They deal with

- the discovery of photoconductivity,
- the external photoeffect and its relation to fluorescence, and
- dark conductivity.

Pochettino [1] discovered in 1906 that anthracene is a **photoconductor**. The anthracene crystal was investigated later, in particular after 1950, as the prototype for photoconductivity and many other electrical, optical and optoelectronic properties of aromatic molecular crystals.

Stark and Steubing [2] in 1908 were the first to investigate the relationship between fluorescence and the photoelectric effect (i.e. the **external photoeffect**), which a few years before had been explained by A. Einstein using the quantum hypothesis of light, i. e. the concept of photons. They carried out their experiments on a large number of different organic solids. This included benzene, naphthalene, and anthracene, but also many other aromatics with N- or OH-substituents. The following quote from one of their publications is still valid today:

“Light emission by fluorescence below $\lambda = 0.5 \mu$ has its origin in the release of energy accompanying the recapture of freed or unsaturated valence electrons by their binding sites in the molecule; this recapture is preceded by a partial or total separation of the electrons from their molecules.”

(cf. Sect. 8.4.2 on the photo-generation of charge carriers).

W. E. Pauli [3] in 1913 measured the excitation spectra for fluorescence and the photoelectric effect in fluorescing organic solids and analysed them. He found that the minimum photon energy required for the initiation of photoemission of electrons is greater than that for the photoexcitation of fluorescence.

The following quote from Pauli's paper is also essentially still correct today, for one can derive from a reading of the paper that his expression "*the lack of parallelism*" (s. below) meant the difference between the excitation spectra for photoemission and those for fluorescence, and "*the agitation*" referred to the excitation of fluorescence:

"The lack of parallelism would however also be explained ... if one assumes that the distance of the electron which is cast out of its binding within the atomic system is extraordinarily small (during the process of agitation) and that therefore the attractive force between the positively-charged atom and the electron remains strong in comparison to the force of the externally-applied field which is pulling the electron away from the atom" (cf. Sect. 8.4.2).

As early as 1910, Koenigsberger and Schilling [4] in their paper "*On the conduction of electricity in solid elements and compounds*" report an investigation of not only elemental solids (Si, Ti and Zr) and minerals (magnetite and pyrites), but also of "*benzene derivatives*". Unlike the work of Stark and Steubing, Koenigsberger and Schilling however studied the "*conduction of electricity*" without optical irradiation, that is the **dark conductivity**. Their "*Examination as to whether electron conductivity or ionic conductivity is present, was ... carefully carried out in various ways, and showed that the former occurs also in compounds (i.e. molecules) far more often than was previously assumed*". Both for anthracene and for naphthalene, these authors find that "*the conduction of electricity takes place by electrons but it is appreciable only in the liquid state; still, a conductivity in the solid state could be detected qualitatively*".

The above-mentioned and other early works on the electrical conductivity of organic molecular crystals and non-crystalline organic solids were continued only sporadically up to about 1960. They made essentially no contribution to the rapid development of solid-state physics during this period. The reason for this was on the one hand the widespread reluctance of solid-state physicists to become involved in chemistry. On the other hand, in the beginning, crystalline systems with only one or a few atoms in their unit cells sufficed to carry out the elucidation of the fundamental phenomena of solid-state physics, such as superconductivity and semiconductor physics.

However, at least after the work of the Hungarian Nobel prize winner for medicine in 1937, the biochemist Albert Szent-Györgyi, it was known that electrical currents play a central role in living systems as well. He pointed out that macromolecules take part in the electron-transfer reactions which are so important for biological systems [5]. The following quotation is taken from his book: "*What drives life is thus a little electric current, kept up by the sunshine. All the complexities of intermediary metabolism are but the lacework around this basic fact.*"

This knowledge contributed to the revival of research on the electrical conductivity of organic solids in the 1950's and to the fact that especially since about 1980, it has experienced an enormous, worldwide boom. The development of electrophotography (xerography), for which C. F. Carlson obtained the decisive patent in 1942, was an important driving force towards the elucidation of the elementary processes in the (photo)-conductivity of organic solids. Xerography – a neologism derived

from ξηρος (dry) and γραφειν (to write) – is based in its central step on the storage of the image which is to be printed via the photoconductivity of insulators. The first experiments with electrophotography were in fact carried out by Carlson using anthracene. Only later did it become clear that α -Se is a better insulator and therefore the better material for this purpose. Today, most photocopier machines make use of organic materials as photoreceptors [M4].

The history of our knowledge of the electrical conductivity of organic solids has been discussed by several authors who were involved in the work on the electrical conductivity of polycyclic aromatic hydrocarbons in the years after 1950 in a special volume of *Molecular Crystals, Liquid Crystals* [6] edited by H. Inokuchi. At the beginning of this newer period of research, there were at least five milestones:

Stimulated by the measurements of Eley on phthalocyanine, Akamatu and Inokuchi in the year 1950 discovered a thermally-activated specific conductivity with an activation energy of $E = 0.39$ eV in violanthrone, and obtained similar values for related aromatic solids [7]. The interpretation given at the time for this value in terms of the model of an intrinsic semiconductor with a band gap $\Delta E_g = 2E$ is, to be sure, obsolete today (see below), but the results clearly showed that no conductivity exists at $T = 0$ and thus no intrinsic charge carriers are present in the crystal.

In 1953, Mette and Pick [8] purified anthracene using a melting technique and thereby obtained the purest starting material then available for their crystals grown from the melt. In their experiments on the dark conductivity of anthracene crystals at temperatures between 80° C and 210° C, they were the first to measure the **anisotropy** of the specific electrical conductivity σ . Their results gave the ratios of the values of σ along the three crystal axes a , b and c : $\sigma_a : \sigma_b : \sigma_c = 1 : 1 : 0.19$ at 148° C. These values hardly differ from those measured with modern methods along the three axes today (see Sect. 8.5).

In 1959/1960, Le Blanc [9] and Kepler [10] investigated the transient **photoconductivity** of high-purity anthracene crystals. The charge carriers were activated by a UV pulse and their mobilities were measured (see Sect. 8.4.1). Both for holes and for electrons, they found values between 0.3 cm²/Vs and 3 cm²/Vs at room temperature. These were dependent on the crystal orientation relative to the electric field and increased on cooling. Their results are still valid today (see Table 8.2 in Sect. 8.5.2).

In 1961, Mark and Helfrich [11, 12] studied the dark conductivity of ca. 50 μ m thick crystals of naphthalene, anthracene, and other aromatic hydrocarbons. In their work, the charge carriers (holes) were injected from an anode into the crystals. The crystals were thus charged and therefore conducting. This charge, like that for example in electronic valves, is termed a space charge. It determines the electric field and limits the current in the crystal. By analysis of the strongly non-linear current-voltage curve, i.e. the non-Ohmic characteristic, Mark and Helfrich were the first to detect the **space-charge-limited currents** (see Sect. 8.4.4) in organic molecular crystals.

Finally, in 1966, Riehl, Becker and Bässler [13] measured the temperature dependence of the dark current due to holes in anthracene crystals. In their experi-

ments, the temperatures of the silver electrodes (anode and cathode) and that of the crystal could be independently varied. It was found that the stationary current depends only on the temperature of the anode. The activation energy was 0.7 eV. It is considerably smaller than the excitation energy of singlet excitons in the anthracene crystal (3.1 eV), and particularly, it is smaller than the gap between the **valence and the conduction bands**, i.e. the **band gap** E_g (cf. Fig. 8.6). In the relaxed anthracene crystal, $E_g^{\text{Ad}} = 4.1$ eV (Fig. 8.7). It follows from Fermi statistics that there is a vanishingly small intrinsic charge-carrier concentration at room temperature and all temperatures below the melting point. Instead, the charge carriers must be injected. For the **injection**, there is a **barrier** at the **contact** between the metal electrode and the crystal (see Sect. 8.4.3.3). The activation energy measured by Riehl, Becker and Bässler was thus not the activation energy for the intrinsic generation of an electron-hole pair, but rather the height of the barrier at the contact, and it was first described by these authors as such.

8.2

Conductivity and Mobility of nearly-free Charge Carriers

The specific electrical conductivity σ is defined by the relation between the current density \mathbf{j} ($|\mathbf{j}| = I/A$, I = current and A = cross-sectional area) and the electric field strength \mathbf{F} :

$$\mathbf{j} = \mathcal{G} \mathbf{F} \quad (8.1)$$

(see Fig. 8.3). In non-cubic crystals, \mathcal{G} is a tensor. Typical values of σ in various solids are shown in Fig. 8.4. They range over nearly 30 orders of magnitude. Values for aromatic molecular crystals are not shown in the figure, because any such value – without detailed information about the dopant concentrations and dopant materials as well as the material of the electrodes – is not significant and would not be characteristic of the pure crystal. In the purest anthracene crystals, values for σ at room temperature have been reported which lie nearly at the lower edge of the scale of Fig. 8.4.

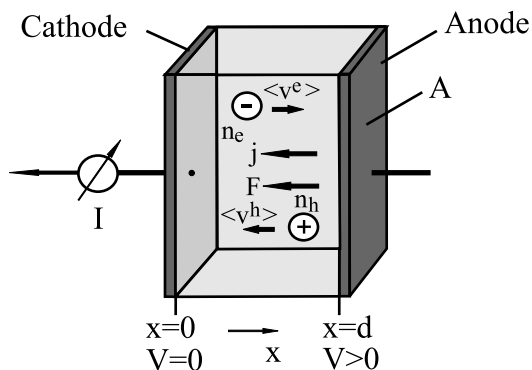


Fig. 8.3 The electrical conductivity:
 I = current, \mathbf{j} = current density,
 A = cross-sectional area and d =
thickness of
the sample, \mathbf{F} = electric field
strength,
 V = applied voltage, $\langle v_d^e \rangle$ and
 $\langle v_d^h \rangle$ are the mean drift velocities
of the electrons and the holes, n_e
and n_h are the densities of
electrons and holes.

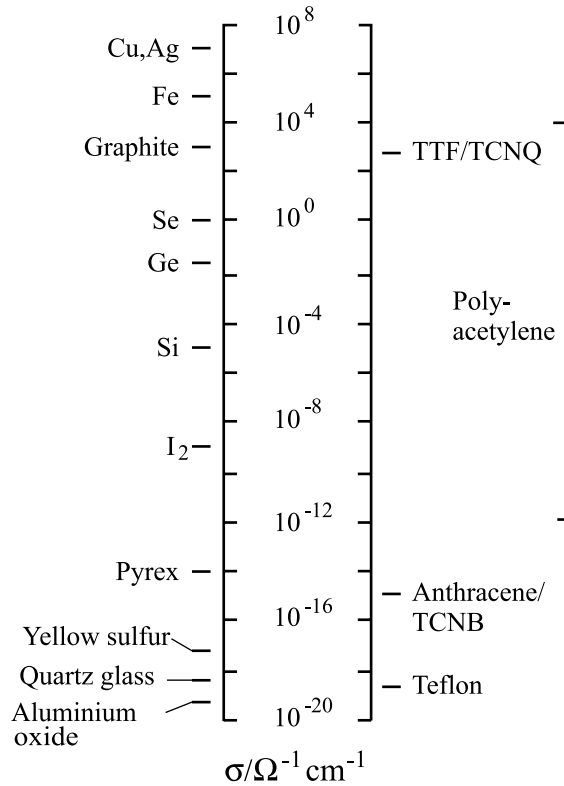


Fig. 8.4 The specific electrical conductivity σ of typical solids at room temperature. TTF/TCNQ is a quasi-one-dimensional organic radical-ion salt, anthracene/TCNB is a three-dimensional weak charge-transfer crystal (see Chap. 9). Pure organic solids with π -electron systems, for example highly-pure anthracene crystals or very pure polyacetyls $(\text{CH})_x$ are insulators, whose conductivity values lie at the lower edge of the scale here. Through doping, the conductivity can be increased by many orders of magnitude. As an example, this is shown for polyacetylene.

In the simplest case of a conducting solid, the current is due to only a single type of charge carrier with a charge q , e.g. electrons ($q = -e$), whose density is n_e . If the charge carriers move with a drift velocity \mathbf{v}_D^e , then an electric current flows with the current density

$$\mathbf{j} = qn_e \mathbf{v}_D^e. \quad (8.2)$$

$\mathbf{v}_D = \langle \mathbf{v} \rangle$ is the mean value of the velocity of all the charge carriers. In an electric field, we have

$$\mathbf{v}_D^e = \frac{\mathcal{G}}{qn_e} \mathbf{F}. \quad (8.3)$$

The relation between \mathbf{v}_D and \mathbf{F} is called the charge-carrier mobility μ :

$$\mathbf{v}_D = \mu \mathbf{F}. \quad (8.4)$$

The mobility μ is thus the drift velocity \mathbf{v}_D of the charge carriers in the given field \mathbf{F} , and it is usually quoted in units of cm^2/Vs . (In non-cubic crystals, μ is also a tensor.) The specific conductivity is then given by

$$\sigma = qn\mu \quad (8.5)$$

and is therefore the product of the two independent quantities n and μ . From a simple measurement of the current I at a given voltage V , μ and n cannot be determined separately (however, see Sects. 8.4.4 and 8.6.4.2).

n and μ are, on the one hand, materials specific. On the other hand, these two materials parameters depend in many solids on the applied field and on the temperature. In particular, in various semiconductors the mobilities can either increase or decrease strongly on increasing the temperature. As mentioned, both cases have been observed in organic semiconductors and will be discussed in later sections of this chapter.

\mathbf{F} and n are local quantities. Only when the charge carriers are homogeneously distributed within the solid is the internal field determined by $|\mathbf{F}| = V/d$, i.e. uniquely by the applied voltage V between plane-parallel electrodes at a spacing d (Fig. 8.1). And only when n and μ are both constant, and thus not dependent on the field strength \mathbf{F} , does Ohm's law hold.

To describe this situation, **Drude** introduced the model which bears his name around 1900, the **Drude model**. He inserted a term describing friction, $m\mathbf{v}_D/\tau$, into the classical equation of motion for an electron gas within a metal:

$$m\dot{\mathbf{v}} + \frac{m}{\tau}\mathbf{v}_D = -e\mathbf{F}. \quad (8.6)$$

Here, m is the mass of the charge carriers, τ is a relaxation time, and \mathbf{v}_D is the drift velocity, which is due to the applied electric field \mathbf{F} and acts in addition to the thermal velocity $\mathbf{v}_{\text{therm}}$. The velocity of the charge carriers is thus $\mathbf{v} = \mathbf{v}_D + \mathbf{v}_{\text{therm}}$. After the electric field is switched off, \mathbf{v} relaxes exponentially with the time constant τ towards $\mathbf{v}_{\text{therm}}$. In the stationary case, ($\dot{\mathbf{v}} = 0$), we have

$$\mathbf{v}_D = -\frac{e\tau}{m}\mathbf{F}. \quad (8.7)$$

With Eq. (8.4), this becomes

$$\mu = -\frac{e\tau}{m} \quad (8.8)$$

and with Eq. (8.5), we obtain the specific conductivity:

$$\sigma = \frac{e^2\tau}{m}n. \quad (8.9)$$

Later, we shall not be concerned with the nearly-free motion of an electron gas, but rather with electrons which to first order in organic solids either occupy the LUMO of a molecule or are missing in the HOMO of a molecule and thereby

give rise to holes. In both cases, the charge carriers polarise their neighbouring molecules in the organic crystal (see Sect. 8.3). Both the electrons in the LUMO as well as the missing electrons (holes) in the HOMO are thus components of the π -electron system. In an ideal single crystal, the sharp HOMO and LUMO states of the molecules become quasi-continuous bands: in the first case, the conduction band, in the second, the valence band.

Before we treat important details and the deviations from this ideal picture, which are very significant in molecular crystals and especially in disordered organic films, we wish in the rest of this section to sketch the differences between the Drude model (Eqs. (8.8) and (8.9)) and the band model for a simple metal; conceptually, this latter model is an important basis for understanding the band conductivity of a nonmetallic solid (cf. Sect. 8.5):

In the band model for a metal, all the energy states $E(\mathbf{k})$ of the electrons below the Fermi energy E_F are occupied and those lying at higher energies ($E > E_F$) are empty, so long as the temperature is not too high, i.e. $k_B T \ll E_F$. \mathbf{k} is the wavevector and $\hbar\mathbf{k} = m\mathbf{v}$ the linear momentum of the conduction electrons. In the \mathbf{k} -space of a simple metal, the occupied states are described by a sphere centred on the origin in the absence of an electric field \mathbf{F} , the Fermi sphere, with the Fermi surface (Fig. 8.5). In an applied electric field $\mathbf{F} = F_x$, owing to the Pauli principle only the electrons on the Fermi sphere can take up energy, i.e. occupy states in \mathbf{k} -space which would be unoccupied for $F = 0$. Therefore, the whole Fermi sphere shifts in stationary equilibrium by the amount

$$\delta k_x = -\frac{e\tau}{\hbar} F_x. \quad (8.10)$$

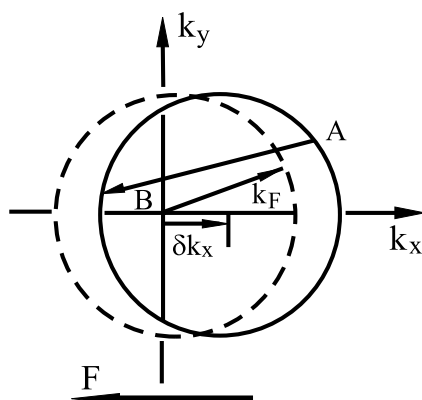


Fig. 8.5 A schematic representation of the shift of the Fermi distribution of the conduction electrons in the \mathbf{k} -space of a metal under the action of an electric field F_x and the scattering processes during the relaxation after switching off F_x . The dashed curve is for $F = 0$, when the distribution is centred around $[0, 0, 0]$. The solid curve indicates the shift of the Fermi

sphere by $\delta k_x = -e\tau(E_F) F_x/\hbar$. E_F is the Fermi energy and $\tau(E_F)$ the scattering time of the conduction electrons on the Fermi surface. δk_x is greatly exaggerated in this sketch. $A \rightarrow B$ represents inelastic scattering processes during relaxation of the occupied states to the unoccupied states on the Fermi surface.

Here, $\tau = \tau(E_F)$ is the relaxation time of those conduction electrons which have acquired the additional momentum $\hbar \delta k_x$ on the Fermi surface and relax back to thermal equilibrium after the electric field is switched off. This relaxation process is an inelastic scattering process in which the electrons which occupy a state A on the Fermi surface, that is, which have wavevectors $\approx k_F$, are scattered into unoccupied states B on the Fermi surface (Fig. 8.5). This scattering can be with a phonon, with a statistical lattice defect, or with an impurity. In a simple metal, the scattering occurs only for the electrons at the Fermi energy, and thus only those electrons which move with the Fermi velocity determine the mobility, and together with it and the concentration n of all the charge carriers, then limit the specific conductivity.

In the simple case in which the parabolic approximation holds, $E(\mathbf{k}) = \hbar^2(k_x^2 + k_y^2 + k_z^2)/2m^* = \hbar^2 k^2/2m^*$ for a conduction band with a constant effective mass m^* of the electrons, we have

$$\frac{1}{m^*} = \frac{1}{\hbar^2} \cdot \frac{d^2 E}{dk^2} = \text{const.} \quad (8.11)$$

The additional momentum transferred by the electric field F_x to the whole Fermi sphere, per electron, is given by

$$m^* \delta v(E_F) = \hbar \delta k_x. \quad (8.12)$$

The stationary additional velocity of the electrons then becomes with Eq. (8.10),

$$\delta v_x = -\frac{e\tau(E_F)}{m^*} \cdot F_x. \quad (8.13)$$

Equations (8.13) and (8.7) are formally identical. Therefore, in this simple band model, the specific conductivity σ and the charge-carrier mobility μ are:

$$\sigma = \frac{e^2 \tau(E_F)}{m^*} \cdot n \quad (8.14)$$

and

$$\mu = \frac{e\tau(E_F)}{m^*}. \quad (8.15)$$

The electrical conductivity σ of a simple metal is thus determined by the product of the density n of all free charge carriers and the relaxation time $\tau(E_F)$ of the charge carriers on the Fermi surface. In this case, in the Drude formula (Eq. (8.9)), the free electron mass m must be replaced by the effective mass m^* . The conductivity has a characteristic temperature dependence: it decreases over a large temperature range with increasing temperature. This decrease is primarily due to the decrease of the mobility and thus to the shortening of the scattering time $\tau(E_F)$ with increasing temperature, since the density n of the charge carriers is not dependent on the temperature.

We point out here, however, that the situation in a semiconductor is more complex, principally for two reasons:

- An electric current in an insulator requires excess charge carriers, that is, the insulator must be charged electrically. This **space charge** can consist of mobile and bound charges. Only the mobile charges contribute to the current, but both can influence the electric field and both are as a rule strongly dependent on the temperature and on the applied voltage. Furthermore, the metal contacts often produce unknown voltage differences. The contact problem and space charge make the interpretation of the current-voltage characteristic $I(V)$ often difficult. $I(V)$ is seldom linear, i.e. Ohm's law is generally not valid in insulators – and thus also not in organic solids which consist of only one type of molecules with conjugated π -electron systems – and most of the interesting properties of the organic semiconductors follow from the analysis of the deviations from Ohm's law.
- But not only the density n , also the mobility μ of the charge carriers is more complicated in semiconductors than in simple metals. The density of the photo-induced or injected charge carriers is as a rule small compared to the number density of the molecules, and the energetic distribution of the electrons and the holes obeys Boltzmann statistics with the Boltzmann factor $\exp(-\Delta E/kT)$. Here, ΔE for electrons in pure crystals is their corresponding energetic position relative to the lower edge of the conduction band (CB or LUMO), and for holes, it is their energetic position relative to the upper edge of the valence band (VB or HOMO) (see Fig. 8.6, Sect. 8.3). The relevant scattering times τ are thus each averages over the scattering times of **all** the charge carriers in the HOMO and the LUMO. Furthermore, the mobilities of electrons and holes are, as a rule, very different. And, above all, these mobilities are so small in many crystalline and in all disordered organic semiconductors that the mean free paths of the charge carriers are equal to the spacing between the molecules. The description of the conductivity in a band model is then not possible and must be carried out within a hopping model, as mentioned in the introduction (cf. Sect. 8.6). While the band model assumes quasi-free charge carriers which are scattered by defects or thermally-excited phonons, hopping models start from localised charge carriers whose transport becomes possible only due to thermal motions. The temperature- and field-dependent mobilities in various organic semiconductors can therefore be quite different.

In the following section, we discuss the nature of the charge carriers in organic semiconductors.

8.3

Charge Carriers in Organic Semiconductors: Polarons, Shallow Traps and Deep Traps

We know from earlier chapters that the model of a molecular crystal as a crystal made of oriented molecules with weak intermolecular coupling forms the basis of our understanding of the physical properties of organic solids. This is also

true of the understanding of the charge carriers which in some way are either produced in the crystal or are injected into it: excess electrons occupy the LUMO of the molecules. The charged molecule, the anion, polarises the molecules in its neighbourhood. The relaxation time of this electronic polarisation is of the order of the inverse frequencies of the optical transitions. In contrast, the transfer time for the charged state to a neighbouring molecule is about a factor of 100 longer, since it is given by a transfer integral whose value is of the same order as that of the exchange integral J , which we treated in Chap. 6. Owing to the weak intermolecular coupling, $J/\hbar c$ is of the order of 100 cm^{-1} .

The **electronic polarisation** of the neighbourhood of the charged molecule thus follows the motion of the charge within the lattice instantaneously and remains spatially limited to the near environment of each charged molecule. One refers to the negative charge carriers in a molecular solid therefore also as small negative **polarons**. Correspondingly, the holes in the HOMO, which are positive charge carriers created by ionisation, are small positive polarons, including the electronic polarisation of their environment.

For an understanding of the electrical conductivity, i.e. the transport of charge carriers in organic semiconductors, we must characterise the energies E_e and E_h of the negative and the positive polarons and if possible measure them (Fig. 8.6). E_e and E_h are denoted as transport levels. To carry a stationary current, they must be populated and depopulated. At each of the contacts, the contact barriers which exist there, that is the differences of the energies of the transport levels of the two contacting materials (metal/semiconductor or semiconductor 1/semiconductor 2), must be overcome in order for the contact to allow the passage of charges. And, on the other hand, the energy gap E_g

$$E_g = E_e - E_h \quad (8.16)$$

is the minimum energy for producing a completely ionised electron-hole pair (compare also Fig. 6.3).

The energies E_e and E_h differ from the energies of the ionised molecules in the gas phase by the polarisation energies P_e and P_h . Due to the high polarisability of the molecules, these polarisation energies are not small (see also Chap. 2). The electronic polarisation energy P_h of the positive polarons is the difference between the ionisation energy I_G of the free molecule and I_C of the crystal:

$$P_h = I_G - I_C. \quad (8.17)$$

P_h can therefore be measured directly using UV photoelectron spectroscopy. P_e is the difference between the electron affinity A_C of the crystal and A_G of the molecules in the gas phase:

$$P_e = A_C - A_G. \quad (8.18)$$

It has yet to be directly determined experimentally, because although for a few molecules A_G is known, A_C is not. If one assumes as a first approximation that

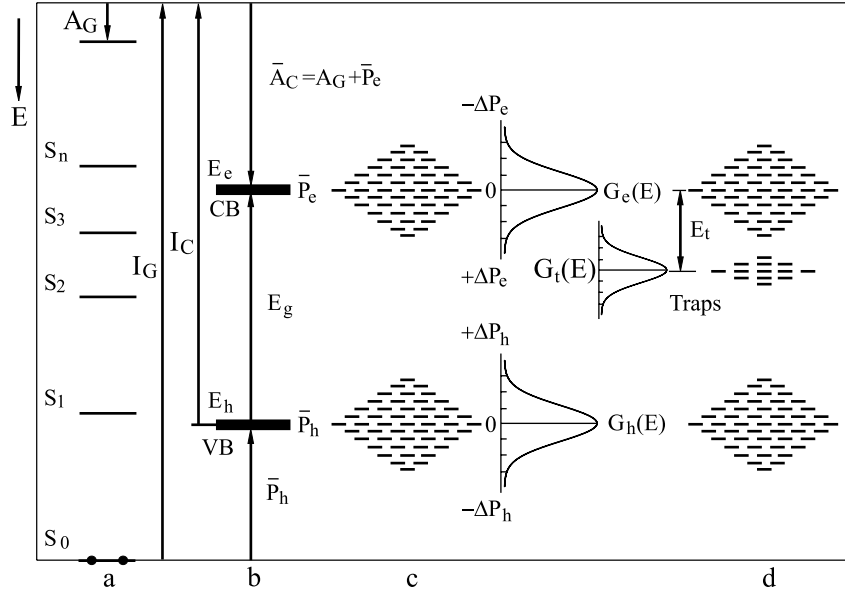


Fig. 8.6 The energy diagram of an organic semiconductor. a: The energy levels of the neutral isolated molecules. S_0 is the electronic ground state, $S_1, S_2 \dots S_n$ are the electronic singlet excited states, I_G is the molecular ionisation energy, A_G the electron affinity of the isolated molecule. b: The energy bands of the ionised states of the ideal crystal. E_h is the energy of holes, VB = valence band = transport level of the holes; E_e is the energy of the conduction electrons, CB = conduction band = transport level of the electrons. \bar{P}_h and \bar{P}_e are the mean polarisation energies of the holes

and the electrons. I_C is the ionisation energy of the crystal. A_C is the electron affinity of the crystal, E_g the energy gap. c: The energy levels of the ionised crystal states with a statistical distribution of polarisation energies. ΔP_h and ΔP_e are the deviations of the polarisation energies from their average values \bar{P}_h and \bar{P}_e , and $G_e(E)$ and $G_h(E)$ are the Gaussian densities of states for electrons and holes. d: The energy levels of traps within the energy gap (only electron traps are shown). E_t is the trap depth, $G_t(E)$ the density of states of the traps. From [M2].

the polarisation energy is determined by the interaction P_{id} of the charge with the dipole moments which it induces, then it is independent of the sign of the charge:

$$P_e = P_h = P_{id} \propto \sum_{k=1}^{N-1} \frac{e^2 \bar{\alpha}}{2r_k^4}. \quad (8.19)$$

Here, $\bar{\alpha}$ is the mean isotropic polarisability and r_k is the distance between the centre of gravity of the charge and molecule k . The index k runs over all the molecules in the crystal. The approximation (8.19) is no longer strictly valid if the interactions of the charge with the permanent quadrupole moments on the neighbouring molecules are taken into account [14]. The quadrupole correction however has no influence on the value of E_g ; instead, it shifts E_e and E_h by the same amount towards higher energies. If one leaves out this correction, then the term diagram of the ionised states in an ideal molecular crystal is defined by the equations (8.16) to

Table 8.1 Average experimental values for the ionisation energy I_G in the gas phase and I_C in the crystal as well as for the electron affinity A_G in the gas phase, and for the band gap E_g (E_g^{Ad}) in organic molecular crystals. From [M1, S. 204], [18] and [24].

	$\langle I_G \rangle / \text{eV}$	$\langle I_C \rangle / \text{eV}$	$\langle A_G \rangle / \text{eV}$	E_g / eV
Benzene	9.2	–	–1.4	~6–7
Naphthalene	8.2	6.8	–0.2	~ 5
Anthracene	7.42	5.77	0.58	4.1*
Tetracene	6.98	5.26	1.03	3.1
Pentacene	6.64	5.01	1.37	2,2
Phenanthrene	8.0	6.5	0.2	–
Pyrene	7.5	5.8	0.5	4.1
Perylene	7.0	5.4	1.1	3.1

(8.19). Figure 8.6b shows the resulting term diagram, and Table 8.1 contains experimental values for the ionisation energies, the electron affinities, and the energy gaps of selected molecules and molecular crystals [15, 16].

Along with the electronic polarisation, there is also a “vibronic” polarisation. This term denotes a **lattice relaxation** in the neighbourhood of the polaron [17]. The decisive frequencies are the phonon frequencies. Vibronic relaxation has the immediate effect that the energy gap is smaller with the relaxation than without it. The former is called the adiabatic energy gap E_g^{Ad} and the latter the optical energy gap, E_g^{Opt} . One-half the difference between them is the relaxation energy E_b for the occurrence of lattice relaxation [18]. Figure 8.7 gives a term diagram which is refined in comparison to that of Fig. 8.6b correspondingly, with the experimentally determined energy values for anthracene crystals. The band gap and its energetic position relative to the vacuum level depend on the spatial extent of the conjugated π -electron system. This is characterised by the term diagrams of the ionised states of the polyacene crystals benzene, naphthalene, anthracene, tetracene, and pentacene (Fig. 8.8) [19].

Thus far, we have considered ideal crystals with perfect lattice periodicity. Only in this limit do we obtain the discrete values of the energy terms shown in Fig. 8.6b and Fig. 8.7. Every deviation from ideal lattice periodicity, e.g. in the neighbourhood of structural defects or – in particular – in non-crystalline solids causes a shift in the terms E_e and E_h . This follows immediately from Eq. (8.19): a deviation of Δr_k from the average value \bar{r}_k produces a corresponding shift of the polarisation energies and thus of the energies E_e and E_h . Compressed regions in the crystal (cf. for example Fig. 4.3) lead to local states with an increased contribution from the polarisation energy ($|P\rangle|\bar{P}\rangle$) and thus to deep or **shallow traps** within the energy gap of the ideal crystal (Fig. 8.6c). **Deep traps** refers to disturbed molecules from whose ions the captured charge carriers can no longer escape by thermal activation; shallow traps are those which can still be thermally activated. Expanded regions of the crystal

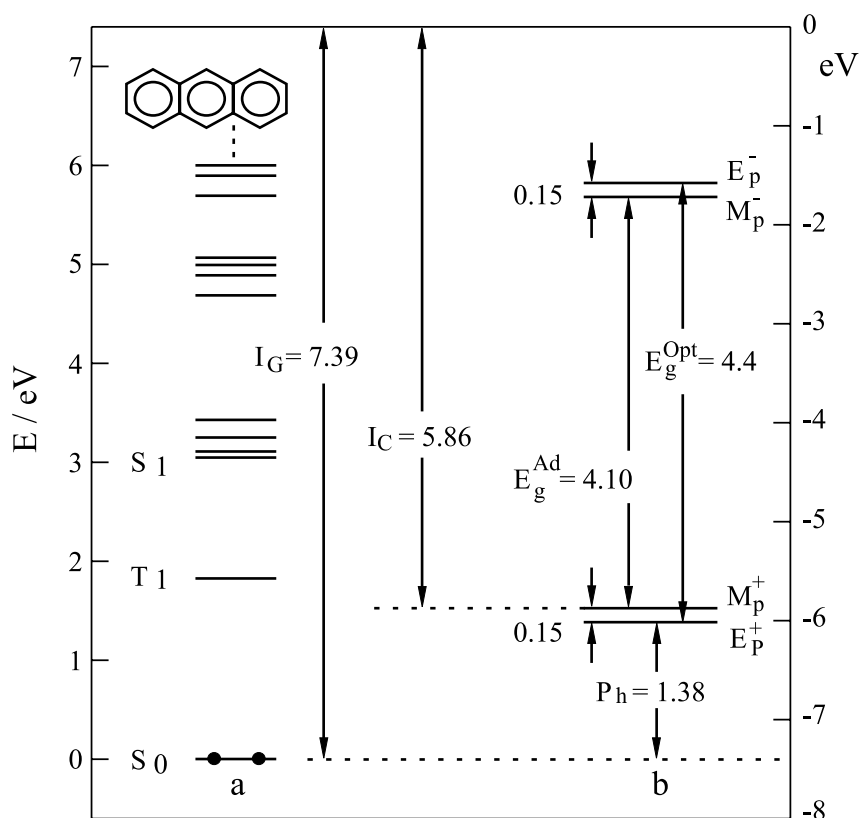


Fig. 8.7 Energy diagram of the anthracene crystal, taking into account lattice relaxation. **a**: the neutral molecule; **b**: ionised states. E_p^- and E_p^+ are the electronic polaron states, M_p^- and M_p^+ are the transport states of the electrons. E_g^{Opt} and E_g^{Ad} are the electronic and the adiabatic energy gaps. V is the vacuum level. For other notation, see Fig. 8.6. After [18].

lead to local states whose energies lie above E_e or below E_h . The statistical distributions of the energies of the localised defects, deep-trapping or shallow-trapping states can be most simply described by a Gaussian distribution for each. These can either be centred on the energies E_e and E_h , or on the average energy E_t of discrete traps (see below), and they have a characteristic width σ (cf. Fig. 8.6c). (σ denotes here of course not the specific conductivity, but rather a parameter of the Gaussian normal distribution which describes its width.) There are two obvious reasons to choose a Gaussian distribution: the profile of excitonic optical absorption bands is roughly Gaussian; and the polarisation energy results from a large number of internal contributions (see Eq. (8.19)), which vary statistically by small amounts around a mean value.

In the case of defects which are not caused by local compression or expansion, but instead by structural modifications or impurity molecules, the traps can also be

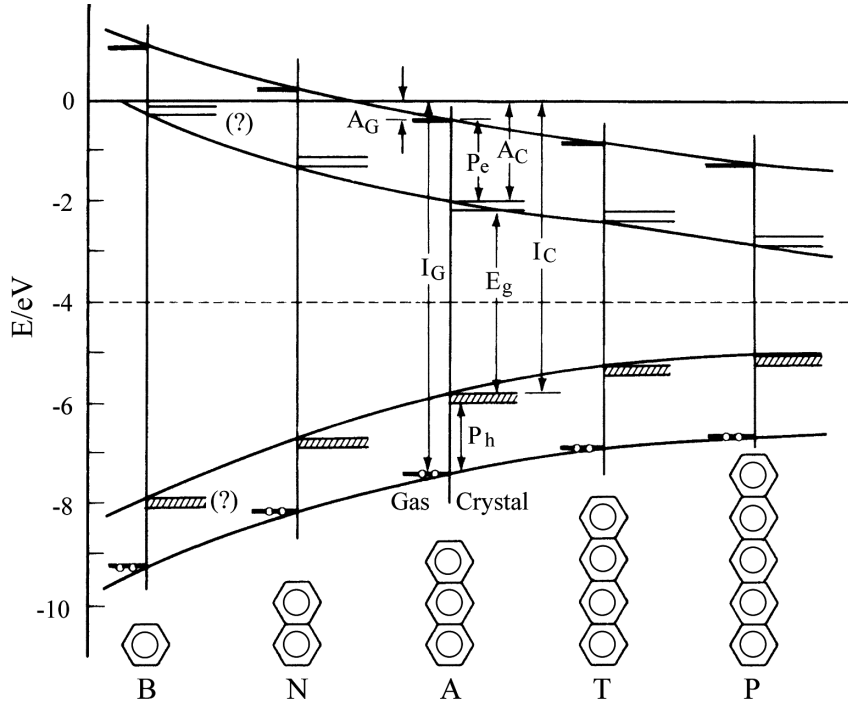


Fig. 8.8 A comparison of the term diagrams of the ionised states of the polyacene crystal series benzene, naphthalene, anthracene, tetracene, and pentacene, with the levels of the isolated molecules. Notation as in Fig. 8.6. From [19].

centred deep within the energy gap. The Gaussian distribution function $G(E)$ for this case, which is sketched in Fig. 8.6d, is then given by:

$$G_t(E) = \frac{N_t}{\sqrt{2\pi} \sigma_t} \exp \left[-(E - E_t)^2 / 2\sigma_t^2 \right]. \quad (8.20)$$

Here, N_t is the overall density of the trapping states, σ_t is the width of the distribution, and E_t is the average trap depth.

The existence of lattice vibrations, shallow traps, deep traps and spatial disorder leads schematically to the following model for charge transport in an electric field \mathbf{F} : in the ideal crystal, the charge carriers (polarons) can move freely at $T = 0$. This case naturally does not occur. When lattice vibrations (phonons) are excited, the lattice periodicity is disturbed. The resulting modulation of the polarisation energy leads to scattering of the charge carriers. Deep traps lead to localised charge carriers; from shallow traps, the charge carriers can be reactivated thermally. Shallow traps thus also act as scattering centres.

8.4

Generation of Charge Carriers and Charge Transport: Experimental Methods

The two basic experimental methods for the investigation of charge transport in organic semiconductors are measurement of the photoconductivity with the time-of-flight method (TOF), and measurement of the dark-current characteristic $I(V)$. In the TOF method, the time dependence of the transient current $I(t)$ is registered following the pulsed generation of excess charge carriers by the internal photoeffect using intense UV light pulses. In the measurement of the dark-current characteristic of the stationary dark current I as a function of the applied voltage V , the excess charge carriers are injected from the electrodes. Information about the mechanisms of charge transport is obtained in both cases from the dependence of the observables on the temperature T and on the electric field F .

The two methods mentioned above will be treated in this section as applied to crystals in the following order: in Sect. 8.4.1, we describe the TOF method for determining the mobility; in Sect. 8.4.2, the required photogeneration of the charge carriers; in Sect. 8.4.3, the injection of excess charge carriers from contacts – necessary for production of dark currents – and the associated space charges in the crystals; and finally in Sect. 8.4.4, space-charge-limited currents. Selected results from crystals and their interpretation follow in Sect. 8.5. In Sect. 8.6, the methods are extended to disordered organic films and discussed in terms of a few examples.

8.4.1

The TOF Method: Gaussian Transport

Figure 8.9 illustrates the principle of a TOF experiment [9, 10, 20]: the crystals or non-crystalline films with typical dimensions of $(50 \text{ mm}^2) \times (1 \mu\text{m} \dots 1 \text{ mm})$ are contacted on each of their large surfaces with metal electrodes, of which the front electrode must be semitransparent to permit photoexcitation. Between the two electrodes, a dc voltage V is applied. Charge carriers (electrons and holes) are generated by δ -shaped light pulses when the quantum energy of the photons, the electric field, and the temperature permit (see Sect. 8.4.2). In the ideal case, the wavelength of the optical excitation is chosen so that the charge carriers are generated in a thin layer behind the irradiated surface, which is small compared to the sample thickness d . This requires that $1/\alpha \ll d$, where α is the absorption coefficient for the excitation light (typically a few $10^5/\text{cm}$, compare Fig. 8.13). A typical pulse length for the optical excitation is 1 ns.

When the voltage applied to the front electrode is positive, the photo-generated electrons at the front electrode are instantaneously discharged. The holes remain in the sample and drift in the electric field through the crystal. Their total charge q , determined by the energy of the excitation pulse, should be kept so small by limiting the latter that the electric field F is fixed by the applied voltage V and the sample thickness d . To achieve this, the condition $q \ll Q$ must be fulfilled, where $Q = C_M V$ is the charge in the measurement cell, i.e. the capacitor formed by the electrodes and the sample, and C_M is its capacity. Then the field is given by

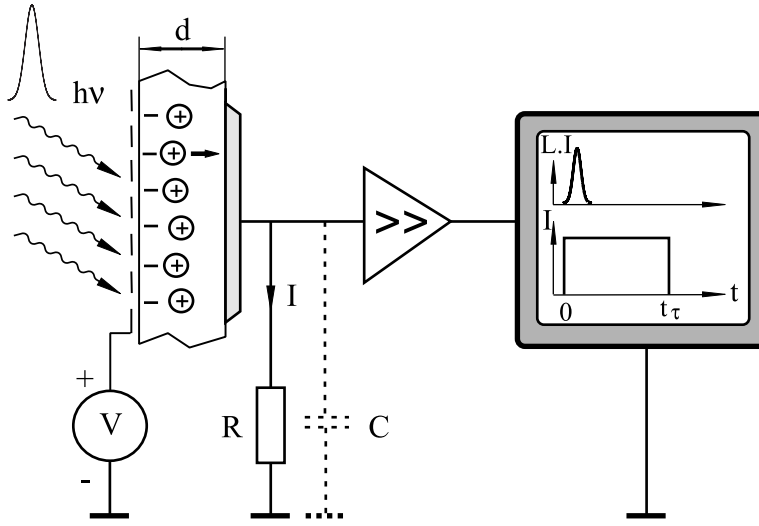


Fig. 8.9 Schematic setup of a TOF experiment. $I(t)$ is the transient of the displacement current following photoexcitation by a δ -shaped UV pulse of intense light L . Its penetration depth behind the semitransparent front electrode is small compared to the thickness d of the sample. The ideal dependence of the displacement current $I(t)$ of holes is illustrated, for a constant, positive voltage V on the front

electrode. The transient ends after the transit time t_τ of the plane-wave packet of holes through the sample. By reversing the polarity of V , the transit time of the electrons can also be measured. A finite width of the excitation pulse L , the finite time constant RC of the circuit, and charge-carrier diffusion cause rounding-off of the transients $I(t)$ at $t = 0$ and at $t = t_\tau$ even for ideal transport. After [20].

$F = V/d$. So long as the drift velocity v_D is constant, a plane-wave, δ -shaped hole-charge packet drifts through the sample and reaches the back electrode after the transit time $t_\tau = d/v_D$. On reversing the polarity, the holes will be discharged at the front electrode and the electrons drift. If no charge carriers are captured in traps during the time t ($0 < t < t_\tau$), then a constant **displacement current** I results. It falls to zero when the charge-carrier packet reaches the back electrode and discharges there. Therefore, the time t_τ is called the transit time. Applying the definition of the mobility μ (Eq. (8.4)), we obtain directly, in the ideal case described above, from a measurement of the transit time t_τ the mobility μ_- of the electrons (negative polarons) or μ_+ of the holes (positive polarons):

$$\mu_{\pm} = d^2 / t_\tau V_{\pm}. \quad (8.21)$$

In order to attain this ideal case, at least the following conditions must be fulfilled:

- The characteristic time constant RC of the circuit must be considerably shorter than the transit time : $RC \ll t_\tau$.
- The length τ_e of the optical excitation must be short compared to the transit time: $\tau_e \ll t_\tau$.
- Diffusion of the charge carriers must be negligible. This condition cannot in principle be ideally met, since the charge-carrier packet will inevitably broaden during the drift time due to the high density gradient initially

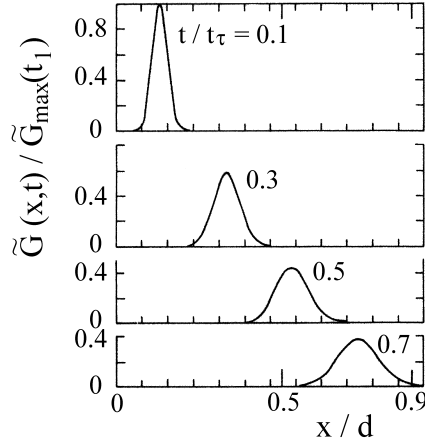
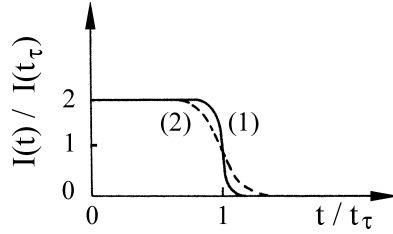


Fig. 8.10 A Gaussian transport process. Above: the distribution function $\tilde{G}(x, t)$ of the charge carriers at various times t . $\tilde{G}(x, t)$ is the probability that a charge carrier will be at the position x at time t , if it was at the position $x = 0$ at the time $t = 0$. x/d is the normalised distance of the charge carriers from $x = 0$, where they were generated. d is the sample thickness (see Fig. 8.9). In Gaussian transport, the transit time t_τ is defined by $\langle x(t_\tau) \rangle = d$. Below: transients of the displacement current $I(t)/I(t_\tau)$. In Gaussian transport, the width of the decay of the transients is governed by diffusive broadening of the charge-carrier packet. For transient (1), the transit time t_τ is longer than for transient (2).



present. This broadening is determined by the Einstein relation between the diffusion coefficient D and the mobility μ

$$\frac{\mu}{D} = \frac{e}{k_B T} \quad (8.22)$$

and leads to a non-rectangular contribution to the transient current (Fig. 8.10). The width of the initially δ -shaped charge-carrier packet is given by its mean square displacement $\langle \Delta x^2 \rangle$:

$$\langle \Delta x^2 \rangle^{1/2} = (2Dt)^{1/2}. \quad (8.23)$$

Thus, the relative width of the initially δ -shaped charge-carrier packet is, using $\langle x \rangle = \langle v_D \rangle F = \mu F t$ and Eq. (8.22),

$$\frac{\langle \Delta x^2 \rangle^{1/2}}{\langle x \rangle} = \frac{kT}{eF} \left(\frac{2}{Dt} \right)^{1/2}. \quad (8.24)$$

Likewise, the relative uncertainty in the transit time is

$$\frac{\Delta t_\tau}{t_\tau} = (2kT/eV)^{1/2}. \quad (8.25)$$

With an applied voltage of $V = 500$ V and at a temperature $T = 300$ K, we obtain $\Delta t_\tau/t_\tau \approx 10^{-2}$. When the transients obey Eqns. (8.24) and (8.25), the transport is termed ideal **Gaussian transport** (cf. Sect. 8.4.2.1).

For the ideal case described, the density of the traps for the charge carriers must be negligible. If only deep traps are present, which cannot be thermally reactivated, the charge-carrier density and with it the transient current will be continuously and irreversibly decreased. For this, the lifetimes τ_D of the immobilised charge carriers in their traps must be clearly longer than the transit time: $\tau_D \gg t_\tau$. The remaining “free” charge carriers drift in spite of the decreasing current in the form of a flat disc to the back electrode and there produce the rectangular but smaller decay at the time t_τ . Even the presence of deep traps thus does not prevent the measurement of the transit time.

In many cases, one observes no sharp decay of the transient current and thus a fundamental deviation from Gaussian transport. The reason for this is that the charge carriers have spread out over the whole sample. This transport is termed **dispersive transport**. It is characteristic of strongly disturbed crystals, or especially of non-crystalline organic solids, and will be treated in Sect. 8.6.

Nearly ideal TOF transients for Gaussian transport are, however, exhibited e.g. by high-purity sublimation-grown anthracene crystals at room temperature [21], Fig. 8.11a. The transit time t_τ for the electrons in this experiment is about $12.5 \mu\text{s}$. On cooling the anthracene crystal to 40 K, one observes for the same orientation of the electric field, ($\mathbf{F} \parallel \mathbf{c}$), a nearly featureless decay of the current (Fig. 8.11b). It is caused by a small density of deep traps. In spite of the decrease in the current, the transit time t_τ can still just be recognised as a small shoulder (here at $2 \mu\text{s}$). From the shortening of the transit time, the increase in the mobility on cooling the sample follows directly (in this example, it is $\mu(40 \text{ K}) / \mu(300 \text{ K}) = 3.6$).

Figure 8.12 gives a second example of the nearly ideal electron transients in a perylene crystal at 300 K and at 40 K [22]. From the strong decrease in the transit

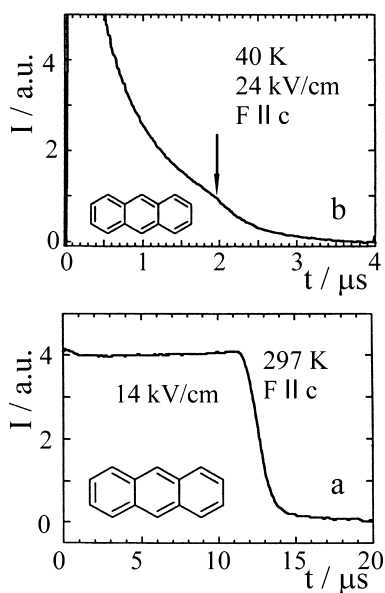


Fig. 8.11 a: Nearly ideal TOF transients for electrons in an anthracene crystal along the \mathbf{c}' direction (the direction with the smallest charge-carrier mobility, compare Table 8.2); $T = 300 \text{ K}$. b: $T = 40 \text{ K}$. As a result of charge-carrier traps from which the charge carriers can be thermally released with only a small probability at the lower temperature, the displacement current decreases so strongly for times $t < t_\tau$ that only a small fraction of the charge carriers arrive at the back electrode and therefore, only a small blip (arrow) is discernible in the transient, in spite of the increased field strength. From the transit time, the field strength and the thickness of the crystal, the mobility can be computed directly. From [21].

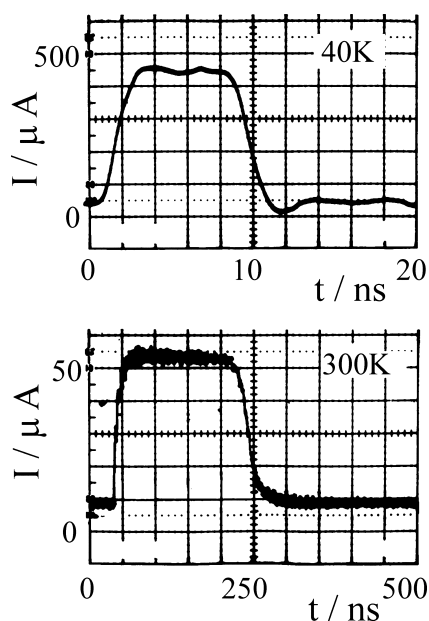


Fig. 8.12 The electron TOF transients of a 225 μm thick perylene crystal disc in the b direction; below, at $T = 300\text{ K}$ and $F = 22\text{ kV/cm}$; above, at $T = 40\text{ K}$ and $F = 35.6\text{ kV/cm}$. Note the strong decrease in the transit time t_t on cooling. After [22].

time on cooling, with the data in the the figure caption we obtain for this example $\mu(40\text{ K}) / \mu(300\text{ K}) = 15$. In a different crystal direction, the temperature dependence is still more pronounced: Fig. 8.1 shows the values of the mobilities in perylene crystals found from the transients using Eq. (8.21). Both the values at room temperature and the temperature dependencies are typical of high-purity organic molecular crystals. Details of the analysis of the dependence of μ on temperature, field strength, and angle in molecular crystals will be given in Sect. 8.5.

8.4.2

Photogeneration of Charge Carriers

In the treatment of photoconductivity in Sect. 8.4.1, we simply mentioned in passing the primary process: the generation of the excess charge carriers using the **internal photoeffect**. In this section, we will treat the details of this process and choose again as an example the anthracene crystal.

An ideal intrinsic photoconductor with a large band gap ($E_g \gg kT$) contains practically no thermally-excited charge carriers. The generation of charge carriers via the internal photoeffect requires a charge separation, i.e. the production of an equal number of electrons in the conduction band (CB) and holes in the valence band (VB). The necessary minimum energy for this process is E_g^{Ad} (see Fig. 8.7). In anthracene, $E_g^{\text{Ad}} = 4.1\text{ eV}$ and is thus considerably larger than the excitation energy of the singlet excitons S_1 , which is about 3.14 eV (cf. Fig. 8.13). In optical excitation with $h\nu + kT > E_g^{\text{Ad}}$, the energy $h\nu$ is therefore sufficient both for the production of excitons and for the generation of free charge carriers.

8.4.2.1 Intrinsic Charge Carrier Separation

We initially restrict ourselves to the simplest process: the linear intrinsic photogeneration of charge-carrier pairs. Their production rate is proportional to the absorbed intensity of photons of the excitation light in the crystal, and requires neither excitonic processes at the crystal surface nor at the contacts, nor does it involve biexcitonic processes.

The quantum yield η of the intrinsic photogeneration is defined as the ratio of the number of generated charge-carrier pairs to the number of photons absorbed. η is dependent on the wavelength of the optical excitation, but also on the electric field and above all on the temperature: the process is thermally activated. Three important experimental results for pure anthracene crystals are shown in Figs. 8.13–8.15: the quantum yield η as a function of the wavenumber of the excitation radiation (Fig. 8.13) illustrates that a minimum energy of the photons of about 3.9 eV is necessary for charge separation [25]. This minimum photon energy is thus smaller than E_g^{Ad} and larger than the energy of the singlet exciton S_1 .

The absolute value of the quantum yield η in anthracene crystals at room temperature is of the order of 10^{-4} [26]: Fig. 8.14 shows its electric-field dependence

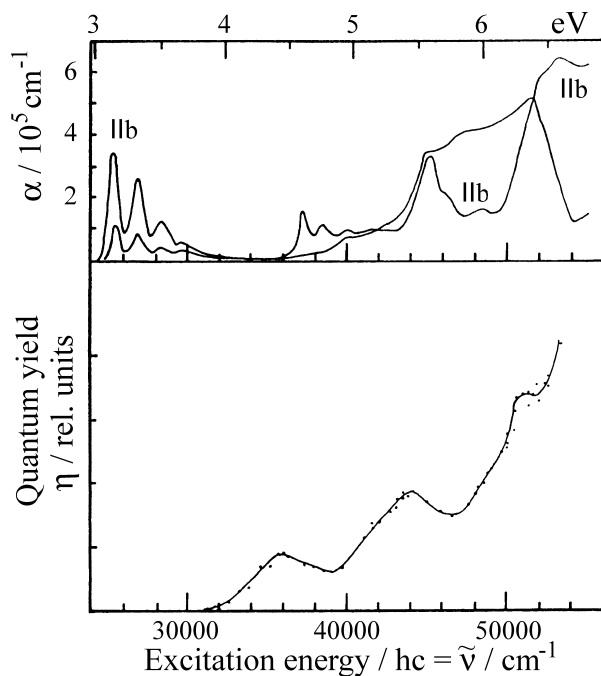


Fig. 8.13 The absorption constant α and the relative quantum yield η for photoelectron generation in anthracene crystals as a function of the excitation wavenumber. Absorption \parallel and \perp to the crystalline b axis. η was measured with unpolarised excitation light. From [25].

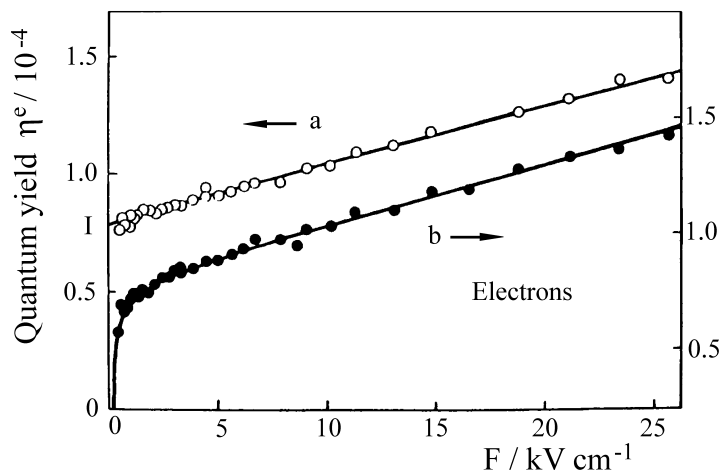


Fig. 8.14 The photoelectron quantum yield η^e as a function of the applied field strength F in an anthracene crystal at room temperature with an excitation wavelength of 225 nm. **a**: a pristine crystal, left-hand ordinate. **b**: a crystal which was irradiated before the experiment, right-hand ordinate. In the linear region, **a** and **b** are identical. According to Onsager's theory for the recombination of ions [29], the ratio $S/I = e^3/8\pi\epsilon\epsilon_0k^2T^2$. Here, $S = d\eta/dF$ is the slope and I the intersection of $\eta(F)$. S/I thus depends only on the temperature T and as the only material constant, it contains the relative dielectric constant ϵ . From [26].

$\eta^e(F)$ for photoelectrons in the field range up to 25 kV/cm at an excitation wavelength of 225 nm (≈ 5.51 eV). For pristine crystals, i.e. crystals which have not been irradiated before the experiment, the quantum yield increases linearly with increasing electric field strength F (Fig. 8.14a). On repeating the experiments with previously irradiated, non-pristine crystals, the increase with increasing field strength for $F > 2$ kV/cm is identical, but for $F < 2$ kV/cm, it is reduced (Fig. 8.14b). The reason for this reduction is the recombination of photogenerated electrons with holes in traps which were produced in the excitation volume of the crystal during the first irradiation and were still present during the second irradiation.

For holes, the experimental data for the electric-field dependence are nearly identical: $\eta^h(F) = \eta^e(F)$. This holds both for pristine and for non-pristine crystals [26].

The separation of electrons and holes to give quasi-free charge carriers is, as mentioned, thermally activated. The activation energy ΔE_a^{ph} was determined from the temperature dependence of the quantum yield [27]. The dependence of the activation energy $\Delta E_a^{\text{ph}}(\lambda)$ on the wavelength of the excitation light λ exhibits two pronounced plateaus (Fig. 8.15): $\Delta E_{a,1}^{\text{ph}} = 0.0675$ eV in the range of $200 \text{ nm} < \lambda < 230 \text{ nm}$ ($\approx 6.2 \text{ eV} > h\nu > 5.4 \text{ eV}$) and $\Delta E_{a,2}^{\text{ph}} = 0.090$ eV in the range of $240 \text{ nm} < \lambda < 280 \text{ nm}$ ($\approx 5.17 \text{ eV} > h\nu > 4.4 \text{ eV}$). For $\lambda > 280 \text{ nm}$, ΔE_a^{ph} increases further. In the whole wavelength range, the sum of the optical quantum energy and the thermal energy is larger than the band gap: $h\nu + kT > E_g^{\text{Ad}}$. This is in particular also true for $\lambda > 300 \text{ nm}$, where $h\nu < E_g^{\text{Ad}}$ holds.

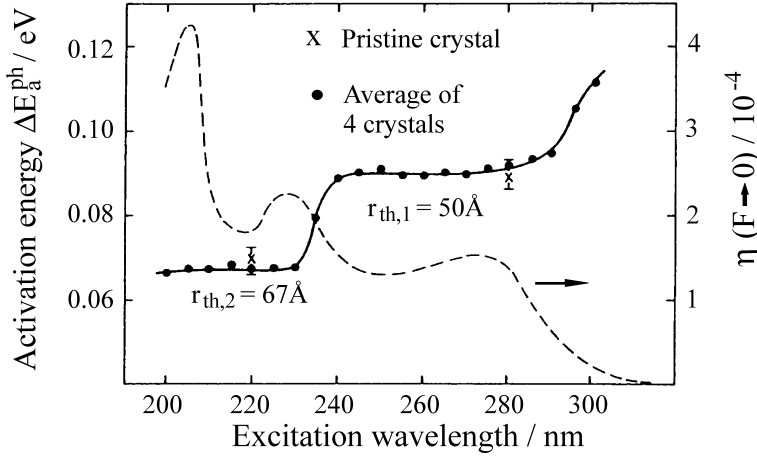


Fig. 8.15 the activation energy ΔE_a^{ph} for photogeneration of charge-carrier separation in anthracene crystals as a function of the excitation-light wavelength. $r_{th,1}$ and $r_{th,2}$ are the spacings of the positive and the negative charges corresponding to the two plateaus in the still Coulomb-bound metastable

charge-carrier pairs (CP states or Charge-Transfer states or geminate pairs) before the final, thermally-activated separation into “free” charge carriers. Dashed: the quantum yield $\eta(F \rightarrow 0)$ (see Fig. 8.14). From [27].

From these experimental results, it follows that the photogeneration of free charge carriers in the anthracene crystal is an autoionisation process. This term refers to the following: the neutral excited states – the singlet excitons – have a configuration interaction with the continuum of ionised crystal states. Autoionisation is the competing process to the much more efficient intramolecular relaxation and thus to recombination of the charge-carrier pairs after the optical excitation. This recombination is also called geminate pair recombination. This means that also in the photogeneration of charge carriers in organic molecular crystals, the molecular properties are dominant in comparison to the solid-state properties.

From the above-mentioned experimental results and data, the following scheme can be derived (Fig. 8.16) for the process of photogeneration [28]: in a first step, the absorption of photons produces singlet excitons S_1, S_2, S_3, \dots . In the second step, autoionisation occurs. With a quantum yield Φ_0 , positively-charged molecule-ions and quasi-free electrons with kinetic energy (“hot electrons”) are produced. In the third step, the hot electrons are thermalised by scattering processes and form metastable charge pairs within the sphere of action of the Coulomb potential of the positive ions (CP states), i.e. radical-anion-radical-cation pairs with spacings of r_{th} . Since the electrons and the holes are thermalised but not yet “free”, the CP states are charge-transfer (CT) excitons whose energy is E_{CP} . Thus, a charge transfer from one molecule to a second molecule at a distance $r_{th} < r_c$ has occurred. r_c is the distance at which the magnitude of the Coulomb energy is just equal to kT :

$$r_c = e^2 / 4\pi\epsilon\epsilon_0 kT. \quad (8.26)$$

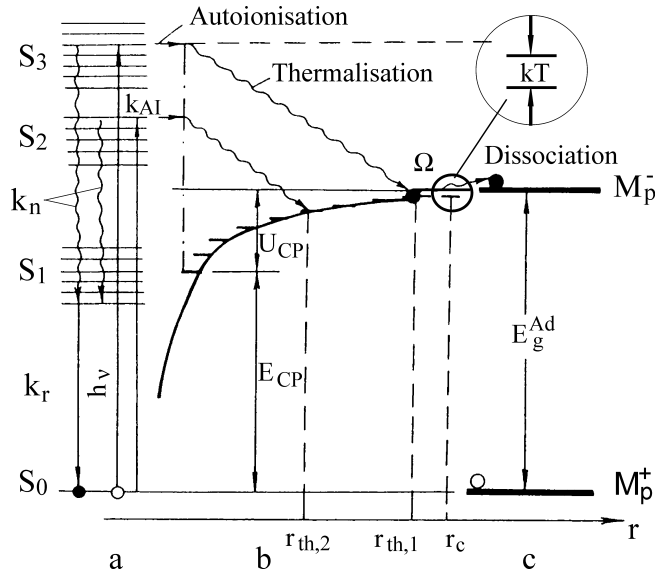


Fig. 8.16 Scheme of the individual steps in the process of intrinsic photogeneration of charge-carrier pairs, $M_p^+ - M_p^-$, in a molecular crystal. The charge carriers are polarons (p). **a:** S_0 = neutral ground state; S_1 , S_2 , S_3 are singlet excitons. Rate constants: k_{AI} for autoionisation, k_n for radiationless and k_r for radiative “intramolecular” recombination (fluorescence). **b:** bound charge-carrier pairs

(CP states or geminate pairs); E_{CP} = energy, U_{CP} = Coulomb binding energy, Ω = dissociation probability of the CP states. r_{th} is the spacing of the molecule-ions M^+ and M^- in the CP state. r_c is the “Coulomb radius”: $kT = e^2/4\pi\epsilon\epsilon_0r_c$. **c:** Ionised states M_p^+ and M_p^- of the charge carriers; E_g^{Ad} is the band-gap energy (see Fig. 8.7). From [28].

In the final step, these bound charge-carrier pairs dissociate by thermal activation. The necessary thermal activation energy for this is $E_a^{ph} = -U_{CP} = E_{CP} - E_g^{Ad}$ and is reduced by an applied electric field which is superposed onto the Coulomb potential, that is by the Stark effect (see Fig. 8.17).

The probability of this dissociation can be described in a modified Onsager model [29], [26–28]. Here, the activation energy for the intrinsic photo-generation of the free charge carriers is determined only by the Coulomb binding energy U_{CP} of the CP state:

$$E_a^{ph} = -U_{CP} = \frac{e^2}{4\pi\epsilon\epsilon_0r_{th}}. \quad (8.27)$$

From the experimentally-determined activation energy at $F \rightarrow 0$, for the two plateau values of $\Delta E_{a,1}^{ph}$ and $\Delta E_{a,2}^{ph}$ we find the two discrete values $r_{th,1} = 50 \text{ \AA}$ and $r_{th,2} = 67 \text{ \AA}$ (cf. Fig 8.15). The two CP states thus defined clearly possess a higher reaction cross-section for autoionisation than other possible CP states.

The total quantum yield $\eta = \eta(h\nu, T, F)$ was treated within a modified Onsager model by Silinsh and Inokuchi [28]. With the approximations of an isotropic density $g(r)$ of the distances r of thermalised electrons from the ionised molecules, no field dependence of Φ_0 , an isotropic dielectric constant ϵ and for small electric

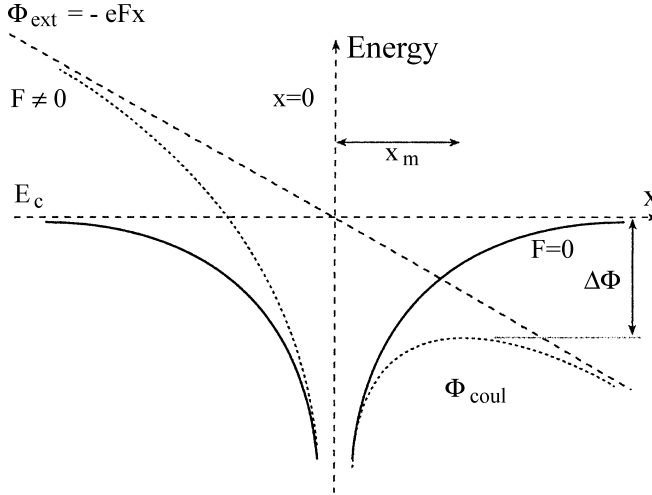


Fig. 8.17 The work function of an electron in a Coulomb field is lowered by an applied electric field F by the amount $\Delta\Phi$. An electron at a distance $x > x_m$ from the positive charge is free.

fields F , one obtains for the quantum yield η a product of the probabilities η_0 for autoionisation to thermal equilibrium and Ω for dissociation:

$$\begin{aligned}\eta(h\nu, T, F) &= \eta_0(h\nu) \cdot \Omega(T, F) \\ &= \eta_0 \left(1 + \frac{eF}{2kT} \right) \int_0^\infty g(r) \exp(-r_c/r) 4\pi r^2 dr.\end{aligned}\quad (8.28)$$

Here, we used

$$\eta_0(h\nu) = \frac{k_{AI}(h\nu)}{k_{AI}(h\nu) + \sum_n k_n(h\nu)}$$

as the fraction of excitons which are ionised, k_{AI} as the rate constant of autoionisation, $\sum_n k_n$ as the sum of all the intramolecular rate constants (see Fig 8.16) and $r_c = e^2/4\pi\epsilon\epsilon_0 kT$ (Eq. (8.26)). One can readily see that the expression (8.28) is plausible by considering only one fixed distance, that is by replacing $g(r)$ by a delta function:

$$g(r) = \frac{1}{4\pi r_{th}^2} \delta(r - r_{th}).$$

Then Eq. (8.28) becomes:

$$\eta = \eta_0 \left(1 + \frac{eF}{2kT} \right) \exp(-U_{CP}/kT). \quad (8.29)$$

A critical test of Eq. (8.28) is a comparison of the quotient S/I with the experimental results. Here, $S = (d\eta/dF)$ is the slope and $I = \eta (F = 0)$ is the intercept of $\eta(F)$ (cf. Fig. 8.14). From Eq. (8.28), we obtain

$$S/I = e^3 / 8\pi \epsilon \epsilon_0 (kT)^2. \quad (8.30)$$

The only materials constant in this equation is the dielectric constant ϵ on the right-hand side. Comparison with the experimental data for S/I in many cases gives surprisingly good agreement [26].

8.4.2.2 Extrinsic and Bimolecular Processes

A marked aspect of intrinsic linear optical charge-carrier separation in polyacene crystals is their low quantum yield. In other organic semiconductors, especially in binary systems with charge-transfer character, it can be considerably higher. However, in polyacene crystals there are also other processes for the optical generation of charge carriers, of which some have notably higher quantum yields: optically-induced charge-carrier injection from an electrode, exciton dissociation in the neighbourhood of an interface with an electrode, the generation of pairs of a free charge carrier with one bound in a shallow trap, production of charge-carrier pairs by exciton-exciton annihilation at high exciton densities, photoionisation of triplet excitons, and still others (see e.g. [M1], Chap. III, p. 481).

Due to its fundamental significance, we wish in the following to briefly describe one of these processes:

In anthracene crystals with ultraclean surfaces, the photogeneration of an equal number of electrons and holes has been observed; these are produced by exciton-exciton annihilation [31]. This requires high excitation densities which are achieved by using a high-intensity pulsed laser. From the quantitative analysis of the quadratic dependence of the photocurrent on the laser intensity (Fig. 8.18), the rate constant for the production of charge-carrier pairs by singlet-singlet exciton annihilation was found to be $\alpha_{ss} = 0.9 \cdot 10^{-12} \text{ cm}^3 \text{ s}^{-1}$. α is defined by the following rate equation for bimolecular processes:

$$\frac{dn}{dt} = \alpha_{ss} [S]^2 + \sigma_s [S] I + k_2 I^2.$$

Here, n is the concentration of the charge carriers, $[S]$ is the concentration of singlet excitons, I the intensity of the UV radiation, σ_s the constant for photoionisation of the singlet excitons, and k_2 is the rate constant for charge-carrier production by two-photon absorption. All three processes are proportional to I^2 . For the separation into individual processes, the spectral dependence of the quadratic photogeneration of charge-carrier pairs was determined and analysed [31].

8.4.3

Contacts, Injection, Ejection, and Dark Currents

In Sections 8.4.1 and 8.4.2, we introduced the basic principles of photoconductivity. Without optical excitation, electric currents can flow in ideal, non-doped organic

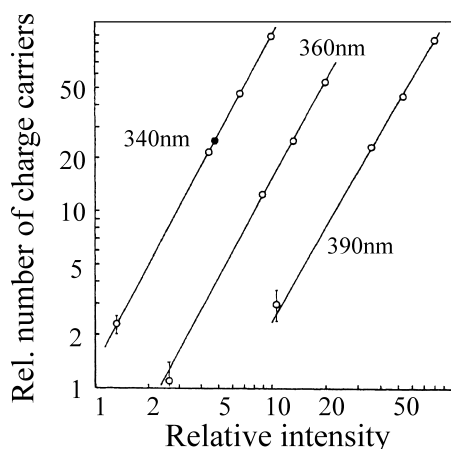


Fig. 8.18 The dependence of the number of photo charge carriers in an anthracene crystal on the intensity of the irradiation at high intensities. The wavelengths of the excitation light were in the range of the absorption of the singlet excitons in which single-photon photogeneration of charge carriers is negligible

(see Fig. 8.13). The units are arbitrary and the scale is shifted for each wavelength for clarity. The solid data point in the 340 nm data corresponds to a photon intensity of $I_0 = 2.5 \cdot 10^{18} \text{ photon cm}^{-2} \text{ s}^{-1}$. The slopes are 1.87 at 340 nm; 1.85 at 360 nm; and 1.77 at 390 nm. From [31].

semiconductors, due to their large band gaps ($E_g \gg kT$), only when the charges come from the external circuit, i.e. when they are injected from one contact and ejected into the other one.

8.4.3.1 Preliminary Remarks and Definitions

When a contact and not the organic semiconductor limits the current, it is referred to as a contact-limited current. When, in contrast, the organic semiconductor itself and not the contacts limit the current, the contacts are referred to as Ohmic contacts. Both cases can be of interest: the first when the current is to be controlled in the circuit independently of the external resistance; and the second, when the process of charge transport in the organic semiconductor is to be investigated.

In the case of an **Ohmic contact**, the density of the free charge carriers at the contact and in its immediate neighbourhood is much higher than the density of free charge carriers in the bulk of the semiconductor, which are e.g. thermally activated from defects. An Ohmic contact thus provides a sufficient reservoir of charge carriers. The term “Ohmic contact” can be misleading in the sense that it does not necessarily mean that the current follows Ohm’s law, i.e. that the current I depends linearly on the voltage V . On the contrary, the characteristic $I(V)$ is linear, and the resistance is Ohmic, only when the voltage V is so low that in the stationary state fewer charge carriers per volume are injected than are present in the bulk through thermal activation (see Sect. 8.4.3.4). As soon as the voltage exceeds this limit, that is when the semiconductor is charged with excess charge carriers and thus has a

stationary space charge, the characteristic becomes nonlinear in a typical manner (see Sect. 8.4.4).

To understand this, we first consider an idealised “circuit device”: let the semiconductor be an organic molecular crystal or a non-crystalline, thin organic film with a large band gap ($E_g \gg kT$) or a high energy spacing between the densities of state (DOS) of the positive and the negative charge carriers (Fig. 8.6). It has no traps or only a negligible density of traps which are occupied in the stationary state; they are as a rule ions when occupied and cannot capture any more charge carriers of the same sign. And finally, let it be contacted with two identical metal electrodes, each of which represents an Ohmic contact. The device is thus a capacitor (see e.g. Fig. 8.3) with the capacity $C = \varepsilon \varepsilon_0 A/d$ (ε is the dielectric constant). With an applied voltage V , the capacitor will charge. Its charge is given by

$$Q = C \cdot V. \quad (8.31)$$

The mean field strength F in this ideal case, up to a numerical factor η , which is of order 1 to 2 (cf. Sect. 8.4.4.), is given by

$$F = \eta \frac{V}{d}. \quad (8.32)$$

Using this expression together with the definitions of the specific conductivity σ and the mobility μ (Eqns. (8.1) and (8.5)) as well as the charge density n ($n = Q/\text{Vol} = Q/Ad$), and with the equation of continuity, $(\partial j/\partial x) = 0$, we find for the current density j :

$$j = \sigma F = en\mu F = e \frac{Q}{Ad} \mu \eta \frac{V}{d} = e \frac{\varepsilon \varepsilon_0 AV}{Ad^2} \mu \eta \frac{V}{d}$$

that is

$$j = \eta \varepsilon \varepsilon_0 \mu \frac{V^2}{d^3}. \quad (8.33)$$

This simple but important equation is called **Child's law** and was originally derived for vacuum electron valves. The current which is flowing through the insulator (or through the vacuum) is termed the **space-charge-limited current (SCLC)** and will be treated in more detail in Sect. 8.4.4. It is proportional to the square of the voltage V and inversely proportional to the third power of the sample thickness d and therefore experimentally clearly distinguishable from an Ohmic current, which is proportional to V/d .

When the ideal case sketched here is realised (we will give some examples of it later), then the mobility μ can be directly determined from the $I-V$ characteristic $j(V)$ (Eq. (8.33)). This is an important aspect, because the temperature dependence and the dependence on electric field of the mobility are the keys to understanding the coupling of the charge carriers to the remaining degrees of freedom, e.g. to the phonons, excitons, or shallow traps of the semiconductor.

To be sure, the ideal case described above is often not realised nor can it be. The most important real cases are the following:

- Often, the materials of the anode and the cathode are necessarily different. The two metals then have different work functions. This leads to a contact potential and produces in the semiconductor an internal, **built-in field** F_{BI} , when the external voltage V is switched off ($V = 0$). For $V \neq 0$, the internal field is then a superposition of the built-in field and the applied field (see Sect. 8.4.3.2).
- In the presence of traps, the injected charge separates into a distribution with a density n_t of trapped charges and n of free charges. The two distributions together determine the internal field $F(x)$, according to the Poisson equation

$$\varepsilon \varepsilon_0 \frac{\partial F}{\partial x} = n_t + n, \quad (8.34)$$

but only the free charge carriers contribute to the current. Only when the injection current is large, i.e. at high applied voltages and thus strong fields, with all the traps occupied in the stationary state, does Child's law hold for a further increase of the applied voltage (Eq. (8.33)) (cf. Sect. 8.4.4).

- The mobility itself also depends in general on the field strength: $\mu = \mu(F)$. This holds in particular for the hopping conductivity in disordered organic semiconductors (see Sect. 8.6), but also for band conductivity in ideal organic molecular crystals (see Sect. 8.5).

In the three following sections 8.4.3.2–8.4.3.4, we treat the contacts, charge-carrier injection, and the Ohmic region of the I – V characteristic; and in Sect. 8.4.4, we return to the space-charge-limited current.

8.4.3.2 Contacts

When two planar metal plates are mounted in vacuum parallel to each other with a small spacing d , and a voltage is applied between them, as long as the voltage V is not too high, and the temperature is moderate, e.g. at room temperature, no current will flow. The reason is well known: the electrons which are present in the metal in sufficiently high numbers would have to be able to diffuse into the vacuum under the influence of the high density gradient present at the surface of the plates; but they cannot “escape”, because the work function Φ_M of the metal, that is the energy required to release an electron into the vacuum, is too large: $e\Phi_M \gg kT$. If they could escape, then a current would flow in a vacuum valve without heating the cathode, since electrons are mobile in vacuum. If the vacuum is replaced by another insulator, e.g. an organic semiconductor (Fig. 8.19) with a large energy gap and a negligibly-small density of thermally-activated charge carriers from defects or doping sites, then current would flow at moderate temperatures, although nothing would be changed in the metal. But the semiconductor has an electron affinity A_c and an ionisation potential I_c (cf. Fig. 8.6). To activate the injection of an electron from metal 1 into an intrinsic semiconductor, the work function Φ_{M1} therefore

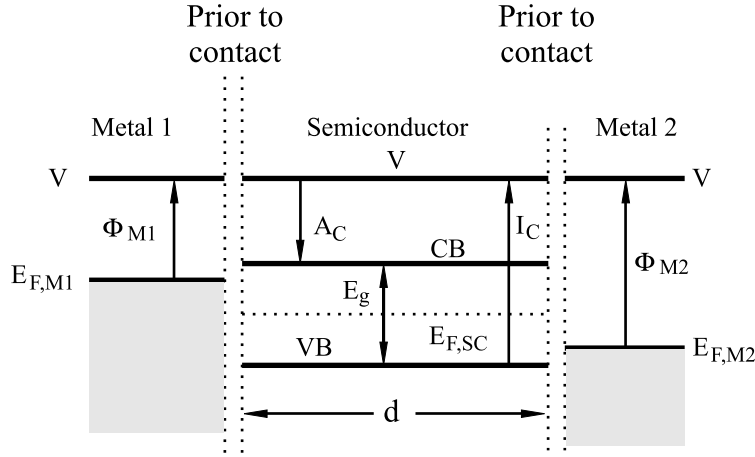


Fig. 8.19 The term diagrams of an (organic) semiconductor SC and two metals M_1 and M_2 , which are not in contact. V is the vacuum energy level, E_F the Fermi energy, Φ the work function, CB the lower edge of the conduction band at the energy E_c , VB the upper edge of the valence band at the energy E_v , E_g the band-gap energy, A_C the electron affinity, I_C the ionisation energy, and d the thickness of the semiconductor sample (cf. also Fig. 8.6).

must be reduced by the electron affinity A_c , and this yields the activation energy Φ_e for the injection of electrons into the semiconductor:

$$\Phi_e = \Phi_{M1} - A_c \quad (8.35)$$

(Fig. 8.19, left).

In order to activate the ejection of an electron from the semiconductor into the metal 2 electrode, analogously the ionisation potential I_c must be reduced by the work function Φ_{M2} and this determines the activation energy for the ejection of electrons from the semiconductor, Φ_h , or – in the usual terminology – for the injection of holes into the semiconductor:

$$\Phi_h = I_c - \Phi_{M2} \quad (8.36)$$

(Fig. 8.19, right).

When the two metals M_1 and M_2 are brought into contact with each other, then an electric current flows for a brief time until the two Fermi levels $E_{F,M1}$ and $E_{F,M2}$ are equalised (Fig. 8.20). The metal M_2 is negatively and metal M_1 positively charged in this process, if $\Phi_2 > \Phi_1$. Between the vacuum levels of the two metals there is then a contact potential V_{BI}

$$V_{BI} = \Phi_{BI}/e = (\Phi_{M2} - \Phi_{M1})/e. \quad (8.37)$$

When the contact is produced via an ideal intrinsic semiconductor of thickness d , then a built-in electric field F_{BI} is established within the semiconductor:

$$F_{BI} = V_{BI}/d \quad (8.38)$$

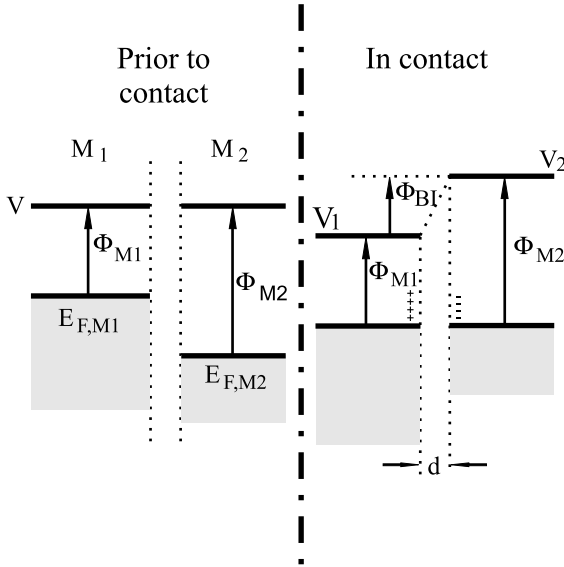


Fig. 8.20 The term diagrams of two metals, M_1 and M_2 , before (left) and after (right) contact is made.

$\Phi_{BI} = (e \cdot \text{contact potential})$; all other notation is the same as in Fig. 8.19.

(Fig. 8.21). To make charge transport possible, a counter-voltage V_{ext} must therefore be applied to contacts with different work functions, which is at least sufficient to compensate the built-in field, $V_{\text{ext}} > -V_{BI}$. The (internal) field strength in this greatly idealised case would then be

$$F = (V_{\text{ext}} - V_{BI})/d \quad (8.39)$$

(Fig. 8.22).

The contacts described above are called **neutral contacts** and are, as mentioned, strongly idealised: firstly, we assumed that the semiconductor is not doped and thus contains no charge carriers of its own, and secondly, we assumed that the contact interfaces consist only of the pure materials, i.e. that they are ideally clean and the states at the surface are the same as those in the bulk. Furthermore, the values of the work functions in the two injection barriers, Φ_e and Φ_h (Eqns. (8.35)

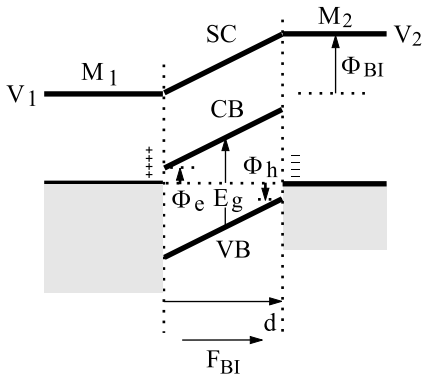


Fig. 8.21 Neutral contacts: the term diagrams of an intrinsic semiconductor in contact with two metals with different work functions: $\Phi_{M2} > \Phi_{M1}$. $F_{BI} = \Phi_{BI}/ed$ is the “built-in field strength”; Φ_e and Φ_h are the activation energies for electrons (e) and holes (h); the remaining notation is as in Figs. 8.20 and 8.19.

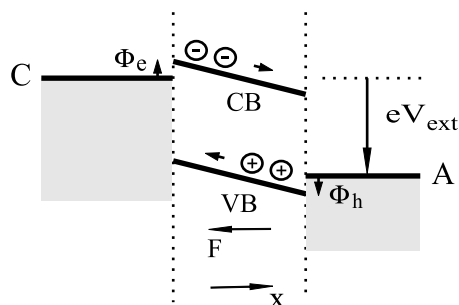


Fig. 8.22 The term diagram of an ideal intrinsic semiconductor with neutral contacts (see Fig. 8.21) and an applied voltage V_{ext} . Here, only the transport levels are shown. F is the electric field strength; the remaining notation is as in Figs. 8.19–8.21. The transport levels in semiconductors are flat and not curved only when the semiconductor is not p- or n-doped

and V_{ext} is so low that the density of injected charge carriers cannot measurably influence the field F . This case is also termed the “flat band case”. When the applied voltage is higher, so many charge carriers are injected that the space charge determines the field within the semiconductor and thereby dominates the charge transport (see Sect. 8.4.4).

and (8.36)) are not necessarily the tabulated values of the pure metals, since often a contact-specific dipole layer is present, which modifies the work function. When very thin dipole layers (only a few Å) are inserted between the metal and the organic semiconductor, e.g. a layer of LiF, the activation energy for charge-carrier injection can be reduced.

In doped semiconductors, depletion zones are formed near the contacts and they thus become **Schottky contacts**, which for one of the two polarities of the applied voltage are inhibiting contacts (Schottky barriers) that prevent the flow of current. This case, which has important applications, will not be treated further here. Dipole layers and Schottky barriers namely do not change the basic necessity of using metals with a small work function for an effective injection of electrons and metals with a large work function for an effective injection of holes. The former are used for the investigation of electron conductivity, the latter for the investigation of hole conductivity, and both for the investigation of bipolar currents. (In the case of bipolar currents, electrons and holes can recombine within the organic semiconductor; compare Chap. 12.)

8.4.3.3 Charge-Carrier Injection – Injection-limited Currents

For the injection of an electron from the metal into the semiconductor, the electron must be emitted with thermal energy from the metal and then either have sufficient kinetic energy to overcome the barrier or else it must tunnel through the barrier (cf. Fig. 8.22). Analogous conditions hold for the injection of holes. We therefore restrict the discussion here to the injection of electrons.

To determine the height of the barrier in an applied electric field $F \neq 0$, we must take into account the so-called **Schottky effect** (Fig. 8.23): an injected electron at a distance x from the metal surface produces a positive image charge in the metal through influence, whose field gives rise to what is termed the image force and

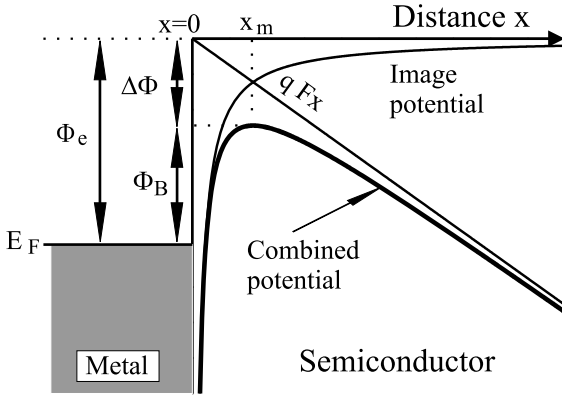


Fig. 8.23 The barrier for the injection of an electron from a metal into a semiconductor with an applied electric field F . Φ_e and $\Phi_B = \Phi_e - \Delta\Phi$ are the barrier heights without and with the image charges taken into account. x_m is a measure of the width of the barrier (see text).

whose potential is called the image-charge potential Φ_{image} (see textbooks on electricity and magnetism):

$$\Phi_{\text{image}} = \frac{e^2}{16\pi\epsilon\epsilon_0} \cdot \frac{1}{x}. \quad (8.40)$$

The superposition of the image potential with the potential Φ_{field} of the applied field F ($\Phi_{\text{field}} = eFx$) lowers the potential barrier Φ_e by an amount

$$\Delta\Phi = \sqrt{\frac{e^3 F}{4\pi\epsilon\epsilon_0}} \quad (8.41)$$

to the effective height of the barrier, $\Phi_B = \Phi_e - \Delta\Phi$. The maximum of the superposed potential lies at a distance x_m from the surface of the metal:

$$x_m = \sqrt{\frac{e}{16\pi\epsilon\epsilon_0 F}}. \quad (8.42)$$

A thermally-emitted electron must reach at least this distance in order that it is not able to recombine. At a typical applied-field strength of $F = 1 \text{ MV/cm}$ and $\epsilon = 4$, we have $\Delta\Phi = 0.19 \text{ eV}$ and $x_m = 9.5 \text{ \AA}$. The Schottky effect thus makes a non-negligible contribution to the effectiveness of thermally-activated injection, which is known as thermionic emission (Fig. 8.24).

The current density j_{RS} for this process, which at high temperatures is also called glow emission, was originally calculated by Richardson for glow cathodes in vacuum valves and, taking the Schottky effect into account, is given by:

$$j_{RS} = A^* T^2 \exp(-\Phi_B/kT). \quad (8.43)$$

Here, $A^* = 4\pi em^* k^2/h^3$ is the effective Richardson constant, which is proportional to the effective mass m^* of the charge carriers and otherwise contains only physi-

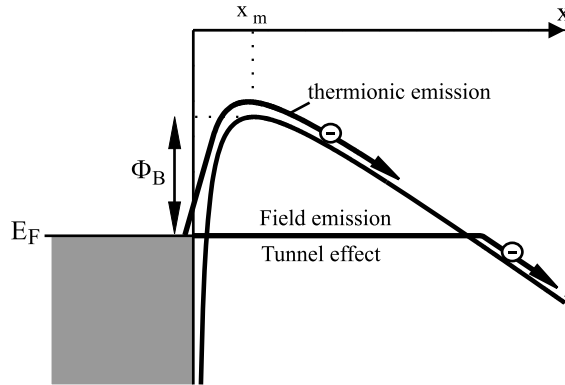


Fig. 8.24 Thermionic emission and field emission.

cal constants. The thermionic current is dominated by thermal activation over the barrier Φ_B . To obtain an Ohmic contact, Φ_B must therefore be small.

A second injection process is the tunnel effect at the Fermi energy of the metal (Fig. 8.24). It is also termed the field effect. For a triangular barrier Φ_B , the tunnel current density has been calculated by Fowler and Nordheim [32]:

$$j_{FN} = \frac{A^*}{\Phi_B} \left(\frac{eF}{\alpha k} \right)^2 \exp \left(-\frac{2\alpha \Phi_B^{3/2}}{3eF} \right). \quad (8.44)$$

In this expression, $\alpha = 4\pi\sqrt{2m^*}/h$. When a measurement of $\ln(j/F^2)$ as a function of $1/F$ yields a straight line, this is an indication of the tunnel effect. From the slope of the line, the value of Φ_B can be computed. To be sure, for this a knowledge of F is required. In Sect. 8.4.4 on the position dependence of F with space-charge-limited currents, we shall see that this problem is non-trivial.

For a real Schottky barrier, the current density in the pass direction is given for $eV > 3kT$ by the so-called Shockley formula:

$$j = AT^2 \exp(-\Phi_B/kT) \exp((eV/nkT) - 1). \quad (8.45)$$

Here, n is an “ideality factor”. For ideal Schottky diodes, $n = 1$ (see textbooks on solid-state physics).

Thermionic emission over the barrier and field emission, that is the tunnel effect through the barrier, are limiting cases. All injection processes of electrons of energy between E_F and $E_F + \Phi_B$ are termed thermionic field emission. These processes have all been described for semiconductors with broad bands. They do not take the molecular character of the organic and particularly the disordered organic semiconductors into account. Here, for example, recombination and the thermalisation of the charge carriers must be considered, similarly to the case of the photogeneration of free charge carriers (compare Sect. 8.4.2). We refer the reader to the more specific articles [33] and [34].

8.4.3.4 Doping – Ohmic Currents

When a semiconductor, due to its large band gap ($E_g \gg kT$), contains practically no intrinsic charge carriers and owing to a low applied voltage also no injected charge carriers, and nevertheless has an appreciable dark conductivity, then it must be doped. The dopants must either be able to activate electrons thermally into the conduction band (they are then referred to as donors and are oxidised to cations if they were previously neutral); or they must be able to thermally activate electrons out of the valence band and thereby be reduced (in this case they are called acceptors and become anions if they were previously neutral, or neutral if they were previously positively charged, for example as radical cations). The two redox or charge-transfer processes yield electrons with a density n in the conduction band and holes with a density p in the valence band (Fig. 8.25). Overall, the sample must remain neutral, that is

$$n + N_A^- = p + N_D^+ \quad (8.46)$$

Furthermore, Fermi statistics apply. The computation of the charge-carrier concentrations n and p for the general case in which both donors at a concentration $N_D = N_D^0 + N_D^+$ and also acceptors at a concentration $N_A = N_A^0 + N_A^-$ are present, is a general problem of semiconductor physics and can be carried out only numerically [35]. For the case of a pure n-type semiconductor, that is a semiconductor which contains only donors and no acceptors, the charge-carrier concentration $n(T)$ and the Fermi energy $E_F(T)$ can, however, be calculated to a good approximation [35]:

$$n \approx 2N_D \left(1 + \sqrt{1 + 4 \frac{N_D}{N_c} \exp(E_d/kT)} \right)^{-1} \quad (8.47)$$

Here, N_c is the density of states in the conduction band and $E_d = E_{LB} - E_D$ is the energy spacing of the donor levels from the lower edge of the conduction band

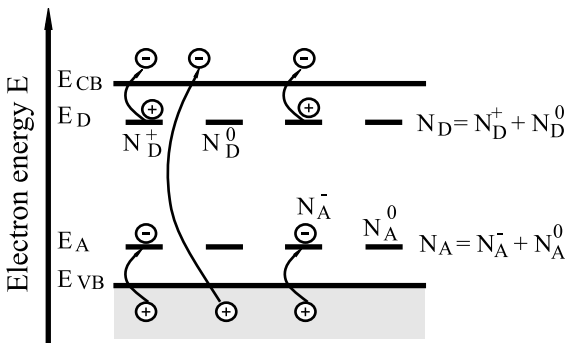


Fig. 8.25 Conduction electrons in the conduction band CB, holes in the valence band VB, and charged and neutral donors D and acceptors A. E = energies, N = densities. +, 0 and – represent charges in units of the elementary charge e .

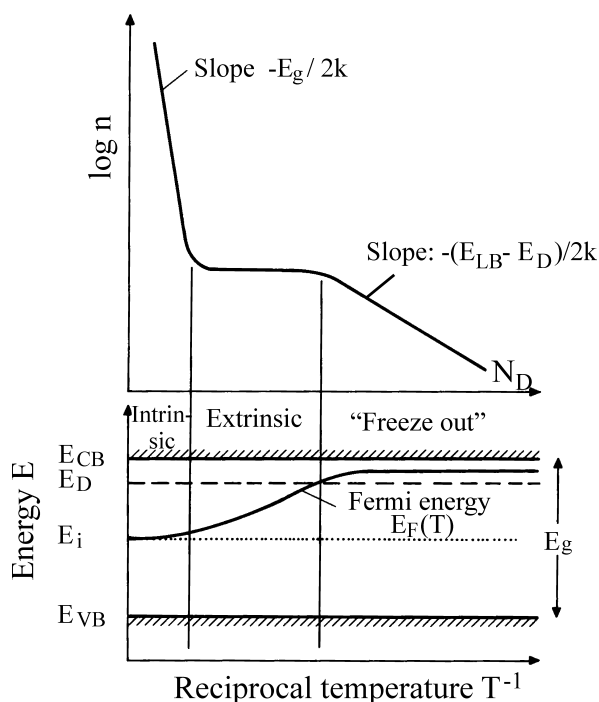


Fig. 8.26 The dependence of the conduction-electron concentration $n(T)$ and the Fermi energy $E_F(T)$ in an n -type semiconductor as functions of the temperature. E_i is the Fermi energy of the intrinsic semiconductor. The other notation is as in Fig. 8.25.

(Fig. 8.25). Figure 8.26 shows $n(T)$ and $E_F(T)$. At low temperature, the energy E_D of the donors follows from the temperature dependence of $n(T)$. In the temperature range of "exhaustion", the donors are maximally oxidised. Intrinsic charge carriers can be released, owing to the width of the band gap E_g , only at still higher temperatures. In organic semiconductors, this case is generally not observed.

When an organic semiconductor is weakly n - or p -doped, thus when dopants lead to the charge-transfer reactions mentioned above, it becomes an Ohmic conductor. A measurement of the specific conductivity σ can then in optimal cases permit the concentration of the dopants to be computed, if the mobility μ is known.

An extensive treatment of **doped molecular semiconductors** can be found in the monograph by Simon and André [M6]. For the elucidation of the electric conductivity of doped organic semiconductors, we must remind the reader that the solubility of dopant molecules in organic single crystals is very limited. Only in very rare cases can foreign molecules be introduced with a concentration of more than 10^{-3} into single crystals, without strongly disturbing their crystal structure or causing aggregation of the dopant molecules. A fundamental requirement for understanding the mechanism of conduction is therefore an analysis of the structure of the dopants introduced and their crystalline or non-crystalline surroundings. In addi-

tion to X-ray diffraction, a number of spectroscopic techniques including optical and IR spectroscopy, Raman spectroscopy, ESR spectroscopy and others are indispensable for this purpose.

Brinkmann *et al.* [59] have extensively investigated the mechanism of conduction in iodine (I)-doped pentacene (PEN) crystals. In their experiments, the iodine concentration in (I/PEN) was varied within a range of $I/PEN < 0.05$ up to 6 atoms per molecule. The iodine doping leads to the formation of PEN^+ radical cations and I^- anions. At the smallest concentrations, (< 0.05) the crystal structure of the PEN remains essentially unchanged. At $0.2 \leq I/PEN \leq 2$, iodine intercalates form from I_3 and I_5 , which are mixed with non-doped regions of PEN. Here, the specific conductivity increases from the value of the non-doped crystal (ca. 10^{-8} S/cm) to around 1 S/cm. In the range of highest doping concentrations, ($I/PEN > 2$), the iodine is located within the ($a-b$) planes of the PEN molecules in the crystal and produces a nearly amorphous material. The conductivity then no longer increases. We will not treat the doped organic semiconductors further in this book; for applications, however, they are certainly of great significance.

8.4.4

Space-Charge Limited Currents

When the current is not injection limited, but instead the cathode and the anode are Ohmic contacts, then the current is limited by the organic semiconductor itself. In the ideal case of an organic semiconductor, which has practically no intrinsic charge carriers owing to its large band gap ($E_g \gg kT$), and only a small density n_0 of charge carriers which have been thermally activated out of ionisable centres, one observes with a low applied voltage only the current due to those charge carriers. The characteristic $j = \sigma F$ is then linear, $\sigma = en_0\mu$ is constant and the field F is constant, independent of the position x within the entire sample (Fig. 8.22). With increasing applied voltage, however, excess charge carriers are injected. As soon as their density becomes larger than n_0 , the organic semiconductor contains a space charge, which determines the internal field and the current to a large extent. The **space-charge-limited stationary currents** require no thermally-activated charge carriers, just like the displacement currents in photo-induced TOF experiments. In ideal organic semiconductors, they are the normal case and were first investigated in organic semiconductors by Mark and Helfrich [11, 12].

The basic idea of the SCLC was sketched in Sect. 8.4.3.1. In the following, we will describe a model with whose help the unipolar space-charge-limited current in an organic semiconductor can be described in more detail and more realistically. As we shall see, Eq. (8.33) with the factor η heuristically introduced in Eq. (8.32) is only an ideal limiting case. As an illustration of the phenomena which are to be explained with this model, Figs. 8.27 and 8.28 show three examples of current-voltage characteristics in organic semiconductors, in analogy to Figs. 8.1 and 8.2.

In a $10\ \mu\text{m}$ thick rubrene crystal, the current $I(V)$ increases linearly with the voltage V for low voltages, then quadratically for higher voltages, with a still higher power at higher voltages, and at the highest voltages again quadratically (Fig. 8.27a).

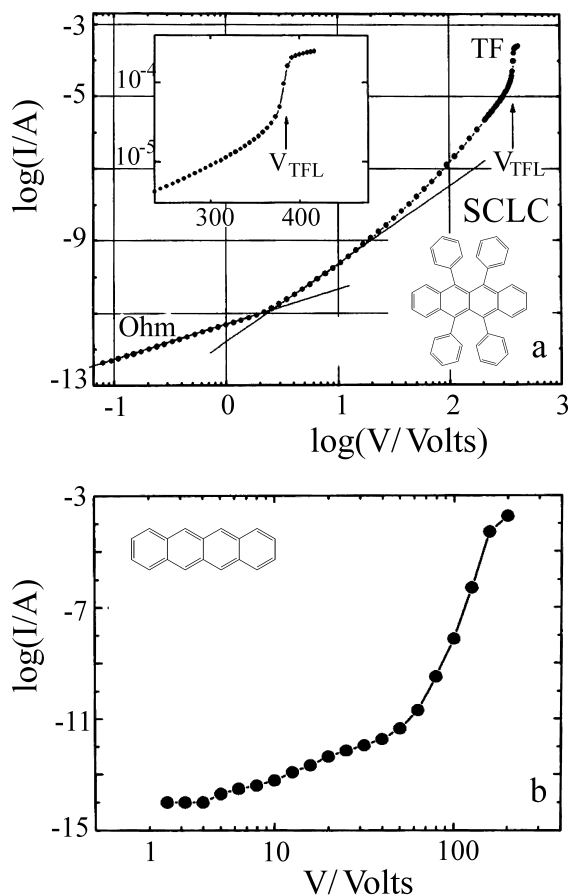


Fig. 8.27 Current-voltage characteristics $I(V)$ of organic single crystals at room temperature. Above: in a $d = 10 \mu\text{m}$ thick rubrene crystal. At low voltages ($V < 2 \text{ V}$), one observes Ohmic behaviour ($I \propto V$); the metal-rubrene contact resistance is small in comparison to the resistance of the crystal. For $V > 2 \text{ V}$, the characteristic is nonlinear: up to about 20 V , one can detect a quadratic increase ($I \propto V^2$), for $V > 20 \text{ V}$, a still steeper increase up to the voltage V_{TFL} , and for $V > V_{TFL}$, again $I \propto V^2$ is seen. The current is space-charge limited in the whole range $V > 2 \text{ V}$. V_{TFL} is the voltage at which all the traps are filled with charge carriers in the stationary state (see Eq. (8.64)). The density N_t of the traps can be derived from the value of V_{TFL} . For $V > V_{TFL}$, Child's law holds (Eq. (8.59)), from which the mobility μ can be directly obtained. Furthermore, from the $I-V$ characteristic, the depth E_t of the traps

can be determined. For the rubrene crystal, $N_t = 10^{15} \text{ cm}^{-3}$ was found. After [36]. Below: from a $d = 30 \mu\text{m}$ thick tetracene crystal. The current was measured along the c' axis. The trap concentration was $N_t = 5 \cdot 10^{13} \text{ cm}^{-3}$ and the mobility $\mu = 0.59 \text{ cm}^2/\text{Vs}$. This value represents a lower limit and agrees rather well with the value of the mobility in the c' direction measured by the TOF method of photoconductivity (cf. Table 8.2). A significant difference between the measurements of μ with the TOF method and from the $I-V$ characteristic depends on the quality of the contacts: since the current is a displacement current in the TOF method, that is, the measurement is carried out within a capacitor, the quality of the contacts plays a less important role than for the measurement of the $I-V$ characteristic, where the contacts must inject charge carriers. After [37].

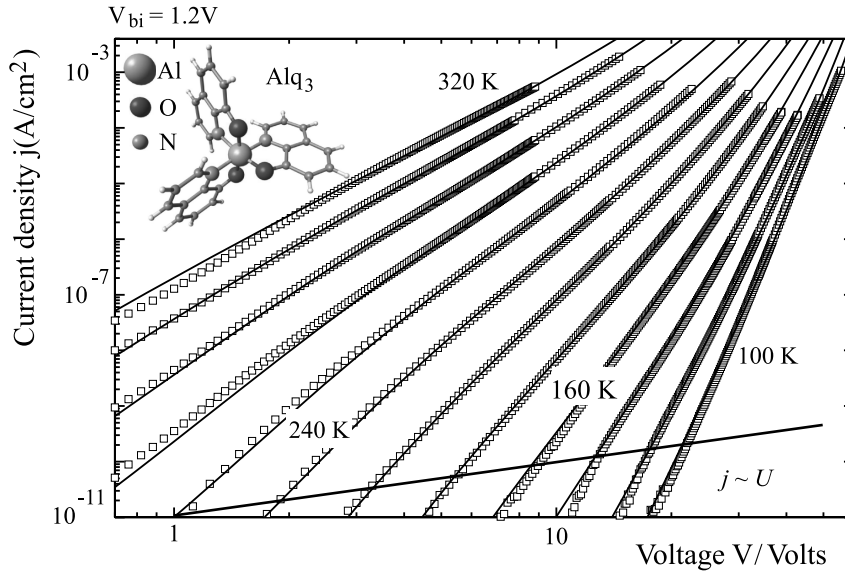


Fig. 8.28 Experimental values and a simulation (solid lines) of the temperature-dependent $j(V)$ characteristics of a partially-crystalline, $d = 294$ nm thick Alq_3 film ($\text{Al}/\text{Alq}_3/\text{Ca}$). The simulation of all the characteristics was carried out using a Gaussian distribution of traps with a density $N_t = 9 \cdot 10^{16} \text{ cm}^{-3}$ and a width $\sigma_t = 0.2$ eV. All the characteristics are much steeper than the Ohmic characteristic $j \propto V$. For details, see Sect. 8.6.5. After [38].

In a $30 \mu\text{m}$ thick tetracene crystal, the current increases quadratically with voltage in the voltage range between 4 V and 50 V and at higher voltages with a higher power. Above $V = 150$ V, a quadratic dependence again seems to appear (Fig. 8.27b). In the non-crystalline 294 nm thick Alq_3 film (Fig. 8.28), the current density $j(V)$ increases extremely nonlinearly at all temperatures between 100 K and 320 K. The comparison with the Ohmic characteristic in Fig. 8.28 demonstrates this directly. All three examples are characteristic of space-charge-limited currents in crystals and in non-crystalline organic semiconductors. We will see later that – for example from the analysis of these characteristics – the mobilities μ and their field and temperature dependencies as well as the concentration N_t and the depth E_t of the charge-carrier traps can be extracted.

The following assumptions enter the model for the space-charge-limited currents (see e.g. M1, 11, 12, 38):

- The material is assumed to be an insulator, i.e. the thermally-generated charge-carrier density is so small that it makes no noticeable contribution to the transport and therefore can be neglected in the model. All the charge carriers which participate in the transport or are captured in traps are excess charge carriers injected from the contacts.
- Diffusion currents are negligible. Then only the drift current determines the overall current. This means, to be sure, that with this model, the current in the reversed-bias direction and in the pass direction for very low voltages near V_{BI} (Eq. (8.37)) cannot be described correctly. As an estimate, we can

assume that the voltage must be at least a few kT/e ($= 26$ mV at 300 K) above V_{BI} in order for the model to be able to describe the experimental results.

- Only one type of charge carriers will be considered. In the following, this will be the electrons in the conduction band or in the LUMO. The treatment of the holes is analogous.
- The organic material is assumed to be homogeneous, that is the materials parameters which determine the mobility and the trapping states are spatially constant within the material.
- As far as not explicitly given, the influence of the contacts will be neglected. In the sense of the SCLC theory, this means that the electric field \mathbf{F} vanishes at the contact: $F(x=0) \equiv F_0 = 0$.
- Shallow traps and deep traps for charge carriers are taken into account. They can have either sharp energy values (discrete trapping states) or they can be distributed over an energy range (see Fig. 8.6). In the latter case, the density n of the free charge carriers is computed using Boltzmann statistics, while the occupation of the shallow and deep trapping states is obtained with Fermi statistics. The Fermi energy E_F , as well as the energy E of the shallow and deep traps, are assumed to be positive when they lie within the band gap.
- The mobility μ is not taken to be constant, but is assumed to be field-dependent. This means that the drift velocity depends in a nonlinear way on the field strength. For numerical simulations, an arbitrary field dependence can be used. (In the case of disordered films, we shall later explicitly investigate the form which is usual for organic materials, $\mu(F) = \mu_0 \exp(\beta\sqrt{F})$ (see Sect. 8.6).)

On the basis of these assumptions, in the following we shall calculate the results of the **SCLC model**, taking into account a **field-dependent mobility**. The coordinate x has the value zero at the injecting electrode (cathode) and d (sample thickness) at the opposite electrode (anode) (Fig. 8.3). The current density \mathbf{j} and the electric field \mathbf{F} are directed from the anode towards the cathode and thus point in $-\mathbf{e}_x$ direction. It is therefore expedient to define the scalar quantities j and F as $\mathbf{j} = -j\mathbf{e}_x$ and $\mathbf{F} = -F\mathbf{e}_x$. The quantities j and F are then positive. Since we consider only electrons, the absolute value of the transport level E_e plays no role and will therefore be set equal to zero. All energy values are thus given relative to E_e (cf. Fig. 8.6), whereby the energy scale is defined in such a way that positive energies lie in the band gap. This notation simplifies the formulation of the equations without limiting their general validity.

We thus obtain the following system of equations:

$$\text{transport equation} \quad j = en\mu F, \quad (8.48)$$

$$\text{Poisson equation} \quad \frac{\varepsilon\varepsilon_0}{e} \frac{\partial F}{\partial x} = n + n_t, \quad (8.49)$$

$$\text{equation of continuity} \quad \frac{\partial j}{\partial x} = 0, \quad (8.50)$$

$$\text{filled charge-carrier traps} \quad n_t = \int \frac{G_t(E)}{1 + \exp((E_F - E)/kT)} dE, \quad (8.51)$$

$$\text{determination of the Fermi level} \quad n = N_e \exp(-E_F/kT), \quad (8.52)$$

$$\text{field-dependent mobility} \quad \mu(F, T) = \mu_0(T) \exp(\beta(T)\sqrt{F}), \quad (8.53)$$

$$\text{or: } \mu = \mu(F, T) \text{ arbitrary} \quad (8.54)$$

$$\text{boundary condition} \quad F(0) \equiv F_0 = 0, \quad (8.55)$$

$$\text{resulting voltage} \quad \int_0^d F dx = V_{\text{ext}} - V_{BI} = V. \quad (8.56)$$

In these equations, n is the density of the free charge carriers, n_t the density of the charge carriers captured in shallow traps, ε the static dielectric constant, N_e the density of states at the transport level E_c , V_{ext} the applied voltage, and $G_t(E)$ gives the density of the trapping states per energy interval dE . N_e in disordered films or in crystals with narrow conduction bands is equal to the number of molecules per unit volume.

The system of Eqns. (8.48)–(8.55) can be immediately collected into an integral from which the local field $F(x)$ can be computed. Here, the current density j is spatially constant due to the lack of recombination processes (Eq. (8.50)). The quantity n_t can initially be written with Eq. (8.52) as a function of the free charge-carrier density n :

$$n_t = \int \frac{G_t(E)}{1 + \exp((E_F - E)/kT)} dE = \int \frac{G_t(E)}{1 + (N_e/n) \exp(-E/kT)} dE.$$

From the transport equation, we find $n = j/e\mu F$. With this, both n and n_t can be written as functions of the field strength F . Setting these results into the Poisson equation, we obtain:

$$\frac{\varepsilon\varepsilon_0}{e} \frac{\partial F}{\partial x} = \frac{j}{e\mu(F)F} + \int \frac{G_t(E)}{1 + (N_e e\mu(F)F/j) \exp(-E/kT)} dE.$$

This equation can be integrated immediately and yields:

$$\int_{F_0}^{F(x)} \frac{\mu(F)F}{1 + \int \frac{G_t(E)}{(j/e\mu(F)F) + N_e \exp(-E/kT)} dE} dF = \int_0^x \frac{j}{\varepsilon\varepsilon_0} dx = \frac{j}{\varepsilon\varepsilon_0} x. \quad (8.57)$$

This integral can be solved exactly for special cases and numerically with high precision for the general case. The quantity finally determined is the upper integration limit of the left-hand integrals, i.e. $F(x)$ as a function of the current density and the electric field F_0 at the contact. Using Eq. (8.57), it is thus possible to apply even more complicated boundary conditions (non-Ohmic contacts), but in particular arbitrary field-dependent mobilities and arbitrary energetic distributions of the shallow traps. The necessary voltage is then found by integration for the electric field (Eq. (8.56)).

Important special cases are: in the theory of SCLC, as it was originally developed for inorganic materials, the mobility is in general treated as a constant, as is normally the case for band transport. In this case, the current-voltage characteristics and the field distribution can be given analytically for some limiting conditions. We consider two of these limiting cases (*i.* and *ii.*) here. From the following results, one obtains important general characteristics of space-charge-limited currents in single crystals. Further limiting cases and the numerical simulation are treated in Sect. 8.6.5.2.

i) Constant **mobility without trapping states** ($\mu = \text{const.}$, $n_t = 0$). In the presence of shallow traps, one finds immediately from the transport and the Poisson equations:

$$F(x) = \sqrt{\frac{2j}{\varepsilon\varepsilon_0\mu}x + F_0^2} \quad (8.58)$$

where F_0 is the field at the injecting contact. F_0 is in general given by the injection characteristic. Setting $F_0 = 0$, we obtain the **Mott-Gurney equation** for the current density (Child's law):

$$j = \frac{9}{8}\varepsilon\varepsilon_0\mu\frac{V^2}{d^3}. \quad (8.59)$$

It is identical with Eq. (8.33), where however here the previously unknown factor η has been determined to have the value 9/8. The position-dependent field strength is then found to be:

$$F(x) = \frac{3V}{2d}\sqrt{\frac{x}{d}}. \quad (8.60)$$

The field thus increases on going away from the contact and reaches the value $3V/2d$ at the opposite electrode, which is 50% higher than in the space-charge free case, in which $F = V/d$ (see Fig. 8.29).

The charge-carrier density is given by $n = j/e\mu F$ and is therefore:

$$n = \frac{3\varepsilon\varepsilon_0}{4ed^2}\sqrt{\frac{d}{x}} \cdot V = \frac{1}{2}\sqrt{\frac{d}{x}}\bar{n} \cdot V \quad (8.61)$$

with the mean charge-carrier density

$$\bar{n} = d^{-1} \int_0^d n(x) dx = \frac{3\varepsilon\varepsilon_0 V}{2ed^2}.$$

The charge-carrier density thus decreases on going away from the contact into the bulk (Fig. 8.29). To be sure, the charge-carrier density diverges in this expression at the injecting contact. This problem does not occur if one takes diffusion currents into account. The case treated above, without shallow traps, will in the following be referred to as **TF-SCLC (trap-free SCLC)**.

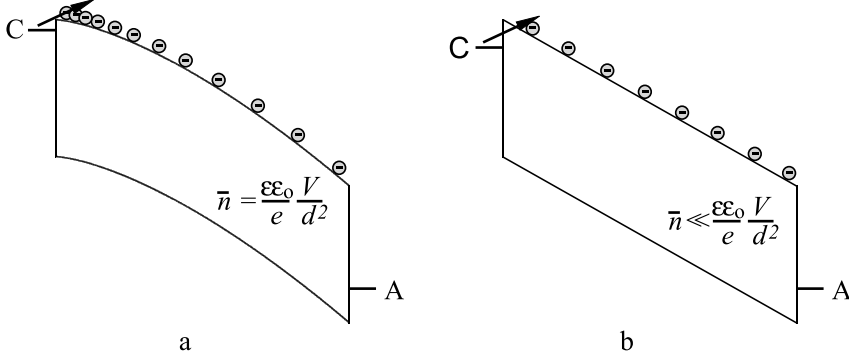


Fig. 8.29 Comparison of the position dependence of the density of conduction electrons $n(x)$ and the energies $E(x)$ of the conduction and the valence bands for space-charge limiting (a) and for injection limiting (b). \bar{n} is the mean density of the charge carriers, C = cathode, A = anode.

ii) Constant **mobility with discrete trapping states**. Only in the rarest cases is an organic solid free of shallow traps and/or charge-carrier traps. As a rule, they are present and decrease the current. How strongly they decrease it depends above all on the density of trapping states, since for low current densities, all of the shallow traps are already filled and the current is thus practically just as great as it would be without trapping states. This is the so-called **Trap-Filled Limit (TFL)**. In the following, the situation with an energetically-discrete trapping level will be treated. We thus replace $G_t(E)$ by a delta function, $G_t(E) = N_t \delta(E - E_t)$, where N_t is the density of the shallow traps and E_t is their depth (see Fig. 8.6). The integral (8.57) which must be computed is then:

$$\int_{F_0}^{F(x)} \mu F \frac{j/e + \chi \mu F}{j/e + (\chi + N_t) \mu F} dF = \int_0^x \frac{j}{\epsilon \epsilon_0} dx = \frac{j}{\epsilon \epsilon_0} x \quad (8.62)$$

with $\chi = N_e \exp(-E_t/kT)$. For high current densities, the quotient in the left-hand integral is equal to one and one obtains the same result as in the case without shallow traps. For very small current densities, j/e can be neglected and the quotient then likewise takes on the constant value Θ with $\Theta^{-1} = 1 + N_t/N_e \exp(E_t/kT)$; then we can have $\Theta \ll 1$. The current-voltage characteristic is then formally identical with the TF-SCLC case, if one replaces the real mobility μ by an effective mobility μ_{eff} :

$$j = \frac{9}{8} \epsilon \epsilon_0 \mu_{\text{eff}} \frac{V^2}{d^3}. \quad (8.63)$$

Here, $\mu_{\text{eff}} = \mu \Theta$. In Fig. 8.30, simulated characteristics for the parameters $\mu = 10^{-7} \text{ cm}^2/\text{Vs}$, $d = 300 \text{ nm}$, $\epsilon_r = 4$, $N_e = 5 \cdot 10^{21} \text{ cm}^{-3}$, and $E_t = 0.5 \text{ eV}$ are shown. Between the region dominated by trapping ($\Theta \ll 1$) and the TFL region ($\Theta \approx 1$),

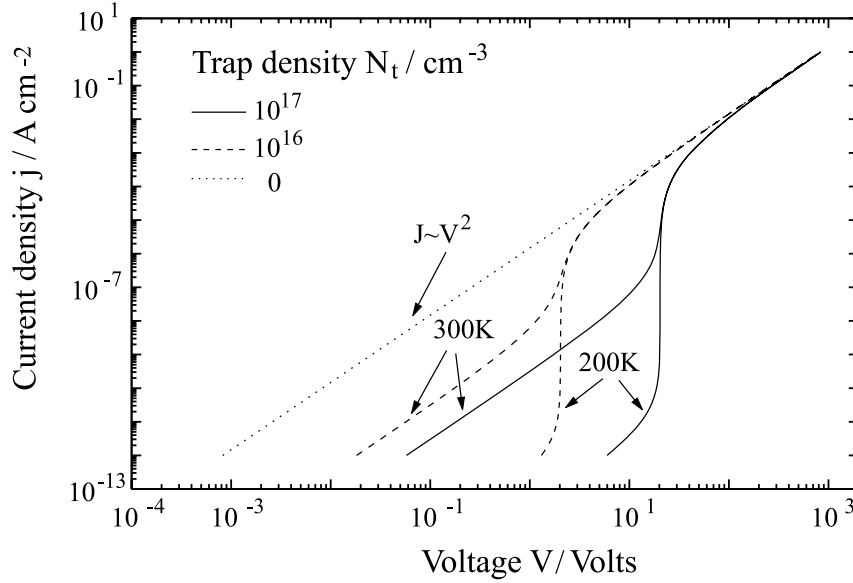


Fig. 8.30 Simulated current-voltage characteristic $j(V)$ with discrete trapping states for various temperatures T and trap densities N_t , with $\mu = 10^{-7} \text{ cm}^2/\text{Vs}$, $d = 300 \text{ nm}$, $\varepsilon = 4$, $N_e = 5 \cdot 10^{21} \text{ cm}^{-3}$ and $E_t = 0.5 \text{ eV}$ (see text). From [38].

there is a sharp transition. The voltage at which this transition takes place is given by

$$V_{\text{TFL}} = \frac{eN_t d^2}{2\varepsilon\varepsilon_0}. \quad (8.64)$$

The simulated current-voltage characteristic (Fig. 8.30) corresponds roughly to the experimentally-determined characteristics for rubrene and tetracene crystals in the non-ohmic range (Fig. 8.27). For the ultrapure tetracene crystals, the values $\mu \approx 1 \text{ cm}^2/\text{Vs}$ for the mobility at room temperature and $N_t < 5 \cdot 10^{13} \text{ cm}^{-3}$, $E_t \approx 700 \text{ meV}$ for the density and the depth of the charge-carrier traps were found [37].

From the case discussed above, with constant mobility and energetically sharply-localised shallow traps, the following results hold:

- With a discrete trapping state, there is an abrupt increase in the current at a voltage of V_{TFL} , at which the trapping states are all filled. From the voltage, the trap density can be determined. The temperature dependence of Θ (for $V < V_{\text{TFL}}$) yields the trap depth. E_T
- Since the range of currents and voltages is always limited, this transition is not always observable experimentally. In the case that it is not, one can initially determine only the effective mobility μ_{eff} ; a direct determination of the mobility with completely filled traps is then not possible.
- If the transition occurs at voltages near the contact potential V_{BI} , the simulation will not yield correct results owing to the fact that diffusion is neglected.

Since $V_{\text{TFL}} \propto d^2$, the sample thickness is the decisive parameter to shift the transition between $\Theta \ll 1$ and $\Theta \approx 1$ into an experimentally accessible voltage range which is also sufficiently high for the simulation ($V_{\text{ext}} - V_{\text{BI}} \gg kT$). The charge-carrier traps become particularly important for thicker samples and can thus best be studied in this case; for thin samples, one is usually already in the TFL range for voltages which lie just above V_{BI} .

- Outside the transition region, the characteristics are formally identical to the TF-SCLC case. From $j \propto V^2$ alone, it thus does not follow that no trapping states are present.

The case described above of an energetically sharply-localised shallow-trap state provides an intuitively clear example of the general properties of charge-carrier traps. In **disordered systems**, this situation is however not very probable. There, trapping states are always **distributed** over a certain range of energies. This case, which will be treated in Sect. 8.6.5.2, leads to an excellent agreement between the SCLC theory and the current-voltage characteristics for non-crystalline semiconductors, and thereby to the quantitative analysis of the mobility and the trap distribution.

8.5

Charge-Carrier Mobilities in Organic Molecular Crystals: Experimental Results and Band Structures

Many organic molecular crystals, in particular the polyacenes naphthalene, anthracene, tetracene, and pentacene as well as e.g. perylene and others, have been grown with exceedingly high quality through improvement of purification and crystal-growth procedures. They contain very small concentrations of impurities and/or structural defects and are therefore often referred to as ultrapure crystals. For the investigation of charge transport in these crystals, one can and must assume that they contain only a few defects and thus few traps, so that in the first approximation, the structures of the valence band (VB) and of the conduction band (CB) (Fig. 8.6) as well as the phonons determine the mobilities μ_h and μ_e of the holes and the electrons.

8.5.1

Band- or Hopping Conductivity?

Whether in a molecular crystal in fact band conductivity or hopping conductivity predominates must be tested using a few simply-defined and physically clear-cut criteria: if the mean scattering time τ (cf. Sect. 8.2) is not long in comparison to \hbar/W , where W is the bandwidth, then no discrete value \mathbf{k} of the wavevector can be attributed to the charge carriers and a description in terms of an energy-band

model $E_e(\mathbf{k})$ or $E_h(\mathbf{k})$ is not possible. For band conductivity, the following condition must therefore be fulfilled:

$$\tau \gg \hbar/W. \quad (8.65)$$

A typical bandwidth of the charge-carrier bands VB and CB in the polyacene crystals is of the order of 0.1–0.5 eV (see Sect. 8.5.4), i.e. $\tau > 10^{-15}$ s must hold if one wants to describe the conductivity in terms of a band model. The states of the charge carriers in a band extend coherently over at least several unit cells. Therefore, for a description within a band model, the mean free path λ of the charge carriers must be long in comparison to the lattice constant:

$$\lambda \gg a_0. \quad (8.66)$$

With $a_0 \approx 0.5$ nm, we thus have the condition that $\lambda \gg 0.5$ nm.

Whether or not these conditions are fulfilled is not simple to determine. In Fig. 8.1, we saw a typical temperature dependence of the mobility in a highly-pure perylene crystal. It is similar to the general temperature dependence $\mu(T)$ of the charge-carrier mobility in inorganic semiconductors (Fig. 8.31): at high temperature, the mobility is limited by scattering of the charge carriers from phonons. In the high-temperature branch, the mobility therefore decreases with increasing temperature, since the scattering probability increases with increasing occupation of the phonon states, that is with increasing temperature. With scattering from acoustic phonons, this decrease follows to first order the relation $\mu \propto T^{-3/2}$ [35].

At very low temperatures, the scattering processes from phonons die out. The mobility in real semiconductors does however not continue to increase with further temperature decreases, but rather it decreases. The reason for this is the increasing effect of scattering of charge carriers from charged defects, that is from ions. In inorganic semiconductors, these are for example ionised donors or acceptors. In the high-purity molecular crystals, ions can form through capture of charge carriers in shallow traps, which are still present in spite of the high purity. The scattering process from the charged traps is “Rutherford scattering” owing to the Coulomb interaction between the charge carriers and the ions for both types of trap. If the

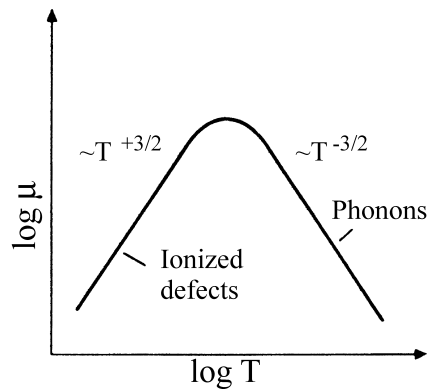


Fig. 8.31 The schematic temperature dependence of the mobility μ of the charge carriers in a doped inorganic semiconductor. At high temperatures, μ is limited by scattering of the charge carriers from acoustic phonons, at low temperatures by scattering from ions. After [35].

concentration of the donors or acceptors in a doped inorganic semiconductor is constant and their energy within the band gap is discrete, then the decrease of the mobility with decreasing temperature follows the relation $\mu \propto T^{+3/2}$ [35].

A comparison of Figs. 8.31 and 8.1 shows that the low-temperature decrease in organic molecular crystals is steeper than described above. Qualitatively, this result is plausible: the scattering probability must in addition to the probability for an individual Rutherford-scattering event also be proportional to the density of the scattering centres. When the traps in the molecular crystal just under the conduction band or just above the valence band are not energetically discrete, but rather form a continuous distribution, then the concentration of active scattering centres increases with decreasing temperature and the mobility decreases more strongly with decreasing temperature than in the case of monoenergetic traps.

Comparison of the two figures 8.31 and 8.1 thus speaks for the validity of the band model even for organic molecular crystals. A confirmation of this supposition can however only result from a quantitative test of the two criteria (8.65) and (8.66), i.e. from a quantitative comparison of experiment and theory. How difficult this question is to answer can be seen from the fact that it has been the subject of intensive discussions since at least 1960. Stimulated on the one hand by very precise experiments on ultrapure single crystals, especially those of Karl and coworkers, and by the increasing applications of organic semiconductors on the other hand, the earlier band-structure calculations [39–41] have been considerably improved using modern quantum-chemical methods [42]. In the following sections, we will first present the most important experimental results for various ultrapure crystals (Sects. 8.5.2 and 8.5.3), and then the results of the band-structure calculations (Sect. 8.5.4). From the comparison, the question posed above as to the mechanisms of limitation of the mobilities can be at least partially satisfactorily answered. In the last subsection (8.5.5), we will then treat methods and results relevant to the identification of traps and other scattering centres for the charge carriers.

Space-charge-limited currents in single crystals will not be treated further here. Their existence in ultrapure organic crystals has been verified beyond a doubt (cf. for example Fig. 8.27). Particularly in thin crystals such as those used in transistors (see Chap. 12), the currents are space-charge limited; for the determination of mobilities, they are however seldom as reliable as TOF experiments using the photoconductivity, due to contact problems between the metal electrodes and the organic crystals.

8.5.2

Temperature Dependence and Anisotropy of the Mobilities

The ultrapure organic molecular crystals naphthalene, anthracene, tetracene, perylene and others have mobilities μ both for holes and for electrons whose values at room temperature all lie around $1 \text{ cm}^2/\text{Vs}$, but are not all the same (Table 8.2). Their temperature dependencies $\mu(T) \propto T^n$ ($n < 0$) at $T < 300 \text{ K}$ are also similar but not identical. In particular, there are clear deviations from the ideal value of the exponent $n = -3/2$ (see Fig. 8.31). The temperature above which the relation

Table 8.2 Charge-carrier mobilities μ at room temperature (as a rule 300 K) and exponents n for the temperature dependence (as a rule on cooling). n is defined by $\mu(T) = \mu(300\text{ K})(T/300\text{ K})^n$. After Karl [24].

Crystal	Charge carrier	Direction	Mobility $\mu/\text{cm}^2\text{V}^{-1}\text{s}^{-1}$	n
Naphthalene	+	a	0.94	-2.8
	+	b	1.84	-2.5
	+	c'	0.32	-2.8
	-	a	0.62	-1.4
	-	b	0.64	-0.55
	-	c'	0.44	+0.04
Anthracene	+	a	1.13	-1.46
	+	b	2.07	-1.26
	+	c'	0.73	-1.43
	-	a	1.73	-1.45
	-	b	1.05	-0.84
	-	c'	0.39	+0.16
Tetracene	+	c'	0.85	≈ -2.5
Biphenyl	-	a	0.42	-1.0
	-	b	1.25	-1.25
	-	c'	0.51	-1
Perylene	-	a	2.37	-1.78
	-	b	5.53	-1.72
	-	c'	0.78	-2.15
Durol	+	a - b plane	5	-2.5
	-	b	8	-2.5
Phenazine	-	a'	0.51	-0.1
	-	b	1.1	-0.65
	-	c	0.29	0.05
Dibromo-naphthalene	+	a	0.36	
	+	b	0.66	
	+	c'	1.07	
	-	a	$1 \cdot 10^{-2}$	
	-	b	$1.2 \cdot 10^{-2}$	
Dibenzothiophene	-	c'	$4.7 \cdot 10^{-2}$	
	+	a	1.34	≈ -3.5
	+	b	1.18	-2
	+	c'	1.57	

$\mu \propto T^n$ with $n = \text{const.} < 0$ is observed is also similar for the various different crystals, about 40 K, but it still varies in different materials and depends on the purity and perfection of the crystals; and finally, the mobilities in all these crystals are anisotropic, i.e. they depend on the direction of the current. The anisotropy, that is the ratio of the maximum to the minimum mobility, is for example for holes in naphthalene about 5, and is thus not very large, and it is of the same order for the different crystals. (We mention here that for the anisotropy of the conductivity

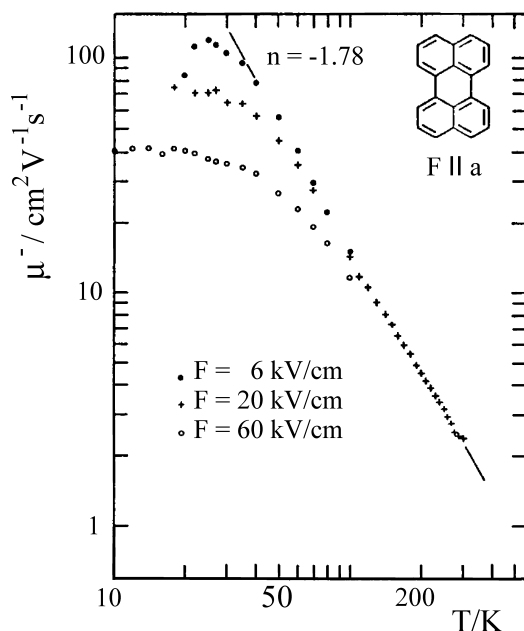


Fig. 8.32 The temperature dependence of the electron mobility in a perylene crystal with the applied electric field parallel to the crystallographic *a* axis. In the high-temperature range, μ is proportional to T^n ($n < 0$). F = applied electric field. After [23].

in organic radical-ion salts with quasi-one-dimensional crystal structures, values of 10^4 and more have been measured (see Chap. 9)).

To illustrate these experimental results, Figs. 8.1 and 8.32–8.35 show some characteristic examples. A detailed treatment can be found in several articles by Karl *et al.* (see e.g. [24, 43]). Figures 8.1, 8.32 and 8.33 show the electron mobilities in perylene crystals for three different crystal orientations. Their comparison shows on the one hand that the values remain of the same order; on the other hand, for example the steep decrease with decreasing temperature in the measurements of Figs. 8.32 and 8.33 is observed only at a somewhat lower temperature than in the measurement shown in Fig. 8.1. One reason for this is the greater degree of perfection of the crystals used for the measurements shown in Figs. 8.32 and 8.33 [23, 43].

How strongly a high defect concentration affects the temperature dependence of the mobility can be seen from the comparison of the experimental results for a perylene crystal with a concentration of 0.17% traps of depth $E_t = 270$ meV (Fig. 8.33). Even near room temperature, the mobility μ decreases steeply with decreasing temperature. In this crystal with defects, hopping conductivity occurs even in the temperature region near 300 K.

Figure 8.34 shows as an example the anisotropy and its temperature dependence for the holes in a perylene crystal in a selected plane. The principal axes of the

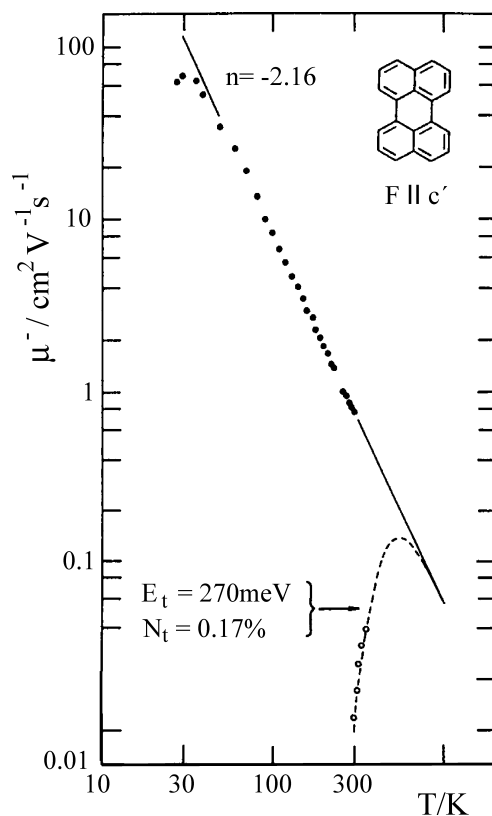


Fig. 8.33 The temperature dependence of the electron mobility in perylene crystals for the applied electric field F parallel to the crystallographic c' axis. Dashed: a perylene crystal with 0.17% traps with a trap depth of $E_t = 270 \text{ meV}$. In the high-temperature range, μ in the pure crystal is proportional to T^n ($n < 0$). After [23].

mobility tensor are only roughly parallel to the monoclinic crystal axes and they are nearly independent of temperature.

Finally, from Fig. 8.32, one can see a characteristic dependence of the mobility on the magnitude of the electric field $|F|$. It will be treated in detail in Sect. 8.5.3.

In ultrapure naphthalene crystals [20] also, the exponents n are different for holes and electrons (Fig. 8.35 and Table 8.2). For holes, the value of $n = -2.8$ also deviates strongly from the ideal value $-3/2$. The reason for this is probably a continuous energy distribution of the shallow charge-carrier traps. Down to the lowest measurement temperature of about 4 K, no decrease in the mobility with decreasing temperature was observed. And also in naphthalene crystals at high electric fields, a decrease of μ with increasing field strength is found.

Qualitatively similar values are found in ultrapure anthracene crystals [21] (Table 8.2). To be sure, the values of the mobilities at low temperature and the ex-

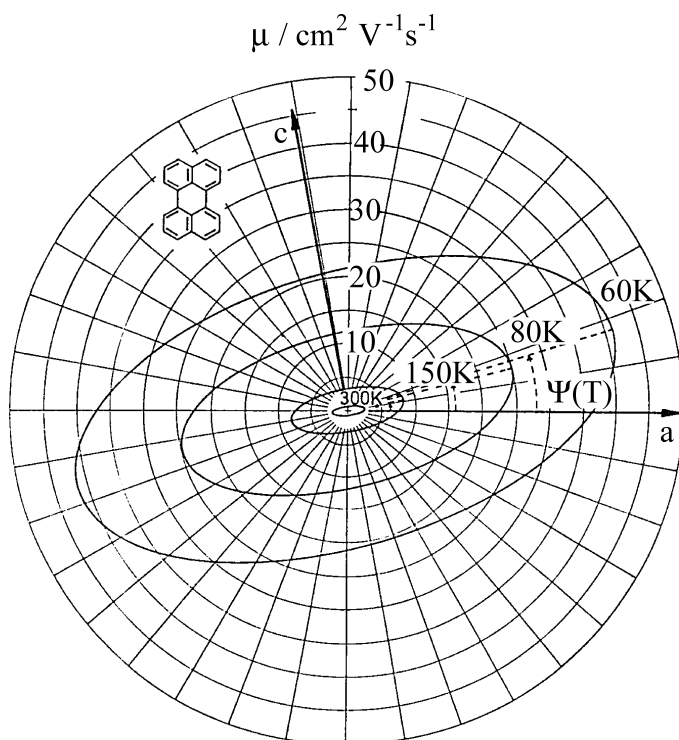


Fig. 8.34 The anisotropy of the electron mobility in a perylene crystal in its $a-c$ plane. The angle Ψ between the direction of maximum mobility and the a axis is weakly temperature dependent. After [24] and [43].

ponents n are somewhat smaller than for naphthalene and perylene crystals. The anisotropy is nearly temperature independent in the anthracene crystal, also.

8.5.3

Electric-field Dependence

At low drift velocities, the mobilities are independent of $|\mathbf{F}|$. This has been confirmed using the TOF method in many cases. An example is given in Fig. 8.36.

With increasing drift velocity, the mobilities at low temperature become however dependent on the **electric field strength** in a characteristic manner: they decrease with increasing field. According to Eq. (8.4), the drift velocity v_D then increases sublinearly with increasing field strength. Figure 8.37 shows a typical example for the drift velocity v_D^h of the holes in an ultrapure naphthalene crystal as a function of the electric field at different low temperatures [20].

The sublinear increase of $v_D(F)$ be interpreted with the aid of a model by Shockley [45], based on the inelastic scattering of charge carriers from longitudinal acoustic phonons. In this model, the assumption is made that the charge carriers scatter

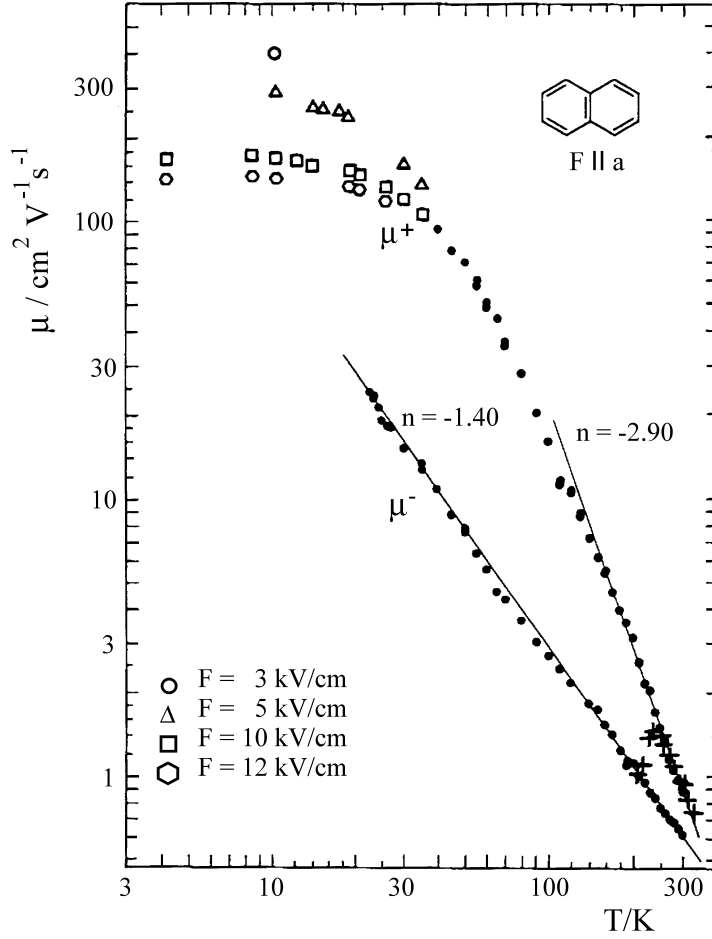


Fig. 8.35 The temperature dependence of the mobilities of the electrons (μ^-) and the holes (μ^+) in a naphthalene crystal with the applied electric field parallel to the crystallographic **a** axis. F = electric field. In the higher temperature range, μ is proportional to T^n ($n < 0$). After [20, 24].

from the crystal potential which is deformed by the longitudinal phonons. According to this model of deformation-potential scattering, v_D is solely determined by the mobility μ_0 at low applied fields ($\mu_0 = \mu (F \rightarrow 0)$) and the mean longitudinal sound velocity c_ℓ , and naturally by the electric field strength:

$$v_D = \mu_0 F \cdot \sqrt{2} \left\{ 1 + \left[1 + \frac{3\pi}{8} \left(\frac{\mu_0 F}{c_\ell} \right)^2 \right]^{1/2} \right\}^{-1/2}. \quad (8.67)$$

It follows from this for $v_D(F)$ at the highest values of the electric field ($\mu_0 F \gg c_\ell$):

$$v_D(F)/\mu_0 F \gg c_\ell \propto \sqrt{F}. \quad (8.68)$$

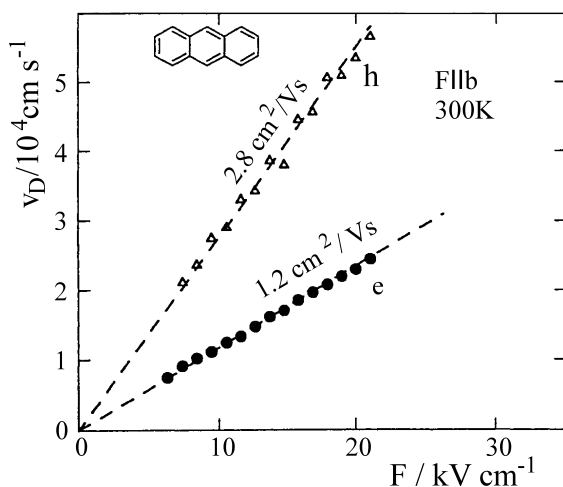


Fig. 8.36 Ohm's law at low drift velocities of the electrons and holes in an anthracene crystal at room temperature along the **b** axis. v_D = drift velocity, F = electric field. After [21].

The solid curves in Fig. 8.37 were computed with only one free parameter in Eq. (8.67), namely the longitudinal velocity of sound $c_\ell = 4 \cdot 10^5$ cm/s. μ_0 is not a fit parameter, since the zero-field mobility follows directly from the measurable slope of $v_D(F)$ for $F \rightarrow 0$ (see Fig. 8.37). The value for c_ℓ obtained in this way agrees surprisingly well with the independently-measured longitudinal sound velocity (compare Table 5.4) and is thus a good indication that the Shockley model for the electron-phonon coupling is also applicable to organic molecular crystals.

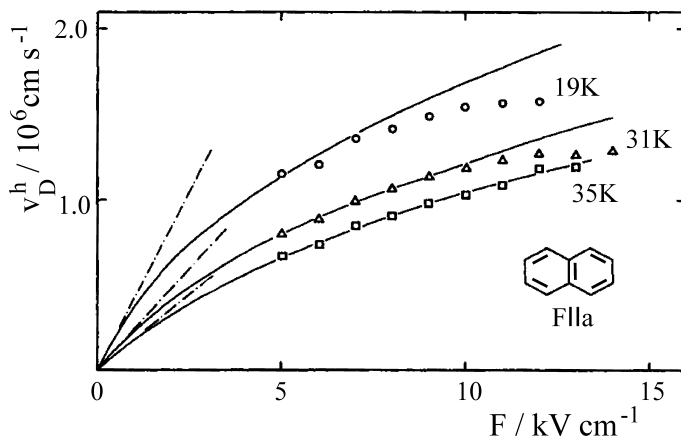


Fig. 8.37 The dependence of the drift velocity v_D^h of the holes on the electric field F in a naphthalene crystal at low temperature in the range of non-Ohmic transport. The slopes at the origin correspond to the zero-field mobilities $\mu(F \rightarrow 0) = 420$ cm²/Vs at 19 K,

235 cm²/Vs at 31 K, and 180 cm²/Vs at 35 K. The solid lines were calculated using the model of deformation-potential scattering and the longitudinal sound velocity $c_\ell = 4 \cdot 10^5$ cm/s (see Eq. (8.66)). From [20].

8.5.4

Band Structures

For an understanding of charge-carrier mobilities, it is necessary to have some knowledge of the band structures $E_e(\mathbf{k})$ and $E_h(\mathbf{k})$ of the excess charge carriers. Here, E_e and E_h are the energies of the electrons and the holes, and \mathbf{k} is their wavevector.

The calculations of Cheng *et al.* [42] are based on the Hartree-Fock-INDO method for calculating the molecular orbitals and transfer integrals t in the van der Waals-bound crystals. The band structures were calculated in the tight-binding approximation. All the crystals for which calculations were carried out have two molecules per unit cell (A and B). Therefore, for both electrons and for holes, there are two bands each: $E_{e,\pm}(\mathbf{k})$ and $E_{h,\pm}(\mathbf{k})$, which are each formed from the symmetric and antisymmetric linear combinations of the molecular wavefunctions of the two molecules A and B of the same type but differing orientations within the unit cell. The energy splitting into two bands each, E_+ and E_- , is analogous to the Davydov splitting of the excitonic bands (see Chap. 6). The calculations assume small concentrations of excess charge carriers. The Coulomb interactions between the charge carriers were therefore not included.

In the tight-binding approximation, the energies of the two excess charge carrier bands of each type, $E_+(\mathbf{k})$ and $E_-(\mathbf{k})$ for the holes and for the electrons, are determined by the transfer integrals t_i^A , t_i^B and t_i^{AB} (see below) between the molecular HOMOs or between the molecular LUMOs:

$$E_{\pm}(\mathbf{k}) = \left(\frac{T_A + T_B}{2} \right) \pm \sqrt{\left(\frac{T_A - T_B}{2} \right)^2 + (V(\mathbf{k}))^2}. \quad (8.69)$$

For crystals with inversion symmetry,

$$T_A = E_A - 2 \cdot \sum_i t_i^A \cdot \cos(\mathbf{k} \cdot \mathbf{r}_i^A) \quad (8.70)$$

$$T_B = E_B - 2 \cdot \sum_i t_i^B \cdot \cos(\mathbf{k} \cdot \mathbf{r}_i^B) \quad (8.71)$$

and

$$V(\mathbf{k}) = -2 \cdot \sum_i t_i^{AB} \cdot \cos(\mathbf{k} \cdot \mathbf{r}_i^{AB}). \quad (8.72)$$

T_A and T_B are the energies of the translationally-equivalent molecules A and B , E_A and E_B are their monomer energies, and the summation runs over all of the **translationally-equivalent** molecules. Here, t_i^A are the intermolecular transfer integrals between a central molecule A in the unit cell $i = 0$ and a molecule A in the unit cell $i \neq 0$. The same holds for t_i^B . In crystals with two equivalent molecules, $E_A = E_B$ and $t_i^A = t_i^B$. \mathbf{r}_i is the distance between the central molecule and the molecule in the i -th unit cell. $V(\mathbf{k})$ is the interaction energy between the A molecules and the B molecules. Here, t_i^{AB} is the intermolecular transfer integral between the

central molecule ($i = 0$) and the translationally-inequivalent molecule in the unit cell i , thus in particular also with the second molecule in the same unit cell $i = 0$. r_i^{AB} is the distance between the two molecules of summand i .

With Eqns. (8.69) to (8.72), the band structures for excess charge carriers in several different polyacene crystals were calculated numerically [42]. As an example, Fig. 8.38 shows the energy bands $E_{\pm}(\mathbf{k})$ for electrons and holes for five different directions of the \mathbf{k} vector in the naphthalene crystal and also the densities of state (DOS) in the conduction band and the valence band. Here, \mathbf{a} , \mathbf{b} , and \mathbf{c} are the crystal axes and $\mathbf{d}_1 = (1/2, 1/2, 0)$ and $\mathbf{d}_2 = (-1/2, 1/2, 0)$ are the directions along the near neighbours in the $(a-b)$ plane, which are degenerate in the monoclinic crystals naphthalene and anthracene, but not in the triclinic crystals tetracene and pentacene. The dispersion along the \mathbf{c} direction is smaller than within the $(a-b)$ plane, which is due to the smaller intermolecular interactions between the $(a-b)$ planes compared to those within the $(a-b)$ planes. Similarly, the mobilities are also higher in the $(a-b)$ plane than between the $(a-b)$ planes (see below).

The bandwidths of the all together sixteen subbands in the monoclinic crystals (or twenty in the triclinic crystals) – both for electrons and for holes, there are two bands each, E_+ and E_- , for each of the five directions of \mathbf{k} calculated, of which two are degenerate in the monoclinic crystals – vary between 4 meV and 500 meV, depending on the direction and the crystal (cf. Fig. 8.38). The overall bandwidths W vary, depending on the crystal and the LUMO or HOMO band (CB or VB) between 372 meV (naphthalene, LUMO) and 738 meV (pentacene, HOMO). Table 8.3 lists the values of the overall bandwidths for the polyacene crystals naphthalene, anthracene, tetracene, and pentacene.

The overall bandwidths are thus larger than kT for all the crystals: $W \gg k_B T$. For the transport properties, the thermal occupation of the bands must therefore be taken into account: at 300 K and lower temperatures, only states in the neighbourhood of the band minima are occupied (cf. Eq. (8.87)).

Table 8.3 Overall bandwidth W for holes in the LUMO and electrons in the HOMO in polyacene crystals. From [42].

Crystal	Overall Bandwidth W/meV	
	HOMO	LUMO
Naphthalene	409	372
Anthracene	509	508
Tetracene	625	502
Pentacene	738	728

The velocities of the charge carriers follow strictly from the band structures: the group velocities $\mathbf{v}(\mathbf{k})$ of the electron and the hole waves are found from band theory to be

$$\mathbf{v}(\mathbf{k}) = (1/\hbar) \cdot \nabla_{\mathbf{k}} E(\mathbf{k}). \quad (8.73)$$

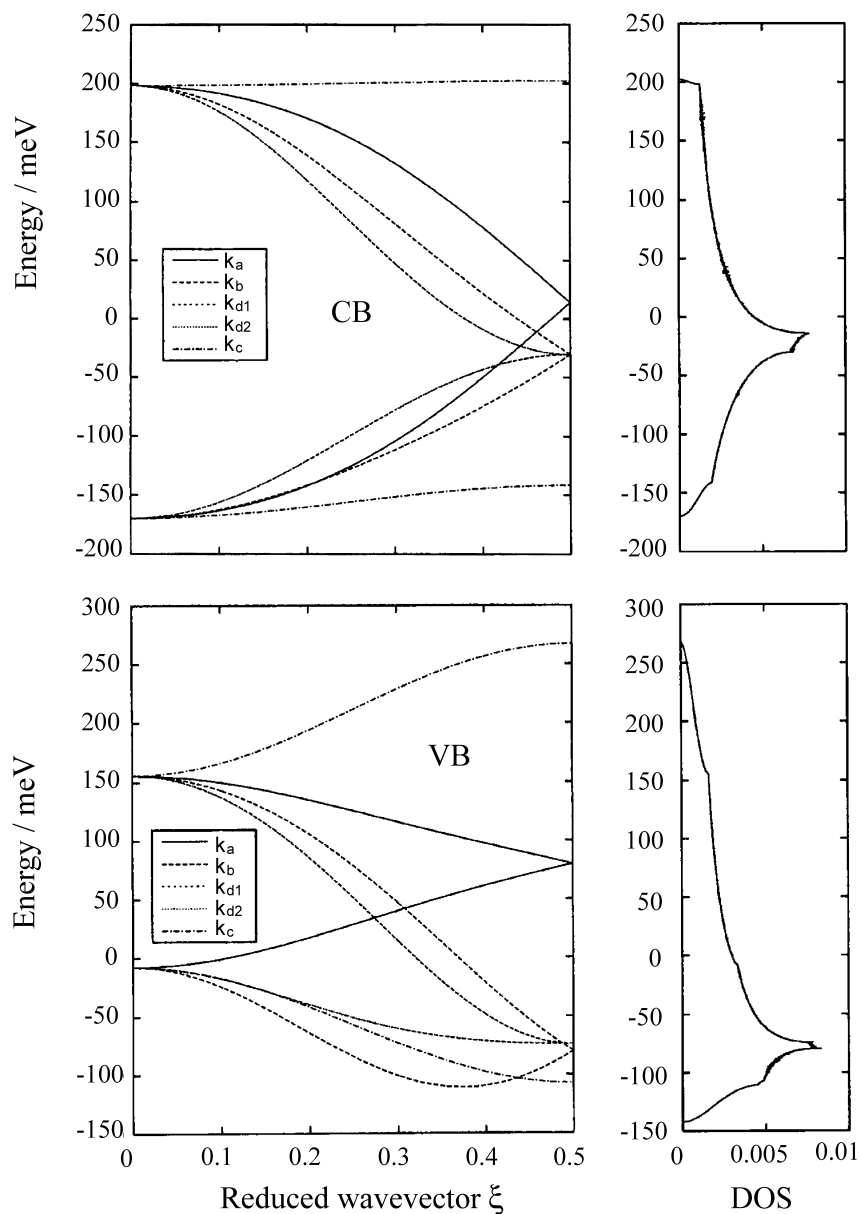


Fig. 8.38 Dispersion relations and densities of state in the naphthalene crystal. Left: the energy $E_{c,\pm}(\mathbf{k})$ of the LUMO or conduction bands (above) and $E_{v,\pm}(\mathbf{k})$ of the HOMO or valence bands (below) for various directions of \mathbf{k} in the naphthalene crystal. \mathbf{a} , \mathbf{b} , and \mathbf{c} are the

crystal directions, \mathbf{d}_1 and \mathbf{d}_2 are the directions along the axis connecting the two inequivalent molecules A and B in the unit cell. Right: densities of states (DOS) in the HOMO and LUMO bands. From [42].

For an approximate estimate of the mobilities, either a constant, isotropic relaxation time τ or a constant, isotropic mean free path λ can be assumed. In these two approximations, the components μ_{ij} of the mobility tensor are found from the Einstein relation (Eq. (8.22)) to be

$$\mu_{ij} = e\tau \langle v_i v_j \rangle / kT \quad (8.74)$$

and

$$\mu_{ij} = (e\lambda/kT) \langle v_i v_j / |\mathbf{v}(\mathbf{k})| \rangle. \quad (8.75)$$

In these expressions, v_i is the i -th vector component of the group velocity, $\mathbf{v}(\mathbf{k})$, and the brackets $\langle \rangle$ denote the averaging over the Boltzmann distribution of the charge carriers in the energy bands:

$$\langle v_i v_j \rangle = \frac{\int \left(\frac{\partial E_+}{\partial k_i} \cdot \frac{\partial E_+}{\partial k_j} \cdot \exp(-E_+(\mathbf{k})/k_B T) + \frac{\partial E_-}{\partial k_i} \cdot \frac{\partial E_-}{\partial k_j} \cdot \exp(-E_-(\mathbf{k})/k_B T) \right) d\mathbf{k}}{\hbar^2 \int (\exp(-E_+(\mathbf{k})/k_B T) + \exp(-E_-(\mathbf{k})/k_B T)) d\mathbf{k}}. \quad (8.76)$$

The two expressions $\langle v_i v_j \rangle$ and $\langle v_i v_j / |\mathbf{v}(\mathbf{k})| \rangle$ were computed numerically and are the essential quantities for the calculation of the charge-carrier mobilities. τ and λ are fit parameters.

The results for $\langle v_i v_j \rangle$ in the naphthalene crystal are shown in Fig. 8.39 for different directions within the crystal. In the directions **a** and **b**, the quantities $\langle v_a v_a \rangle$ and

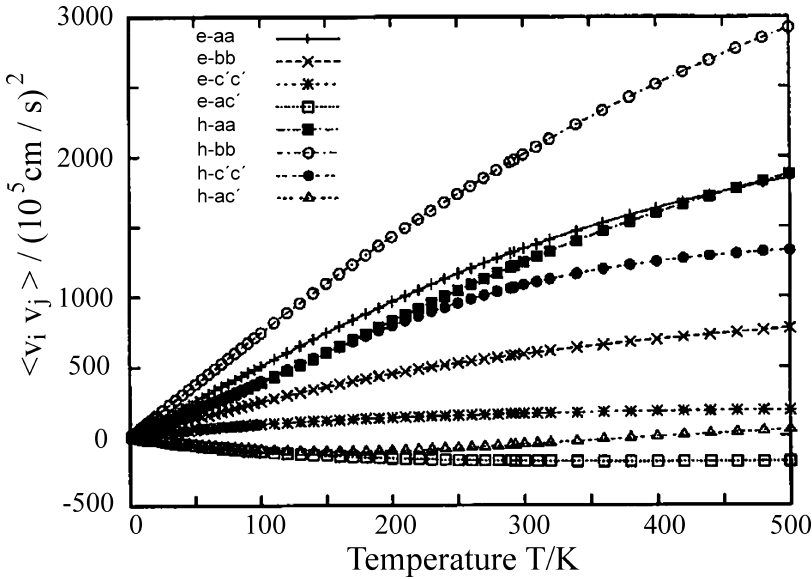


Fig. 8.39 The temperature dependence of the quantities $\langle v_i v_j \rangle$ (see Eq. (8.75)) in the naphthalene crystal for electrons (e) and holes (h) in different directions within the crystal (**a**, **b**, **c'**). After [42].

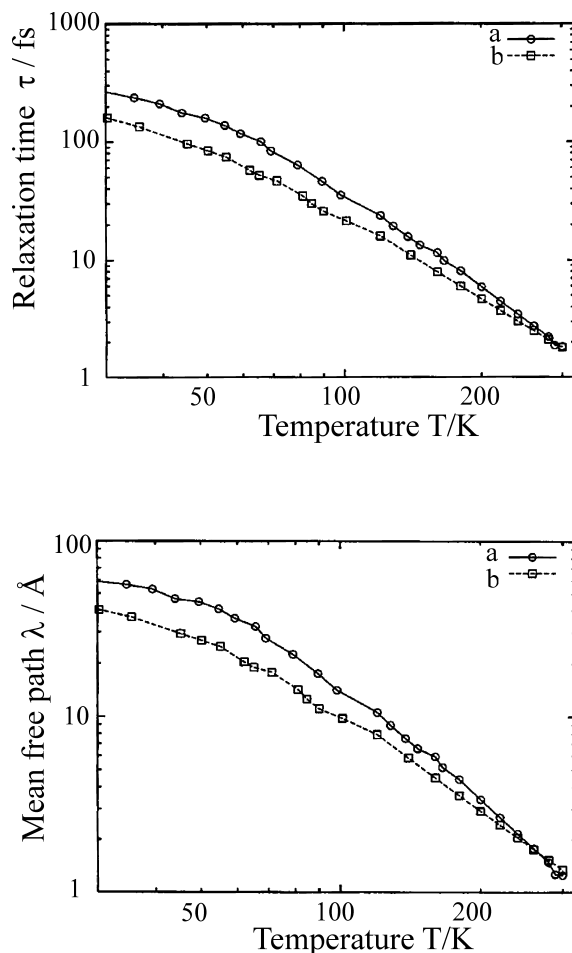


Fig. 8.40 The temperature dependence of the relaxation time τ (above) and the mean free path λ (below) for the holes in the naphthalene crystal. The values of τ and λ were calculated using Eqns. (8.73) and (8.74) with the experimentally determined values of the mobilities μ . From [42].

$\langle v_b v_b \rangle$ increase roughly linearly with temperature T for $T < 300$ K. In the c' direction, these quantities saturate at around 100 K, because the bandwidths in the c' direction are considerably smaller than those within the $(a-b)$ plane.

Using these theoretical results for the quantities $\langle v_i v_j \rangle$ and Eqns. (8.74) and (8.75), a comparison with the experimentally determined temperature-dependent mobilities μ_{ij} (see e.g. Fig. 8.35) yields the relaxation times τ and the mean free path λ as functions of the temperature. The results for holes in the naphthalene crystal are shown in Fig. 8.40. It follows that for $T < 150$ K, the conditions for the existence of band conductivity (Eqns. (8.64) and (8.65)) are well fulfilled in high-purity naphthalene crystals within the $(a-b)$ plane. The same holds for other ul-

trapure organic molecular crystals at low temperatures. Already at room temperature, however, τ and λ have values which no longer fulfill the conditions (8.64) and (8.65). At room temperature and above, the electrical conductivity even in ultra-pure organic molecular crystals must be treated in terms of a hopping mechanism. Hopping mechanisms are the normal case for most of the organic crystals at room temperature and above, and especially for the non-crystalline organic solids at all temperatures (see Sect. 8.6).

8.5.5

Charge-Carrier Traps

Impurities, doping, defects and other disturbances of the lattice periodicity as a rule inhibit charge transport so strongly, that with increasing concentration of the disturbing sites, the charge transport especially at low temperatures is limited by the disturbances (see e.g. [44]). Impurity molecules in the host crystal, e.g. tetracene molecules in an anthracene crystal, represent traps for charge carriers. They are characterised by their energy depth E_t , their concentration N_t , and their molecular structure.

Shallow traps can, after being filled at lower temperatures by an electrical current, be thermally emptied by heating the crystal, and they then lead to an increase in the dark current. Figure 8.41 gives as an example the thermally-stimulated discharge current from the traps in an anthracene crystal whose electron traps were previously filled at a lower temperature; the crystal was thus charged at a low temperature. The corresponding experiment was carried out with the same crystal also

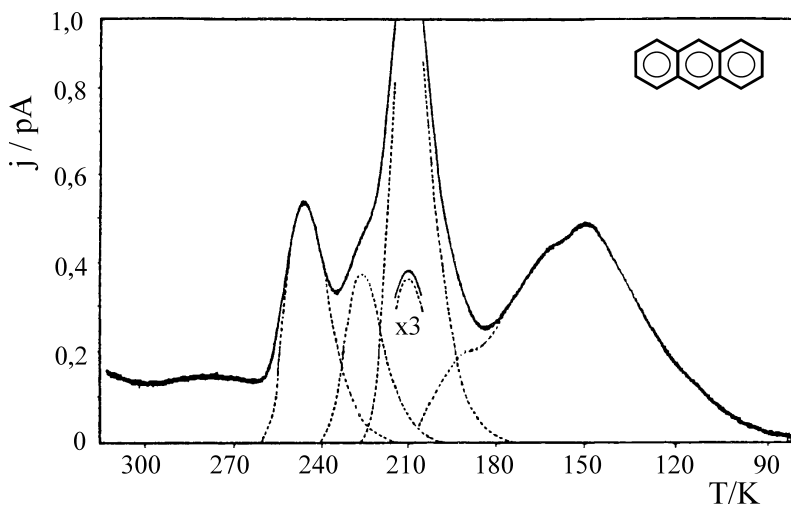


Fig. 8.41 Thermally-stimulated electron current in a highly-pure anthracene crystal whose traps were previously filled at $T = 70$ K by means of a stationary photocurrent. From the temperatures at which the current attains its maximum values, the trap depths can be determined. After [44].

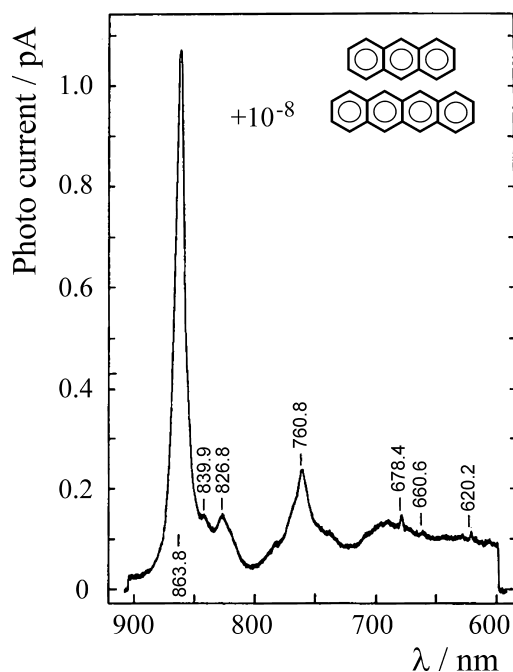


Fig. 8.42 The excitation spectrum of the photocurrent of an anthracene crystal doped with tetracene at 77 K, whose traps were filled before the photoexcitation. The excitation spectrum corresponds to the 0,0 transition and the vibronic series of the doublet-doublet transition $D_1 \leftarrow D_0$ in the tetracene radical-cation. From [44].

for the holes. From the complex evaluation of the peaks at different temperatures, in suitable cases the depths of the traps can be determined [44].

Deeper traps can in some cases be emptied by **irradiation with light**. Figure 8.42 shows as an example the excitation spectrum of the photocurrent in an anthracene crystal which was doped with 10^{-8} tetracene molecules and whose hole traps were previously filled at a lower temperature, so that the anthracene crystal contained tetracene radical-cations before the excitation. The excitation spectrum shows the 0,0 transition and the vibronic series of the energetically lowest doublet-doublet transition $D_1 \leftarrow D_0$ in the tetracene radical-cation. The combined evaluation of the thermally and the optically-stimulated currents yielded in this special case a value $E_t^h = 0.42$ eV for the depth E_t^h of the hole traps represented by tetracene in an anthracene crystal [44].

Along with the thermal and optical emptying of occupied traps, excitons can also empty them. In particular the long-lived triplet excitons T_1 can be excited in a substantial stationary concentration. The excitation is usually carried out optically, but it can also be performed electrically through simultaneous injection of electrons and holes from both electrodes. In any case, the triplet excitons have a long lifetime and can couple, for example magnetically, to the charge carriers.

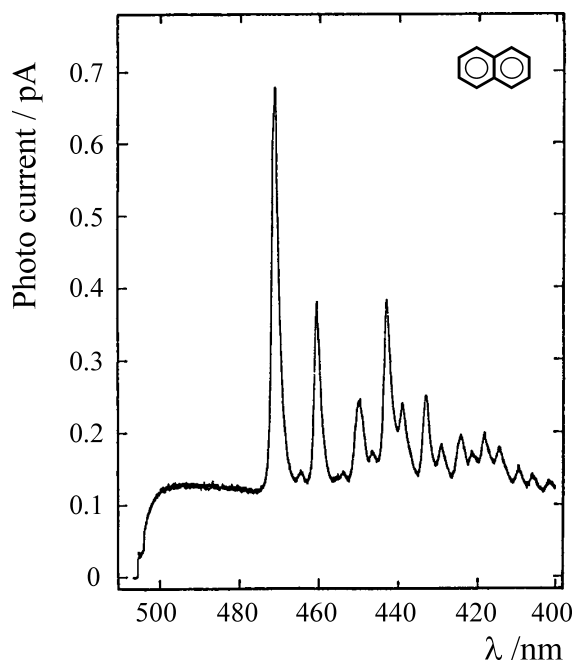


Fig. 8.43 The excitation spectrum of the photocurrent in a high-purity naphthalene crystal after its traps had been filled at $T = 77$ K. The spectrum consists of the 0,0 transition and the vibronic series of the strongly forbidden $T_1 \leftarrow S_0$ transition. In this way, primarily triplet excitons T_1 are excited, which empty the charge-carrier traps by annihilation and thus contribute to the current. After [44].

The excitation energy $E(T_1)$ of the triplet excitons is e.g. in the naphthalene crystal larger than a typical trap depth. An exciton is therefore energetically able to empty a charge-carrier trap and thus to increase the current. Figure 8.43 shows the excitation spectrum of photoconduction of a high-purity naphthalene crystal whose traps were previously filled at 77 K. Here, the forbidden 0,0 transition at $21\,208\text{ cm}^{-1}$ ($\lambda = 471.5\text{ nm}$) and the vibronic series of the $T_1 \leftarrow S_0$ transition in the naphthalene crystal were observed [44].

Charge-carrier traps can not only be emptied, but also completely filled in the stationary state by high current densities. Then the defects no longer act as traps, but rather as potential scattering centres.

8.6

Charge Transport in Disordered Organic Semiconductors

While in the previous sections of this chapter we treated organic semiconductors which consist of single crystals of molecules with conjugated π -electron chains, in

this section we shall consider disordered organic semiconductors. They are important in particular because many organic semiconductor substances do not – or only with great difficulty – permit the growth of single crystals. They consist of molecules or polymers with cyclic or non-cyclic π -electron systems and are as a rule prepared in the form of thin films.

The number of molecules from which disordered organic semiconductors can be prepared is very large. As examples, we will treat those molecules or polymers here whose semiconducting properties have been especially well investigated and which consist entirely or to a large extent of hydrocarbons. Often, these molecules are larger, but not very much larger, than the polyacenes. Their synthesis is a branch of organic chemistry. Many of these molecules are so stable, particularly in vacuum, that they can be evaporated or sublimed without degradation. For purification or preparation of films, this is equally important as for applications in technical products, e.g. in organic light-emitting diodes (OLEDs) or as photovoltaic elements (see Chap. 11). Due to their size and structure, these molecules usually have no trivial names (such as e.g. “anthracene”), but instead are named according to the IUPAC rules (cf. textbooks on organic chemistry) and in addition are denoted by abbreviations. In the following, we shall restrict ourselves to a few selected examples of disordered organic semiconductors, which however are typical and have been very thoroughly investigated. However, there is no real model substance for the disordered organic semiconductors, comparable for example to anthracene for organic semiconductor crystals.

Films of these molecules can in many cases be prepared by controlled evaporation in vacuum onto a substrate. In other cases, they are spun onto the substrate from solution. After evaporation of the solvent, amorphous or partially crystalline or liquid-crystal films are formed, whose thickness can in many cases be varied in a controlled way.

The lateral homogeneity of the evaporated or spun films is sufficient for experiments on charge transport through the films, if they are carefully prepared. In the case of evaporated films, this is in many cases also true of extremely thin films, e.g. of 20 nm thickness and with an area of $2 \times 2 \text{ mm}^2$.

Soluble polymers can likewise be prepared in the form of thin films by spinning the solution onto a substrate and then evaporating the solvent. Insoluble polymers can in suitable cases be spun in the form of their soluble precursors and then after evaporation of the solvent be converted into the insoluble polymer by elimination of the substituents which rendered them soluble. A well-known example of this is poly(para-phenylene-vinylene) (PPV).

When the substrate of a thin film has a metallic conductivity, it can serve as back electrode and the metallic front electrode for experiments on charge transport can e.g. be evaporated onto the film. In this way, one obtains a device such as is shown in Fig. 8.3. When the substrate is not itself an electrical contact, both electrodes are often applied to the surface of the film with a well-defined geometry for experiments on charge transport. In this case – and also in the case that both contacts were applied to the insulating substrate before the preparation of the film and are thus on the lower surface of the film – the electric field is in principle inhomoge-

neous, but not limited to the surface of the film, if the film thickness is small in comparison to the spacing of the electrodes on the surface. For quantitative analysis, this can be problematic, but for practical applications it is often an advantage.

A comparison of the charge-carrier mobility μ , the transients in time-of-flight measurements (TOF), and the current-voltage characteristic $I(V)$ demonstrates the differences between disordered and crystalline systems:

- The mobilities of the charge carriers in disordered films are smaller by orders of magnitude than in crystals and their temperature dependencies are inverse over a large temperature interval (compare Figs. 8.1 and 8.2).
- The transients from TOF experiments on disordered films, in contrast to the transients from crystals (cf. Fig. 8.12), only rarely exhibit a step indicating the arrival of the charge carriers at the back electrode on a linear time scale. Figure 8.44 shows a typical example, the TOF transients from a $5.6 \mu\text{m}$ thick film of high-purity DEH glass (DEH is *p*-diethylamino-benzaldehyde-diphenylhydrazone) at various temperatures [46]. Only at high temperature can one observe an initially constant current and then a step at the transit time t_τ in a linear $I(t)$ plot. At low temperatures, the transient is featureless in a linear plot; only in a log-log plot can the kink at $t = t_\tau$ be clearly discerned.

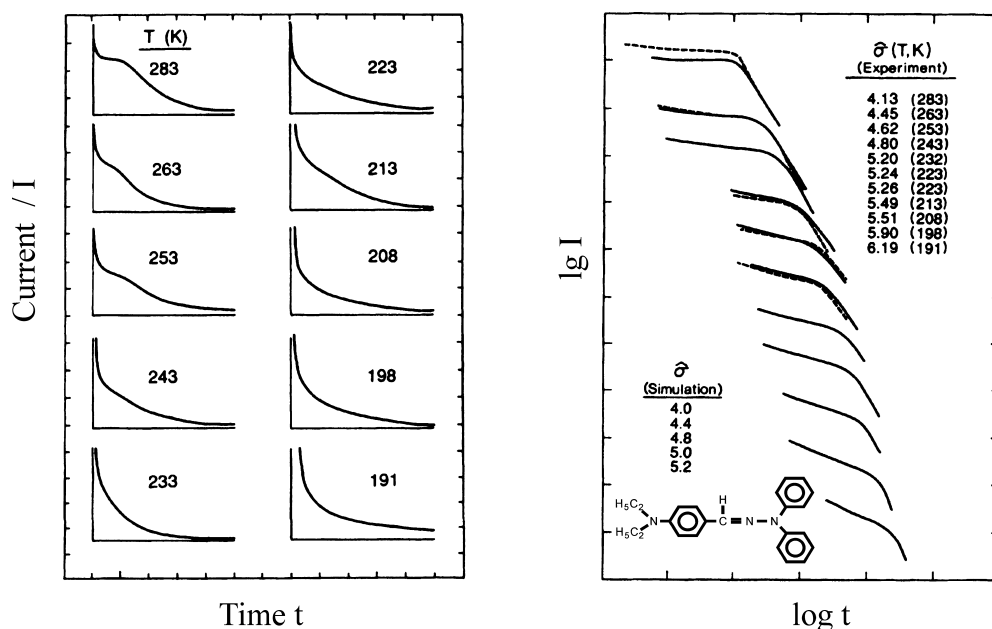


Fig. 8.44 Left: experimental TOF transients for hole transport in a $5.6 \mu\text{m}$ thick DEH glass at various temperatures. DEH = *p*-diethylamino-benzaldehyde-diphenylhydrazone. $F = 0.6 \text{ MV/cm}$. Right: the same transients in a double logarithmic plot. Dashed: a

simulation with a width of $\sigma = 0.101 \text{ eV}$ for the energy distribution function of the states. The experimental transient for $\hat{\sigma} = \sigma/kT = 4.45$ is nearly identical with the simulation for $\hat{\sigma} = 4.4$. From [46].

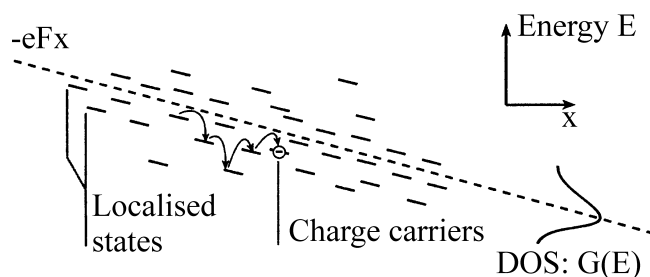


Fig. 8.45 Schematic of hopping transport in a disordered organic semiconductor. The energy distribution of the states (DOS) is assumed in the Bässler model to be a Gaussian distribution function $G(E)$ with a width σ (compare Eq. (8.77)). The hopping processes parallel to the electric field F take place either to neighbouring molecules with lower energies, or to neighbours with higher energies (cf. Eqns. (8.78) and (8.79)).

- The current-voltage characteristics from disordered films are to be sure just as nonlinear as those from molecular crystals, but the typical structure along the $I - V$ characteristic of the space-charge-limited current in crystals is not so strongly pronounced in the disordered films. This can be seen for example by comparison of Figs. 8.27 and 8.28. However, as we shall see in Sect. 8.6.5, the current in high-purity disordered films is likewise space-charge limited and has been analysed in detail as such.

Charge transport in disordered films is an example of hopping transport. Its origin lies in the energetically inhomogeneous distribution of the localised transport states of the holes and the electrons (Fig. 8.6c). This produces a distribution of the energy differences and the hopping probabilities for the charge carriers during transport to the neighbouring molecules (Fig. 8.45).

Numerous models have been proposed for hopping transport (see e.g. [M1], [M2]). Conceptionally the simplest and physically most well-founded is the model of Bässler [47], which we will outline in the next section. In the sections thereafter, we will present typical experimental results for the temperature and electric-field dependencies of the mobility and for the temperature, field and thickness dependence of the dark current $I(V)$ as a function of the applied voltage in disordered organic semiconductors.

8.6.1

The Bässler Model

The Bässler model [47] for hopping transport in disordered organic solids is based on a few plausible hypotheses:

- The basic units of charge transport are molecules or segments of molecules (sites), whose energies E for the hole or electron transport states are defined

in terms of a Gaussian distribution function $G(E)$ of the density of states (DOS) (see Figs. 8.6 and 8.45):

$$G(E) = (2\pi\sigma^2)^{-1/2} \exp(-E^2/2\sigma^2). \quad (8.77)$$

All these states are localised. The origin of the energy scale lies at the centre of the DOS. σ is the width of the distribution. The distribution itself is based on the stochastic variation of the polarisation energies (cf. Sect. 8.3). This energy distribution is also termed **diagonal disorder**.

- The hopping rate v_{ij} between two sites i and j is assumed to be the product of a prefactor v_0 , a factor which takes the overlap of the wavefunctions into account, and a Boltzmann factor [48]:

$$v_{ij}(\uparrow) = v_0 \exp\left(-2\gamma a \frac{\Delta R_{ij}}{a}\right) \exp\left(-\frac{E_j - E_i - eF(x_j - x_i)}{kT}\right) \quad (8.78)$$

$$v_{ij}(\downarrow) = v_0 \exp\left(-2\gamma a \frac{\Delta R_{ij}}{a}\right). \quad (8.79)$$

Here, for (8.78): $E_j - E_i - eF(x_j - x_i) > 0$ holds, while for

(8.79): $E_j - E_i - eF(x_j - x_i) < 0$.

E_i and E_j are the energies of the transport states of the two sites within their distribution in zero field $G(E)$, F is the electric field, ΔR_{ij} the value of the distance between the two sites, a is their mean spacing, γ is the decay constant of the exponentially decreasing wavefunction (the inverse Bohr radius in the case of hydrogen-like wavefunctions) and $eF(x_j - x_i)$ is the difference of the additional electrostatic energies of the sites in the electric field F along the x direction. Equations (8.78) and (8.79) mean that for thermal activation of a hopping process $v_{ij}(\uparrow)$ to an energetically higher state, no other activation energy is necessary besides the difference of the energies of the transport states, which is a function of the electric field. Hopping processes $v_{ij}(\downarrow)$ to energetically lower-lying sites require no activation. Thus, naturally, $v_{ij} \neq v_{ji}$.

The overlap parameter $2\gamma \Delta R_{ij}$ is likewise not sharp, but rather statistically distributed. The distribution is assumed to be a Gauss function with a width Σ . The distribution of the overlap parameters is termed the **non-diagonal disorder**. σ and Σ are the two important materials parameters in the Bässler model for hopping transport in disordered semiconductors.

The model cannot be solved analytically in closed form. Bässler *et al.* therefore constructed a model sample with $70 \times 70 \times 70$ sites and, using a Monte-Carlo method, simulated the charge transport. The simulation was thus an idealised experiment.

One result of the Bässler model is the relaxation of the excess charge carriers towards thermal equilibrium after their production by photoexcitation (Fig. 8.46). The equilibrium energy $\langle E_\infty \rangle$ of the charge carriers which were generated with

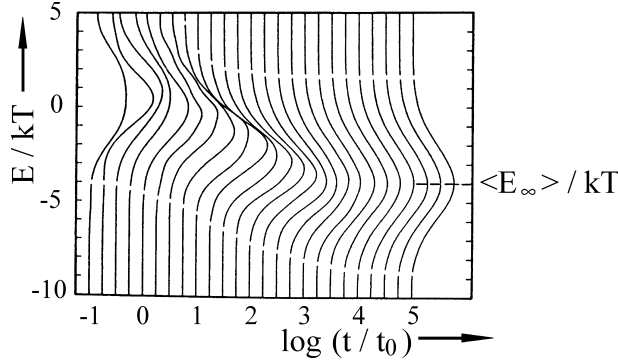


Fig. 8.46 A Monte-Carlo simulation of the time dependence of the distribution of charge-carrier energies as a Gauss function of the states (DOS) with a width σ . The centre of the energy of the distribution of excess charge carriers relaxes in $\lim_{t \rightarrow \infty}$ to the value $\langle E_{\infty} \rangle = \lim_{t \rightarrow \infty} \langle E(t) \rangle = -\sigma^2/kT = -\sigma \hat{\sigma}$. In the example shown, $\hat{\sigma} = \sigma/kT = 2$. After [47].

$F = 0$ and at $t = 0$ within the distribution function $G(E)$ is negative, temperature dependent, and has a simple form:

$$\langle E_{\infty} \rangle = \lim_{t \rightarrow \infty} \langle E(t) \rangle = -\frac{\sigma^2}{kT} = -\sigma \hat{\sigma} \quad (8.80)$$

with the normalised width

$$\hat{\sigma} = \sigma/kT. \quad (8.81)$$

It is thus plausible that the charge transport must be thermally activated with the energy E_{∞} . The result of Bässler for the mobility with low electric fields is:

$$\mu = \mu_0 \exp \left[-\left(\frac{T_0}{T} \right)^2 \right] \quad (8.82)$$

where

$$T_0 = \frac{2\sigma}{3k}. \quad (8.83)$$

μ_0 is the mobility of the hypothetical disorder-free semiconductor at the temperature $T \rightarrow \infty$.

With this, we can determine the width σ or the normalised width $\hat{\sigma}$ of the distribution function from the temperature dependence of the mobility μ , if the experimental results for $\mu(T)$ can be described by Eq. (8.82).

8.6.2

Mobilities in High-Purity Films: Temperature, Electric-Field, and Time Dependence

One of the many impressive and typical examples of the experimental results for the temperature dependence of the mobility in high-purity films containing only

one type of molecules is the hole mobility in a MPMP film (Fig. 8.2). The film was prepared by thermal precipitation from the vapour phase (sublimation) [49]. Its thickness was $8.7 \mu\text{m}$. The temperature dependence of the hole mobility obeys Eq. (8.82) almost perfectly over a range of about four orders of magnitude in the mobility: $\lg(\mu/\mu_0) \propto -T^{-2}$. (One can readily convince oneself that distinguishing between $f(T) \propto -T^{-2}$ and $f'(T) \propto T^{-1}$ in the temperature range studied requires a high precision in the measurement of the temperature and the electric current.) From the slope at the lowest electric fields, one obtains a value for the width of the DOS: $\sigma = 0.098 \text{ eV}$. From the field dependence, whose origin will be treated later in this section, one obtains in addition the width of the non-diagonal disorder: $\Sigma = 2.0$. In van der Waals-bonded organic solids, the overlap parameter is of the order of $2\gamma a = 10$ ($\gamma \approx 0.5 \text{ \AA}$, $a \approx 10 \text{ \AA}$). This means that the relative width of the distribution of this parameter, $\Sigma/2\gamma a$, is about 20%.

Using a Monte-Carlo method for the computation of the charge transport in the framework of the Bässler model, the temperature and field dependencies of the TOF transients and the charge-carrier mobilities were simulated for numerous disordered organic photo-conductors [M4], [46], [47]. Figure 8.44b shows the simulation of the TOF transients of the holes in a film of DEH at various temperatures with a single value of $\sigma = 0.101 \text{ eV}$ for the width of the Gaussian distribution function of the transport states. Similarly, from a Monte-Carlo simulation based on the Bässler model, the temperature dependence of the hole mobility μ in DEH films was obtained (Fig. 8.47). Here, also, the experimental values of the mobilities were calculated from the thickness d of the films and the transit times $\langle t_\tau \rangle$ using the relation $\mu = d/F\langle t_\tau \rangle$ (cf. Eq. (8.21)). The values of $\langle t_\tau \rangle$ were derived from the intercepts of the asymptotes in a log-log plot of the transients (Fig. 8.44). The simulation of the temperature dependence of the mobility (Fig. 8.47) was carried out with the same value for the width of the distribution function, $\sigma = 0.101 \text{ eV}$, with which the transients were also simulated.

In addition to the temperature dependence, the disordered organic materials also exhibit a characteristic electric-field dependence $\mu(F)$. A series of experimental results from a large number of disordered organic semiconductors suggests that the mobility quite generally has the following form:

$$\mu(F) = \mu(F=0) \exp(\beta\sqrt{F}). \quad (8.84)$$

Here, $\mu(F=0)$ is the zero-field mobility and β is called the field amplification factor. Both parameters have in general a strong temperature dependence. It is most frequently observed as the so-called Poole-Frenkel form:

$$\mu(F, T) = \mu_\infty \exp\left(-\frac{\Delta_0 - \beta_{PF}\sqrt{F}}{kT_{\text{eff}}}\right), \quad T_{\text{eff}}^{-1} = T^{-1} - (T')^{-1}. \quad (8.85)$$

In this expression, μ_∞ , Δ_0 , β_{PF} and T' are constants. The name of Eq. (8.85) derives from its similarity to the Poole-Frenkel law [50].

In Fig. 8.17, the idea behind the Poole-Frenkel effect is illustrated. The basic assumption is that charged trapping states exist which are neutralised immediately

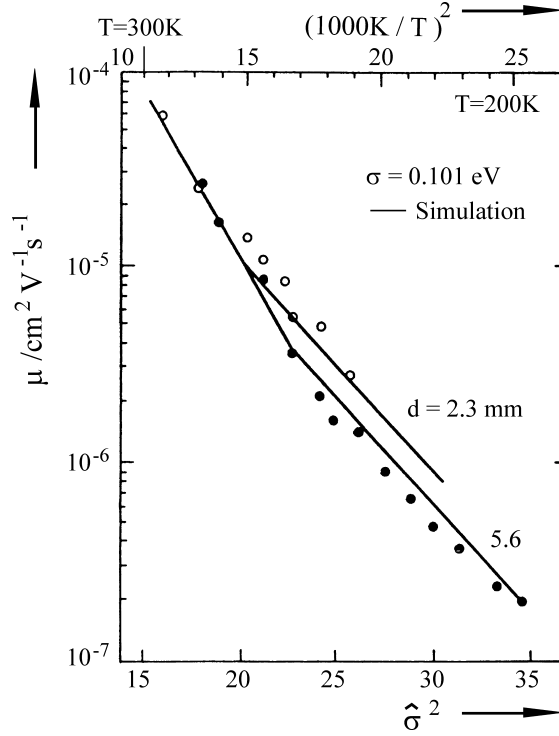


Fig. 8.47 The temperature dependence of the hole mobility $\mu = d/F(t_\tau)$ in DEH (see Fig. 8.44). \circ and \bullet are the experimental values for two different sample thicknesses, $d = 2.3 \mu\text{m}$ and $5.6 \mu\text{m}$. The lines give the simulation results with $\sigma = 0.101 \text{ eV}$. From [46].

on capturing a charge carrier. These shallow traps thus have a Coulomb potential which is superposed onto the external potential. In the direction of the electric field F , the potential thus has a maximum at $x_m = \sqrt{e/4\pi\epsilon\epsilon_0 F}$. The lowering of the energy barriers at x_m relative to the field-free case is then

$$\Delta\Phi \equiv \beta_{PF}\sqrt{F} = \sqrt{\frac{e^3}{\pi\epsilon\epsilon_0}}\sqrt{F}, \quad (8.86)$$

with which the probability for passing the barrier increases by $\exp(-\Delta\Phi/kT)$, so the mobility is then given by

$$\mu(F, T) = \mu_\infty \exp\left(-\frac{\Delta_0 - e\sqrt{eF/\pi\epsilon\epsilon_0}}{kT}\right). \quad (8.87)$$

This equation is formally identical to Eq. (8.85), although the constant T' does not occur here. The presence of T' was explained by the assumption that the transition to the excited state does not take place via a single phonon, but rather through a multiphonon process [51].

Formally, it is possible to derive Eq. (8.85) from the Poole-Frenkel effect. To be sure, there are considerations that speak against this model conception. For example, the distance of the potential maximum x_m from the trapping state at typical values of the electric field is about an order of magnitude greater than the usual hopping distance between two molecules of ca. 0.5–1 nm ($x_m = 6$ nm for $F = 10^5$ V/cm and $\varepsilon = 4.0$). Therefore, the \sqrt{F} behaviour in the exponent of the mobility cannot simply be explained by the Poole-Frenkel effect.

However, the Bässler model likewise gives a $\exp(\sqrt{F})$ dependence. The reason for this is the field dependence of the hopping rate (Eq. (8.78)). The overall field and temperature dependence according to this model for the hopping conductivity in disordered materials at high fields ($F > 10^5$ V/cm) is given by:

$$\begin{aligned} \mu(\sigma, \Sigma, F, T) \\ = \mu_0 \exp \left[- \left(\frac{2}{3} \frac{\sigma}{kT} \right)^2 + C \left(\left(\frac{\sigma}{kT} \right)^2 - 2.25 \right) \sqrt{F} \right] \text{ for } \Sigma < 1.5 \end{aligned} \quad (8.88)$$

$$\begin{aligned} \mu(\sigma, \Sigma, F, T) \\ = \mu_0 \exp \left[- \left(\frac{2}{3} \frac{\sigma}{kT} \right)^2 + C \left(\left(\frac{\sigma}{kT} \right)^2 - \Sigma^2 \right) \sqrt{F} \right] \text{ for } \Sigma \geq 1.5. \end{aligned} \quad (8.89)$$

Here, $C = 2.9 \times 10^{-4} \sqrt{\text{cm/V}}$ is an empirical constant.

The $\mu \propto \sqrt{F}$ dependence has in fact been found experimentally for many disordered organic films (see e.g. [M4] and [47]). In MPMP (Fig. 8.2), in the whole field range investigated, no deviations were found within the experimental error limits. This can be very simply demonstrated by calculating the dimensionless quantity S from Eq. (8.88):

$$S := \frac{\partial \ln(\mu/\mu_0)}{\partial \sqrt{F}} = C(\hat{\sigma}^2 - \Sigma^2). \quad (8.90)$$

S thus increases linearly as T^{-2} . This dependence can be tested directly by experiment and used as an indicator for the applicability of the Bässler model. Figure 8.48 shows $S(\hat{\sigma}^2)$ for MPMP. Together with the temperature dependence with $F = \text{const}$ and the electric-field dependence with $T = \text{const}$, the values quoted above for the two physically well-defined materials constants σ and Σ as well as for the empirical constant C were obtained. A further example of the \sqrt{F} dependence will be treated in Sect. 8.6.3.

Aside from the temperature and field dependencies of the mobilities in disordered organic semiconductors, the explicit form of the TOF transients was investigated (see e.g. Fig. 8.44). A particularly typical example is shown in Fig. 8.49: the TOF transient of the hole photocurrent of a $10 \mu\text{m}$ thick film of the commercially available, purified polymer PVK (poly-(N-vinyl-carbazole)) at $T = 279$ K after an excitation pulse of width 10 ns and an applied voltage of $V = 400$ V [52]. The hopping transport of the holes takes place in this system between the carbazole side

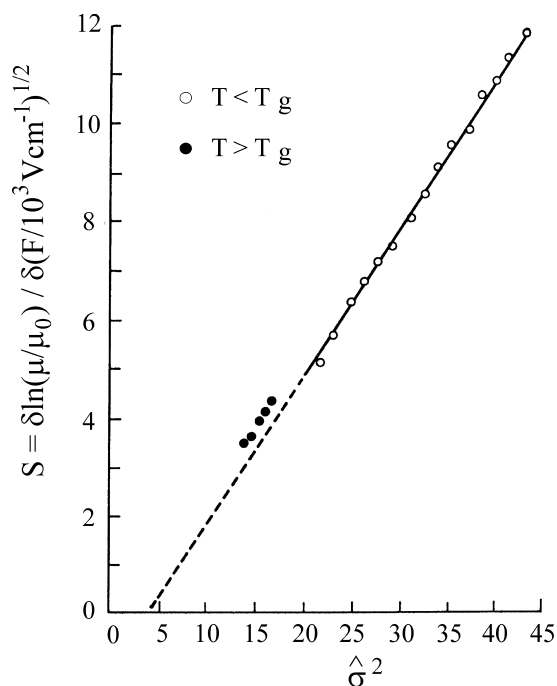


Fig. 8.48 The temperature dependence of the field dependence of the mobility μ in MPMP. The quantity $S := \partial \ln(\mu/\mu_0) / \partial \sqrt{F}$ is plotted as a function of the quantity $\hat{\sigma}^2$. $\hat{\sigma} = \sigma/kT$; F is the electric field, T_g the glass temperature. From [49].

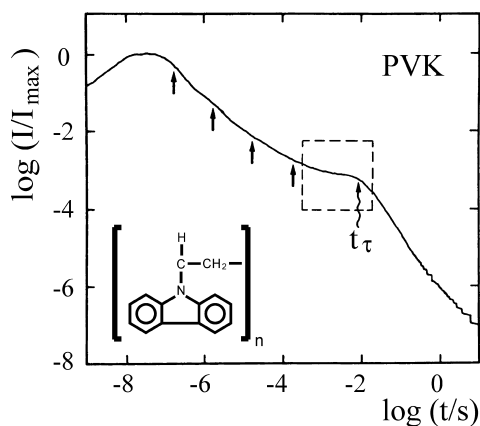


Fig. 8.49 TOF hole-conduction transients in a polyvinyl-carbazole (PVK) film of thickness $d = 10 \mu\text{m}$ at $T = 279 \text{ K}$ after an excitation pulse of width 10 ns and an applied voltage of $V = 400 \text{ V}$, as a log-log plot. The time scale spans eight decades and the measurement is composed of five individual curves acquired over different time intervals, whose limits are marked by arrows. t_τ is the transit time. After [52].

groups of the polymer. Immediately after the excitation pulse, in a time interval of $100 \text{ ns} < t < 10 \mu\text{s}$, one observes in a log-log plot a slope of -1 . This corresponds to a maximally-dispersive transport, in which the charge carriers are not yet relaxed. With increasing time, the slope decreases, until at $t \rightarrow t_r$ it is extremely small. At somewhat higher temperatures ($T = 335 \text{ K}$), a slope of 0 is measured. This corresponds to a time-independent current and thus to a dispersion-free transport at $t \rightarrow t_r$. Obviously, the charge carriers have come into thermal equilibrium at the higher temperature even before the transit time, that is before the fastest ones have reached the back electrode. At the lower temperature, the relaxation process is evidently not yet completed at the time t_r , so that the charge carriers are discharged before they can relax.

For $t > t_r$, the slope is about -1.5 . The current thus decreases by seven orders of magnitude over a time range of about 9 decades, and can be interpreted within a single transient in terms of a gradual transition from dispersive to non-dispersive transport.

The interpretation of these experimental data for the TOF transients in PVK within the Bässler model [53] explains the temperature and time dependence of the hole transport quantitatively in terms of an intrinsic DOS of width $\sigma = 0.080 \text{ eV}$ and additional traps with a molar concentration of 0.1% and a depth of 0.4 eV .

To conclude this section on hopping transport in disordered molecular films and its description by the Bässler model, we remind the reader once again of the **fundamental differences** compared to the temperature dependence of the mobilities in crystalline systems: the mobilities in **disordered films** are at room temperature orders of magnitude smaller than those in crystals, and they decrease with decreasing temperature, in contrast to the increase of the mobilities with decreasing temperature in **perfect crystals**. The charge-carrier transport in ultrapure crystals is band transport at low temperatures, in which the charge carriers are scattered by thermally-activated phonons. In the hopping transport in disordered systems, the charge-carrier transfer becomes possible only through thermal excitations.

8.6.3

Binary Systems

Not only in high-purity disordered films, which contain only one type of molecule or polymer, but also in disordered binary systems, which in principle can have a charge-transfer character, charge transport is a hopping process, which in many cases also can be described by the Bässler model. An example is shown in Fig. 8.50, which gives the temperature and field dependence of the hole mobility in tri-para-tolylamine (TPTA)-doped)biphenol-A-polycarbonate (BPPC; see Fig. 8.51) [54]. At all temperatures, the field dependence obeys the \sqrt{F} relation. If the zero-field mobility $\mu(F=0)$ is extracted from it for each temperature by extrapolation, then it also follows the temperature dependence described by the Bässler model (Fig. 8.51). The extrapolation of this dependence to very high temperatures ($T^{-2} \rightarrow 0$) yields $\mu_0 = 0.1 \text{ cm}^2/\text{Vs}$, i.e. a physically very plausible value. It is of the same order of magnitude as the mobilities found for molecular crystals at high temperatures. For

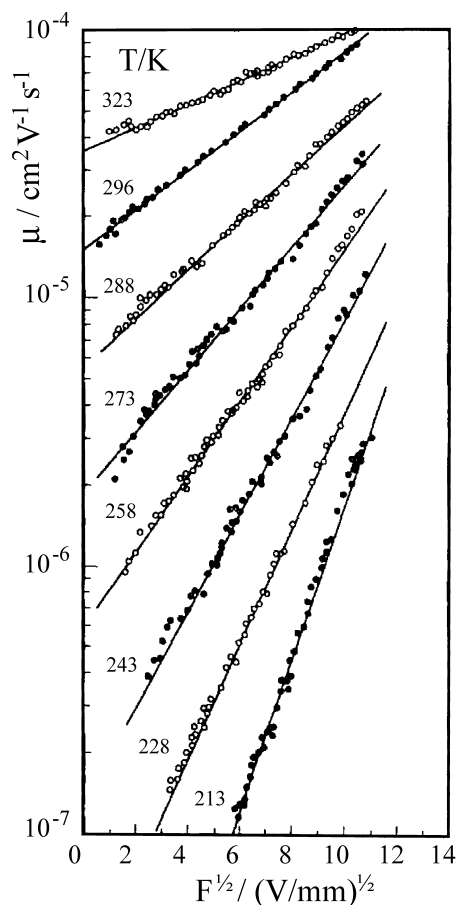


Fig. 8.50 The charge-carrier mobility in a binary system: the field dependence of the hole mobility of TPTA-doped BPPC at different temperatures is shown. TPTA = tri-para-tolylamine, BPPC = biphenol-A-polycarbonate (see Fig. 8.51). From [54].

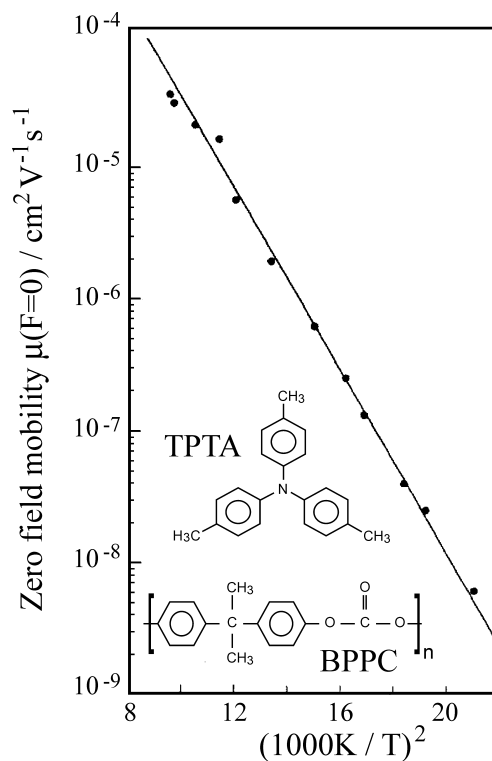


Fig. 8.51 The charge-carrier mobility in a binary system: molecular structures and temperature dependence of the zero-field mobility $\mu(F=0)$ of TPTA-doped BPPC. From [54].

the binary systems, the Bässler model can therefore also be considered to give a realistic description of charge transport.

8.6.4

Discotic Liquid Crystals

The liquid-crystalline state has been known for more than a century, as the so-called mesophase. It has a finite viscosity and at the same time anisotropic physical properties. **Mesogenic systems** do not lose all their long-range order suddenly above their melting points; instead, as their temperature is increased, the positional long-

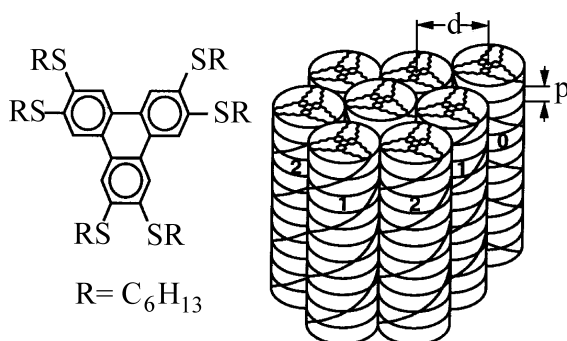


Fig. 8.52 The molecular structure of the triphenylene sulphur derivative HHTT and a sketch of its liquid-crystalline columnar *H* phase. The *H* phase exhibits long-range intracolumnar correlations and thus also a lateral correlation between the columns. Column 0 is shifted relative to columns 1 and 2 by $p/2$ and has the opposite helicity compared to columns 1 and 2. The lattice parameter in the *H* phase is $d = 21.74 \text{ \AA}$. After [55].

range order of the molecules is lost in one, two, or three dimensions. Only at the clear point does the possibly still-extant positional or orientational long-range order of the molecules vanish. Mesogenics are thus positioned between the crystals and disordered systems. How this is reflected in the charge-carrier mobility will be demonstrated here with an example.

One group of liquid crystals consists of disc-shaped, so-called discotic molecules. A well-studied example of charge transport in discotic liquid crystals is provided by the triphenylene derivative HHTT (Fig. 8.52) [55]. HHTT forms columnar phases in which the molecules are stacked “like a roll of coins”. In the mesogenic phase D_h , the molecular planes are perpendicular to the stacking axis and the stacks are ordered hexagonally. Between the crystalline phase (*K*) at low temperatures and the D_h phase, a further liquid-crystalline phase *H* exists, with genuine long-range order (Fig. 8.53). Above the D_h phase lies the isotropic phase *I*. Figure 8.54 shows the temperature dependence of the charge-carrier mobility of HHTT along the columns in

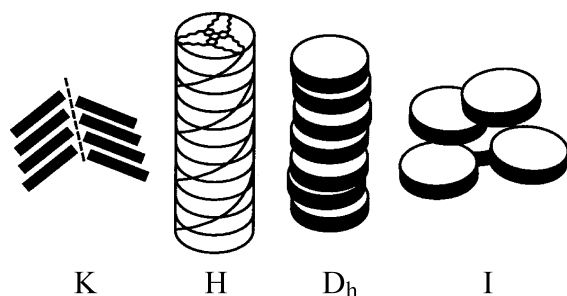


Fig. 8.53 Phases of HHTT: *K* = microcrystalline; *H* = mesogenic, long-range order with a correlation length $> 800 \text{ \AA}$; D_h = mesogenic phase; *I* = isotropic phase. From [55].

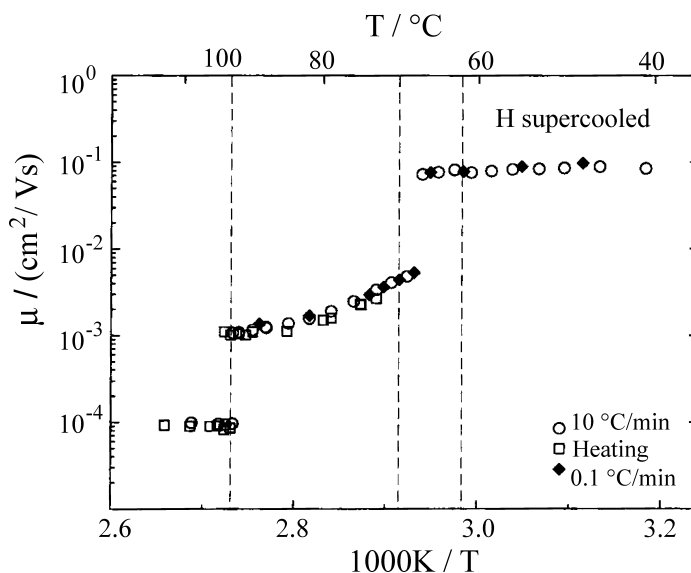


Fig. 8.54 The temperature dependence of the charge-carrier mobility of the liquid crystal HHTT. The Arrhenius plot shows μ (T^{-1}) at an electric field of 2.0×10^4 V/cm for various thermal treatments of HHTT: cooling from $I \rightarrow D_h$ at $0.1^\circ\text{C}/\text{min}$ or $10^\circ\text{C}/\text{min}$, and heating from $K \rightarrow D_h$. (Compare Fig. 8.53.) The vertical dashed lines mark the corresponding transition temperatures. From [55].

the I , D_h and H phases. At each phase transition, a jump in the mobility is observed. In the I phase, μ is already relatively high in comparison to disordered molecular semiconductors, and is temperature independent. In the D_h phase, μ increases with decreasing temperature to values up to ca. $5 \cdot 10^{-3} \text{ cm}^2/\text{Vs}$. One does not observe a thermal activation as in the disordered systems, but instead the opposite. The reason for this is the increase of the molecular and columnar order with decreasing temperature. In the H phase, μ attains the value $0.1 \text{ cm}^2/\text{Vs}$ and is thus comparable with single crystals in terms of charge transport. For the detailed analysis of these results, we refer the reader to the original literature ([55]).

8.6.5

Stationary Dark Currents

Stationary dark currents in disordered thin films which contain no intrinsic charge carriers require the injection of charge carriers. If Ohmic contacts have been prepared, then the stationary dark current is not limited by the contact resistance, but instead by the mobility and the injected space charge. Since about 1985, stationary dark currents through disordered thin films have attracted great interest, especially since at that time, suitable contacting methods were developed to permit injection of both electrons from the one electrode as well as holes from the other. This made

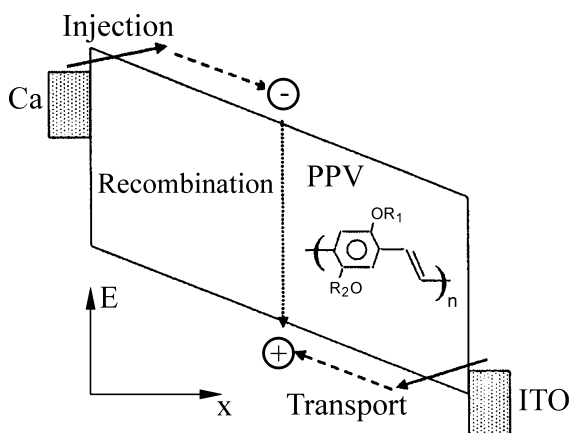


Fig. 8.55 Scheme of the bipolar current, and the structure of the soluble polymer PPV (poly(dialkoxy-para-phenylene-vinylene)). Here, $R_1 = \text{CH}_3$ and $R_2 = \text{C}_{10}\text{H}_{21}$. From [56], [57].

it possible to observe a stationary bipolar current. Figure 8.55 shows schematically the injection of a bipolar current into a polymer film. When electrons and holes recombine radiatively within the film and this radiation can be coupled out of the device, it is called an organic light-emitting diode (OLED). OLEDs will be treated in Chap. 11.

In order to understand the dark current through disordered films, primarily experiments with unipolar currents must be carried out and analysed. In Sect. 8.6.5.1, we will therefore initially present a few typical and important experimental results on dark currents in selected disordered films of molecules or polymers. In Sects. 8.6.5.2 and 8.6.5.3, we then give the analysis of these results. Beyond a simple measurement of the temperature and voltage dependence of the current, $I(V, T)$, this analysis is reasonable only if the experiments were carried out on carefully and reproducibly prepared films and the parameters film thickness d , temperature T and applied voltage V_{ext} were varied over the widest range possible.

8.6.5.1 Selected Experimental Results

The following experimental results were obtained from two groups of carefully prepared samples, **PPV polymer films** and molecular Alq_3 vapour-deposited films. They were chosen from the large number of molecular and polymeric films which have been studied, because the fundamental empirical results in these two groups of samples can be especially clearly presented.

Figure 8.56 shows the hole current–voltage characteristic of a PPV polymer film (PPV = poly-(para-phenylene-vinylene), see Fig. 8.55) for three different film thicknesses at room temperature as a log-log plot. The hole current was attained through a suitable choice of the work functions of the electrode: indium-tin oxide (ITO) injects holes, Au injects no electrons. All three characteristics are parallel. The current

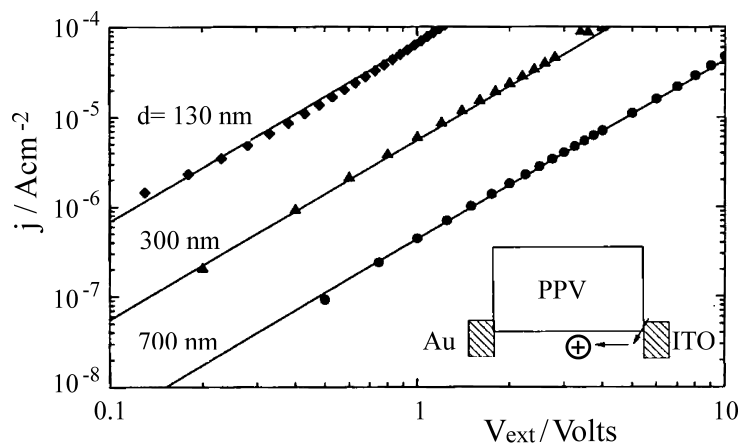


Fig. 8.56 Voltage and film-thickness dependence of the hole current density j_h in a soluble poly(dialkoxy-para-phenylene-vinylene) film (see Fig. 8.55). V_{ext} is the applied voltage, d the PPV film thickness, ITO stands for indium-tin oxide. From [56], [57].

density j is in each case proportional to the square of the voltage V and furthermore roughly proportional to the third power of the thickness d : $j \propto U^2/d^3$ [56], [57].

Figure 8.57 shows the electron current, likewise in PPV at room temperature, which was again obtained through a suitable choice of electrodes. In this case, they are made of Ca, and inject electrons, but no holes. The electron current does not increase quadratically, but rather with a much higher power of the voltage than the

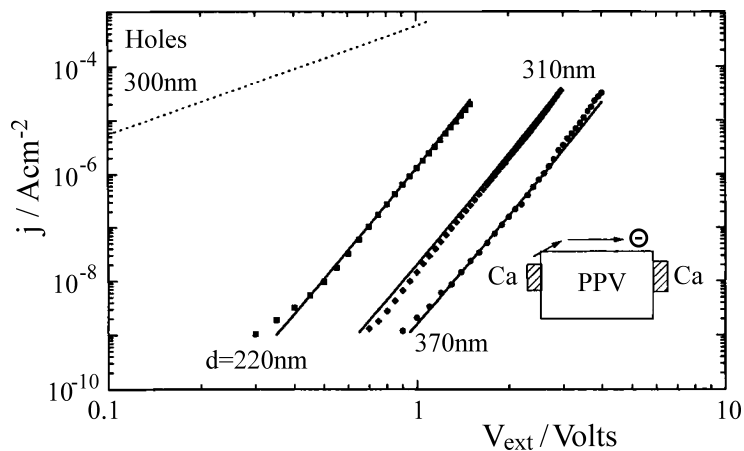


Fig. 8.57 Voltage and film-thickness dependence of the electron current density j_e in a soluble poly(dialkoxy-para-phenylene-vinylene) film (see Fig. 8.55). V_{ext} is the applied voltage, d the PPV film thickness. From [56], [57].

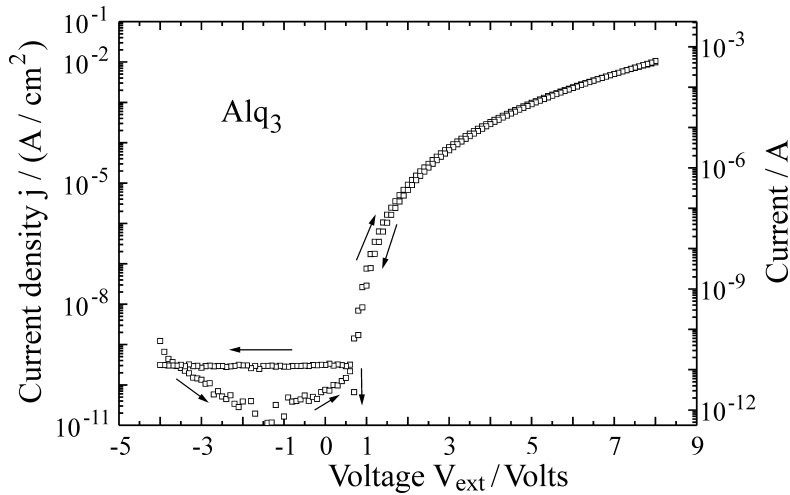


Fig. 8.58 A typical current-voltage characteristic from a Al/Alq₃/Ca device at room temperature. The thickness of the Alq₃ layer was $d = 97$ nm and its area was $A = 4.4$ mm². A voltage sweep from -4 V to $+8$ V and back is shown. The electron current

density in this diode in the pass direction at $V = +8$ V is about 10^6 times larger than in the inhibit direction. The two different metal electrodes generate a contact voltage $V_{BI} \approx +1$ V (vertical arrow). After [38].

hole current (with about the seventh power). The sample-thickness dependence is also very much stronger than for the hole current [56, 57]. Both these results can be directly read off from Fig. 8.57.

With evaporated molecular films, one observes a similar situation [38]. Figure 8.58 gives the characteristic of the unipolar electron current in an Alq₃ film at room temperature. The contacts are Ca as electron injector and aluminium as counter electrode. The difference in their work functions generates a built-in voltage $V_{BI} \approx 1$ V. Only when $V > -V_{BI}$ does current begin to flow. In the pass direction, at $V \approx 4$ V, it is already a factor of 10^6 larger than in the inhibited direction.

Figure 8.59, corresponding to Fig. 8.56, shows the dependence of the current-voltage characteristic on the layer thickness: at a constant mean electric field strength of $5 \cdot 10^5$ V/cm, the current density increases in inverse proportionality to the thickness (compare the scaling in Fig. 8.60).

Finally, as last and most important experimental result, Fig. 8.28 (which we have already seen in another context) shows the temperature dependence of the $j(V)$ characteristic for the electron current in Alq₃ with a layer thickness of $d = 294$ nm. Clearly, the temperature, along with the layer thickness, is a decisive parameter in determining the behaviour of the extremely nonlinear characteristics in this system. For example, the current increases by a factor of about 40 on doubling the voltage V at 320 K, and at 100 K, by a factor of about 10^5 . And for $V = 8$ V, the ratio of the current at 160 K to that at 320 K is roughly 10^8 .

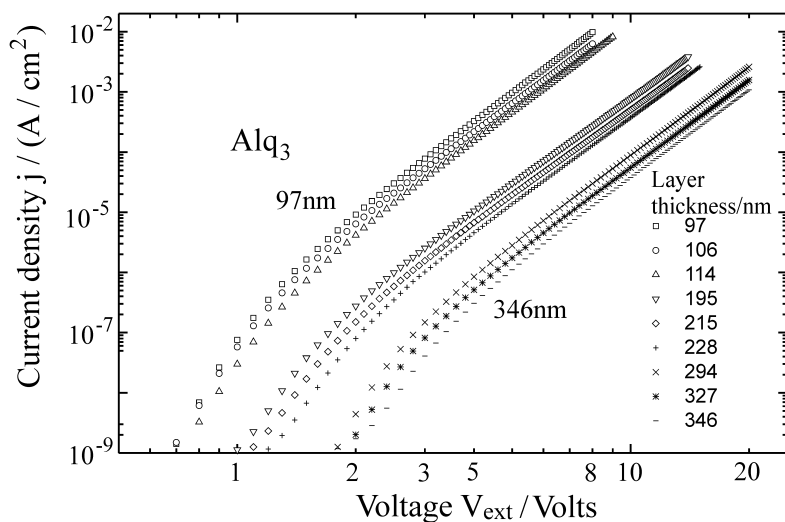


Fig. 8.59 The influence of the layer thickness on the current-voltage characteristic of Al/Alq₃/Ca diodes at room temperature. From [38].

In order to analyse these very notable experimental results on the dark current of injected charge carriers in disordered films, we first describe in the next Sect. 8.6.5.2 the model of space-charge-limited currents for the case that the semiconductor is not an ultrapure single crystal, but rather a disordered molecular film.

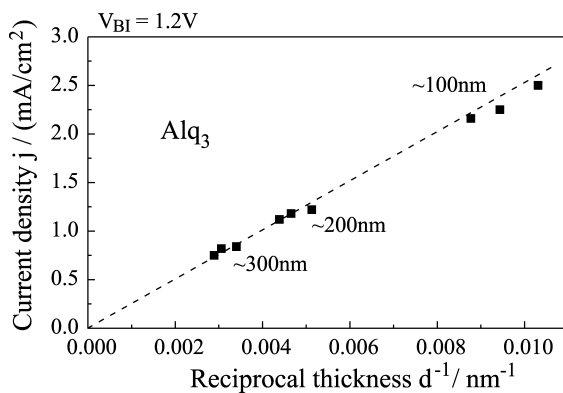


Fig. 8.60 Scaling of the electron current density j in Al/Alq₃/Ca diodes with the inverse layer thickness d^{-1} at room temperature for a mean electric field strength $\bar{F} = 5 \cdot 10^5$ V/cm. From [38].

8.6.5.2 The Theory of Space-Charge Limited Currents in Disordered Films

In Sect. 8.4.4, we formulated a model for space-charge-limited currents and gave the solution of the system of Eqns. (8.48)–(8.56) for a simple special case. The most extensive special case in Sect. 8.4.4 was that of constant (i.e. independent of the field strength) mobility and discrete trapping states. The experimental results described in Sect. 8.6.5.1 in disordered films demonstrate, without a detailed analysis, that it is out of the question to try to understand them with this simple special case. On the other hand, the model itself was formulated very generally: in principle, from Eq. (8.56), the I – V characteristic for an arbitrary trap distribution and a mobility with an arbitrary field and temperature dependence can be computed or simulated. It is therefore possible to test the model critically using the experimental results from disordered films. To this end, we first continue directly the considerations of Sect. 8.4.4 and begin with the case of **energetically distributed trapping states** with a constant mobility, for which analytic solutions can be obtained [58], and then turn to the general case. Finally, we will consider some useful scaling laws.

The properties of energetically-distributed charge-carrier traps are above all in disordered organic semiconductors of considerable significance for the analysis of real current-voltage characteristics. We consider the following two energy distributions for shallow traps: an exponential distribution, with its maximum at the transport level E_e (compare Fig. 8.6):

$$G_{\text{exp}}(E) = (N_t/E_t) \exp(-E/E_{t,\text{exp}}) \quad (8.91)$$

and the Gaussian distribution with its maximum at $E_{t,\text{Gauss}}$, below E_e , and a width σ :

$$G_{\text{Gauss}}(E) = \frac{N_t}{\sqrt{2\pi}\sigma} \exp\left(-\frac{(E - E_{t,\text{Gauss}})^2}{2\sigma^2}\right). \quad (8.92)$$

For both distributions, $E \geq 0$ and $\int_0^\infty G(E) dE = N_t$ hold.

First, we consider the exponential trap distribution G_{exp} (Eq. (8.89)). For this distribution, as mentioned, there is an analytic approximate solution [58]. It yields

$$n_t = N_t (n/N_e)^{1/\ell} \quad (8.93)$$

with $\ell := E_t/kT > 1$. The number n_t of filled shallow traps thus slowly increases with the density of free charge carriers; its increase is slower at low temperatures. The field strength and the charge-carrier density are found to be:

$$F(x) = \frac{2\ell + 1}{\ell + 1} \frac{V}{d} \left(\frac{x}{d}\right)^{\ell/\ell+1} \quad (8.94)$$

$$n(x) = \frac{\bar{n}}{\ell + 1} \left(\frac{x}{d}\right)^{\ell/\ell+1}. \quad (8.95)$$

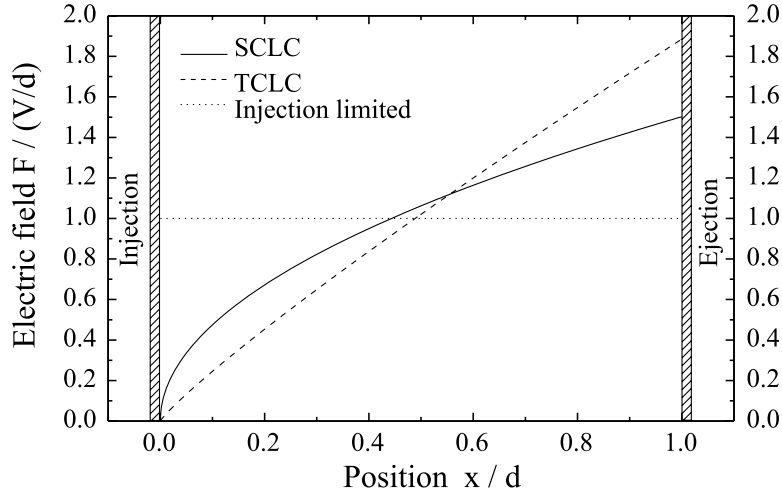


Fig. 8.61 The relative depth dependence of the electric field strength in the trap-dominated (TCLC) and in the filled-trap/trap-free (SCLC) voltage ranges, as well as for injection limiting. $E_t = 0.2$ eV, $T = 300$ K, $\ell = E_t/kT \approx 7.8$. After [38].

The field strength increases for large ℓ (that is for $E_t \gg kT$) nearly linearly with distance from the electrode and is thus steeper than in the case of the trap-free, space-charge-limited current (TF-SCLC). The field increase at the counterelectrode is likewise larger in comparison to the trap-free TF-SCLC case – there, the field is nearly twice as strong as in the case of injection-limited currents (cf. Fig. 8.61). The free charge-carrier density also drops more rapidly in going from the contact into the bulk of the semiconductor. The current-voltage characteristic is given by:

$$j_{\text{exp}} = e\mu N_e \left(\frac{2\ell + 1}{\ell + 1} \right)^{\ell+1} \left(\frac{\ell}{\ell + 1} \frac{\varepsilon \varepsilon_0}{e N_t} \right)^{\ell} \frac{V^{\ell+1}}{d^{2\ell+1}}. \quad (8.96)$$

It exhibits the following typical features: firstly, the characteristic is steeper than in the TF-SCLC case; secondly, it obeys a power law; and thirdly, the layer thickness has a considerably greater influence on the characteristic than in the case without trapping states. These features are all the more prominent for higher ℓ , and thus the lower the temperature. The voltage range in which these power laws are valid, that is in which no substantial filling of the trapping states has occurred, is called the TCLC region (TCLC for Trap-Charge-Limited Currents), since the current in this case is limited by the fact that charge carriers are immobilised in shallow traps.

The voltage V_{TFL} at which the trapping states are for the most part filled is given by

$$V_{\text{TFL}} = \frac{ed^2}{\varepsilon \varepsilon_0} \left[\frac{9}{8} \frac{N_t^{\ell}}{N_e} \left(\frac{\ell + 1}{\ell} \right)^{\ell} \left(\frac{\ell + 1}{2\ell + 1} \right)^{\ell+1} \right]^{1/(\ell-1)}. \quad (8.97)$$

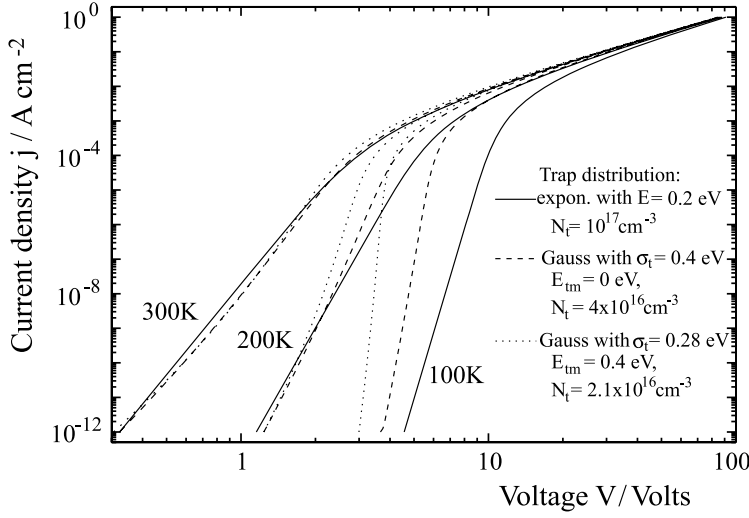


Fig. 8.62 Comparison of the simulated current-voltage characteristics for exponential and Gaussian trap distributions, as a log-log plot. The simulations were carried out for temperatures of 100 K, 200 K, and 300 K. The other parameters are: $\mu = 10^{-5} \text{ cm}^2/\text{Vs}$, $\varepsilon_r = 4$, $d = 300 \text{ nm}$, and $N_c = 2 \cdot 10^{21} \text{ cm}^{-3}$. The parameters for the trap distributions are given in the figure. From [38].

Above V_{TFL} , the characteristic again approaches the TF-SCLC case, and it therefore again becomes flatter. In a log-log plot, one thus finds a typical, strongly negative curvature of the characteristic in the transition region (see Fig. 8.62).

For the Gaussian distribution (Eq. (8.92)), there is also an approximate analytic solution; it is, however, valid only for deep trapping states ($E_{t,\text{Gauss}} > E_F$). With $m := (1 + 2\sigma^2/16k^2T^2)^{1/2}$ and $N'_t = (N_t/2) \exp(E_{t,\text{Gauss}}/mkT)$, the characteristic is found to be given by [58]:

$$j_{\text{Gauss}} = e\mu N_c \left(\frac{2m+1}{m+1} \right)^{m+1} \left(\frac{m}{m+1} \frac{\varepsilon\varepsilon_0}{e^m N'_t} \right) \frac{V^{m+1}}{d^{2m+1}}. \quad (8.98)$$

This characteristic is formally identical to Eq. (8.96), so that experimentally, distinguishing between an exponential and a Gaussian trap distribution is not readily achieved [58]. Only when the temperature can be varied over a very wide range is it possible to differentiate between these distributions. Figure 8.62 shows the characteristics for various trap distributions with otherwise identical parameters. The values of the parameters were chosen so that the characteristics are nearly the same at $T = 300 \text{ K}$. At this temperature, for all three distributions one finds characteristics which are similar to a power law (before the trapping states are filled). One sees that in practice, it is impossible to decide which trap distribution applies on the basis of only one measured characteristic. Only when the temperature is varied over a large range is it possible to obtain information on the trap distribution by comparing the measured data with simulated current-voltage characteristics.

In the general case that there is both an energy distribution of traps and a dependence of the mobility on the electric field, the system of equations (Eqns. (8.48)–(8.56)) could as yet not be analytically solved. This case is however realistic, in particular for disordered organic semiconductors. Therefore, a numerical simulation based on Eq. (8.57) is necessary. It was carried out for the model system Alq₃, and successfully tested by comparison with experimental data over a large range of the variable parameters (see Sect. 8.6.5.3).

From our previous considerations in this chapter (including subsection 8.4.4), we can see that the film thickness d of the transport layer has a strong influence on the current-voltage characteristics of space-charge-limited currents. Indeed, from the following **scaling laws**, one can directly read off via the thickness dependence of the current at a given mean electric field $\bar{F} = V/d$ whether the traps have a significant influence on the characteristic, without the need for precise knowledge of the field dependence of the mobility. Furthermore, one can also immediately read off whether the assumption of an ideal Ohmic contact is an allowed approximation, which is one of the central preconditions for the SCLC model:

- **Injection limiting:** the contact cannot deliver a sufficient number of charge carriers to establish a space charge. In an insulator, the electric field between the contacts is then per definition homogeneous: $F(x) = F = V/d$. In this case, the characteristic as a function of F is determined by the injection current. Then the current density for a given field strength is independent of the layer thickness, without regard to the details of the injection.
- **Space-charge-limited current without shallow traps / with filled traps** (TF-SCLC or SCLC): the contact is Ohmic and space charges at the contact limit the flow of current. From Eqns. (8.59) and (8.62), one can immediately see that $j = f(V/d)/d$ and thus $j(\bar{F} = \text{const}) \propto d^{-1}$. This scaling law states that for a given mean electric field, the current density decreases inversely proportional to the layer thickness of the organic semiconductor.
- **Space-charge-limited current with energy-distributed trapping states** (TCLC region): for exponential or Gaussian trap distributions, one finds $j \propto \bar{F}^{\ell+1}/d^\ell$. Thus, as a scaling law, we obtain $j(\bar{F} = \text{const.}) \propto d^{-\ell}$ with $\ell > 1$. Other trap distributions should give similar scaling laws if a suitable parameter is chosen as a function of the energy distribution and the temperature. It can be shown that the field-dependent mobility has no influence on this scaling. The layer-thickness dependence with distributed trapping states is thus clearly more predominant than in the case of trap-free transport, in particular at low temperatures.

Thus, even without a precise analysis of the characteristics, one can determine the limiting factor for current flow solely by regarding its dependence on layer thickness.

8.6.5.3 Analysis of Selected Experimental Results

In this final section, we describe the analysis of the selected experimental results from Sect. 8.6.5.1 using the model for space-charge-limited currents.

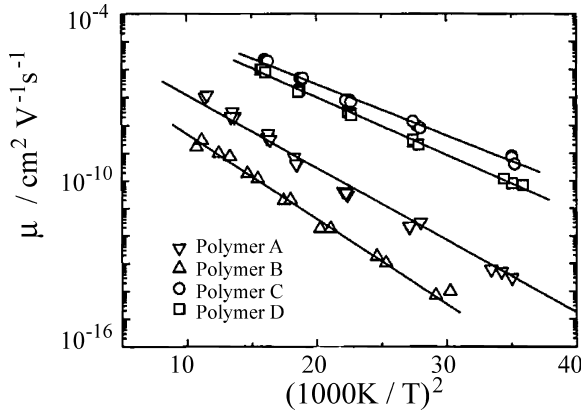


Fig. 8.63 The temperature dependence of the zero-field hole mobility μ ($F \rightarrow 0$) of four differently-substituted PPV derivatives. The data were fit to the model for hopping transport with a Gaussian distribution of the transport states: $\ln(\mu/\mu_0) \propto (T_0/T)^2$ (see Eq. (8.82)). From [56], [57].

Holes in PPV Derivatives: the current-voltage characteristics $j(V)$ (Fig. 8.56) obey Eqns. (8.59) or (8.63) to high precision. The current is thus space-charge limited and not injection limited. The effective mobility at room temperature can be determined directly from the characteristics. The field and temperature dependence of various PPV derivatives can be described by the Bäessler model for hopping transport or by further developments based on this model [56], [57]. Figure 8.63 shows as an example the temperature dependence of the hole mobilities μ of four different PPV derivatives in the temperature range between 320 K and 170 K. The four samples differ in terms of the substituents R_1 and R_2 (see Fig. 8.55). All four temperature dependencies obey Eqns. (8.77) or (8.87). The values for the width σ of the Gaussian distribution of the transport levels (HOMOs) obtained from the data for these four examples are: 112 meV, 121 meV, 93 meV, and 99 meV. They are thus again of the order of magnitude of 100 meV, which is obviously typical of disordered molecular or polymer films.

Electrons in PPV: The electron current in PPV is smaller than the hole current (Fig. 8.57). Its strong field dependence is typical of a trap dominated space-charge-limited current with an energy distribution of the traps. The experimental values of the characteristics (Fig. 8.57) obey Eq. (8.96) or (8.98) with a distribution parameter $\ell = E_t/kT$ for an exponential or m for a Gaussian distribution. The fit to the measurements shown in Fig. 8.57 yields the value $E_t/k = 1500$ K, that is $E_t = 130$ meV [56], [57], and thus again a value of the order of 100 meV.

Electrons in Alq₃: the layer-thickness dependence of the current density (Figs. 8.59 and 8.60) is $j \propto d^{-1}$ at a high and constant field strength. It follows from this that the contact is Ohmic and the current is space-charge limited and not limited by the contact. This is the basic condition for the model of space-charge-limited currents. The $j(V)$ characteristics for a film thickness of $d = 294$ nm (Fig. 8.28) and the corresponding characteristics for smaller thicknesses are determined by energy-

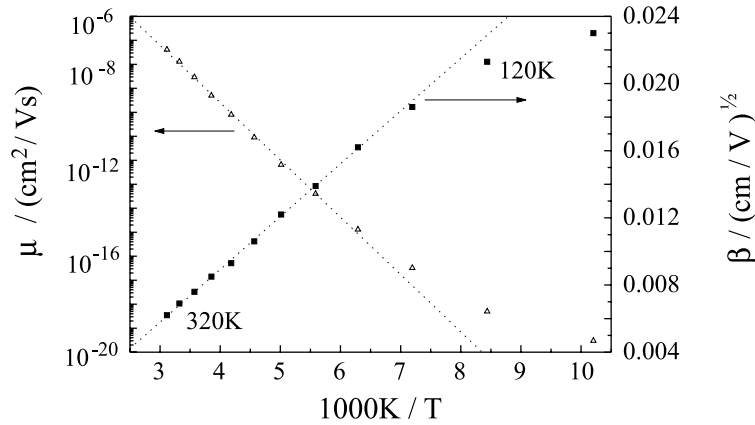


Fig. 8.64 The temperature dependence of the zero-field mobility μ_0 and the field-amplification factor β of the mobility $\mu = \mu_0 \exp(\beta\sqrt{F})$ for space-charge-limited current in a 294 nm thick Alq₃ film. The extrapolation to very high temperatures yields $\mu_0 (T \rightarrow \infty) = 2.5 \text{ cm}^2/\text{Vs}$. After [38].

distributed shallow traps, according to what we have seen in Sect. 8.6.5.2. The simulation of the $j(V)$ characteristics for a Gaussian trap distribution and a field-dependent mobility $\mu(F) = \mu_0 \exp(\beta\sqrt{F})$ leads to excellent agreement with the experimental values (compare Fig. 8.28). With the values for the width of the distribution of 0.2 eV, the overall shallow-trap density of $9 \cdot 10^{16} \text{ cm}^{-3}$, and the relative dielectric constant of 4.4 ± 0.2 , one obtains nearly identical curves for the experimental data and the simulation over a current range of up to eight orders of magnitude. At each temperature, only the two fit parameters μ_0 and β (see Eq. (8.53)) were used. These parameters are strongly temperature dependent (Fig. 8.64). The zero-field mobility at infinitely high temperature follows from a formal extrapolation: $\mu_0 (T \rightarrow \infty) = 2.5 \text{ cm}^2/\text{Vs}$, i.e. once again a value whose order of magnitude is similar for all the organic semiconductors. For a detailed discussion of these results, we refer the reader to the original literature [38].

The examples of current-voltage characteristics in disordered films with Ohmic contacts treated quantitatively here are individual cases which were studied especially carefully and which made use of samples that were prepared under very well-controlled conditions. The details of the results should not be generalised. However, at least the width of the energy distribution of the transport levels of about 100 meV appears to be typical of disordered organic semiconductors. It follows from the examples that the current in disordered films of organic semiconductors with Ohmic contacts can still be quantitatively described by the model for space-charge-limited currents, possibly using a simulation, even when shallow or deep traps are present and when the mobilities are field and temperature dependent. Due to the strongly nonlinear dependence of the current on voltage and layer thickness, this is a non-trivial result. At this point, we wish to emphasize once more that not only different materials, but also different preparation techniques for films of one and the same material can lead in detail to different conductivities in disor-

dered films: the reproducibility of the experimental results depends very sensitively on carefully-controlled sample preparation.

Problems

Problem 8.1. Intrinsic conductivity:

Compute the (fictitious) value of the specific electrical conductivity of a pure anthracene crystal at room temperature. How large would the homogeneous charge-carrier density (number of charge carriers per molecule) have to be, in order to attain a specific conductivity of $1 \Omega^{-1} \text{ cm}^{-1}$?

Problem 8.2. Photo-induced charge-carrier generation in conjugated polymers:

In the following papers, the process of charge-carrier generation in conjugated polymers was investigated: V. GULBINAS, D. HERTEL, H. BÄSSLER *et al.*, *Phys. Rev. Lett.* **89**, 107401 (2002); and D. HERTEL, H. BÄSSLER *et al.*, *Chem. Phys. Lett.* **361**, 99 (2002).

In the first article, the authors were able to demonstrate that the photo-charge carriers are generated through dissociation of singlet excitons and that in addition, a strong electric field is necessary. The experiment shows that field-assisted photoionisation is a secondary process, which originates from a primary neutral state. In the second article, the quenching of the fluorescence and the quantum yield of the charge carriers generated were measured simultaneously as a function of the strength of an applied electric field. Both the quenching of the fluorescence and the quantum yield of charge-carrier generation increase superlinearly with the electric field strength. This experiment demonstrates that a metastable electron-hole pair is formed from the fluorescing singlet state, whose lifetime at room temperature lies in the range of microseconds and which can escape from its Coulomb potential only with the aid of an external field.

Discuss these two papers in detail.

Problem 8.3. Space-charge limited currents:

Derive the two equations (8.59) and (8.63) for space-charge limited currents without traps and with filled traps, respectively, from the system of Eqns. (8.48)–(8.56). Discuss the experimental results on organic single crystals (Fig. 8.27).

Literature

Monographs and Books

- | | |
|--|--|
| <p>M1 M. POPE and CH. S. SWENBERG, <i>Electronic Processes in Organic Crystals and Polymers</i>, Oxford University Press (1999)</p> | <p>M2 E. A. SILINSH and V. ČÁPEK, <i>Organic Molecular Crystals</i>, AIP Press (1994)</p> |
| | <p>M3 J. D. WRIGHT, <i>Molecular Crystals</i>, 2nd ed., Cambridge University Press (1995)</p> |

- M4** P. M. BORSENBERGER and D. S. WEISS, *Organic Photoreceptors for Imaging Systems*, Marcel Dekker, Inc., New York (1993)
- M5** K. C. KAO and W. HWANG, *Electrical Transport in Solids*, Pergamon Press, Oxford (1981)
- M6** J. SIMON and J. J. ANDRÉ, *Molecular Semiconductors*, Springer-Verlag (1985)
- M7** W. BRÜTTING, ed., *Physics of Organic Semiconductors*, Wiley-VCH (2005)

References

- 1 A. POCHETTINO, *Acad. Lincei, Rendiconti* **15**, 355 (1906)
- 2 A. STARK and W. STEUBING, *Physikalische Zeitschrift* **9**, 481 (1908)
- 3 W. E. PAULI, *Ann. Phys.* **40**, 667 (1913)
- 4 J. KOENIGSBERGER and K. SCHILLING, *Ann. Phys.* **32**, 179 (1910)
- 5 A. SZENT-GYÖRGYI VON NAGYRAPOLT, *Science* **93**, 609 (1941); *Introduction to a Submolecular Biology*, Academic Press, New York, Chapter 3 (1960)
- 6 *Mol. Cryst. and Liq. Cryst.* **171** (1989), Guest Editors: H. Inokuchi, M. Sano, Y. Maruyama and N. Sato
- 7 D. D. ELEY, *Nature* **62**, 819 (1948); H. AKAMATU and H. INOKUCHI, *J. Chem. Phys.* **18**, 810 (1950)
- 8 H. METTE and H. PICK, *Zeitschr. F. Physik* **134**, 566 (1953)
- 9 O. H. LE BLANC, JR., *J. Chem. Phys.* **30**, 1443 (1959)
- 10 R. G. KEPLER, *Phys. Rev.* **119**, 1226–1229 (1960)
- 11 P. MARK and W. HELFRICH, *J. Appl. Phys.* **33**, 205 (1962)
- 12 W. HELFRICH, in: *Physics and Chemistry of the Organic Solid State*, Vol. III, edited by D. Fox, M. Labes and A. Weissberger, Interscience Publishers (1967)
- 13 N. RIEHL, G. BECKER and H. BÄSSLER, *Phys. Stat. Sol.* **15**, 339 (1966)
- 14 N. SATO, H. INOKUCHI and E. A. SILINSH, *Chem. Phys.* **115**, 269 (1987)
- 15 K. SEKI, *Mol. Cryst. Liq. Cryst.* **171**, 255 (1989)
- 16 E. C. M. CHEN and W. E. WENTWORTH, *Mol. Cryst. Liq. Cryst.* **171**, 271 (1989)
- 17 L. SEBASTIAN, G. WEISER and H. BÄSSLER, *Chem. Phys.* **61**, 125 (1981); (with G. PETER) *Chem. Phys.* **75**, 163 (1983)
- 18 E. A. SILINSH and A. J. JURGIS, *Chem. Phys.* **94**, 77 (1985)
- 19 N. KARL, *Festkörperprobleme* **14**, 261 (1974)
- 20 W. WARTA and N. KARL, *Phys. Rev. B* **32**, 1172 (1985)
- 21 N. KARL and J. MARKTANNER, *Mol. Cryst. Liq. Cryst.* **335**, 149 (2001)
- 22 N. KARL, in: *Spektroskopie amorpher und kristalliner Festkörper*, Hrsg.: D. Haarer und H. W. Spiess, Steinkopf-Verlag Darmstadt (1995)
- 23 W. WARTA, R. STEHLE and N. KARL, *Appl. Phys. A* **36**, 163 (1985)
- 24 N. KARL, Organic Semiconductors, in: *Landolt-Boernstein (New Series)*, Group III, Vol.17 Semiconductors, edited by O. Madelung, M. Schulz and H. Weiss, Springer Verlag, Heidelberg, p. 106 (2000)
- 25 N. GEACINTOV and M. POPE, *J. Chem. Phys.* **50**, 814 (1969)
- 26 R. R. CHANCE and C. L. BRAUN, *J. Chem. Phys.* **59**, 2269 (1973)
- 27 R. R. CHANCE and C. L. BRAUN, *J. Chem. Phys.* **64**, 3573 (1976)
- 28 E. A. SILINSH and H. INOKUCHI, *Chem. Phys.* **149**, 373 (1991)
- 29 L. ONSAGER, *Phys. Rev.* **54**, 554 (1938)
- 30 R. H. BLATT, C. L. BRAUN and J. F. HORNIG, *J. Chem. Phys.* **49**, 1967 (1968)
- 31 C. L. BRAUN, *Phys. Rev. Lett.* **21**, 215 (1968)

- 32 R. H. FOWLER and L. NORDHEIM, *Proc. Roy. Soc.* **119A**, 173 (1928)
- 33 E. M. CONWELL and M. W. WU, *Appl. Phys. Lett.* **70**, 1867 (1997)
- 34 V. I. ARKHIPOV, E. V. EMELIANOVA, Y. H. TAK and H. BÄSSLER, *J. Appl. Phys.* **84**, 848 (1998)
- 35 See e.g. H. IBACH and H. LÜTH, *Festkörperphysik*, Springer Verlag, Heidelberg (1995)
- 36 V. PODZOROV, S. E. SYSOEV, E. LONGINOVA, V. M. PUDALOV and M. E. GERSHENSON, *Appl. Phys. Lett.* **83**, 3504 (2003)
- 37 R. W. I. DE BOER, M. IOCHENSEN, T. M. KLAPWIJK and A. F. MORPURGO, *J. Appl. Phys.* **95**, 1196 (2004)
- 38 W. BRÜTTING, S. BERLEB and A. MÜCKL, *Organic Electronics* **2**, 1–36 (2001); S. BERLEB, Dissertation, Universität Bayreuth (2001)
- 39 J. L. KATZ, S. A. RICE, S. I. CHOI and J. JORTNER, *J. Chem. Phys.* **39**, 1683 (1963)
- 40 R. M. GLAESER and R. S. BERRY, *J. Chem. Phys.* **44**, 3797 (1965)
- 41 D. C. SINGH and S. C. MATHUR, *Mol. Cryst. Liq. Cryst.* **27**, 55 (1973)
- 42 Y. C. CHENG, R. SILBEY, D. A. DA SILVA FILHO, J. P. CALBERT, J. CORNIL and J. L. BRÉDAS, *J. Chem. Phys.* **118**, 3764 (2003)
- 43 N. KARL, Charge Carrier Mobility in Organic Crystals, in: *Organic Electronic Materials*, edited by R. Farchioni and G. Grosso, Springer-Verlag (2001)
- 44 N. KARL, in: *Defect Control in Semiconductors*, edited by K. Sumino, Elsevier Science Publishers B. V., pp. 1725 ff (1990)
- 45 W. SHOCKLEY, *Bell Systems Technical Journal* **30**, 991 (1951)
- 46 P. M. BORSENBERGER, L. T. PAUTMEIER and H. BÄSSLER, *Phys. Rev.* **B 46**, 12145 (1992)
- 47 H. BÄSSLER, *phys. stat. sol. (b)* **175**, 15 (1993)
- 48 A. MILLER and E. ABRAHAM, *Phys. Rev.* **120**, 745 (1960)
- 49 P. M. BORSENBERGER, L. PAUTMEIER and H. BÄSSLER, *J. Chem. Phys.* **95**, 1258 (1991)
- 50 J. FRENKEL, *Phys. Rev.* **54**, 647 (1938)
- 51 A. YELON and B. MOVAGHAR, *Phys. Rev. Lett.* **65**, 618 (1990)
- 52 E. MÜLLER-HORSCHÉ, D. HAARER and H. SCHER, *Phys. Rev.* **B35**, 1273 (1987)
- 53 U. WOLF, H. BÄSSLER, P. M. BORSENBERGER and W. T. GRUENBAUM, *Chem. Phys.* **222**, 259 (1997)
- 54 P. M. BORSENBERGER, *J. Appl. Phys.* **68**, 6263 (1990)
- 55 D. ADAM, Dissertation, Universität Bayreuth (1994); D. ADAM, F. CLOSS, T. FREY, D. HAARER, H. RINGSDORFF, P. SCHUHMACHER and K. SIEMENSMEYER, *Phys. Rev. Lett.* **70**, 457 (1993)
- 56 P. W. M. BLOM and M. J. M. DE JONG, *IEEE J. Select Top Quant Electron* **4**, 105 (1998)
- 57 P. W. M. BLOM and M. C. J. M. VISENBERG, *Materials Science and Engineering* **27**, 53 (2000)
- 58 M. A. LAMPERT and P. MARK, *Current Injection in Solids*, Academic Press, New York (1970)
- 59 M. BRINKMANN, V. S. VIDEVA, A. BIEBER, J. J. ANDRÉ, P. TUREK, L. ZUPPIROLI, P. BUGNIN, M. SCHAER, F. NUESCH and R. HUMPHRY-BAKER, *J. Phys. Chem. A* **108**, 8170 (2004)

9

Organic Crystals of High Conductivity

9.1

Donor-Acceptor Systems

In Chap. 8, we treated organic crystals which are composed of a single type of molecules. As we expect of organic substances, these crystals are semiconductors or insulators. The LUMOs of the molecules form the conduction band, the HOMOs form the valence band, and the energy gap is large compared to $k_B T$. At room temperature, typical values of the conductivity are less than about $10^{-14} (\Omega \text{ cm})^{-1}$, and values of the mobilities are less than around $1 \text{ cm}^2/\text{Vs}$. The lowest-lying optical excitation states of these substances are Frenkel excitons.

In this chapter, we deal with a different group of organic crystals: those whose unit cells are composed of two partners in a stoichiometric ratio, often in the ratio 1:1 or 2:1. Here, one of the partners is an electron donor D with a small ionisation energy I_G , e.g. tetrathio-fulvalene (TTF), the other is an electron acceptor A with a high electron affinity A_G , e.g. tetracyano-quinodimethane (TCNQ) (see also Figs. 2.8 and 2.17). The index G means that the values apply to the gas phase (cf. Fig. 8.6 and Table 8.1). During crystal growth, molecular ions D^+ and A^- are formed. In this process, the charge transfer δ is not necessarily a whole elementary charge per molecule. In particular, the degree of charge transfer for a stoichiometric ratio of 2:1 is often near to one elementary charge per unit cell, that is $1/2$ per molecule for one of the two partners. The donors must therefore not be completely oxidised and the acceptors not completely reduced. The intermolecular bonding is then not due solely to the van der Waals forces; rather, there is a more or less strong ionic or charge-transfer contribution, i.e. a Coulomb bonding (cf. Sect. 2.4). The energy of the CT bonding is composed of the difference between I_G and A_G of the donor and the acceptor as well as, in the crystal, the stabilising Coulomb forces between the ions, i.e. the Madelung energy E_M , corresponding to the ionic contribution. In the crystal, $E_M > |I_G - A_G|$ must hold. The ionic contribution to the binding energy is $E_B = -E_M + (I_G - A_G)$. E_M is, to be sure, difficult to compute, since one cannot approximate the charge distribution with point charges, as is often possible in ionic crystals (see problem 2.4). For the spatially-extended molecules, this approximation is too rough; instead, one must know the charge distribution within the molecules as well as the degree of CT, δ ($\delta \leq 1$).

Within this group of crystals, there are those with a **high dark conductivity**, which presumes that some particular geometrical and electronic conditions are fulfilled. Early examples (1954) are the complexes of polycyclic aromatics, such as for example the perylene cations with halogen anions, which exhibit conductivities in the range from $1\text{--}10^{-3} (\Omega \text{ cm})^{-1}$ at room temperature [1]. In 1973, the complex of tetrathio-fulvalene and tetracyano-quinodimethane, for short $\text{TTF}^+ \cdot \text{TCNQ}^-$, was found to have a room-temperature conductivity of $5 \cdot 10^2 (\Omega \text{ cm})^{-1}$, increasing up to $1.5 \cdot 10^4 (\Omega \text{ cm})^{-1}$ at 66 K [2] (its crystal structure is shown in Figs. 2.8 and 2.17). The radical-ion salt copper dimethyl-dicyano-quinonediimine, $(2,5\text{-DM-DCNQI})_2^- \text{Cu}^+$, exhibits a specific conductivity of $5 \cdot 10^5 (\Omega \text{ cm})^{-1}$ at $T = 3.5 \text{ K}$ (Figs. 1.12, 1.7 and 9.14) [3]. This value is comparable with the room-temperature conductivity of copper. It is, as mentioned, the highest conductivity which has as yet been measured in an organic crystal; exceptions are naturally the organic superconductors (see Chap. 10). In addition to their high conductivities, one observes in the radical-ion salts also other properties which are typical of highly-conducting solids or metals: for example, the radical-ion salt (di-fluoranthene)-hexafluorophosphate $(\text{Fa})_2^+ \text{PF}_6^-$ (Fig. 2.18) also exhibits a metallic reflectivity (Fig. 1.8) at room temperature – in addition to its high dc-conductivity (Fig. 1.13).

The three **radical-ion salts** named above are typical representatives of the highly conducting organic CT crystals. They will be treated in more detail in the following sections of this chapter. In their nomenclature, it is usual to distinguish between radical-ion salts, radical-cation salts, and radical-anion salts: in the radical-ion salts of type $\text{TTF}^{\bullet+} \cdot \text{TCNQ}^{\bullet-}$, both organic partners are ions **and** radicals, since the closed electronic shells of the two initially neutral organic molecules also generate radicals in the process of charge transfer. (A radical ion has in addition to its charge also an unpaired electron spin.) In the **radical-cation salts** of type $(\text{Fa})_2^{\bullet+} \text{PF}_6^-$, only the organic partner $(\text{Fa})_2^{\bullet+}$ is a radical; the anion PF_6^- however has closed electronic shells and thus no spin, when $\delta = 1/2$ per Fa molecule, i.e. 1 elementary charge per PF_6 . Conversely, in the **radical-anion salts** of the type $(\text{DCNQI})_2^{\bullet-} \text{Cu}^+$, the cation Cu^+ has closed electronic shells and therefore no spin when $\delta = 1$ per Cu atom. In the two last-named cases, the inorganic counterions have tightly-bound electron systems and thus to a good approximation make no contribution to the electrical conductivity.

Organic crystals with high dark conductivities have become an active and extensive area of research in recent decades. We refer the reader to the review articles [M1, M4, M5] and [4].

9.2

Strong CT Complexes, Radical-ion Salts

In crystals which are composed of donors and acceptors, one can distinguish two limiting cases: weak CT complexes and strong CT complexes or radical-ion salts. The boundary between the two groups is fuzzy.

Weak CT complexes are constructed of molecules with closed shells. In their ground states, the charge transfer between the two partners is very small; both partners are thus practically neutral. The contribution of ionic mesomeric limiting structures to the bonding between the molecules is weak. In the electronically-excited state, the ionic limiting structures appear, and the charge transfer can be much larger. They crystallise in general with mixed stacking (Fig. 9.1a). Their electrical conductivity is – at least in the ground state – often higher than the semiconductors treated in Chap. 8, but still not very high. Anthracene is for example a molecule which can form such weak CT complexes with a variety of acceptor molecules. See in this connection the examples given in Chaps. 1 and 2, anthracene-TCNB (Fig. 1.6) and in Chap. 6, anthracene-PMDA (Fig. 6.14).

Strong CT complexes and radical-ion salts have, in contrast, a clear-cut ionic character. Even in their ground states, they consist of more or less strongly positively- and negatively-charged ions. The charge transfer is often favoured by a chemical stabilisation of at least one of the partners of the cation-anion pair formed, which accompanies the ionisation. Chemical stabilisation can occur through aromatisation of non-aromatic π -electron systems or through delocalisation of the charge across larger aromatic π systems.

In the compounds which are composed of donors and acceptors in a ratio other than 1:1, the charge is correspondingly distributed: with a ratio of 2:1, two partners with (formally) one-half elementary charge each have a singly-charged partner.

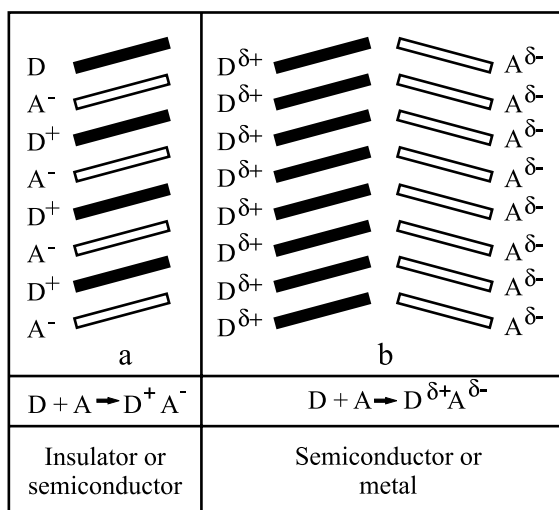


Fig. 9.1 The arrangement of the molecular ions in single crystals of organic CT complexes. **a:** mixed stacking of donor (D) and acceptor (A) molecules; such crystals are insulators or semiconductors. **b:** separate stacking with partial electron transfer ($\delta \leq 1$); such crystals exhibit high metallic conductivities along the stacks or they are semiconductors with a strong anisotropy.

The degree of charge transfer can be measured by the fraction δ (see also Sect. 2.2.4). $\delta = 0.5$ means the transfer of one-half charge per molecule, or of a whole charge to every second molecule. Partial charge transfer thus leads to mixed-valence states. In the conducting radical-ion salts, as a rule $\delta < 1$ per organic molecule. In the above-mentioned complex TTF-TCNQ, for example, in the ground state at room temperature, $\delta = 0.59$.

Typical and important for the strong CT and the radical-ion crystals is in many cases an arrangement of donors and acceptors in separate stacks, as in the compound TTF-TCNQ, Fig. 2.17. This is shown schematically in Fig. 9.1b.

Whether two partners crystallise in separate or in mixed stacks results from the delicate balance of the forces. Intermolecular forces which favour separate stacking are donor-acceptor interactions between D° and D^+ or between A^- and A° , or else the presence of a specific attraction between D^+ and A^- , so that an edge-to-edge contact of the molecules is favoured instead of face-to-face. The attractive Coulomb interaction between the stacks competes with the repulsion of the same charges within the stacks. For two given partners, it is often difficult to predict which stacking they will adopt. The stacking can also be influenced in some cases by the method of crystal growth. Reliable theoretical predictions of the crystal structures of CT salts are thus possible only to a limited extent and one must therefore depend on the measured crystal structures in order to understand the individual interactions.

In the stacks, both types of molecule-ion are frequently slanted relative to the stacking axis and also form a herringbone pattern together (compare e.g. TTF-TCNQ, Fig. 2.8). In other radical-ion crystals, for example in $(\text{Fa})_2\text{PF}_6$, the molecular planes are perpendicular to the stacking axis (cf. Fig. 2.18). The electrical conductivity is highest along these stacks. The largest anisotropy in the conductivity, namely 10^3 and more, is observed in those crystals with a perpendicular orientation of the molecular planes relative to the stacking axis. When the crystal in contrast is constructed of mixed stacks, DADADA... (see Fig. 9.1a), then a high electrical conductivity is not observed.

Table 9.1 The specific electrical conductivities at room temperature of some CT complexes and radical-ion salts of TCNQ (the structures of the molecules are given in Fig. 9.12).

	$\sigma/(\Omega \text{ cm})^{-1}$
TTF-TCNQ	$5 \cdot 10^2$
HMTSeF-TCNQ	$2 \cdot 10^3$
TTF-TCNQ ₂	$1 \cdot 10^2$
BEDT-TTF-TCNQ	$5 \cdot 10^1$
TSeF-TCNQ	$1 \cdot 10^4$
Quinolinium-TCNQ ₂	$1 \cdot 10^2$
NMP-TCNQ	$2 \cdot 10^2$
Li-TCNQ	$5 \cdot 10^{-6}$
Cs ₂ ·(TCNQ) ₃	$2 \cdot 10^{-3}$

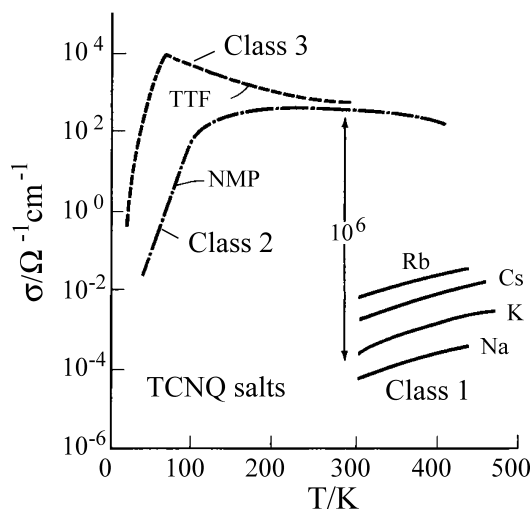


Fig. 9.2 The temperature dependence of the electrical conductivity σ of highly-conducting TCNQ salts along the stacking axis. TCNQ is in each case the acceptor; TTF, NMP, and the alkali atoms are donors. The meanings of the abbreviations are given in Fig. 9.12. The three classes 1, 2, and 3 are explained in the text. After [5] and [M1, p. 592].

In many radical-ion salts with separate stacks, one finds conversely a high electrical dark conductivity, sometimes also with metallic character. One then refers to **organic metals**. We shall concern ourselves with these salts in more detail in the following sections of this chapter. There are, however, also numerous strong CT complexes with separate stacks in which the conductivity is lower. Table 9.1 lists the conductivities of some CT complexes and radical-ion salts of TCNQ.

One can divide the conducting CT complexes and radical-ion salts with separate stacks phenomenologically into three classes which differ especially in the temperature dependence of their conductivities ([5] and [M1], Chap. V; see Fig. 9.2):

Class 1: the crystals have a conductivity which increases with increasing temperature, with an activation energy of a few tenths of an eV (0.3–0.5) and conductivities between 10^{-8} and 10^0 ($\Omega \text{ cm}^{-1}$). Among these is the salt $\text{Cs}_2(\text{TCNQ})_3$ (Fig. 9.3). In it, the TCNQ molecules are not stacked equidistantly, but rather they form trimers [6]. This is called alternating stacking, and leads to semiconducting behaviour [5].

Class 2: crystals in which the conductivity at low temperatures increases with the temperature, then passes through a broad maximum T_m , and with further increasing temperature again becomes lower. The maximum in the conductivity often lies around twice the room-temperature value of ca. 100 ($\Omega \text{ cm}^{-1}$). A typical example of this class is the salt (N-methylphenacinium)-TCNQ (Fig. 9.4) [5]. Here, the charge transfer is large and temperature dependent. For $\delta = 1$, the conductor becomes an insulator.

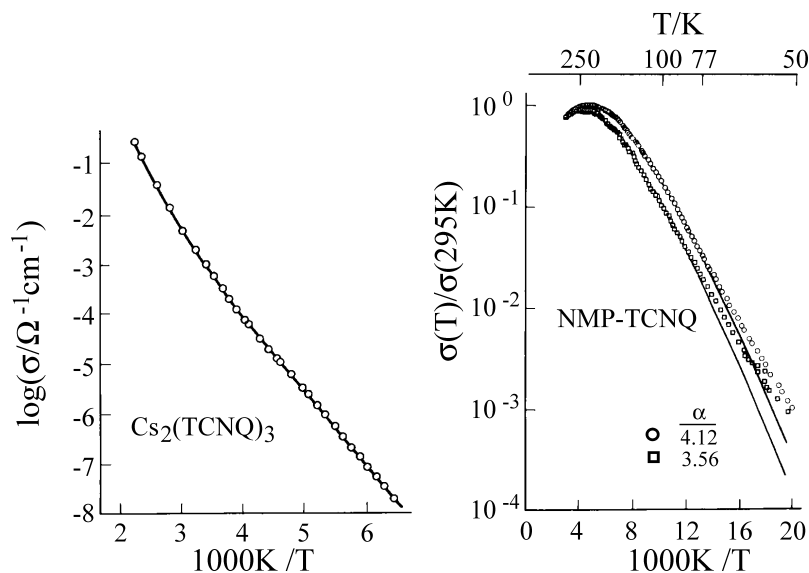


Fig. 9.3 The conductivity σ of $\text{Cs}_2(\text{TCNQ})_3$ along the stacking axis as a function of the inverse temperature, as an example of a CT crystal of class 1. After [6].

Fig. 9.4 The conductivity σ of NMP-TCNQ as a function of the inverse temperature, as an example of a CT crystal of class 2. For the definition of α , see the text. After [5] and [M1, p. 601].

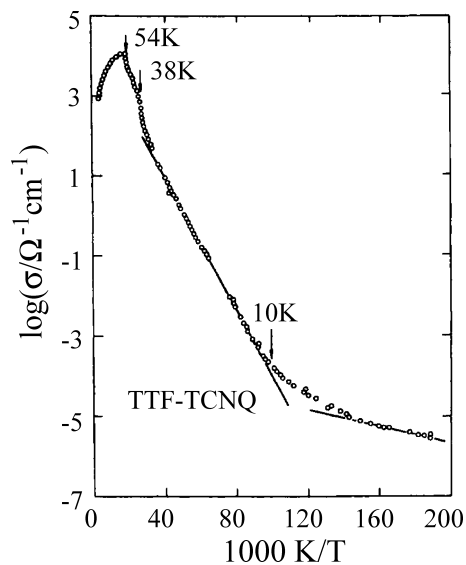


Fig. 9.5 The conductivity σ of TTF-TCNQ along the stacking axis as a function of the inverse temperature, as an example of a CT crystal of class 3 with a very high conductivity. At $T = T_p = 54\text{ K}$, the Peierls transition occurs, and at $T = 38\text{ K}$, there is a structural phase transition. After [7].

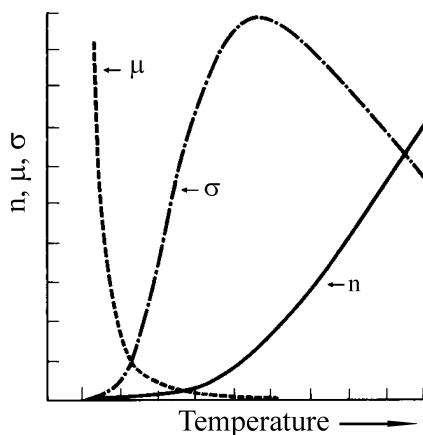


Fig. 9.6 The temperature dependence of the electrical conductivity $\sigma = en\mu$. The maximum of the conductivity in crystals of class 2 is found from the charge-carrier concentration $n \propto e^{-E_g/2k_B T}$. (E_g is the band gap, and the mobility $\mu \propto T^{-\alpha}$.) From Pope [M1].

Class 3: in the third class, the organic metals, the conductivity increases steeply in the high-temperature region with decreasing temperature, reaching values of 500–1000 ($\Omega \text{ cm}$)^{−1} at 300 K and often 100 times more at the maximum, T_m . On further decreasing of the temperature, the conductivity in most cases again drops sharply, and the metal becomes a semiconductor or an insulator. An example is TTF-TCNQ (cf. Fig. 9.5, [7]). In this class, δ is noticeably smaller than one per molecule.

In a simple phenomenological model, one can describe the temperature dependence of the conductivity $\sigma = en\mu$ for all three classes with a common formula [5]:

$$\sigma(T) = AT^{-\alpha} e^{-\Delta E/k_B T}. \quad (9.1)$$

In Eq. (9.1), $T^{-\alpha}$ is the temperature dependence of the mobility μ and $e^{-\Delta E/k_B T}$ is that of the charge-carrier concentration n . $\sigma(T)$ has a maximum at $T_m = \Delta E/k_B \alpha$ when ΔE is independent of the temperature (see Fig. 9.6). In class 1, $T_m \gg 300 \text{ K}$; in class 2, T_m is 250–300 K; and in class 3, $T_m \ll 300 \text{ K}$.

In class 1, the second exponential term is dominant. The activation energy ΔE for the concentration of the charge carriers is relatively large and has values of a few tenths of an eV; the mobility exponent is $\alpha \geq 4$. In class 3, with $\Delta E/k_B \ll 300 \text{ K}$, the strong decrease of the conductivity with increasing temperature for $T > T_m$ is due solely to the mobility, with $\mu \sim T^{-\alpha}$, where α is between two and four. In simple metals, the exponent α is one for electron-phonon scattering when the temperature T is high. This scattering mechanism must thus be different in the organic metals from that in simple metals. The often-observed sharp decrease of $\sigma(T)$ at very low temperatures is not explained by Eq. (9.1) with $\Delta E = 0$. In class 2, the charge-carrier concentration n is thermally activated; it thus increases with increasing temperature. Here, $\Delta E = 0.2$ to 0.4 eV . The scattering from phonons also increases with increasing temperature, giving $\mu \sim T^{-\alpha}$ with $\alpha = 2.5 \dots 4$. From this, the temperature dependence $\sigma(T)$ shown schematically in Fig. 9.6 results.

To which class a particular system belongs is determined by the electronic structure of the molecules and the crystal and can be predicted theoretically in most cases only with difficulty from knowledge of the structural elements.

The high conductivity originates from the fact that the mostly planar molecules lie with their planes parallel and equidistant to one another, or nearly equidistant, and the highest occupied π orbitals of the molecules are only partially occupied owing to the charge transfer. The molecular-plane spacing is smaller (typically 3.1–3.5 Å) than that expected from the van der Waals bonding. Thus, the π orbitals of the neighbours in the stacks have a sufficiently strong overlap. The electrons flow in supramolecular π orbitals; that is, they are spread over a whole series of molecules. This is the language of the chemists.

The physicist prefers to speak of a conduction band. The conduction electrons in the conduction band are delocalised along the stack axis and can move to first approximation only parallel to this axis, i.e. they can be scattered also only along this axis. Their energy $E(\mathbf{k})$ is, as in every crystal, a function of their \mathbf{k} vectors, that is of their quasi-momenta $\mathbf{p} = \hbar\mathbf{k}$. Typical bandwidths for \mathbf{k} parallel to the stacking axis, thus for motion of the electrons in this direction, are of order 0.2 to 0.5 eV. One can measure them using photoelectron spectroscopy.

Depending on the crystal structure of the one-dimensional stacks and on whether a Peierls transition occurs or not (more on this subject will be given in Sect. 9.3), the states in the one-dimensional bands are wholly or partially filled. The CT crystals can therefore be semiconductors or metallic conductors. If at high temperature metallic conductivity is present and at a lower temperature T_p a Peierls phase transition occurs, the metal becomes a semiconductor at $T < T_p$, or an insulator.

9.3

The Organic Metal TTF-TCNQ – Peierls Transition and Charge-Density Waves

TTF-TCNQ crystals appear black in reflected light at room temperature, and olive green in transmitted light. We shall take this compound as an example here of a CT- or radical-ion salt with metallic conductivity. This is shown in particular by the temperature dependence of the conductivity (Fig. 9.5). As in a metal, the conductivity increases strongly with decreasing temperature over a large range between 300 K and 54 K. It reaches its maximum of ca. $1.5 \cdot 10^4 (\Omega \text{ cm})^{-1}$ at 54 K. The increase is due to the mobility; the number of charge carriers remains constant. This follows from measurements of the magnetic susceptibility and ESR. The steep increase in the conductivity obeys a $T^{-\alpha}$ law with $\alpha > 2$.

The temperature dependence of the conductivity and thus also the mobility between 300 K and 54 K is based in part on the lattice contraction, which is largest in the stacking direction with decreasing temperature; in the main, however, it is due to the decreasing interactions of the charge carriers with the phonons as the temperature is lowered. The high numerical value of α implies that the electron-

phonon scattering must be different in a one-dimensional system from that in other molecular crystals and in metals. Below 54 K, the crystal becomes semiconducting or insulating.

In contrast to the usual inorganic metals, the conductivity is strongly anisotropic. The high values are found parallel to the stacking axis, which is the long axis of the usually needle-shaped crystals. Perpendicular to this axis, the conductivity is several orders of magnitude smaller; the conductivity is thus one-dimensional. This results in the sharp phase transition at 54 K from the metal to a semiconducting or insulating phase, the so-called Peierls transition. Here, the conductivity decreases by more than an order of magnitude within a very small temperature interval (cf. Fig. 9.5).

The **Peierls transition**, characteristic of one-dimensional metallic systems, is a static, periodic lattice distortion at its transition temperature T_P , which produces a semiconducting or insulating state for $T < T_P$. The lattice distortion is accompanied by a spatially periodic modulation of the density of the conduction electrons, a **charge-density wave**. The two periods are the same and depend only on the filling of the conduction band: their lattice vector is given by $2k_F$, that is twice the Fermi wavevector k_F .

We treat the model of the Peierls transition in the following in some detail due to its fundamental importance for one-dimensional conductivity. We first discuss the approximation of free electrons which can move in only one dimension within the length L (1-d). The energy of the **free electrons** is

$$E(k) = \frac{\hbar^2}{2m} k^2 \quad (9.2)$$

(Fig. 9.7). With periodic boundary conditions, the discrete values of the wavevectors k are equidistant:

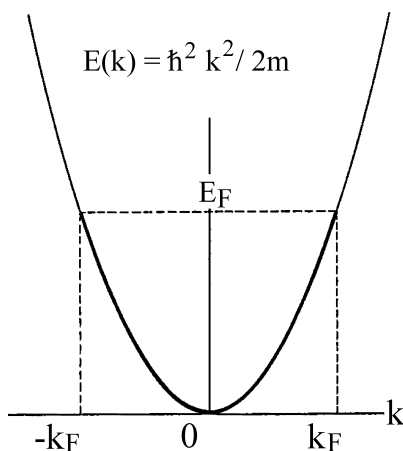


Fig. 9.7 The conduction band of free electrons in one dimension. E = energy, k = wavevector, m = mass. The states are occupied up to the Fermi energy E_F and have there the Fermi wavevector k_F or $-k_F$.

$$k = \pm \ell \frac{2\pi}{L}, \ell = 0, 1, 2, \dots \quad (9.3)$$

The density of states in reciprocal space is then

$$D(k) = 2 \cdot L/2\pi = L/\pi \quad (9.4)$$

since each state can be occupied by two electrons with opposite spins according to the Pauli principle. The normalised wavefunctions are $\phi(r) = (\ell/\sqrt{L})e^{ikr}$.

At $T = 0$, N electrons occupy the states up to the Fermi energy E_F with wavevectors $k = -k_F$ and k_F . They form the “contents” of the conduction band. The Fermi wavevector k_F and the Fermi energy are determined by the number density of the electrons, $n = N/L$. At finite temperature $T \neq 0$, the occupation probability $f(E)$ of a state of energy E is given by the Fermi distribution function $f(E)$:

$$f(E) = \frac{1}{e^{(E-E_F)/k_B T} + 1}.$$

Here, E_F is the chemical potential (or the Fermi energy for $T \rightarrow 0$). With the density of states $D(E)$ = number of states per energy interval, the chemical potential is determined by the condition

$$N = \int_0^\infty f(E) D(E) dE. \quad (9.5)$$

At $T = 0$, $f(E) = 1$ for $E < E_F$ and $f(E) = 0$ for $E > E_F$. Then we have

$$N = \int_0^{E_F} D(E) dE. \quad (9.6)$$

The density of states $D(E) dE = D(k) dk = D(k) \cdot (dk/dE) dE$ using Eqns. (9.2) and (9.4) becomes

$$D(E) = \frac{\sqrt{2mL}}{\pi \hbar} \cdot \frac{1}{\sqrt{E}}. \quad (9.7)$$

With Eq. (9.6), the Fermi energy is

$$E_F = \frac{\pi^2 \hbar^2}{8m} n^2 \quad (9.8)$$

and the Fermi wavevector is

$$k_F = \frac{\pi}{2} n \quad (9.9)$$

follow for free electrons in a one-dimensional, bounded space of length L .

In a **periodic** 1-d **potential** with the spatial period a_M (the index M stands for the metallic state which we will introduce later), the wavevector space (reciprocal

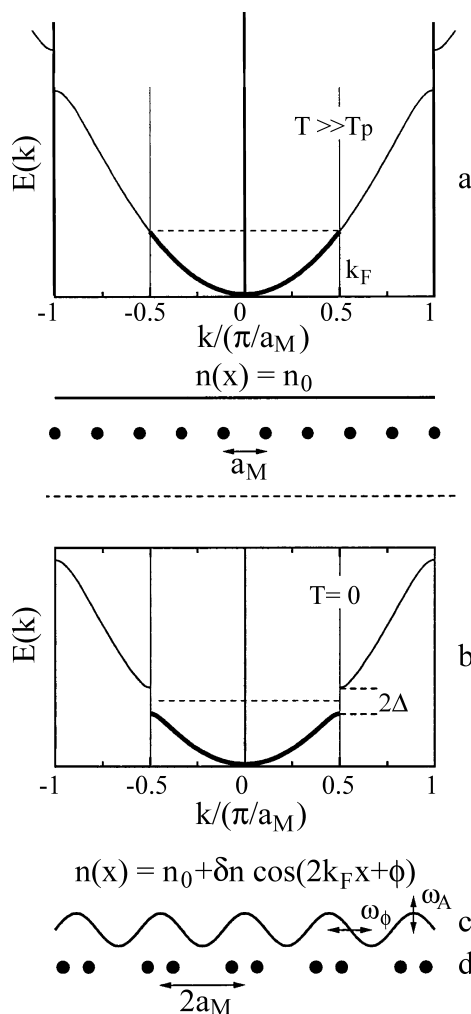


Fig. 9.8 The Peierls transition and the charge-density wave in a one-dimensional metallic electron system with a periodic crystal potential. a_M is the lattice constant.

a: The band model of the metallic state.

$E(k)$ is the energy of the conduction electrons, k their wavevector, n the electron density in the metallic state.

b: The band model of the insulating state which is produced by the Peierls transition. 2Δ is the energy gap at $k = k_F$.

c and d: charge-density wave and the static distortion of the lattice. δn is the amplitude of the density modulation.

A special case is shown, where the metallic band is exactly half filled; the Fermi wavevector k_F is therefore exactly $\pi/2a$ and the spatial periods of the charge-density wave and the lattice distortion are exactly $2a_M$. When the metallic band is less than half filled, and thus $2k_F$ is $< \pi/a$, the two spatial periods remain equal, but are $> 2a_M$.

When the spatial period of the charge-density wave and the lattice distortion are in an integral ratio with the lattice constant a_M , the Peierls distortions of the charge-density wave are termed commensurate; otherwise, they are incommensurate.

ω_ϕ and ω_A are possible excitations of the charge-density wave.

space) is divided as usual into Brillouin zones (BZ). The 1st BZ extends from $q = -\pi/a_M$ to $+\pi/a_M$ (Fig. 9.8a). When the amplitude V of the potential is weak and can be treated as a perturbation, the band splits at the boundary of the 1st BZ. The band gap is then $2V$. When the one-dimensional system has two electrons per unit cell, then $n = 2/a_M$. Then, $k_F = \pm\pi/a_M$, the band is thus filled and the one-dimensional system is an insulator. When however $n < 2/a_M$, e.g. $n = 1/a_M$ and therefore $|k_F| < \pi/a$, for the example $|k_F| = 0.5\pi/a_M$, the system becomes metallic. This is the simplest picture of an intrinsic semiconductor or a metal. $N < 2/a_M$ corresponds to a partial and $n = 1/a_M$ a full CT degree δ per unit cell in an organic metal (CT complex, class 3), independently of how many molecules are in the unit cell. If it contains e.g. two acceptors and one donor (as in $(\text{DCNQI})_2\text{Cu}^+$), or two donors and one acceptor (as in $(\text{Fa})_2^+ \text{PF}_6^-$), then for $n = 1/a_M$, the CT degree of the

conducting organic 1d stacks is 0.5 per molecule. In TTF-TCNQ, $\delta = 0.59$. Then both organic 1-d stacks contribute to the metallic conductivity.

The particular characteristics of the one-dimensional system are the following:

1. The density of states in the one-dimensional (1-d) system is $D(E) \propto 1/\sqrt{E}$ (Eq. (9.7)); in the 2-d system, it is constant, and in the 3-d system $\propto \sqrt{E}$ (see textbooks on solid-state physics, e.g. [M2], [M3]).
2. The Fermi wavevectors in 1-d systems are $k_F \propto n$ (Eq. (9.9)), in 2-d systems $\propto n^{1/2}$, and in 3-d systems $\propto n^{1/3}$.
3. In the most important process which limits the electrical conductivity in a pure metal, the relaxation of the electrons by inelastic scattering from phonons, in a 1-d metal only those scattering processes are allowed in which the wavevector of the electrons after the scattering has the value $-k_F$ when it was $+k_F$ before the scattering, and *vice versa*. The reason for this limitation, which holds only for 1-d metallic systems, is simple: the energy of the phonons is always small compared to the Fermi energy. Thus, only those scattering processes are allowed which remain in the neighbourhood of the Fermi surface, and thus only with those phonons whose wavevector q is equal to about $2k_F$. For scattering processes from phonons with the wavevector $q \neq 2k_F$, the laws of energy conservation and of conservation of the wavevector (i.e. of linear momentum) in the 1-d metal cannot be simultaneously fulfilled. In 2-d and 3-d metals, however, phonons with arbitrary wavevectors can contribute to the scattering (see Fig. 9.9).

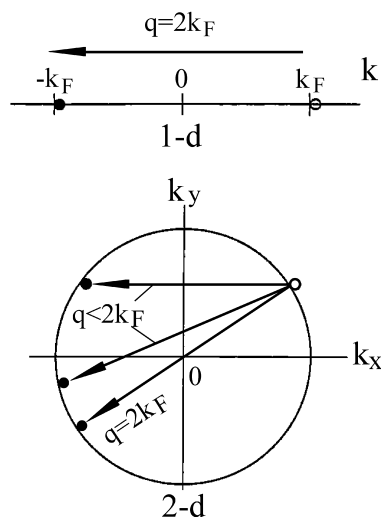


Fig. 9.9 Electron-phonon scattering in a one-dimensional (1-d) and in a two-dimensional (2-d) metallic system. Since the Fermi energy is always large compared to the phonon energies, the single-phonon scattering processes are limited to the immediate neighbourhood of the Fermi surface. In the 1-d system, the Fermi "surface" consists of only two points and the conduction electrons can be scattered only from k_F to $-k_F$. In the (isotropic) 2-d case, the Fermi "surface" is a circle and the conduction electrons can be scattered from one state into any other state on the "Fermi circle". In the 1-d case, the electron system can thus interact only with phonons whose wavevector is $q = 2k_F$. In the 2-d and the 3-d cases, the conduction electrons can interact with the whole spectrum of phonons.

The **Peierls transition** results from these properties of the 1-d metal [8]. Primarily, this phase transition is the instability of the periodic potential with respect to a distortion which is caused by the phonons and has the wavevector $q = 2k_F$. If e.g. in a half-filled 1-d band $k_F = 1/2\pi/a_M$, then the wavevector of the potential distortion

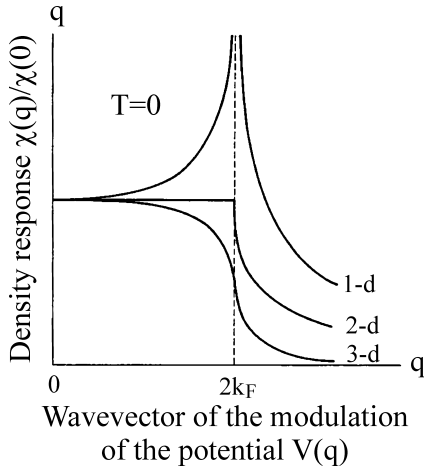


Fig. 9.10 The density-response function χ . $\chi(q)$ describes the redistribution $\delta n(q)$ of the electron density by a periodic modulation $V_q(q)$ of the potential as a function of the wavevector q (cf. also Fig. 9.8). In a 1-d system, χ has a singularity at $q = 2k_F$. This singularity does not exist in 2-d- and 3-d systems. From [9] and [M4], Chap. 2.

will be π/a_M . This corresponds to a spatial period of $2a_M$; thus, for this special case, to a doubling of the size of the unit cell (Fig. 9.8d). This doubling holds however only when the CT degree is $\delta = 1$ per unit cell, i.e. the Fermi wavevector is $k_F = 1/2\pi/a_M$, and the 1-d conduction band is therefore exactly half full. For other CT degrees, $2k_F \neq \pi/a_M$. Then the periods of the metallic 1-d lattice and the superlattice do not in general form an integral ratio. When they do have an integral ratio, the distortion and the associated charge-density wave are called commensurate, and otherwise incommensurate. The $2k_F$ distortion has been observed in several organic metals by means of X-ray structural analysis (see Sect. 9.6.2).

The origin of the distortion is the reaction (the “response”) of the conduction electrons in the 1-d metal to a **periodic modulation of the periodic potential**. The amplitude n of the electron density in the 1-d metal exhibits an increasing and divergent component when the wavevector of the potential $V_q(q)$ of the periodic modulation of the lattice potential (which is due to the phonons), i.e. the wavevector q of the periodic perturbation, has the value $q = 2k_F$. Figure 9.10 shows the so-called polarisation function or density-response function $\chi(q)$. It describes the redistribution $\delta n(q)$ of the electron density $n(q)$ in the presence of this periodic potential $V_q(q)$:

$$\delta n(q) = -\chi(q) V_q(q). \quad (9.10)$$

The divergence of the density-response function $\chi(q)$ occurs only in a 1-d metal [M4, M2, Chap. 17]. It gives rise to the collective state of the electrons (the charge-density wave) and the static lattice distortion with the same period $q = 2k_F$, as well as the opening of an energy gap at the Fermi energy E_F (Fig. 9.8c).

The fundamental mechanism of the Peierls transition, that is the spontaneous modulation of the charge density and the lattice periodicity, is thus relatively simple to understand: in a 1-d metal, in which all the states with $k \leq k_F$ are occupied, a modulation of the lattice – which is due to the phonons and has the wavevector $q = 2k_F$ – mixes states in the neighbourhood of k_F with states in the neighbourhood

of $-k_F$ and thus leads to a splitting 2Δ at the Fermi level. This allows a lowering of the energies of all the occupied states. It is compensated by the increase in the elastic lattice energy and thus leads to the formation of a stable energy gap, the stable lattice distortion, and the charge-density wave with a wavevector $2k_F$. This phenomenon can be observed only at low temperatures. At higher temperatures, the Peierls distortion is quenched by the phonons and the energy gap closes. The phase transition temperature is called the Peierls temperature T_p . The phase transition is strongly pressure dependent in the soft organic crystals. It is also suppressed by 2- or 3-dimensional couplings of the charge carriers and is therefore observable only when the one-dimensionality, i.e. the anisotropy in the metallic conductivity is strong.

The details of the theory of the Peierls transition cannot be dealt with here; we refer the reader to the extensive works of Kagoshima *et al.* [M4], Rice *et al.* [9], Lee *et al.* [10] and Schulz [11].

The most important results of this theory are the following:

- i) In the framework of the so-called “mean-field” theory, in which the fluctuations in the 1-d metal lattice are neglected, the energy gap $2\Delta = 0$ for $T \geq T_p^{MF}$. Below T_p^{MF} the energy gap opens continuously with decreasing temperature, analogously to the BCS theory of superconductivity, and at $T \rightarrow 0$, it has the value

$$2\Delta(T=0) = 3.5k_B T_p^{MF}. \quad (9.11)$$

Essential parts of the BCS theory can be taken over in the mean-field theory of the Peierls transition if one replaces the Debye energy $\hbar\omega_D$ in the superconductor by the Fermi energy E_F in the metal. Since $E_F/\hbar\omega_D \approx 10 - 100$, the Peierls phase transition temperatures are considerably higher than the critical temperatures of BCS superconductors.

- ii) The frequency Ω_{2k_F} of the phonons which are responsible for the Peierls transition has, for $T \geq T_p^{MF}$, the temperature dependence

$$\Omega_{2k_F}^2 \propto \omega_{2k_F}^2 \cdot \ln(T/T_p^{MF}). \quad (9.12)$$

Here, ω_{2k_F} is the high-temperature frequency. For $T \rightarrow T_p^{MF}$, with $\Omega_{2k_F} \rightarrow 0$, the lattice distortion becomes static. The $2k_F$ phonons in one-dimensional metals are therefore also referred to as soft modes.

- iii) In the mean-field approximation for the description of the Peierls transition, all the lattice fluctuations except those with the wavevector $q = 2k_F$ are neglected. Fluctuations are however particularly effective in highly one-dimensional systems: in contrast to 3-d systems, phase transitions in 1-d systems are seriously influenced by fluctuations. The relation between the real phase-transition temperature T_p and the experimentally observable ground-state energy gap $2\Delta(T=0)$ is, taking the fluctuations in one-dimensional metals into account:

$$2\Delta(T=0) > 3.5 k_B T_p. \quad (9.13)$$

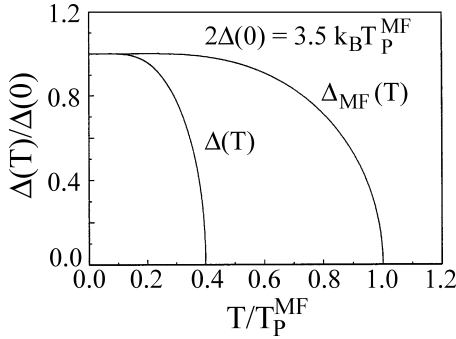


Fig. 9.11 The temperature dependence of the real Peierls energy gap $\Delta(T)$ and the energy gap $\Delta_{MF}(T)$ obtained from the BCS theory (see text).

The real phase-transition temperature T_p is thus smaller than the mean-field temperature T_p^{MF} . In TTF-TCNQ, $T_p = 54$ K. The energy gap $2\Delta(T \rightarrow 0)$ can be directly determined from the slope of the $\sigma(T^{-1})$ curve (Fig. 9.5) at low temperatures: $2\Delta(T \rightarrow 0) = k_B \cdot 450$ K [12]. The ratio $2\Delta(T = 0)/k_B T_p = 8.5$ is thus considerably larger than 3.5 in TTF-TCNQ crystals.

This implies also that the temperature dependence of the real energy gap $\Delta(T)$ in highly one-dimensional systems taking account of the fluctuations is different from the mean-field theory prediction for the temperature dependence of the energy gap, $\Delta_{MF}(T)$. Figure 9.11 shows this in-principle result [11], which can be experimentally tested, since $\Delta(T = 0)$ and T_p can be directly measured (see e.g. [12]).

A further consequence of the fluctuations is the opening of a so-called pseudo energy gap. This refers to a strong decrease of the density of states compared to the metallic density of states in the temperature range between T_p and T_p^{MF} . This pseudo energy gap is also observed in one-dimensional organic metals above the real phase-transition temperature T_p (see Sect. 9.6).

So far, we have treated the Peierls transition in terms of free electrons by introducing the periodic lattice potential and finally the particular case of $2k_F$ scattering in the electron-phonon coupling in a 1-d metal, which was the origin of the lattice distortion and the charge-density wave, both with a wavevector $2k_F$. The period of the distortion thus depends only on the filling of the bands. In this free-electron approximation, the Coulomb repulsion U between the conduction electrons was neglected and only their kinetic energy was considered. In order to include the Coulomb repulsion, the Peierls transition can also be treated in the approximation of bound electrons, i.e. in the tight-binding model. This approximation leads among other things to $4k_F$ charge-density waves. For more on this subject, we refer the reader to e.g. [M4], Chap. 2.4.

Furthermore, in treating the electrical conductivity we have thus far considered only single-particle excitations and, in particular at $T < T_p$, only thermal excitations of the charge carriers across the Peierls band gap 2Δ . As we shall see later, the charge-density wave itself can also be transported. This charge-density-wave transport is strongly frequency and electric-field dependent (see Sect. 9.6.6).

9.4

Other Radical-ion Salts and CT Complexes

There are a large number of strong CT complexes or radical-ion salts. Many organic compounds can be oxidised to radical cations by a suitable partner (e.g. perylene) \bullet^+ or reduced to radical anions (e.g. TCNQ \bullet^-). Figure 9.12 shows a variety of such molecules. The complexes can consist of two organic molecules, as in the case of TTF-TCNQ. One of the partners can however also be an inorganic ion, e.g. Cu^+ in $(2,5\text{-Dimethyl-DCNQI})_2^- \text{Cu}^+$ or also Ag^+ , Li^+ , Cs^+ , Na^+ , K^+ , Rb^+ (see Sect. 9.5) or PF_6^- , as in the radical-cation salt $(\text{fluoranthene})_2^+ \cdot \text{PF}_6^-$ (see Sect. 9.6).

In the following, we wish to summarise the most important characteristics of organic metals:

- The crystal lattices consist of separate stacks, either of planar organic donors and planar organic acceptors, or of planar organic radical ions and suitable inorganic counterions.

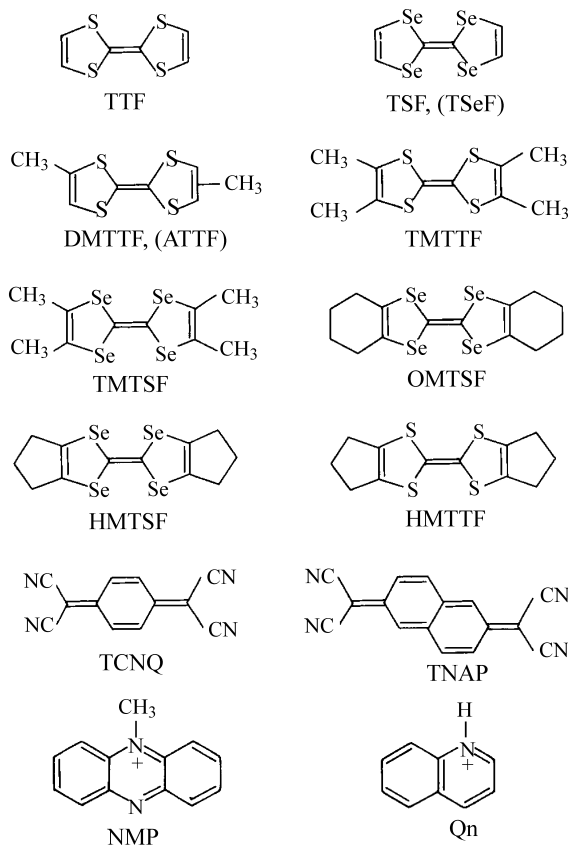


Fig. 9.12 The structure of some organic donor and acceptor molecules which are the structural units of highly-conductive radical-ion salts.

- The stacks are as a rule partially charged, i.e. they contain on the average charged and non-charged molecules, e.g. “TTF–TCNQ” = $(\text{TTF}^{+0.59} - \text{TCNQ}^{-0.59})$.
- The organic molecules form pseudo-one-dimensional conductors. In the metallic state, the organic molecular ions are equidistant when the unit cells contain only one molecule per anion or cation stack (example: TTF–TCNQ). When the unit cells contain two organic molecules per anion or cation stack, the dimers of these molecular ions are equidistant in the metallic state (e.g. $(\text{Fa})_2\text{PF}_6$). At low temperatures, in general a Peierls transition occurs in the one-dimensional metals, whereby a $2k_F$ superstructure is formed within the lattice. The stacking axis is the axis of highest conductivity, and is also the long axis of the needle-shaped crystals. The anisotropy of the electrical conductivity is large.
- In order to maintain metallic behaviour even at very low temperatures, charge bridges between the one-dimensional stacks are necessary to establish a higher dimensionality.

In this chapter, we will not discuss the **weak CT complexes** further. In these complexes, at least in the ground state, the charge transfer δ is not large. They in general crystallise in mixed, alternating stacks. We have already mentioned the example systems anthracene-tetracyanobenzene or A-TCNB (cf. Fig. 1.6) and anthracene-pyromellitic acid-dianhydride or A-PMDA (cf. Fig. 6.14).

The conductivities of these crystals lie typically in the range of 10^{-8} to $10^{-12} \Omega^{-1}\text{cm}^{-1}$, clearly higher than those of pure anthracene crystals, for example. Their ground states, as shown by photoelectron spectra, are similar to anthracene, with 5–10% CT character. The triplet states T_1 are likewise similar to anthracene, as seen in their optical spectra. The $S_1 \leftarrow S_0$ absorption is, however, very different; it is a typical CT absorption. As its photoconductivity shows, the charge separation in anthracene-PMDA takes place in the S_1 state with an activation energy of 0.14 eV. The mobilities are similar to those of anthracene.

In the two next sections, we wish to enter into more detail for two groups of radical-ion salts, because they demonstrate in a particularly impressive way the variety of interesting physical properties of organic metals and highly-conductive organic radical-ion salts: these are the radical-ion salts with dicyanoquinone-diimine (DCNQI), already mentioned in Chap. 1 (Sect. 9.5), and the likewise previously mentioned radical-cation salts with fluoranthene (Fa) (Sect. 9.6).

9.5

Radical-Anion Salts of DCNQI

Numerous 2,5-disubstituted N,N'-dicyanoquinone-diimine molecules, R_1 , R_2 -DCNQI (R_1 , R_2 = CH₃, CH₃O, Cl, Br, I) (compare Fig. 1.12) form 2:1 radical-anion salts with different monovalent metal ions (Cu⁺, Ag⁺, Li⁺, Na⁺, K⁺, Rb⁺, Tl⁺, and NH₄⁺). The crystals, which are usually black, grow preferentially in the form

of long (3–15 mm) thin (20–150 μm) rods on electrocrystallisation from an acetonitrile solution. The axis of the rods is the stacking axis of the molecules. Their structure, already shown in Chap. 1 (Fig. 1.7), exhibits a stacking arrangement of the DCNQI structural elements. Each metal-ion chain is surrounded by 4 stacks of the organic ligands. The crystal structures of the numerous different salts which are distinguished by their substituents R_1 , R_2 or metal ions are all very similar. Well over 50 different salts have been investigated.

These radical-anion salts also provide a nice example of the way in which organic materials offer the possibility of broad variation of their physical properties through the multiplicity of compounds obtainable from organic chemistry. A good survey of this group of substances is given by the review article of Hünig *et al.* [13] and, somewhat older, by Kato [14].

Here, we are in the main interested in their electrical conductivities. We first consider the **non-Cu salts**. Their cations are simply charged, while the formal charge of DCNQI is $-1/2$ in these salts. This means that the conduction electrons have their origin in the one-dimensional (organic) $p\pi$ band, which is one-fourth filled. The non-Cu salts are one-dimensional metal-like semiconductors with conductivities of typically 50 to 300 ($\Omega\text{ cm}$) $^{-1}$ at room temperature. From the temperature dependence, an activation energy of 30–70 meV is found. Down to 200 to 150 K (depending on the substituent), their conductivity changes only a little, then it decreases strongly, until they become complete insulators, similar to the Cu salts shown in the two lower curves in Fig. 1.12. The “metal” turns into an insulator.

In addition to the interactions via the π electrons along the stacking axis, which are in the first instance responsible for the charge-carrier mobility, there is also the possibility of an electronic connection between the stacks via the central metal ions, i.e. between the central metal ion and the nitrogen in the CN group of DCNQI. Such a bridging function between the stacks can be performed especially well by the Cu ion with its d electrons. In this respect, the **Cu salts**, with which we shall mainly be concerned in the following, are distinguished from the other salts. With these bridges, the one-dimensional conductivity can become three-dimensional, with a $p\pi d$ band. This is shown clearly in the structure diagram in Fig. 9.13. The ratio of the conductivities parallel and perpendicular to the stacks in most DCNQI salts lies around 5000, but for the Cu salt (dimethyl-DCNQI) $_2$ Cu, a ratio of only $\sigma_{\parallel}/\sigma_{\perp} = 15 \pm 5$ is observed.

The Cu ions in Figs. 1.7 and 9.13 are tetrahedrally coordinated. The unit cell contains four DCNQI molecules and two Cu ions. The exact degree of the charge transfer t from Cu to the DCNQI can be determined using different methods, for example by X-ray structural analysis or photoelectron spectroscopy, or else with FIR spectroscopy [14]. The copper is found to be in a mixed-valent state with a charge of $+4/3$ ($\text{Cu}^+ : \text{Cu}^{2+} = 2 : 1$), with fluctuations in the metallic state. Each DCNQI molecule then carries a charge of $-2/3$. Formally, the copper ions are thus Cu^{2+} (Cu(II)). In Cu-DCNQI salts which exhibit a Peierls transition, the Cu ions can be detected by ESR at $T < T_p$. The interplanar spacing between the DCNQI molecules along the tetragonal axis is only 3.18 Å [15, 16].

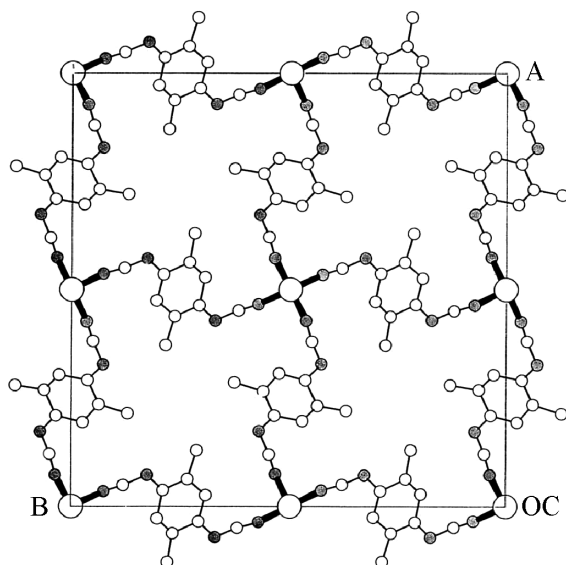


Fig. 9.13 *a, b* projection of the crystal structure of $(2,5\text{-dimethyl-DCNQI})_2 \text{Cu}$. $\bigcirc = \text{Cu}$, $\bullet = \text{N}$, $\circ = \text{C}$. The thick valence lines indicate the Cu-N coordination. One can readily recognise the bridging function of the Cu atoms via the CN groups (compare also Fig. 1.7). After [14] and [16].

The extremely high conductivity and the metallic character of its temperature dependence down to the lowest temperatures shown by one of the Cu compounds, the copper salt with two methyl groups on DCNQI (Fig. 1.12, uppermost curve, and Fig. 9.14), show why one refers to organic metals. The conductivity of this salt is – at low temperatures, for $T < 0.4 \text{ K}$ – as high as that of copper at room temperature, and it decreases continuously with increasing temperature, as is typical of metals. Below 15 K, it no longer changes significantly. Between 30 K and room temperature, the decrease of σ is roughly proportional to $T^{-2.3}$. But even at room temperature, it is still around $10^3 (\Omega \text{ cm})^{-1}$. The contribution of the conduction electrons to the magnetic susceptibility, not shown here, exhibits the behaviour of a Pauli paramagnet, again typical of metals, down to very low temperatures; i.e. it is independent of the temperature.

If we now pose the question as to the nature of the conduction mechanism and why a metallic character is observed, then to answer it, we must make use of a whole series of different experimental techniques of molecular physics and solid-state physics, including for example the influence of pressure and measurements with NMR. The method of ESR spectroscopy can also give important information [15, 17]. Through such measurements, we know for example that the high conductivity occurs mainly along the stacks, in particular those of the organic structural units. This can be seen especially from the influence of the mobile

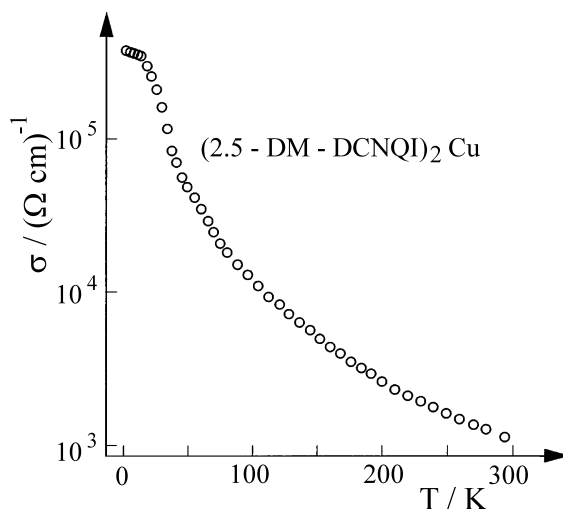


Fig. 9.14 The temperature dependence of the conductivity σ of (2,5-dimethyl-DCNQI)₂ Cu single crystals along the stacking axis. From [3].

charge-carrier spins on the relaxation behaviour of the proton spins in the DCNQI molecules [15].

It is interesting to compare the conductivity behaviour of various salts from this group which differ either in terms of their metal ions (see above) or in terms of the substituents on the DCNQI molecule. Examples of this are shown in Figs. 1.12 and 9.15. It is important for such a comparison that the different salts have the same crystal structure and merely somewhat different lattice parameters, slightly different spacings between the structural units, and slightly varied orientations [16]. The masses of the atoms and the moments of inertia of the molecules – and thus the lattice dynamics (phonons) also differ slightly. These small changes in the structural parameters can lead to large changes in the physical properties. Not only variation of the side groups R_1 , R_2 (one also refers to “internal pressure”), but also applied, “external” pressure [18] can give rise to such changes.

Only a few DCNQI copper salts are metallic conductors down to the lowest temperatures. Most of the salts show a behaviour like that seen in the lower curves in Figs. 1.12 and 9.15. The relatively high conductivity at room temperature initially increases a little on lowering the temperature, then there is a strong or even abrupt decrease into the semiconducting or insulating region. This behaviour of a “metallic semiconductor” is typical of one-dimensional conductors in which a Peierls transition puts an end to the metallic state. Such compounds therefore are not candidates for “molecular wires” (see Chap. 12), in any case not at low temperatures.

Especially impressive is the observation that the deuteration of just two subgroups of the DCNQI molecules can provoke a drastic change in the temperature dependence of the conductivity (Fig. 9.15). Unusually sharply reversible phase tran-

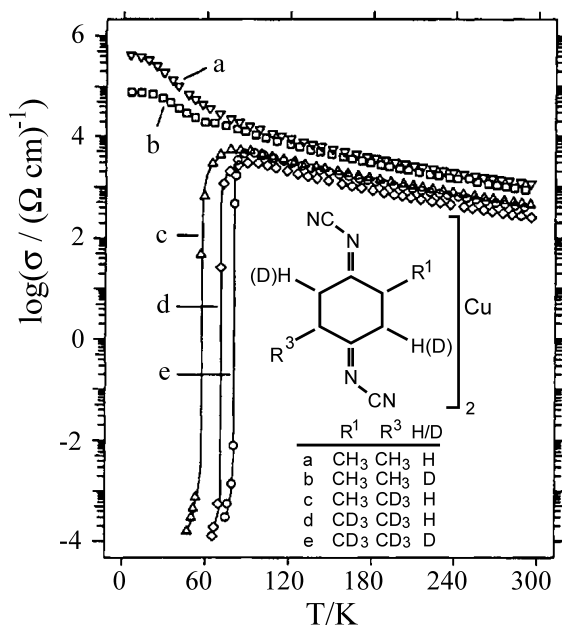


Fig. 9.15 The temperature dependence of the electrical conductivity σ of variously deuterated single crystals of $(2,5\text{-dimethyl-DCNQI})_2 \text{Cu}$. One can see the strong effects of even small variations in the crystal parameters. Only the crystals with deuterated methyl groups undergo a Peierls transition. The crystals a and b, in contrast, remain metallic conductors down to the lowest temperatures. From [16].

sitions from the metallic phase into the insulating phase within 1–2 K produce a decrease in the conductivity by a factor of 10^7 to 10^8 . Deuteration of one CH_3 group to CD_3 raises the transition temperature to 58 K, with two deuterated CH_3 groups it is at 78 K, and with still further deuteration of the molecule it rises to 82 K. In Table 9.2, the structural data of the non-deuterated crystal of the Cu-dimethyl salt (d_0 , curve a in Fig. 9.15) is compared with that of the salt where the six hydrogen atoms of the two CH_3 groups have been replaced by deuterium (d_6 , curve c in Fig. 9.15). The differences between their two structures are minimal. Deuteration of the CH_3 groups leads to a (minor) contraction of the unit cell, because the C-D bonds are somewhat shorter than C-H bonds due to their smaller zero-point energy. This shrinking of the groups leads to a contraction of the intermolecular spacings and thus to an “internal pressure”. It can be compared with the influence of an external pressure [14], [16].

The relatively small changes in the geometrical and electronic configuration of the copper compound shown in the uppermost curves in Fig. 1.12 and in the two upper curves a and b in Fig. 9.15 are apparently sufficient to partially lift its one-dimensionality by increasing the interstack interactions via the bonds between the central Cu ion and the CN groups of the DCNQI. Here, the Cu^{2+} d states (d^9) medi-

Table 9.2 An example of the change in structural data through deuteration. Non-deuterated (2,5-dimethyl-DCNQI)₂Cu (*d*₀, curve **1a** in Fig. 9.15) is compared to the 6-fold-deuterated salt (in its two methyl groups; *d*₆, curve **1c** in Fig. 9.15). From [16]. Here, *a* and *c* are the lattice constants and *V*_{cell} is the volume of the unit cell. It contains

four DCNQI molecules and 2 Cu ions. α is the coordination angle which is formed by a N-Cu-N bridge. The distance between two DCNQI molecules in a stack is *d* _{π - π} . The spacing between the Cu and N atoms in a Cu-N coordination is *d*_{Cu-N}. Between the Cu stacks, the minimum distance of two Cu atoms is *d*_{Cu-Cu}.

Crystal temperature	<i>d</i> ₀ 295 K	<i>d</i> ₀ 20 K	<i>d</i> ₆ 295 K	<i>d</i> ₆ 20 K
<i>a</i>	21.606 Å	21.654 Å	21.619 Å	21.693 Å
<i>c</i>	3.8811 Å	3.792 Å	3.8744 Å	3.776 Å
<i>V</i> _{cell}	1811.7 Å ³	1778.0 Å ³	1810.8 Å ³	1776.7 Å ³
α (N-Cu-N)	124.8°	126.3°	124.8°	128.5°
<i>d</i> _{π-π}	3.213 Å	3.145 Å	3.208 Å	3.122 Å
<i>d</i> _{Cu-N}	1.984 Å	1.972 Å	1.986 Å	1.966 Å
<i>d</i> _{Cu-Cu}	12.76 Å	12.70 Å	12.76 Å	12.70 Å

ate the intermolecular interactions between the π orbitals of the organic molecules in neighbouring stacks. These in turn reduce the one-dimensionality and suppress the Peierls transition, so that the high metallic conductivity remains intact down to low temperatures.

A small modification of the structure of the molecular units thus suffices to cause drastic changes in the conductivity behaviour [17].

The charge-carrier mobility is based on the overlap of the π orbitals of the DCNQI molecules in the stacks. The high conductivity is due as in every conductor to the partial filling of the conduction band. Conduction along the Cu chains is not possible, because the Cu⁺ ions have closed electronic shells and because their spacing is too large. In the Cu salts of DCNQI, the Cu-Cu distance is about 50% greater than in Cu metal.

Detection of the conduction electrons by ESR is not feasible in the conductive Cu salts. Owing to the spin-orbit coupling and their pseudo-three-dimensional character (see below), the relaxation times are too short and therefore the linewidths too large [17]. There is thus an anticoincidence here between high conductivity and ESR [18]. In the one-dimensional conducting state of the Li salts of DCNQI, with a smaller spin-orbit interaction, the electron-spin resonance can, in contrast, indeed be observed.

The paramagnetism of the conduction electrons, not observable by ESR, can however be detected by a measurement of the magnetic susceptibility. In the region of metallic conductivity, one observes in the contribution of the conduction electrons a nearly temperature-independent Pauli susceptibility, well known from metals. In those crystals which undergo a Peierls transition and become semiconductors or insulators at low temperatures, the Pauli susceptibility is transformed into a Curie-law behaviour. The susceptibility then increases with further decreasing tem-

perature as expected of localised, decoupled spins. In this temperature range, the ESR of the localised spins of the Cu^{2+} ions is observed. From the ESR linewidth, one can also conclude that the Cu is in a mixed-valent state, which fluctuates in the metallic phase, with an average charge of $+4/3$, $g = 2$, $\text{Cu}^+ : \text{Cu}^{2+}$ ratio = 2 : 1 [15], [16]. An ESR signal from spins localised on the organic molecular stacks could not be detected. Presumably, a charge-density wave is formed along these stacks [16], accompanied by spin pairing within the DCNQI stacks [18]. At still lower temperature (6–8 K), an antiferromagnetic ordering of the Cu^{2+} spins with a corresponding decrease in the susceptibility begins to occur.

The dimensionality of the conduction behaviour of “molecular conductors” can be explored nicely in detail in the Cu salts of DCNQI. In those crystals which undergo a Peierls transition, the equidistant arrangement of the DCNQI molecules in the stacks is disturbed by a dimerisation (or else a trimerisation), so that each pair of molecules is separated from the neighbouring pairs by a somewhat larger spacing. This structural modification converts the metallic-conducting crystal into an insulator (or a semiconductor with a large band gap); its electrical resistance changes by many orders of magnitude at the critical temperature within a small temperature range, and this change is reversible; hysteresis can however occur. An example for this is shown in Chap. 12. We shall return to this point in the treatment of light-induced phase transitions in Chap. 12.

If a Peierls transition occurs in a Cu salt of DCNQI, this means that the central Cu atoms can no longer produce a sufficiently strong interstack interaction via the CN groups and thereby guarantee a higher dimensionality. This case can occur on lowering the temperature and bringing about the minor distortion of the crystal structure accompanying the Peierls transition. For a sufficient interstack interaction, a very subtle geometrical and energetic overlap of the orbitals of the Cu ions with those of the CN groups is necessary. This can be reduced on lowering the temperature. The overlap can, by the way, recur at still lower temperatures under certain conditions [19]. This is termed reentry behaviour, because the overlap can change again on decreasing the temperature still further, due to the contraction of the crystal. An example of this is shown in Fig. 12.5.

The Peierls transition can be reversed in some DCNQI crystals through optical excitation. The conductivity of the crystal is in this case increased by up to eight orders of magnitude by a short light pulse. To detect this effect, the (transient) electric conductivity must be measured in the excited state. More on this subject will likewise be presented in Chap. 12.

Various different applications of the conductivity properties of the DCNQI salts have been suggested [13]. The very rapid change in microwave reflectivity with light-induced phase transformations in partially-deuterated $[2,5\text{-DMe-DCNQI}]_2$ Cu alloys can be used for fast microwave switching [20]. Thin films of special DCNQI salts can be used as sensors for paramagnetic gases such as O_2 and NO [21]. Applications in electrophotography have also been discussed.

To conclude this section, we would like to mention that much of what has been learned about the organic metals can be applied to the field of organic supercon-

ductivity. The first organic superconductor to be discovered was the radical-ion salt $(\text{TMTSF})_2\text{PF}_6$. More on this topic will be given in Chap. 10.

9.6

Radical-Cation Salts of the Arenes

In Sect. 9.5, we treated the radical-anion salts of DCNQI. There, we especially emphasized the often strong effects of minor variations in the organic anions and/or the inorganic cations on the physical properties of the CT salts. In this Sect. 9.6, we treat the radical-cation salts of the arenes. First, we want to present some different experimental methods for studying the physical properties of CT salts using as an example the $(\text{Fa})_2\text{PF}_6$ crystal.

The radical-cation salts of type $(\text{Fa})_2^+\text{PF}_6^-$ are notable for their simple molecular and crystal structures. The organic molecules are the arenes, that is pure, planar aromatic hydrocarbons, and their stacking axis is perpendicular to the molecular planes (compare Fig. 2.18). Along with the fluoranthene salts, the corresponding perylene, pyrene and naphthalene salts have been investigated. Furthermore, the inorganic counterions PF_6^- have been substituted by e.g. AsF_6^- , SbF_6^- or also mixtures of these. The common features of these highly-conducting salts are a strong one-dimensionality and the Peierls transition to a ground state with a charge-density wave (CDW) (cf. Sect. 9.3). At temperatures above the Peierls phase-transition temperature T_p , these salts are in a quasi-metallic state, which differs from a true metal in that among other things both its specific electrical conductivity as well as its magnetic susceptibility increase with increasing temperature. Both are lower than in a pure metallic state in which the charge-carrier concentration and the Pauli susceptibility of the conduction electrons are constant. The reason for this are the fluctuations at $T > T_p$, which in these highly-one-dimensional systems extend over a large temperature range.

The Peierls instability and the high degree of one-dimensionality are observable in a whole series of different experiments. These include the dc conductivity in low applied fields (see Sect. 9.6.1 and Fig. 1.13), the diffuse reflections of the $2k_F$ superlattice in X-ray scattering (Sect. 9.6.2), the reflection spectra from the FIR up to the UV spectral ranges (Sect. 9.6.3), the magnetic susceptibility (Sect. 9.6.4), the conduction electron spin resonance, and nuclear resonances (Sect. 9.6.5), as well as the nonlinear electrical conductivity at high applied electric fields or at high frequencies (Sect. 9.6.6). Most of these methods are also employed for the study of the other radical-ion salts, e.g. TTF-TCNQ or the DCNQI salts. They will therefore be treated as examples in this Sect. 9.6.

9.6.1

Direct-current Conductivity

Figure 1.13 shows the temperature dependence of the specific conductivity σ parallel to the highly conducting crystal axis of a $(\text{Fa})_2\text{PF}_6$ crystal as an Arrhenius plot

over the temperature range between room temperature and 15 K. In this temperature range, the value of σ varies over more than 15 orders of magnitude. At $T < 20$ K, the crystal resistance for typical sample dimensions is nearly $10^{16}\Omega$. Its temperature dependence $\sigma(T)$ can be subdivided into four regions (A)–(D) (see Fig. 1.13):

The high temperature region (A) is notable for a relatively high conductivity of several $100 (\Omega \text{ cm})^{-1}$ at room temperature. The anisotropy, that is the ratio of the conductivities parallel and perpendicular to the stacking axis, is $\sigma_{\parallel}/\sigma_{\perp} \approx 10^4$. Together with other experimental results (see below), one therefore refers to a quasi-one-dimensional metal in this temperature range. From the decrease in the conductivity with decreasing temperature in region (A) and from other experimental results, it follows that in region (A), there is no genuine metallic conductivity. The crystals are thus often referred to as quasi-metallic in the high temperature range.

At $T = T_p = 182$ K, the Peierls transition takes place. The phase transition temperature T_p can be determined very precisely from the sudden jump in the slope of $\sigma(T)$ at $T = T_p$ [22]. From the results of variation of the counterion $X^- = \text{PF}_6^-$, AsF_6^- or SbF_6^- , it follows that T_p depends on the size of the counterion and thus on the weak interstack interactions, i.e. on the three-dimensional coupling of the conducting stacks to each other.

Below T_p , σ decreases sharply with decreasing temperature, owing to the opening of the energy gap in region (B), and then in region (C) changes to a thermally activated behaviour with a constant slope in the Arrhenius plot. From it, the value of the ground-state energy gap $2\Delta(T \rightarrow 0)$ can be found. In $(\text{Fa})_2\text{PF}_6$ crystals of the highest crystal quality, it is equal to about 90 meV.

In region (D), the value of σ is already so low that it is presumably determined by small concentrations of impurities or defects from which charge carriers can be thermally activated. This region (D) will therefore not be dealt with further in the rest of this section.

Brütting *et al.* have treated the conductivity of quasi-one-dimensional CDW systems in the framework of the Boltzmann equation (see e.g. [M2] or [M3]) with scattering from longitudinal acoustic phonon [23, 24]. For the temperature dependence of the conductivity $\sigma(T)$, they derived an integral equation which, aside from the temperature-dependent energy gap $2\Delta(T)$, contains only a single materials parameter C :

$$\sigma(T) = \frac{C}{2k_B T} \int_0^{\infty} \frac{x^2 + 2x\gamma}{(x + \gamma)^2} \frac{e^{x+\gamma}}{(e^{x+\gamma} + 1)^2} dx. \quad (9.14)$$

Here, $x = \varepsilon/k_B T$, $\gamma = \Delta(T)/k_B T$, ε is the energy of the charge carriers, and the materials parameter is

$$C = \frac{2e^2 N_c M c_s^2}{\pi \hbar a} \left(\frac{\hbar v_F}{E_{ac}} \right)^2. \quad (9.15)$$

In this expression, N_c is the number of conducting chains per unit area, M is the molecular mass, c_s the velocity of sound, v_F the Fermi velocity, a the lattice constant

of the linear stacks, and E_{ac} the so-called acoustic deformation potential constant. For E_{ac} , the usual approximation in solid-state physics is employed: $E_{ac} = 2/3 E_F$, with E_F = Fermi energy ([25, p. 200]).

The integral in the integral equation (9.14) can be computed only by numerical methods, but analytical solutions are possible in three limiting cases: for the case that $\Delta \gg k_B T$,

$$\sigma(T) = \frac{C}{\Delta(T)} \ln(1 + e^{-\Delta(T)/k_B T}). \quad (9.16)$$

For $T \ll T_p$, the energy gap has reached its ground-state value of $2\Delta(0)$. Then Eq. (9.16) becomes

$$\sigma(T) = \frac{C}{\Delta(0)} e^{-\Delta(0)/k_B T}. \quad (9.17)$$

When the energy gap vanishes, the integral in Eq. (9.14) has the value 1/2 and we then obtain

$$\sigma(T) = \frac{C}{4k_B T} = N_c e^2 D(E_F) \tau_F v_F^2. \quad (9.18)$$

$D(E_F)$ is the density of states at the Fermi energy. Eq. (9.18) describes the known temperature dependence of the electrical conductivity of a metal at high temperatures: $\sigma \propto T^{-1}$.

Figure 9.16a shows the temperature dependence of the energy gap, $\Delta(T)$ (solid curve), as obtained from a measurement of the magnetic susceptibility of the conduction electrons (see Sect. 9.6.4 and [24]). With this information, the experimental temperature dependence $\sigma(T)$ was fitted to Eq. (9.14) (Fig. 9.17). The fit shows that the essential characteristics of $\sigma(T)$ from room temperature down to about 50 K, with a variation of more than eight orders of magnitude, are correctly described by this equation. It is thus justified to use Eq. (9.14) alone for the determination of the energy gap $\Delta(T)$ and the constant C . Figure 9.16a shows the energy gap $\Delta(T)$ (dashed curve), as determined directly from the conductivity $\sigma(T)$ (Fig. 1.13) using Eq. (9.14). From this fit, the constant C is also obtained (Table 9.3).

Table 9.3 Materials parameters obtained from the electrical conductivity of the $(\text{Fa})_2\text{PF}_6$ crystal (24). C = constant of the transport equation (Eqns. (9.13) and (9.14)); $2\Delta(0)$ is the energy gap for $T \rightarrow 0$; m^* the effective mass of the charge carriers, v_F the Fermi velocity (see Table 9.4), M is the molecular mass, and c_s the velocity of sound in the crystal.

$\frac{C}{\text{eV}/\Omega \text{ cm}}$	$\frac{\Delta(0)}{\text{meV}}$	$\frac{m^* = \frac{\Delta(0)}{v_F^2}}{m_0}$	$\frac{M c_s^2}{\text{eV}}$	$\frac{c_s}{\text{m/s}}$	$\frac{M}{u}$
236	90	0.23	0.42	449	202

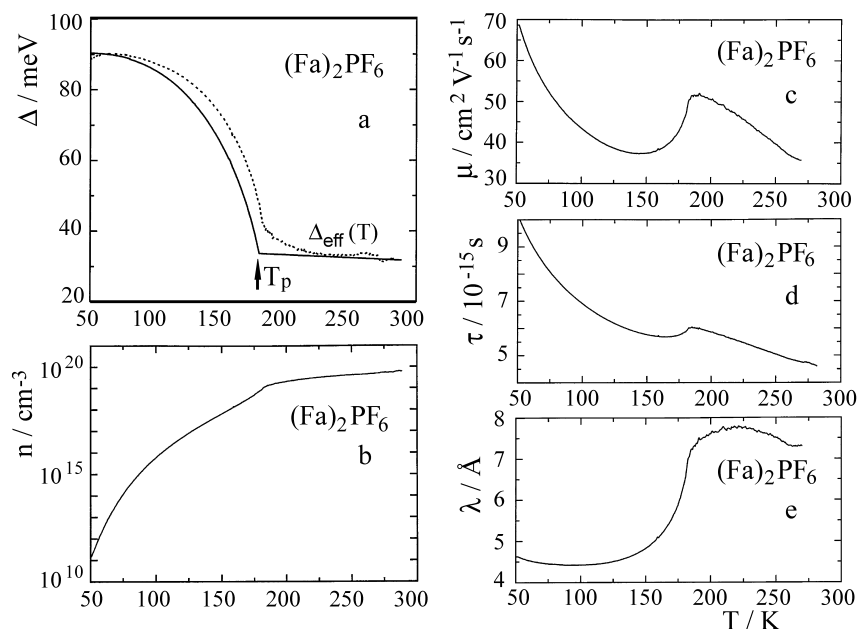


Fig. 9.16 Analysis of the conductivity measurements: temperature dependence of electronic properties derived for the $(\text{Fa})_2\text{PF}_6$ crystal: **a** of the energy gap 2Δ at $q = 2k_F$, **b** of the concentration n , **c** of the mobility μ , **d** of the mean scattering time τ , and **e** of the mean free path λ of the charge carriers in the

$(\text{Fa})_2\text{PF}_6$ crystal. Δ_{eff} is the effective or pseudo-energy gap for $T > T_p$. $\Delta(T)$ was determined both from the magnetic susceptibility of the charge carriers (solid curve) and from the conductivity $\sigma(T)$ (dashed curve). T_p is the transition temperature of the Peierls phase transition. From [24].

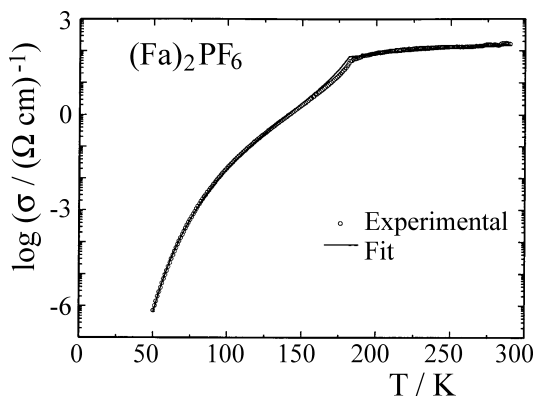


Fig. 9.17 Fit of the experimental data for the dc conductivity $\sigma(T)$ of the $(\text{Fa})_2\text{-PF}_6$ crystal to the conductivity formula (Eq. (9.14)). After [23].

An important result of this analysis of the temperature dependence of the conductivity, $\sigma(T)$, is the existence of an effective energy gap for $T > T_p$, which can also be seen in the measurements of the magnetic susceptibility of the conduction electrons (cf. Sect. 9.6.4). It is characteristic of these highly-one-dimensional conductors and has its origin, as mentioned, in fluctuations above the phase-transition temperature T_p for the Peierls transition [26].

From the temperature dependence of the conductivity, numerous other transport properties can be derived [23], [24]. Figure 9.16b shows the charge-carrier concentration $n(T)$. It makes the dominant contribution to the temperature dependence $\sigma(T)$ of the conductivity. At room temperature, $n = 6 \cdot 10^{19} \text{ cm}^{-3}$ and thus about a factor of 30 smaller than one charge carrier per unit cell. The reason for this is the existence of the effective energy gap. From the charge-carrier concentration, with $\sigma = en\mu$ we also obtain the temperature dependence of the mobility, $\mu(T)$ (see Fig. 9.16c). At room temperature, it is clearly larger than in pure molecular crystals (cf. Chap. 8). Its temperature dependence in the neighbourhood of the Peierls transition is evidently determined by the lattice distortion which occurs there. Only at temperatures far below T_p does the mobility increase continuously with decreasing temperature, as in all conducting crystals with small defect concentrations.

Finally, the mean scattering time τ (Fig. 9.16d) and the mean free path (Fig. 9.16e) of the charge carriers were also extracted from the data. From these two results, one can see that the charge-carrier transport is on the boundary between band and hopping transport over the whole range of temperatures studied.

9.6.2

X-Ray Scattering

In addition to the sharp Bragg reflections from which the crystal structure was determined (see Chap. 2, Fig. 2.18), the X-ray diffraction diagram of a $(\text{Fa})_2\text{PF}_6$ crystal also exhibits **diffuse superlattice reflections** [27], even at room temperature. On cooling, they become sharper, and at 20 K, the by now **sharp superlattice reflections** are seen at the positions of the reciprocal-lattice vectors $\mathbf{q} = (1/2, 0, 0)$. It follows from this that the wavevector of the charge-density wave is $\mathbf{q}_{CDW} = 2\mathbf{k}_F = 0.5\mathbf{a}^*$. With $a^* = 2\pi/a$, then $k_F = \pi/2a$. The model of a half-filled conduction band in the quasi-metallic state is thus directly confirmed by X-ray diffraction. The wavelength of the charge-density wave is then found to be $\lambda_{CDW} = 2\pi/q_{CDW} = 2a$, that is, it is commensurate with the lattice. The temperature dependence of the intensity of the $2k_F$ superlattice reflections exhibits – independently of the determinations of the band gap $2\Delta(T)$ from the conductivity and from the magnetic susceptibility – a BCS-like curve with a Peierls phase-transition temperature $T_p \approx 180 \text{ K}$.

The results of X-ray scattering thus on the one hand show that around 180 K, the Peierls transition to the CDW ground state occurs, and on the other, that above the Peierls transition over a large temperature range, fluctuations between the metallic and the semiconducting states are present.

9.6.3

Optical Reflection Spectrum

(Fa)₂PF₆ crystals and similar radical-cation salts, e.g. those of perylene, are not transparent even when the samples are very thin. However, they have crystal surfaces with a high reflectivity (see Fig. 1.8). It is due to the contribution of the free charge carriers. From the **reflection spectrum**, information about the electronic properties can be obtained. In this subsection, we will therefore consider the reflection spectrum of (Fa)₂PF₆ crystals over a large spectral region from the FIR to the UV.

Figure 9.18 gives the reflection spectra $R(\omega) = I_r(\omega)/I_i(\omega)$ of polarised electromagnetic radiation in the wavelength range from 80 cm⁻¹ to 50 000 cm⁻¹ ($\hat{=}$ 10 meV to 6 eV) for the two polarisation directions of the electric-field vector, parallel and perpendicular to the stacking axis at room temperature [28]. Here, I_r is the reflected and I_i the incident intensity. The reflectivity R_{\parallel} between 10 meV and 800 meV is more than 80% and decreases by more than three decades up to around 1.2 eV. This decrease is termed the plasma edge. In the high-energy spectral range ($E > 2$ eV), one can discern the structures of individual interband transitions, which we shall however not discuss further here. The reflectivity R_{\perp} is smaller than 10% over the whole spectral range with the exception of a few resonances in the IR region.

For the analysis of the reflection spectra, we consider as usual the frequency-dependent complex dielectric tensor $\tilde{\epsilon}(\omega)$. We restrict ourselves here to the case that the direction of polarisation is parallel to the stacking axis, and denote the real and imaginary parts of the complex dielectric function as usual: $\epsilon(\omega) = \epsilon_1(\omega) + i\epsilon_2(\omega)$. It is related to the complex index of refraction, $\hat{n} = n_1 + in_2$, via $\hat{n} = \sqrt{\epsilon}$. The real part of

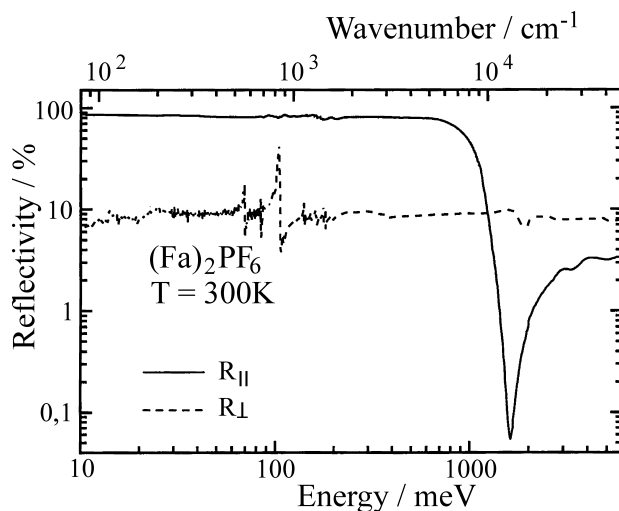


Fig. 9.18 Reflection spectra polarised parallel and perpendicular to the stacking axis, R_{\parallel} and R_{\perp} , of a (Fa)₂PF₆ crystal at $T = 300$ K. From [28].

the frequency-dependent or optical conductivity $\sigma^{opt}(\omega)$ is related to the imaginary part $\varepsilon_2(\omega)$ of the dielectric function:

$$\sigma^{opt}(\omega) = \varepsilon_0 \omega \varepsilon_2(\omega). \quad (9.19)$$

To determine $\sigma^{opt}(\omega)$ from a measurement of $R(\omega)$, for metals one generally uses the Drude-Lorentz model (see e.g. [M2], Chap. 1). In this model, the conduction electrons and the positively-charged ions are treated as a plasma and all contributions to ε which do not originate with the free charge carriers are combined in the constant ε_∞ . One then obtains for the dielectric function of a metal:

$$\varepsilon(\omega) = \varepsilon_\infty - \frac{\omega_p^2}{\omega^2 + i\omega/\tau} \quad (9.20)$$

with the plasma frequency

$$\omega_p^2 = \frac{Ne^2}{\varepsilon_0 m_{opt}^*}. \quad (9.21)$$

τ is the relaxation time. ω_p is called the unshielded plasma frequency and m_{opt}^* is the optical effective mass. N is the density of the charge carriers. Neglecting the damping term ω/τ , Eq. (9.19) yields a zero for $\varepsilon(\omega)$ when

$$\omega = \omega_{p,s} = \omega_p / \sqrt{\varepsilon_\infty} \quad (9.22)$$

is fulfilled. $\omega_{p,s}$ is referred to as the shielded plasma frequency. For $\omega < \omega_{p,s}$, $\varepsilon_1 < 0$ and thus the reflectivity is $R = 1$, since the electromagnetic radiation cannot propagate within the metal. For $\omega > \omega_{p,s}$, $\varepsilon_1 > 0$. The electromagnetic radiation can then propagate in the metal. The reflectivity therefore drops off at the plasma edge ($\omega = \omega_{p,s}$). The fit of the experimental data (Fig. 9.18) to the Drude model yields the values listed in Table 9.4 for $\hbar\omega_{p,s}$, $\hbar\tau$, and ε_∞ . With the charge-carrier density $N = 1.68 \cdot 10^{21} \text{ cm}^{-3}$, the value for m_{opt}^* is found. The optical conductivity at the frequency 0, $\sigma_0 = \sigma(\omega \rightarrow 0)$, follows from Eqns. (9.19) and (9.20) with

$$\sigma_0 = \varepsilon_0 \omega_p^2 \tau \quad (9.23)$$

Table 9.4 Materials parameters obtained from the optical reflection spectra of the $(\text{Fa})_2\text{PF}_6$ crystal (28). ω_p is the unshielded plasma frequency, τ the mean scattering time, ε_∞ the background dielectric constant, σ_0 the optical conductivity for $\omega \rightarrow 0$, m_{opt}^* the effective mass of the charge carriers, v_F the Fermi velocity, and E_F the Fermi energy.

$\hbar\omega_p$ eV	$\frac{\tau}{10^{-15} \text{ s}}$	ε_∞	$\frac{\sigma_0}{(\Omega \text{ cm})^{-1}}$	$\frac{m_{opt}^*}{m_0}$	$\frac{v_F}{10^7 \text{ cm/s}}$	$\frac{E_F}{\text{eV}}$
1.63	4.9	2.1	2660	0.85	3.1	0.63

and is found to be $\sigma_0 = 2660 \text{ } (\Omega \text{ cm})^{-1}$ (see Table 9.4). On cooling the $(\text{Fa})_2\text{PF}_6$ crystal to 10 K, one can observe the Peierls transition in the reflection spectrum at 180 K and also an energy gap of ca. 150 meV [28].

9.6.4

Magnetic Susceptibility

The measurement and analysis of the magnetic susceptibility can give further independent information on the electronic structure of the $(\text{Fa})_2\text{PF}_6$ crystals. In particular, from the temperature dependence of the susceptibility, the effective energy gap $2\Delta_{\text{eff}}$ above the Peierls-transition temperature T_p can be directly derived.

For this, we consider the static magnetisation $M = \chi B/\mu_0$ of a para- or diamagnetic solid in an applied magnetic field \mathbf{B} . We limit our considerations here to the case where the direction of the applied field is parallel to the stacking axis. The susceptibility in a conducting solid is in general the sum of three electronic contributions: $\chi(T) = \chi^{\text{dia}} + \chi^{\text{Curie}}(T) + \chi^{\text{c.e.}}(T)$. In organic solids with π -electron systems, the diamagnetic contribution χ^{dia} has the largest magnitude. Since it is negative and temperature independent, it can be uniquely separated from the two paramagnetic contributions in the analysis of the experimental temperature dependence $\chi(T)$.

The Curie contribution χ^{Curie} is due to unpaired spins, e.g. the spins in paramagnetic centres or impurities, and it is characterised by the Curie law: $M_{\text{Curie}} = \chi^{\text{Curie}}(T)B = C \cdot B/T$. Here, M_{Curie} is the Curie contribution to the magnetisation and $C = N_{\text{Curie}}\mu^2/k_B$ is the Curie constant. N_{Curie} is the density of the paramagnetic centres and μ their magnetic moment. From a measurement of the temperature dependence of $\chi^{\text{Curie}} \propto 1/T$, the density N_{Curie} of the paramagnetic centres or the impurities can be found. It is, even in the highest-purity radical-cation salts, still of the order of magnitude of 10^{-4} mol/mol.

The contribution of the conduction electrons to the electronic magnetisation is that of Pauli paramagnetism in a classical 3-d metal:

$$M_{\text{Pauli}} = \chi^{\text{c.e.}}B = \mu_0 \frac{N_e \mu^2}{k_B T_F} B \quad (9.24)$$

where the Fermi energy is $k_B T_F \gg k_B T$ (see e.g. [M3], Chap. 14). N_e is the density of the conduction electrons in the metal. In contrast to the Curie susceptibility, the contribution $\chi^{\text{c.e.}}$ of the conduction electrons to the susceptibility of a Pauli paramagnet is, owing to the Pauli principle, independent of the temperature and is reduced by the factor T/T_F per spin.

In the $(\text{Fa})_2\text{PF}_6$ crystal [29] and in the related naphthalene, pyrene, and perylene salts [30]–[32], the contribution $\chi^{\text{c.e.}}$ was determined experimentally by separating the contributions χ^{dia} and $\chi^{\text{Curie}}(T)$ from the total susceptibility χ using their signs and their temperature dependencies. We will consider here the experimental results for the $(\text{Fa})_2\text{PF}_6$ crystal and their analysis [29]. Figure 9.19 shows the temperature dependence $\chi^{\text{c.e.}}(T)$. The absolute values are within the error limits identical to the susceptibilities obtained using conduction-electron spin resonance (see Sect. 9.6.5). $\chi^{\text{c.e.}}(T)$ exhibits two characteristic temperature regions: one with

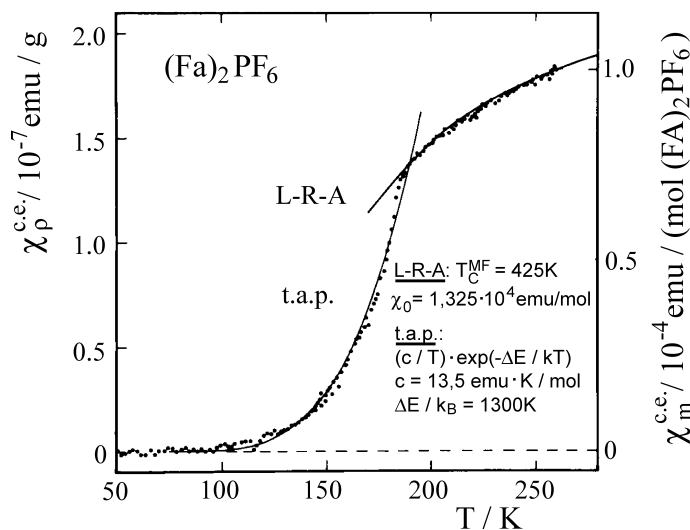


Fig. 9.19 The temperature dependence of the contribution $\chi^{\text{c.e.}}$ of the conduction electrons to the magnetic susceptibility of the $(\text{Fa})_2\text{PF}_6$ crystal with the direction of the static magnetic field \mathbf{B} parallel to the stacking axis \mathbf{a} . (The susceptibility is given here in cgs-Gaussian units: on the left-hand ordinate as χ_ρ in emu/g (i.e. cm^3/g), on the right-hand ordinate as χ_m in emu/(mole $(\text{Fa})_2\text{PF}_6$), with

$M_m = 549.5 \text{ g/mol } (\text{Fa})_2\text{PF}_6$.) Solid curves: calculated temperature dependence for thermally-activated paramagnetism (t.a.p.) and for the paramagnetism of the conduction electrons with an effective energy gap of $2\Delta_{\text{eff}}(T)$ in the quasi-metallic state for $T > T_p$, according to the Lee-Rice-Anderson model (L-R-A). From [29].

a strong rise with increasing temperature for $T < 185 \text{ K}$, and one with a weak rise with increasing temperature for $T > 185 \text{ K}$. Evidently the Peierls transition is also clearly recognisable in the susceptibility of the conduction electrons. Furthermore, $\chi^{\text{c.e.}}$ is not temperature independent in the temperature range $T > T_p$, as in a classical Pauli paramagnet.

The low-temperature region can be described in terms of a thermally-activated Curie paramagnetism (t.a.p.). The formula and data are shown in Fig. 9.19. The high-temperature region can be described formally by the above-mentioned Lee, Rice and Anderson (L-R-A) model, which takes into account the fluctuations of the 1-d metal for $T > T_p$ [26]. One of the two constants fitted in this region is the Pauli susceptibility χ_0 for $T \gg T_p$. Comparison with the experimental data in Fig. 9.19 shows that for $T_p < T < 300 \text{ K}$, the value of $\chi^{\text{c.e.}}(T)$ is always smaller than χ_0 (for example, $\chi^{\text{c.e.}}(250 \text{ K})/\chi_0 = 1/1.3$).

Making use of a thermodynamic model of charge-density waves in one-dimensional conductors [33], the temperature dependence $\chi^{\text{c.e.}}(T)$ in the entire temperature range measured was analysed [29]. This model contains – aside from the Pauli susceptibility χ_0 – only the temperature-dependent energy gap $2\Delta_{\text{eff}}(T)$:

$$\frac{\chi^{\text{c.e.}}}{\chi_0} = 2 \int_A^\infty \frac{x}{(x^2 - A^2)^{1/2}} \frac{e^x}{(e^x + 1)^2} dx \quad (9.25)$$

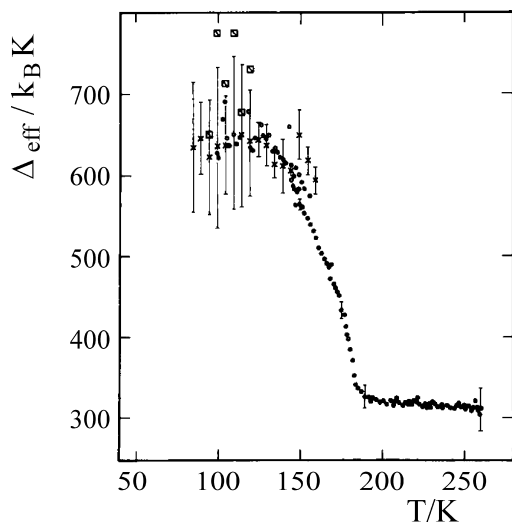


Fig. 9.20 The temperature dependence of half the effective energy gap, $\Delta_{\text{eff}}(T)$, of the $(\text{Fa})_2\text{PF}_6$ crystal, computed from the temperature dependencies of the static magnetic susceptibility $\chi^{\text{c.e.}}(T)$ and the ESR intensity χ^{ESR} of the conduction electrons. From [29].

with $x = \varepsilon/k_B T$ and $A = \Delta_{\text{eff}}/k_B T$. ε is the energy of the charge carriers. The energy zero-point is chosen to be in the centre of the band gap. For the density of states $D(\varepsilon, \Delta_{\text{eff}})$, the following simple function is assumed:

$$D(\varepsilon, \Delta_{\text{eff}}) = D_0 \frac{|\varepsilon|}{\sqrt{\varepsilon^2 - \Delta_{\text{eff}}^2}} \quad \text{for } |\varepsilon| \geq \Delta_{\text{eff}} \quad (9.26)$$

$$D(\varepsilon, \Delta_{\text{eff}}) = 0 \quad \text{for } |\varepsilon| < \Delta_{\text{eff}}. \quad (9.27)$$

Using the value of χ_0 , the temperature dependence of the energy gap, $\Delta_{\text{eff}}(T)$, was determined from the experimental values using this expression (Fig. 9.20). It shows qualitatively the same temperature dependence as was found from the temperature dependence of the specific electrical conductivity (cf. Fig. 9.16a). In particular, it exhibits the effective band gap above the Peierls transition, which is caused by the fluctuations of the one-dimensional CDW conductor and has the result that even above the Peierls transition, no genuine metallic conductivity is present.

9.6.5

Spin Resonance of the Conduction Electrons (ESR)

Making use of electron-spin resonance in the radical-ion salts, in particular the diffusion constant D and the hyperfine interaction constant A of the electron spins can be measured. One thus obtains independent information on the dynamics and the spatial distribution of the conduction electrons within the stacks.

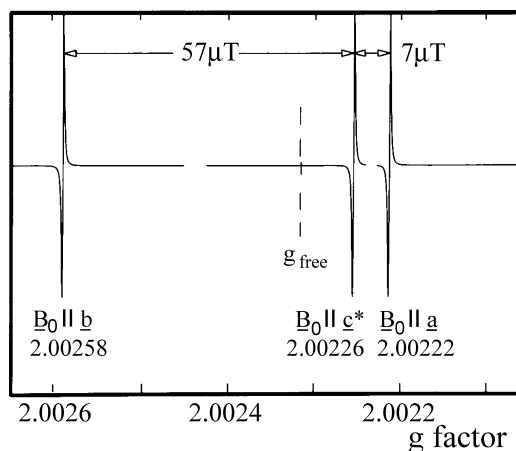


Fig. 9.21 The ESR spectrum of the $(\text{Fa})_2\text{PF}_6$ crystal for three different orientations of the crystal relative to the applied magnetic field. The g -factor is shown along the abscissa. After [34].

Figure 9.21 gives the ESR spectrum of the $(\text{Fa})_2\text{PF}_6$ crystal at room temperature for three different directions of the applied magnetic field B_0 relative to the crystal axes a , b and c^* [34]. For each orientation, the entire ESR spectrum consists of a single extremely narrow resonance line (Fig. 9.22a). Its linewidth (the width between the maxima of the differential ESR line) in the crystals of highest quality is $\Delta B_{pp} = 10 \text{ mG}$ [35].

In contrast to the ESR spectra of radical ions in solution, all traces of hyperfine structure are thus missing in the ESR spectrum of these crystals. The reason for

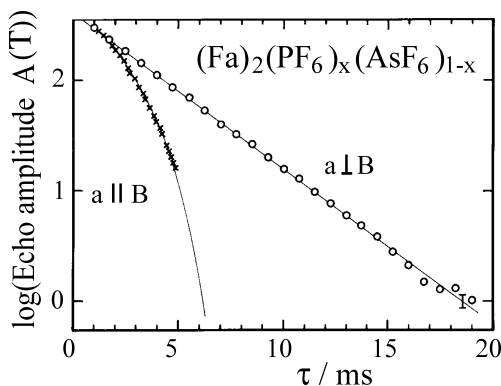


Fig. 9.22 The conduction-electron spin-echo amplitude $A(\tau)$ from a $(\text{Fa})_2\text{PF}_6$ crystal in a constant magnetic field B_0 with a constant magnetic-field gradient $G_{\parallel} B_0$ at room temperature. For the orientation $B_0 \perp a$, one observes a mono-exponential decay; for $B_0 \parallel a$, the spin diffusion along the stacking axis a causes an additional decay as in Eq. (9.26). From [34].

this is an extreme motional narrowing (see also Chap. 7): the conduction electrons move at the Fermi velocity in the stacks of radical ions and this averages out the hyperfine coupling of the electron spins to the nuclear spins.

The ESR line of the $(\text{Fa})_2\text{PF}_6$ crystal is homogeneous. It corresponds to a free-induction signal of the transverse magnetisation $M_x(t) = M_0 \exp(-t/T_2)$ with the transverse relaxation time $T_2 = 9$ s. Both with respect to the extremely narrow resonance line and to the corresponding extremely long transverse relaxation times, the radical-ion salts differ from normal metals (e.g. Li or Na), in which the ESR lines are much broader. The reason is the almost negligible spin-orbit coupling in the aromatic compounds.

The long transverse relaxation times could be exploited to determine experimentally the **diffusion constant** D of the charge carriers [36], [34]. For this measurement, Hahn sequences and other electron-spin-echo experiments were carried out in applied magnetic fields \mathbf{B}_0 , with a constant magnetic field gradient \mathbf{G} superposed parallel to \mathbf{B}_0 . When the spins diffuse within the time interval 2τ , i.e. the time between the first 90° pulse and the echo after the 180° pulse at time τ , they arrive at locations where the coherence of the spin precession is destroyed owing to the field gradient. This leads to an additional decay of the echo amplitude $A(\tau)$:

$$A(\tau) = A_0 e^{-2\tau/T_2} e^{-2/3 \cdot \gamma^2 G^2 D \tau^3}. \quad (9.28)$$

Figure 9.22 shows the echo amplitude $A(\tau)$ for the two orientations of \mathbf{B}_0 and \mathbf{G} parallel and perpendicular to the stacking axis \mathbf{a} . For $\mathbf{B}_0 \perp \mathbf{a}$, one can observe an exponential decay with the transverse relaxation time. For $\mathbf{B}_0 \parallel \mathbf{a}$, the decay is much faster and not mono-exponential. From the fit of $A(\tau)$ to Eq. (9.26), one obtains the values of the diffusion constant of the charge carriers at room temperature parallel and perpendicular to the stacks: $D_{\parallel} = (1.3 \pm 0.3) \text{ cm}^2/\text{s}$ and $D_{\perp} < 10^{-3} \text{ cm}^2/\text{s}$. The spin-echo experiments are thus an additional proof of the high anisotropy of the charge-carrier motion in radical-cation salts.

With the value of the Fermi velocity v_F from Table 9.3, we obtain from D_{\parallel} an independent value of the scattering time: $\tau_{\parallel} = D_{\parallel}/v_F^2 = 1.3 \cdot 10^{-15} \text{ s}$. It is to be sure somewhat different from the values determined from the optical reflection spectra and from the conductivity (Table 9.4), but the differences are negligible considering the different counterions and the very diverse methods and approximations in the data analyses.

The extremely narrow ESR line (Fig. 9.23a) could be made use of to measure the **hyperfine coupling** of the conduction electrons to the nuclear spins [35]: due to the polarisation P_n of the nuclear spins in the applied magnetic field \mathbf{B}_0 , the average hyperfine field of all the nuclear spins is superposed onto the applied field and leads to a smaller shift $\Delta\nu_{\text{ESR}}$ of the ESR resonance frequency ν_{ESR} in comparison to the ESR resonance frequency without hyperfine coupling or without nuclear-spin polarisation:

$$\Delta\nu_{\text{ESR}} = \frac{1}{2} (A_{zz}/h) \cdot P_n. \quad (9.29)$$

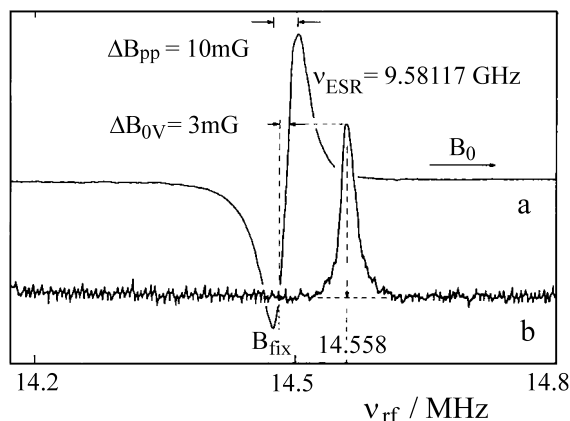


Fig. 9.23 The Overhauser shift ΔB_{OV} of the ESR line from a $(\text{Fa})_2\text{PF}_6$ crystal at room temperature. **a:** the ESR line at a fixed microwave frequency ν_{ESR} . **b:** the change in the ESR signal with an additional fixed applied magnetic field $B_0 = B_{\text{fix}}$ and irradiation with a variable radio-frequency field of frequency $14.2 \text{ MHz} < \nu_{\text{rf}} < 14.8 \text{ MHz}$. From [35].

A_{zz} is the component of the hyperfine tensor in the B_0 direction. $\Delta\nu_{\text{ESR}}$ is called the **Overhauser shift**. It is analogous to the Knight shift $\Delta\nu_{\text{NMR}}$ of the nuclear-spin resonance frequency ν_{NMR} in the presence of conduction electrons with a polarisation P_e :

$$\Delta\nu_{\text{NMR}} = \frac{1}{2}(A_{zz}/h)P_e. \quad (9.30)$$

The Overhauser shift is very small: the contribution to $\Delta\nu_{\text{ESR}}/\nu_{\text{ESR}}$ of the protons is of order 10^{-6} and that of less abundant nuclear spins, e.g. ^{13}C , is of order 10^{-9} [34]. Their measurement is accomplished by a double resonance technique. The shift ΔB_{OV} of the resonance field for ESR is measured at a constant ESR-microwave frequency ν_{ESR} (e.g. 9.4 GHz), while at the same time a strong radio-frequency field with the variable frequency ν_{rf} is applied. When $\nu_{\text{rf}} = \nu_{\text{NMR}}$, the nuclear-spin resonance, e.g. the nuclear-spin resonance of the protons at $\nu_{\text{rf}} = \nu_p$, will be saturated. This produces equal populations of the two nuclear-spin Zeeman levels, causing the nuclear-spin polarisation P_n to vanish. This leads according to Eq. (9.27) to a shift of the ESR resonance field by an amount

$$\Delta B_{OV} = -\frac{h}{g\mu_B}\Delta\nu_{\text{ESR}}. \quad (9.31)$$

Figure 9.23b shows the experimental result for saturation of the proton-spin resonance in a $(\text{Fa})_2\text{PF}_6$ crystal: the spectrum $\Delta B_{OV}(\nu_{\text{rf}})$ is the indirectly measured nuclear-spin resonance line of the protons. From the absolute value of ΔB_{OV} at the maximum, that is at the proton-spin resonance frequency ν_p , applying Eq. (9.29), the average hyperfine coupling A_{zz} of all the protons can be directly determined. Similar experiments were carried out with ^{13}C nuclei [34].

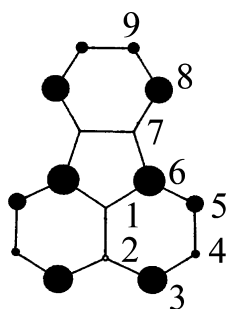


Fig. 9.24 A graphic simulation of the experimentally-determined local p_z spin and charge-carrier densities. The diameter of the circles is proportional to the spin density. From [37].

The hyperfine coupling between a conduction electron and a proton or a ^{13}C nucleus is directly proportional to the probability density of the conduction electron at the site of the ^{13}C nucleus or the nucleus to which the proton is bound. By selective deuteration and thereby marking of particular C atoms in the molecules, and additionally by measuring the Knight shift [37], the spatial distribution of the conduction electrons was determined. Figure 9.24 shows the results schematically. A comparison with Fig. 2.18 reveals that the conduction electrons are concentrated on the $2p_z$ orbitals of the $(\text{Fa})_2^+\bullet$ radical ions which have the strongest overlap in the stack with their two nearest neighbours. This result can also be formulated differently: the radical-cation salts of the pure aromatic hydrocarbons crystallise in such a way that the overlap integrals of the neighbouring HOMOs are maximised.

To end this section, we mention that the narrow ESR line, its anisotropic and field-independent g -factor, and the excellent chemical stability of highly-purified $(\text{Fa})_2\text{PF}_6$ crystals can be used for very precise magnetic field measurements as well as for the stabilisation of ESR spectrometers [38]. For magnetic-field measurements, in a range between the terrestrial magnetic field and several Tesla, a field resolution of at least 10^{-8} Tesla was achieved. For the stabilisation of the field/frequency ratio B_0/ν_{ESR} , a stability of 10^{-9} was obtained [34].

9.6.6

Charge-Density-Wave Transport

Thus far, in Sect. 9.6 we have considered the electronic structure and the single-particle excitations of $(\text{Fa})_2\text{PF}_6$ crystals as examples of radical-cation salts. For single-particle charge transport at $T < T_p$, a thermal activation of the charge carriers across the energy gap is necessary. It corresponds to a frequency of $f_\Delta = 4.4 \cdot 10^{13}$ Hz, thus an excitation in the infrared spectral range.

Aside from the single-particle excitations treated up to now, there are for $T < T_p$ both additional contributions to the direct current as well as excitations at lower frequencies than f_Δ . These are the contributions of the charge-density wave (CDW) to the current. In contrast to the current of the uncorrelated charge carriers, i.e. the single-particle current, the current or the **motion of the charge-density wave** can be detected in the nonlinear current-voltage characteristic on exceeding a threshold electric field F_T through an increase in the noise power in the nonlinear range of the conductivity as well as through a strong frequency dependence of the conduc-

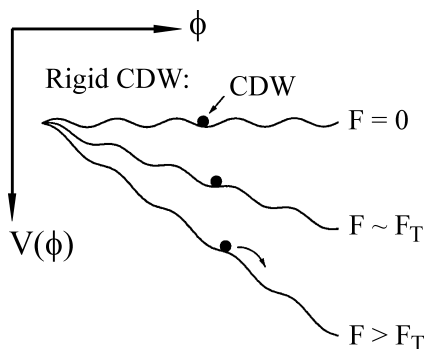


Fig. 9.25 A schematic model of the transport of the rigid charge density wave CDW in an electric field F . (Here, the rigid CDW is symbolised by a point, in analogy to the centre of gravity of a rigid body.) F_T is the threshold field strength, $V(\phi)$ the lattice potential, and $\phi = 2k_F x$ the phase.

tivity and the dielectric constant in the FIR, microwave, and low-frequency ranges, i.e. at $f < f_\Delta$. We will present these experiments in the following. To do so, we use a simple picture of the charge-density wave (Fig. 9.25). It can to first order be treated as a rigid body. If it is commensurate with the lattice, that is if for example $k_F = \pi/2a$, then it is anchored to the lattice potential $V(\phi)$. If it is incommensurate, that is if $k_F < \pi/2a$, its period is thus larger than $2a$, then it is likewise anchored, because the crystal contains defects, e.g. lattice structural defects. It follows for the transport of the charge-density wave that only for fields above the threshold value F_T can it be transported (Fig. 9.25).

This can be seen in deviations from Ohm's law in the direct-current conductivity and in the noise: Fig. 9.26 shows the constant Ohmic conductivity over several orders of magnitude of the electric field F for two different arene-radical-cation salts, as well as the strongly nonlinear increasing conductivity at field strengths above a **threshold field** F_T . The value of F_T is dependent on the quality of the crystal and lies in the range between 0.1 and 1 V/cm. In this nonlinear region of the conductivity, that is in the range of decreasing differential resistance, the **noise voltage** rises sharply (inset in Fig. 9.26) [39]. This is typical of the transport of charge-density waves [40].

The transport of the charge-density wave can be especially clearly seen in the frequency dependence of the conductivity $\sigma(\omega)$ and of the dielectric constant $\varepsilon(\omega)$. Both dependencies were measured with the method of dielectric spectroscopy on $(\text{Fa})_2\text{PF}_6$ crystals between two metal contacts, thus in capacitors with $(\text{Fa})_2\text{PF}_6$ as dielectric, in the frequency range from 10^{-4} Hz to $3 \cdot 10^9$ Hz [41]. At a temperature of $T = 290$ K, i.e. above the Peierls transition, where the conductivity of the crystals is around $1000 (\Omega \text{ cm})^{-1}$, the real part σ of the conductivity in this experiment is limited by the contact resistance. It is independent of the frequency (Fig. 9.27). Below the Peierls transition, one observes a broad temperature-dependent structure in the range of low and medium frequencies, and the beginning of a steep increase with increasing frequency at high frequencies. From the analysis of these spec-

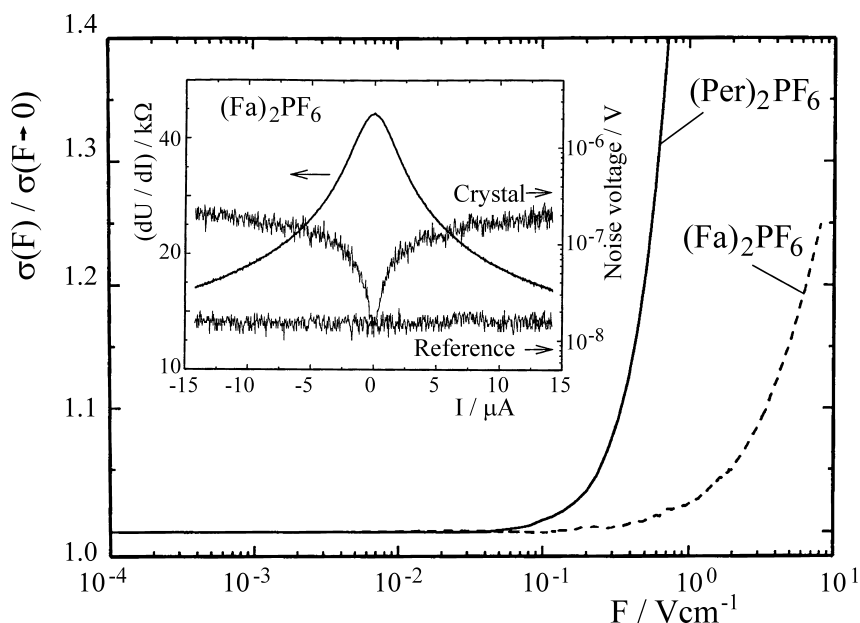


Fig. 9.26 The nonlinear conductivity of $(\text{Fa})_2\text{PF}_6$ - and $(\text{Per})_2\text{PF}_6$ crystals. The threshold field strengths F_T lie at about 1 V/cm and 0.1 V/cm. Inset: the differential resistance and the noise voltage of a $(\text{Fa})_2\text{PF}_6$ crystal as well as the noise voltage from a reference resistance of the same value (see text). After [39].

tra, the so-called **pinning frequency** $\omega_0/2\pi$ could be estimated. It lies in the range between 10^{11} and 10^{12} Hz and is the frequency with which either the anchored charge-density wave or deformations of the charge-density wave oscillate around their equilibrium positions (see also Fig. 9.8).

Complementary to the real part $\sigma(\omega)$ of the conductivity is the real part $\varepsilon'(\omega)$ of the dielectric function. $\varepsilon'(\omega)$ exhibits a frequency dependence at temperatures between 105 K and 40 K which corresponds to Debye relaxation. The resulting polarisation is described in simplified form by

$$\varepsilon'(\omega) = \varepsilon_\infty + \frac{\varepsilon_{st} - \varepsilon_\infty}{1 + (\omega\tau)^2}. \quad (9.32)$$

Here, ε_∞ and ε_{st} are the dielectric constants for $\omega \rightarrow \infty$ and for $\omega \rightarrow 0$ and τ is the relaxation time. A quantitative evaluation of the temperature dependence of the relaxation time shows a thermally-activated relaxation probability. The value for its activation energy Δ is the same as the value of Δ obtained from the dc conductivity. It follows that the mechanism for the relaxation must be scattering of the charge-density wave from free charge carriers [41].

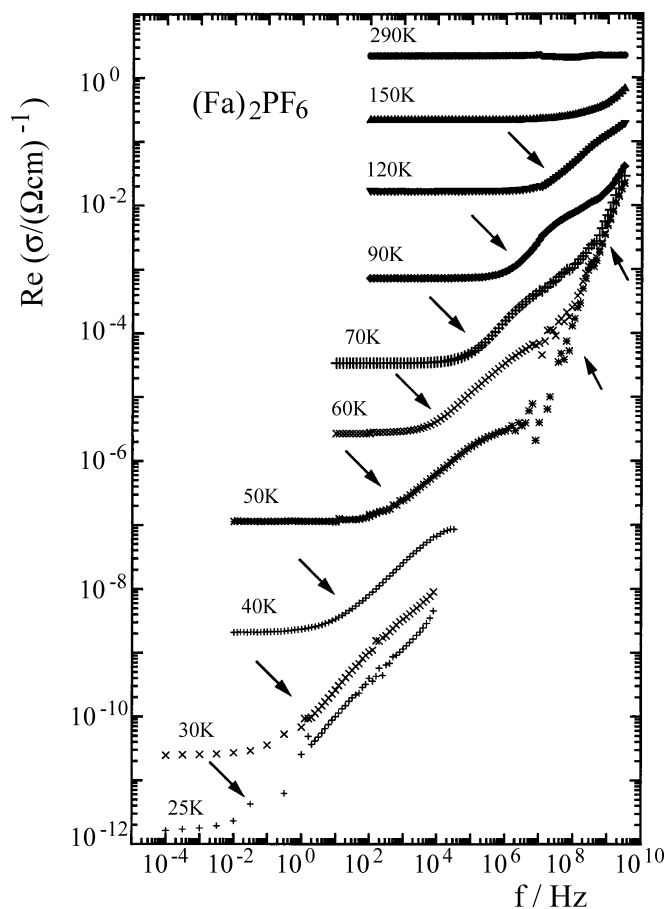


Fig. 9.27 The real part $\sigma(\omega)$ of the conductivity of a $(\text{Fa})_2\text{PF}_6$ crystal at different temperatures. The curve at 290 K is determined by the contact resistance of the electrodes.

\times indicates the strongly temperature-dependent low-frequency mode, $+$ the beginning of a high-frequency mode below the Peierls transition, that is for $T < T_P = 182$ K (see text).

From [41].

Problems for Chapter 9

Problem 9.1. The optically-induced “reversed Peierls transition”:

In the $\text{Cu}(\text{DCNQI})_2$ radical-anion salt in the neighbourhood of the Peierls phase-transition temperature, it was found that the insulating state can be switched optically on a time scale of less than 20 ps into the conducting state (F. O. KARUTZ, H. C. WOLF *et al.*, *Phys. Rev. Lett.* **81**, 140 (1998)). This optical switching process was termed a “reversed Peierls transition”. From the current transients, it was found that the switched volume must be at least 100 times larger than the directly photo-

excited volume. From this, a quantum yield of 100 charge carriers per photon follows. Furthermore, it was found that the phase transition presumably propagates with the velocity of sound ($3 \mu\text{m/ns} = 3 \times 10^5 \text{ cm/s}$, cf. Table 5.4).

Discuss the details of this paper.

Problem 9.2. The Fermi energy and the Pauli susceptibility:

Consider the charge carriers in the $(\text{Fa})_2^+\text{PF}_6^-$ radical-cation salt at high temperatures in a rough approximation as a free electron gas in a one-dimensional potential well, and compute for this case

- The Fermi energy E_F and the Fermi temperature, and
- the Pauli susceptibility.

Compare these values with those of genuine simple metals and with the measured values in the $(\text{Fa})_2^+\text{PF}_6^-$ crystal at 300 K (Fig. 9.19).

Discuss the reasons for the differences.

Literature

Monographs and Books

- | | |
|---|---|
| <p>M1 M. POPE and Ch. S. SWENBERG, <i>Electronic Processes in Organic Crystals and Polymers</i>, Oxford University Press (1999)</p> <p>M2 N. W. ASHCROFT and N. D. MERMIN, <i>Solid State Physics</i>, 2nd ed., Holt Rinehart and Winston (1987)</p> <p>M3 Ch. KITTEL, <i>Introduction to Solid State Physics</i>, 8th ed., John Wiley and Sons (2004)</p> | <p>M4 S. KAGOSHIMA, H. NAGASAWA and T. SAMBONGI, <i>One Dimensional Conductors</i>, Springer Series in Solid State Sciences 72, Springer Verlag, Heidelberg (1988)</p> <p>M5 <i>Semiconductors and Semimetals</i>, Vol. 27: <i>Highly Conducting Quasi-One-Dimensional Organic Crystals</i>, edited by Esther Conwell, Academic Press, Boston, San Diego (1988)</p> |
|---|---|

References

- | | |
|--|--|
| <p>1 H. AKAMATU, H. INOKUCHI and Y. MATSUNAGA, <i>Nature</i> 173, 168 (1954)</p> <p>2 J. T. DEVREESE, R. P. EVRARD and R. P. VON DOREN (eds), <i>Highly Conducting One-Dimensional Solids</i>, New York Plenum Press (1979); J. P. FERRARIS and T. F. FINNEGAN, <i>Sol. State Comm.</i> 18, 1169 (1976); L. B. COLEMAN, M. J. COHEN, D. J. SANDMAN, F. G. YAMAGUCHI, A. F. GARITO and A. J. HEEGER, <i>Sol. State Commun.</i> 12, 1125 (1973)</p> | <p>3 A. AUMÜLLER, P. ERK, G. KLEBE, S. HÜNIG, J. U. v. SCHÜTZ and H. WERNER, <i>Angew. Chem.</i> 98, 759 (1986); H. C. WOLF, <i>Nachr. Chem. Techn. Lab.</i> 37, 350 (1989)</p> <p>4 D. JÉROME and H. J. SCHULZ, <i>Advances in Physics</i> 31, 299 (1982)</p> <p>5 A. J. EPSTEIN, E. M. CONWELL and J. S. MILLER, <i>Ann. N.Y. Acad. Sci.</i> 313, 183 (1978)</p> <p>6 J. S. BLAKEMORE, J. E. LANE and D. A. WOODBURY, <i>Phys. Rev.</i> B18, 6797–6806 (1978)</p> |
|--|--|

- 7 M. J. COHEN and A. J. HEEGER, *Phys. Rev.* **B16**, 688–696 (1977)
- 8 R. E. PEIERLS, *Quantum Theory of Solids*, Oxford Univ. Press (1955)
- 9 M. J. RICE and S. STRÄSSLER, *Sol. St. Comm.* **13**, 125 (1973); **13**, 1389 (1973)
- 10 P. A. LEE, T. M. RICE and P. W. ANDERSON, *Phys. Rev. Lett.* **31**, 462 (1973); *Sol. St. Comm.* **14**, 703 (1974); P. A. LEE and P. W. ANDERSON, *Phys. Rev.* **B19**, 3970 (1979)
- 11 H. J. SCHULZ, in: D. Jérôme and L. G. Caron, *Low Dimensional Conductors and Superconductors*, Plenum, New York, p. 95 (1985)
- 12 S. ETEMAD, *Phys. Rev.* **B13**, 2254 (1976)
- 13 S. HÜNIG and E. HERBERTH, *Chem. Reviews* **104**, 5535 (2004)
- 14 R. KATO, *Bull. Chem. Soc. Jpn.* **73**, 515 (2000)
- 15 J. U. v. SCHÜTZ, U. BAIR, D. BAUER, W. BIETSCH, M. KREBS and H. C. WOLF, *Synth. Met.* **55**, 1809 (1993)
- 16 K. SINZGER, S. HÜNIG, M. JOPP, D. BAUER, W. BIETSCH, J. U. v. SCHÜTZ, H. C. WOLF, R. K. KREMER, T. METZENTHIN, R. BAU, SAEED I. KHAN, A. LINDBAUM, C. L. LENGAUER and E. TILLMANNS, *J. Am. Chem. Soc.* **115**, 7696 (1993); S. HÜNIG *et al.*, *Angew. Chem.* **104**, 896 (1992)
- 17 J. U. v. SCHÜTZ, D. BAUER, S. HÜNIG, K. SINZGER and H. C. WOLF, *J. Phys. Chem.* **97**, 12030 (1993)
- 18 D. GOMEZ, H. SCHMITT, J. U. VON SCHÜTZ, A. WACHTEL and H. C. WOLF, *J. Chem. Phys.* **104**, 4198 (1996)
- 19 J. U. v. SCHÜTZ, D. GOMEZ, H. WACHTEL and H. C. WOLF, *J. Chem. Phys.* **105**, 6538 (1996)
- 20 F. O. KARUTZ, J. U. VON SCHÜTZ, H. WACHTEL and H. C. WOLF, *Phys. Rev. Lett.* **81**, 140 (1998)
- 21 S. HAMM, J. U. VON SCHÜTZ, H. WACHTEL and H. C. WOLF, *J. Phys. D* **25**, 1345 (1992)
- 22 W. BRÜTTING, W. RIESS and M. SCHWOERER, *Ann. Physik* **1**, 409–422 (1992)
- 23 P. H. NGUYEN, G. PAASCH, W. BRÜTTING and W. RIESS, *Phys. Rev.* **B45**, 5172–5181 (1994)
- 24 W. BRÜTTING, P. H. NGUYEN, W. RIESS and G. PAASCH, *Phys. Rev.* **B51**, 9533–9543 (1994)
- 25 J. M. ZIMAN, *Prinzipien der Festkörpertheorie*, Verlag Harry Deutsch (1975); *Principles of the Theory of Solids*, Cambridge University Press, Cambridge (1972)
- 26 P. A. LEE, T. M. RICE and P. W. ANDERSON, *Phys. Rev. Lett.* **31**, 462–465 (1973)
- 27 V. ILAKOVAC, S. RAVY, J. P. POUGET, W. RIESS, W. BRÜTTING and M. SCHWOERER, *Journal de Physique* (Paris) **IV**, **3**, C2, 137–140 (1993)
- 28 D. BERNER, V. M. BURLAKOV, G. SCHEIBER, K. WIDDER, H. P. GESERICH, J. GMEINER and M. SCHWOERER, *Solid State Communications* **97**, 863–867 (1996); Th. SCHIMMEL, B. KOCH, H. P. GESERICH and M. SCHWOERER, *Synthetic Metals* **33**, 311–327 (1989)
- 29 U. KÖBLER, J. GMEINER and E. DORMANN, *Journal of Magnetism and Magnetic Materials* **69**, 189–198 (1987)
- 30 B. PONGS, G. FISCHER and E. DORMANN, *J. Phys. Condens. Matter* **14**, 8655–8662 (2002)
- 31 B. PONGS, T. WOKRINA, S. MATEJCEK, C. BUSCHHAUS and E. DORMANN, *Eur. Phys. J. B* **28**, 289–297 (2002)
- 32 R. DESQUIOZ, M. HOFFMANN and E. DORMANN, *Eur. Phys. J. B* **16**, 403–410 (2000)
- 33 D. C. JOHNSTON, *Phys. Rev. Lett.* **52**, 2049–2052 (1984)
- 34 G. DENNINGER, *Mol. Cryst. Liq. Cryst.* **171**, 315–331 (1989); G. DENNINGER, W. STÖCKLEIN, E. DORMANN and M. SCHWOERER, *Chem. Phys. Lett.* **107**, 222–226 (1984)
- 35 W. STÖCKLEIN and G. DENNINGER, *Cryst. Liq. Cryst.* **136**, 335–360 (1986)
- 36 G. G. MARESCH, M. MEHRING, J. U. VON SCHÜTZ and H. C. WOLF, *Chem. Phys.* **85**, 333–340 (1984); G. G.

- MARESCH, A. GRUPP, M. MEHRING, J. U. VON SCHÜTZ and H. C. WOLF, *J. Physique* **46**, 461–464 (1984)
- 37** D. KÖNGETER and M. MEHRING, *Phys. Rev. B* **39**, 6361–6369 (1989)
- 38** E. DORMANN, G. DENNINGER, G. SACHS, W. STÖCKLEIN and M. SCHWOERER, *Journal of Magnetism and Magnetic Materials* **54–57**, 1315–1316 (1986)
- 39** W. RIESS and W. BRÜTTING, *Physica Scripta*, Vol. **T49**, 721–725 (1993)
- 40** S. BHATTACHARYA, J. P. STOKES, MARK O. ROBBINS and R. A. KLEMM, *Phys. Rev. Lett.* **54**, 2453–2456 (1985)
- 41** C. MATH, W. BRÜTTING and W. RIESS, *Europhys. Lett.* **35**, 221–226 (1996)

10

Organic Superconductors

10.1

Introduction

From the preceding chapters, we know that among the great variety of organic solids, there are – in addition to insulators and semiconductors – also metals (or at least materials with a metallic conductivity). The next question must be: are there also organic materials which are superconducting? For the experimentalist, this means that below a materials-specific critical temperature T_c , the electrical resistance vanishes; the substance behaves like an ideal diamagnet with a magnetic susceptibility $\chi = -1$, and there is an energy gap $E_g(T) = 2\Delta(T)$ in the electronic density of states in the superconducting state. It is largest at $T = 0$, decreases with increasing temperature, and vanishes at T_c . The gap can be measured using tunnel spectroscopy or infrared-reflection spectroscopy.

According to the theory of Bardeen, Cooper, and Schrieffer (BCS) [1], superconductivity is a consequence of the mutual motion of coupled pairs of conduction electrons with the same magnitudes, but opposing directions of their momenta and spins. One electron polarises and distorts the surrounding crystal lattice, so that the second electron is attracted to it. Thus, an effective bonding between the two electrons is produced, which together form a so-called Cooper pair. The Cooper pairs are the charge carriers of the superconductor. They experience no scattering by phonons, impurities, defects, or other inhomogeneities in the lattice. The reason for the properties of the Cooper pairs is the spatial extent of their wavefunctions, of order between 10 and 100 nm, and the fact that they are Bosons (see general textbooks on solid-state physics). This means on the one hand that within the spatial extension of a Cooper pair, many thousand or million other Cooper pairs are present and on the other, all of these Cooper pairs are in one and the same quantum state. If for example one Cooper pair were to scatter on a phonon, then all the other Cooper pairs would have to scatter at the same time, in order for them to all remain in the same quantum state. Owing to the multiplicity of coupled Cooper pairs, this would require an enormous energy difference, which can never be supplied or taken up by individual phonons or lattice structural elements. When there is no scattering of the Cooper pairs, however, an electrical resistance, as is produced e.g. by the scattering of mutually independent conduction electrons at the Fermi

surface of a metal, is not possible. The energy gain connected with the formation of the Cooper pairs leads to the opening of the energy gap.

According to the BCS theory, in superconductivity there is a relation between the energy gap Δ and the critical temperature, $2\Delta(0) = 3.52 T_c$ (in the case of weak electron-phonon coupling). $\Delta(0)$ is the value of the energy gap at $T = 0$ K.

If not phonons, as with the Cooper pairs, but rather excitons in highly-polarisable organic molecular crystals or polymers produce a pair coupling between electrons – thus if the pair formation comes about through exchange of electronic excitations (excitons or plasmons with typical energies of 1 eV), and not via the exchange of the considerably less energetic phonons – then according to Little [2], it should be possible to obtain superconductivity at much higher temperatures. Such speculations led to considerable activity in the search for organic superconductors.

These hopes have, to be sure, not been fulfilled. Instead of an “excitonic” superconductor, motivated by the suggestion of Little, experimentalists have since found a large number of organic superconductors with conventional, or in any case not excitonic coupling mechanisms.

The organic superconductors can be divided into three classes:

- radical-ion salts, consisting of an organic cation as donor and a (frequently inorganic) acceptor, preferentially with one-dimensional conductivity;
- other donor-acceptor compounds as charge-transfer salts, in which both partners can be organic molecules, with quasi-two-dimensional conductivity;
- Fullerenes; these are salts with C_{60} as acceptor and an inorganic donor.

Table 10.1 Transition temperatures T_c and critical pressures p_c of some organic superconductors.

	T_c /K	p_c /kbar
Bechgaard salts		
(TMTSF) ₂ ClO ₄	1.4	0
(TMTSF) ₂ PF ₆	1.1	6.5
ET salts		
β -(BEDT-TTF) ₂ I ₃	1.5	0
	7.6	0.5
κ -(BEDT-TTF) ₂ Cu (NCS) ₂	10.4	0
κ -(BEDT-TTF) ₂ Cu[N(CN) ₂]Br	11.6	0
κ -(BEDT-TTF) ₂ Cu[N(CN) ₂]Cl	13	0.3
C₆₀ compounds		
K ₃ C ₆₀	18	0
Rb ₃ C ₆₀	30.7	0
	33	0
Cs ₃ C ₆₀	40	14
Rb ₂ CsC ₆₀	32.5	0

The common feature of most organic superconductors (with the exception of the Fullerenes) is a strong anisotropy. The variety of structures is very great and small changes in the molecular and structural configurations can lead to significant changes in physical behaviour. Table 10.1 lists some typical organic superconductors and their critical temperatures T_c .

Readers who wish to study the organic superconductors in detail are especially referred to the book by Ishiguro *et al.* [M1]. Other important reviews can be found in [M2] and [3].

10.2

Mainly One-dimensional Charge-Transfer Salts as Superconductors; Bechgaard Salts

The best-known organic superconductors, the so-called Bechgaard salts [4], [5], are radical-cation ionic salts of TMTSF, with tetramethyl-tetraselena-fulvalene as donor (Fig. 10.1). The first organic superconductor to be discovered was the compound synthesised in 1979 by Bechgaard, $(\text{TMTSF})_2\text{PF}_6$ that is TMTSF as electron donor and the inorganic ion PF_6^- as acceptor. The acceptor PF_6^- has a high electronegativity. An electron from two TMTSF molecules is transferred to a PF_6^- group. Each PF_6^- thus carries the charge $q/e = -1$ and each TMTSF molecule on the average the charge $q/e = +0.5$ [4]. To be sure, this salt becomes superconducting only under a relatively high pressure of 6 kbar. Its critical temperature T_c is about 1 K. There are many more Bechgaard salts with the same donor, and as counterion AsF_6^- , SbF_6^- , TaF_6^- , ReO_4^- , FSO_3^- , ClO_4^- , and others. Only the salt $(\text{TMTSF})_2\text{ClO}_4$ is superconducting under normal pressure; for all the other compounds, a more or less high applied pressure is necessary.

The crystal structure $(\text{TMTSF})_2\text{PF}_6$ is shown in Fig. 10.2. The structure of the other Bechgaard salts is very similar. The nearly planar TMTSF molecules are arranged in stacks along the crystallographic *a* axis and weakly dimerised, as we have already seen in Chap. 9 for other radical-ion salts. Along these axes, the conductivity in the metallic state is highest. The interplane spacing is 3.6 Å. The resulting large overlap of the π -orbitals in the stacking direction with the unfilled conduction band of the stack gives rise to a metallic electrical conductivity in the

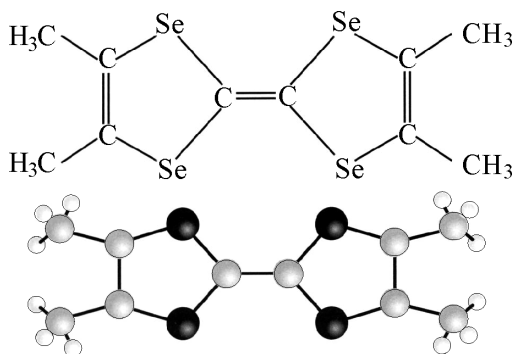


Fig. 10.1 The molecular structure of tetramethyl-tetraselena-fulvalene, TMTSF for short. The molecule is planar, which favours a stacking of the molecules within the crystal.

range of up to ca. $500 (\Omega \text{ cm})^{-1}$ along this direction. The conductivity σ_b , perpendicular to the plane of the page in Fig. 10.2b is much smaller. The smallest is σ_c , the conductivity in the direction in which the stacks are separated by the PF_6^- anions (see Fig. 10.3). Ratios such as $\sigma_a : \sigma_b : \sigma_c = 30000 : 100 : 1$ are typical of the Bechgaard salts. These salts are therefore nearly one-dimensional conductors with a temperature dependence of their conductivity that is characteristic of these (compare Figs. 10.3 and 10.4). By electrocrystallisation, one can obtain them in the form of long, thin needles with the *a* axis in the long axis of the needles. Here, the oxida-

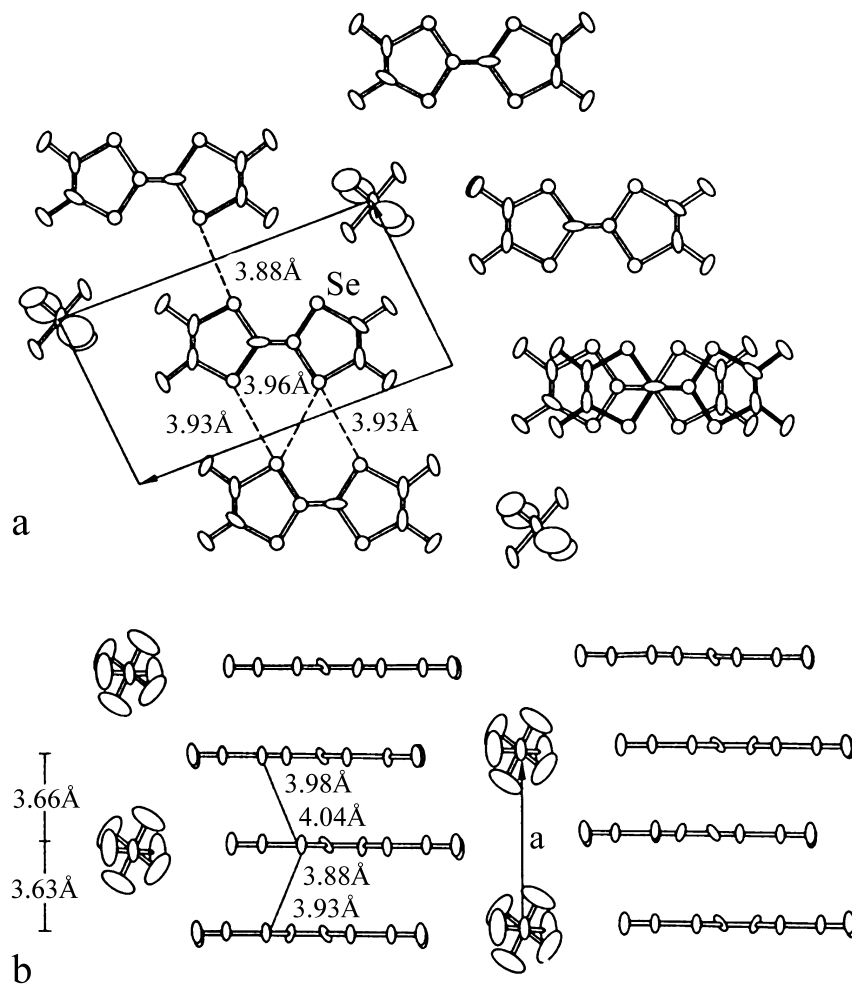


Fig. 10.2 The crystal structure of the Bechgaard salt $(\text{TMTSF})_2\text{PF}_6$, the first organic superconductor. The H atoms are – as usual – left off for clarity. The PF_6^- anions are arranged between the stacks of the organic molecules. The perpendicular spacing within the stacks

alternates between 3.66 and 3.63 Å. In addition, the distances between the nearest-neighbour S atoms are given. The stacking direction is the crystallographic *a* axis. From [5].

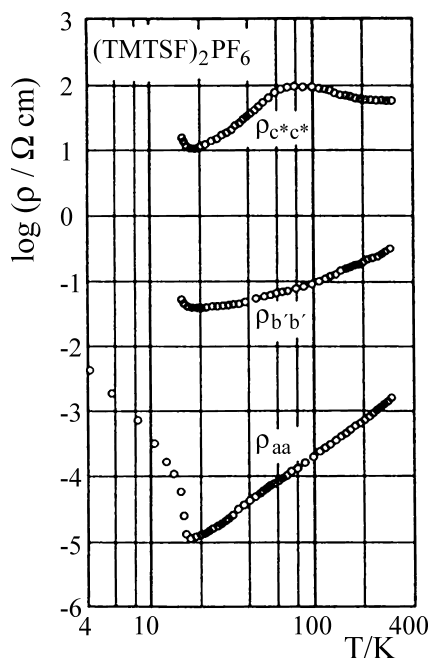


Fig. 10.3 $(\text{TMTSF})_2\text{PF}_6$: its resistance ρ as a function of the temperature, without applied pressure, and with the electric field parallel to the crystallographic axes \mathbf{a} , $\mathbf{c}^* = \mathbf{a} \times \mathbf{b}$, and $\mathbf{b}' = \mathbf{c} \times \mathbf{a}$. From [5].

tion of the donor or the reduction of the acceptor molecules takes place in solution near one of the electrodes. Small crystals grow there in times of hours to weeks (see also Chap. 3).

For their physical properties, it is very important that the Bechgaard salts, particularly also $(\text{TMTSF})_2\text{PF}_6$, are not completely one-dimensional (see also Chap. 9). At low temperatures, they to be sure exhibit a Peierls transition from metallic to insu-

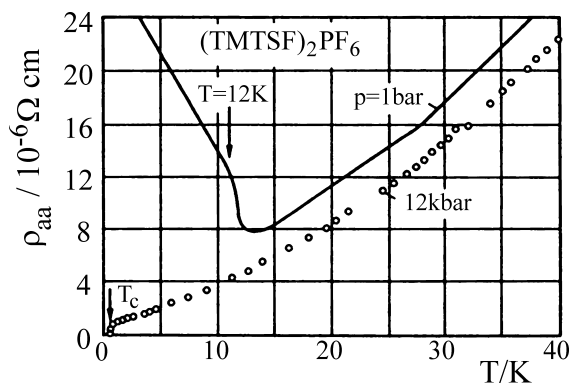


Fig. 10.4 $(\text{TMTSF})_2\text{PF}_6$: electrical resistance ρ as a function of the temperature, without applied pressure and under a pressure of 12 kbar, measured along the \mathbf{a} direction. Without applied pressure, at $T = 12$ K there is a metal-semiconductor transition. At 12 kbar, this transition is missing, and instead at ca. 1 K, the sample becomes superconducting. After [5].

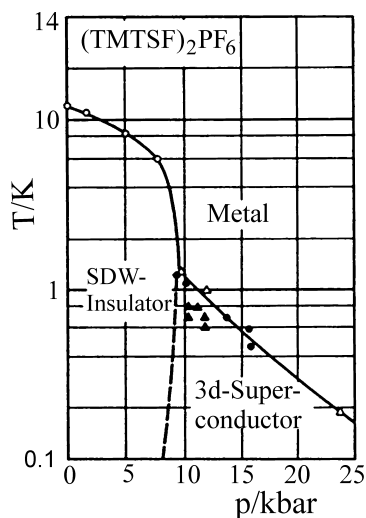


Fig. 10.5 (TMTSF)₂PF₆: a phase diagram for the transition temperature as a function of the applied pressure. The data points are due to different authors. At low temperatures and low applied pressures, one observes the behaviour of an insulator with spin-density waves. At low temperature and high pressure, the substance is superconducting; at higher temperature it is metallic. Crystallographic data: triclinic, $a = 7.29 \text{ \AA}$, $b = 7.71 \text{ \AA}$, $c = 13.52 \text{ \AA}$, $\alpha = 83.39^\circ$, $\beta = 86.27^\circ$, $\gamma = 71.01^\circ$. (From [4]).

lating behaviour, typical of one-dimensional conductors. However, a charge-density wave is not formed at the transition, but instead a spin-density wave (SDW), that is a periodic antiferromagnetic ordering of the conduction electrons. Application of pressure can prevent the localisation transition, and the substance then becomes superconducting at ca. 1 K (compare Fig. 10.4). The applied pressure increases the overlap of the molecular orbitals and thereby also increases the dimensionality from one-dimensional to two- or three-dimensional.

There are a number of anions, more than 10, with which nearly isomorphous Bechgaard salts can be synthesised. The counterions provide charge neutrality and influence the spacing of the stacks and the planar spacing of the nearly planar TMTSF ions within the stacks. Small structural differences, however, can have a great effect on the conductivity properties. Only one of these salts, (TMTSF)₂ClO₄, has a sufficiently small anisotropy even without applied pressure so that it remains metallic on cooling and exhibits a transition to the superconducting state at 1.4 K. In all these salts, phase transitions can be induced by pressure and temperature changes, leading to Peierls ordering, antiferromagnetic ordering, other ordered states and also to superconductivity. Figure 10.5 shows a portion of the phase diagram of (TMTSF)₂PF₆ as a function of the temperature and the pressure. Here, three phases are indicated: in addition to the superconducting phase at low temperature and higher pressures, there is a phase in which the substance is semiconducting with spin-density waves as excitations, and a metallic phase.

10.3

Quasi-Two-dimensional Charge-Transfer Systems as Superconductors

The second, considerably larger group of organic superconductors has as their organic basic structural unit the donor molecule bisethylenedithio-tetrathio-

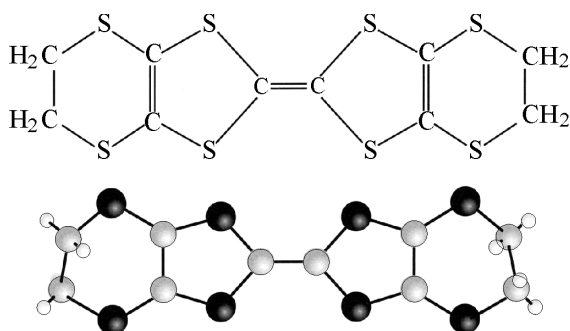


Fig. 10.6 The molecular structure of bis(ethylenedithio)tetrathiofulvalene, for short BEDT-TTF. The molecule is larger and less planar than TMTSF (Fig. 10.1).

fulvalene, BEDT-TTF, for short ET, or some related molecules from which charge-transfer salts can be prepared. Figure 10.6 shows the structure of ET. These molecules are not as planar as those of TMTSF. The ET molecules as cations form salts with a larger number of monovalent anions X of composition $(ET)_mX_n$. Most of the ET superconductors have the composition 2:1, that is $(ET)_2X$, with varying crystal structures. By no means all of the ET salts become superconducting. Like the Bechgaard salts, most of them are prepared by electrocrystallisation. In this process, the donor molecules D are oxidised at one electrode (see Chap. 3) and then crystallise with the monovalent anions A^- present in the electrolyte, frequently with the composition $D_2^+A^-$.

Here, we will take the salt $\beta\text{-(ET)}_2\text{I}_3$ as an example. This salt becomes superconducting even at normal pressure, with a critical temperature of $T_c = 1.5$ K. With a moderate applied pressure, T_c can be increased to 8 K.

The crystal structure is shown in Fig. 10.7, and the transition from the normal to the superconducting state is illustrated in Fig. 10.8. In these salts, there are a number of somewhat different crystal structures or phases which differ in the detailed

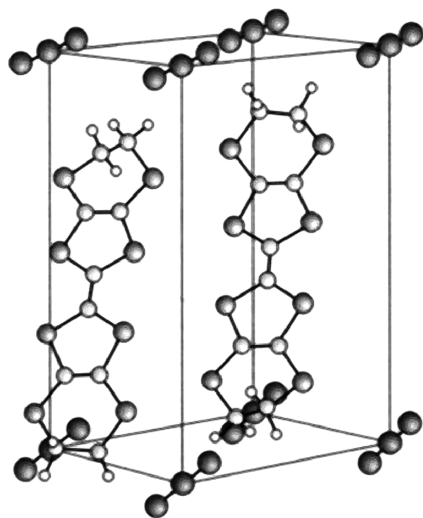


Fig. 10.7 The crystal structure of $\beta\text{-(BEDT-TTF)}_2\text{I}_3$ at room temperature. This is a nearly two-dimensional metal, in which the conducting BEDT-TTF planes, with a small anisotropy, are separated from each other by the anionic planes. Data for the unit cell: triclinic, α -Phase: $a = 9.211$ Å, $b = 10.850$ Å, $c = 17.488$ Å, $\alpha = 96.95^\circ$, $\beta = 97.97^\circ$, $\gamma = 90.75^\circ$. β -Phase: $a = 6.615$ Å, $b = 9.100$ Å, $c = 15.286$ Å, $\alpha = 94.38^\circ$, $\beta = 95.59^\circ$, $\gamma = 109.78$. From [M2].

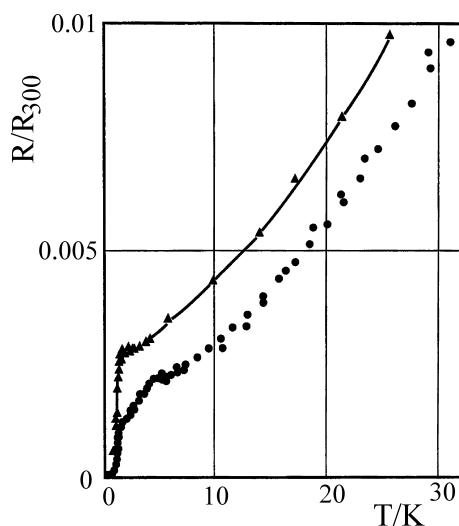


Fig. 10.8 The temperature dependence of the resistance of β -(ET) $_2$ I $_3$ at standard pressure. Above: crystal platelets. Below: crystal needles. The resistance R relative to its value at 300 K is plotted. After [M1], Fig. 5.36.

arrangement of the ET molecules relative to each other within the planes occupied by these molecules. Figure 10.7 shows the so-called β phase. Other phases are denoted by Greek letters. The different phases, especially α and κ , differ only slightly in their molecular arrangements, but show considerable differences in their physical properties.

Within the planes, the molecules, as usual in organic metals, are arranged in stacks. Owing to the considerably greater overlap with neighbouring stacks in the same plane as compared to the Bechgaard salts, the anisotropy of the conductivity within the planes is not very strong. The planes of the anions lie between these highly-conducting planes. They are responsible for the fact that the conductivity perpendicular to the (BEDT-TTF) planes can be many orders of magnitude smaller than that within the planes. These salts are thus quasi-two-dimensional conductors and therefore do not undergo a Peierls metal-insulator transition. They can also be grown as single crystals of high quality by electrocrystallisation.

In an applied magnetic field at low temperatures (2 K and lower), one can observe a collective behaviour of the delocalised electrons at high fields (more than a few T) and with high-purity samples, namely magnetic-field oscillations. These are:

- the de Haas-van Alphen effect, that is a periodic oscillation in the magnetic susceptibility with changes in the applied magnetic field;
- and the Shubnikov-de Haas effect, that is a periodic oscillation of the electrical resistance with changes in the applied magnetic field.

Both effects are based on the quantised motion of the charge carriers with closed orbits in k space. These effects can be used to study the topology of the Fermi surfaces. For more on this topic, we refer to the specialised literature: [6] and [M1].

There are a large number (more than 100) of different organic superconductors of this type. The highest critical temperature was measured for κ -(BEDT-TTF) $_2$ Cu[N(CN) $_2$]Cl as 13 K; to be sure, under a low applied pressure of 0.3 kbar.

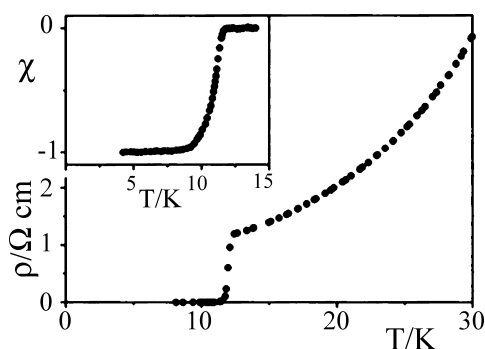


Fig. 10.9 κ -(BEDT-TTF) $_2$ Cu[N(CN) $_2$]Br: the temperature dependence of the specific electrical resistance ρ , measured perpendicular to the planes, as well as (in the inset) the magnetic susceptibility χ , measured in a magnetic field of 0.1 mT. When the sample becomes superconducting at T_c , it becomes a perfect diamagnet. This can be used to demonstrate that the superconducting phase is spread over the entire sample and is a bulk property. From [3].

At normal pressure, the isostructural salt κ -(BEDT-TTF) $_2$ Cu $^-$ [N(CN) $_2$]Br attains a critical temperature of 11.5 K. Figure 10.9 shows the specific electrical resistance ρ of this compound measured perpendicular to the planes, as well as the magnetic susceptibility χ as a function of the temperature T , measured with a SQUID system in a magnetic field of 0.1 mT. At the critical temperature T_c , the electrical resistance vanishes and the measured susceptibility of $\chi = -1$ corresponds to complete diamagnetism. From the signal strength, it follows that the entire sample had become superconducting; its superconductivity is thus a bulk property. There is also an ET salt in which both partners are organic molecules, namely (BEDT-TTF) $_2$ SF $_5$ CH $_2$ CF $_2$ SO $_3$, with $T_c = 4.5$ K at normal pressure.

10.4

The Nature of the Superconducting State in Organic Salts

The organic superconductors are, as mentioned, strongly anisotropic conductors and are superconductors of type II. In these superconductors, below the lower critical field B_{C1} , in the so-called Meissner phase, the entire bulk of the sample is superconducting. In the region between B_{C1} and the upper critical field B_{C2} , the “Shubnikov phase”, the magnetic flux penetrates the sample in quantised “flux tubes”. Above B_{C2} , the substance is a normal conductor. In type I superconductors there is in contrast only one critical field, B_C , at which the Meissner phase undergoes a direct transition into the normal-conducting state. The two critical magnetic fields B_{C1} and B_{C2} lie far apart in organic superconductors and are therefore often not measurable with a single experimental setup. If the magnetic field is applied perpendicular to the superconducting planes, then B_{C1} is typically in the range of a few mT in the ET compounds, while B_{C2} is a few T. The coherence lengths, that is the distance at which the electrons are coupled to form Cooper pairs, are a

few nm within the planes, while they are considerably shorter in the perpendicular direction. In $(\text{TMTSF})_2\text{ClO}_4$, the coherence length along the stack direction is ca. 80 nm, and along the perpendicular crystal axes, it is ca. 35 nm or 2 nm [M3]. In this last direction, it is thus less than the lattice spacing in the c direction. A three-dimensional coherence beyond the boundaries of the planes is thus possible only by coupling via the Josephson effect. If the magnetic field is applied parallel to the superconducting planes, B_{C1} is smaller by a factor of between 10 and 100, and B_{C2} is correspondingly increased by a factor of 10. The magnetic penetration depth is quite large. Depending on the direction of the applied field and the substance, it lies in the range of several μm .

The question of the nature of the superconducting state in the radical-ion salts can still not be unambiguously answered even after more than 20 years of intensive research. In the conventional superconductors, the phenomenon can be explained through the BCS theory by the formation of Cooper pairs. Here, the attractive interaction between two electrons is mediated by phonons. The total spin of the Cooper pairs is $S = 0$, and their total orbital angular momentum is $L = 0$. The pair wavefunction is an s -function. The concept of the Cooper pairs as spin singlets can evidently also be applied to the radical-ion salts. This can for example be shown by measurements of the NMR spin-lattice relaxation time in the superconducting state [3].

However, whether the coupling mechanism is the electron-phonon interaction as in conventional superconductors could not be unambiguously demonstrated in all the cases investigated. The usual proof of this is the isotope effect. It is based on the fact that an isotopic substitution and thus a change of the mass of the nuclei within a molecule also has an influence on the phonon spectrum and thus on the electron-phonon coupling. Heavier isotopes lead to a lower critical temperature. Here, along with other difficulties, there is the problem that on substitution of the atoms in the molecules by heavier isotopes, there will also be minor modifications of the lattice parameters, so that after substitution, the influence of the masses on the superconductivity cannot be measured independently of other effects. Studies of the phonon dispersion and the phonon density of states by neutron scattering below T_c have in some cases shown clear-cut changes compared to the normal-conducting state.

For the further characterisation of superconductivity in organic materials, the energy gap 2Δ and the associated density of states must be investigated. These quantities are studied by means of tunnel spectroscopy across interfaces and by infrared reflection spectroscopy.

Measurements of the energy gap 2Δ with tunnel or with microwave spectroscopy have yielded values in some experiments which are compatible with the BCS value for weak coupling, $2\Delta/kT_c = 3.52$. However, values were also determined which were noticeably higher.

Figure 10.10 shows an example of a measurement of the energy gap by a tunneling experiment. The measurement gives the tunnel resistance between two crystals of β -(BEDT-TTF) $_2\text{I}_3$ in the superconducting state. The tunnel barrier here is the vacuum between the two minimally separated crystals [7]. The plot of dV/dI , the dif-

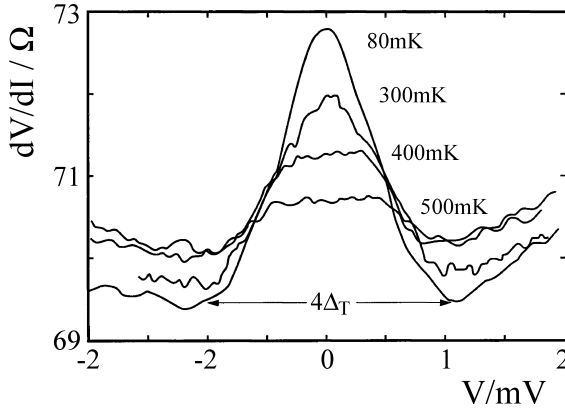


Fig. 10.10 The differential tunnel resistance dV/dI of β $(\text{BEDT-TTF})_2\text{I}_3$ in the superconducting state at various temperatures T . $4\Delta_T$ is the full width at $d^2V/dI^2 = 0$ and is a measure of the band gap at the given temperature T (see text). From [7].

ferential tunnel resistance as a function of the tunneling voltage V , is bell-shaped with its maximum at $V=0$. The halfwidth $2\Delta_T$ at the base of this curve (where the first derivative has its minima) should be a measure of the superconducting energy gap at the given temperature T . In the example of Fig. 10.10, $2\Delta_{T=80\text{mK}} = 1\text{ meV}$ and $T_c = 1.35\text{ K}$. For $2\Delta_T/kT_c$, a value of 8 instead of 3.5 is thus found; the latter would be expected from the BCS theory for weak electron-phonon coupling. In the case shown here, the deviation can be explained on the basis of strong coupling. It thus does not mean that the BCS mechanism cannot be applied here.

In spite of many experiments, with other methods as well [3], a clear answer to the question of the coupling mechanism and thus of the mechanism of the superconductivity itself has not been found, although there are many indications that a phonon-induced coupling exists and therefore conventional BCS behaviour.

Especially for the strongly anisotropic materials, there are however experiments which seem to indicate unconventional superconductivity. As coupling mechanisms for the Cooper pairs, non-phononic interactions, e.g. magnetic correlations, have been discussed. It is also not completely certain whether the pair wavefunctions have s -state symmetry or instead have p - or d -wave symmetry. There are many parallels to the inorganic high-temperature superconductors.

The current state of knowledge can be summarised as follows: there is as yet no complete consensus as to the nature of the superconducting state in organic superconductors. More on this subject can be found in [3] and [M1].

10.5

Three-dimensional Superconductivity in Fullerene Compounds

Pure Fullerene (C_{60} , Fig. 10.11) crystallises in a face-centered-cubic structure with a lattice parameter of 14.15 \AA . Crystallised C_{60} is an insulator. It can however be

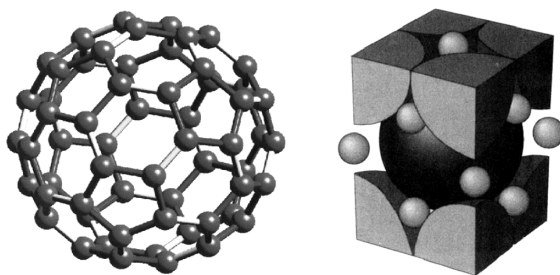


Fig. 10.11 The structure of a C_{60} molecule (left) and the face-centered-cubic structure of the C_{60} molecular crystal (right). The lattice parameter is $a = 14.15 \text{ \AA}$. From [12] and [M3].

made into a metallic conductor by doping. In normal C_{60} , there are no charge carriers, since the energy bands of the electrons are either completely filled or else are empty. One can obtain a metal through doping either by partially filling the conduction band (electron doping) or by partially emptying the valence band (hole doping). Per unit cell in the crystal, there are two tetrahedral and one octahedral interstitial sites; this makes doping with foreign atoms possible. The insertion of monovalent elements, especially the alkali metals Li, Na, K, Rb, or Cs, led to the observation of a metallic conductivity [8] and shortly thereafter in K_3C_{60} to the discovery of superconductivity below 18 K [9]. The C_{60} superconductors are C_{60} radical-anion salts.

The alkali metals act here as donors, which make a metal of the semiconductor C_{60} as acceptor, with an energy band gap of ca. 2.3 eV via half-filling of the conduction band. The system behaves similarly to the radical-anion salts which we have already treated (Sects. 9.2 and 9.3). C_{60} is a good electron acceptor. It consists entirely of carbon atoms and is thus not actually an organic molecule. Superconducting Fullerene salts however have properties which are like those of the organic molecular salts. These are above all the important role played by the π electrons in charge transport, and the existence of relatively narrow bands with a low electron density.

In the past years, more than 20 superconducting Fullerene compounds have been discovered, in particular of the types A_3C_{60} and A_2BC_{60} (A and B stand for alkali metals). The highest critical temperature achieved so far is 40 K (in Cs_3C_{60} at 14.3 kbar), and 32.5 K (at normal pressure, in Rb_2CsC_{60}). Figure 10.12 shows the transition from normal conduction to superconductivity for a few Fullerene salts, measured via the magnetic susceptibility.

Studies in an applied magnetic field show that we are dealing here with type II superconductivity, with a lower and an upper critical field; their values are very different: B_{C2} is 50 T and higher, and B_{C1} is 15–120 G [M3]. The coherence lengths lie around a few nm, and the magnetic penetration depths are 200–800 nm. All of the observations so far indicate that Fullerene superconductivity can be understood within the framework of the conventional BCS theory with moderately strong electron-phonon coupling. More about this subject may be found in Ishiguro [M1] and in the review articles by Baenitz [10] and Gunnarson [11].

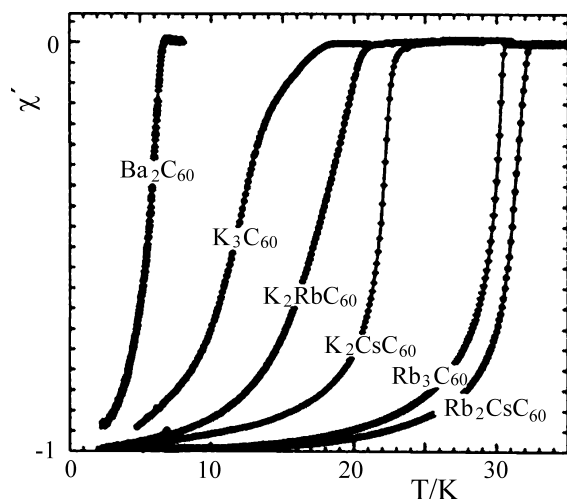


Fig. 10.12 Transition curves for superconductivity in the alkali- and alkaline-earth-doped Fullerene crystals. The real part χ' of the ac susceptibility, normalised for $T \rightarrow 0$ K to -1 (i.e. the value for ideal diamagnetism), is plotted against the temperature. After [10].

The physics of organic superconductivity is an interesting area of research with many open questions remaining. To be sure, this field has strong competition from the inorganic high-temperature superconductors. But we can certainly count on some future interesting developments in the field of organic superconductivity.

Literature

Monographs and Books

- | | |
|--|---|
| <p>M1 T. ISHIGURO, K. YAMAJI and G. SAITO, <i>Organic Superconductors</i>, 2nd ed., Springer (1998)</p> <p>M2 J. M. WILLIAMS, J. R. FERRARO, R. J. THORN, K. D. CARLSON, U. GEISER, H. H. WANG, A. M. KINI and M.-H.</p> | <p>WHANGBO, <i>Organic Superconductors</i>, Prentice Hall (1992)</p> <p>M3 W. BUCKEL and R. KLEINER, <i>Supraleitung</i>, 6th ed., Wiley-VCH Verlag (2004)</p> |
|--|---|

References

- | | |
|--|---|
| <p>1 J. BARDEEN, L. N. COOPER and J. R. SCHRIEFFER, <i>Phys. Rev.</i> 108, 1175 (1957)</p> <p>2 W. A. LITTLE, <i>Phys. Rev. A</i> 134, 1416 (1964)</p> | <p>3 J. WOSNITZA, <i>Physikalische Blätter</i> 56(4), 41 (2000)</p> <p>4 D. JÉROME, A. MAZAUD, M. RIBAUT and K. BECHGAARD, <i>J. Phys. Lett.</i> 41, L95 (1980); D. JÉROME, <i>Physica</i> 109/110B, 1447 (1982)</p> |
|--|---|

- 5 C. S. JACOBSEN, K. MORTENSEN, N. THOROUGH, D. B. TANNER, M. WEGER and K. BECHGAARD, *Chem. Scri.* **17**, 103 (1981)
- 6 J. WOSNITZA, *Fermi Surfaces of Low-Dimensional Organic Metals and Superconductors*, Springer (1996)
- 7 A. NOWACK, U. POPPE, M. WEGER, D. SCHWEITZER and H. SCHWENK, *Z. Physik B* **68**, 41 (1987)
- 8 R. C. HADDON *et al.*, *Nature* **350**, 320 (1991)
- 9 A. F. HEBARD *et al.*, *Nature* **350**, 600 (1991)
- 10 M. BAENITZ, *Physik in unserer Zeit* **30**, 167 (1999)
- 11 O. GUNNARSON, *Rev. Mod. Phys.* **69**, 575 (1997)
- 12 C. H. PENNINGTON, *Rev. Mod. Phys.* **68**, 855–910 (1996)

11

Electroluminescence and the Photovoltaic Effect

In Chaps. 5–10, we treated primarily individual, intrinsic properties of organic solids: phonons, excitons, spin excitations, semiconducting properties, metallic conductivity, and superconductivity. Our main interest was directed in particular to excitations in the **bulk** of the organic solids.

In this chapter, we will deal with the **combination of electrical and optical properties**. Here, along with the bulk properties, also the **interfaces** between the electrical contacts and the organic solids, as well as the interfaces between different organic solids, will play a central role. We restrict ourselves in this chapter to two electrooptical effects: electroluminescence and the photovoltaic effect. The two phenomena are complementary:

For **both**, so-called devices with one or more organic semiconductor layers between two metallic or metallic-conducting electrodes must be prepared. The anode and the cathode differ in their work functions. Furthermore, either the cathode or the anode must be semitransparent. In the case of **electroluminescence** (Sect. 11.1), the device is called an organic light-emitting diode, (**OLED**) (Fig. 11.1). In it, an external voltage source V generates a bipolar current I in the organic semiconductor in such a way that the two types of charge carrier from the opposite electrodes, the electrons from the cathode and the holes from the anode, drift towards each other (Fig. 11.2). When the initially free charge-carrier pairs meet, they can create electronically-excited molecules or excitons in the organic layer, which then recombine radiatively; this electroluminescence is then emitted through the semitransparent electrode. The intensity of the emitted luminescence is the luminosity of the OLED.

In the **photovoltaic effect** (Sect. 11.2), radiation which enters the device from outside via the semitransparent electrode produces electronically-excited molecules or excitons after absorption of the photons in the organic layer. These excitation states dissociate immediately after their formation via ultrafast processes and generate free charge-carrier pairs, which then drift apart in opposite directions as a bipolar current: the electrons to the cathode and the holes to the anode. The charges thus produced give rise to a potential difference between the two electrodes and thus to an internal electric field in the organic layer which prevents further charge transport when the external circuit is open, even with continuing irradiation. When it is closed, a continuous current flows as long as the irradiation continues. The prod-

uct of the existing potential difference V and the current I is the electric power of the **photovoltaic cell**. It is called a **solar cell** when the irradiation consists of white light, whose entire spectrum is more or less strongly absorbed and contributes to the production of excitons.

The thickness of the organic layer or, in multilayer devices, of the organic layers, is as a rule in the range between 10 and a few 100 nanometers. The electrooptics of organic devices is thus also a nanotechnology. The optimisation of the contacts and the layer thicknesses is – along with the intrinsic materials parameters – of central importance for the efficiency of the devices, i.e. for the luminous yield of electroluminescent devices or for the electric power of photovoltaic cells. The devices must therefore be optimised by both controlled variation of the layers and layer thicknesses and by comparison with simulations.

11.1

Electroluminescence: Organic Light-Emitting Diodes (OLEDs)

11.1.1

Historical Remarks

The phenomenon of electroluminescence in organic solids has been known since the 1960's: at that time, Pope *et al.* [1] and Helfrich and Schneider [2] discovered and investigated the electroluminescence of **anthracene crystals** between two electrodes, an anode and a cathode. The thickness of the highly-purified anthracene crystal platelets was large in these first experiments: 10–20 μm or 1–5 mm. The two electrodes on the surfaces of the crystal platelets were “silver paste” or liquid, highly concentrated solutions of NaCl. The necessary external voltages varied between 50 and 2000 V. Later, Williams and Schadt [3] were the first to construct a “display”, likewise from anthracene crystals, but with solid, laterally-structured electrodes, and they encapsulated it to prevent its degradation in the air.

Owing to the high voltages – made necessary by the high layer thickness of the anthracene crystal platelets – and due to the mechanical fragility of the single crystals, research on the applications of electroluminescence in organic solids was not very intensive in the following years. This changed drastically after Tang and van Slyke [4] in 1987 developed thin, **low-molecular organic evaporated films** and Burroughes, Bradley, Friend *et al.* [5] in 1990 used thin, spun organic **polymer films** instead of the anthracene crystal used earlier for the fabrication of organic LEDs. Both types of organic materials contain conjugated π -electron systems. They are organic semiconductors (see Chap. 8) and fluoresce (see Chap. 6). Both types have since been named OLEDs (Organic Light Emitting Diodes). Since these results were published, worldwide research and development activities have been established in the OLED field, leading in 1998 to the first commercially-produced monochrome display. In the intervening years, several firms have developed colour display monitors.

The technical specifications of these monitors are impressive: they luminesce in the entire visible spectrum, they are bright and efficient. They are thinner and lighter than LCD monitors (liquid crystal displays) and are therefore especially suited for portable equipment. They are intrinsically emissive, and thus require no background illumination, and they have a display angle of nearly 180° . Furthermore, they are fast and thus suitable for rapid video sequences. The image points (pixels) can be switched to a completely dark state, so that higher contrast can be obtained.

More advanced OLED displays have a high resolution: e.g. the 20" screen display introduced by IDTech, CMO and IBM in May 2003 (20 inch picture diagonal) has 1280×780 pixels in three colours each (cf. Table 11.1). The emitters of these displays are low-molecular organic evaporated films. The active control of the emitting pixels in this display is carried out by a matrix of semiconductor devices based on amorphous silicon. The maximum operating luminosity L_0 of the display lies between 300 and 500 Candela per square meter (cd/m^2) and is thus about 3 to 5 times higher than that of a television screen under normal conditions. The switching time is less than 1 ms and the contrast higher than 1 000. At $100 \text{ cd}/\text{m}^2$, the operating life is probably more than 10 000 hours.

There are in the meantime comparable products from several firms. For example, Philips introduced a 13" monitor in July 2004 on the basis of light-emitting polymers; it is produced using the technology of inkjet printing. The number of pixels is 576×324 . Other manufacturers have reported switching times of < 0.01 ms and a large number of available colours. Table 11.1 gives a brief and incomplete list. This table will certainly be outdated by the time this book is published, since

Table 11.1 A selection of OLED display manufacturers with their most significant specifications. M stands for low-molecular evaporated films, P for polymers, S for evaporated with a shadow mask, Ti for ink-jet printing.

Manufacturer	Screen diagonal (inches)	OLED Material	Structuring	Pixel number	Date of publication
Pioneer		M	S		01-Jan-98
Sony	13	M	S	800×600	17-Apr-01
Toshiba Matsuhita	17	P	Ti	1280×768	16-Apr-02
Sony	24	M	S	1024×768	01-Jan-03
Kodak	2.2	M	S		02-Mar-03
IDTech	20	M	S	1280×768	18-Mar-03
Epson	40	P	Ti	1280×768	18-May-04
Samsung	17			1600×1200	18-May-04
Sony	3.8	M	S	480×320	14-Sep-04
Philips	13	P	Ti	576×324	July 2004

developments in this field, driven by a potentially enormous market, are rapid and successful. (See also [M1].)

We shall therefore not further discuss the technical applications of OLEDs. In future, they will presumably lead to large-area light sources in addition to large video displays. Instead, in the following we will treat the physical fundamentals of OLEDs, considering a few selected organic materials as examples.

11.1.2

The Principle of the OLED

Figure 11.1 shows a cross-sectional view through the simplest device structure of an OLED. It consists of an organic layer between two electrodes, an anode and a cathode. The typical thickness of the organic layer is less than 100 nm. The surface area of the layer is in principle arbitrary: thus far, OLEDs with an active area between $1\ \mu\text{m}^2$ and more than 50cm^2 have been constructed. The whole layer structure is mounted on a substrate, which for example can be made of glass or a flexible polymer sheet, or also a silicon wafer. The airtight cemented cover layer of glass (encapsulation) serves to protect the inner layers from oxygen, water, etc. One of the two metallic or metallic-conducting electrodes must be semitransparent to permit the light produced to exit the device. This is often the anode, which is then frequently made of indium-tin oxide (ITO), which is electrically conducting and transparent. In newer developments, however, transparent cathodes are also used, which consist of a thin film of a non-noble metal [6]. This arrangement is called a

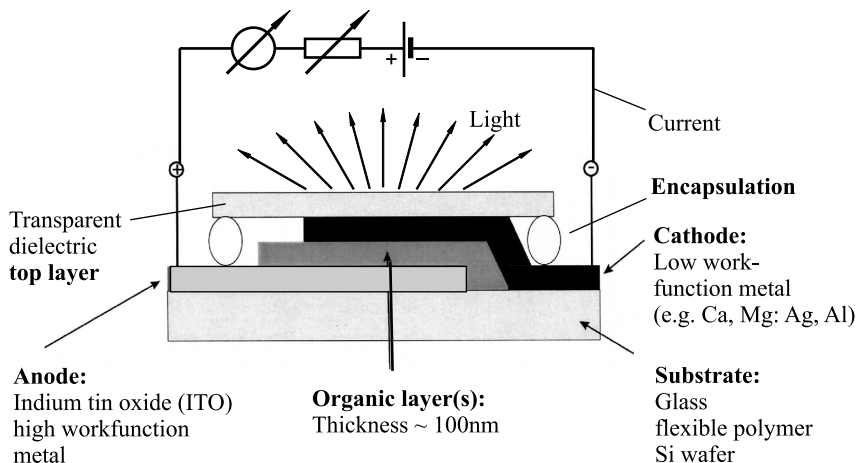


Fig. 11.1 A cross-section through the simplest form of an organic light-emitting diode (OLED). One of the two metallic or metallic-conducting electrodes must be semitransparent to permit the luminescence to exit the device. In the example in this figure, this is the cathode. Typical thicknesses of the organic layer(s) between the electrodes are

between 10 nm and 100 nm. The surface areas of OLEDs fabricated up to now lie between $1\ \mu\text{m}^2$ and 50cm^2 . However, especially upwards, there are no limits in principle. The airtight cemented cover layer of glass serves to protect the organic layer(s) from air and water (encapsulation). Typical operating voltages lie between > 1.5 and 10 V.

top emitting OLED. When Si substrates for active control of the electrodes or other non-transparent substrates are used, this arrangement has the advantage that the light can be emitted upwards, i.e. not through the substrate.

The operating principle of the OLED is similar to that of inorganic LEDs. Figure 11.2 illustrates the four fundamental processes in an energy-level diagram for an external voltage applied in the pass direction. These processes are: **1** injection and **2** transport of the charge carriers, **3** their binding to form excitons, and **4** their recombination accompanied by the emission of light. The organic layer is characterised by its two energy levels HOMO and LUMO (see Chap. 8). Both levels are not sharp in these non-crystalline layers, but are drawn in Fig. 11.2 as sharp levels for clarity. Both the energy gap and the exciton energy, and thus the wavelength

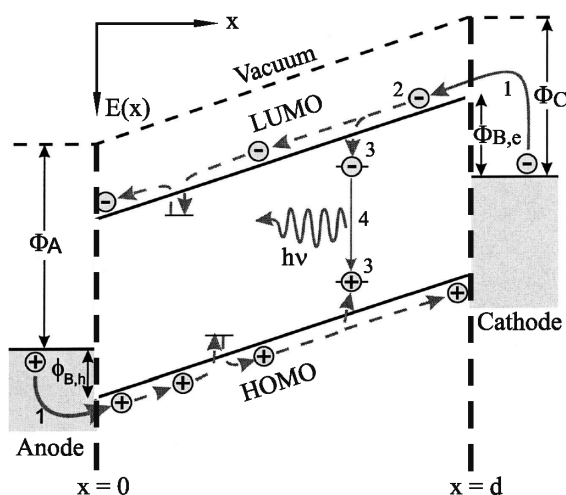


Fig. 11.2 The term diagram and charge-carrier processes in an OLED consisting of a single organic layer (one-layer OLED). **1** injection, **2** charge-carrier transport, **3** binding of charge-carrier pairs (electron-hole pairs) to give Frenkel excitons, and **4** recombination of the excitons with emission of the luminescence. The organic semiconductor layer with a thickness d is contacted between the two metal electrodes which have different work functions. For current to flow, charges must be transported. These can be either electrons, which are injected from the cathode into the organic semiconductor and occupy the LUMO there, i.e. they form radical anions. Or they can be holes, which are injected from the anode into the organic semiconductor and occupy its HOMO, i.e. they form radical cations. The energies $E(x)$ of the HOMO and the LUMO are a function of the location x and

of the sum of the contact voltages of the two different metal electrodes and the applied voltage. The term diagram is shown for the case that an external voltage source is applied with its polarity chosen to allow the current to flow in the pass direction through the diode. If its polarity is reversed (inhibit direction of the diode), neither electrons nor holes can be transported. Only when the current is bipolar in the pass direction, thus only when both electrons and holes can flow, can excitons be formed where the two types of charge carrier meet. Their radiative recombination is the electroluminescence. A typical value of the energy gap (HOMO-LUMO energy gap) is 3 eV. Typical binding energy of the excitons: 0.5 eV. Φ_A and Φ_C are the work functions of the anode and the cathode. $\Phi_{B,h}$ and $\Phi_{B,e}$ are the activation barriers for the injection of holes and of electrons.

of the emitted light, are materials dependent (see Chaps. 6 and 8). With the great variety of applicable organic semiconductors to choose from, it has been possible to fabricate OLEDs for the whole visible spectral range.

The anode is made of a metal with a large work function Φ_A . It can inject holes through one of the interfaces into the HOMO of the organic layer. For this to occur, the activation barrier $\Phi_{B,h}$ must be overcome. The cathode is made of a non-noble metal with a lower work function Φ_C . From it, electrons can be injected via the opposite interface into the LUMO. The activation barrier for this process is $\Phi_{B,e}$. The contact of the two different electrodes across the organic layer produces the contact voltage Φ_{BI} and the built-in internal field. It prevents the transport of the injected charge carriers when no external voltage is applied (cf. Sect. 8.4.3). Only when the external voltage (negative at the cathode and positive at the anode) is larger in magnitude than the contact voltage can a current flow. This case is shown in Fig. 11.2.

When electrons and holes meet, they can initially form charge-transfer excitons and then electronically-excited singlet or triplet states. Both excitation states can decay radiatively and thus contribute to the electroluminescence. Every non-radiative contribution to the decay reduces the light yield of the OLED. As a rule, fluorescence from the singlet excitons is predominant in OLEDs. There are however also important triplet emitters (see below).

The mobilities μ of the charge carriers in the materials from which OLEDs are fabricated are low in comparison to the mobilities in organic molecular crystals (see Chap. 8). Furthermore, they are very different in the different materials: there are some materials in which predominantly electrons are transported ($\mu_e \gg \mu_h$), and some in which mainly holes participate in the transport ($\mu_h \gg \mu_e$). Hole-transport materials, e.g. the naphthyl-phenyldiamine-biphenyl derivative NPB, have a relatively low ionisation energy and therefore form radical cations preferentially and reversibly. Electron transport materials, e.g. Alq₃, have a relatively high electron affinity and thus form radical anions preferentially and reversibly.

When in the stationary state equal numbers of holes and electrons are injected per unit time, but e.g. the hole mobility is much higher than the electron mobility, then in a single-layer OLED, the recombination occurs very near the cathode. This leads as a rule to an increase in non-radiative recombination and thus to a reduction of the light yield. If different numbers of holes and electrons are injected and transported per unit time, then that part of the charge carriers which is in excess, i.e. a part of the current, cannot contribute to the production of light. This too reduces the efficiency of the OLED.

Nevertheless, even such simple single-layer OLEDs function well. Figure 11.3 shows a single-layer OLED made with the polymer PPV (see Fig. 11.5) in operation with an applied voltage $V = 4.5$ V. Their luminescence can be seen from the last row of a large auditorium. However, they are inefficient and have a limited operating life.

To understand how the efficiency η of OLEDs was improved markedly in the course of only a few years, we wish to define and analyse this most important characteristic of an OLED in the following:

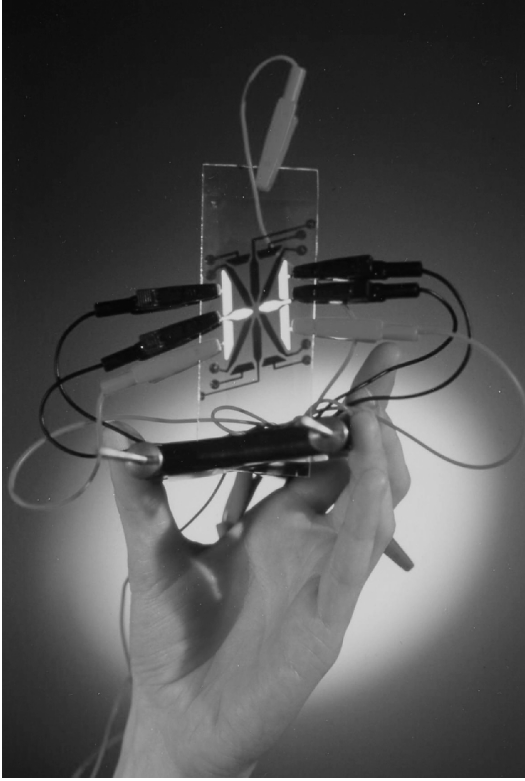


Fig. 11.3 A 16-segment display with a single-layer OLED. The active organic layer is made of PPV. The glass plate serves as substrate and is coated with ITO; the black dots are the contacts for the Al cathodes. The OLED segments which are supplied with a voltage of 4.5 V emit light, the others remain dark. (Prepared by J. Gmeiner, University of Bayreuth, 1992.) Compare the coloured plate in the Appendix.

The efficiency of an OLED characterises the external light yield relative to the electric power, $\eta_E(\text{ext})$. It is defined as the ratio of the specific light emission M to the electrical power density input [7]:

$$\eta_E(\text{ext}) = \frac{M}{jV}. \quad (11.1)$$

Here, $M = \Phi/A$, Φ is the light current and A is the emitting area. The unit of the specific light current or specific light emission is $[M] = 1 \text{ lm/m}^2$ ($\text{lm} = \text{lumen}$) [8]. j is the current density and V the operating voltage between the anode and the cathode of the OLED. The unit of η_E is $[\eta_E] = 1 \text{ lm/W}$. M , j and V can be measured directly and thus, η_E is an observable. For a Lambertian source [8], $M = \pi L_0$. Here, L_0 is the luminosity $L(\Theta)$ emitted perpendicular to the surface, i.e. at an angle $\Theta = 0$ to the surface normal (see Fig. 11.13). The unit of L is $[L] = 1 \text{ cd/m}^2$. $\eta_E(\text{ext})$

is directly correlated with the external quantum yield $\eta_\phi(\text{ext})$. It is defined as the ratio of the number of photons emitted out of the device to the number of injected charge carriers. Due to the losses of photons on coupling out of the device, we have

$$\eta_\phi(\text{ext}) = \eta_{\text{tr}} \eta_\phi(\text{int}). \quad (11.2)$$

Here, $\eta_{\text{tr}} < 1$. The coupling-out losses occur in the main by total reflection. If, as in the arrangement shown in Fig. 11.1, the light is emitted upwards through a glass layer and the substrate or the anode totally reflect, then

$$\eta_{\text{tr}} \approx \frac{1}{n^2}. \quad (11.3)$$

In this expression, n is the highest index of refraction within the OLED [9].

$\eta_\phi(\text{int})$ is the number of photons produced within the emitting material per charge carrier. It cannot be measured in a simple way, but can be estimated. The following estimate holds the key to the optimisation of an OLED:

$$\eta_\phi(\text{int}) = \gamma \eta_r \eta_{\text{PL}}. \quad (11.4)$$

In this equation, γ is the charge equilibrium factor, η_r is the probability of exciton formation from one electron-hole pair, and η_{PL} is the quantum yield for the photoluminescence.

η_{PL} is defined as the ratio of the number of emitted photons to the number of absorbed photons in photoluminescence. If triplet states can be neglected, since in the usual molecules the intersystem crossing rate and the phosphorescence probability are negligibly small (cf. Chap. 6), then η_{PL} is the fluorescence probability. For “good” molecules, it has a value between 0.5 and 1.

η_r in singlet emitters is the probability of formation of a singlet exciton. As mentioned, triplet excitons are not competitive in the usual materials in comparison to singlet excitons in terms of luminescence. However, they are formed by recombination. The probability of forming a triplet exciton is in fact statistically three times greater than that of forming a singlet exciton, since the distributions of the spin orientations of the unpaired electrons and holes are isotropic and every triplet state is threefold degenerate. Therefore, $3/4$ of all the excitons which are formed by electron-hole pairs are triplet excitons, and for the singlet emitters, $\eta_r = 1/4$. Important exceptions are found in triplet emitters. They are composed of molecules which contain heavy nuclei (see below).

γ is the ratio of the numbers of injected electrons and holes, and is called the charge equilibrium factor. If all the injected electrons and holes are consumed by recombination, then $\gamma = 1$. When the electron and the hole currents are unequal, then $\gamma < 1$.

All together, the external quantum yield is thus

$$\eta_\phi(\text{ext}) = \eta_\phi(\text{int}) \eta_{\text{tr}} = \gamma \eta_r \eta_{\text{PL}} \eta_{\text{tr}}. \quad (11.5)$$

Even if the electron and hole currents are equal ($\gamma = 1$), and even if the organic layer has a large photoluminescence quantum yield, e.g. $\eta_{\text{PL}} = 50\%$, the external

quantum yield of an OLED with singlet emitters in which the fluorescence must exit through a glass plate remains small: $\eta_{\phi}(\text{ext}) \approx 1 \cdot 25\% \cdot 50\% \cdot \frac{1}{6} \approx 2\%$. From this estimate, it becomes clear which measures must be taken to optimise OLEDs in order to obtain high values of the efficiency: use of the triplet states and reduction of the reflection losses. Furthermore, the balance between the electron and the hole currents must be maintained, and emission layers with high quantum yields for luminescence must be employed. In the two following subsections, we shall see that efficient OLEDs must be fabricated with many layers, of which each one optimises one of the individual processes of electroluminescence and does not perturb the other processes seriously.

11.1.3

Multilayer OLEDs

Using both low-molecular evaporated films and polymer films, multilayer OLEDs of high efficiency have been constructed. The structures of some molecules often used for evaporated films are shown in Fig. 11.4, and the monomers for polymer films in Fig. 11.5. The purpose of the fabrication of multilayer OLEDs is the independent optimisation of the individual processes which were described in Sect. 11.1.2, with the goal of achieving high-efficiency OLEDs: injection and transport of the electrons and holes, balance between the currents of electrons and holes, recombination, use of triplet states, and reduction of reflections in the transmission of the luminescence to the outside of the OLED. In the following, we will treat a few typical examples of OLEDs prepared with low-molecular evaporated films. We emphasize, however, that also multilayer OLEDs made with polymers can yield comparable results and information.

The optimisation of the efficiency using multilayer OLEDs can in principle be attained, as mentioned, by optimising each layer for an individual process, provided it is neutral for the other processes. For this purpose, at least the following layers are necessary (see Fig. 11.8): a hole injection layer (metal anode), a hole transport layer (HTL), an emission layer (EML), an electron transport layer (ETL), an electron injection layer (metal cathode), and a reflection-reducing cover layer (dielectric) over the semitransparent electrode (cathode or anode), as well as the encapsulation for protection against air and water. This multilayer concept requires an additional optimisation of the interface phenomena between the layers. Furthermore, it requires the optimisation of the interference which occurs because the emission layer is within the cavity resonator formed by the electrodes acting as mirrors and the internal organic dielectric layers. All together, the optimisation process is thus complex.

The simplest multilayer OLED consists of two organic layers (Fig. 11.6), one EML which is at the same time an ETL (e.g. Alq_3), and an HTL (e.g. NPB). Alq_3 is a singlet emitter. The layer thicknesses can be optimised so that the electron and hole currents are equal and that the recombination and thus the emission occur in the Alq_3 , and there in a thin layer near the interface to the HTL. This allows the

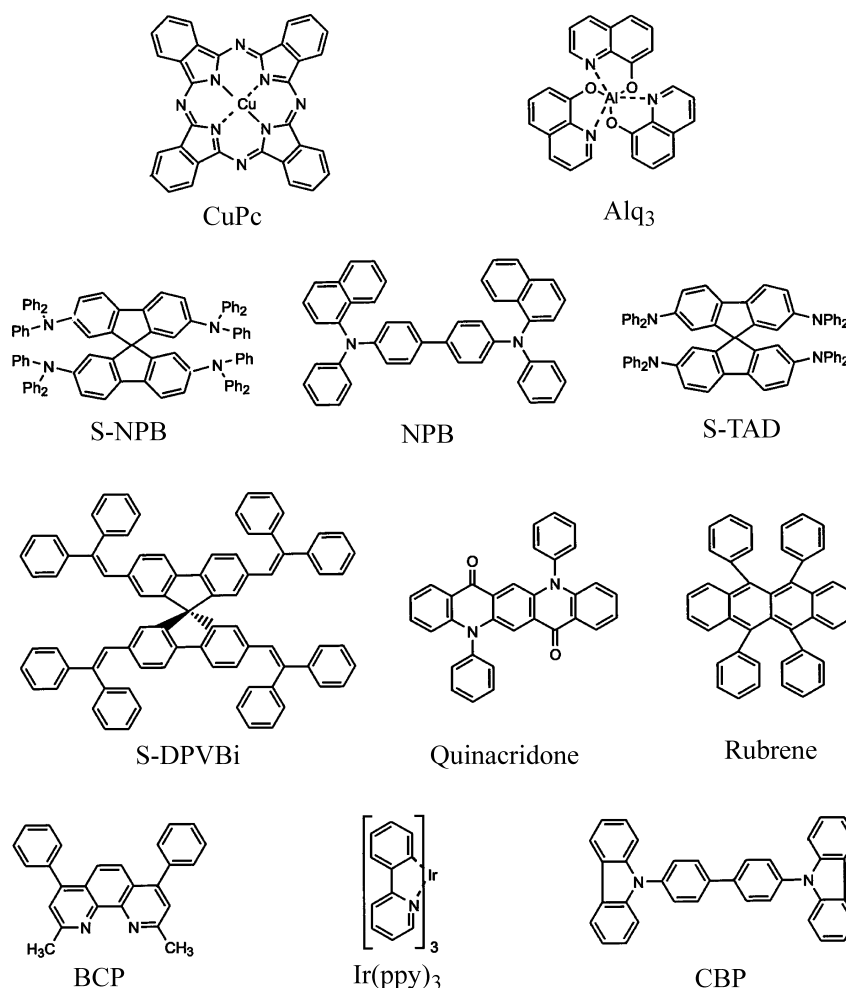


Fig. 11.4 Often-used molecules in low-molecular evaporated films for the fabrication of OLEDs. Many of these molecules have no trivial names and are therefore denoted by abbreviations. CuPc is copper phthalocyanine.

non-radiative recombination in the neighbourhood of the cathode to be minimised and the position of the emission within the cavity to be determined.

A further improvement is the introduction of a copper phthalocyanine (CuPc) layer between the anode and the hole transport layer (Fig. 11.7). The CuPc layer was originally introduced as a hole injection layer. Its essential functions are however the optimisation of the electric field within the two organic layers and protection of the Alq₃ layer against an excess of holes. Holes form radical cations in Alq₃. But Alq₃ has a high value of the electron affinity, i.e. it tends strongly towards formation

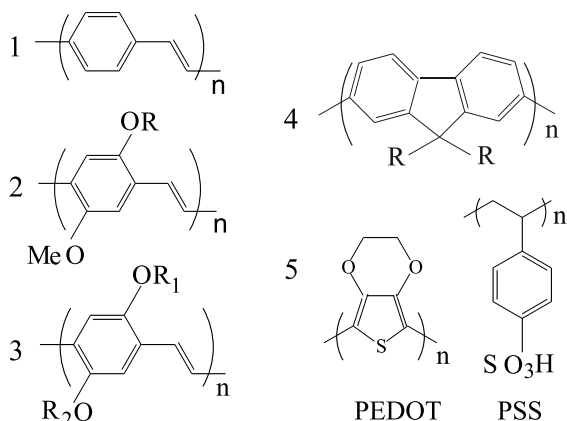


Fig. 11.5 Frequently-used monomers for spun-on or printed polymer layers used in the fabrication of OLEDs. 1: unsubstituted insoluble PPV = poly-paraphenylene; 2: MeH-PPV (Me = CH₃, H = ethylhexyl); 3: substituted PPV (for R₁ and R₂, there are a

number of organic and/or inorganic substituents available); 4: polyfluorene; 5: PEDOT = poly-3,4-ethylene-dioxi-thiophene; PSS = polystyrol-sulfonate; PEDOT : PSS (= BAYTRON) is used as anode material.

of a radical anion. Holes therefore lead to the degradation of this layer and thus to a reduction of the operating life of the OLED [10].

With a dielectric cover layer of ZnSe over the semitransparent Ca cathode, by a suitable choice of the layer thickness, both a high efficiency and good colour purity could be obtained. Here, the constructive interference of the directly emitted radi-

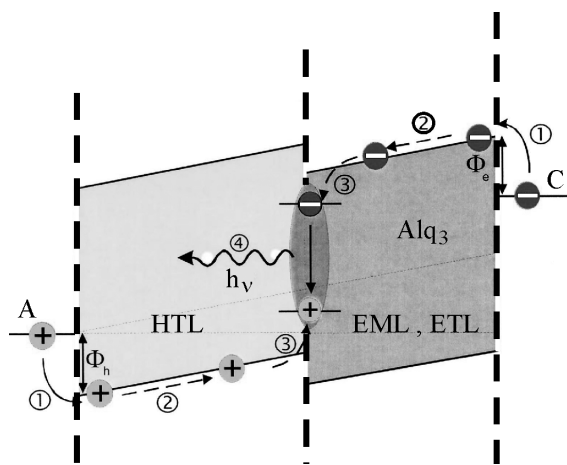


Fig. 11.6 The structure and schematic energy diagram of a two-layer OLED. With a suitable choice of the layer thicknesses, recombination occurs in the emission layer (EML) Alq₃ in the neighbourhood of the HTL/Alq₃ interface layer. Alq₃ is simultaneously the electron transport

layer (ETL). HTL is a hole transport layer. It can be made of e.g. NPB. The energy diagram is drawn for $V > -V_{BI}$ (V is the externally-applied voltage, V_{BI} the contact voltage). A = anode, C = cathode.

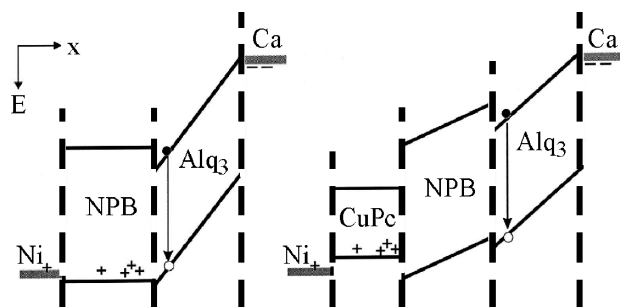


Fig. 11.7 A schematic energy diagram $E(x)$ for $V > -V_{BI}$ of a NPB/Alq₃ OLED without and with an additional CuPc layer as anode. This additional layer controls the field distribution within the layers and protects the Alq₃ layer against excess holes. From [10].

ation with that reflected by the anode was optimised (cf. Fig. 11.8 and Sect. 11.1.4) [6].

The construction of a highly-efficient OLED from five organic layers between the two electrodes is illustrated in Fig. 11.9. It contains in particular an EML made of CBP which has been doped with the triplet emitter Ir(ppy)₃ (compare Fig. 11.4). This molecule was originally introduced by Baldo *et al.* [12]. The lifetime of its T_1 state is $< 1 \mu s$, i.e. short. The reason for this is the spin-orbit coupling, which is due to the high nuclear charge ($Z = 77$) of the Ir. The T_1 state of Ir(ppy)₃ is therefore not a pure triplet state and its luminescence quantum yield is high for the same reason. With a doping concentration of $\geq 5\%$, the triplet excitons of CBP are almost completely “harvested” by T_1 states of Ir(ppy)₃, so that these then emit the luminescence (see the term diagram in Fig. 11.9, upper part, and also Chap. 6). This system is therefore referred to as a “luminescence harvesting system”. The additional BCP layer between the doped CBP-EML and the Alq₃ layer serves as a

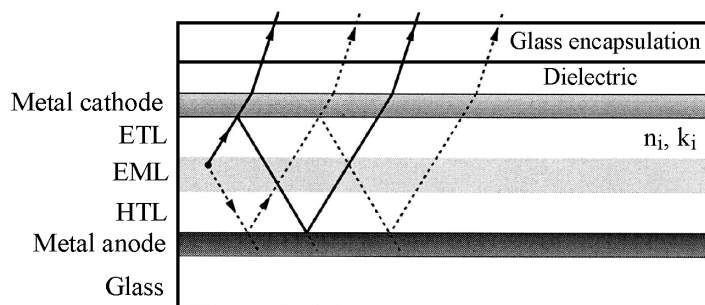


Fig. 11.8 The structure of an OLED with three organic layers and a dielectric cover layer. HTL refers to the hole transport layer, EML to the emission layer, ETL to the electron transport layer. n_i and k_i are the optical constants of the layers (for their definitions, see Sect. 11.2.3). The dielectric is an antireflection layer. After [6, 10].

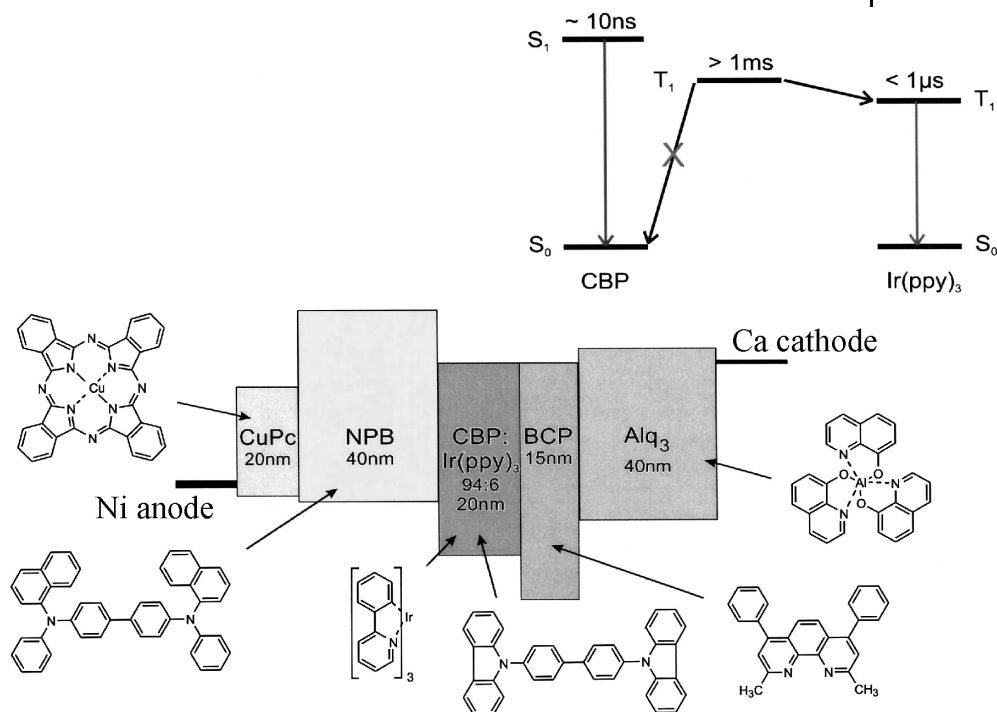


Fig. 11.9 The structure and energy diagram of a high-efficiency “phosphorescent” OLED made with several organic layers. The energy diagram on the upper right shows the non-radiative population of the triplet state of Ir(ppy)_3 , from which the electroluminescence is emitted. The diagram is drawn for an applied voltage of $V = -V_{BI}$. After [10].

buffer layer for the holes (hole blocking layer, HBL). Thus the injection of holes into the Alq_3 layer is prevented. The latter serves only as an ETL, and thus does not emit light in this multilayer OLED design.

The most important electrooptical properties of this and similar highly efficient multilayer OLEDs made of molecular evaporated layers of polymer layers will be discussed in the following subsection on the basis of examples.

11.1.4

Electro-optical Properties

In this final subsection on OLEDs, we wish to show some selected, characteristic experimental results using the example of the multilayer OLEDs of the type shown in Fig. 11.9, and to explain them [10].

Figure 11.10 shows the two most important observables of an OLED, the current density j (left-hand ordinate) and the luminosity L_0 (right-hand ordinate), each in a semilogarithmic plot as a function of the applied voltage V . The structure of this OLED included no reflection-reducing cover layer over the cathode. The anode

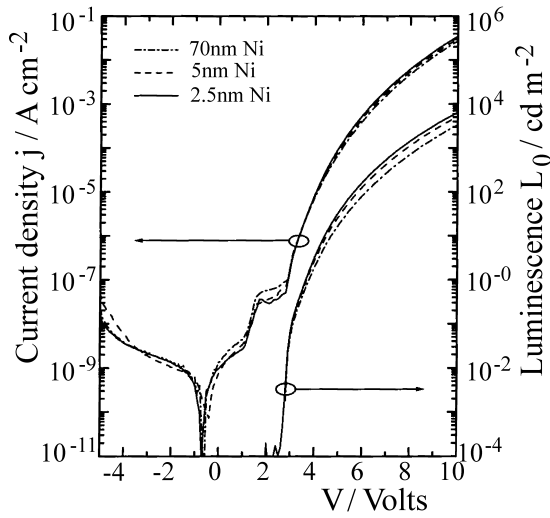


Fig. 11.10 The current density j and the luminosity L_0 of the multilayer OLED of the type shown in Fig. 11.9, both plotted logarithmically as functions of the applied voltage on a linear scale. Three experimental curves for three Ni anodes of differing

thickness are shown. The two thin Ni films are on an Al substrate (see text). The order of the layers as seen from the vacuum is thus Al/Ni/CuPc.... In the case of the two thin Ni films, the Al substrate acts as a reflector. From [10].

was varied: it consisted of a 70 nm thick layer of pure Ni, or of a 5 nm or a 2.5 nm thick Ni film deposited onto a 70 nm Al substrate. The two thinner Ni injection layers are transparent, so that the reflection of the luminescence takes place on the Al substrate beneath them, which has a better reflectivity. The current-voltage characteristics of these three different OLEDs are almost identical diode characteristics. At about 2.5 V, the OLED begins to emit light. The luminosities are however

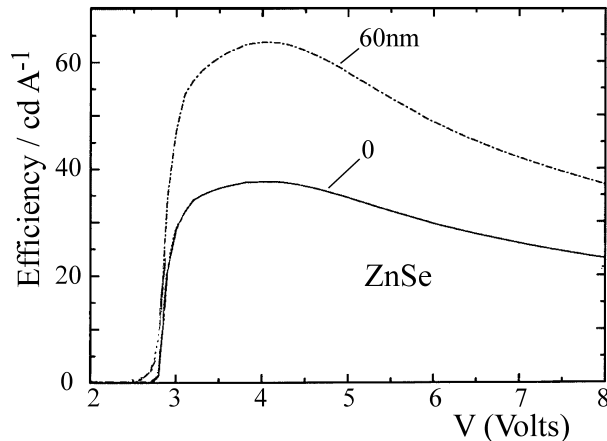


Fig. 11.11 Improvement of the efficiency by means of a ZnSe antireflection layer 60 nm thick. From [10].

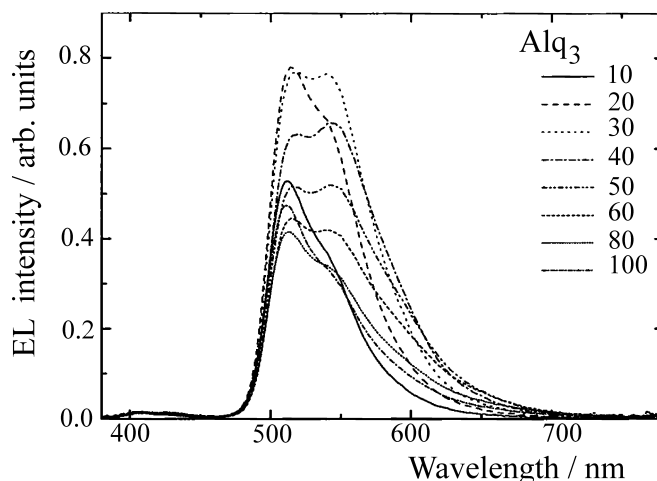


Fig. 11.12 The dependence of the emission spectra on the thickness of the Alq_3 layer in an OLED of the type shown in Fig. 11.9, in which this Alq_3 layer is not the emission layer (see text).

markedly different: at 4 V operating voltage, the luminosity of the OLED with the 2.5 nm Ni anode is around 1.6 times higher than that of the OLED with the pure Ni anode. Such small differences are important for applications and can be discovered only by careful experimentation. A quantitative analysis of the results shown in Fig. 11.10 yields an external efficiency of $L_0/j = 40 \text{ cd/A}$ for the OLED with the 2.5 nm Ni anode.

This already rather high value could be improved further by adding a reflection-reducing ZnSe layer onto the semitransparent cathode. Figure 11.11 shows the efficiency as a function of the operating voltage V , with and without the antireflection layer. With a 60 nm thick ZnSe layer, the efficiency was further increased by about a factor of 2.

As an example of the dependence of the OLED properties on the organic layer thicknesses, Fig. 11.12 gives the emission spectra on variation of the Alq_3 layer thickness between 10 and 100 nm. The width, the shape, and the intensity of the emission lines depend on the thickness of the Alq_3 layer, although all the luminescence is emitted by the Ir(ppy)_3 and the Alq_3 layer itself does not emit light. The thickness of the Alq_3 layer however has a clear-cut influence on the interference effects within the OLED, which as mentioned represents a cavity resonator for the light. In this cavity, the relative and the absolute intensities of the two emission bands of the Ir(ppy)_3 emitter depend on its position within the resonator, on the optical constants of the materials of the resonator, and on the wavelengths of the bands.

The level of quality that has been achieved in OLEDs can be seen also from their radiation characteristics: Fig. 11.13 shows the angular distribution of the emitted intensity in a polar diagram for the multilayer OLED (Figs. 11.9 and 11.10). Its

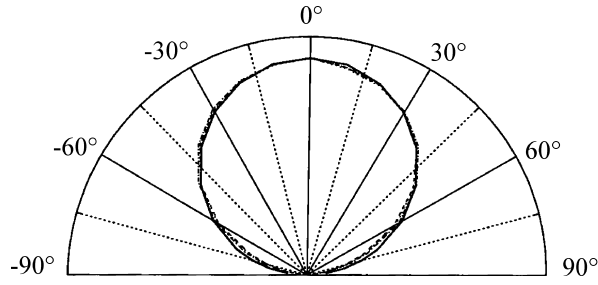


Fig. 11.13 The angular radiation characteristic of the multilayer OLED of the type shown in Fig. 11.9 in comparison to a Lambertian source. The agreement is nearly perfect.

emission characteristic is nearly identical with that of a Lambertian source. Therefore, the viewing angle for OLED display monitors is very large.

For the fabrication of fast-responding displays, the time dependence of the electroluminescence after switching on or off of the operating voltage is the limiting factor. Figure 11.14 shows a typical example for the rise of the luminescence as a function of the time after switching on the voltage (4 V). The electroluminescence signal appears after a well-defined delay time t_D (here ca. 50 μs). It is determined by the charge-carrier mobilities and by the layer thicknesses. (The RC time constant for the entire circuit including the OLED is much shorter and is around 0.1 μs .)

We shall not go further into the details of these experimental results here, but instead refer the reader to the original literature cited. These results are meant to give an example of the current state of development of OLEDs.

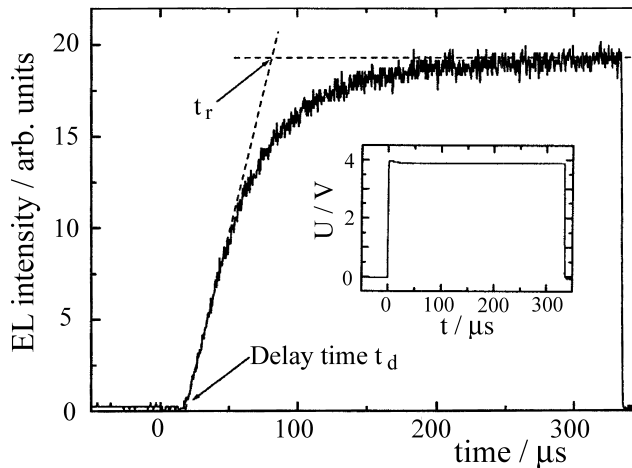


Fig. 11.14 The time dependence of the electroluminescent intensity of the multilayer OLED of the type shown in Fig. 11.9 after switching on the operating voltage V . The delay time t_D is limited by the charge-carrier mobilities and the layer thicknesses: only at the time when the electrons and the holes in the bipolar current within the OLED initially meet up does the device begin to luminesce.

11.2

Photovoltaic Effect: Organic Photovoltaic Cells

The general structure of a photovoltaic cell is similar to that of an OLED (Fig. 11.1): one or more thin organic layers between two metal electrodes with differing work functions. One of the two electrodes must be semitransparent. The photovoltaic effect is, as mentioned, complementary to electroluminescence: the cell is illuminated from the outside through the semitransparent electrode, the light is absorbed in the organic layer or layers, and it then provides electrical power to the closed external circuit. The photovoltaic effect thus involves a charge separation – a charge-transfer process – following photoexcitation. In organic systems, the charge separation into separate electron-hole pairs occurs from photoexcited molecules or from photoexcited Frenkel excitons, that is – not as in solar cells made of inorganic semiconductors – by direct photoexcitation of the electron-hole pairs across the band gap. This is the most significant difference between organic and inorganic solar cells. The lowest excitation energy of the organic molecules is smaller than the band gap, and the binding energy E_B of the Frenkel excitons is of the order of 0.4 ... 1.2 eV in organic systems (see Chap. 6 and Sect. 8.3). At room temperature, $E_B \gg kT$. Thus, the photoexcited molecules or the Frenkel excitons in organic systems cannot be thermally dissociated. Instead, their dissociation takes place either within a single homogeneous organic layer or, with a much higher efficiency, in donor-acceptor systems and there either at the interface between a discrete donor and a discrete acceptor layer, or at the “contacts” between donor and acceptor molecules in a mixed donor-acceptor layer.

The photovoltaic effect in organic solids was observed for the first time on anthracene crystals in 1959 by Kallmann and Pope [22]. For the fabrication of the first organic solar cells, chlorophyll-like low-molecular-mass **dyes** based on porphyrins and phthalocyanines were used [13]. Tang, as early as 1986, with a solar cell containing **two layers** with planar interfaces between copper phthalocyanine (CuPc) and a perylene derivative, was able to demonstrate a power efficiency of nearly 1% [14]. Here, CuPc was the electron donor and the perylene derivative was the electron acceptor. The electron acceptor is also termed the hole donor in this context. With the photoinduced charge transfer from conjugated **polymers** to Fullerene, C_{60} , in 1992, semiconducting polymers also became available for the fabrication of organic solar cells [14]. Along with two-layer systems [16], [17], **mixed systems** were also employed [18]. Here, the electron donor, e.g. the polymer PPV, and the acceptor, C_{60} , are not present as two separate layers, but are mixed within a single layer. With a polythiophene/ C_{60} system, high efficiencies of about 5% were achieved in 2004 [19].

All organic systems are characterised by a high absorption coefficient: at the maximum of the absorption spectrum, it is of the order of 10^5 cm^{-1} (cf. Chap. 6). Organic solar cells therefore contain layers whose thickness is less than the wavelength of light. Making use of multiple reflections, e.g. at mirrored interfaces, the layer thicknesses can be reduced to well under 100 nm. This is another differ-

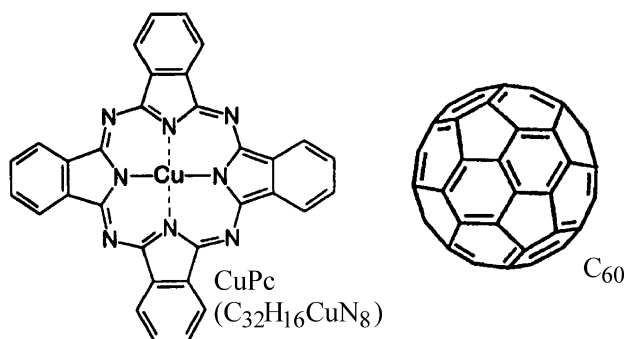


Fig. 11.15 The donor (CuPc) and acceptor (C₆₀) molecules of a typical organic photovoltaic cell.

ence compared to solar cells made with inorganic semiconductors. The small layer thicknesses also permit a low electrical series resistance and a high internal electric field (built-in field), which is due to the difference in the work functions of the two electrodes and has an influence on the drift velocities of the charge carriers (see Sect. 8.4.3).

In the next subsections, we will describe organic solar cells, their physical fundamentals and typical experimental results, using as an example the system CuPc/C₆₀ (Fig. 11.15).

11.2.1

Exciton Dissociation

The decisive mechanism for generating free charge carriers in an organic solar cell is, as mentioned, the dissociation of the strongly bound, photoexcited excitons. In order to be efficient, this dissociation must take place on a time scale which is short compared to all competing processes. These are above all radiative recombination (fluorescence and phosphorescence), non-radiative recombination by phonon creation (heat), and recombination processes at the metal electrodes. Dissociation of the excitons in the donor-acceptor systems of the photovoltaic elements, e.g. in the system CuPc/C₆₀, must therefore be an ultrafast charge transfer. Making use of time-resolved experiments with femtosecond laser pulses, it could be determined in similar systems that this process takes place on a time scale of < 100 fs at the donor-acceptor contact [20]. In comparison to the processes of radiative and non-radiative recombination, which occur on a ns and sub-ns time scale, the dissociation process is thus several orders of magnitude faster.

For the CuPc/C₆₀ system, the dissociation process is explained in Fig. 11.16: the upper part of the figure shows the electron transfer. Following photoexcitation of the donors (CuPc), first the strongly-bound excitons are excited. Their binding energy E_B is about 0.6 eV, and their energy states lie between the HOMO and the LUMO. If in the immediate neighbourhood of the CuPc donor there is an acceptor molecule (C₆₀), then charge transfer takes place from the excited CuPc to the LUMO of the C₆₀ on a 100 fs time scale, as shown above; i.e. extremely fast in com-

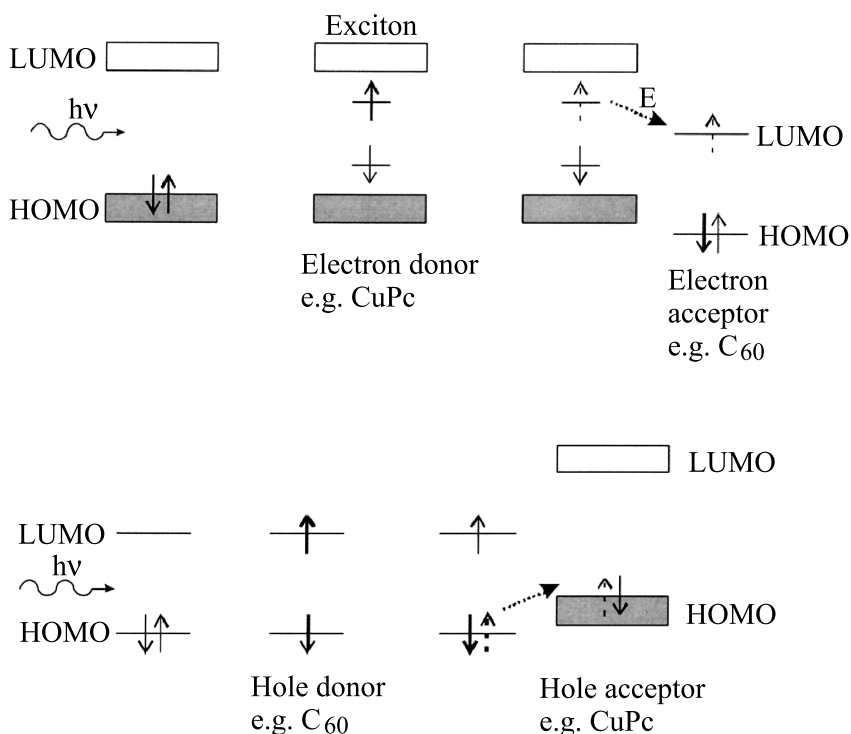


Fig. 11.16 The scheme of photoinduced charge transfer (above: electron transfer; below: hole transfer). Three important steps are: (i) the absorption of radiation by the charge donor; (ii) the generation of an exciton, and (iii) the ultrafast charge transfer (into the LUMO of the electron acceptor or the HOMO of the hole acceptor, with formation of a positive radical ion at the charge donor) on a sub-picosecond time scale. From [21].

parison to the competing processes and therefore with a quantum yield of nearly 100%. Without photoexcitation, no charge transfer can occur. After the dissociation, there are (CuPc)^{•+} radical cations and (C₆₀)^{•-} radical anions, and thus charge carriers: holes in the CuPc and electrons in the C₆₀.

The lower part of Fig. 11.16 shows the mirror-image process of hole transfer. After photoexcitation of the C₆₀, the hole transfer takes place at the interface to the hole acceptor, into the HOMO of CuPc. Here, again, holes are generated in the HOMO of the CuPc and free electrons in the LUMO of the C₆₀. Thus, both photon absorption by C₆₀ as well as by CuPc can contribute to charge-carrier generation (see below).

The energetic condition for photoinduced electron transfer is given by $I_{D^*} - A_A + E_{B,D} < 0$. Here, I_{D^*} is the ionisation energy of the excited donor, A_A the electron affinity of the acceptor, and $E_{B,D}$ is the binding energy of the exciton in the donor. Figure 11.17 shows the energy relationships for the two-layer system CuPc/C₆₀ between an ITO electrode on the CuPc and an Al cathode on the C₆₀ layer (left) as

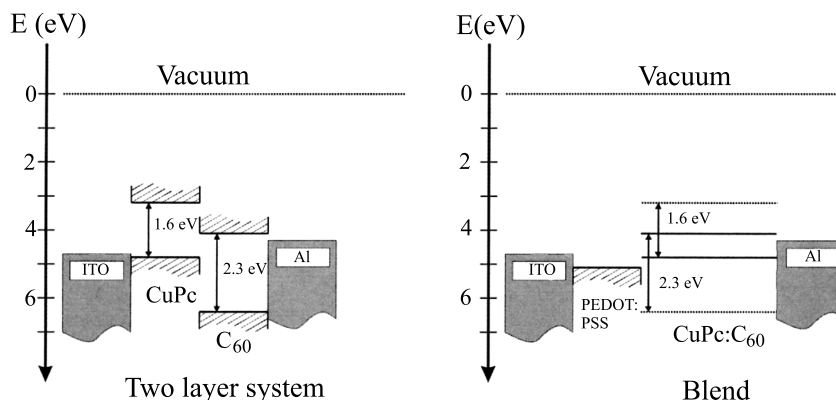


Fig. 11.17 The energy-level diagram for the two-layer system CuPc/C₆₀ (left) between an ITO anode and an aluminium cathode; and for the mixed system CuPc:C₆₀ between an ITO anode with a PEDOT:PSS buffer layer, and an aluminium cathode (right). The level scheme is shown for the case that the layers are not yet in contact. After making contact, the Fermi levels equalise, so that the HOMOs and the LUMOs are bent in such a way that the electrons drift

to the cathode and the holes to the anode. Both types of charge carriers are generated on irradiation. The absorption of the radiation produces excitons which separate into electron-hole pairs in an ultrafast dissociation process: in the layer system at the donor-acceptor layer interface, in the mixed system at the points of contact between the donor and the acceptor molecules. After [21].

well as for the mixed system CuPc:C₆₀ between an ITO-PEDOT:PSS anode and an Al cathode (right). The energy levels are shown before contacting the layers. The decisive quantity for electron transport is the LUMO of C₆₀ and for hole transport, the HOMO of CuPc. On contact, the Fermi levels are equalised, and thus a bending of the HOMO and LUMO levels occurs in such a way that the electrons generated by the dissociation drift to the Al electrode and the holes to the ITO electrode (see Sect. 8.4.3).

11.2.2

Photovoltaic Characteristics

The directly-measurable quantities of a photovoltaic cell are the short-circuit photocurrent I_{sc} (sc = short circuit), the open-circuit voltage V_{oc} (oc = open circuit), the filling factor (FF), the external quantum yield IPCE and the efficiency η_p . Figure 11.18 illustrates these quantities with a current-voltage characteristic curve from a typical photovoltaic cell with and without illumination. The dark current-voltage curve is a typical diode characteristic. With illumination, the characteristic shifts in the negative current range ($I < 0$) due to the photogenerated charge carriers.

When the cell is short circuited ($V = 0$), the **short-circuit photocurrent** I_{sc} flows. With monochromatic illumination, one can obtain from it e.g. the spectral dependence of the charge-carrier generation. The voltage at which the current just ceases to flow is called the **open-circuit voltage** V_{oc} . It is mainly determined by the energy

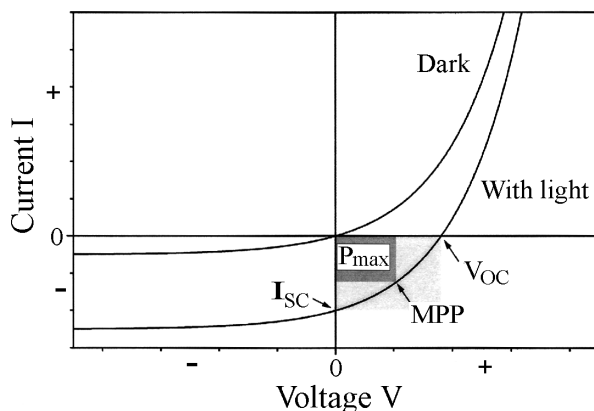


Fig. 11.18 A current-voltage characteristic $I(V)$ from a photovoltaic cell without and with illumination (dark and light characteristics). I_{sc} is the short-circuit photocurrent, V_{oc} the open-circuit voltage, and MPP the maximum-power point, where the power is P_{max} .

levels of the materials used, that is by the HOMOs and the LUMOs of the organic layers and by the work functions of the electrodes. The maximum electric power P_{max} which can be drawn from a photovoltaic cell is given by the maximum power point MPP. The **filling factor FF** is defined as

$$FF = \frac{P_{max}}{V_{oc} I_{sc}} = \frac{V_{MPP} I_{MPP}}{V_{oc} I_{sc}}. \quad (11.6)$$

FF is thus given by the ratio of the dark grey and light grey areas in Fig. 11.18. FF is a measure of the quality of a photovoltaic cell. It is essentially determined by the series resistance of the cell and therefore by the mobilities of the charge carriers in the organic part of the cell. Typical values of the filling factor are 0.75–0.85 for Si cells and 0.5–0.6 for good organic cells.

The **external quantum yield** or **IPCE** (incident photon to current efficiency) is defined as the quotient of the number of incident photons and the number of charge carriers output to the external circuit. It is smaller than the internal quantum yield for conversion of the absorbed photons into charge carriers within the cell, because it takes into account losses due to reflection, recombination, and scattering. In contrast to the internal quantum yield, which can attain values of nearly 100% (see above), the value of the external quantum yield can be measured directly from the short-circuit current density j_{sc} , with $j_{sc} = I_{sc}/A$, where A is the active area of the cell, and the incident light intensity is I_0 . At a given wavelength λ , we have

$$IPCE/\% = \frac{j_{sc}/(\mu A \cdot cm^{-2})}{I_0/(mW \cdot cm^{-2})} \cdot \frac{124}{\lambda/nm}. \quad (11.7)$$

For low intensities, the short-circuit current j_{sc} is proportional to the intensity I_0 . The quantity

$$s(\lambda) = \frac{j_{sc}(\lambda)}{I_0(\lambda)} \quad (11.8)$$

is referred to as the **spectral sensitivity** $s(\lambda)$. It is an important parameter for the specification of a photovoltaic device.

The **efficiency** η_p is the maximum electric power P_{max} per light power P_L ,

$$\eta_p = \frac{P_{max}}{P_L} = \frac{V_{oc} \cdot j_{sc}}{I_0} \cdot FF. \quad (11.9)$$

For a powerful, effective photocell, one thus requires a large filling factor, a high short-circuit current, and a high open-circuit voltage. It is not sufficient to optimise only one of these quantities if one wishes to produce an efficient photovoltaic cell or solar cell.

11.2.3

CuPc/C₆₀ Solar Cells

For the optimisation of a photovoltaic cell or a solar cell, it is necessary to determine the optical constants of all the materials involved, including the electrodes. Only then is it possible to model the cell and in particular the thicknesses of the thin, absorbing layers so that e.g. the photon flux density at

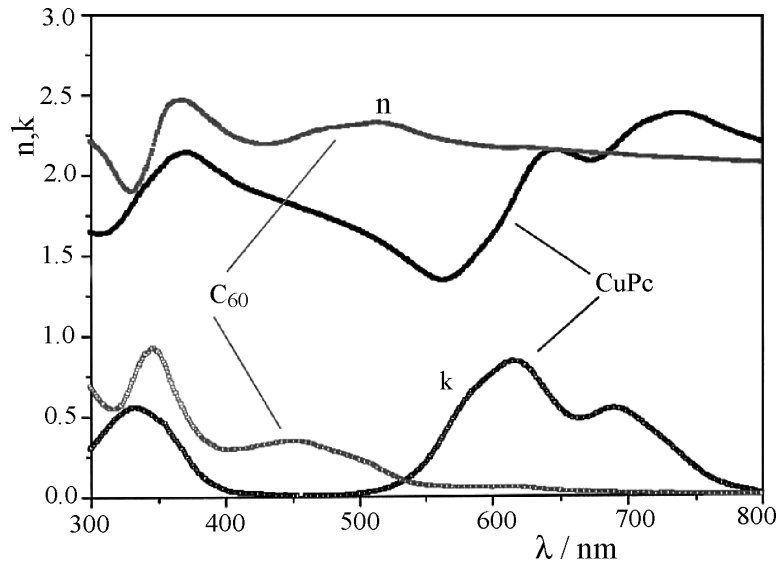


Fig. 11.19 The optical constants of CuPc and C₆₀. $n(\lambda)$ is the index of refraction, $k(\lambda)$ is the absorption index, and λ the wavelength of the light. After [21].

the donor-acceptor interface is maximal [20]. The damped electromagnetic wave $\mathbf{E}(x, t) = \mathbf{E}_0 e^{-i(\tilde{k}_m x - \omega t)}$ is characterised by its frequency ω and its complex wavevector \tilde{k}_m in matter. \tilde{k}_m is found from the wavevector k_0 in vacuum and the complex index of refraction \tilde{n} in the material: $\tilde{k}_m = k_0 \tilde{n}$. Here, $k_0 = 2\pi/\lambda_0$, $\lambda_0 = 2\pi c/\omega$, and

$$\tilde{n} = n - ik. \quad (11.10)$$

n is the real part of the index of refraction, and k is the absorption index. It is related to the absorption coefficient $\alpha(\lambda)$ of the material:

$$\alpha(\lambda) = 4\pi k(\lambda)/\lambda. \quad (11.11)$$

k and n are termed the two **optical constants** of a material.

Figure 11.19 shows these two constants for CuPc and C₆₀ in the visible spectral range [21]. The absorption indices of the two materials exhibit a nearly complementary behaviour over the whole visible spectral range. According to Eq. (11.11), then also the absorption constants $\alpha(\lambda)$ behave in such a way that the entire visible spectral range can be employed for the absorption, if the layer thicknesses are chosen suitably. The order of magnitude of the absorption constants follows directly from Eq. (11.11): for $k = 1$, $\alpha = 2.5 \cdot 10^5 \text{ cm}^{-1}$.

Figure 11.20 shows the calculated normalised photon flux density $Pd(x)$ within the two-layer system ITO/CuPc/C₆₀/Al for two different C₆₀ layer thicknesses and

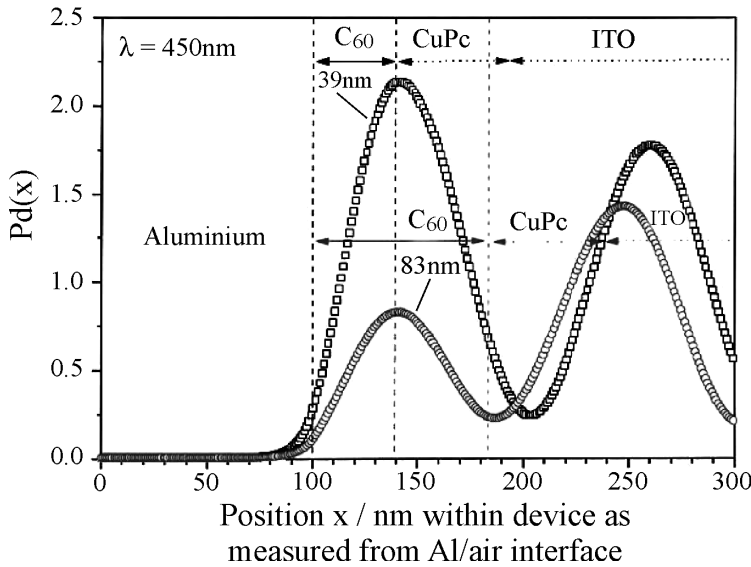


Fig. 11.20 Calculated, normalised photon flux densities $Pd(x)$ as a function of the distance x from the Al/air interface in a CuPc/C₆₀ two-layer photovoltaic cell [ITO (175 nm)/CuPc (57 nm)/C₆₀ (x)/Al (100 nm)] on illumination at the wavelength $\lambda = 450 \text{ nm}$, for two different C₆₀ layer thicknesses, $x = 39 \text{ nm}$ (\square) and

83 nm (\circ). $Pd = 1$ corresponds to the same light intensity as before entering the photocell, $Pd > 1$ means an increase in the intensity through constructive interference, and $Pd < 1$ a reduction through destructive interference. From [21].

for a wavelength of $\lambda = 450$ nm [21]. x is the position within the device, measured from the Al/air interface. $Pd(x)$ is defined as the quotient of the squares of the electric field strength in the material and the electric field strength of the incident light. Values of $Pd > 1$ thus mean an increase in the photon density within the cell in comparison to the photon density of the incident light. This increase is due to constructive interference. In the example shown in Fig. 11.20, it has its **maximum** at the CuPc/ C_{60} interface when the thickness of the C_{60} layer is 39 nm. If the C_{60} layer were about twice as thick, at (83 nm), then the interference **minimum** would be at the interface. Just as in multilayer OLEDs (Sect. 11.1), it is here also of decisive importance to optimise the layer thicknesses, since for the function of photovoltaic cells, the light intensity must be high at the location where the excitons are to be generated in order to create electron-hole pairs nonradiatively. In the case of OLEDs, the layer thicknesses must be optimised in such a way that the electron and hole densities are large at locations where excitons are to be generated which recombine radiatively.

Figure 11.21 compares the experimental current-voltage characteristics without illumination (dark characteristic) and under white-light illumination (light characteristic) for the two-layer system ITO/CuPc (30 nm)/ C_{60} (30 nm)/Al and for

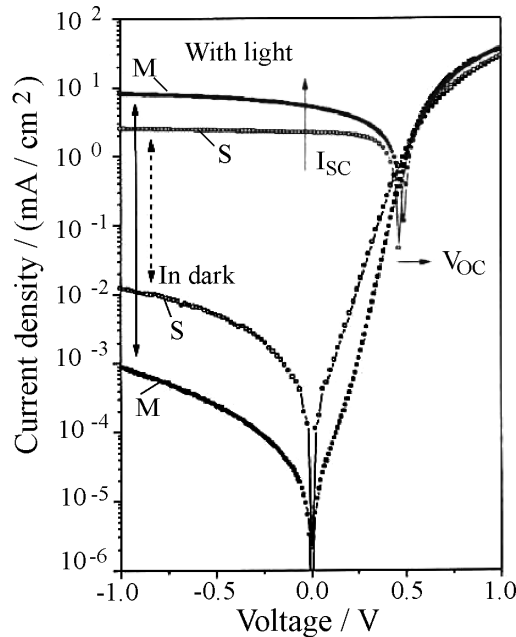


Fig. 11.21 The current-voltage characteristics $j(V)$ in the dark and under white-light illumination (solar cell) of intensity 46 mW/cm^2 , from a two-layer system (S) and a mixed-layer system (M), each consisting of CuPc and C_{60} .
 S: [ITO(113 nm)/CuPc(30 nm)/ C_{60} (30 nm)/Al];
 M: [ITO(30 nm)/PEDOT:PSS(35 nm)/CuPc: C_{60} (80 nm)/Al].
 From [21].

the mixed-layer system ITO/PEDOT:PSS/CuPc:C₆₀(80 nm)/Al. The illumination with an intensity of 46 mW/cm² was produced by a Xe lamp [21]. The comparison of the dark characteristics shows directly that the rectifier effect in the mixed system is more than an order of magnitude stronger than in the layer system. This effect is due to the use of the PEDOT:PSS anode. From the light characteristics, one can also see directly that the short-circuit photocurrent in the mixed system is more than a factor of two higher than in the layer system. This is due to the larger reaction volume for exciton-dissociation processes in the mixed system as compared to the layer system. The open-circuit voltages V_{oc} are 0.47 V for the layer system and 0.49 V for the mixed system.

The quantitative evaluation of these characteristics yields the filling factors FF . They are larger in the mixed system (up to 58%) than in the two-layer system (34%). Together with the white-light intensity of 46 mW/cm², corrected to the solar spectrum, this yields a higher power efficiency, $\eta_p = 1.9\%$ for the CuPc:C₆₀(80 nm) mixed-layer system. In the two-layer system, $\eta_p = 1.2\%$. Compared to the polymer/C₆₀ systems mentioned earlier, the low-molecular systems thus show good photovoltaic properties, which as seen from Eq. (11.9) can be improved still further by increasing the filling factors FF and the open-circuit voltages.

Whether organic solar cells will be commercially employed in the future will be decided by economic aspects. It is certain, however, that their fabrication is simpler and cheaper than that of silicon-based solar cells. Furthermore, they have the advantage that they can be produced on flexible and light substrates. In addition, solar cells based on polymer systems can be fabricated using printing technology. For technical applications, however, their efficiencies must be improved, for example by employing organic materials with higher mobilities. Also, as in the case of the OLEDs, the problems of encapsulation for protection from air and water must be solved, in order to obtain a long operating life.

Literature

Monograph

- M1 K. MÜLLEN and U. SCHERF, eds., *Organic Light-Emitting Devices*, Wiley-VCH (2006)

References

- 1 M. POPE, H. P. KALLMANN and P. MAGNANTE, *J. Chem. Phys.* **38**, 2042 (1963)
- 2 W. HELFRICH and W. G. SCHNEIDER, *Phys. Rev. Lett.* **14**, 229–231 (1965); *J. Chem. Phys.* **44**, 2902–2909 (1966)
- 3 D. F. WILLIAMS and M. SCHADT, *Proc. IEEE*, March 1970, p. 476 (1970)
- 4 C. W. TANG and S. A. VAN SLYKE, *Appl. Phys. Lett.* **51**, 913–915 (1987)
- 5 J. H. BURROUGHES, D. D. C. BRADLEY, A. R. BROWN, R. N. MARKS, K. MACKAY,

- H. FRIEND, P. L. BURNS and A. B. HOLMES, *Nature* **347**, 539–541 (1990)
- 6 H. RIEL, S. KARG, T. BEIERLEIN, B. RUHSTALLER and W. RIESS, *Appl. Phys. Lett.* **82**, 466–468 (2003)
- 7 T. TSUTSUI and K. YAMAMOTO, *Jpn. J. Appl. Phys.* **38**, 2799, 2803 (1999)
- 8 See textbooks on experimental physics, e. g. D. MESCHÉDE, *Gerthsen Physik*, 21. Auflage, Springer Verlag
- 9 N. GREENHAM, R. FRIEND and D. BRADLEY, *Advanced Materials* **6**, 491–494 (1994)
- 10 W. RIESS, T. A. BEIERLEIN and H. RIEL, *phys. stat. sol. (a)* **201**, 1360–1371 (2004)
- 11 H. RIEL, S. KARG, T. BEIERLEIN, W. RIESS and K. NEYTS, *J. Appl. Phys.* **94**, 5290–5296 (2003); H. RIEL, Dissertation, Universität Bayreuth (2002)
- 12 M. BALDO, S. LAMANSKY, P. BURROWS, M. THOMPSON and S. FORREST, *Appl. Phys. Lett.* **75**, 4–6 (1999); C. ADACHI, M. A. BALDO, M. E. THOMPSON and S. R. FORREST, *J. Appl. Phys.*, **90**, 5048 (2001); S. FORREST, *J. Appl. Phys.* **90**, 5048–5051 (2001)
- 13 C. W. TANG and A. C. ALBRECHT, *J. Chem. Phys.* **62**, 2139 (1975)
- 14 C. W. TANG, *Appl. Phys. Lett.* **48**, 183 (1986)
- 15 N. S. SARICIFTCI, L. SMILOWITZ, A. J. HEEGER and F. WUDL, *Science* **258**, 1474 (1992)
- 16 N. S. SARICIFTCI, D. BRAUN, C. ZHANG, V. I. SRDANOV, A. J. HEEGER, G. STUCKY and F. WUDL, *Appl. Phys. Lett.* **62**, 585 (1993)
- 17 J. J. M. HALLS, K. PICHLER, R. H. FRIEND, S. C. MORATTI and A. B. HOLMES, *Appl. Phys. Lett.* **68**, 3120 (1996); *Synth. Met.* **77**, 277 (1996)
- 18 G. YU, J. GAO, J. C. HUMELIN, F. WUDL and A. J. HEEGER, *Science* **270**, 1789 (1995)
- 19 Siemens Information Number CT 200401.001 (2004)
- 20 N. S. SARICIFTCI and A. J. HEEGER, *Int. J. Mod. Phys. B* **8**, 237 (1994)
- 21 TH. STÜBINGER, Dissertation, Universität Bayreuth (2004)
- 22 H. KALLMANN and M. POPE, *J. Chem. Phys.* **30**, 585 (1959)

12

Towards a Molecular Electronics

12.1

What is Molecular Electronics and What Will it Do?

The concept of “molecular electronics” describes an interdisciplinary research area which deals with the questions of how molecular systems and molecular materials might find applications in electronics, photonics, and optoelectronics. We can perhaps define molecular electronics as follows: it includes those processes and phenomena in which organic molecules, individually or in larger numbers, play an active role in the processing, transferring and storage of information [1–5].

Can the present-day electronics based on silicon and related inorganic semiconductor materials, in particular micro- to nanoelectronics, be extended in the not-too-distant future to include electronics with molecules which makes use of molecular functional units and applies their specific molecular properties? Can molecular devices be integrated into circuits based on silicon? The fascinating aspect of such ideas is a conceivable further miniaturisation beyond that possible with inorganic semiconductors, combined with the enormous variability which is offered by organic chemistry, and perhaps also the greater ease of development and fabrication of devices based on such materials.

The goal of molecular physics is to find molecules which can carry out various functions in a molecular electronics, e.g. as switching elements or as conductors (“molecular wires”). The required molecular properties are described in the book by Haken and Wolf, *Molecular Physics and Elements of Quantum Chemistry*, Chap. 22 [1] and here, briefly, in Sect. 12.2. In “**monomolecular**” molecular electronics, one makes use of **single molecules** or isolated functional units to carry out electronic functions. These molecules must be connected to other units of the device. This type of molecular electronics in the narrow sense is not the subject of this book, which is instead concerned with the solid state.

We must rather consider molecular electronics in a wider sense. Every electronic unit whose function is based on a molecular property can be considered to be a molecular-electronics device. Thus, we can define a “**macroscopic**” molecular electronics. A first success story on the road to molecular electronics have been the colour displays based on OLEDs (see Chap. 11). The pixels of these displays consist

of organic molecules which are addressed by an active matrix based on amorphous silicon.

The path to single molecules as switching elements, and thereby from mono-molecular to macroscopic molecular electronics, is long. After finding molecules with the desired properties, one will have to investigate:

- whether the molecules retain their functionality in a crystal or in an ordered film, and whether they can be structured into a suitable device architecture;
- whether they are uniquely addressable while retaining their function;
- whether they can arrange and organise themselves via supermolecular interactions and maintain their locations within the structure;
- how they can be connected to each other and to the outside world;
- and whether they are sufficiently stable and do not give rise to undesirable chemical reactions with their neighbours.

Furthermore, a way must be found to permit the transfer of information between the molecules and the macroscopic world. An information exchange with other molecular-electronic subunits and, via an interface, with conventional electronic devices must be possible. Research in these areas is still in its infancy. In any case, molecular electronics will require molecules as switching elements and as connecting “wires”. These applications are discussed in the next Sects. 12.2 and 12.3.

Light-induced phase transitions apply to the structures of entire crystals or crystallites. These are thus genuinely macroscopic processes. They will be treated in Sect. 12.4.

Finally, aside from the OLEDs and solar cells described in Chap. 11, a series of other devices for “macroscopic” molecular electronics have been demonstrated, in which numbers of organic molecules carry out a specific function. We mention rectifiers, transistors, and storage elements. These will be discussed in Sects. 12.5, 12.6, and 12.7. Instead of a crystal, most of the conceivable applications in molecular electronics will presumably make use of organised and structured films. The preparation and characterisation of such films is therefore particularly important [21, 22]. We shall, however, not treat it in detail here.

12.2

Molecules as Switches, Photochromic Effects

The possibility of modulating a particular physical property of a molecular system with an external stimulus, e.g. with light or with an electric field, is of central importance when one wishes to design molecular or supermolecular devices. Therefore, molecular systems are being sought which can be switched reversibly between different states. They must permit the reversible selection of a physical property of the supermolecular or macroscopic system by means of a directed and rapid stimulus, for example a light pulse.

Such an active system will be referred to here as a **molecular switch**. To recall the molecular physics, we give here a brief example of switches based on polychromic compounds. For more details, we refer to the original literature [6–10].

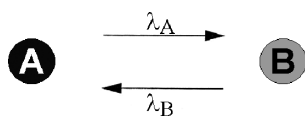


Fig. 12.1 The photochromic effect: a molecule in the configuration A is transformed to configuration B by light of wavelength λ_A . Light of wavelength λ_B brings the molecule back to the initial state A.

What photochromism means is demonstrated in Fig. 12.1: using light of wavelength λ_A or λ_B , a molecule can be reversibly switched back and forth between two configurations A and B. Without light, both configurations are stable. The process should be repeatable through many cycles without ageing. Thus, irreversible light-induced reactions, e.g. the photopolymerisation of diacetylene crystals (see Chap. 3), are *not* considered as possible molecular switches.

A class of substances which fulfills these conditions are the fulgides (Fig. 12.2). Equally useful and frequently investigated are the diaryl-ethenes and the dithienyl-ethenes (Fig. 12.3) and similar molecules. In both cases, the photochromism is based on a bonding isomerisation. Here, a π bond is transformed into a σ bond, accompanied by a ring closure. This leads in solution to a new absorption line

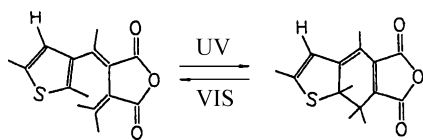


Fig. 12.2 Molecules as switches: the molecule thiophene-fulgide is photochromic and can be switched reversibly by light between the two valence-isomeric configurations shown. The open bond lines denote CH_3 groups.

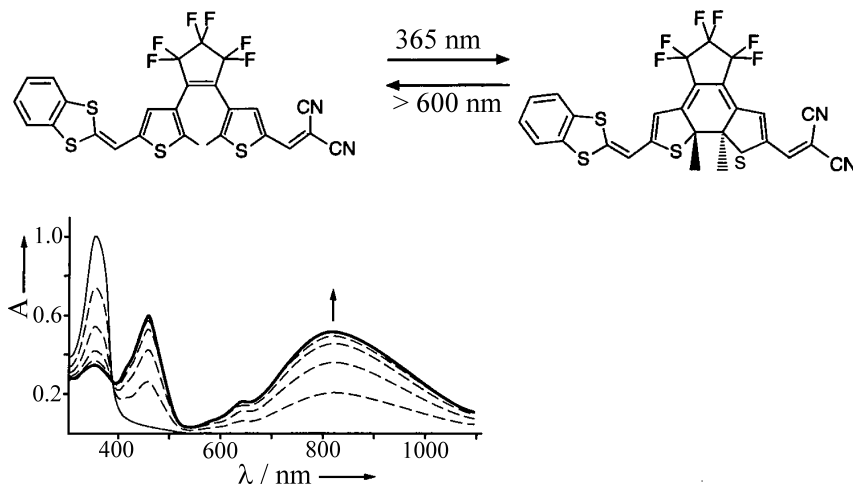


Fig. 12.3 Above: example of a dithienyl-ethene molecule. At the left, the open configuration; at the right, the closed configuration. The open configuration contains two short chains of conjugated double bonds (six carbon atoms each). The closed configuration contains a longer chain of conjugated double bonds

within the molecule (twelve carbon atoms). This results in a new absorption at 800 nm. The lower part of the figure shows the change in the absorption Δ through irradiation of the open configuration with light of $\lambda = 365$ nm. After [8].

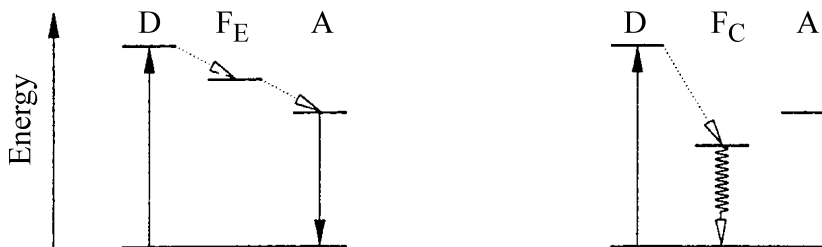
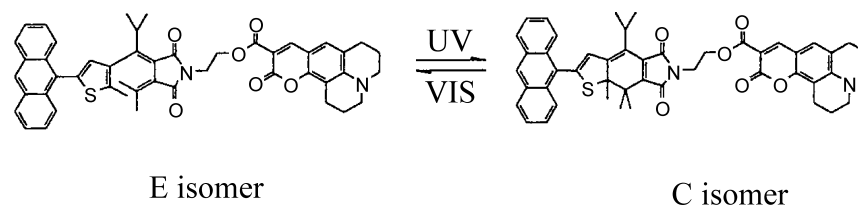


Fig. 12.4 A molecular switch: as the E isomer, the fulgide molecule transfers excitation energy from the donor (an anthryl group) to the acceptor (a coumarin group). The fluorescence of the latter can be observed when state D is optically populated. When the fulgide is switched into its C configuration, its S_1 state acts as a trap and the acceptor cannot be excited. This process can be repeated many times. From [7].

in the visible and thus to a colouration. The process is reversible and is termed “bleaching out”.

The molecules can be varied over a broad range by adding different substituents and changing the structures. The substructure which is responsible for switching is left intact, but the wavelength required for the switching can be modified over a wide range. The switching process is rapid, with times on the order of picoseconds [6]. Figure 12.4 demonstrates that such molecules can carry out a switching function. The supermolecule shown there can pass energy from the donor, an anthryl group (left) to the acceptor coumarin (right) only when the central fulgide molecule is in its open state *E*. In the closed state *C*, it is in a lower-lying S_1 state. In this state it acts as a trap for the excitation energy, which therefore cannot pass from the anthryl to the coumarin, so that the latter does not fluoresce. The fulgide molecule thus serves the function of a molecular switch operated by light. The coumarin fluorescence acts here as an indicator for the switching process [7]. All this refers to the behaviour of the molecules in solution.

In the solid state, things become more difficult. The two photochromic configurations require different amounts of space; in the closed configuration, the molecules are essentially planar. Due to the ring opening, they take on a non-planar configuration. Thus, the photochromic switching process is reversible only when sufficient free volume is available. This is evidently true to a certain extent in amorphous films; in crystals and in regularly-ordered films, in contrast, a reversible photochromic switching is in general not possible, or is possible only within a surface

layer. Only in some special diaryl-ethenes have reversible photochromic reactions been observed in single crystals [9]. Here, the possibility of an application of the photochromic switching process in a crystalline medium opens up.

This discussion is intended to give a brief insight into the field of molecular switches. There are many other examples, in biological systems as well [11]. But reversible molecular switching in the solid state, in single crystals or in the polycrystalline phase, remains problematic and frequently cannot be achieved.

12.3 Molecular Wires

The ability to connect by means of “wiring” is an important precondition for the fabrication of networks of molecular-electronic elements. For this purpose, as well as for the connection to macroscopic devices, one requires connecting wires on a molecular scale. The search for suitable molecular conductors has up to now been more a goal for molecular physics than for solid-state physics. We refer in this connection to Sects. 21.5 and 22.4, as well as 22.5, in the textbook by Haken and Wolf [1].

A reminder of the molecular physics: there are many long chainlike molecules in which electrons, especially π -electrons in conjugated systems, are delocalised over a large region and through many bonds. These delocalised electrons can in principle serve as bridges to transport charges from one end of a molecular functional unit to the other; they thus take on the function of molecular wires. Examples of such molecules are the polyenes, the oligo- and poly-thiophenes, poly-pyrroles and other polymers.

The word “wire” needs a further explanation. In a molecular donor-bridge-acceptor unit, the bridge is in general important, as it can facilitate the transfer of electrons from the donor to the acceptor. In this sense, one often refers to a “molecular wire”, which has the ability to conduct electrons. This terminology can, however, lead us astray, since it plays on an imagined analogy between the path of electrons through organic molecules and their path along a metallic conductor.

The conduction of electrons through single molecules is however in all known cases not an Ohmic conductivity, but rather a tunneling process. Molecular wires facilitate an electron transport relative to the vacuum, but they differ from metallic wires in terms of the order of magnitude as well as the mechanism of the conductivity.

In order to understand the conductivity of single molecules and to be able to use them as wires, one must deal with the problem of the contacts. There must be a mechanism for bringing the charges into the conducting molecule and an understanding of how they are transported along it. We refer the reader in this connection to the corresponding sections in [1] as well as in [2] and [3]. A summary of relevant methods and results can be found in [12].

In searching for molecular wires, one can also consider the highly-conducting crystals from the group of radical-ion salts, the so-called organic metals (cf.

Chap. 9). In these, the electrical conduction is one-dimensional along the organic molecular ions, which are stacked parallel to each other. The conductivity along the stacks can, as pointed out in Chap. 9, have metallic character. In particular, owing to its temperature dependence, it is termed metallic. If one wants to make these “wires” of molecular salts arbitrarily thin, however, one meets up with a physical limit. One-dimensional metallic conductivity becomes unstable at low temperatures. A phase transition occurs through dimerisation, the Peierls transition, leading to an insulating phase (compare Figs. 1.12 and 9.15). This problem was already discussed in detail in Chap. 9, particularly in Sects. 9.5 and 9.6, using as examples the radical salts of DCNQI and of the arenes, respectively.

A single chain of molecules in an organic crystal cannot serve as a “molecular wire”, at least not at low temperatures. One requires at least several stacks which are connected together.

12.4

Light-Induced Phase Transitions

We have already seen that in organic molecular crystals, transitions between energetically nearby phases occur frequently. They can for example be induced by changes in the temperature or by applied pressure. For molecular electronics, such phase transitions could become quite interesting, provided that they can be controlled with light.

A nice example is provided by the radical-ion salts of DCNQI. We have already pointed out in Sect. 9.5 that these include a great variety of salts which differ in terms of the metal ions or in terms of the substituents on DCNQI (CH_3 , I, Br and others), but which have essentially the same crystal structures (Fig. 1.7). The minor differences in the intermolecular spacings and the mutual orientations of the molecules within the crystal can however lead to great differences in their physical properties [13]. In Figs. 9.15 and 12.5, it becomes clear that in contrast to normal Cu dimethyl DCNQI, i.e. h_8 , the deuteration of the six CH_3 protons to d_6 leads to a Peierls transition in the range of ca. 70 K from a metallic to an insulating phase, reversibly and in a very narrow temperature interval. This behaviour could be made use of for a molecular switch. If, as in h_8 , the phase transition is suppressed, then this is because the Cu ions act as bridges between the DCNQI stacks and therefore convert the one-dimensional system into a three-dimensional one (cf. Sect. 9.5).

To give sufficiently strong interstack interactions, a very subtle geometric and energetic overlap of the orbitals of the Cu ions and the CN groups is necessary. It can be reduced by lowering the temperature, owing to the resulting contraction of the crystal, so that a Peierls transition occurs. At still lower temperatures, the interstack interactions can under certain circumstances again become stronger, so that a reentry behaviour is observed, since the overlap continues to change with the continuing contraction on cooling to still lower temperatures. This behaviour is exhibited by the mixtures of non-deuterated (h_8) and deuterated (d_6) material in Fig. 12.5 (compare also [14]).

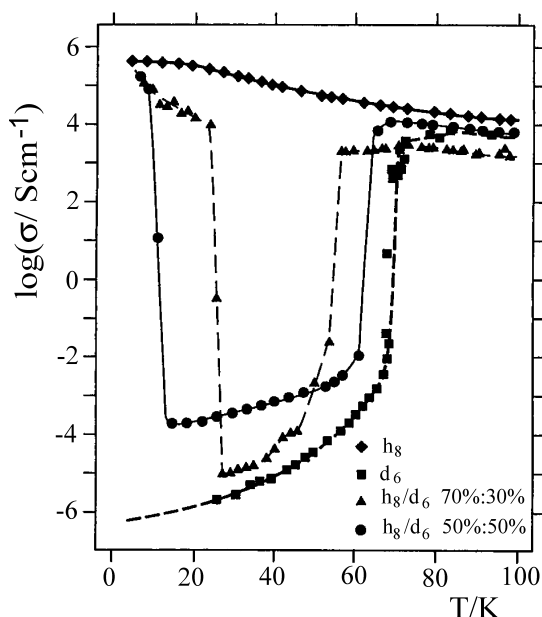


Fig. 12.5 The conductivity σ as a function of the temperature in crystals of $(\text{Me-Me-DCNQI})_2\text{Cu}$. h_8 means non-deuterated, d_6 means that the two CH_3 groups are fully deuterated; also, two mixtures are shown. One can discern the phase transitions in the deuterated substances as well as a hysteresis and re-entry into the conducting phase at low temperatures. After [14] (see also Fig. 9.15).

The Peierls transition can be suppressed by transferring the molecules in the crystal in the neighbourhood of the phase transition to a transient optically-excited state using an intense light pulse, thus changing the geometrical and electronic overlap of the orbitals as compared to the ground state. The Peierls transition can thus be switched off through optical excitation (cf. [15]). In order to detect such an inverse Peierls transition, one must measure the electrical conductivity in the optically-excited state, i.e. in a time window of nanoseconds. This can be accomplished with the method of optically-induced transient electrical conductivity [15]. An experimental setup for this method is shown in Fig. 12.6.

An experimental result is shown in Fig. 12.7. Following excitation with a short light pulse in the temperature range of the upper phase transition (upper part of the figure) or the lower transition (lower part of the figure), the conductivity changes from insulating to highly conducting, varying over orders of magnitude. This high conductivity persists for a time of many 100 nanoseconds, the time in which the crystal relaxes back to the state before the optical excitation. One must of course experimentally verify that the effect is not purely thermal, i.e. that it is not due to warming of the crystal by the light pulse or production of additional charge carriers by the photoeffect (middle part of the figure, far from the phase transition). For details of these questions, see the original literature [14], [15].

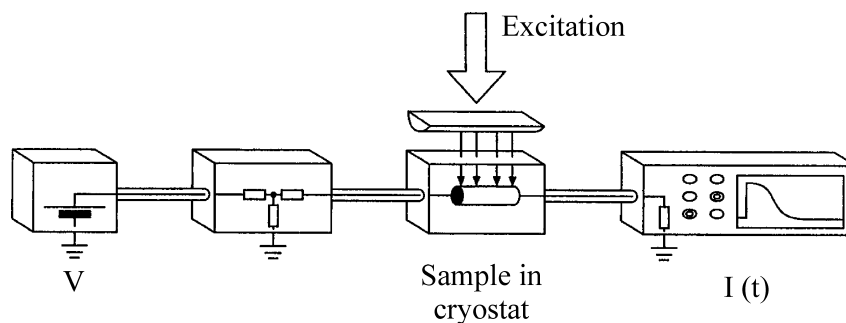


Fig. 12.6 Setup (schematic) for measurements of the optically-induced transient conductivity, OITEL. From [15].

In any case, these experiments show that the organic metals introduced here can also serve as **switches**, in which an optical pulse can be used to change the electrical conductivity of the whole crystal bulk over many orders of magnitude, rapidly and reversibly.

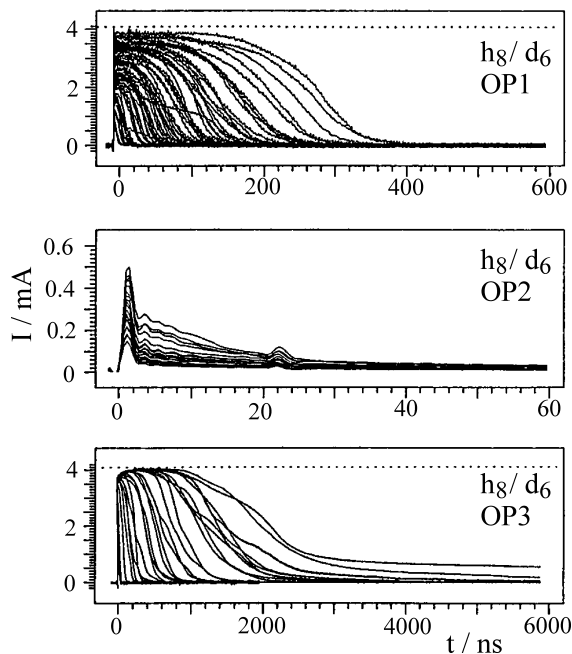


Fig. 12.7 The transient current, i.e. the current as a function of the time following a light pulse in crystals of (Me-Me-DCNQI)₂Cu as a mixture of h₈/d₆ (see Fig. 12.5), following optical excitation with a ps light pulse. The measurement was carried out at three different temperatures in the insulating region: OP1 and OP3 near the phase transition at higher and lower temperatures (reentry, compare

Fig. 12.5); OP2 is a measurement in the non-conducting range between the two phase transitions. While in OP1 and OP3, the high metallic conductivity is restored after a period of ns to ms, in the range of OP2 only short-lived charge carriers are produced, which give rise to a much shorter and smaller conductivity increase. Note the different scales. From [15].

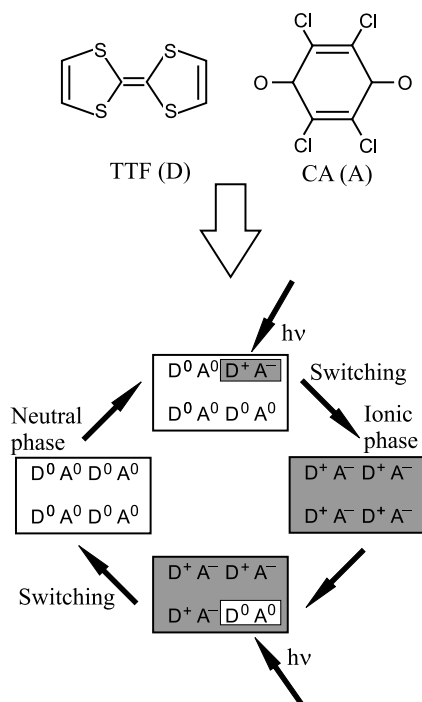


Fig. 12.8 A schematic representation of the phase transition between the neutral (D^0A^0) and the ionic (D^+A^-) phases following population of a local CT excitation, as a series of cooperative CT-interactions in the CT complex crystal TTF/CA (TTF = tetrathio-fulvalene, CA = chloranile). The arrows $h\nu$ refer to irradiation with light pulses to populate the local CT excitation. After [16].

Another example of a photoinduced phase transition is exhibited by the donor-acceptor crystal tetrathio-fulvalene (TTF)-chloranile (CA), see Fig. 12.8. TTF-CA crystallises as quasi-one-dimensional mixed stacks, and thus does not belong in the group of the highly-conducting crystals. It has two characteristic phases: in the high-temperature or “neutral” phase N, charge transfer between the donor (TTF : $D^{+\delta}$) and the acceptor (CA : $A^{-\delta}$) is rather weak, $\delta = 0.3$. In the low-temperature phase, the “ionic” phase I, the charge transfer increases to $\delta = 0.6$. The transition temperature is 82 K. The N–I phase transition is accompanied by a dimerisation within the lattice; it can thus also be regarded as a type of Peierls transition.

Both phase transitions can be triggered by optical pulses [16]. The crystal is excited by an 80 fs pulse in the region of its CT absorption at temperatures between 77 and 105 K, thus near the transition temperature. The phase transition is detected by the changes in the reflection spectrum of the crystal. It is found that the phase transitions occur with a delay of 500 to 800 fs. Evidently it requires this time for an optically-excited local CT state to be converted into a macroscopic “ionic” I or “neutral” N phase. Here, cooperative electron-electron and electron-lattice interactions are presumably the driving forces for these photoinduced phase transitions. This is demonstrated by the dependence of the transition on the light intensity. The phase transitions are shown schematically in Fig. 12.8. For further details of this process, which is still not understood in all its aspects, we refer the reader to the original literature [16].

There are other interesting examples of light-induced phase transitions. For example, H. Matsuzaki *et al.* report on a light-induced transition from the diamagnetic to the paramagnetic phase at room temperature in a radical crystal in *Phys. Rev. Lett.* **91**, 017403 (2003).

12.5

Molecular Rectifiers

An old and still important goal of molecular electronics is the production of a molecular rectifier. This concept refers to molecules or functional units which can be arranged mutually parallel in a molecular architecture and are structured in such a way that an electric current flows through them asymmetrically; their electrical conductivity is thus considerably higher in one direction than in the opposite direction.

Such a molecular functional unit is shown schematically in Fig. 12.9. It contains at one end a molecular group A which serves as an electron acceptor, for example a molecule with CN groups as substituents. At the other end, there is a molecular group D with donor properties, which readily gives up electrons. In between, there is an insulating bridge, which however can be tunneled through by charge carriers. Such a functional group should have a polar character and preferentially conduct current from D to A (in the case of electrons) or *vice versa* for holes.

The problem of making contacts proved to be a difficult obstacle to producing a molecular rectifier, as well as the difficulty of establishing an electrical connection from the contacts to a metal or semiconductor interface. This was finally achieved using the molecule HDQ-3CNQ (hexadecyl-quinolinium-tricyanoquinone-dimethanide) [17] (Fig. 12.10), schematically $T-D^+-\pi-A^-$. Here, D^+ refers to quinolinium, the electron donor, π refers to a π -electron bridge, and A^- stands for tricyanoquinone-dimethanide, the acceptor. T represents the hexadecyl group. It is attached to the actual rectifier molecule so that using the Langmuir-Blodgett technique, monomolecular LB films can be prepared in which the molecules have a unique orientation.

The molecules were laid onto an Al electrode as an LB film in one or in several layers. The counterelectrode, likewise Al, was evaporated in vacuum (Fig. 12.11). Using this arrangement, current-voltage curves were measured and are shown in Fig. 12.12. They do in fact exhibit a rectifier characteristic. From the measured data, an electron transfer rate of $k_{ET} = 0.5$ electrons per molecule and second was calculated.

This, then, demonstrates the possibility of fabricating a unimolecular rectifier. More details can be found in the summary article [18]. Technical applications

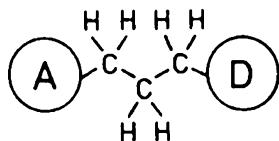


Fig. 12.9 The structure formula of a molecular functional unit which can act as a “molecular rectifier”. A is an electron acceptor group, D a donor group. See also D. HAARER, *Informationstechnik* **34**, 4 (1992).

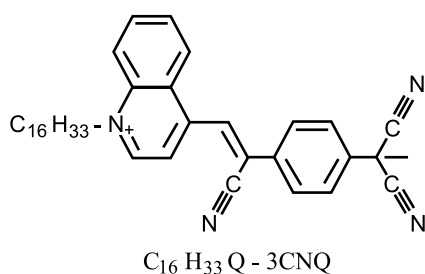


Fig. 12.10 The structure of the molecule HDQ-3CNQ, which can act as a molecular rectifier [17].

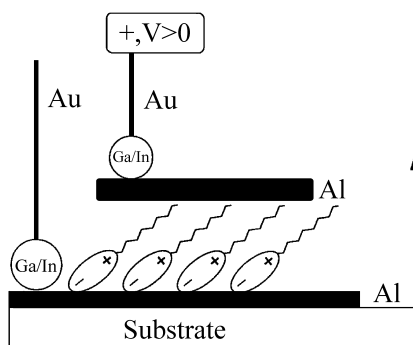


Fig. 12.11 An experimental setup for the measurement of molecular rectification by HDQ-3CNQ. The electrical contact is established using a Ga/In alloy in order to maintain the same electrical conditions at both electrodes. From [17].

would, however, seem to lie in the distant future, not least due to the poor stability of the molecular films with time.

12.6

Molecular Transistors

Perhaps the most important functional unit in micro- and nanoelectronics is the transistor. Research in the area of organic transistors is in a state of rapid development.

In a field-effect transistor (Fig. 12.13), the current which flows through a semiconductor between two electrodes (the source and the drain) can be controlled by

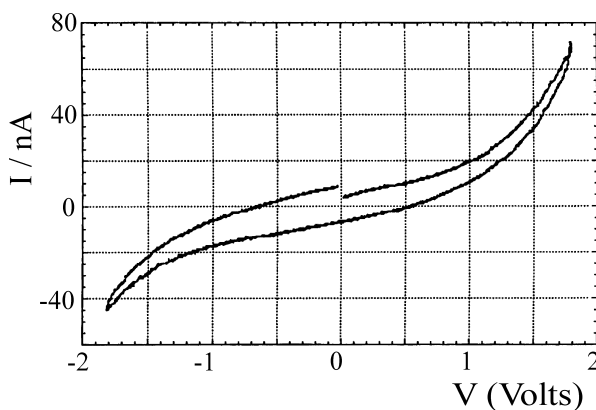


Fig. 12.12 Current-voltage characteristics of a molecular rectifier, corresponding to the arrangement shown in Figs. 12.10 and 12.11. From [17].

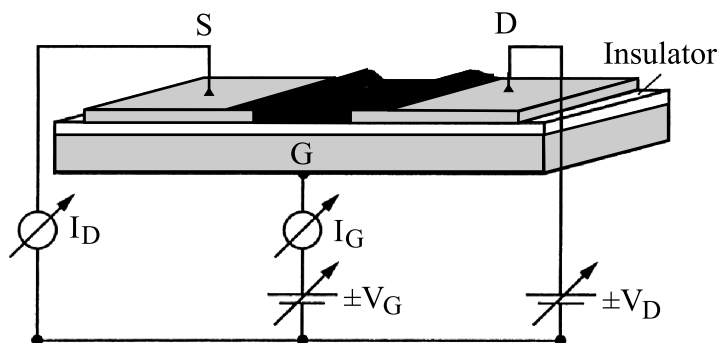


Fig. 12.13 An organic thin-film field-effect transistor, schematic. The current I_D in a weakly semiconducting organic film (black) between two electrodes S (source) and D (drain) can be controlled by the gate (G) voltage V_G . The latter influences charge carriers capacitively in a thin layer of the

semiconductor, the channel. The insulating dielectric (white) can for example be made of SiO_2 or an alkyl-trichlorosilane on a Si substrate, or it can be a polymer film or some other insulating thin organic film. The dimensions are given in the text.

an electric field which is applied to a third electrode (the gate). This electrode is insulated from the semiconductor by a thin dielectric layer, e.g. of SiO_2 . The typical thickness of this layer is 150 nm. Up to 2005, the thinnest reported gate dielectric, a self-arranged monolayer (SAM) of alkyl-trichlorosilane, had a thickness of only 2.5 nm [19]. The gate voltage is applied between the gate and the source or the drain. It leads via the field effect to an accumulation of charge in a very thin, conducting **channel** in the interface layer between the semiconductor and the insulator. For possible applications, the typical channel dimensions (length and width) are in the range of micrometres. The current between the source and the drain electrodes flows through the channel; the strength of the current depends on the gate voltage, which determines the number of free charge carriers in the channel, as well as on the materials property charge-carrier mobility μ . Without an applied gate voltage, no current (or only a very small current) flows between the source and the drain. This is the “off” state. Typical transistor characteristics, giving the drain current as a function of the voltage between the source and the drain with the gate voltage as parameter, are shown in Fig. 12.14. With increasing drain voltage, the current reaches a saturation value. From it, one obtains the on/off ratio.

A field-effect transistor offers in an elegant form the possibility of injecting charge carriers into an insulator or a semiconductor without disturbing the inner balance of the semiconductor, as happens when it is doped with impurities or guest molecules. With this “field-effect doping”, one can vary the number density of the charge carriers over a wide range through small changes in the gate voltage. With the electric field in the dielectric, the current between the source and the drain can therefore be amplified by many orders of magnitude. Thus, very high on/off ratios for the source-drain current can be obtained in switching the gate voltage on or off. In practice, one aims at a value of this ratio of $> 10^6$.

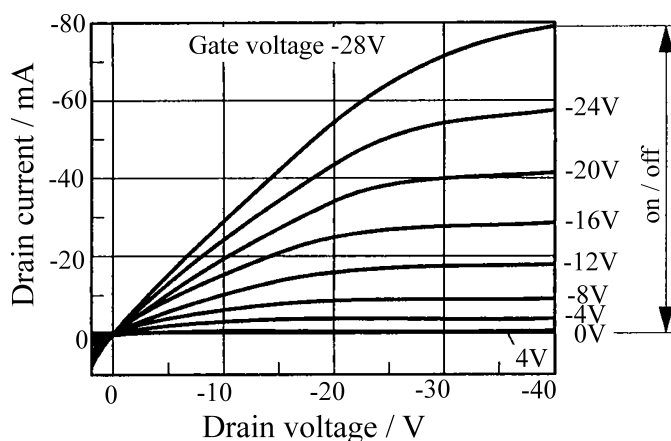


Fig. 12.14 Typical transistor characteristics: the drain current as a function of the drain voltage with the gate voltage as parameter. From the saturation value of the current, the on/off ratio can be determined. These characteristics were measured with a polymer transistor. After [25].

The switching speed of a transistor and thus also the on/off ratio is limited by the transit time of the charge carriers from the source electrode through the channel to the drain electrode. The shorter the channel length L (typically a few μm) and the higher the charge-carrier mobility μ , that is the velocity of the charge carriers per unit of field strength, the faster the switching time of the transistors. For the maximum switching frequency, the expression $f_{\text{max}} \sim \mu \cdot V_{\text{ds}}/L^2$ holds, where V_{ds} is the drain-source voltage. The on/off ratio, i.e. the ratio between the maximum and the minimum current, should be $> 10^6$, so that operation in the MHz range is possible. (With inorganic transistors, one can employ considerably higher frequencies owing to the higher mobilities in these materials.)

The channel length L is limited by the process technology with which one can apply the electrodes at a well-defined, small spacing. The charge-carrier mobility in the organic semiconductors used up to now – these are in particular polymers such as polythiophene or oligothiophene layers, or evaporated films of small molecules such as pentacene – lies in the range between 10^{-2} and about $2 \text{ cm}^2/\text{Vs}$ (compare Figs. 12.15 and 8.27). It depends strongly on the degree of ordering in the organic semiconductor material and on its purity. Most favourable is high-purity, single-crystalline material. In rubrene crystals, values up to $15 \text{ cm}^2/\text{Vs}$ have been achieved [20].

With regard to the question of the applicability of a particular organic material in molecular electronics, the preparation methods play a critical role. Frequently, one is interested in preparing thin or ultrathin films. Organic materials can be deposited as thin films onto a number of different substrates – glass, metal foils, polymer foils. An overview of various possibilities for producing and structuring of such films can be found for example in [21] and [22]. In particular, the gate

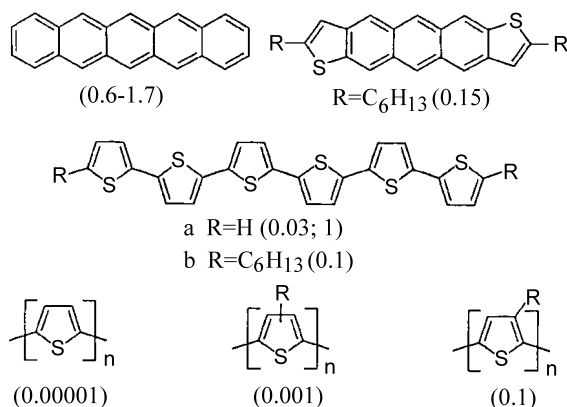


Fig. 12.15 Examples of p-type semiconducting organic materials with high charge-carrier mobilities. (The values in brackets are in $\text{cm}^2\text{V}^{-1}\text{s}^{-1}$ at room temperature. The second value for **a** was measured in a single crystal.) From [33].

dielectric must be as thin as possible, so that with low gate voltages, high charge-carrier densities can be obtained [19].

When the organic semiconductor layer is applied by sputtering, chemisorption (self assembly), or by epitaxy onto the insulator or substrate, then it is important for obtaining high charge-carrier mobilities in the channel between the source and the drain that the molecules lie parallel to each other with their long axes perpendicular to the substrate. In any case, a π stacking parallel to the substrate must be the goal; the mobility of the charge carriers from the source to the drain is then greatest.

In terms of their mobility, inorganic transistors are greatly superior to organic transistors. In crystalline silicon, one can readily achieve hole mobilities of $\mu > 500 \text{ cm}^2/\text{Vs}$. In comparison to transistors fabricated from inorganic semiconductors, organic transistors are therefore much slower (cf. the review articles [21], [23], [24]).

In organic transistors, in the first instance the semiconductor material is naturally organic. As a substrate, one often chooses Si, and as insulation layer, as mentioned, SiO_2 or an organic material. However, the insulation layer and the substrate can also be made with polymers, thus yielding completely organic transistors, which are flexible, robust and small (a few μm). Such “plastic chips” are expected to have interesting applications [21], [25].

For high currents, organic layers with high charge-carrier mobilities are being sought. In polycrystalline layers, the current is limited by the hopping conduction across the grain boundaries. Therefore, layers with large crystallites are favourable. In amorphous layers, there are to be sure no grain boundaries, but here also, as a result of the disordered packing of the molecules in the layer, the mobilities attainable are not very high (see Chap. 8, especially Sect. 8.6).

If we hope to construct organic transistors which are competitive with the inorganic semiconductor materials that are available with fast switching times, then the mobility in the organic materials must be increased. This proved up to now most

successful by orienting molecules with electronically-interacting π systems onto a substrate in the form of extended domains, giving in the limit monocrystalline layers.

The best currently-reported organic field-effect transistors with layered structures make use of oligo- and poly-thiophenes as semiconductor material (Fig. 12.15), as well as pentacene. After preparation by vacuum sublimation, using these materials (at room temperature) it was possible to achieve mobilities up to a few $\text{cm}^2 \text{V}^{-1} \text{s}^{-1}$ with an on/off ratio of 10^6 . This is quite adequate for simpler applications. Improvements are being intensively sought. The search continues with some success also for n (electron)-conducting materials and preparation methods for them, as a complement to the presently predominant p (hole)-conductors. p -conducting transistors are predominant in particular because organic substances are often readily photo-oxidisable; traps for electrons are thus produced and n -type conductivity is suppressed. Progress in fabricating n -channel transistors is summarised in [26].

As materials for hole injection, metals with high work functions such as Au or Ag are particularly suitable. Metals with low work functions such as e.g. Mg are suitable as electron injectors. The work functions of the source and drain electrodes must be adapted to the HOMO and LUMO levels of the organic semiconductor. It has also been possible to make bipolar transistors, that is, transistors with n -type and p -type conductivity. This can be achieved by fabricating heterostructures with two different molecules in the transistor layer. Especially interesting is the light emission from bipolar organic field-effect transistors. Details are given in [27]. The most ambitious goal of these efforts is an electrically-pumped organic laser. For the required population inversion, more molecules must be in the radiative excited state within the active volume than in the ground state.

The ultimate step for achieving higher mobilities is the use of high-purity single crystals as transistor material. With tetracene, pentacene, and rubrene, clear-cut progress has already been made [20]. To be sure, the effective mobilities obtained are still lower than the intrinsic mobilities. This is presumably due to the perturbation of the ideal crystal structure by the attached electrodes. This assumption is supported by the differences in the charge-carrier mobilities found from I/V curves and with the time-of-flight method [28].

The organic transistor certainly has an interesting future. If one wishes to use organic transistors, then ways must be found to connect many transistors into logical units and to make integrated circuits. In fact, there are already commercial products of this type, the so-called plastic chips [25].

In summary, we can say that organic semiconductors have demonstrated sufficiently high mobilities and on/off ratios so that organic transistors can be applied to the production of circuits, at least in certain cases. Their fabrication, even on an industrial scale, is relatively simple [24], [25], and even complex circuits have already been produced. However, major efforts will still be required in order to elucidate the central materials questions and to further improve the chances for applications of organic electronic circuits. A problem of decisive importance is also, as with all applications of organic materials, their stability over longer times.

12.7

Molecular Storage Units

Can molecules in a crystal or in a matrix also be used as storage units for information? Can molecular systems be placed in a stable state which is measurably different from their initial state by light absorption, and can the information thus stored be read out or erased by a second light quantum? Can such a functional unit attain a storage density which approaches the density of the molecules within a solid or on a surface?

An interesting *ansatz* for this problem is based on photochemical or photophysical hole-burning. The principle is explained in Fig. 12.16. The emission as well as the absorption spectra of molecules in a solid matrix, or also in an organic glass, consists in general of relatively broad bands. They are inhomogeneously broadened, since the molecules, which have intrinsically sharp absorption and emission lines, experience a multiplicity of different local environments in the matrix, with different values of the so-called solvent shift. The observed spectrum is then a superposition of many individual sharp lines, and one observes only their broad envelope.

If, by absorption of monochromatic light, i.e. a laser beam, a molecule can be so modified in its structure or in its interaction with the local environment that a laser pulse of the same wavelength cannot – even at a later time – again be absorbed (bleaching), then this molecule is excluded from the ensemble of molecules which contribute to the broad, inhomogeneous absorption line. In the broad absorption band, a “hole” then appears at the position of the individual absorption of the bleached molecule. This forms the basis of the method of **hole-burning** (cf. Fig. 12.17).

A structural modification of a molecule (tautomerism) can lead to hole-burning when the two tautomeric configurations are inequivalent with respect to the lo-

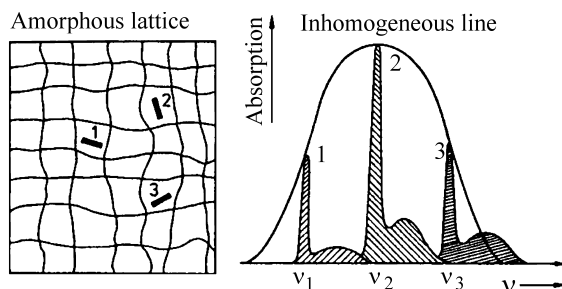


Fig. 12.16 Inhomogeneous broadening of the molecular spectral lines in a matrix as the basis of the process of hole-burning. In an amorphous or disordered lattice, the electronic excitation terms and thus the transition frequencies of a molecule are distributed over a broad range of energies, because the molecules experience different local

environments (left-hand figure). Each individual configuration has a particular absorption spectrum, consisting of the zero-phonon line and the phonon sidebands. The overall absorption results from a superposition of the individual absorptions (right-hand figure). After [34].

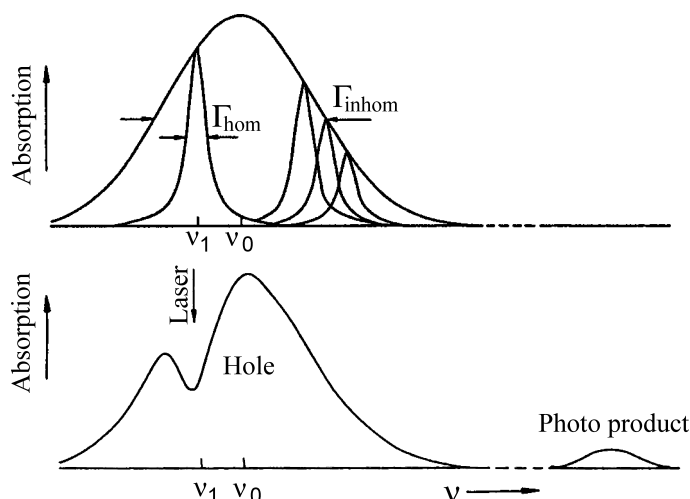


Fig. 12.17 Photochemical hole-burning: within an inhomogeneously-broadened spectral line, narrow-band laser light is applied. A hole is then burned into the broad absorption line, with the spectral width of the laser light or with the homogeneous linewidth Γ_{hom} . The absorption line of the photoproduct appears at some other location within the spectrum. From [35].

cal environment and differ spectrally in terms of different solvent shifts. The first molecule on which this process was successfully investigated was porphyrin in a solid solution (see Fig. 12.18). Here, the hole-burning is based primarily on a change in the molecular structure. It is thus an example of photochemical hole-burning.

Especially in glasses and in solid matrices with strongly inhomogeneously-broadened absorption lines of the molecules within them, one can obtain sharp molecular absorption lines and sharp holes by applying this principle with narrow-band laser light. If the quantum energy of the laser light is varied by small steps, many holes can be burned adjacent to one another in the broad absorption line.

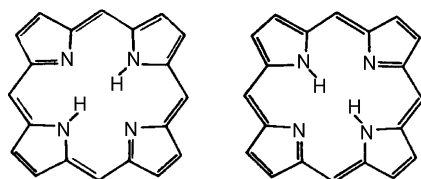


Fig. 12.18 In the molecule porphyrin (free base form), the two central H atoms can be switched back and forth between two configurations by light (photo-isomerisation). This leads in a solid solution to a “hole” in the absorption spectrum. Optical hole-burning with organic molecules was first demonstrated

using this molecule. Only at low temperatures can the isomerisation be produced by light. At room temperature, the central protons are rapidly mobile between the two configurations. This can be demonstrated using proton-spin resonance.

Then one can try to construct an information storage device with a high storage density using molecular systems. In the theoretically most favourable case, at He temperature densities of 10^{12} bits/cm², that is, considerably more than with magneto-optical memories (10^8 bits/cm²), should be achievable. At room temperature, the density would still be 10^{10} bits/cm². A serious problem in constructing such a storage device is, to be sure, its poor long-term stability, in particular when using light irradiation, and also the question of reversibility and the need for low temperatures. More on this subject is given in [29].

Interesting applications of the principle of hole-burning have been reported in optical holography, using biological molecules or polymers [30], [31]. However, we shall not go further into the details of that work, nor of the applications of hole-burning to molecular spectroscopy.

Some other possibilities for data storage using molecular systems have been discussed and investigated, for example the use of photorefractive organic materials [32]. These are materials in which illumination leads to a charge separation; the resulting dipoles can then be oriented by an applied electric field. This finally produces a measurable change in the index of refraction of the material as a function of the illumination intensity. This is promising for applications to holographic data storage.

A practical application is in this case, as with other techniques for information storage using molecular materials, not yet on the horizon. We will therefore not go further into the details.

References

- 1 H. HAKEN and H. C. WOLF, *Molecular Physics and the Fundamentals of Quantum Chemistry*, 2nd ed., Springer, Heidelberg (2004)
- 2 J. JORTNER and M. RATNER (eds.), *Molecular Electronics*, Blackwell Science, Oxford (1997)
- 3 A. AVIRAM and M. RATNER (eds.), *Molecular Electronics*, New York Acad. Sci. (1998)
- 4 J. M. LEHN, *Supramolecular Chemistry*, VCH, Weinheim (1995)
- 5 H. C. WOLF, *Nachr. Chem. Techn. Lab.* **37**, 350 (1989)
- 6 M. HANDSCHUH, M. SEIBOLD, H. PORT and H. C. WOLF, *J. Phys. Chem. A* **101**, 502 (1997)
- 7 J. WALZ, K. ULRICH, H. PORT, H. C. WOLF and F. EFFENBERGER, *Chem. Phys. Lett.* **213**, 321 (1993)
- 8 S. L. GILAT, ST. H. KAWAI and J.-M. LEHN, *Chem. Eur. J.* **1**, 275 (1995)
- 9 M. IRIE, TH. LIFKA and K. UCHIDA, *Mol. Cryst. Liq. Cryst.* **297**, 81 (1997); S. KOBATAKE, T. YAMADA and M. IRIE, *Mol. Cryst. Liq. Cryst.* **344**, 185 (2000); M. IRIE, *Chem. Rev.* **100**, 1685 (2000)
- 10 ST. H. KAWAI, S. L. GILAT, R. PONSINET and J.-M. LEHN, *Chem. Eur. J.* **1**, 285 (1995)
- 11 I. WILLNER and SH. RUBIN, *Angew. Ch.* **108**, 419 (1996)
- 12 D. K. JAMES and J. M. TOUR, *Chem. Mater.* **16**, 4423 (2004); R. L. MC CREERY, *Chem. Mat.* **16**, 4477 (2004)
- 13 J. U. VON SCHÜTZ, D. BAUER, K. SINZGER and H. C. WOLF, *J. Phys. Chem.* **97**, 12030 (1993); K. SINZGER, *J. Am. Chem. Soc.* **115**, 7696 (1993)

- 14 D. GOMÉZ, H. SCHMITT, J. U. VON SCHÜTZ, H. WACHTEL and H. C. WOLF, *J. Chem. Phys.* **104**, 4198 (1996)
- 15 F. O. KARUTZ, J. U. VON SCHÜTZ, H. WACHTEL and H. C. WOLF, *Phys. Rev. Lett.* **81**, 140 (1998)
- 16 S. KOSHIHARA, Y. TAKAHASHI and H. SAKAI, *J. Phys. Chem. B* **103**, 2592, (1999); S. TAKAHASHI, S. KOSHIHARA, F. MINAMI, Y. TOKURA and T. KODA, *Synth. Met.* **103**, 1961 (1999)
- 17 R. M. METZGER and M. P. CAVA, in [3] p. 95; R. M. METZGER *et al.*, *J. Am. Chem. Soc.* **119**, 10460 (1997)
- 18 R. M. METZGER, *Chem. Rev.* **103**, 3803 (2003)
- 19 H. MALIK, H. KLAUK, U. ZSCHIESCHANG, G. SCHMID, C. H. DEHM, M. SCHÜTZ, M. MAISCH and F. EFFENBERGER, *Nature* **431**, 963 (2004)
- 20 R. W. I. DE BOER, M. E. GERSHENSON, A. F. MORPURGO and V. PODZOROV, *phys stat. sol. (a)* **201**, 1302 (2004); V. PODZOROV, S. E. SYSOEV, E. LONGINOVA, V. M. PUDALOV and M. E. GERSHENSON, *Appl. Phys. Lett.* **83**, 3504 (2003)
- 21 G. HOROWITZ, *Adv. Mat.* **10**, 367 (1998); F. GARNIER, G. HOROWITZ, X. PENG and D. FICHO, *Adv. Mat.* **2**, 592 (1990)
- 22 FORREST ST. R., *Nature* **428**, 911 (2004)
- 23 H. E. KATZ and Z. BAO, *J. Phys. Chem. B* **104**, 671 (2000)
- 24 C. D. DIMITRAKOPOULOS and P. R. L. MALEFANT, *Adv. Mater.* **14**, 99 (2002) Review
- 25 W. CLEMENS and W. FIX, *Physik-Journal* **2**, Nr. 2, 31 (2003); H. E. A. HUITEMA *et al.*, *Nature* **414**, 599 (2001)
- 26 C. R. NEWMAN, C. D. FRISBIE, D. A. DE SILVA FILHO, J. L. BREDAS, P. C. EWBANK and K. R. MANN, *Chem. Mater.* **16**, 4436 (2004)
- 27 C. ROST, D. J. GANDLACH, S. KARG and W. RIESS, *J. Appl. Phys.* **95**, 5782 (2004); C. ROST, S. KARG, W. RIESS, M. A. LOI, M. MURGIA and M. MUCCHINI, *Appl. Phys. Lett.* **85**, 1613 (2004); E. J. MEIJER, D. M. DE LEEUW, S. SETAYESH, E. VAN VEENENDAAL, B.-H. HUISMAN, P. W. M. BLOM, J. C. HUMMELEN, U. SCHERF and T.M. KLAPWIJK, *Nature Materials* **2**, 678 (2003)
- 28 R. W. I. DE BOER, M. JOCHENSEN, T. M. KLOPWIJK, A. F. MORPURGO, J. NIEMAX, A. K. TRIPOTHI and J. PFLAUM, *J. Appl. Phys.* **95**, 1196 (2004)
- 29 R. AO, L. KÜMMEL and D. HAARER, *Adv. Mat.* **7**, 495 (1995)
- 30 C. BRÄUCHLE, N. HAMPP and D. OESTERHEIT, in: *Molecular Electronics*, edited by M. Decker (1996)
- 31 U. P. WILD *et al.*, *Pure and Appl. Chem.* **64**, 1335 (1992)
- 32 F. WÜRTHNER, R. WORTMANN and K. MEERHOLZ, *Chem. Phys. Chem.* **3**, 17 (2002)
- 33 F. WÜRTHNER, *Angew. Chem.* **113**, Nr. 6, 1069 (2003)
- 34 J. FRIEDRICH and D. HAARER, *Angew. Chem.* **96**, 96 (1994)
- 35 S. VÖLKER, *Ann. Rev. Phys. Chem.* **40**, 499 (1989)

Appendix: Coloured Plates

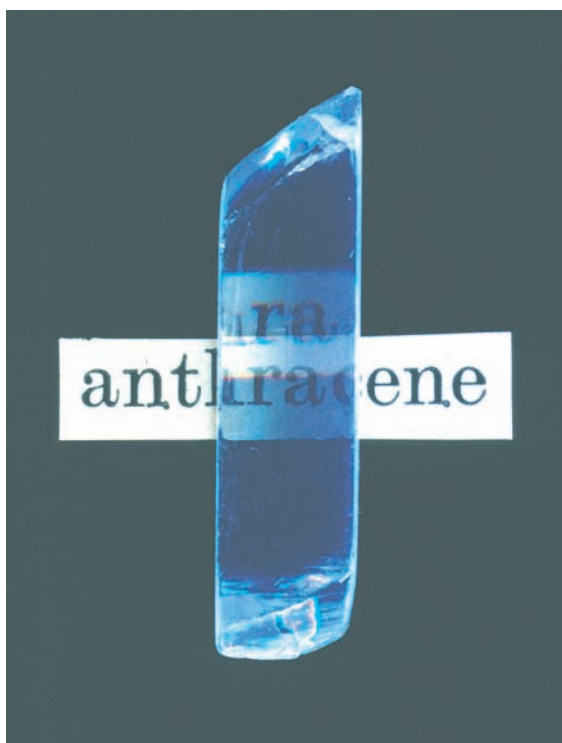


Fig. 1.4 An anthracene single crystal made by the Bridgman crystal-growth method, then cleaved and polished. The length of the crystal is about 2 cm and its thickness 1 cm. Along the direction of sight in this photograph, the c' direction, the strong double refraction is apparent. Image provided by N. Karl [1].

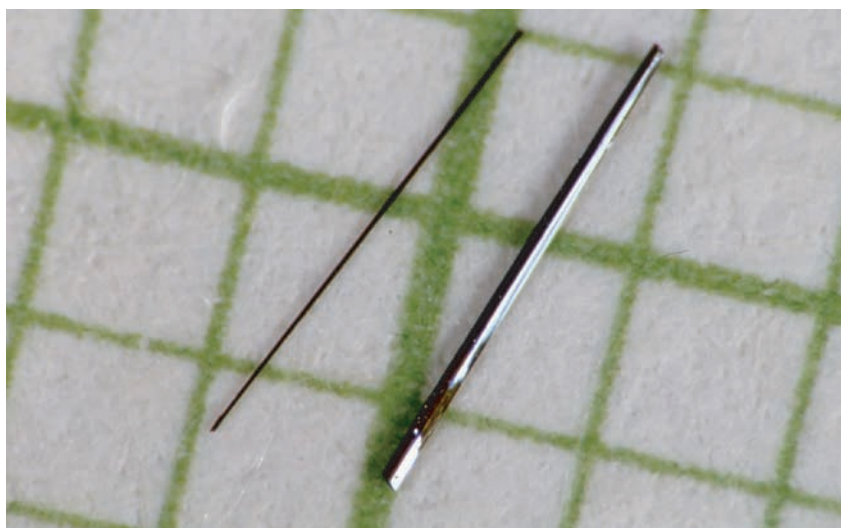


Fig. 1.8 Two crystals of the radical-cation salt (di-fluoranthrene) hexafluorophosphate, $(\text{Fa})_2^+\text{PF}_6^-$. The right surface of the right-hand crystal is orientated in such a way that it reflects the light coming from the light source on the right. Its reflectivity is metallic due to the high conductivity of the crystal parallel to its long axis (**a** axis, see Fig. 2.18). The grid corresponds to 1 mm².

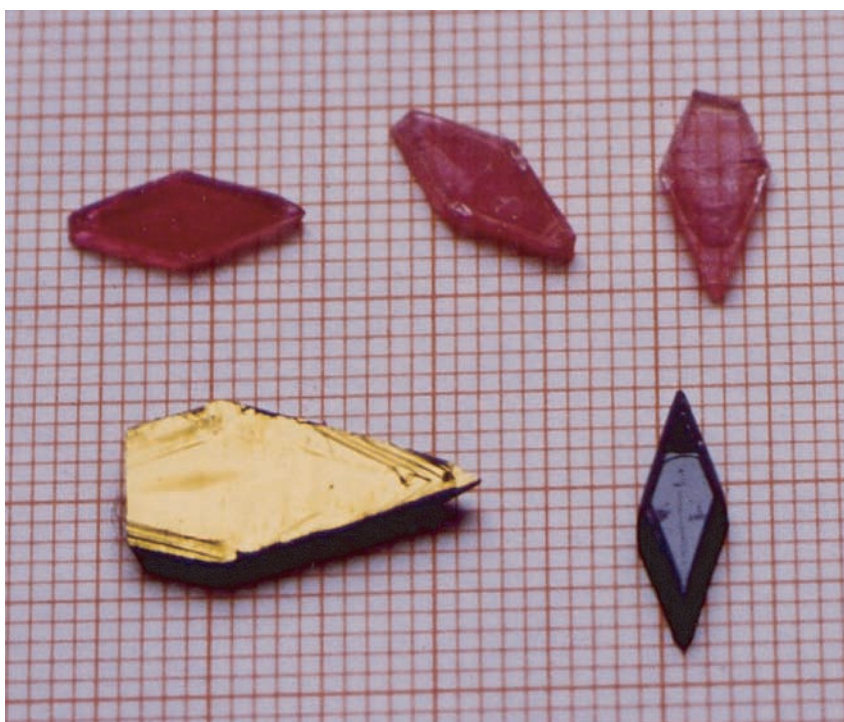


Fig. 1.11 Two single crystals of the polydiacetylene paratoluyyl-sulfonyl-oximethylene-diacetylene (TS6). Above: three monomer crystals, illuminated with linearly polarised light. The polarisation direction of the light is horizontal, and the **b** axis of the polymer chains is oriented parallel to the long axis of the crystals. The polymer crystals strongly reflect light (below left) when the light

is polarised parallel, and almost not at all (below right) when the light is polarised perpendicular to the axis of the polymer chains. The monomer crystals contain only a small fraction of polymerised chains and are thus opaque (above left) when the light is oriented parallel, but transparent (above right) when the light is perpendicular to the **b** axis.

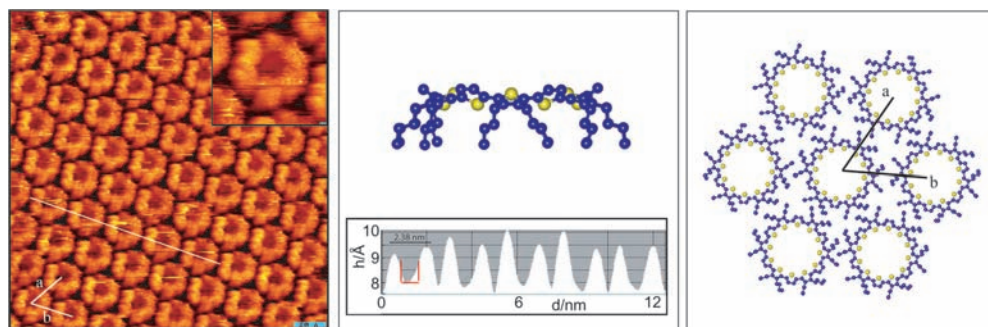


Fig. 2.23 The self organisation of cyclo [12] thiophene (C[12]T) on HOPG (Highly-Oriented Pyrolytic Graphite). The portion shown on the left is an area of $28 \times 28 \text{ nm}^2$. At the upper right in the picture, an enlargement of $6.7 \times 6.7 \text{ nm}^2$ is shown. In the centre section, below, we see an STM scan along the white line

in the left image, passing over seven macrocycles. Above centre: the calculated equilibrium conformation of C[12]T. Right-hand portion of the figure: a computed model of a two-dimensional hexagonal crystal of C[12]T. With the kind permission of Ms. Mena-Osteritz [13].

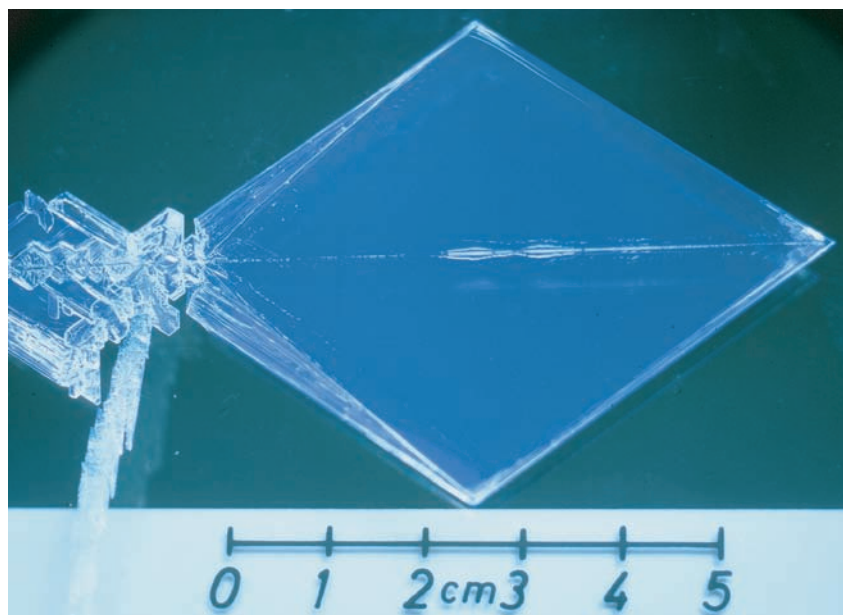


Fig. 3.8 A large anthracene crystal, prepared by plate sublimation under an inert gas atmosphere, $60 \times 60 \text{ mm}$ in size and with a thickness of 0.4 mm . From [3].

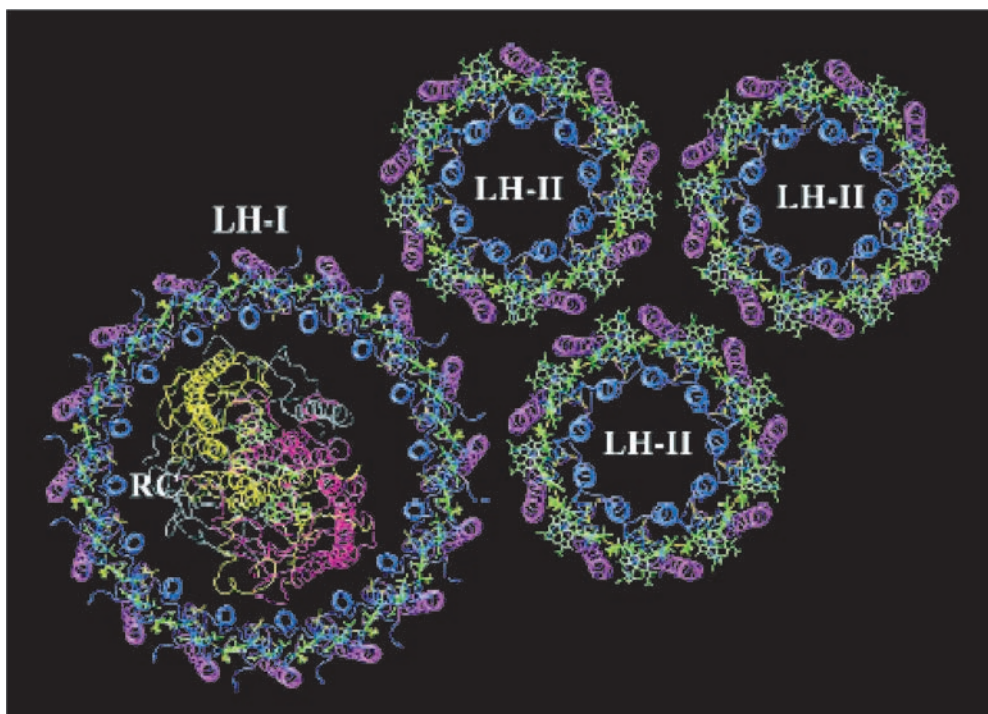


Fig. 6.27 The reaction centre (RC) and the light-harvesting complex in the photosynthetic apparatus of the bacterium *rhodospseudomonas sphaeroides*. Between the helices of the apoproteins (magenta and blue), the bacterio-chlorophyll (BChl) molecules (green and blue) of the light-harvesting complexes

LH II (outer part) and LH I (inner part) are ordered in a ring-shaped and nearly coplanar arrangement. In the middle of LH I is the reaction centre with the two BChl molecules of the “special pair”. From [53]. See also [M6], Sect. 20.7.

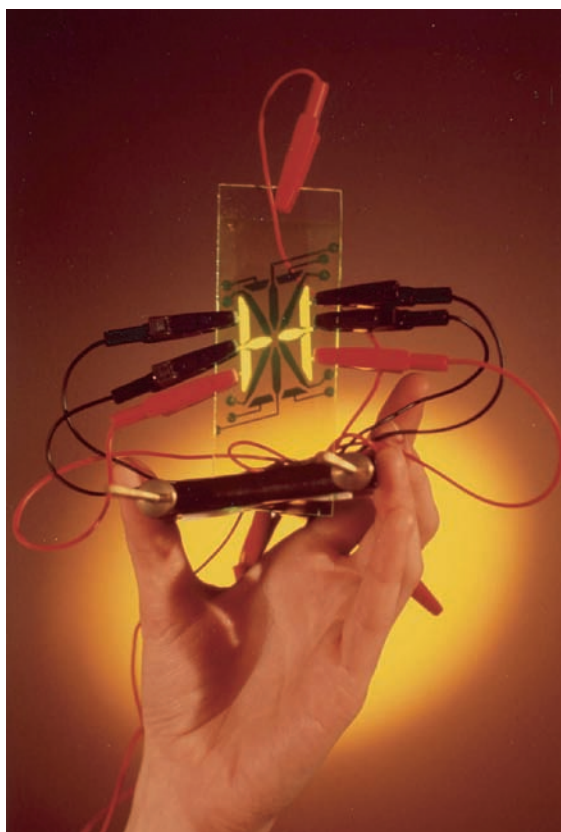


Fig. 11.3 A 16-segment display with a single-layer OLED. The active organic layer is made of PPV. The glass plate serves as substrate and is coated with ITO; the black dots are the contacts for the Al cathodes. The OLED segments which are supplied with a voltage of 4.5 V emit light, the others remain dark. (Prepared by J. Gmeiner, University of Bayreuth, 1992).

Index

- X-traps, 132
 β -(BEDT-TTF) $_2$ I $_3$, 352, 357, 360
 κ -(BEDT-TTF) $_2$ Cu (NCS) $_2$, 352
 κ -(BEDT-TTF) $_2$ Cu[N(CN) $_2$]Br, 352, 359
 κ -(BEDT-TTF) $_2$ Cu[N(CN) $_2$]Cl, 352, 358
 π bond, 3
 π orbitals, 314
 π -electron systems, 226
 π -electrons, 3
 σ bonds, 2
 σ electrons, 3
 d electrons, 324
 d orbitals, 327
 n -octane, 35
 (2,5-Dimethyl-DCNQI) $_2$ Cu $^+$, 322
 (BEDT-TTF) $_2$ SF $_5$ CH $_2$ CF $_2$ SO $_3$, 359
 (DCNQI) $_2$ Cu $^+$, 308
 (Fa) $_2$ PF $_6$, 310, 330
 (Fa) $_2^+$ PF $_6^-$, 34, 43, 308
 (TCNQ) $_3$, 311
 (TMTSF) $_2$ ClO $_4$, 352, 356, 360
 (TMTSF) $_2$ PF $_6$, 352, 353, 356
 (TTF)-chloranile, 399
 (di-fluoranthene)-hexafluorophosphate, 308
 (fluoranthene) $_2^+$ PF $_6^-$, 322
effet solide, solid-state effect, 212
 0,0 transitions, 129
 1,4-dibromo-naphthalene, 39
 2,3-dimethyl naphthalene, 2

 A-PMDA, 323
 A-TCNB, 323
 absorption coefficient, 125, 129
 absorption spectrum, 131, 133
 acceptor, 34, 42, 253
 acridine, 2, 213
 activation barrier, 370
 adiabatic energy gap, 231

 ADMR, 215
 aliphatic compounds, 6
 aliphatic molecules, 34
 alkanes, 35, 41
 alkyl-trichloro-silane, 402
 Alq $_3$, 257, 370, 373
 Alq $_3$ vapour-deposited films, 293
 amphiphilic molecules, 47
 anisotropy, 43, 310, 315, 323, 331, 354, 358
 anisotropy of the mobility, 265
 annihilation, 163, 165, 167
 antenna molecules, 171
 anthracene, 2–4, 6, 10–12, 15, 27, 36, 42, 51, 52, 64, 70, 77, 79, 81, 91, 92, 104, 110, 121, 126, 142, 143, 145, 147, 150, 157, 158, 186, 199, 200, 217, 222, 231, 238, 265, 268, 309
 anthracene-PMDA, 42, 309
 anthracene-pyromellitic acid-dianhydride, 151, 323
 anthracene-TCNB, 40, 309
 anthracene-tetracyano-benzene, 7, 323
 antiferromagnetic ordering, 329, 356
 aromatic compounds, 36
 aromatic hydrocarbons, 2, 6, 35
 aromatic molecules, 34
 atom-atom interactions, 107
 atom-atom potentials, 31, 32, 34, 107
 autoionisation, 241

 Bässler model, 282, 287, 289, 301
 bacterio-chlorophyll, 171
 band conductivity, 219, 263
 band gap, 223, 317
 band model, 228
 band model for a metal, 226
 band structures, 272
 bandwidth, 263, 273
 BAYTRON, 16, 373

- BCP, 373, 376
- BCS theory, 351, 352, 360, 362
- Bechgaard salts, 352, 353, 356
- BEDT-TTF, 357
- benzene, 2, 35, 116
- benzofurane, 2
- benzothiophene, 76
- binary systems, 289
- biphenyl, 110, 186
- bipolar current, 293, 365
- bipolar transistors, 405
- bisethylene-dithiolo-tetrathio-fulvalene, 357
- bonding isomerisation, 393
- Born-Meyer potential, 30
- Bosons, 351
- BPPC, 289
- bridging function, 324
- Bridgman crystal, 5, 66, 82, 411
- Bridgman crystal-growth process, 65
- Brillouin zone, 94
- Buckingham potential, 30
- buffer layer, 377
- built-in field, 248, 370
- C₆₀, 72, 381
 - compounds, 352
 - optical constants, 387
 - superconductors, 362
- carbazole, 2
- carbene, 188
- CBP, 376
- CDW, 330
- channel, 402–404
- characteristic phonons, 111
- charge bridges, 323
- charge equilibrium factor, 372
- charge separation, 238, 381
- charge transfer, 34, 42, 253, 307, 310, 324, 381
- charge transport, 12, 234
- charge transport in disordered organic semiconductors, 279
- charge-carrier concentration, 217, 313, 334
- charge-carrier density, 224, 260
- charge-carrier dissociation, 365
- charge-carrier generation, 303
- charge-carrier mobility, 224, 403, 404
- charge-carrier mobility in organic molecular crystals, 263
- charge-carrier pairs, 365
- charge-carrier traps, 257, 258, 277
- charge-density wave, 315, 320, 321, 329, 330
- charge-density-wave transport, 343
- charge-transfer complexes, 7
- charge-transfer crystals, 2, 3
- charge-transfer excitons, 149, 150, 173, 370
- charge-transfer interactions, 42
- charge-transfer states, 130
- chemical stabilisation, 309
- chemisorption, 49
- Child's law, 246, 247, 260
- chlorophyll, 171
- chromatography, 58
- circuits, 405
- classes of materials, 5
- clathrates, 40
- coherence, 147, 148, 160
 - length, 147, 359, 362
 - of triplet excitons, 188
 - time, 147
- coherent, one-dimensional triplet excitons, 203
- columnar phases, 291
- combination of electrical and optical properties, 365
- commensurate charge-density wave, 319, 334
- compressibility, 105
- conduction band, 130, 226, 263, 314
- conduction electrons, spatial distribution, 343
- conduction-electron spin resonance, 337
- conductivity, 43, 217, 223, 313–315, 323, 330, 331, 354, 358
 - high, 314
 - metallic, 43
 - optical, 336
- conductors, 42
- constant mobility with discrete trapping states, 261
- constant mobility without trapping states, 260
- contact barriers, 229
- contact potential, 247, 248
- contact voltage, 370
- contacting, 400
- contacts, 245, 247, 258, 280, 395
- Cooper pairs, 351, 359, 360
- copper dimethyl-dicyano-quinonediimine, 308
- copper phthalocyanine, 374
- Coulomb bonding, 307
- Coulomb energy, 241
- Coulomb forces, 33
- Coulomb interaction, 54, 136

- Coulomb potential, 241
- Coulomb repulsion, 29
- covalent bonding, 9
- cover layer, 368, 373, 375
- critical magnetic fields, 359
- critical pressure, 352
- critical temperature, 352, 358, 362
- crystal growth, 63
- crystal growth by electrocrystallisation, 67
- crystal growth by sublimation, 63
- crystal growth from solution, 66
- crystal growth from the melt, 65
- crystal structures, 36
- crystalline phase, 291
- crystallographic data, 37, 39
- crystals of high conductivity, 307
- Cs₃C₆₀, 352, 362
- CT absorption, 152
- CT complexes
 - strong, 308, 309
 - weak, 309
- CT excitation, 152
- CT excitons, 150, 152, 153
- CT state, 151
- Cu dimethyl DCNQI, 396
- Cu ions as bridges, 396
- Cu salts of DCNQI, 324
- Cu₂O, 149
- Cu⁺(DCNQI)₂^{•+}, 34, 43
- CuPc, 373, 374
 - optical constants, 387
- CuPc/C₆₀, 382
- current density, 223
- current-voltage characteristic, 246
 - of a solar cell, 384, 388
 - of disordered films, 282
- cyclo [12] thiophene, 49

- D-A complex, 34, 42, 151
- D-A crystal, 6, 67, 151
- D-A systems, 307
- D-A-complex crystals, 39
- dark conductivity, 220, 222
- Davydov bands, 142
- Davydov splitting, 93, 126, 127, 132, 134, 138, 142–144, 154, 195, 198, 272
- DCNQI, 7, 12, 68, 328, 396
- de Haas-van Alphen effect, 358
- deep traps, 228, 231
- defects, 75, 84, 277
- deformation-potential scattering, 270
- DEH, 281
- delayed fluorescence, 127, 139, 160, 163–167, 170

- delocalisation, of electrons, 15
- density of state, 273
- density of trapping states, 259
- density-response function, 319
- depletion zones, 250
- deuteration, 326
- diacetylene, 43, 46, 70
- diagonal disorder, 283
- diaryl-ethenes, 393
- dibenzothiophene, 2
- dibromo-naphthalene, 141, 146, 161, 203
- dichloro-anthracene, 149
- dielectric constant, 344
- dielectric function, 336
- differential tunnel resistance, 361
- diffusion, 90, 113, 120, 158, 235
- diffusion coefficient, 121, 158, 159, 200, 236
- diffusion coefficient of the charge carriers, 341
- diffusion currents, 257
- diffusion length, 159
 - for triplet excitons, 202
- diffusion of triplet excitons, 200
- dimer spectra, 138
- dimerisation, 42
- dimers, 38, 134, 143, 180
- dimethyl-anthracene, 83, 110
- dimethyl-naphthalene, 83, 110
- dipolar disorder, 83, 113
- dipole layer, 250
- dipole moments
 - fluctuating, 27
- dipole-dipole interaction
 - electrical, 25
- discotic liquid crystals, 290
- discotic molecules, 291
- dislocations, 79
- dispersion energy, 29
- dispersion relations, 146
- dispersive forces, 27
- dispersive interactions, 36
- dispersive transport, 237, 289
- displacement current, 235
- display monitors, 366
- dissociation of excitons in photovoltaic cells, 381, 382
- distillation, 58
- dithienyl-ethenes, 393
- donor, 34, 42, 253
- donor-acceptor complexes, 6, 34
- donor-acceptor crystals, 6, 39, 42, 83

- donor-acceptor interface in photovoltaic cells, 381
- dopants, 70, 253
- doping, 253, 277
- doping, C₆₀, 362
- drain, 401
- drift current, 257
- drift velocity, 217, 224, 225, 235
- Drude, 225
- Drude model, 225
- Drude-Lorentz model, 336
- dynamic nuclear-spin polarisation, 212
- dynamics, of triplet states, 178, 209
- EEDOR, 186
- effective band gap, 339
- effective energy gap, 334
- effective mass, 227
- effective mobility, 261, 262
- efficiency, 386
 - OLED, 370, 373
- efficiency of a solar cell, 381, 389
- efficiency of OLED
 - external, 379
- Einstein relation, 236, 275
- ejection, 248
- electrets, 15, 16
- electric-field dependence of the mobility, 269
- electroabsorption, 151
- electrocrystallisation, 67, 324, 357
- electrodes, 365
- electroluminescence, 16, 365
 - time dependence, 380
- electron acceptor, 307
- electron affinity, 34, 42, 229, 247, 307, 370
- electron distribution, 3
- electron donor, 307
- electron injection, 405
- electron spin polarisation (OEP), 204
- electron transport materials, 370
- electron-electron double resonance, 186
- electron-hole pair, 229
- electron-hole separation, 240
- electron-phonon coupling, 271, 321, 362
- electron-phonon interaction, 360
- electron-phonon scattering, 315
- electron-spin resonance, 177, 178
- electronic polarisation, 229, 231
- electronics with molecules, 391
- electrons in Alq₃, 301
- electrons in PPV, 301
- electrooptics, 366
- electroreflection, 151
- emission layers, OLED, 373
- emission spectra of a multilayer OLED, 379
- encapsulation, 368, 373
- ENDOR, 77
- energetically distributed trapping states, 297
- energy bands for electrons and holes, 273
- energy conduction, 125, 126, 140, 141, 148, 156, 159
- energy exchange, 126, 140, 141, 148, 159
- energy gap, 247, 320, 331, 360
- energy transfer, 125, 126, 140, 141, 148, 159
- energy transport, 126, 140, 141, 148, 159
- energy-level diagram, OLED, 369
- epitaxy, 50, 71
- equation of continuity, 258
- ESR, Electron-Spin Resonance, 177, 314, 328
- ESR line, 341, 343
- ESR linewidth, 196
- ESR powder spectra, 191
- ESR spectrum, 340
- ET salts, 352
- ET superconductors, 357
- evaporated films, 366
- evaporation of films, 280
- excess charge carrier bands, 272
- excess charge carriers, 228, 234, 245, 255, 257
- exchange integral, 229
- exchange interaction, 139, 143, 161
- exchange narrowing, 196
- exchange of energy, 125, 126
- excimer excitons, 156
- excimers, 38, 154–156
- excitation spectra, 220
- excitation spectroscopy, 125, 139, 161
- excitation spectrum of photoconduction, 279
- excited states, 130
 - optical, 127
- exciton annihilation, 163, 165, 167, 168
- exciton band, 142
- exciton band structure, 146
- exciton coherence, 79
- exciton diffusion, 158
- exciton dispersion relations, 145
- exciton dissociation, 244, 382
- exciton fission, 168, 169
- exciton motion, 126
- exciton states, 83
- exciton-exciton annihilation, 244
- exciton-phonon interaction, 147

- excitonic bands, 134, 139
- excitonic processes, 163
- excitonic superconductor, 352
- excitons, 13, 77–79, 90, 125, 126, 140, 141, 145, 148, 158, 159, 173
- excitons, OLED, 369
- exhaustion, 254
- exponential trap distribution, 297
- external quantum yield of a solar cell, 385
- fatty acids, 47
- Fermi energy, 227, 316
- Fermi level, 248, 258
- Fermi sphere, 226, 227
- Fermi statistics, 253
- Fermi surface, 226, 227
- Fermi velocity, 227
- Fermi wavevector, 315, 316
- field dependence of the hopping rate, 287
- field emission, 252
- field-dependent conductivity, 344
- field-dependent mobility, 258, 285
- field-effect doping, 402
- field-effect transistor, 401
- filling factor, 385, 389
- films, 8, 47, 71, 403
 - structuring, 403
- fine structure, 180, 199
- fine structure of the ESR spectrum, 178
- fine-structure constants, 178, 184, 186, 188, 191, 195, 199
- fission, 168
- fluctuating dipole moments, 27, 28
- fluctuations, 330
- fluctuations at the Peierls transition, 334, 338
- fluctuations between the metallic and the semiconducting states, 334
- fluoranthene, 2, 12, 68
- fluoranthene salts, 330
- fluorene, 2, 213
- fluorescence, 128, 129, 138, 169, 220
- fluorescence spectrum, 62, 131
- force constants, 108
- forces, 25
 - intermolecular, 4, 25
 - intramolecular, 4, 25
- foreign molecules, 75
- free charge carriers, 223
- Frenkel defects, 78
- Frenkel excitons, 14, 15, 51, 126, 139, 150
 - photovoltaics, 381
- frequency dependence of the conductivity, 344
- fulgides, 393
- Fullerene, 361
- Fullerene compounds, 362
- functional unit, 401, 406
- furane, 2
- gate, 402
- gate dielectric, 402
- Gaussian distribution function, 233
- Gaussian distribution of traps, 299
- Gaussian transport, 236
- Ge, 149
- geminate pair recombination, 241
- generation of charge carriers, 234
- glow emission, 251
- gradient sublimation, 58, 59, 65
- grain boundaries, 82
- group velocity, 273
- guest, 75
- guest molecules, 75
- Hückel LCAO-MO theory, 18, 19, 22
- Hückel model, 16
- HBL, 377
- HDQ-3CNQ, 400
- heat of sublimation, 32, 52
- Heitler-London model, 17
- herringbone pattern, 35
- heterocyclic compounds, 2
- hexamethyl-benzene, 37, 141
- HHTT, 291
- high dark conductivity, 308
- hindered rotation, 113
- historical remarks, 220, 366
- hole injection, 405
- hole transport materials, 370
- hole-burning, 406
- holes, 226
- holes in PPV derivatives, 301
- holographic data storage, 408
- holography, 408
- HOMO, 225, 229, 273
- hopping conductivity, 219, 263
- hopping frequency, 197
- hopping mechanism, 277
- hopping model, 228
- hopping processes, 147, 158
- hopping rate, 283
- hopping time, 148
- hopping transport, 282
- hot band spectroscopy, 145
- hot electrons, 241
- hybrid crystals, 51
- hybrid orbital, 18

- hydrogen bonds, 34
- hydrogen molecular ion, 16
- hydrogen molecule, 17
- hyperfine coupling, 342, 343
- hyperfine coupling of the conduction electrons, 341
- hyperfine interaction, 186, 202
- hyperfine structure, 198
- identification of traps and other scattering centres, 265
- image force, 250
- image-charge potential, 251
- impurities, 70, 75, 84, 232, 277
- inclusion crystals, 40
- incommensurate charge-density waves, 319
- indium-tin oxide, 368
- inductive forces, 26
- infrared absorption, 100
- injection, 217, 234, 247, 248, 292
 - OLED, 369
- injection barrier, 223, 249
- injection layers, OLED, 373
- injection limiting, 300
- injection of electrons, 250
- injection-limited currents, 250
- inorganic semiconductors, 122, 173
- inorganic-organic hybrid crystals, 51
- insulators, 42, 43, 217
- integrated circuits, 16
- intercalates, 255
- interfaces, 365
- interference, OLED, 373
- intermolecular forces, 4, 25
- intermolecular potentials, 30
- internal conversion, 129
- internal electric field, 365
- internal field, 247, 255
- internal photoeffect, 238
- inter-stack interactions, 327, 329
- intersystem crossing, 129, 178, 205
- intersystem crossing rate, 129
- intramolecular forces, 4, 25
- intramolecular relaxation, 241
- intrinsic charge carriers, 255
- intrinsic fluorescence, 132
- intrinsic photo-generation, 239
- inverse Peierls transition, 397
- ionic bonding, 9
- ionisation energy, 307, 370
- ionisation limit, 129
- ionisation potential, 42, 247
- Ir(ppy)₃, 373, 376
- island structures, 50
- isotope effect, 360
- isotopic mixed crystals, 75, 138
 - naphthalene – isotopic mixed crystals, 192
- ITO, 368
- Jahn-Teller instability, 188
- Josephson effect, 360
- K₃C₆₀, 352
- Lambertian source, 371
- Langmuir balance, 48
- Langmuir-Blodgett films, 36, 47–49, 72
- Langmuir-Blodgett technique, 400
- lattice distortion, 315, 320, 321
- lattice dynamics, 107
- lattice energy, 25
- lattice periodicity, 233
- lattice potential, 107
- lattice relaxation, 231
- layer-thickness dependence of the current density, 301
- layered structure, 35
- lead halides, 51
- Lennard-Jones potential, 30
- libration, 89, 93
- lifting of degeneracies, 134
- light current, 371
- light emission from bipolar field-effect transistors, 405
- light yield, OLED, 371
- light-induced phase transitions, 329, 392, 396, 400
- linewidths, 133
- local field, 259
- long-term stability, 408
- luminosity, 367, 371
- luminosity of an OLED, 365
- LUMO, 225, 229, 273
- Madelung energy, 307
- magnetic dipole-dipole coupling, 114, 181, 183
- magnetic dipole-dipole interaction, 214
- magnetic field oscillations, 358
- magnetic quantum number, 181, 190
- magnetic susceptibility, 314, 325, 328, 330, 337, 359
- mean free path, 264, 276
- mean square displacement, 236
- MeH-PPV, 373
- Meissner phase, 359

- melting point, 28
- mesogenic phase, 291
- mesogenic systems, 290
- metal-semiconductor phase transition, 315
- metallic bonding, 9
- metallic semiconductor, 326
- microwave-induced delayed phosphorescence, 207
- mini-exciton ESR, 193, 198
- mini-excitons, 134, 136, 139, 172, 192, 195, 199
- mixed crystals, 70
- mixed stacking, 309
- mixed systems, photovoltaic cells, 381
- mobilities in disordered films, 281
- mobility, 217, 224, 234, 236, 246, 258, 263, 275, 313, 404, 405
 - OLED, 370, 380
- mobility in single crystals, 217
- mobility in vapour-deposited films, 218
- mobility tensor, 268, 275
- model for the space-charge-limited currents, 257
- model of the Peierls transition, 315
- molecular conductors (wires), 395
- molecular crystals, 5, 89–91, 93, 104, 107, 110, 113
- molecular devices, 391
- molecular dynamics, 89
- molecular electronics, 16, 391
 - macroscopic, 391
 - monomolecular, 391
- molecular functional unit, 400
- molecular orbitals, 272
- molecular rectifier, 400
- molecular sponges, 42
- molecular storage units, 406
- molecular structures, 2
- molecular switch, 392
- molecular vibrations, 89
- molecular-beam epitaxy, 49
- motional narrowing, 196, 198, 341
- Mott-Gurney equation, 260
- MPMP, 218, 285, 287
- multilayer OLED, 373, 376
- nanotechnology, 366
- naphthalene, 2, 22, 34, 36, 95, 100, 143, 191, 199, 265, 268, 269
 - energy bands, 273
 - isotopic mixed crystals, 179, 205
- neutral contacts, 249
- neutron diffraction, 90
- neutron scattering, 97
- NMR spectrum, 113
- noise voltage, 344
- non-diagonal disorder, 283
- non-radiative recombination, 370, 374
- nonpolar molecules, 34
- nonpolar organic solids, 10
- normal modes, 91
- normal vibrations, 92
- NPB, 370, 373
- nuclear magnetic resonance, 113
- nuclear spin temperature, 213
- nuclear spin-lattice relaxation, 123, 200
- Ohm's law, 225, 228
- Ohmic contact, 245
- Ohmic currents, 253
- on/off ratio, 405
 - transistor, 402
- one-dimensional bands, 314
- one-dimensional behaviour, 43
- one-dimensional metal, 331
- one-dimensional metallic systems, 315, 318
- one-dimensionality, 330
- Onsager model, 242
- open-circuit voltage, 384, 389
- operating life, 367
- optical detection of magnetic resonance (ODMR), 178, 186–188, 203, 212
- optical double resonance, 212
- optical emptying of traps, 278
- optical energy gap, 231
- optical nuclear-spin polarisation, 212
- optical pumping, 212
- optical spin polarisation, 204
- optically-induced charge-carrier injection, 244
- optically-induced transient electrical conductivity, 397
- optimisation of a photovoltaic cell, 386
- orbitals, 16
- organic light-emitting diode (OLED), 293, 365, 366
- OLED principle, 368
- organic metals, 311, 325
- organic molecular-beam epitaxy, 71
- oriented gas, 10, 91, 126
- oscillator strength, 129, 134, 138, 143
- Overhauser effect, 212
- Overhauser shift, 342
- p-TS6, 47
- packing coefficient, 35
- pair spectroscopy, 163

- pantacene, 2
- paraffins, 41
- parity, 130
- Pauli paramagnet, 325
- Pauli paramagnetism, 337
- Pauli principle, 29, 226
- Pauli susceptibility, 328, 347
- PEDOT, 16, 373
 - PSS, 384
- Peierls instability, 12
- Peierls phase-transition temperature, 330
- Peierls temperature, 320
- Peierls transition, 314, 315, 318, 319, 330, 331, 397
 - theory of, 320
- pentacene, 36, 255
 - transistor, 405
- Perovskite structure, 51
- perylene, 2, 35, 38, 110, 144, 155, 217, 264, 265, 267, 322
- phenantrene, 42
- phonon dispersion relations, 96, 97, 100, 101, 106–109
- phonon energy, 30
- phonon scattering, 318
- phonons, 11, 89, 93, 94, 103, 263, 319
- phosphorescence, 128, 129, 138
- phosphorescence spectrum, 131
- photoacoustic spectroscopy, 125
- photochemical or photophysical hole-burning, 406
- photochromic switching process, 394
- photochromism, 393
 - single crystals, 395
- photoconduction
 - excitation spectrum, 279
- photoconductivity, 220, 222, 234, 265
- photoelectrets, 15
- photoelectron spectroscopy, 229
- photoexcitation, 217
- photogeneration, 234
- photogeneration of charge carriers, 238
- photon flux density in a solar cell, 387
- photorefractive organic materials, 408
- photosynthesis, 126, 171
- photovoltaic cell, 366, 381
- photovoltaic characteristics, 384
- photovoltaic effect, 365
- phthalocyanines, 381
- pinning frequency, 345
- pixels, OLED, 367
- plasma edge, 335
- plasma frequency, 336
- plastic chips, 404
- plate sublimation, 63
- PMDA, 151
- point defects, 78
- Poisson equation, 247, 258
- polar organic solids, 11
- polar substituents, 39
- polarisability, 26, 36, 230
- polarisation energy, 229
- polarisation of optical transitions, 136, 143
- polarons, 228, 229, 235
- poly-diacetylene crystals, 43, 68
- poly-(N-vinyl-carbazole), 287
- poly-para-phenylene-vinylene, 373
- polyacene crystals, 109, 231
- polyacenes, 263
- polymer films, 366
- polymer single crystals, 8, 43, 68
- polymerisation, 69
- polymers, OLED, 367
- polymers as thin films, 280
- polystyrol-sulfonate, 373
- polythiophene/C₆₀, 381
- Poole-Frenkel effect, 285, 287
- porphyrin, 381, 407
- porphyrin molecule, 42
- potentials
 - intermolecular, 30
- PPV, 370, 373, 381
- PPV polymer films, 293
- pressure
 - external, 326, 327
 - internal, 326, 327
- pressure dependence of T_c for superconductivity, 356, 357
- pseudo energy gap, 321
- PSS, 16, 373
- purification, 57
- PVK, 287
- pyrazole, 2
- pyrene, 2, 38, 42, 77, 155
- pyridine, 2
- pyrrole, 2
- quadrupole correction, 230
- quadrupole moments, 28
- quantum yield, 239
 - OLED, 372
- quantum yield of photogeneration of charge carriers, 242
- quasi-metallic state, 330, 331
- quinacridone, 373
- quinoline, 207
- quinoxaline, 2, 209, 211

- radiation characteristics, 379
- radiationless transitions, 128
- radical anions, 370
- radical cations, 253, 370
- radical-anion salts of DCNQI, 323
- radical-cation salts of the arenes, 330
- radical-ion, 42
- radical-ion crystals, 2, 3, 7
- radical-ion salts, 7, 11, 12, 33–35, 42, 43, 54, 67, 78, 153, 308, 314, 322
- radicals
 - Alq3, 374
- Raman scattering, 90, 99
- Raman spectrum, 102
- Rb₂CsC₆₀, 352, 362
- Rb₃C₆₀, 352
- reciprocal lattice, 95
- recombination, 240
 - OLED, 369
- recrystallisation, 58
- rectifier molecule, 400
- rectifiers, 392
- reentry behaviour, 329, 396
- reflection spectrum, 125, 153, 335
- relaxation of the excess charge carriers, 283
- relaxation time, 225, 227, 229, 276
- reorientation, 115, 118
- reproducibility, 303
- repulsive forces, 29
- resonance interaction, 132, 136, 143–145
- reversed Peierls transition, 346
- Richardson constant, 251
- Richardson equation, 251
- rotational vibrations, 93
- rubrene, 373
 - transistor, 405
- S-DPVBi, 373
- S-NPB, 373
- S-TAD, 373
- salts, 33
- SAM, 71
- scattering diagram, 99
- scattering of charge carriers, 227, 269
- scattering of charge carriers from charged defects, 264
- scattering of charge carriers from phonons, 264, 269
- scattering time, 228, 263
- Schottky barrier, 252
- Schottky contacts, 250
- Schottky defects, 78
- Schottky effect, 250
- scintillator crystals, 15
- SCLC, 246
- SCLC model, 258
- selection rules for intersystem crossing, 208
- self assembly, 49, 71
- self diffusion, 79, 113, 120
- self organisation, 49
- self trapping, 152, 156
- self-assembled monolayers, 52
- semiconductors, 42, 217
- semitransparent electrode, 365
- sensitised delayed fluorescence, 161
- sensitised fluorescence, 62, 157, 159, 160, 162, 170
- shallow traps, 228, 231, 258, 261
- shallow-trap distribution, 259
- short-circuit photocurrent, 384
- Shubnikov phase, 359
- Shubnikov-de Haas effect, 358
- silicon wafer, 368
- simulation of TOF transients, 285
- single-layer OLED, 370
- singlet excitons, 241
 - OLED, 370
- singlet states, 128
- singlet-singlet annihilation, 167
- singlet-triplet annihilation, 167
- SiO₂, 402
- solar cells, 366, 381
- solid-state polymerisation, 45
- solubility of dopant molecules, 254
- solvent shift, 132, 136
- sound velocity, 103, 104
- source, 401
- space charge, 228, 234, 246, 255
- space-charge-limited current, 222, 246, 255, 303
- space-charge-limited current with energy-distributed trapping states, 300
- space-charge-limited current without shallow traps / with filled traps, 300
- space-charge-limited currents in disordered films, 297
- space-charge-limited stationary currents, 255
 - in rubrene crystals, 255
 - in tetracene crystals, 257, 262
- spectral sensitivity, 386
- spectroscopic techniques, 62, 84
- spin eigenfunctions, 181
- spin exchange, 198
- spin Hamiltonian, 189, 194
- spin quantisation in triplet states, 181

- spin resonance of the conduction electrons, 339
- spin-density wave, 356
- spin-lattice relaxation, 113, 205, 211
- spin-lattice relaxation of protons, 202
- spin-lattice relaxation time, 115, 117, 118
- spin-orbit coupling, 129, 148, 183, 208, 209, 212
- spinning of films, 280
- spiral dislocations, 80
- SQUID, 359
- stacking axis, 310
- stacks, 42
 - separate, 310
- stationary dark currents in disordered films, 292
- step dislocation, 80
- stimulated emission of microwaves, 205, 211
- storage density, 408
- storage elements, 392
- structural data, 31
- structural defects, 75, 78, 231, 232
- structure of an OLED, 368
- structures, 34
- sublimation, 58
- sublimation crystals, 81
- sublimation energy, 31, 32
- sublimation enthalpy, 79
- substituents
 - polar, 39
- superconductivity, 362
 - critical temperature, 351
 - donor-acceptor compounds, 352
 - electrical resistance, 351
 - energy gap, 351, 352
 - Fullerides, C₆₀, 352
 - magnetic susceptibility, 351
 - one-dimensional, 353
 - radical-ion salts, 352
 - three-dimensional, 361
 - two-dimensional, 356
- superconductors, 351
- superlattice, 319
- superlattice reflections, 334
- supramolecular, 314
- surface excitons, 153, 154, 173
- surfaces, 12
- switches
 - molecular, 391
 - organic metals, 398
- switching speed of a transistor, 403
- switching times, 367
- tautomerism, 406
- TCLC, 298
- TCNQ, 42, 307, 311, 322
- technical applications, 16
- temperature dependence, 313, 314, 330, 331, 334, 354
- temperature dependence of the characteristic, 295
- temperature dependence of the energy gap, 339
- temperature dependence of the hole mobility, 285
- temperature dependence of the magnetic susceptibility, 337
- temperature dependence of the mean free path, 334
- temperature dependence of the mobility, 217, 264, 265, 284, 334
- temperature dependence of the real energy gap, 321
- tempering, 51
- tensile strength, 45
- tetracene, 2, 36, 126, 157, 168, 265
 - transistor, 405
- tetrachloro-benzene, 187
- tetracyano-quinodimethane, 307
- tetramethyl-tetraselena-fulvalene, 353
- tetraphenyl-porphyrin, 41
- tetrathio-fulvalene, 307
- thermally-stimulated discharge current, 277
- thermionic emission, 251, 252
- thermionic field emission, 252
- thiol end groups, 49
- thionaphthene, 76
- thiophene, 2
 - transistor, 405
- threshold field strength, 344
- time-of-flight method(TOF), 234
 - experiments on disordered films, 281
 - method, 234
 - transients, 287
 - transients in anthracene crystals, 237
 - transients in perylene crystals, 237
- TMTSF, 353
- topochemical reactions, 43
- topology of Fermi surfaces, 358
- TPTA, 289
- transfer integrals, 272
- transistor characteristics, 402
- transistors, 16, 265, 392, 401
- transit time, 235
- transition temperature, 352

- translational vibrations, 89, 93
- transmission electron microscopy, 72
- transmission losses, 372
- transparent cathodes, 368
- transport equation, 258
- transport layers
 - OLED, 373
- transport level, 229
- transport of charge carriers
 - OLED, 369
- transport properties, 334
- trap depth, 233, 262
- trap-charge-limited currents, 298
- Trap-Filled-Limit (TFL), 261
- trapping states, 258
- traps, 163, 258
- triplet emitter Ir(ppy)₃, 376
- triplet emitters
 - OLED, 370
- triplet ESR spectrum, 179
- triplet exciton fusion, 168
- triplet excitons, 143, 144, 160, 177, 187, 188, 199, 214
 - OLED, 372
- triplet mini-excitons, 177, 180
- triplet states, 128, 177
- triplet-exciton ESR, 199
- triplet-triplet annihilation, 163, 165
- triplet-triplet annihilation – magnetic-field dependence, 165
- triplet-triplet annihilation processes, 164
- TTF, 42, 307
- TTF-TCNQ, 42, 310, 313, 314, 321, 322
- TTF⁺-TCNQ⁻, 34, 308
- tunnel effect, 252
- tunnel resistance, 360
- tunnel spectroscopy, 351
- tunneling process, 395
- twinning, 39
- two-electron spin functions, 182
- two-layer systems, photovoltaic cells, 381
- two-photon spectroscopy, 130
- type I superconductors, 359
- type II superconductors, 359, 362
- ultrafast charge transfer, 382
- ultrapure crystals, 263, 265
- unimolecular rectifier, 400
- unit cell, 35
- urea, 41
- vacancies, 78
- valence band, 226, 263
- van der Waals attraction, 30
- van der Waals bonding, 9–11, 25, 104
- van der Waals forces, 27
- van der Waals interaction, 4, 109, 120
- variability, 13
- velocity of sound, 270
- vibronic relaxation, 231
- Wannier excitons, 14, 51, 149, 150
- weak CT complexes, 323
- wires
 - molecular, 391
- work function, 247, 250, 370
- X traps, 75–78, 186
- X-ray scattering, 334
- X-ray topography, 85, 86
- xerography, 221
- Y traps, 77
- Zeeman energies, 189
- Zeeman splitting, 178, 189
- zero-field components, 178
- zero-field resonance, 178, 186
- zero-field splitting, 178
- zero-field transitions, 186
- zero-phonon line, 152
- ZnSe, 375
- zone refining, 58, 59